Transactions of the ASME®

Technical Editor
H. L. JULIEN (1998)

Associate Technical Editors
Advanced Energy Systems
M. J. MORAN (1999)
Gas Turbine
D. COOKE (1999)
H. NELSON (1999)
J. PETERS (1999)
J. N. SHINN (1996)
Internal Combustion Engines
D. ASSANIS (1999)
Power
D. LOU (1998)

BOARD ON COMMUNICATIONS
Chairman and Vice President
R. MATES

OFFICERS OF THE ASME
President, **KEITH B. THAYER**
Executive Director, **D. L. BELDEN**
Treasurer, **J. A. MASON**

PUBLISHING STAFF
Managing Director, Engineering
CHARLES W. BEARDSLEY
Director, Technical Publishing
PHILIP DI VIETRO
Managing Editor, Technical Publishing
CYNTHIA B. CLARK
Managing Editor, Transactions
CORNELIA MONAHAN
Production Coordinator
VALERIE WINTERS
Production Assistant
MARISOL ANDINO

Transactions of the ASME, Journal of Engineering for Gas Turbines and Power (ISSN 0742-4795) is published quarterly (Jan., April, July, Oct.) for $195.00 per year by The American Society of Mechanical Engineers, 345 East 47th Street, New York, NY 10017. Periodicals postage paid at New York, NY and additional mailing offices. POSTMASTER: Send address changes to Transactions of the ASME, Journal of Engineering for Gas Turbines and Power, c/o THE AMERICAN SOCIETY OF MECHANICAL ENGINEERS, 22 Law Drive, Box 2300, Fairfield, NJ 07007-2300.
CHANGES OF ADDRESS must be received at Society headquarters seven weeks before they are to be effective. Please send old label and new address.
PRICES: To members, $40.00, annually: to nonmembers, $195.00. Add $30.00 for postage to countries outside the United States and Canada.
STATEMENT from By-Laws. The Society shall not be responsible for statements or opinions advanced in papers or . . . printed in its publications (B7.1, par. 3).

INDEXED by Applied Mechanics Reviews and Engineering Information, Inc. Canadian Goods & Services Tax Registration #126148048

Journal of Engineering for Gas Turbines and Power

Published Quarterly by The American Society of Mechanical Engineers

VOLUME 119 • NUMBER 4 • OCTOBER 1997

TECHNICAL PAPERS

(Contents continued on p. 986)

(Contents continued)

Journal of Engineering for Gas Turbines and Power

Biography

Dr. A. V. (Sheenu) Srinivasan

The recipient of the 1997 International Gas Turbine Institute Scholar Award, Dr. Amrutur V. "Sheenu" Srinivasan, is president of Strategic Technologies International, Inc., a research and development consulting firm. He also serves as Distinguished Visiting Professor of Mechanical Engineering at Worcester Polytechnic Institute, Worcester, Massachusetts. Dr. Srinivasan, who lives in Glastonbury, Connecticut, has blended teaching, scholarship, and technical expertise in the course of a career spanning nearly 30 years.

Dr. Srinivasan has taught at the University of Iowa, the University of Florida, Yale University, the Hartford Graduate Center, and the University of Connecticut. His industrial experience has been mainly in aerospace research at Kaman Aerospace Corporation, Pratt & Whitney Aircraft, and United Technologies Research Center. He is the author of numerous technical publications in the areas of vibrations, aeroelasticity and damping and, more recently, smart structures. In 1989, he was awarded a U.S. patent in the area of vibration control through shape memory alloys. He was elected a Fellow of the ASME in 1985.

The International Gas Turbine Institute Scholar Award is bestowed upon an individual who submits a learned and comprehensive paper making a significant and timely contribution to the science and practice of gas turbine engineering.

The 1997 IGTI Scholar Paper

Flutter and Resonant Vibration Characteristics of Engine Blades

A. V. Srinivasan
Worcester Polytechnic Institute,
Worcester, MA 01609
Fellow ASME

This paper presents an in-depth study of blade vibration problems that seriously impact development of advanced gas turbine configurations. The motivation for this study arises from the author's conviction that structural integrity of power plants is the dominant factor that influences the quality, reliability, and marketability of the product. Implications of this study in the context of potential R&D challenges and opportunities of interest to industry, governments, and academia are discussed.

Introduction

"I am going to make a gas turbine before I quit and it is going to have higher efficiency than the reciprocating gas engine, and it is going to run without vibration . . ." (Glenn Warren, 1914).

"On axial compressor blade vibration we have gone very cautiously and I believe have not met the problem in all its bleakness; the dark days are still ahead" (Hayne Constant, 1947).

"Suppression of vibratory fatigue is the design challenge" (Clarence Danforth, 1967).

"Failure of fan blades on the B-1's General Electric engines is the suspected cause in both incidents . . ." (*Los Angeles Times,* 1991).

". . . [T]he engine failures are a continuation of fourth stage turbine blade cracking problems that first surfaced in the Pratt and Whitney F100-229 powerplant . . ." (*Aviation Week & Space Technology,* 1994).

"Engine high cycle fatigue is the Air Force's #1 readiness issue" (John Deutch, 1995).

Glen Warren's dream and Hayne Constant's fears notwithstanding, it is fair to say that engine blades, whose designs have evolved through sophisticated aeromechanical efforts, continue to vibrate and fail industry-wide and thus the design challenge continues. One of the objectives of this paper is to present a perspective from which the complex problem of blade failures can be viewed in order to assess the state of the art and to outline issues that deserve to be addressed in future R&D efforts.

The successful operation of a power plant depends largely upon the structural integrity of its rotating parts. The structural integrity in turn depends upon the ability of the machine to withstand steady and vibratory stresses. In the case of jet engines, vibration-induced fatigue failure of rotor blades is a problem of major concern to the designer. Engine certification requirements demand that measured stress levels meet design specifications. The critical nature of the problem becomes apparent when one notes that there can be as many as a thousand blades of different dynamic characteristics in one engine of advanced design. It is this large number and variety of blades that continues to engage researchers and designers in attempting redesigns to mitigate vibration failures.

Vibratory failures occasionally occur in engine blades during final test phases, even though analytical predictions and rig testing may not have indicated a problem. Such was the case with the F-100 program in which first-stage fan blade failures occurred during qualification tests. Even worse is the occurrence of failure of blades after an engine has successfully passed qualification tests and production has begun, as in the case of the J85-21. Undoubtedly, the worst types of failures are those that occur in flight. One such example is the Cathay Pacific flight from Los Angeles during which a wide chord blade on an RB 211-524 G/H experienced a "primary failure" at 21,000 feet, the first of its kind for a component whose design had served well over 12 million engine hours.

These experiences are by no means limited to aircraft engines. More recent industry-wide incidents of failure of turbine blades of land-based gas turbines have raised a new awareness in regard to structural integrity in that segment of gas turbine business. The reported events pertain to loss of blades in the last stages of the machinery due to resonance as well as flutter. The consequences are no less severe. For example, engine development problems that cause delays in commissioning a medium-sized 500 MW power plant can lead to a loss of revenue of "as much as $2.5 million per week!" (*Financial Times,* Sept. 2, 1996).

Such experiences impose technical challenges on engineers who provide the basic design tools. This in turn should alert those in the forefront of research and development to be certain that no stone is left unturned in the quest for understanding the physical aspects of engine technology, to provide a scientifically based design procedure calibrated through a wide variety of test programs.

Such incidents suggest a lack of adequate design tools but they also point to another fact: In the quest for improved efficiency and higher thrust-to-weight ratio, higher stage loading, higher pressures, reduced axial gaps, we are pushing at the boundaries through increased speeds (over 460 m/s fan tip speed) and temperature (upward of 1930°C), radically new blade profiles, lower aspect ratios, etc. Such changes have meant considerations of three-dimensional stress analyses, plate and shell type modes of vibration, and introduction of new damping concepts. Not all these new ideas and tools have fully matured and therefore the challenge to structural dynamicists continues. Thus a clear understanding of the dynamic characteristics of bladed disk assemblies and identification of the governing aeromechanical parameters, as well as their influence on the aeroelastic characteristics, becomes critical in the design phase.

The most common types of vibration problems that concern the designer of jet engines include (*a*) resonant vibration occurring at an integral order, i.e., multiple of rotation speed, and (*b*) flutter, an aeroelastic instability occurring generally as a nonintegral order vibration, having the potential to escalate, unless checked by any means available to the operator, into larger and larger stresses resulting in serious damage to the

Contributed by the International Gas Turbine Institute and presented at the 42nd International Gas Turbine and Aeroengine Congress and Exhibition, Orlando, Florida, June 2–5, 1997. Manuscript received at ASME Headquarters February 1997. Paper No. 97-GT-533. Associate Technical Editor: H. A. Kidd.

machine. The associated failures of engine blades are referred to as high cycle fatigue failures.

More often than not, the particular speeds at which certain resonant conditions may lead to high cycle fatigue failure of blades will become evident only in component or engine testing. Measured resonances are characterized by frequencies that are exact multiples of engine orders (integral order vibration), so that on the Campbell diagram they track the engine order line. Another important feature of resonant stresses is that their amplitudes rise rapidly during acceleration toward a resonant speed, reach a peak at the resonant speed, and rapidly fall off after passing through the speed.

A rational procedure to calculate flutter and resonant characteristics of blades requires advances in:

1 assessment of flow defects at the location they originate and as they are transported along,
2 unsteady aerodynamics of cascades under a wide variety of flow conditions expected in the operating range,
3 structural vibration frequencies and modes of interest over the operating range,
4 quantification of damping in the system due to nonaerodynamic sources,
5 estimate of material properties (fatigue strength, ultimate strength, modulus of elasticity, etc.) for the configuration at the temperatures expected in the operating range, including the influence of processing, defects, etc., leading to the calculation of structural integrity, and
6 identification of dissimilarities in aerodynamic parameters (gap/chord, stagger, incidence, etc.) and structural parameters (frequencies, mode shapes and damping, etc.) and accounting for their influence in a statistical sense.

Each of these items is, in a sense, a discipline in its own right and advances can occur only through systematic and thorough analytical developments (in each of the areas) calibrated through laboratory, rig and engine testing. There appear to be no short cuts.

The unsteady aerodynamics needed are of two types: The first type leads to calculations of aerodynamic damping and the second type predicts pressures that act on blades (assumed to be not vibrating) due to flow variations in the stream. The flow variations are sensed periodically by the rotor blades during each revolution and lead to forcing functions. The nature and extent of aerodynamic damping, superposed on the corresponding contributions from nonaerodynamic damping, determine the stress levels expected in resonant vibration and establish susceptibility to flutter. Clearly, calculations of the aerodynamic forces depend upon the profile of blades, cascade solidity, stagger angle, incidence, and the conditions of flow (i.e., subsonic, transonic, or supersonic), etc. The computational aspects are quite complex even for simple configurations such as, for example, a flat plate cascade at zero incidence in a subsonic flow. Additional complexities arise when one considers actual blade profiles and recognizes flow conditions in which shock and separation can occur within a passage.

The structural dynamic characteristics of a bladed-disk assembly include not only the natural frequencies of vibration of the assembly at various speeds within the operating range but also the mode shapes and damping. These characteristics serve as input to calculations of either resonant vibration or flutter. Therefore, the prediction of forced vibration levels or instability will depend upon both the accuracy in calculation of the aerodynamic forces discussed above and the structural characteristics.

Vibrations of engine blades occur in an aerodynamic environment and therefore it is only appropriate that significant advances in the aerodynamic and structural dynamic characteristics be realized. The subject matter is an interdisciplinary one requiring expertise in aerodynamics of cascades as well as structural dynamics of bladed-disk assemblies leading to aeroelasticity of blades. It is clear that no significant progress can be made in this important field without close interaction among experts and a mutual understanding of the contributing disciplines, along with increased emphasis on conceptualization, theorizing, and testing out ideas in the laboratory, on rigs and finally on engines.

Under the auspices of the American Society of Mechanical Engineers, four volumes covering bladed-disk assembly vibration have been published (Srinivasan, 1976; Ewins and Srinivasan, 1983; Kielb and Rieger, 1985; Kielb et al., 1987) and the papers appearing in these volumes serve as good background on the subject. In addition, two AGARD volumes on the subject of aeroelasticity of axial-flow turbomachines edited by Platzer and Carta (1987, 1988) will serve as an important source of reference for the variety of blade vibration problems discussed in this paper.

In the following, fundamental aspects of this subject will be presented in order to raise awareness in engineers interested in this technology area, to provide a stimulus to researchers and a guideline to funding agencies.

In-context definitions of certain terminologies commonly used in this field of study and practice are included in the appendix for the convenience of those who are interested in the field of blade dynamics but are not familiar with it.

Vibrations of Individual Blades

Typical rotors from the front end to the back end, as illustrated in Fig. 1, display varying sizes, aspect ratios, and hub–tip ratios of blades. In a typical bladed-disk assembly, as shown in Fig. 2, a number of these blades (about 30 or so in fans and over 100 in turbines) are mounted on a support structure, such as a hub or a disk, to assemble a rotor. But we begin with an examination of dynamic characteristics of individual blades. An understanding of the dynamic characteristics of individual blades is necessary in order to be able to interpret the dynamics of the assembly. Deceptively simple, the modal characteristics of individual blades can sometimes be difficult to calculate or measure because of the geometry of blades: the relatively thick and complex shape of the root structures; the extremely thin trailing edges; the varying heights of blades at leading and trailing edges; blade twist and tilt, etc. See, for example, the tip profile of the blade shown in Fig. 2. All these aspects present challenges to modeling, even if the blade is solid. Measurement presents its own challenges, as will be evident later. Clearly, additional difficulties arise if blades are hollow and/or contain complex cooling passages.

Initially the geometry of blades is largely dictated by aerodynamic performance requirements. The final design, however, has to meet both structural and aerodynamic needs. Blade twist structurally couples chordwise motion with motion perpendicular to the chord, the so-called flap motion. The geometry of engine blades is such that, in general, the blades do not experience pure bending or pure torsional motions. Instead, torsional and bending oscillations become coupled in each mode of vibration with varying amounts of contributions from each type of deformation. With every additional aerodynamic insight, blade profiles may change, sometimes drastically, and introduce new challenges to structural modeling. Unusual geometries show unusual structural characteristics and thus the need continues for continually upgrading analytical procedures to calculate vibration characteristics of blades. Beam-like blades may be replaced by plate or shell-like profiles, shrouded blades may be replaced by shroudless blades with wide chord or with large sweep; all such changes introduce different modal content in the vibration modes.

A Case History. In one design problem pertaining to blading of large turbochargers, a method for minimizing blade vibration amplitude was attempted with a lacing wire threaded through a hole in the blades. The principle was that, at a care-

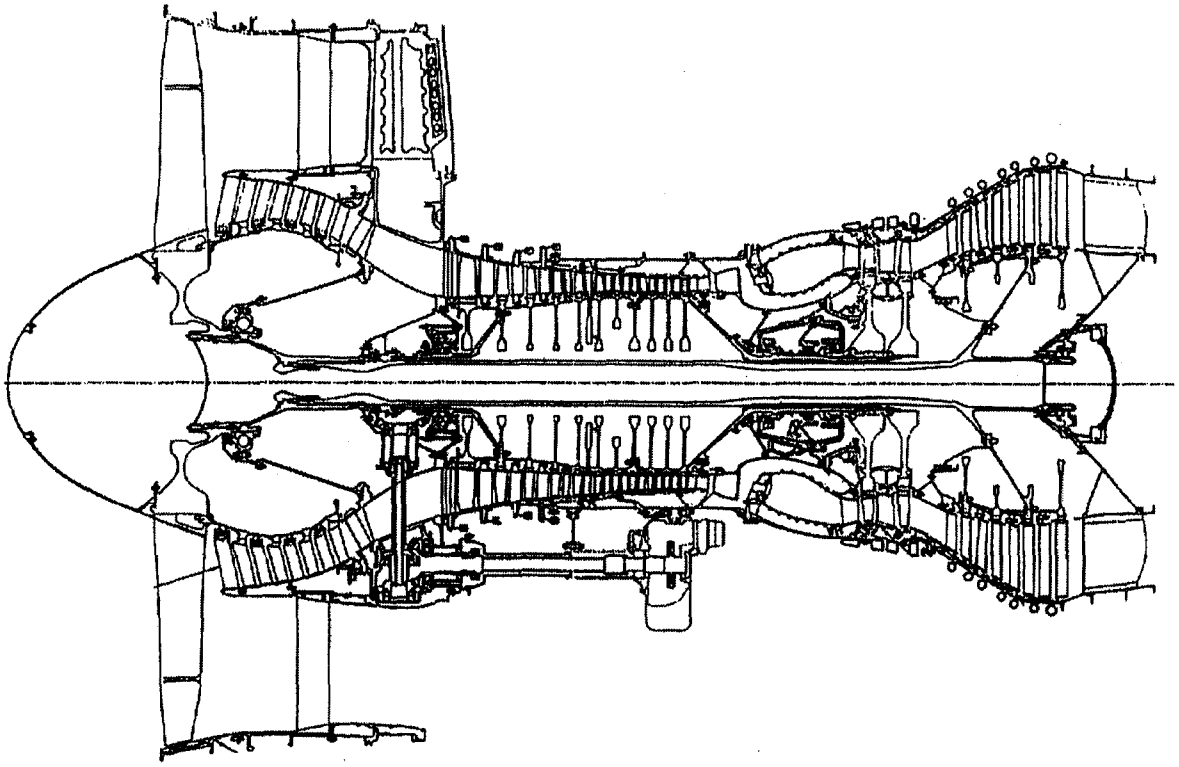

Fig. 1 An aircraft engine configuration

fully selected antinode, sufficient vibratory motion would allow rubbing between the wire and blade to provide damping. The location of such a hole to pass the wire through the blades was to be determined by analysis to "ensure safe stress levels when full load conditions are caused by centrifugal forces . . . without weakening the blade by introducing high stress concentrations in highly stressed areas" (Chapman and Wang, 1987). Thus, the design goal was to maximize damping through the use of lacing wires and the design problem was the location of the hole. Several individual blades were tested using (1) modal analysis with (*a*) impulse, (*b*) white noise, and (*c*) sinusoidal excitations applied at the leading edge and later at the trailing edge, and (2) using (*c*) with an optical measurement system based on Electronic Speckle Pattern Interferometry (ESPI). Thus, a total of six separate test methods were employed to measure natural frequencies and, more important, mode shapes.

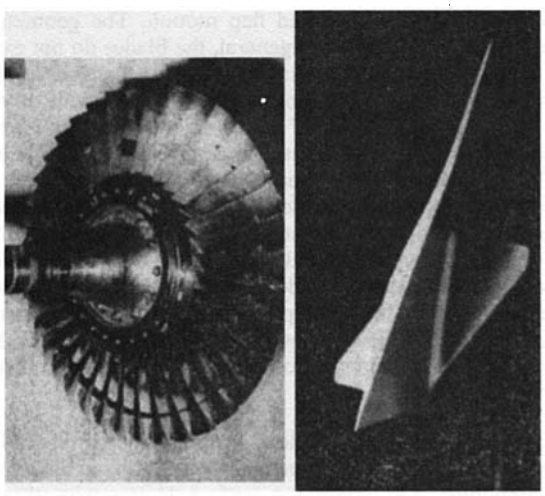

Fig. 2 NASA 1800 ft/sec rotor and its tip profile

Each test program produced modes that varied from slightly different to completely new sets leading to an anomaly between test results.

The test data could not be used to interpret and classify the modes in the conventional manner (flap, edge, torsional, and stripe) and no decision could be made in regard to the location of the hole. Therefore, it was decided to resort to finite element analysis with an eventual model comprising "90 elements with 20 nodes per element . . . with 2115 possible degrees of freedom reduced to 60 master degrees of freedom." The blade was assumed fully fixed at its root. The calculations did not reveal the number of modes found in tests and an edge mode suggested by the analysis was not among those measured (see Fig. 3).

In general, finite element approaches are reliable and are used in design analysis of blades along with optimization techniques. The latter provide "a significant acceleration of the whole design process . . ." (Frischbier et al., 1996). In exceptional situations, as noted in the case discussed above as well as by Frischbier et al., a simultaneous investigation involving both analysis and testing becomes mandatory in order to influence the design process and enhance understanding of vibratory characteristics.

It is important to note here that the differences among tests, as well as between test and finite element method (FEM) results, were not minor and could not be attributed to usual reasons such as method of excitation, mass of accelerometer, and choice of blade height in the analysis, or the assumed boundary condition for the root. The piezoelectric crystal used to excite the blades did distort higher frequency modes. Further, the results from modal analysis lacked modal content from any motion perpendicular to their sensitive direction, as would occur in an edgewise motion. Similarly, ESPI results "would suggest out of plane motion (i.e., blade flap motion) for an inclined plane moving in-plane (i.e., edge mode)." Thus, the precise selection of an antinode could not be made.

The eventual resolution of modal identification and interpretation became possible through additional tests conducted on

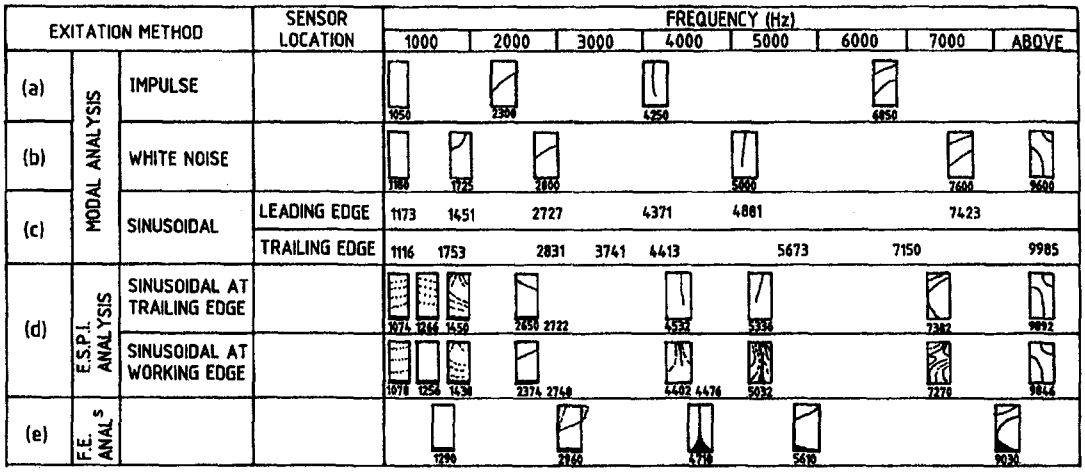

Fig. 3 Case history test data and analyses (Chapman and Wang, 1987)

seven "blades" (plates, each of which was machined to enhance one parameter such as taper, camber, twist, etc.) A careful cataloging of the test results and corresponding finite element analyses of all the plates suggested how certain closely spaced modes could combine to produce spurious modes (i.e., modes that appear as natural modes but which are in fact combinations of closely spaced modes). The reader is encouraged to refer to the cited paper for additional details. It is interesting to note that a similar project was undertaken, although for different reasons (lack of agreement among various FEM packages), by engineers at NASA and the Air Force Aeropropulsion Laboratories by "precision machining a set of twisted plates and testing them in two laboratories" (Kielb et al., 1985).

This discussion sets the stage to alert analysts and experimentalists alike about how important it is to pay meticulous attention to detail, and not take what is measured or calculated for granted, unless a thorough and critical evaluation is made every time. If problems such as those highlighted in this case could occur in what appeared to be a routine investigation of a single blade, we can only imagine what lies ahead in this study when it examines analyses and test data for bladed-disk assemblies in an aerodynamic environment obtained in laboratories, rigs, or engines! On a positive note, it is essential to recognize that the problems that arose in the case described above were indeed solved through persistence and proper engineering analysis and judgment.

Analytical Approaches. While finite element methods will continue to serve as numerical tools to model real blades and bladed-disk assemblies, it is essential to underscore the need to study and develop analytical approaches for several reasons. An appreciation of formulating complex problems using basic principles of applied mechanics is a necessary background to verify and interpret results from essentially numerical approaches. Advances in analytical formulations can stimulate and provide a basis for new and better numerical approaches. Viewing a blade vibration problem in the context of elasticity, plate and shell theories, nonlinear dynamics, and fracture mechanics offers an opportunity to develop a firm foundation in basic principles in a university environment and help address problems concerning realistic blade profiles.

One such formulation was introduced by Petricone and Sisto (1971) to model a low-aspect-ratio helicoidal plate (Fig. 4) using the Raleigh–Ritz procedure based on the principle of potential energy. The latter states that "Of all displacements satisfying given boundary conditions, those which satisfy the equilibrium conditions make the potential energy V assume a stationary value. For stable equilibrium, V is a minimum." A brief discussion of the approach with some results is given below.

With

$$\bar{r} = (r\cos\theta)\bar{i} + (r\sin\theta)\bar{j} + c\theta\bar{k}$$

$$V_\epsilon = C\iint \{(\epsilon_1 + \epsilon_2)^2 - 2(1-\upsilon)(\epsilon_1\epsilon_2 - \tfrac{1}{4}\epsilon_{12}^2)\}\,dA$$

$$V_\kappa = D\iint \{(\kappa_1 + \kappa_2)^2 - 2(1-\upsilon)(\kappa_1\kappa_2 - \tfrac{1}{4}\kappa_{12}^2)\}\,dA$$

$$V_a = -\tfrac{1}{2}\rho t\omega^2 \iint (u^2 + v^2 + w^2)\,dA$$

where the ϵs represent normal and shear strains, κs represent curvatures, u, v, and w represent displacements, $C = Et/2(1-\upsilon^2)$, and $D = Et3/24(1-\upsilon^2)$.

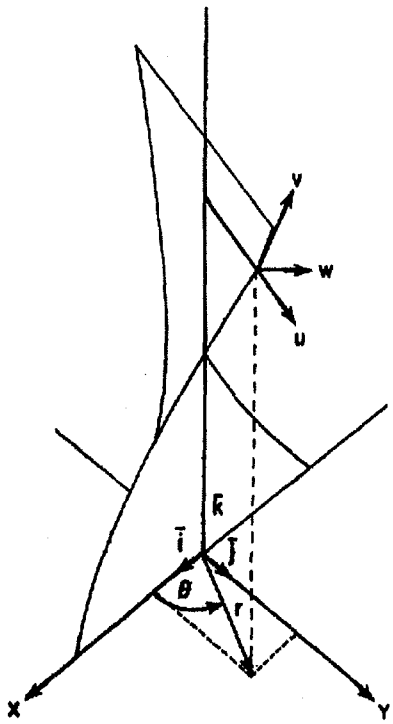

Fig. 4 A helicoidal "blade"

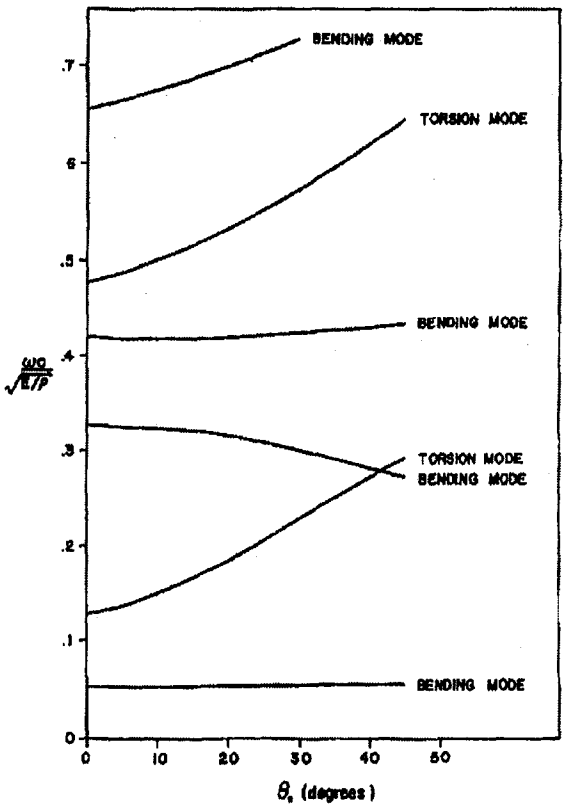

Fig. 5 Influence of twist on natural frequencies (Petricone and Sisto, 1971)

$$V_t = V_\epsilon + V_\kappa + V_a,$$

$$\epsilon_1 = \partial u/\partial r, \quad \epsilon_2 = 1/\alpha(\partial v/\partial\theta) + r/\alpha^2(u),$$

$$\epsilon_{12} = \partial v/\partial r - r/(\alpha^2)v + (1/\alpha)\partial v/\partial\theta + (2C/\alpha^2)w$$

with similar expressions for the curvatures in terms of u, v and w and their derivatives. The variables $u(r, \theta)$, $v(r, \theta)$ and $w(r, \theta)$ are represented as summation of products of functions of r only and functions of θ only. For example, $u(r, \theta) = \Sigma\Sigma\ a_{ij}R(r)\Theta(\theta)$, with similar expressions for v and w. The constants a, and corresponding constants b and c, are the unknowns. The functions within the summation sign are assumed to be Legendre polynomials. Clearly, substituting the assumed functions into the energy expressions and invoking Raleigh–Ritz, the derivatives $\partial V_t/\partial a_k$, etc., are computed and equated to zero. The resulting simultaneous algebraic equations are solved for the unknowns a, b, and c.

Only the highlights of results are described below and the reader is referred to the cited paper for details. First of all, the analysis is used to study the influence of twist on the natural frequencies of a helicoid. As shown in Fig. 5, the first and the third bending modes are not sensitive to changes in blade twist, the frequency of the second bending mode decreases and the fourth bending mode is characterized by in-plane vibration, with chordwise bending, whose frequency increases sharply with twist. Variation of these frequencies, with respect to aspect ratio and twist, is presented in Fig. 6. The lower two surfaces represent the first two predominantly longitudinal bending modes, whereas the top two surfaces represent combined bending (chordwise and in-plane motions, respectively). At aspect ratios beyond about 1.4 and at zero twist angle, a role reversal takes place between the top two surfaces, i.e., stripe modes jump up to the upper surface and membrane modes jump down to the lower surface, as can be seen more clearly in Fig. 7. Some additional observations may be made. Note that the ratio second

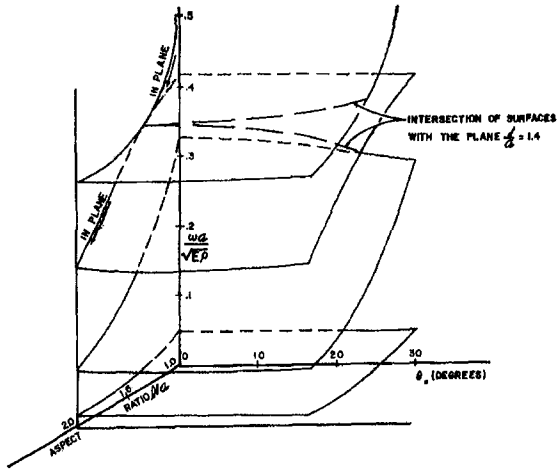

Fig. 6 A frequency "surface" (Petricone and Sisto, 1971)

bending frequency/first bending frequency is always near 6. Further, the coalescence between frequencies for the 1T (first torsion) and 2B (second bending) modes evident in Fig. 7 occurs for higher aspect ratios especially for flat plate-like configurations.

Efforts to model large-size rotors typical of stationary gas turbines have led to a "consistent second-order moderately thick plate theory for the disc" and includes, for the blade model "shear deformation, rotary inertia effects, blade twist, centrifugal effects, warping function of bending and torsion" (Irretier and Rzadkowski, 1994).

While assessment of the value of analytical approaches is left to the judgment of individuals, it is argued that analytical formulations provide valuable insights to the trained eye and may be exploited in the design process.

Vibration of Disks

Compared to blades, disks are simple circularly symmetric structural components with a purely structural function, i.e., to support the blades and transfer torque between blades and the

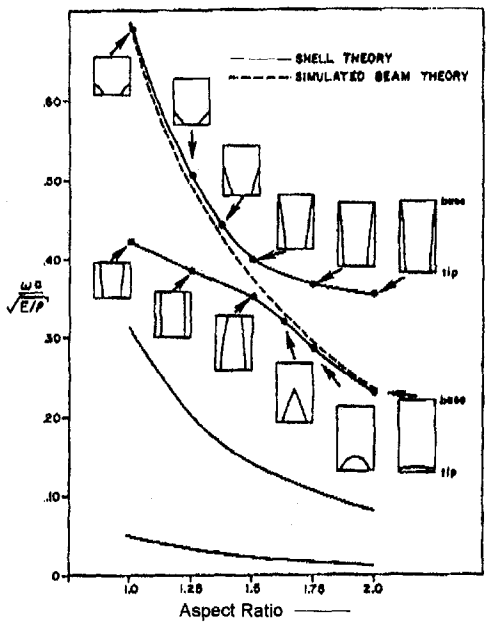

Fig. 7 Influence of aspect ratio on natural frequencies (Petricone and Sisto, 1971)

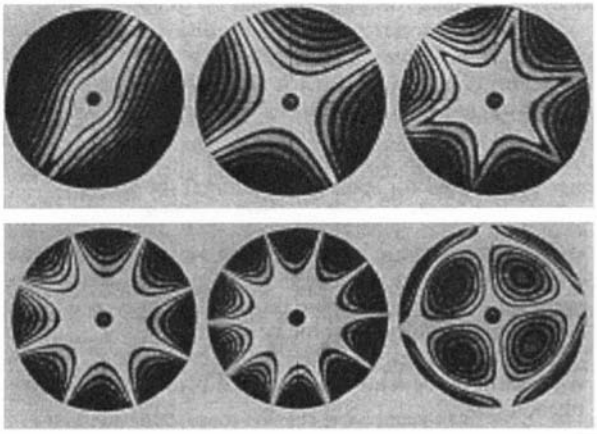

Fig. 8 Disk modes (MacBain et al., 1979)

shaft throughout the speed regime. As a component of a bladed-disk assembly, a typical disk may participate in the vibratory motion of the assembly depending upon the flexibility of the disk. Being circular, disks experience vibratory modes, which have nodal diameter and nodal circle patterns as shown in Fig. 8 (MacBain et al., 1979). These modes may be fixed relative to the disk or may travel in the same or opposite direction to that of the rotor speed.

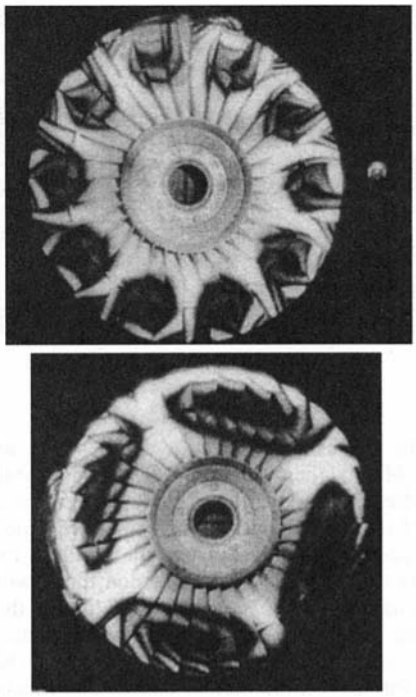

Fig. 9 Holographic images of a shrouded fan (Mickolajczak et al., 1975)

Vibration of Bladed-Disk Assemblies

Structural Dynamic Aspects. From the viewpoint of aeroelasticity of gas turbine engines, bladed-disk assemblies (fan, compressor, and turbine rotors) are the components of particular interest, because analyses and tests occur at this level in order to develop design systems. The blades of the assembly are, of course, the aerodynamic components of the assembly, and the aerodynamics of cascades plays a major part in the calculation of flutter and resonance.

An understanding of the dynamic characteristics of blade assemblies is crucial to the calculation of flutter and resonance of rotors. These characteristics are different from those of individual blades because of any coupling among blades due to either shrouds and/or support structure. Bladed-disk assemblies experience system modes of vibration, which are influenced by characteristics of individual blade vibration; the support structure including part-span or tip shrouds; speed; temperature; damping, and the nature and extent of mistuning among the blades.

Not only are accurate frequencies of vibration (for all modes of interest in the operating range) needed, but also accurate mode shapes are necessary because of their use in the calculation of flutter and forced responses. The modes for the assembly, by their very nature, involve variation of amplitudes along the blade surface, which in turn may vary circumferentially. This gives rise to a pattern, such as shown in Fig. 9 (Mikolajczak et al., 1975), for a shrouded-fan rotor of the type shown in Fig. 10 (Srinivasan and Cutts, 1983a). These patterns illustrate vibratory motion captured as a hologram and are described as 5 and 2 nodal diameter patterns. They were obtained in tests conducted on a stationary fan with shrouds glued together. The modes represent a standing wave with the blades at and close to the nodal diameters experiencing predominantly torsional motion and those at and close to the antinodes experiencing a predominantly bending motion. A higher system mode may include a nodal circle at some location along the blade span. During operation of the engine, this vibratory pattern may be a standing wave and/or a traveling wave in or opposite to the direction of the rotor speed. Traveling waves are commonly observed in engine operation. A backward-traveling wave, whose speed becomes equal to the rotor speed, is identified as a stationary wave and the corresponding rotor speed is interpreted as resonant speed.

These features are usually displayed in a frequency-speed diagram known as a *Campbell diagram.* In order to draw a Campbell diagram, it is necessary to have calculations or measurements of natural frequencies of a bladed-disk assembly with respect to rotor speed for each circumferential wave number (nodal diameter) and radial wave number (nodal circle). The intersection of these characteristics with the engine order lines (per rev. and noted as EO in the illustration) define the resonant speeds, i.e., the speeds at which forced vibration will be undesirable. For example, in Fig. 11 (Pfeiffer, 1985), the intersection points are shown for two and three nodal diameter pattern modes as well as higher modes. The nearly horizontal lines represent the manner in which the frequencies of vibration for a given pattern varies with speed. The reason for the two closely spaced lines for each pattern shown in Fig. 11 is due to any asymmetry in the otherwise circularly symmetric system and will be discussed later.

An examination of a typical Campbell diagram reveals not only resonant frequencies, but also their proximity to each other. In calculations made for a blisk rotor (a shroudless rotor design

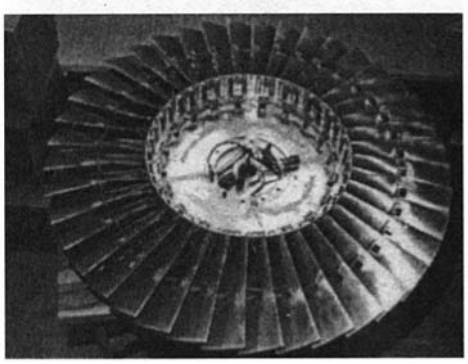

Fig. 10 A part-span shrouded fan

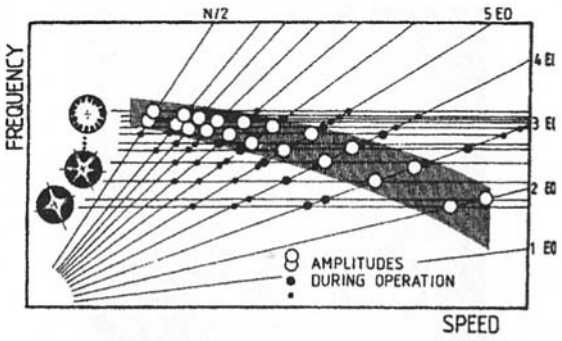

Fig. 11 A Campbell diagram

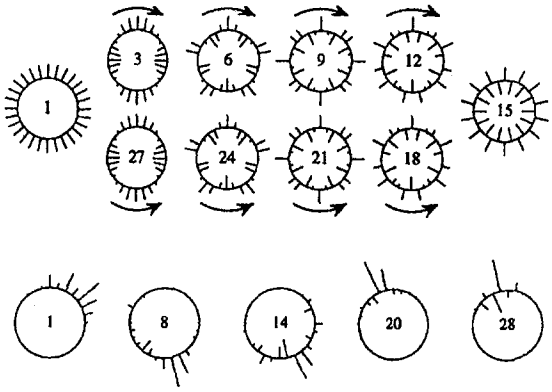

Fig. 13 Modes of tuned and mistuned rotors (Ottarsson and Pierre, 1993)

in which the blades are integral with the disk; see Fig. 12, courtesy of MTU), the Campbell diagram showed that, at zero speed, the frequencies for the second bending mode differed from that of the first torsion mode by a mere 2 percent. With increased speeds, the frequency of the bending mode would increase, but the frequency of the torsion mode would experience little change. Such an observation allowed the designers to recognize the potentially dangerous interaction between modes that could lead to aeroelastic instabilities. The blisk was redesigned through "a numerical optimization technique . . . leading to a significant improvement in design quality and development time" (Frischbier et al., 1996).

The regularity of vibratory patterns depends upon the extent of similarity in the dynamic characteristics of individual blades, i.e., the level of mistuning. If the latter is low, i.e., the geometric and structural characteristics of blades are essentially identical, the resulting vibratory pattern may be easily categorized as a certain nodal diameter/nodal circle mode. On the other hand, a mistuned system is likely to show a system mode whose variation around the rotor may defy easy description (Fig. 13, Ottarsson and Pierre, 1993). Aerodynamic and/or structural nonuniformities around a rotor have been known to influence natural modes, forced responses, and flutter conditions of rotor blades. As suggested earlier, nonuniformities arise due to nonconstant gap/chord, incidence angles or blade frequencies, etc., which influence cascade aerodynamics. A more complete discussion of this feature is included later in sections dealing with flutter and forced vibration.

The introduction of shrouds to provide an elastic support at part-span of fan blades was motivated by flutter prevention. Shrouds are integral protuberances on the individual blades that interlock at speed, in an assembled rotor, to form a ring that couples the blades to provide a stiffer assembly. In earlier designs, adjacent blades were tied together by rods "whose ends were screwed into threaded bushes set in the blade forms" (Armstrong, 1967). This technique proved to be unsuitable because of stress concentrations at the holes in the airfoils and therefore the modified concept of shrouds ("snubbers") was introduced (Fig. 14) and is currently in use industry-wide. These shrouds constitute the integral protuberances referred to above.

Maximum stage stability is obtained by locating the "shroud ring" at about two-thirds of the distance from the blade root to the blade tip. The introduction of this feature to blades also introduced a certain level of uncertainty. Because the blades bear against each other as they untwist at speed to form a "continuous ring," they have a tendency to rub at these interfaces during vibration. The extent of this rub and the resulting potential for damping have been subjects of scrutiny for nearly two decades, yet no acceptable analysis has emerged. As a result, analyses have made assumptions in regard to the boundary conditions that include extreme cases of a fully locked shroud and a freely slipping shroud. The need to pay attention to shroud boundary conditions became apparent when natural frequency calculations for certain rotors failed to correlate with measured data, as shown in the Campbell diagram of Fig. 15 and the corresponding influence on mode shape shown in Fig. 16 (Srinivasan et al., 1978). In Fig. 15, agreement appears to arise with the so-called freely slipping shroud, i.e., without any friction. This is by no means an assurance that the prevailing

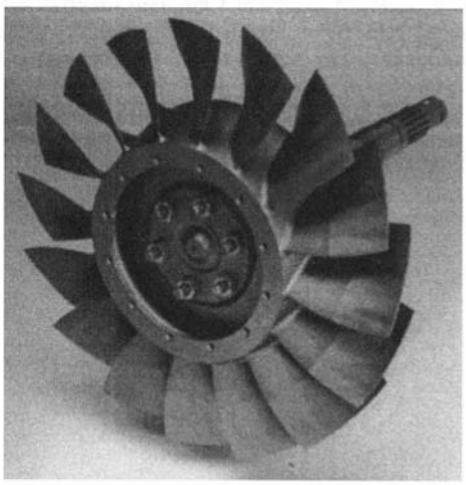

Fig. 12 An MTU "blisk" rotor

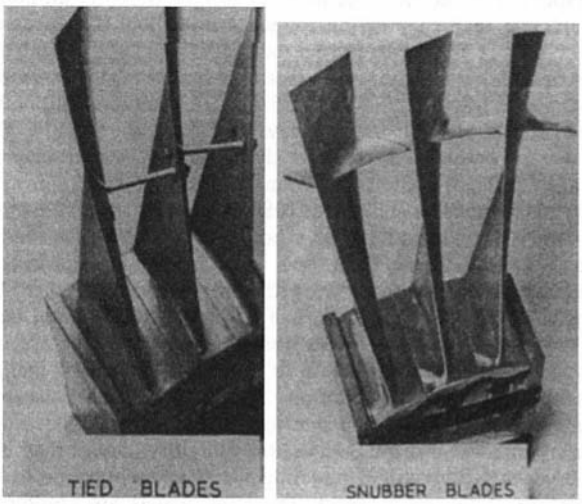

Fig. 14 "Tied" and "snubber" blades (Armstrong, 1967)

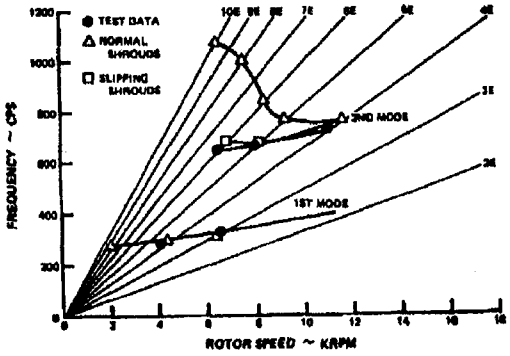

Fig. 15 Shrouded-fan Campbell diagram (Srinivasan et al., 1978)

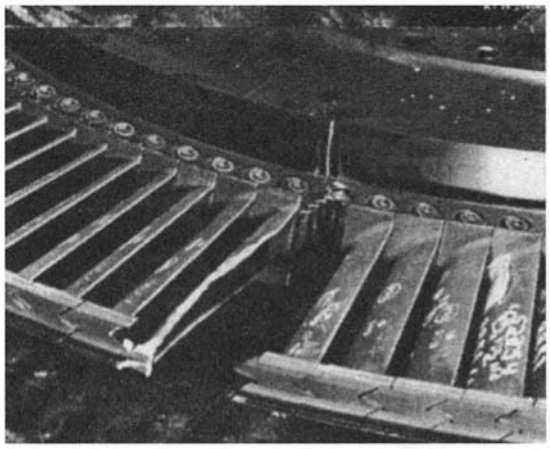

Fig. 17 Tip-shrouded blades

boundary condition truly represents that condition, especially because a visual examination of shroud surfaces after rig and engine tests clearly shows signs of rubbing.

Accurate specification of boundary conditions at the shroud interfaces is important not only to determine resonant speeds but, more important, in predicting the mode shapes of the bladed-disk system. Figure 16 shows the difference in the ratio of bending to torsional deformation for a shrouded fan as a function of the radial distance from shroud to tip. "Slipping shrouds" assumed that the degrees of freedom capable of slipping do so with no accompanying force at the interface. The so-called ball joint shroud condition has made the assumption that no translational motion is permitted at the interfaces, but rotation can take place without any accompanying moments. As will be evident later, this variation in mode shapes has considerable significance in establishing aeroelastic stability because these numbers are used directly in a work/cycle calculation and therefore prediction of susceptibility to flutter is dependent on the accuracy of these mode shapes.

Integral and interlocking shrouds are incorporated on the tips of low-pressure turbine blades of many aircraft engines and these provide additional stiffness as well as a sealing function. The geometry of the tip shrouds is Z shaped and different from the geometry of part-span shrouds of fans (Fig. 17), but their function is the same, that is, to maintain a preload along the circumference during engine operation.

Shrouds do wear and the contact at the interfaces becomes less tight, leading to changes in the dynamic characteristics of the assembly. Engine strain gage data from a variety of tests have shown coupled modes obtained for a tight shroud condition degenerate into first flap and first edgewise cantilever type modes at lower frequencies when the shrouds become slack (Hall and Armstrong, 1976).

The industry-wide practice is to place the frequencies of integral order vibration in the low engine orders (2E, 3E, and sometimes 4E and 5E) either outside the operating range of rotor speeds or at lower speeds within the operating range. Higher order resonances, as high as 30E or above, need to be examined in some cases. Whether these are considered dangerous or not at a given level of excitation will depend upon the magnification factors, which require accurate computations of blade damping.

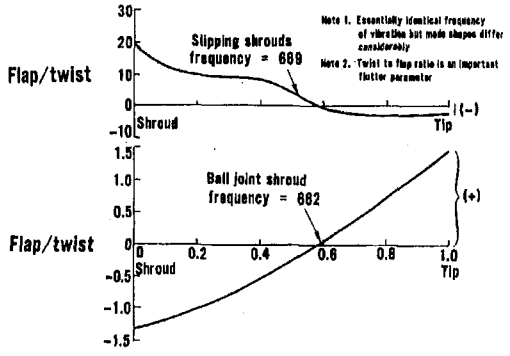

Fig. 16 Mode shapes for different shroud boundary conditions

Structural Dynamic Modeling

An attempt to develop an analysis to model shrouded blades was made by the author (Srinivasan et al., 1978) and the elements of that approach and principal results are discussed below. A key element of this approach is the ability to examine a variety of laws of friction at rubbing interfaces.

The approach to computing the dynamics of a bladed-disk assembly is discussed through the example of fan blades coupled through shrouds only. It is therefore assumed that the support structure is rigid. The starting point for this approach is modal amplitudes (eigenvectors) and frequencies (eigenvalues) of a single blade. The dynamic flexibility of a blade may be expressed as

$$(\alpha) = (\Phi)[m_{ii}(\Omega_i^2 - \omega^2)]^{-1}(\Phi)^T$$

where (Φ) is an assembly of eigenvectors, one column for each mode whose natural frequency is Ω_i, ω is the forcing frequency, and m_{ii} represents the modal masses.

But $\{q\} = (\alpha)\{f\}$ where the vector $\{q\}$ represents vibratory motion (displacements and rotations) at any point on an individual blade surface and therefore includes motion at the interfaces. $\{f\}$ represents external forces acting on the blades. With reference to Fig. 18, we may state that at the rth and sth interfaces, $(q_{r''})$ and $(q_{s''})$ are those degrees of freedom that maintain continuity there. Similarly $(q_{r'})$ and $(q_{s'})$ represent those degrees of freedom that can experience slipping motion. Thus $\{q\}$ consists of $\{q_b, q_{r'}, q_{r''}, q_{s'}, q_{s''}\}$. Then the above equation for $\{q\}$ represents five vector equations for the nine unknown vectors, which include, in addition to the five vectors stated above, the forces that correspond to the r and s degrees of freedom, i.e., $\{f_{r'}, f_{s'}, f_{r''}, f_{s''}\}$. The required additional four equations are obtained by enforcing boundary conditions at the interface as follows. Continuity and cyclic symmetry conditions in $\{q_s\}$ and $\{f_s\}$ provide

$$\{q^N\}_{r''} = \{q^N\}_{s''}e^{-i\beta} \quad \text{and} \quad \{f^N\}_{r''} = \{f^N\}_{s''}e^{-i\beta}$$

At the slipping degrees of freedom, we require equilibrium of forces. This requirement enforced at the rth and sth interfaces

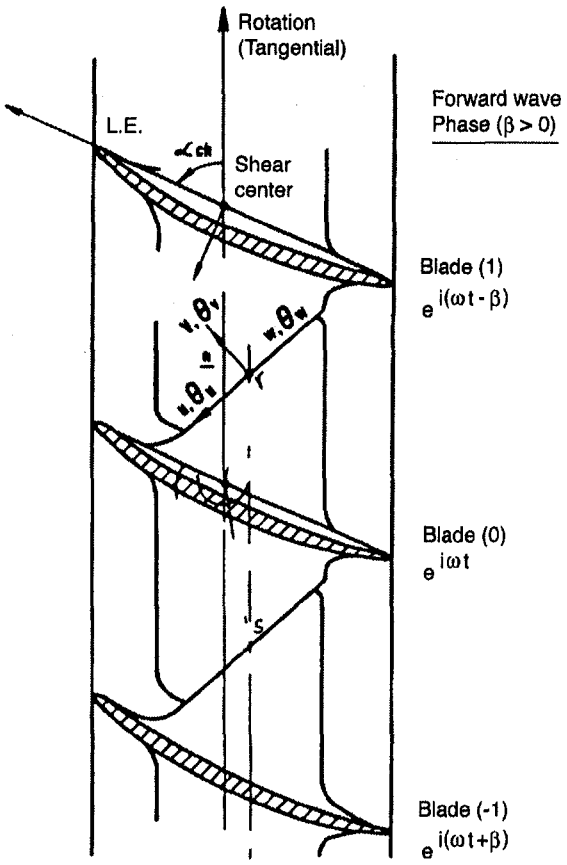

Fig. 18 Shroud boundary conditions

provides the remaining two equations. These may be shown to be

$$\{f_{r'}\} = -\{f_{s'}\}e^{i\beta}$$

$$2i\omega(D)[\{q_{s'}\}e^{-i\beta} - \{q_{r'}\}] + \{f_{s'}\}e^{i\beta} - \{f_{r'}\} = 0.$$

We now have nine equations in nine unknowns and a forced response calculation can be made by a simultaneous solution of the set of equations. Reference may be made to the paper for details. Note that the formulation lends itself to try out different models of friction (matrix (D)) at the interfaces. Calculations made with individual blade modes for a research fan blade show fast convergence around 30 modes and compare very well with corresponding results from NASTRAN. Further details can be found in the paper.

Aeroelastic Aspects

Flutter and resonance are aeroelastic phenomena and therefore the parameters that influence them include aerodynamic, structural, and a combination of the two. The challenge is to design rotors that simultaneously meet both structural and aerodynamic requirements. Flutter is driven by vibration of blades and the extent of resulting unsteadiness in the flow. Resonance, on the other hand, is driven by flow defects.

There are several sources of aerodynamic excitation, arising out of aero and structural design of the engine, which can lead to resonant vibration of engine blades. As remarked earlier, flow entering an engine inlet meets with static obstructions (struts, vanes, etc.) and rotating obstructions (blades) in its path from the inlet to the exhaust. Thus, the flow inside the engine is anything but uniform, either upstream or downstream of a given rotor stage. It is inherently unsteady. Wakes, potential pressure disturbances, circumferential flow distortions, shocks in passages, secondary flows, etc., produce, at a given speed, pressure variations that act as time-varying forces on a spinning blade. A good discussion of these sources of stimuli is presented by Kielb and Chiang (1992) and Chiang and Kielb (1993), with an extensive list of references relevant to this study, and the reader is referred to those papers for additional details.

An essentially complete list of parameters that influence the aeroelastic aspects of blade vibration is included below:

- gap/chord, number of blades
- blade geometry, blade twist
- hub/tip ratio
- aspect ratio
- stagger
- shroud location and shroud angle
- tip speed
- incidence angle, blade loading
- separation point
- pressure distribution on blade surface, shock position and motion
- inlet and exit conditions
- relative inlet Mach number
- distortion pattern
- velocity and pressure defects
- reduced frequency
- interblade phase angle
- mode shape
- mechanical damping
- extent of coupling among blades
- mistuning

Clearly some parameters will be more predominant than others at certain specific aeroelastic conditions. A discussion in regard to some of these parameters and their influences follows.

Reduced Frequency. An important parameter that is also a measure of unsteadiness is the so-called reduced frequency k. It is defined as $b\omega/V$, where b is the semi-chord, ω is the frequency of vibration in radians/sec, and V is velocity of air relative to the blade. Some researchers use blade chord instead of semi-chord to define k. The parameter can be interpreted as the ratio of time taken for a fluid particle to flow past the length of a semi-chord to the time taken for the airfoil to execute one cycle of vibration. Another interpretation can be given as follows (Fig. 19):

"Consider an airfoil of chord length $2b$ oscillating at a frequency of $\omega = 2\pi/T$ in a stream moving past it at a velocity V, as shown above. A sinusoidal wake will be formed, which is imbedded in the free stream and hence also moves relative to the airfoil at a velocity V, with wavelength $\lambda = VT = 2\pi V/\omega$. If we divide the airfoil chord by this wavelength we obtain $(2b/\lambda) = (2b\omega/2\pi V) = (k/\pi)$. Thus, at low reduced frequency ($k \sim 0.05$) the wavelength is very large relative to the chord while at high reduced frequency ($k \sim 1$) the wavelength is not so large relative to the chord" (Platzer and Carta, 1988). Thus the reduced frequency is the ratio of the circumference of a circle of radius b and the wavelength of the wake; the larger the wavelength, the smaller is the k. In either interpretation, it is clear that for small values of the reduced frequency, the flow is quasi-steady and for large values unsteady effects become dominant. For values close to 1, both quasi-steady and unsteady effects need to be considered in formulations. The value of the

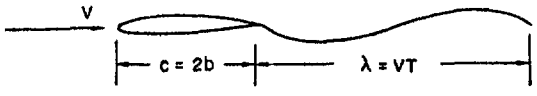

Fig. 19 An interpretation of reduced frequency (Platzer and Carta, 1988)

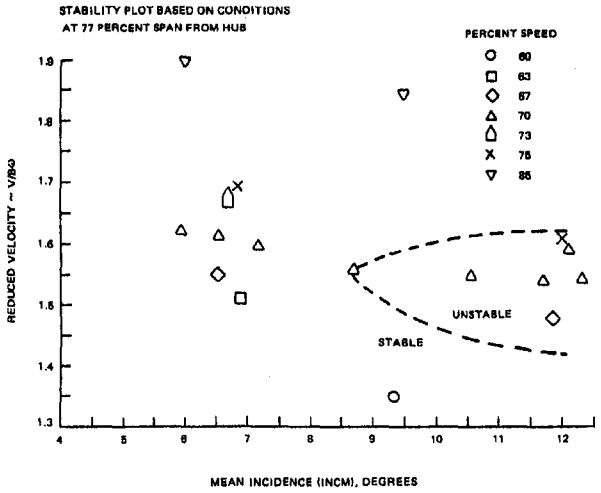

Fig. 20 TS-22 "stall flutter" data (Stargardter, 1979)

parameter k at which flutter has been observed in fans and reported for some rotors is as follows:

P&W research rotor	0.4 to 0.6	(Mikolajczak et al., 1975)
TS 22	0.6 to 0.65	(Stargardter, 1979)
NASA test rotor	0.5 to 0.7	(Kielb and Kaza, 1983)
NASA engine tests	0.7 to 0.75	(Lubomski, 1980)
First fan rotor	0.7	(Kurkov, 1984)

Generally, the experience has been that flutter events in the first mode have been observed for reduced frequencies less than about 0.4 and between 0.4 and 0.7 for modes with a predominantly first torsion mode.

Attempts to correlate "stall flutter" were made in the past by plotting reduced velocity (inverse of reduced frequency) against incidence angle. Rig testing on the TS 22 fan revealed that a strong correlation does not exist because at a given incidence, a unique reduced velocity does not distinguish between flutter and flutter-free conditions. This can be seen clearly in Fig. 20 (Stargardter, 1979) in which flutter conditions prevail over a wide range of incidence angles for a limited range of reduced velocities.

Shroud Location/Angle. The location of the shroud and the mating angle (i.e., the angle of the shroud interface with reference to, for example, blade chord) influence the mode shape as well as the normal load on the interfaces. The effect on the mode shape is seen in the context of torsion and bending of the blade profile, which directly influences the extent of aeroelastic stability. The normal load controls the extent of tightness at the interfaces, which, in turn, requires a balance between any loss of stiffness and increased damping due to shroud rub.

Pressure Distribution, Shock Position, and Motion. Measurement of unsteady pressures made with blade-mounted kulites in the TS 22 test program (Stargardter, 1979) revealed that only about a quarter chord from the leading edge experiences relatively higher pressures. Thus it appears that contribution to unsteady work, which influences flutter, comes mostly from action confined to the leading edge section of the blades.

Inlet Pressure and Temperature. Tests conducted by Jeffers and Meece (1975) and Mehalic et al. (1977) as well as by Lubomski (1980) have shown that inlet conditions do affect the flutter boundary. "For an engine operating at a given inlet temperature, corrected speed, and corrected flow, inlet pressure affects only the density term in the unsteady work expression. Because density is directly proportional to inlet pressure, an increase in pressure produces an increase in the unsteady work and, consequently, the aerodynamic damping. If the system has positive aerodynamic damping, increasing inlet pressure is stabilizing. However, if the aerodynamic damping is negative, increasing inlet pressure is destabilizing. A system that has negative aerodynamic damping can be stable if the positive mechanical damping is large enough to make the total system damping positive. This system can be made unstable at the same operating condition by increasing inlet pressure until the negative aerodynamic damping overcomes the positive mechanical damping" (Jeffers and Meece, 1975).

In addition, Lubomski, in the tests referred to earlier, measured a drop of about 3 to 4 percent in the flutter frequency as inlet pressure increased. The relationship was essentially linear over a range in which the inlet pressure was doubled. Furthermore, his tests confirm the need to recognize that flutter velocity is a function of incidence angle, inlet pressure, and inlet temperature. The change in the frequency of flutter with respect to inlet pressure and temperature suggests nonlinear effects present in the prevailing aerodynamics and/or vibratory modes.

Jeffers and Meece found that a NASTRAN calculation of chordwise bending due to inlet pressure, for the F100 first-stage fan, was significant enough to affect leading edge metal angle, camber, and cascade stagger. The normalized incidence variations due to this effect predicted for the tip region were such that at least a portion of the stability dependence on inlet pressure could be attributed to airfoil deformation due to steady-state aerodynamic loading.

Coupling. Vibratory modes of realistic blade profiles are almost always coupled. By this we mean that the contents of a given mode of vibration include displacements perpendicular and parallel to the chord and torsion of the profile. In general the displacements vary along the chord and span of the blade. With finite element capabilities commonly applied in today's computing environment, we no longer need to refer to these modes as "coupled bending-torsion" modes. Suffice it to simply recognize modes and frequencies and perhaps comment on one or another predominant feature of the modes. In that context, what we calculate could be and almost always are coupled modes and there is no reason to emphasize the obvious and common feature in our discussion.

On the other hand the coupling we need to discuss in the context of engine rotors may pertain to either mechanical and/or aerodynamic coupling in which assembly or system modes may occur. Mechanical coupling among vibrating blades occurs due to shrouds and/or support structure such as a disk or hub. Clearly the extent of coupling is a distinct function of the compliance of the support structure. If the latter is essentially rigid and the blades are shroudless, the only coupling that concerns us is aerodynamic. However, if the coupling is provided by a compliant support, then the assembly modes can develop fully and be well defined. An extreme example of such coupled modes is illustrated in Fig. 21 from tests conducted on a rubber wheel (Stargardter, 1966). The aeroelastic behavior can differ markedly depending upon the magnitude of mechanical and/or aerodynamic coupling. In an assembly or system mode in which the blades respond as participating members in a cascade, the nature of such a mode will vary from a very distinct mode to one that may defy any description around the rotor (for example, the mistuned modes in Fig. 13).

When the solution to a flutter or resonance problem is sought in terms of a set of degenerate modes (i.e., eigenmodes of the structure), one states that the solution is obtained by summing on all contributing modes. For example, for a given circumferential mode, a series of blade modes may be coupled to represent the response (Srinivasan and Fabunmi, 1984). Gerolymos, in his attempt to calculate aerodynamic damping for an assembly of 38 shrouded fan blades (1993) used the aeroelastically coupled modes for the wave numbers +4 and −4 (forward and

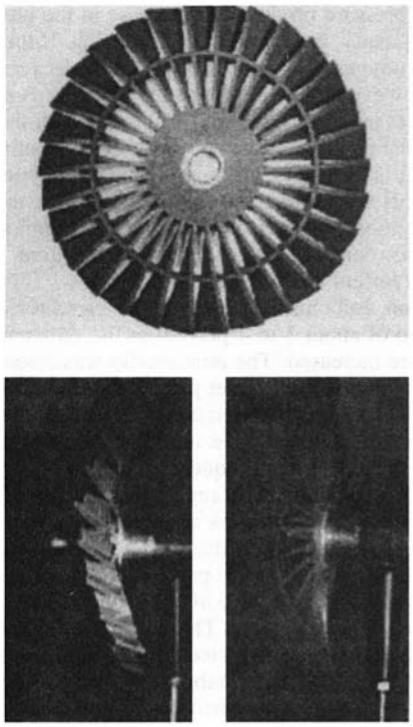

Fig. 21 Vibrating rubber wheels (Stargardter, 1966)

backward traveling waves). These coupled modes were obtained by coupling six modes, i.e., using a summation on 6 blade modes, whose frequencies were 235, 408, 626, 688, 805, and 901 Hz, respectively. Numerical integration of three-dimensional Euler equations provided the required unsteady pressures. An interesting conclusion of this study is that even though the effects of coupling the six blade modes were found to be relatively small on unsteady pressures, the effect on aerodynamic damping was not small as the calculations indicated a drop of about 30 percent in damping when the coupling among the blade modes was included in the calculations.

Interblade Phase Angle. Interblade phase angle is a phase relationship that represents the motion of a blade with respect to other blades. For example, in a well-defined traveling wave mode, the motion of a blade can be shown to be identical to the motion of its neighbor except for a phase angle between them. Thus, each blade will experience exactly the same motion except at a slightly different time. In real systems, vibratory modes may or may not be well-defined. If one could visualize the pattern of vibratory motion by considering it frozen at an instant of time, then the pattern can be broken into its harmonics, each of which is associated with a well-defined mode with an interblade phase angle. Thus, unsteady aerodynamic forces acting on blades at a given set of aero and structural parameters can be defined as the sum of all contributing harmonics. These assumptions are inherent in frequency domain analyses. As the phase relationships must add up to 360 deg (and multiples thereof) as one moves from one blade to another around the rotor, an interblade phase angle can be defined as $\beta = 2\pi n/N$, where n represents the wave number and N is the number of blades. With this definition, clearly one could consider the contributing harmonics to contain all integer values of n, leading to as many βs as the number of blades. In the time-domain approach no such assumption will be needed, as will be described later, and the βs found in the process of such calculations may not necessarily be restricted to this definition. In any case, unsteady aerodynamic coefficients resulting from aeroelastic modeling of vibrating cascades depend principally upon reduced frequency and interblade phase angle in a complicated manner. A list of such values with their real and imaginary parts was tabulated by Whitehead (1962) for flat plate cascades vibrating in incompressible flow. These coefficients can be used to calculate lift forces and moments due to translation and rotation for prescribed values of geometric parameters, reduced frequency and interblade phase angle. Such a complex relationship is depicted in Fig. 22 (Forsching, 1989) for a compressor cascade.

Mistuning. More will be said about this parameter later, but it is important to note here that mistuning is usually specified by measures of departure of aerodynamic and structural parameters from corresponding reference values.

Flutter

Among a variety of phenomena that cause concern in regard to blade failures, perhaps the most serious is flutter. A principal reason for such concern is that flutter is an aeroelastic instability, and once initiated it cannot be stopped in most cases. In an instability condition the aerodynamic forces induced due to blade vibration feed energy into the structure, and thus stresses escalate with each additional cycle of vibration. This is precisely the reason for the special attention that the flutter problem receives industry-wide. An important feature of flutter is that the resulting vibration is nonintegral and therefore the frequency–speed characteristic does not "ride" the engine order line, as is clear from Fig. 23. Test engineers are trained to keep an eye on this feature during engine/rig testing. When the frequency-speed characteristic "rides" the engine order line, it is watched for resonant conditions at an integral order, as evident in Fig. 23. When it departs from the engine order line, then the potential for an aeroelastic instability can be high. However, experienced test engineers report that low level flutter type stresses may occur occasionally and do not necessarily build up, as can be seen in Fig. 24 (Lubomski, 1980). This suggests that other prevailing mechanisms (structural and aerodynamic) may limit flutter events.

Engineers and scientists who have contributed to the study of cascade flutter have identified vulnerable regions on the familiar

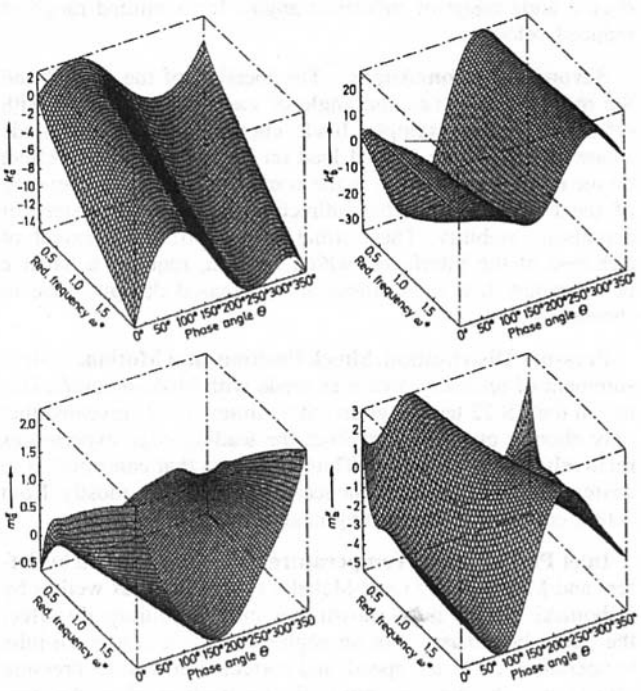

Fig. 22 Unsteady aerodynamic coefficients (Forsching, 1989)

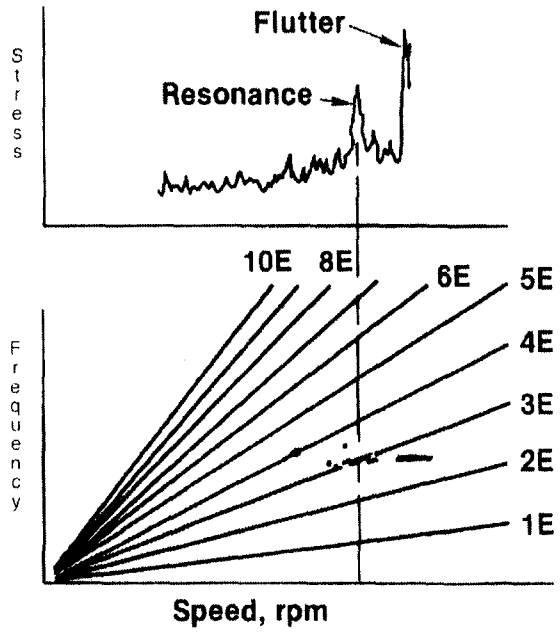

Fig. 23 Campbell diagram from engine test data

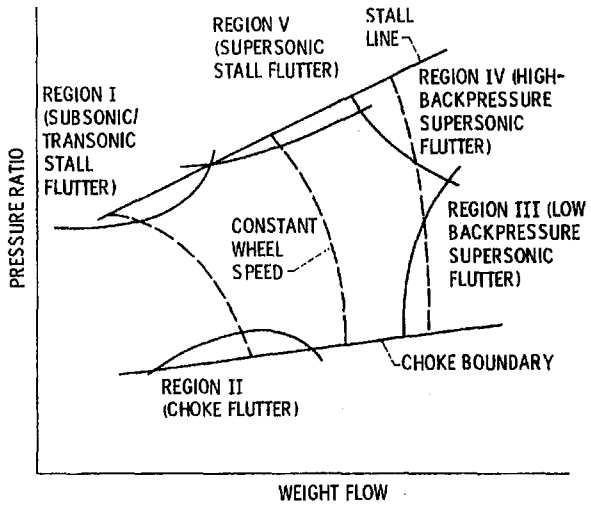

Fig. 25 Compressor stability map (Lubomski, 1980)

compressor map such as shown in Fig. 25 (Lubomski, 1980). Based on test experience with three engines, two of which were turbofans and the third, a turbojet engine, Lubomski identifies aerodynamic and/or aeroelastic phenomena that dominate different regions of flutter. This allows the analysis to focus on enhancing the particular feature noted therein, in order to develop a prediction capability appropriate to the region and the type of flutter of interest. Naming a phenomenon does not solve the problem, but it can offer approaches to analyses appropriate to the complex aerodynamic processes that need to be included in modeling the instability. The performance map is only a guide and these definitions of flutter regions are influenced by experience and continue to evolve. Back in 1972, it was stated in a symposium devoted to the aeroelasticity of turbomachines that ". . . these boundaries fall either at a fairly low pressure ratio with the stability boundary on the low-pressure side of the characteristics or else they fall on the high-pressure side of the characteristic. In some cases you can almost run into a wall as you come up in speed. Perhaps they are more speed sensitive. In other cases you may find areas where you run into an island where there is both an upper and lower boundary inside the characteristic. . . . It is unstable within this island and stable everywhere outside of the island" (Tramm, 1972). An additional aspect contributing to the critical nature of flutter problems was pointed out by Jeffers and Meece in their report on the "F-100 fan stall flutter problem" (1975). Engine tests confirmed flutter occurring in the third coupled above-shroud-torsion mode at a nonintegral order frequency at about 1000 Hz. This was unexpected because rig tests had indicated "stall flutter response" around 800 Hz in the second coupled mode shown in Fig. 26. All such observations increase the level of concern and the need to understand underlying mechanisms.

Table 1 is a compilation of the characteristics of different types of flutter noted on the stability maps of Fig. 25. The test data referred to in this table (Figs. 27, 28) are flutter events obtained from engine tests (Lubomski, 1980). The data represent nonintrusive measurements of tip deflection of each blade recorded as a reflection of laser light from blade tips. Details may be obtained from the reference. Any event that may start in one or two passages is likely to spread through a cascade and develop into a system mode as shown in Fig. 29.

Unsteady Aerodynamic Models

There are two distinct types of unsteady aerodynamic analyses needed for aeroelastic analysis of a row of blades. For

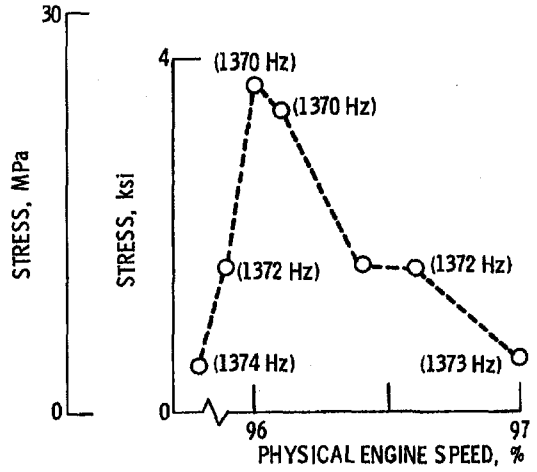

Fig. 24 System mode instability (Lubomski, 1980)

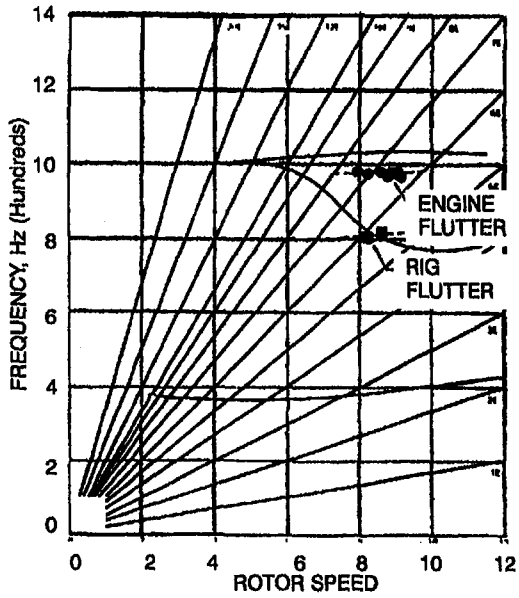

Fig. 26 Rig versus engine stall flutter (Jeffers and Meece, 1975)

Table 1 Characteristics of types of flutter

Type of Flutter	Operating Conditions	Vulnerable Component	Flow Conditions	Governing Parameters	Vibratory Modes	Typical Responses
Separated flow (stall)	Part speed, near surge boundary, subsonic, part speed, transonic, design speed	Fans, front stages of compressors	High incidence, flow separation	Mach number, reduced frequency, incidence, stage inlet conditions	Bending, torsion, plate modes, coupled modes develop suddenly	See Fig. 27
Choke	Part speed	Mid and aft stages of compressors	Negative incidence, higher in-passage Mach numbers	Mach number, reduced frequency, incidence	Bending or torsion modes	See Fig. 28
Supersonic/ unstalled	High corrected speeds	Fan blades	Supersonic relative flow, attached	Mach number, reduced frequency, interblade phase angle, shock position	Bending or torsion modes, mistuned	
Supersonic/ stalled	Close to 100% speed	Fan blades	High loading, supersonic tip, strong shocks	Mach number, reduced frequency	Limited data	

calculation of flutter susceptibilities, the objective is to predict forces acting on a blade surface due to vibration of the cascade of blades under uniform inlet and exit flow conditions. For resonance calculations, the objective is to predict forces acting on a blade surface due to deviations from perfectly uniform flow conditions at inlet or exit. Until recently, the unsteady aerodynamic analyses that have been used in aeroelastic and aeroacoustic design applications were based on classical linearized inviscid flow theory, which is applicable to lightly loaded thin airfoil cascades. Very efficient semi-analytical solution procedures were developed for two-dimensional, attached, subsonic flows, high-frequency transonic flows, and supersonic flows with subsonic or supersonic axial velocity components. As classical analyses were found to be inappropriate for application to transonic flows and to account for blade loading, the next level of modeling addressed these issues. This led to general two-dimensional, inviscid, analyses such as, for example, Euler analyses, which address unsteady flows with strong shocks. While the improved models are efficient and meet some of the needs of the designer, they do not account for other potentially important unsteady phenomena such as "finite amplitude excitation, viscous boundary layer displacement and separation, large shock excursions, etc." (Verdon, 1993). These requirements spurred additional research aimed at providing more realistic and comprehensive modeling capabilities. Current advancements focus on solving the Euler and Navier–Stokes equations on time-dependent grids that deform with blade motion. Research efforts to apply these CFD procedures to single as well as multiple rows continue in order to provide prediction capabilities that capture as many physical conditions as possible within the constraints of computational resources. A thorough review of the techniques is provided by Verdon, along with a list of 85 references, and should be consulted by serious students of unsteady aerodynamics of cascades. Approaches discussed in the review

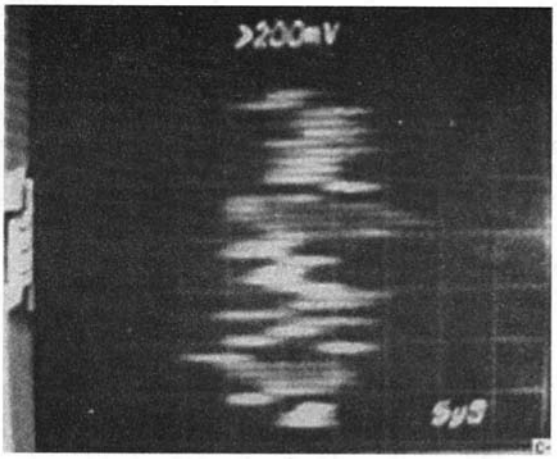

Fig. 27 Separated flow flutter (Lubomski, 1980)

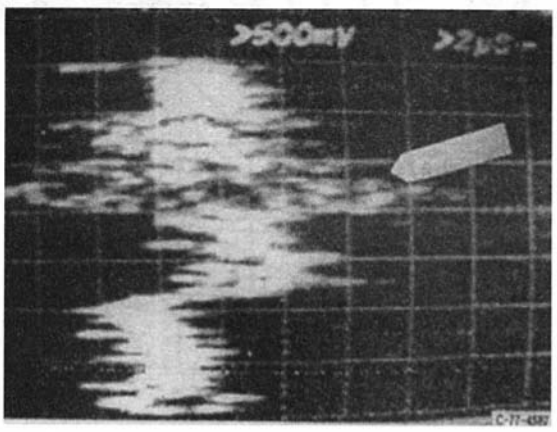

Fig. 28 Choke flutter (Lubomski, 1980)

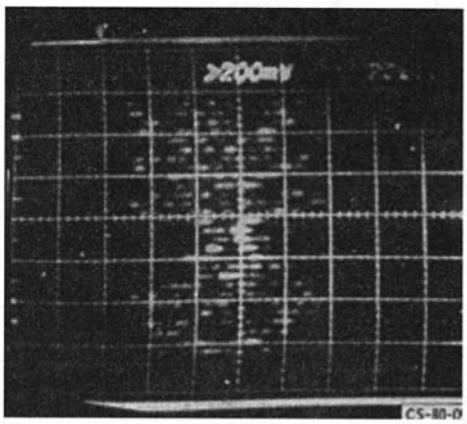

Fig. 29 System mode flutter (Lubomski, 1980)

include both analytical and computational procedures. Of similar interest are a series of systematic studies of standard airfoil configurations in which theoretical and experimental cascade unsteady flow results were compared (Bölcs and Fransson, 1986; Fransson, 1987; Fransson and Verdon, 1991, 1992).

As discussed above, modeling levels for unsteady aerodynamics relevant to gas turbine rotor blades can vary from a full potential flow representation to an Euler model for inviscid flows and a Navier–Stokes representation for viscous flows. Within each level there could be a variety of sublevels depending upon additional assumptions. Among current emphases in research to advance existing capabilities in this field, three aspects appear to be engaging researchers. The first pertains to consideration of nonlinearities in the flow. Preliminary results from a two-dimensional "time-accurate Euler/Navier–Stokes analysis" of high Reynolds number subsonic and transonic unsteady flows relevant to the solution of flutter problems has shown that unsteady surface pressures agree very well with corresponding predictions from a linearized inviscid analysis. However, the exception appears to be in unsteady transonic flows where "shocks develop and their motions cause significant nonlinear contributions" (Ayer and Verdon, 1996). The second emphasis pertains to three-dimensional modeling of unsteady aerodynamic flows. Comparison between a three-dimensional theory (lifting surface theory) and strip theory to calculate unsteady aerodynamic work done in supersonic and transonic flows in a particular cascade shows that differences can be significant in transonic flows (Namba, 1987). More recently, Hall and Lorence (1993) have concluded that "strip theory can be a poor predictor of aerodynamic damping" based on comparison between "experimental results and other aerodynamic analyses." The third area of interest is in the study of interactions among blade rows. Again, in a recent study Buffum (1995) attempted to use "isolated blade row unsteady aerodynamic analyses" to determine the influence of coupling among three blade rows through a set of influence coefficients. This study shows that "interaction effects can be destablizing" in its application to flutter. Similarly the forced response calculations show that "interaction effects can result in a significant increase in resonant response . . .".

Aeroelastic Modeling

Frequency Domain Approaches. Flutter analyses can be formulated in one of two domains: frequency domain or time domain. Frequency domain approaches begin with assumptions of blade motion (harmonic in time) and with constant interblade phase angle. Further, the aeroelastic forces are assumed to be functions of blade motion and the set of unsteady aerodynamic coefficients (lift and moment coefficients due to plunging and pitching motion) are calculated for a prescribed interblade angle and reduced frequency. The governing equations of motion can then be shown to reduce to a complex eigenvalue problem,

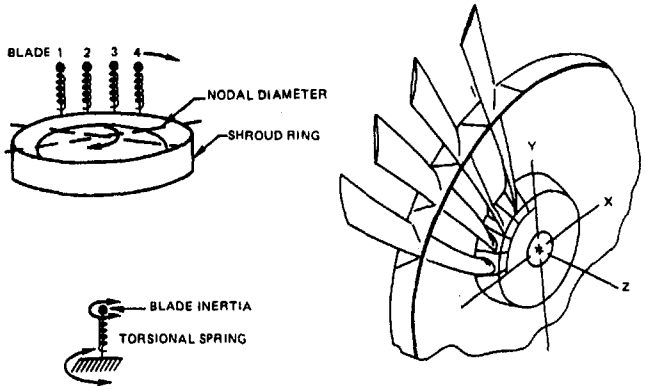

Fig. 31 Above-shroud blade model (Srinivasan and Kurkov, 1981)

the solution of which provides the frequencies whose real part represents the frequency of oscillation and the imaginary part represents damping. When the eigenvalue problem is solved for all possible interblade phase angles at a prescribed reduced frequency, the solution can be plotted as a locus such as shown in Fig. 30 (Whitehead, 1965) from which the susceptibility to aeroelastic instability can be determined. The imaginary part of the eigenvalue in Fig. 30 is a measure of damping and the real part is a measure of frequency of vibration. Imaginary parts are plotted against corresponding real parts for each interblade phase angle to obtain the locus shown in the figure. The sign of the imaginary part determines the interblade phase angle or phase angles at which instability may occur. This approach has been extended to the study of mistuned systems by several researchers. The time domain approach will be discussed later in this section. Shrouded blades that experience vibratory motion essentially above the shroud have been modeled as single-degree-of-freedom oscillators mounted on a flexible ring (Fig. 31). Such a model was attempted to examine the first-stage fan flutter in an advanced engine (Srinivasan and Kurkov, 1981). The ring structure was characterized by a dynamic influence coefficient matrix whose elements vary as a function of the excitation frequency. Thus coupling is not a constant and changes as the frequency is swept.

The eigenvalues for the condition of mechanical coupling only vary unsymmetrically with respect to a datum frequency, as shown in Fig. 32 for a twelve-bladed assembly. The frequencies of the coupled system can be higher or lower and depend upon the wave number. With the same "blades" coupled additionally through aerodynamics, we now have damping in the system and the eigenvalues are complex. The real and imaginary parts of the eigenvalues shown in Fig. 33 can be viewed as before as a locus. In a sense, the size, i.e., the area, of this locus is a measure of the strength of coupling. Notice the rather

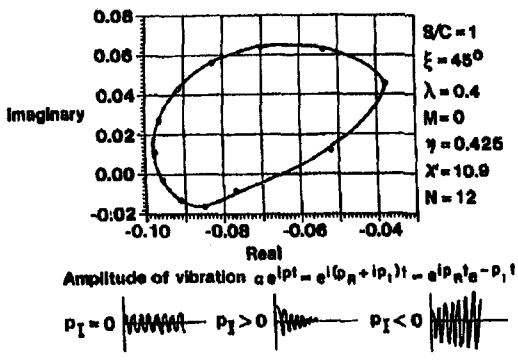

Fig. 30 Locus of eigenvalues (Whitehead, 1965)

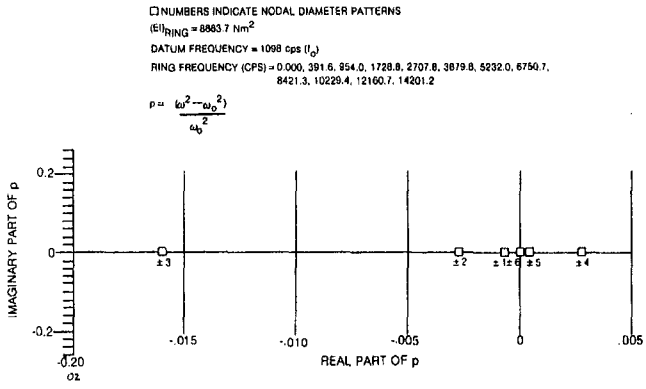

Fig. 32 Eigenvalues with only mechanical coupling among blades

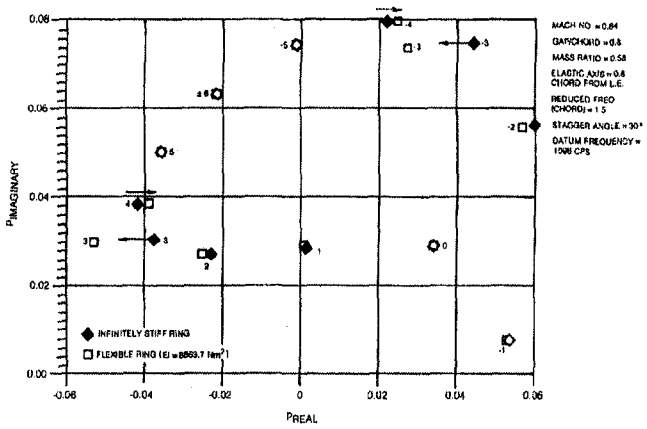

Fig. 33 Eigenvalues with mechanical and aerodynamic coupling

meager change in the frequencies (real part) for the aerodynamically coupled system. The more significant feature is aerodynamic damping, which can be either positive or negative. Thus, at certain wave numbers, the system could become unstable. In the example shown in Fig. 30, the system may experience flutter at interblade phase angles corresponding to $n = 1, 2, 3$ and perhaps $n = 4$. However, for the example shown in Figs. 31–33, the system is shown to be flutter-free. Flutter analyses in which the solution is sought in the form of a harmonic motion at a frequency can predict only susceptibility to instability. Thus calculated negative and positive damping values and the corresponding interblade phase angles must be interpreted as showing only a trend because the solution is not strictly valid for the damped condition.

An analysis that includes both translation and rotation of beam-like blades was carried out (Srinivasan and Fabunmi, 1984) in which the unsteady forces were represented as lift and moments. The latter are integrated effects of forces distributed along the chord and are acceptable for high aspect ratio beam-like blades because the variation of displacements along the chord is minimal. However, for the type of motion implied in the modes displayed in Fig. 34, clearly the variation of pressures along the chord is such that integrated effects are likely to be a poor representation of the physics. Analytically it is a more direct step to use pressures that are the output from an aerodynamic code, and the unnecessary step involving integration of these pressures to obtain lifts and moments can be skipped. Such an approach, which uses unsteady pressures directly in a flutter calculation, was developed recently (Srinivasan and Tavares, 1995) and is suitable for solving mistuned low aspect ratio blades. Thus, for a cascade of aerodynamically coupled wide chord blades as shown in Fig. 35,

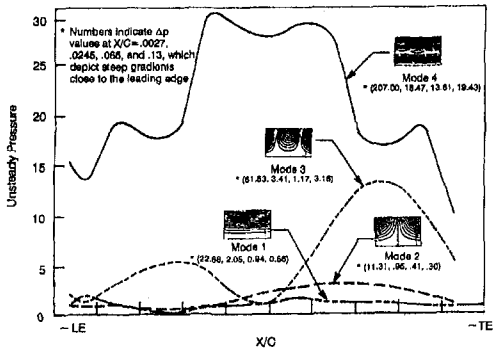

Fig. 34 Unsteady aerodynamic pressures acting along the chord at 50 percent span

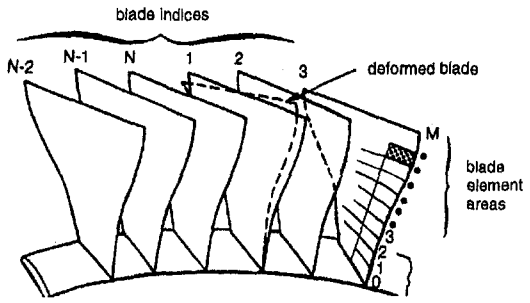

Fig. 35 Cascade of cantilevered blades (Srinivasan and Fabunmi, 1984)

$$P_{hl}^{k} = \sum_{n=1}^{N} (\Delta P_{hh,l}^{kn} q_{hl}^{n} + \Delta P_{hs,l}^{kn} q_{sl}^{n}) \Delta a$$

where Δa = area of the element shown in the figure. An understanding of the physical meaning of the above representation may be obtained by noting that $\Delta P_{hh,l}^{kn}$ represents the unsteady pressure differences along h at element l due to a unit vibratory amplitude of the lth element of the nth blade vibrating along the h direction. A multiplication with the corresponding vibratory motion q provides the desired ΔP. With these definitions along with the definition of $\{q\} = [\Phi]\{\eta\}$ where η represents the generalized coordinates and $[\Phi]^k = [\{\phi_1\}, \{\phi_3\}, \ldots, \{\phi_n\}]^k$ represent eigenvectors for the kth blade, the differential equations of motion

$$[m]\{\ddot{q}\} + [K]\{q\} + \{P\} = 0$$

can be shown to reduce to an eigenvalue problem. $[K]$ and $[m]$ represent stiffness and mass matrices for the kth blade and the vector $\{P\}$ represents the corresponding aeroelastic forces calculated above. The latter, as we have seen before, is expressed in terms of the blade motions q.

An analysis based on this approach was conducted for an assembly of 12 "blades" (flat plates) with the following values for the parameters: gap/chord = 1, stagger angle = 45 deg, Mach number = 0.8, aspect ratio = 0.6, and mass ratio = 150. Figure 34 is a plot of the magnitude of unsteady pressures acting on the chord at 50 percent span for the indicated modes at an interblade phase angle of 30 deg, computed using an analysis by Smith (1973) modified to include chordwise motion. The modification itself is rather straightforward as the formulation allows for a general description of motion along the chord. The values shown in Fig. 35 at the very beginning and the very end are, of course, unsteady pressures close to the leading and trailing edges, respectively.

A word of caution in using ΔPs is in order. Clearly, the use of unsteady pressure differences is valid for low cambered, thin, flat-plate-like profiles. Otherwise, a further modification is necessary to work with unsteady pressures around the blade profile along with corresponding vibratory motions perpendicular and tangential to the elements in question. Also, a further implication in the procedure is that strip theory is valid. Because of that implication, the matrix of aeroelastic forces is as shown below with a diagonal band. A more realistic approach in which calculations for unsteady pressures include the influences of every element on every blade surface would lead to a fully populated matrix.

$$\begin{bmatrix} \Delta P_{hh,1}^{kn} & \Delta P_{hs,1}^{kn} & & & & \\ \Delta P_{sh,1}^{kn} & \Delta P_{ss,1}^{kn} & & & & \\ & \Delta P_{hh,2}^{kn} & \Delta P_{hs,2}^{kn} & & & \\ & \Delta P_{sh,2}^{kn} & \Delta P_{ss,2}^{kn} & & & \\ & & & \ddots & & \\ & & & & \Delta P_{hh,N}^{kn} & \Delta P_{hs,N}^{kn} \\ & & & & \Delta P_{sh,N}^{kn} & \Delta P_{ss,N}^{kn} \end{bmatrix}$$

The calculations for the 12-bladed assembly were extended

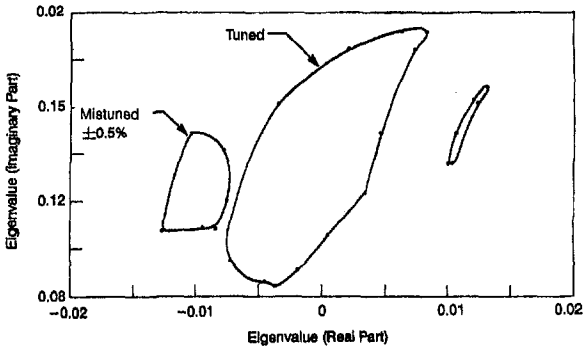

Fig. 36 Effect of mistuning on flutter; M_n = 0.8, k = 2.16, Mode 2

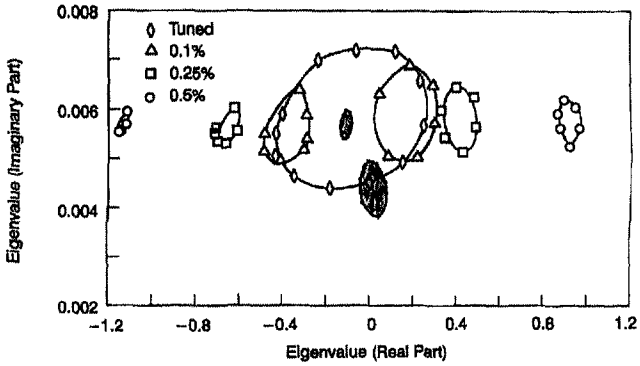

Fig. 38 Effect of mistuning on flutter, M_n = 0.8, k = 4.55, Mode 3

to study the influence of mistuning due to slight differences in frequencies or mode shapes. With only 0.5 percent alternate mistuning, the locus of eigenvalues for the second mode (reduced frequency 2.16) splits into two parts as shown in Fig. 36. Earlier investigations had shown that for reduced frequencies less than 1, such a split in the locus of eigenvalues occurs for alternate mistuning levels far higher than 0.5 percent. For example, for a cascade of 56 blades with a higher aspect ratio, under a variety of flow conditions (Mach numbers 0, 0.5, 1.15, and 1.4), it was found that the locus split around 5 percent alternate mistuning levels (see Fig. 37, Kielb and Kaza, 1983; note: the real part of the eigenvalue represents damping here). Those results were obtained using lift and moment coefficients unlike using unsteady pressures as was done for the low aspect ratio blades under discussion here. It appears that the reduced frequency plays a very significant role in decoupling the blades. At an even higher reduced frequency (4.55) corresponding to the third mode, the splits in the locus of eigenvalues begin to occur at as low a departure as 0.1 percent difference in the frequencies and continue as shown in Fig. 38. Another interesting feature studied pertains to an assembly with identical blade frequencies but with different mode shapes for every other blade, i.e., alternate mistuning through differences in mode shapes. The locus corresponding to this condition splits "vertically" (i.e., in the damping coordinate, unlike the split shown in Fig. 37, which occurs along the frequency coordinate) as shown in Fig. 38. Modes 3 and 4 were used as alternating mode shapes of blades and the analysis frequency corresponds to that of mode 3.

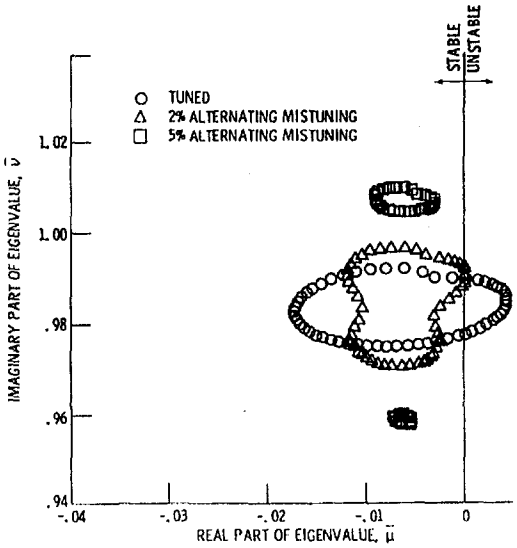

Fig. 37 Effect of mistuning on flutter (Kielb and Kaza, 1983)

A comment in regard to mistuned mode shapes is in order. At very high frequencies, the modal density is rather high, and therefore small differences in blade frequencies can lead to small differences in mode shapes.

It is possible that the small number of blades, i.e., only 12, used in the example given above may have influenced these results and therefore no general conclusions can be drawn. But if the trend is any indication, then small changes in mode shapes can be unfavorable as one part of the split locus tends toward lower values of damping, a feature totally unlike that observed in earlier studies with frequency mistuning. Thus, the general understanding that mistuning is favorable from the point of view of avoiding flutter is questionable if the trends observed above hold true for realistic cascades of blades.

Time Domain Approach. The frequency domain formulation is restricted to linear systems and the assumptions referred to above can be justified in some cases. For example, invoking the fact that the mass ratio parameter (mass of blade/equivalent mass of air) for metal blades has high values, the flutter frequency may be considered to be the same as the blade's natural frequency. Thus, reduced frequencies are input quantities and not part of the solution. Similarly, as blades in tuned systems vibrate in well-defined modes, each mode with a specific interblade phase angle, interblade phase angles can also be input quantities and calculations made at all possible phase angles allow one to identify the most vulnerable modes. This has been the approach that analysts have taken in the past three decades and design procedures have been developed on that basis. They have even been extended to low aspect ratio mistuned blades as discussed above.

There are advantages to such frequency domain approaches. First, the formulations are straightforward, and familiar to structural dynamicists. Further, coding a formulation to solve for eigenvalues is a task for which most analysts have direct experience and the computing expense, even for real rotor systems, can be low.

Time domain approaches, which are being examined more recently, do not make any assumptions in regard to either reduced frequency or interblade phase angle. The entire field equations are solved and the "initial conditions are the steady flow field and a small disturbance applied to the blades in the cascade" (Bakhle et al., 1992). Preliminary results obtained with a time marching CFD aeroelastic solver for a five-bladed cascade of typical section of a propfan at reduced velocities of 4.8 and 5.6 show the blade responses in pitching and plunging motions as functions of time (Fig. 39).

The time domain formulations such as the one discussed above have the advantage of predicting the reduced frequency and interblade phase angles and therefore remove limitations inherent in frequency domain solutions. In typical turbomachinery applications, the mass ratio is high, unlike in the field of wing aeroelastics. Thus, the assumption could then be made

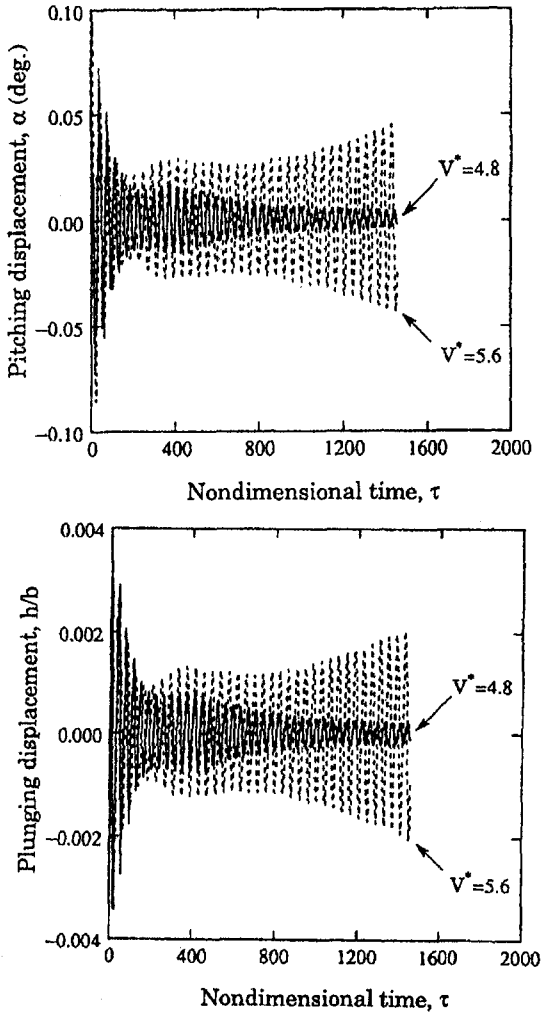

Fig. 39 Time domain solution, pitching, and plunging motion (Bakhle et al., 1992)

that the frequency at flutter is known. The same cannot be said in regard to the interblade phase angles. In general, the latter may assume any value as long as the condition of closure is met. Thus, in time domain analyses, the representation of the physical system is more realistic. Further the method is applicable to nonlinear structural and aerodynamic models. Extension to mistuning appears straightforward. However, CPU time needed by a time domain flutter approach is likely to be considerably larger than that for a linearized frequency domain approach. As a design-analysis tool, however, "the time domain approach may only be appropriate for use in situations where nonlinear effects may be important . . ." (Bakhle, 1996).

Flutter events observed in engine tests by Lubomski and discussed earlier have pointed to phenomena vastly more complicated than are currently modeled. As observed earlier and as shown in Figs. 27, 28, and 29, flutter phenomena may initially involve only a few passages, may include flow separation and is influenced by inlet conditions. These are but a few features that need to be included in advanced modeling efforts.

Furthermore, we need to pay attention to increased sensitivity of some blisk designs to flutter (Fig. 40, courtesy Allied Signal) and to determine structural and aerodynamic parameters that contribute to loss of damping in these designs.

Mistuning and Flutter. Alternate frequency mistuning in which a population of blades has two distinct frequencies, one of which is higher than the other, and is arranged alternately as high, low, high, etc., has been studied by several researchers. This is analytically an easy and interesting case to study and it provides insights into the behavior of mistuned systems. For example, a mode shape such as displayed in Fig. 41 (Srinivasan and Kurkov, 1981) is an indication of the influence of alternate frequency mistuning. Note how the amplitudes alternate between high and low and the interblade phase angle is almost, but not quite, a constant. This suggests a predominant harmonic on which another, a less predominant harmonic, rides. But a more important reason to study such a simple type of mistuning is that it may be viable in practice if analyses establish its potential to increase flutter velocities. Clearly this arrangement is one of many possibilities available to improve flutter characteristics. As will be observed later, the eventual arrangement may be influenced by the statistics of the large sample of blades, which can be used in building a particular rotor in a large fleet of engines.

As observed earlier, mistuning occurs due to *any* asymmetry around a rotor. This obviously includes parameters, such as gap/chord ratio, that influence unsteady aerodynamics of cascades. A study of such an aerodynamically detuned system was made by Hoyniak and Fleeter (1986). Results for a twelve-bladed rotor indicated a stabilizing influence, which depended strongly on the relative locations of the center of gravity and elastic axis of the airfoil. Clearly more research efforts are warranted before design procedures can be influenced.

The pattern of the locus of eigenvalues is not always as clear and well defined as that shown in Fig. 30. Small values of frequency mistuning appear to lead to a clear pattern, e.g., small alternate mistuning leads to a distortion of the pattern in which the locus develops a "waist." Further increase in the magnitude of mistuning breaks the locus into two distinct loci, as observed in Fig. 41 (Kielb and Kaza, 1983). This is because of the increase in the frequency difference between alternate blades, which tends to "split" the rotor into two distinct ones, each with its own characteristic locus. However, in realistic rotors (such as the one for which the performance map is shown in Fig. 42) in which frequencies have a general distribution such as shown in Fig. 43, the locus of eigenvalues loses clear and simple definition and assumes a somewhat erratic pattern as can be seen from Fig. 44. Equally general is the distribution of blade amplitudes around the rotor, a Fourier analysis of which shows the many harmonics (Fig. 45) present in a mode.

Resonant Response

The flow conditions of air drawn through fan stages of an engine and delivered to compressors generally vary in space and time at any engine stage. Similar conditions prevail in the turbine stages. Consider for now changes taking place in space only. Any such variation of flow parameters in the annulus at a given rotor stage is sensed by a rotating blade during each revolution; therefore, blades experience pressures, velocities, incidence, temperatures, etc., that vary periodically in time. Also, a blade may experience unsteady forcing due to other causes such as, for example, shocks moving in blade passages or the effect of shocks in the vicinity of the rotor stage up or downstream. In addition to the aerodynamic sources, mechanical sources of excitation due to blade rub, meshing of gear teeth, foreign object ingestion, etc., can all produce forces at frequencies that may lead to forced vibration in an individual blade mode or a system mode. Only the effects of aerodynamic stimuli are included in the discussion here. While every effort is made to avoid resonant conditions based on a Campbell diagram, experience has shown that it is simply impossible to do so for all resonances.

It is important to note that the changes referred to the above need not be uniform around the circumference and, further, as they approach blade rows and propagate through the machine, they experience additional changes dictated by the changes in geometry of stators and rotors, temperature, special features

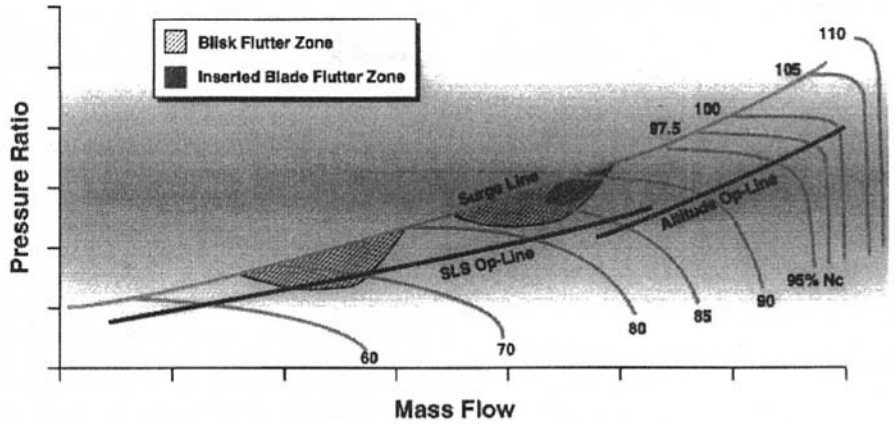

Fig. 40 Sensitivity of blisk design to flutter

such as bleed holes, aerodynamic losses, manifestation of shocks in passages, and a host of other conditions that prevail in an operating jet engine. In addition, unforeseen events such as, for example, a broken vane or seal, an errant probe, or nonuniform combustion around the annulus, all add to the nonuniformity mentioned above and contribute to the forcing functions acting on a blade. A glance at Fig. 46 (Ball, 1993) is enough to appreciate the flow conditions/complexities that prevail in a blade passage. The environment is inherently unsteady in that interactions take place between the aerodynamic forces on the one hand and the elastic and inertial forces on the other. The result is a complex dynamic process that leads to a variety of phenomena, including forced vibration and/or instability.

From the viewpoint of the structural dynamicist, the questions relate to an accurate estimate of aerodynamic forcing functions and determining the conditions under which the pattern of varying forces match any bladed-disk assembly vibratory modes both in time and space. It is this matching that leads to resonance and the resulting stress amplitude is controlled by damping due

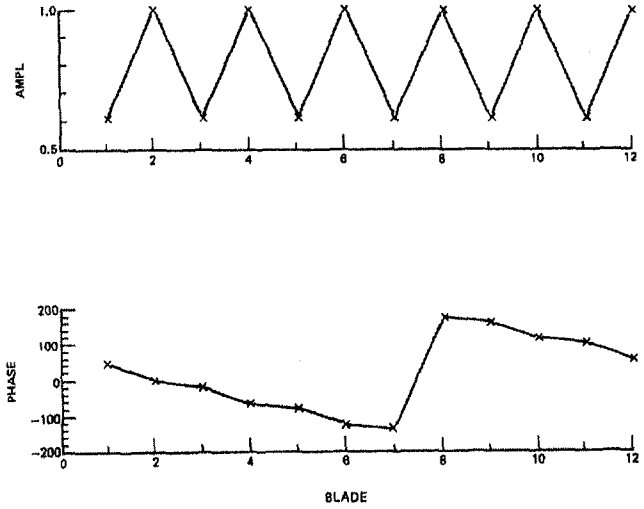

Fig. 41 Eigenvector for an alternately mistuned system

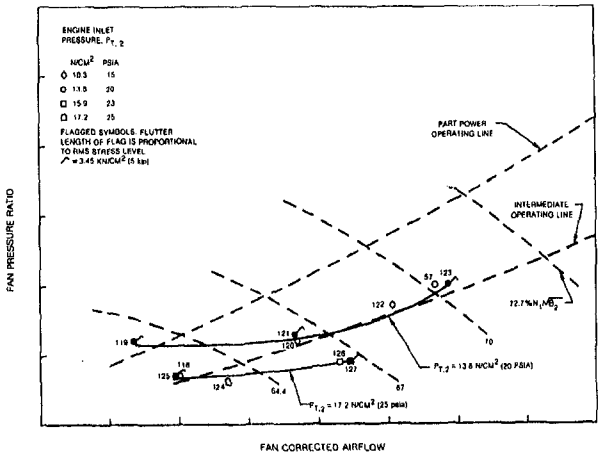

Fig. 42 Fan performance map

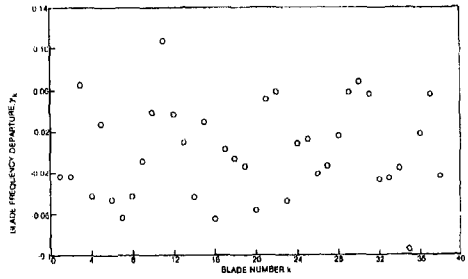

Fig. 43 Departure of individual frequencies from the mean

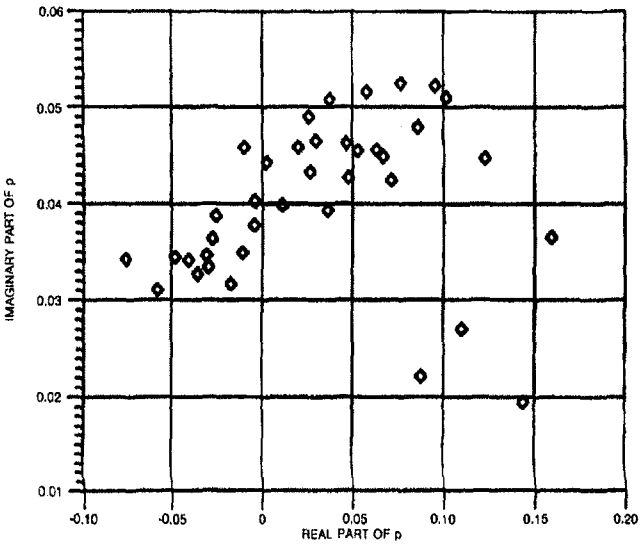

Fig. 44 Eigenvalues for conditions at Test Point 125 of Fig. 41

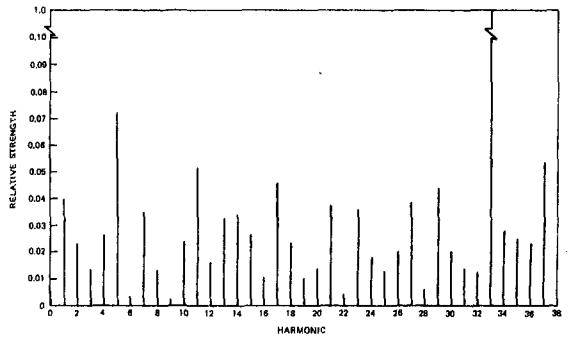

Fig. 45 Harmonics corresponding to the lowest eigenvalue in Fig. 43

to aerodynamic and structural sources. Therefore, the reliability of predicting resonant stresses depends upon the accuracy of prediction of aerodynamic forces, bladed-disk assembly modes and damping available in the system.

Some Incidents of Failure. Consider some of the failures that have occurred in recent years. Each of the cases cited here is unique, requiring unique solutions, which imposed severe demands on time and expenditure for the engine companies. One month after the development version of the F119 powerplant went to test in 1993, a severe high-pressure turbine blade problem appeared. The diagnosis of the problem is said to have taken 11 months. Shock waves, originating in the high-pressure turbine blades and reflected back from downstream low pressure turbine vanes, were suspected to be the cause of high cycle fatigue failures. The problem was resolved by changing the curvature of the vanes and increasing the number of vanes. Engine tests were conducted with the redesigned vane stage "for about 32 hours at 40 different speeds corresponding to 40 specific resonant frequencies" (Kandebo, 1994). At each speed, the blades were allowed to accumulate 10 million cycles at each frequency and showed an acceptably low level of stresses.

In another incident, about an hour into an engine endurance testing program, a JAS-39 Gripen production engine experienced an LPT blade failure, which was traced to "blockage in three fuel nozzles in the combustor liner of the engine, leading to incomplete combustion and a vibration problem" (*Flight International,* Feb. 2, 1994).

Yet another example pertains to a problem that plagued the T55-L-11 circa 1970 in Vietnam, which led to "a progressive failure of the power turbine second-stage rotor blades. The blades on this turbine stage were long and had interlocking blade tip shrouds, which in time wore out due to rubbing, thereby resulting in the blades becoming free standing. With the lack of blade support, a vibratory resonance occurred that eventually produced blade failure. At times sufficient torsional force was generated to tear loose the complete power turbine and shaft. The overspeeding turbine not only tore off the tailpipe, but it could pepper the aircraft with shrapnel. In addition, the power turbine second stage was located aft of the combustor and had only a light shield around it that was insufficient to withstand the ballistic force of a four inch long turbine blade. As a result, blades that failed went through the shroud and into the aircraft." (Leyes and Fleming, 1997).

Incidents of the type presented above, and many more that may have been reported or otherwise, simply point to the urgent need for a sound technological basis to resolve blade vibration problems due to forced vibration.

Aerodynamic Analyses. The analytical tools that are needed to estimate maximum stress levels are drawn from (*a*) aerodynamic analyses capable of calculating the magnitude and phase of forcing functions, (*b*) analyses to provide an estimate of aerodynamic damping, (*c*) analyses or test data to predict the magnitude of nonaerodynamic damping, and (*d*) structural analyses leading to the calculation of forced vibration response. As will be seen, a prediction system can combine (*b*) and (*c*), and use (*a*) and (*d*) to develop a set of governing equations of motion from which forced vibration response can be calculated. Thus, an accurate estimate of blade vibration amplitudes can be made and these can be used in calculating stresses and blade life.

Wakes and inlet distortions are mainly total pressure variations. Crosswinds, gusts, wakes from wings, pylons, nonuniform inlets, burner outputs, severe maneuvers during flight, etc., produce inlet distortions that are convected through the cascade. Wakes are usually trailing edge wakes coming from one or more upstream blade rows and may persist through several rows. Potential disturbances are variations in static pressure, which may originate either upstream or downstream. The flow defects from any of these sources lead to time-varying stimuli or forcing functions. Some analyses assume that these defects are "frozen" and therefore do not consider inevitable changes, especially for cascades experiencing higher loads. Clearly such restrictive assumptions influence our ability to develop a reliable resonant stress prediction system. The challenge and the need to calculate accurately these unsteady aerodynamic forces, due to all sources of excitation referred to earlier, cannot be overemphasized. Similar challenges lie in the areas of accurate structural analyses including the estimation of system damping.

Some improvements have occurred in modeling both structural and aerodynamic aspects. Forced vibration and flutter analyses in the decades of the '70s and '80s modeled a blade section as a typical section encompassing a bending and torsional spring. The ease with which ideas can be tested in analysis of typical sections continues to make this a popular choice at least in the initial stages. Later investigations have used finite element

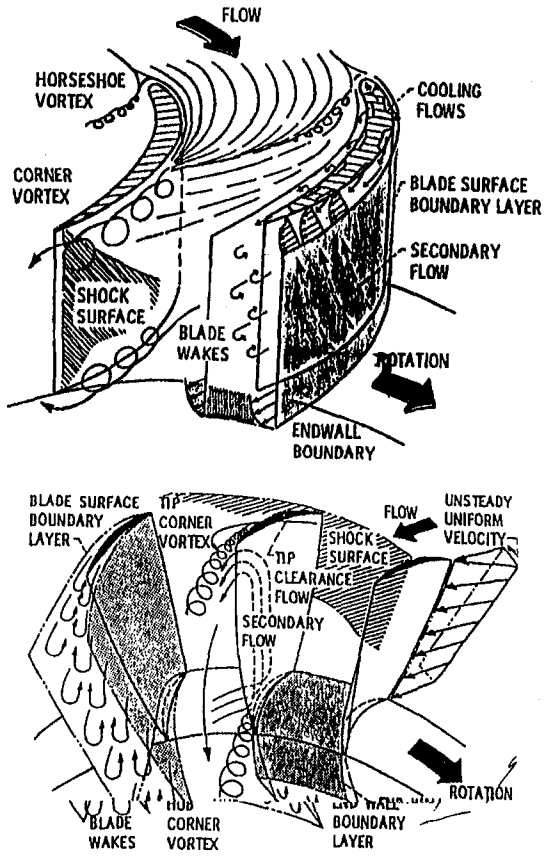

Fig. 46 Flow conditions in compressor and turbine cascades (Ball, 1993)

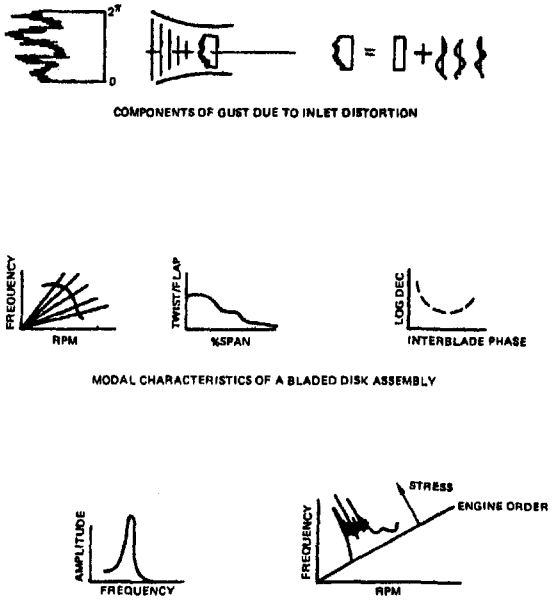

Fig. 47 Schematic of design analysis

analyses, notably NASTRAN, to calculate mode shapes for realistic blade profiles. Such mode shapes generally include displacements and rotations at each mesh point. Thus, forced vibration and flutter analyses have been carried out by using motion along and perpendicular to the chord using corresponding unsteady pressures (Srinivasan and Fabunmi, 1984; Forsching, 1994). Unsteady aerodynamic capability is crucial to successful prediction of either flutter or resonance, and design tools properly calibrated with experimental and engine experience are a must if we are to reduce risks of failure and improve structural integrity of rotor stages.

Assuming that these developments continue and provide the required tools, a procedure to assess blade life can be presented schematically as shown in Fig. 47. The starting point is a distortion pattern at a location, as shown in Fig. 47. At the top of the figure is a schematic of how such a distortion may look at a selected radius along the blade span and the manner in which it "deforms" as it approaches the rotor of interest. The modified distortion pattern can be separated into its harmonics, and the remaining steps lead to calculation of stresses at various selected locations on blades. A sum of such stresses, due to the harmonics of interest, is the desired stress at a given speed. But, it is likely that the only harmonic of interest at an integral order is the one corresponding to the specified engine order.

A systematic study to calculate forced response levels in a fan and a turbine and compare results with corresponding measured data was reported by Chiang and Kielb (1993). Flow defects due to wake disturbances were modeled with a "semi-empirical rotor wake/vortex model" from Majjigi and Gliebe (1984) and "measured data for inlet distortion and a quasi-3D Euler code" due to Holmes et al. (1988) to represent pressure disturbances. Several references are cited in the paper and may be studied to examine how wake data, empirical models, and CFD approaches have been used by several researchers to compute forcing functions. Based on measurements, Manwaring and Wisler (1993) caution that "blading with very large wake defects may require nonlinear analysis," while "linear analysis methods, in which the unsteady part of the flow is linearized about a steady, nonlinear flow, yield reasonably accurate predictions of the unsteady loading in many turbomachinery applications."

A Simplified Calculation Procedure. An appreciation of the physics involved in calculating amplitudes of forced vibration can be obtained by equating W_G, work done by gust forces (forces induced, for example, due to inlet distortion) to W_A, the work done by aerodynamic damping forces.

$$W_G = \int (C_g G e^{i\theta}) A\phi(x)\,dx$$

$$W_A = \int (C_D A\phi) A\phi(x)\,dx$$

$$W_G = W_A$$

$$A/G = \int C_G e^{i\phi}\phi(x)\,dx \Big/ \int C_D\phi^2\,dx$$

where C_gG is the aerodynamic force, due, for example, to a distortion in the flow. A is amplitude of vibration, $\phi(x)$ is the blade mode shape, C_DA is the aeroelastic force induced due to blade vibration, and θ is the phase angle between the forcing function and blade motion. To insure a maximum, we check the following:

$$\partial/\partial\theta(A/G) = 0 \quad \text{and} \quad \partial^2/\partial\theta^2(A/G) < 0.$$

Thus the work done by aerodynamic forces is proportional to the amplitude, whereas the work done by damping forces is proportional to the square of the amplitude. The procedure currently used industry-wide is a modal approach leading to the solution of a matrix equation, as discussed in the section on flutter.

Mistuning and Resonant Response. The vibration characteristics of real bladed-disk assemblies include effects of mistuning. A direct consequence of this nonuniformity is that analyses can no longer assume cyclic symmetry. Further, lack of symmetry leads to the so-called frequency splitting and double modes for each circumferential mode. Thus, a mode such as a 2 nodal diameter pattern around an assembly can occur at two closely spaced frequencies. The extent of the spread between the two frequencies depends upon the level of mistuning. At the first frequency, the nodal lines correspond to the antinodes at the second frequency. In any case, the effect of such double modes is to "crowd" the Campbell diagram, as is evident in Fig. 11 (Pfeiffer, 1985).

A cursory glance at the Campbell diagram shows so many intersections between frequency–speed characteristics and the engine order lines that resonant conditions with some mode at some speed are entirely possible. The only way one could determine if a particular resonant condition is dangerous is through an estimate of the stress level. Designing the rotor to operate safely through such resonances is to assure that there is damping available in the aeroelastic system, sufficient to keep the stress levels to an acceptable minimum. Such an assurance cannot always be given, especially for low-order resonances. The current design practice is to keep the first bending mode above 1E or 2E at top speed and to separate the first torsion and second bending modes.

Influencing Parameters. Some comments in regard to parameters that influence the behavior of mistuned systems are in order here. Clearly, the extent of mistuning, i.e., the departure of individual frequencies from a reference frequency, such as, for example, an arithmetic mean frequency, is an obvious measure. Measured or calculated values of "blade alone" frequencies are used. Measurement implies a laboratory setup, which must assure a fixed boundary condition at the blade root, which needs to be identical for tests conducted on each blade; not an easy task. These "static frequencies" are then corrected to account for the rotor speed at which resonant stress calculations are desired. With this measure, a parameter could be defined that accounts for the coupling among blades arising through shrouds, disks, and aerodynamics. If we were to assume that mechanical coupling is uniform around the rotor, then the ratio

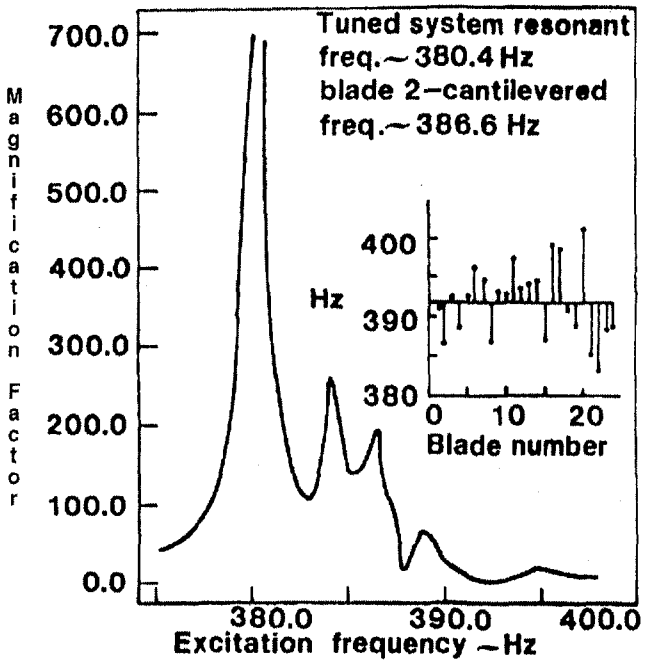

Fig. 48 Response of a mistuned system (Ewins, 1969)

of the mean frequency and the frequency of the tuned coupled system can serve as a parameter. Depending on the nature of the mechanical coupling, i.e., shrouds and/or disks, the coupled system frequencies could either be higher or lower than the nominal frequency. Other structural parameters may include the number of blades, mode shapes, and damping.

Principal Features. One consequence of mistuning is an uneven distribution of vibratory energy among all blades of a rotor. As discussed earlier, the mode shape pattern may be so erratic that it defies a definition of a predominant harmonic. An interesting way of displaying the effects of mistuning is shown in Fig. 13 (Ottarsson and Pierre, 1995). For a 30-bladed tuned system, note how the modal patterns involve similar forward ($n = 3$) and backward ($n = 27$) traveling waves. However, when the system is mistuned, note the thoroughly dissimilar distribution of amplitudes with no obvious pattern. This poses an immediate problem to test engineers who have to determine the blades to be gaged in a rig or engine test program. The amplitude of vibration of a blade depends upon its own characteristics, as well as its location around the rotor. The result is that some blades experience amplitudes far larger than the rest. For example, the response of a particular blade in a mistuned system shown in Fig. 48 contains several peaks over the frequency range shown. This is unlike a single peak the blade would experience had it been part of a tuned assembly. In a rig test of a compressor rotor, three neighboring blades, whose natural frequencies were about 9 and 24 percent higher than the lowest frequency, were arranged in order of high, higher, and low frequency around the rotor. Under aerodynamic excitation at 140 Hz, the neighboring blades experienced highly uneven stresses that varied as $4x$, x, and $10x$, respectively, where x is the lowest stress measured in the three blades (Fig. 49). The frequency spread noted above in the rig tests is not typical of compressor rotors.

Early Efforts. Experience in the past three decades with engines and rigs has brought out convincing evidence that blades mounted on a rotor do not have identical vibratory characteristics, i.e., the frequencies of individual blades (and perhaps mode shapes, and damping values) may be slightly different from each other. The result is that blade response to aerodynamic stimuli is not identical either, so that a mistuned system has multiple resonances and a distinct scatter is noticed in blade amplitude and phase, even when the stimulus is regular, i.e., of a given order. This was established through the pioneering efforts of Whitehead (1965, 1966). The rationale for including this phenomenon in design considerations is that engine blades are likely to wear nonuniformly in service in any case, due to a variety of reasons, even if all the blades on a given rotor were identical to start with. Thus, the questions that are being asked are not in regard to the validity of the phenomenon but more in regard to the extent or level of mistuning present or anticipated.

A focus of research in the '70s was on understanding the dynamics of mistuned bladed-disk assemblies and establishing the validity of the phenomenon of mistuning. It appears that the development of new engines at about the same time industry-wide provided the impetus to examine this phenomenon as a possible source of blade failures that could not be explained otherwise. It became clear that small departures in individual frequencies from a datum frequency could result in unacceptable levels of vibration in some blades on rotors subjected to forced vibration and fatigue failure. This led to development of a reliable calculation procedure to estimate the extent of escalation in blade stresses with respect to the corresponding tuned system. Data from laboratory testing, rigs, and engines were used to calibrate analyses to further help acceptance of the analyses by the design community. The results of one such effort are illustrated in Figs. 50, 51, and 52 and represent calculations for the first turbine rotor of an advanced engine. The analysis that served as the basis of this calibration has been published (El-Bayoumy and Srinivasan, 1975).

Statistical Approaches. Although the levels of increased stresses due to mistuning predicted by different investigators varied over a wide range (21 to upward of 200 percent), each group of researchers appears to have rationalized their findings on the basis of modeling preferences. While it was generally agreed that mistuning was not desirable from a forced vibration point of view, it was clear that it was inevitable. More importantly, it was found that certain types and levels of mistuning could indeed enhance aeroelastic stability of rotors. Research efforts continue to determine ways in which this feature could be exploited in practice to address flutter susceptibilities of rotors. While procedures were established to determine the extent of vulnerability of some blades on a rotor for a given distribution of a parameter such as blade frequency, the basic question remained in regard to changes that might occur over time in that distribution as the rotor went into service. Any distribution, no matter how carefully measured, cannot be expected to remain the same and will change in some unknown manner. Further, it was simply too costly to discard blades merely because their fundamental frequency was a certain percentage off the recommended margin. Also, the phenomenon raised serious questions in regard to the selection of blades for gaging in order to be certain that the absolute maximum escalation in stress is in fact measured. For all these and other reasons, the need to develop an approach on the basis of statistics became clear.

The obvious limitation was the deterministic nature of the analyses and therefore statistical approaches that recognize the random nature of these changes were sought. Research efforts in the 1980s and 1990s have concentrated on this aspect of mistuning. The earliest attempt in this direction was aimed at obtaining "an estimate of expected time of failure of an assembly of 24 blades under excitation by a stationary Gaussian white noise process" (Sogliero and Srinivasan, 1980). The estimate was based on generating 240 numbers from a table of normal random variables and multiplying each with a standard deviation and adding the mean blade frequency. The resulting histograms for each standard deviation are shown in Fig. 53. Thus, from each population ten bladed-disk assemblies could be de-

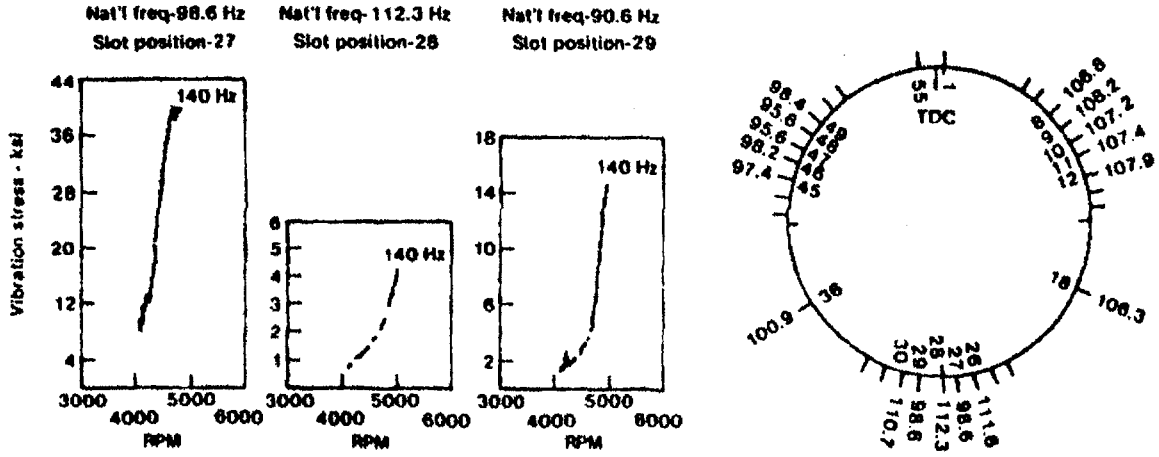

Fig. 49 Compressor rig test data

fined. Blade amplitudes (and stresses) were calculated using the dynamic system modeled (Fig. 54) in the publication referred to above. Using the Palmgren–Miner hypothesis, the expected time to failure was calculated. The shortest time to failure is noted for each assembly leading to ten points shown on the Weibull plots of Figs. 55 and 56 for the ten assemblies. The expected life is seen to increase a thousandfold when the damping ratio is doubled.

The efforts in the mid 1980s and early 1990s continued in academia to develop a statistical basis for analysis of mistuned assemblies (Basu and Griffin, 1986; Griffin, 1988; Griffin and Sinha, 1985; Huang, 1982; Sinha, 1986; Sinha and Chen, 1988, 1989). At the same time an additional focus of research was aimed at studying the underlying mathematics by defining the

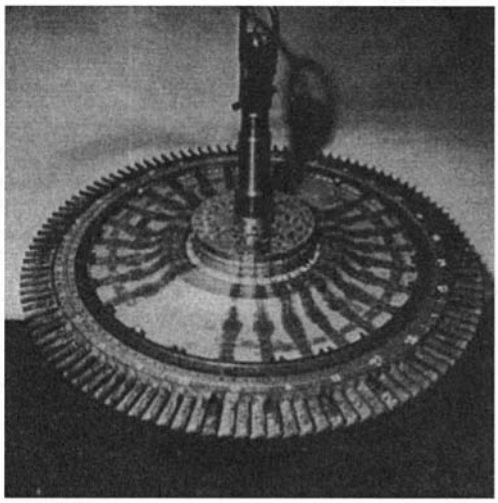

Fig. 50 A first turbine rotor

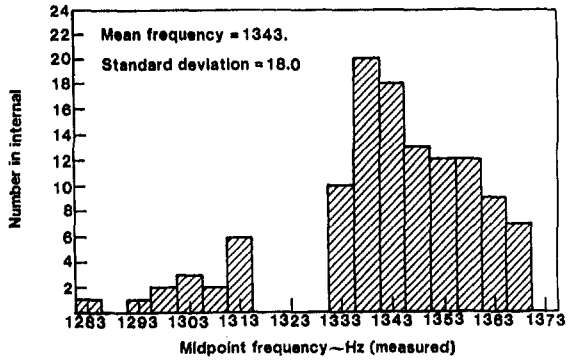

Fig. 51 Histogram of turbine blade frequencies

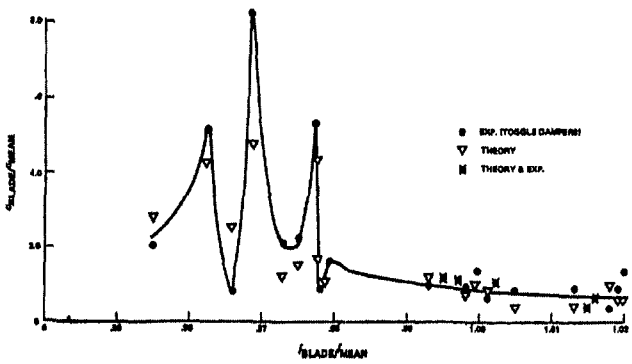

Fig. 52 Response of mistuned 1T blades

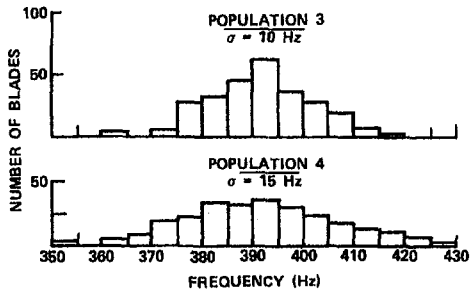

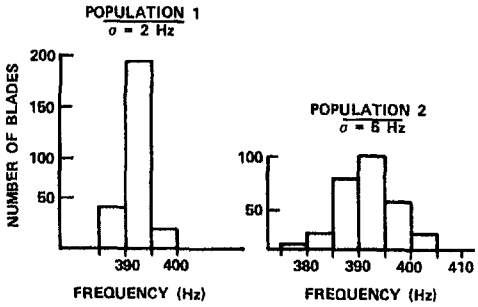

Fig. 53 Histograms of blade populations (Sogliero and Srinivasan, 1980)

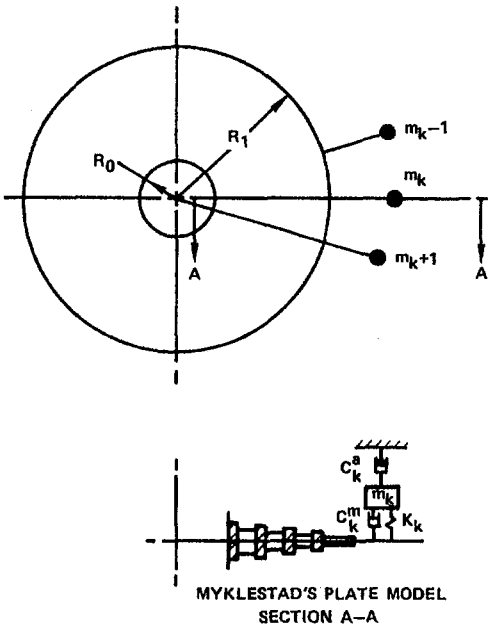

Fig. 54 Dynamic model of mistuned rotor

DAMPING RATIO = 0.001	WEIBULL ESTIMATES	
BLADE FREQUENCY POPULATION	$\hat{\eta}$	$\hat{\beta}$
▲ N (391.8 Hz, 2 Hz)	35.5	1.63
◆ N (391.8 Hz, 5 Hz)	130.0	1.08
● N (391.8 Hz, 10 Hz)	13900	0.44
■ N (391.8 Hz, 15 Hz)	72819	0.47

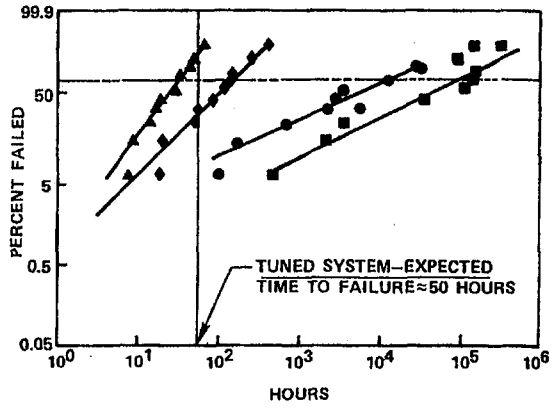

Fig. 55 Time to failure of mistuned blades, damping ratio = 0.001

DAMPING RATIO = 0.002	WEIBULL ESTIMATES	
BLADE FREQUENCY POPULATION	$\hat{\eta}$	$\hat{\beta}$
▲ N(391.8 Hz, 2Hz)	32974	1.95
◆ N(391.8 Hz, 5Hz)	77524	1.34
● N(391.8 Hz, 10Hz)	5673303	0.47
■ H(391.8 Hz, 15Hz)	38031005	0.49

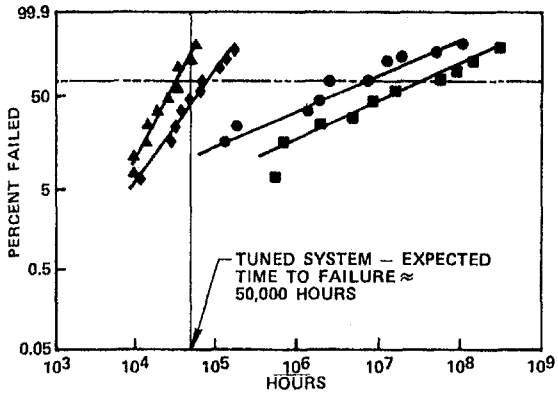

Fig. 56 Time to failure of mistuned blades, damping ratio = 0.002

area as a multiparameter perturbation problem of disordered systems (Wei and Pierre, 1988a, b, 1990; Ottarsson et al., 1994; Ottarsson and Pierre, 1993, 1995; Mignolet and Christensen, 1990; Mignolet and Lin, 1993, 1997). Thus the questions pertinent to the analysis of perturbed systems appeared to take hold. For example, it was obvious that modeling mistuned systems in the context of perturbation mathematics required a base system about which the influence of a small perturbation parameter could be studied. It was argued that strong coupling among blades meant that the small frequency departures from a reference frequency could serve as the required parameter. Thus, the tuned system would serve as the base system to be perturbed. However, if the coupling is weak, then the base system would be the coupled mistuned system itself and perturbation would be examined with the small coupling as the obvious parameter. This of course leaves the middle range somewhat unclear. In this intermediate range the recommendation was to use "Monte Carlo simulations . . . as none of the perturbation schemes yields satisfactory results" (Wei and Pierre, 1990). This limitation appears to have been successfully removed by Mignolet et al. (Lin and Mignolet, 1997).

The new perspectives and formulations have yet to mature to address the critical questions in regard to design guidelines, high cycle fatigue life, blades that need to be instrumented, etc., but they have successfully articulated the influences of key parameters. For example, it was concluded that weakly coupled mistuned systems may experience larger stresses than their counterpart. With a Monte Carlo simulation of a 12-bladed assembly Ottarsson and Pierre (1993) demonstrated the influence of coupling as shown in Fig. 57. With reference to the figure, they state, "Of great importance is the curve labeled 99%. The values on this curve denote the mistuning-induced amplification of maximum response that will only be surpassed

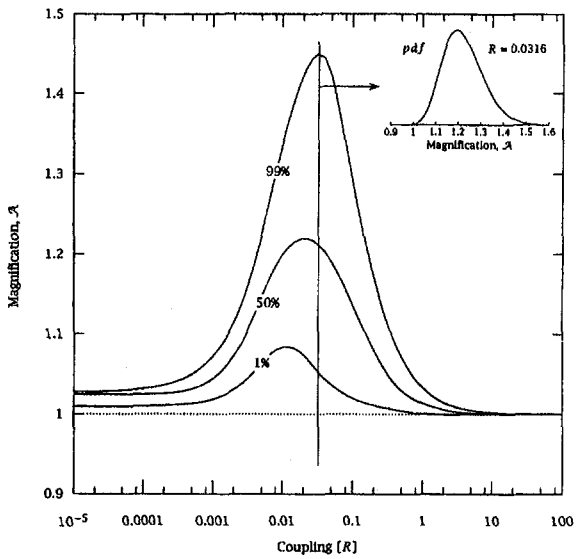

Fig. 57 Influence of coupling on mistuned systems (Ottarsson and Pierre, 1995)

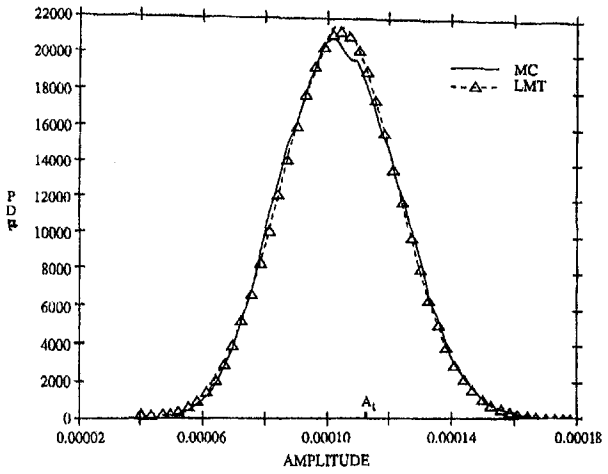

Fig. 58 Correlation of MC simulations with LMT (Mignolet and Lin, 1997)

by 1% of all realizations of mistuned systems. We will say that when this value deviates greatly from unity, mistuning effects are high. From the 1% curve we see that a 12-bladed assembly will almost certainly experience larger amplitudes than the tuned system since the curve is above $\lambda = 1$ throughout nearly the entire range of coupling." From the figure, it is also obvious that the amplification factors are no larger than 1 for strong coupling and greater than 1 for small values of coupling. In regard to the number of blades on a rotor, it was concluded that the larger the number of blades, the greater the influence of mistuning. The influence of standard deviation of frequencies in a population of blades was shown to be a linear increase in the largest amplitude up to a certain value, 0.1 percent in the example studied by Wei and Pierre (1990), and then a rapid decrease with increased standard deviation. However, more recent research results obtained by Mignolet (1996) show the percent increase to be closer to 1 percent.

These studies have made it clear that Monte Carlo approaches to simulate mistuned rotors may "require thousands of realizations, which is a monumental task unless the number of degrees of freedom per realization is kept within reason." In many cases, this may limit the number of degrees of freedom per sector to be less than ten (Ottarson and Pierre, 1993). However, the recent introduction of an adaptive perturbation scheme (Lin and Mignolet, 1997) allows a substantial reduction in computing time without compromising the accuracy of results. A reduction in CPU time of more than an order of magnitude has been shown to be possible with this new approach. This development allows Monte Carlo simulations to remain as popular tools for comparison purposes.

Further analyses of bladed-disk assemblies in this context have proceeded on the basis of Monte Carlo simulations (MC) in the order of 100,000 or so. In view of the large computational effort associated with these simulations, alternate approaches have used perturbation schemes aimed at developing simple closed-form probabilistic models of the random forced response of bladed disks, from which fatigue life can be estimated. Central to these analyses is a probability density function (p.d.f.) that quantifies the probability that, for a given population of blades (with known statistics in regard to the distribution of one or more parameters), the amplitude of vibration of blades exceeds a certain prescribed threshold. An excellent correlation with simulation results has recently been obtained (Fig. 58) by one such approach based on a limit distribution (LMT) (Mignolet and Lin, 1997). These results appear to be quite promising and with further validation with more advanced dynamic models, the approach can be accepted and applied in practice.

High Cycle Fatigue. In the past, a primary design consideration for bladed-disk assemblies was low cycle fatigue. The data base developed over the past three decades has served well in bringing LCF-related failures under control. However, the changes that have occurred during this period in the design and development of blades and disks have led to failures due to high cycle fatigue. The problem looms large at the present time and the attempted fixes have been very expensive. The U.S. Air Force estimates an expenditure of about $100 million/year to inspect and fix high cycle fatigue related problems. Roughly two-thirds of these problems are judged to be unexpected. There is an overwhelming acceptance within the concerned community that a rational basis needs to be developed to address this serious problem. Similarly, there is an appreciation of the role of mistuning in high cycle fatigue failures. Since the influence of mistuning is inevitable, serious consideration is given industry-wide to examine whether the phenomenon could be exploited in design to minimize vibratory failures through deliberate mistuning of blades.

An additional feature that needs to be considered in high cycle fatigue is the transient response of blades during run-up or run-down of machines. Recent efforts by Irretier (1997) include considerations of parabolic changes in the natural frequencies due to centrifugal field as well as nonlinear damping effects due to friction.

A good discussion of approaches to mitigate a variety of stress problems due to forced vibration is provided by Cardinale et al. (1980). Failure due to resonance at lower modes, such as first bending or torsion, may include fracture of an entire blade and its attachment. Such a failure may cause large unbalance and severe secondary damage. The damage could be even greater if the blade is not contained. At higher modes, such as second torsion or second or third bending, only an outer portion of a blade may fracture, causing some unbalance and significant secondary damage. At even higher modes, only a portion of the tip may break off, causing minimal damage.

Forced vibration problems can be resolved by redesign aimed at modifying (*a*) the vulnerable frequencies, (*b*) the stimuli, or (*c*) damping potential. Clearly, frequency modification can be obtained by changes in geometry (taper, shrouds, aspect ratio, hub tip ratio, etc.). Control of stimuli will depend on identification of the sources and may require changes in the number of vanes and/or blades, solidity, modification of vane schedule, altering the magnitude of distortion by, for example, changing spacing of the source location, bleed ports, etc. Additional damping may be obtained by means of designing dampers such as platform or blade to blade dampers. Finally, estimates of blade life based on a proven statistical basis can serve the design community to enhance the structural integrity of jet engine blades.

Before concluding this section, it is necessary to acknowledge the insight of Danforth who, back in 1967, recognized the critical aspect of fatigue of engine components when he warned "suppression of vibratory fatigue is the design challenge." It has taken the community nearly 30 long years to begin to look at this problem with the seriousness it deserves. Danforth emphasized the challenge by observing that, in his experience, the common denominator of nearly 70 percent of all engine component failures was fatigue. Further, he notes that fatigue life definition requires a "statistical treatment: for material fatigue strength, aerodynamic oscillatory excitation forces, parts manufacturing, assembly, and resulting steady-state and vibratory stress response . . .". A summary of his recommendations, given below, is as valid today as it was in 1967! He suggested that parts can be made insensitive to fatigue by refining geometric details to avoid stress concentrations, conducting heavily instrumented tests to verify design intent, and establishing allowable stresses based on interactions between steady and vibratory stresses. He further emphasized the need to capitalize on the feedback from the ultimate test facility of actual service.

No better recommendation can be made than to urge that we now pay close attention to these recommendations in developing a superior product with the intended structural integrity.

Nonaerodynamic Damping of Engine Blades

Material Damping. As observed earlier, escalation of stresses due to flutter can be minimized only if there is adequate damping in the system. System damping is the sum of available aerodynamic damping and mechanical damping. The contribution to the latter can come from material as well as through any rubbing action at interfaces. Similarly, stresses due to resonance are minimized by damping and the resulting amplitudes are used in the calculation of blade fatigue life. For the materials currently in use for manufacturing blades (titanium-based and nickel-based alloys), contribution to material damping is essentially negligible. Loss factors (η defined below) measured for a fan blade of titanium alloy (8-1-1) were as low as 0.0003 in first and second bending modes and even lower in the torsion mode (0.0001). These tests were conducted on a single blade in vacuum with the root welded to a "massive block" to eliminate any damping at the root structure. In fact, resonance sweep tests on the blade could not be conducted in vacuum because of the very low damping. Data could be obtained only by a gradual increase of vacuum conditions up to a certain limit and an estimate of material damping could be obtained by projecting the data. These tests are fully described in the report to NASA (Srinivasan et al., 1981) and may be referred to for additional details. The contribution from material damping is therefore generally neglected, but the situation may change with the introduction of new and different materials in the future.

Different researchers use different measures to report damping and the relationship among them is listed below for convenience. Let Δf = differences in frequencies on either side of a natural frequency at half-power points, δ = log decrement, ζ = ratio of damping coefficient to critical damping coefficient, and Q = amplitude factor. Then we can show that

$$\eta = \Delta f/f_n = \delta/\pi = 2\zeta = 1/Q.$$

Damping Due to Dynamic Friction. When engine blades manufactured with high-strength materials with low inherent damping operate in environments offering low positive or negative aerodynamic damping, the ability of the rotor to withstand vibratory stress due to resonance or flutter depends almost entirely on the extent of damping due to friction at rubbing interfaces. The interfaces of particular interest to us are shown in Figs. 14 and 59 (Cardinale et al., 1980) and include shroud contacts typical of part-span-shrouded fan blades and platform type dampers, which are designed to minimize vibratory amplitudes of turbine blades. The prevailing mechanism is one of dynamic friction at the interfaces, and certain relevant characteristics of the phenomenon are discussed below.

The phenomenon of friction between contacting surfaces is an elusive physical mechanism that defies clear comprehension. The complexity of friction damping arises from variations in the type of time-dependent motions developing at an interface. These variations in the relative motion at the contacting surfaces span the extremes between microslip and gross motion and include local slip, stick-slip motion, chatter, etc. The parameters that control the resulting motion include surface characteristics, normal forces holding the surfaces together and their distribution, properties of materials in contact, surface treatments, temperature, frequency of vibration, and coefficient of dynamic friction. It is assumed that a sublayer of decreased resistance is formed at the interface between rubbing components. One speaks of dry friction forces when the sublayer is in a solid phase. The phenomenon is clearly nonlinear and the feasibility of linearization needs to be established in each application.

In the context of vibration engineering, the basic requirements are to (a) quantify the nature and magnitude of vibratory motion at these interfaces, (b) quantify the nature and magnitude of friction forces that are manifested between contacting interfaces of vibrating components, and (c) predict the extent of damping that may be present. Clearly (a) and (b) are interdependent. Within the present context, friction forces are considered to be useful, i.e., they control vibratory amplitudes, which otherwise may escalate. On the other hand, any consideration of friction forces cannot ignore the influence of these forces on wear of the components, resulting in loss of useful life of machines. The phenomena of friction and wear are thus inseparable.

Early Efforts. An excellent treatment of the science of friction and wear is found in *Friction and Wear: Calculation Methods* (1982) by the Russian authors Kragelsky, Dobychin, and Kombalov. The chapter on "Dry and Boundary Friction" should be of special interest to researchers in this field and has an excellent treatment of the subject beginning as far back as 1508, when Leonardo da Vinci established the simple law of friction, which assumed the friction force to be proportional to the normal load. Researchers should also find the three volumes of the book *Friction, Wear, Lubrication* (1981), edited by Kragelsky and Alisin, interesting. Another book, also by Russian authors Panovko and Gubanova, entitled *Stability and Oscillation of Elastic Systems* (1965) treats the subject of self-induced oscillations with dry friction. In addition, the proceedings volume of a NASA-sponsored symposium on "Interdisciplinary Approach to Friction and Wear" edited by Ku (1968) contains material that covers the several aspects of surface topography, friction, adhesion, wear, etc. Another source of reference on this interdisciplinary topic is a paper by Oden and Pires (1983), which provides a thorough discussion of the physical aspects of dynamic friction and points to the need to include the deformability of interfaces in the normal direction. These books and reports, along with the papers that will be referred to in the sections below, have served as the basis for the viewpoints presented here. Because of the interdisciplinary nature of the subject matter, no claim will be made that all the relevant literature has been surveyed here.

Interface Characteristics. Surfaces of real components used in engineering practice are never ideally smooth, so that when they come into contact with each other, the contact cannot be continuous and only certain parts of the surfaces will carry the applied load. Thus, the true contact area is the sum of those parts of the surfaces where the interaction between the bodies is strong. The true contact area is the result of penetration or crushing of individual asperities and, therefore, the contact area increases with increasing deformation.

Mechanical deformation at an interface occurs due to either penetration of surfaces with ploughing or continuous formation and rupture of welds. All these processes are influenced by the environment. As observed by Kragelsky et al. (1982), "In spite of the complex nature of mechanical, physical, and chemical processes involved, it is still possible to pinpoint certain principles which are common to all friction and wear processes." They are outlined below:

1 The contact between solids occurs at discrete points because of surface roughness.
2 Increase in load leads to increase in contact area due to increase in number of contact points. Therefore, the real pressure at any point increases only slightly.
3 Tangential resistances are additive. Dissipation of energy in the formation and rupture of an individual frictional bond is determined by the resistance in overcoming molecular interaction at points of contact, and the mechanical ploughing effects.
4 Three interconnected processes occur simultaneously in sliding contact: (a) interaction of the surfaces, (b) changes in the surface layers and films, and (c) rupture of the surface layer.

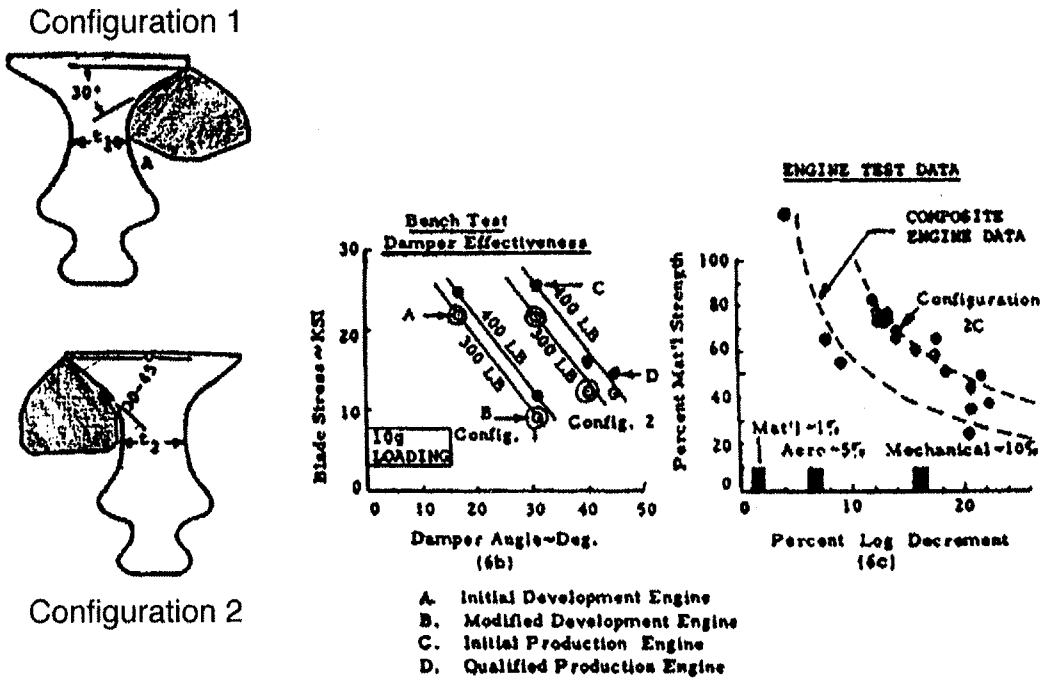

Fig. 59 Bench test optimization of blade damper (Cardinale et al., 1980)

5 Surface sliding requires formation and rupture of a thin layer (weakened layer of base material or films) whose shear strength must be less than the shear strength of the substrate.

Modeling Friction Forces. The simple law of friction established by Leonardo da Vinci assumed the friction force to be proportional to the normal load acting on the interface. The apparent simplicity of this relationship has been the primary reason for its use in most studies of dry friction. However, in addition to the problem of obtaining a reliable estimate of the constant of proportionality, i.e., the coefficient of friction μ, the representation $F = \mu N$ leads to computational complications even when applied to the study of a single-degree-of-freedom system, as shown by Den Hartog (1931). Oden and Pires (1983) have discussed the mathematical and physical difficulties associated with such a representation. Nevertheless, a substantial number of attempts have been made and continue to be made to use modifications of this basic model (Jacobsen, 1930; Zhuralev, 1940; Pian, 1957; Goodman, 1960; Bowden and Tabor, 1964; Greenwood and Williamson, 1964; Yeh, 1966; Earles and Williams, 1972; Mayer and Mowbray, 1975; Annigeri, 1976; Antoniou et al., 1976; Bielawa, 1977; Griffin, 1980; Rimkunas and Frye, 1979; Pratt and Williams, 1981; Srinivasan et al., 1981; Beards, 1981; Srinivasan and Cassenti, 1986). Such modifications are adaptations of the basic model to the analysis of particular components under study. More advanced modifications have been attempted recently and show promise of more accurate representation of friction forces at interfaces (Sanliturk and Ewins, 1996; Menq et al., 1991; Griffin and Menq, 1991).

Coefficient of Friction. An accurate estimate of friction forces induced at interfaces in relative vibratory motion depends on the accuracy with which the coefficient of sliding friction can be estimated. Srinivasan et al. (1981) attempted to measure the coefficient of friction for titanium alloy bars coated with tungsten carbide. The results showed that while variations occurred with respect to normal load, frequency of excitation and velocity, no obvious correlation with any of the variables was evident. This raises serious questions in regard to functional representation of forces of friction.

Additional Influencing Parameters. An important consideration in modeling friction forces is including the possibility of the rise and fall of the interfaces as the contacting bodies move along the asperities in the contacting planes (Fig. 60) (Srinivasan and Cassenti, 1986).

In a similar manner, the motion at an interface in the plane of contact can be two dimensional and the nature of this biaxial

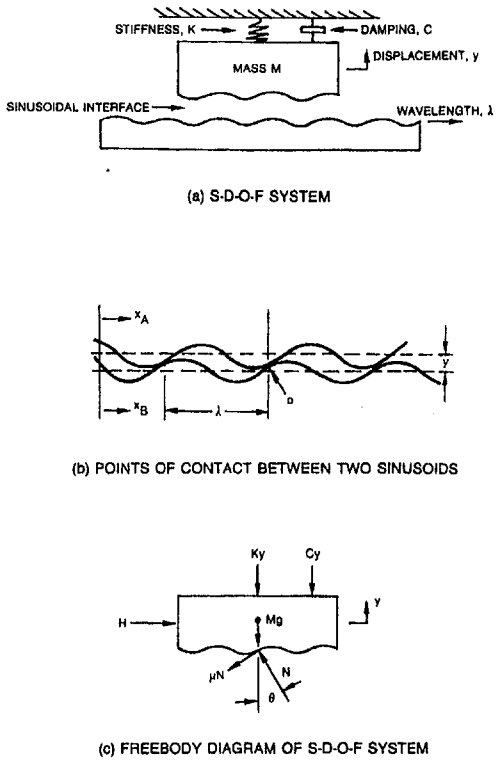

Fig. 60 Vertical degree of freedom and friction (Srinivasan and Cassenti, 1986)

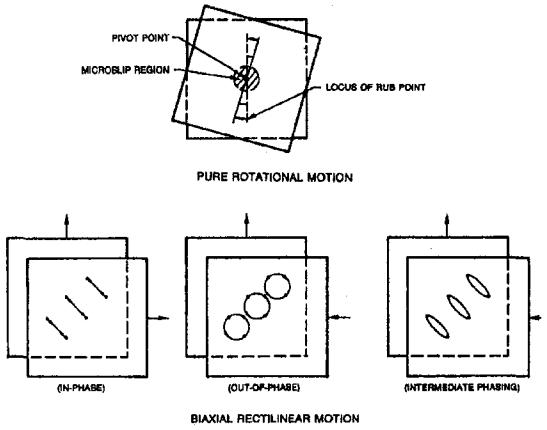

Fig. 61 Biaxial motion and friction (Srinivasan and Cassenti, 1986)

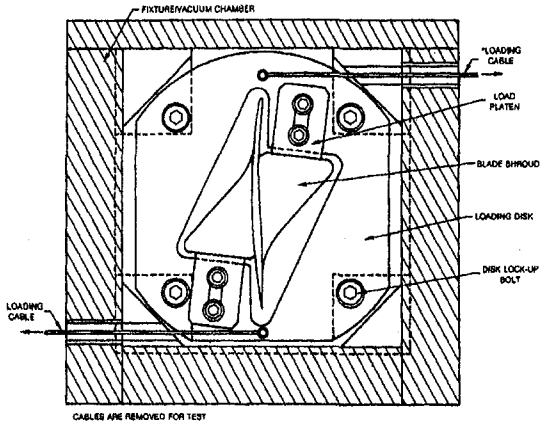

Fig. 62 Shroud loading device for investigation of fan blade shroud damping mechanism (Srinivasan et al., 1981)

motion can be one of the types shown in Fig. 61. These motions are indeed the type of motions typical of vibratory displacements at shroud interfaces. Recently, Menq et al. (1991) and Sanliturk and Ewins (1996) have developed analyses that model the types of two-dimensional motions represented in Fig. 61.

Damping Due to Rubbing at Shroud Interfaces. In the case of part-span shrouded blades, untwisting of the blades under centrifugal pull brings neighboring blades into contact at the shrouds. Determination of the precise nature of conditions at such an interface continues to be an unresolved problem defying both analysis and measurement. Major parameters that control the nature and extent of friction damping at the shroud to shroud interface are: centrifugal loading, roughness of surfaces, level of external excitation, shroud location on the blade, blade geometry, and shroud geometry. Details of a variety of analytical approaches to model shroud damping may be obtained from several publications referred to above. Highlights of two test programs will be presented below (Srinivasan and Kurkov, 1981; Srinivasan and Cutts, 1983a, b). First, the results of tests performed on a single fan blade to measure damping due to rubbing motion at shroud interfaces are discussed. Next, the discussion pertains to measurement of shroud motion at ten interfaces of a fan assembly. These tests are considered unique and it is believed that the measured data are useful in our continuing efforts to model damping at shroud interfaces.

The fan blade used in these tests was the same titanium blade used in material damping tests and was welded at its root to a massive block. It was provided with a means for applying a static normal load on the shroud surfaces. The whole assembly was mounted in a vacuum chamber and subjected to harmonic excitation. The shroud normal loads and input acceleration levels were varied and the stress response at the ASMT (Above-Shroud-Maximum-Thickness) position was monitored. Damping levels were estimated from transient response curves resulting from abrupt cancellation of input signals.

The loading platens (Fig. 62), which were used to apply normal loads on the shrouds, have a rectangular rubbing surface designed to mate with the curved perimeter of the shroud interface. The platens were made of titanium alloy (8-1-1) and hard-faced with tungsten carbide to be compatible with the surface treatment on the shroud interfaces. The loading disk holding the load platens (Fig. 63) was positioned around the blade so that the platens rested on the shroud surfaces. A cable and weight system was used to impose a normal load on the shrouds. Upon reaching the required torque (and hence, the required normal load on the shroud interfaces), the disk was locked in position and the cables were removed. Complete air tightness was achieved by capping the access holes on the fixture. This setup assured constant shroud loading through the series of tests.

The response plot for tip flapwise acceleration during a frequency sweep is shown in Fig. 64. This was performed at a relatively low applied torque (5.2 Nm) and so the boundary conditions at the shroud interface represented neither a fully locked nor a freely slipping condition. In fact, during this series of tests, a rattling type of motion was observed at the shroud location and resulted in a number of peaks occurring at 260 Hz (bending), 475 Hz (second bending), and 880 Hz (torsion). Decay tests were performed from which the damping levels in each of these modes were measured: 1110 Hz (torsion) and 1440 Hz (second bending). Upon increasing the applied torque, it was noted that the number of nonlinear responses diminished and the three above-shroud modes manifested themselves (Fig. 65) at 278 Hz (bending). Response included some participation from the "free" blade bending mode at 93 Hz.

A characteristic of the response curves is a flat peak over a significant bandwidth around the resonance, as shown in Fig. 66. Results of vibratory decay tests for mode 1 are shown in

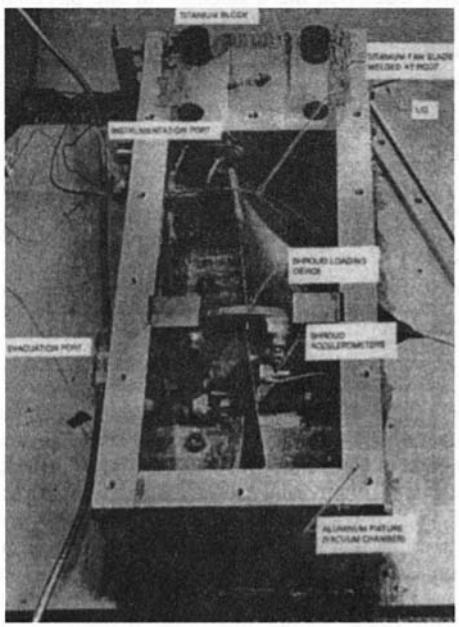

Fig. 63 Shroud damping experiment

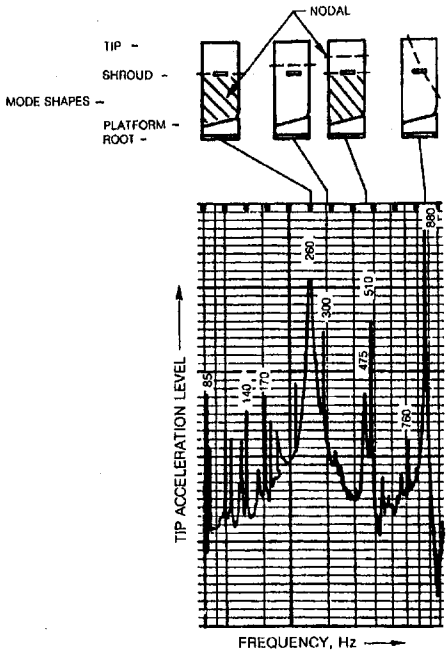

FREQUENCY, Hz	RESPONSE DESCRIPTION
85	NONLINEAR — MODIFIED FIRST FREE BLADE BENDING MODE
140	NONLINEAR — HIGH FREQUENCY RESPONSE
170	NONLINEAR — HIGH FREQUENCY RESPONSE
260	ABOVE SHROUD BLADE BENDING (f-LAP) MODE ($\eta = 0.003$)
300	NONLINEAR — MODIFIED SECOND FREE BLADE BENDING MODE
475	ABOVE SHROUD BLADE SECOND BENDING MODE ($\eta = 0.003$)
510	NONLINEAR — HIGH FREQUENCY RESPONSE
760	NONLINEAR — HIGH FREQUENCY RESPONSE
880	ABOVE SHROUD BLADE TORSION ($\eta = 0.001$)

Fig. 64 Response of shrouded blade at low normal load

Fig. 67. After testing, the platens were removed and their rubbing surfaces examined. The majority of wear occurred at the outer corners of the surfaces even though initially the surfaces were essentially true and tight against the entire length. It is likely that initially some of the new hard-facing may have quickly worn off, allowing the load to move outward and concentrate on a small area, since the loading device was not able to adjust automatically to the new contact condition.

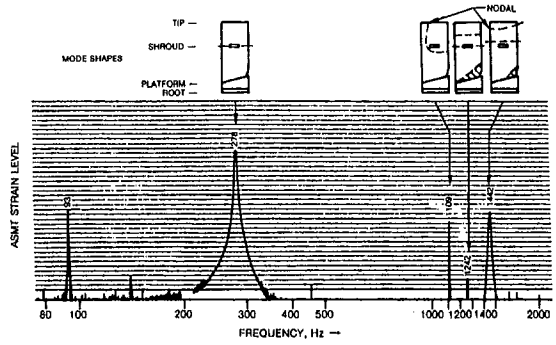

FREQUENCY, Hz	RESPONSE DESCRIPTION
93	NONLINEAR — MODIFIED FIRST FREE BLADE BENDING MODE
278	ABOVE SHROUD BLADE BENDING (FLAP) MODE
1109	ABOVE SHROUD BLADE TORSION
1242	NONLINEAR — MODIFIED SECOND BENDING MODE
1442	ABOVE SHROUD SECOND BENDING MODE

Fig. 65 Response of shrouded blade at high normal load

The loss factors measured in these tests are summarized below:

Shroud load, N	Mode	Period	ASMT stress, MPa (pk)	η
150	1F	3.566–3.579	41–63	0.034–0.056
300	1F	3.563–3.580	61–134	0.024–0.044
500	1F	3.558–3.566	39–195	0.024–0.034
150	1T	0.893–0.894	5.5–9.2	0.0052
300	1T	0.893–0.894	6.1–20	0.0055–0.0082
500	1T	0.891–0.893	7.7–28	0.0040–0.0084

It may therefore be noted that loss factors for torsion modes are an order of magnitude less than those for the bending modes.

The results from a feasibility study to determine the potentials of using an optical instrumentation system, shown in Fig. 68 (a gallium arsenide photo-emitting diode, Texas Instruments Type TIL24, and a silicon position sensing detector, UDT Type PIN-SC/4D, pair), to measure extremely small motions at a

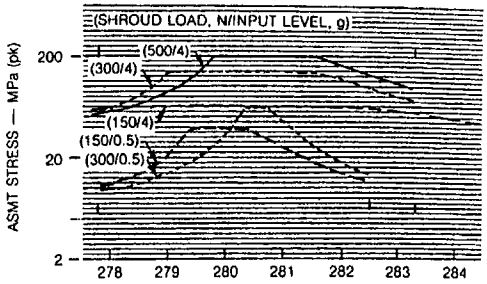

Fig. 66 Response characteristics at various shroud load conditions

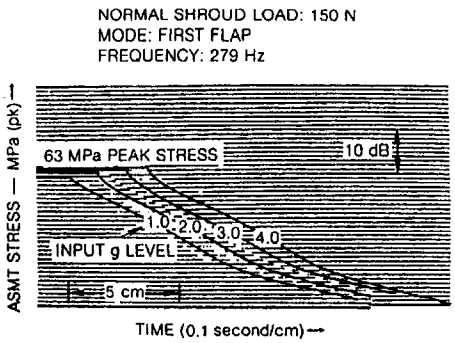

Fig. 67 Shrouded fan blade damping tests

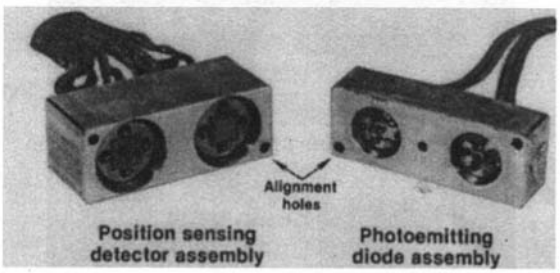

Fig. 68 Shroud motion measurement device

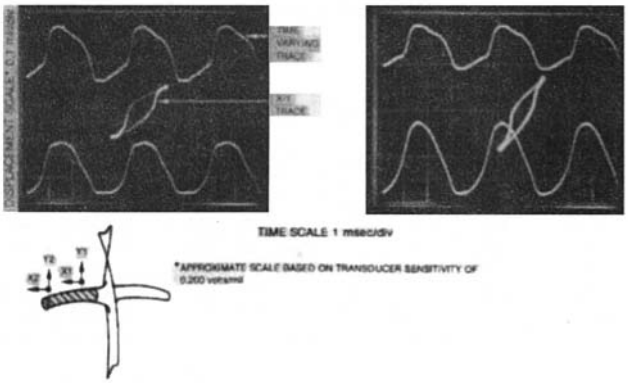

Fig. 69 Recorded shroud motion for the first blade mode

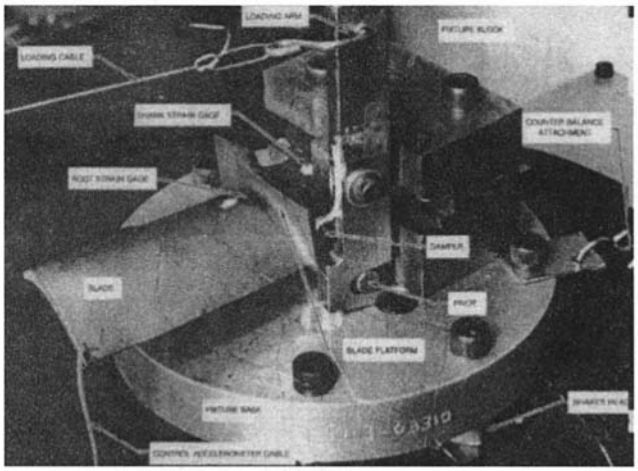

Fig. 71 Turbine blade damper test

shroud interface, are shown in Fig. 69. Details of the design of the optical system and the electronic circuitry may be obtained from the reports submitted to the Air Force (Srinivasan and Cutts, 1983a). The study established that vibratory motions as small as 50×10^{-6} in. could be measured. Clean signals representing the X and Y motions at two locations along the shroud interface were measured as shown in Fig. 69.

This system was developed and used in tests of a 40-blade part-span-shrouded fan assembly (Fig. 70), designated as R-80, spinning at 1200 rpm in an evacuated spin rig. Ten interfaces of adjacent blades #24 through #34 were selected as locations at which the optical devices were mounted. The assembly was excited through a system of piezoelectric crystals mounted on each airfoil just above the shroud location. The excitation system could excite standing or traveling waves. The vibratory motions measured were of a microslip nature. In addition to these motions, static relative displacements were also measured at different speeds, which indicated a somewhat predominant Y motion, with the implication that the motion is predominantly bending with some torsion in it. The nature of shroud vibratory motion varied with the type of system mode of the assembly. For example, in the first family of modes, the motion along the interface was negligible, but the motion along the radial direction was one of pivoting of one shroud against another with the magnitudes about an order of magnitude higher than those measured in the second family of modes. A detailed study of the report will convince the reader that the interfacial characteristics change from one family of modes to another and therefore analytical modeling of boundary conditions needs to take this into account.

These results reinforce the need to develop a data base from more similar tests, conducted under carefully controlled conditions in rigs. Shroud motion data obtained under these conditions, for a variety of shroud configurations, can be invaluable in validating analyses of the type reported recently (Srinivasan and McFarland, 1996) to predict functional forms for friction forces at vibrating interfaces.

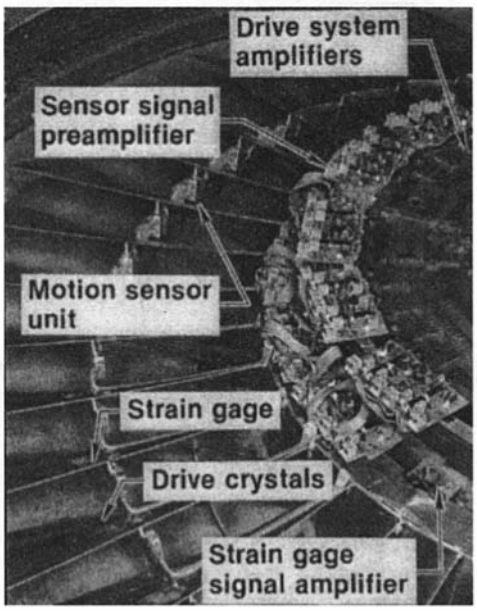

Fig. 70 Instrumented fan to measure shroud slip

Turbine Blade Dampers. A device of the type shown in Fig. 59, which is a simple metallic piece, serves as a damper, when one end of it is attached to a support, such as, for example, a cover plate. In an operating engine, centrifugal forces acting on the damper lift it gradually and, at a certain speed, it fully engages the platform at a predesigned location. The concept, which has been developed over the past three decades or so, is now commonly employed industry-wide and is based on the principle that relative motion can take place as the blade vibrates and this relative motion can dissipate vibratory energy and prevent blade amplitudes from escalating to undesirable levels. Estimates of Q around 30 are considered possible with such a device. The principal parameters that govern the performance of such a device are: contact load, roughness of rubbing surfaces, level of external excitation, location of the contact region, and mass and stiffness of the device. Analytical models of this particular type of device have been examined by Griffin (1980); Srinivasan and Cutts (1983b); Cardinale et al. (1980); Allen and Sidenstick (1980); Dowell and Schwartz (1983); and Sinha and Griffin (1984). In this paper, a summary of results obtained in an experimental program is presented to serve as a basis for a physical understanding of the mechanisms at play in such a design. Tests were conducted on a single, second-stage turbine blade of an advanced engine to which a damper of the type described above was attached, as shown in Fig. 71. The blade had a three fir tree root configuration and a platform located at about 27.7 percent blade span, and had a generous trailing edge overhang to accommodate the damper. Details of the design may be obtained from the report submitted to NASA (Srinivasan et al., 1981). Testing consisted of setting the platform load and input acceleration level and exciting the blade in the vicinity of its fundamental mode. It was found that there was a threshold of both frequency and input level, below which the blade showed no significant response. Once the threshold is crossed, the blade's response was dependent on the normal load. If the latter was "high," the response mode might correspond to a

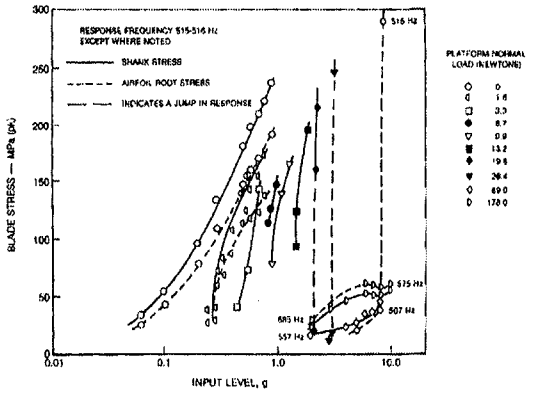

Fig. 72 Damper test data

"stuck" damper condition. If the g levels continued to increase, then a condition at which the damper breaks contact might be reached. Under those conditions, the blade would "plunge" into a lower mode, resulting in the jumps in stress, as shown in Fig. 72. A careful examination of the response curves reveals that the airfoil stresses, which begin by being lower than that measured on the shank, gradually become higher for "larger" loads at higher g levels. This is a clear indication of a change in mode shape in the course of changing load conditions. In any case, stress reductions of nearly 50 percent can occur either due to damping or due to change in mode shape through this device.

An important issue in regard to the prime variable for use in design was introduced by Cardinale et al. (1980) as shown in Fig. 59. Comparison between their results from bench tests and engine tests has led to a design philosophy in which they consider the damper angle to be the prime variable, rather than the damper load. However, it is fair to say that each manufacturer may choose the prime variable in design based on experience.

Before concluding this section, it is necessary to look at two more sources of damping due to rubbing action at interfaces: damping at root structure and damping due to inserts into hollow spaces inside blades. Insofar as damping available at dovetail of blade root is concerned, the data (Srinivasan et al., 1981) show rapid reduction in damping occurs with increasing normal load on the rotor. Thus, in practice, for an advanced fan at operating speeds, the centrifugal load acting on blades is so high that little or no relative motion at the root–disk interface is likely. Thus, contribution from this source of damping at operating speeds is projected to be minimal, although measurements made in some bench tests show Q values comparable to shroud and platform damping levels. However, design changes incorporating retention techniques that permit relative motion at the root location can be examined and introduced in order to exploit this source for enhancing damping due to microslip.

An attempt was made to examine the effectiveness of preloaded inserts, in hollow blade-like plates, on damping (El-Aini et al., 1996). The dampers tested were a variety of sheet metal devices configured to fit inside the chambers of these plates. Bench tests have shown 2 to 3 percent shift in frequencies due to damper mass and a vibratory stress reduction of about an order of magnitude. The viability of this concept in the context of damping and wear needs to be established in spin tests.

Summarizing the observations made so far, and on the basis of a variety of sources cited, one could state that the Q values for material, root, shroud, and platform damping may vary as follows: 3000 to 10,000 for material damping, 50 to 140 for root damping, 180 to 2500 for shroud damping, and 15 to 250 for platform damping. It is necessary to reiterate that the values of Q obtained from friction damping are mode shape dependent. The values quoted above are valid for vibration in a first mode only. A comparable Q for aerodynamic damping can be estimated to be in the region of 160–500.

Conclusions and Recommendations

It must now be clear that much has occurred in the past three decades to improve our understanding of vibratory behavior of gas turbine blades. About thirty years ago, we knew very little about the phenomenon of mistuning. Even though mistuning blades is not a standard feature in the design of rotors, the phenomenon has been exploited in at least a couple of instances to redesign flutter-prone rotors. This has been made possible by research and development efforts stimulated by engine and rig experiences within the past three decades. During the same period, empiricism to determine susceptibility of rotors to flutter has yielded to elaborate prediction systems. The latter combine unsteady aerodynamic pressures acting on vibrating cascades with modes of bladed-disk assemblies to predict aerodynamic damping. A similar experience holds for computing resonant response of blades. The design goal in regard to resonance used to be set with reference to the Campbell diagram by attempting to place low-order resonant frequencies such as 2E or 3E outside the range of operating speeds. Research efforts in the past two decades have led to calculation procedures to estimate forcing functions due to distortion and other disturbances in the flow. Forced response calculations are made using these forcing functions along with finite element models and optimization procedures to design an assembly. It was always clear that estimates of flutter conditions or resonant stresses were dependent on accurate estimates of aerodynamic as well as nonaerodynamic damping, but serious efforts to identify sources of the latter began only in the 1980s. Several investigations addressing material and friction damping potentials discussed in the body of this paper have led to a better understanding of the issues.

However, it would be inaccurate to state that the aforementioned research efforts have all matured to the point that they have been successfully adapted into design systems. Even when they are, caution is exercised before design decisions are made on the basis of new findings. While there are a variety of reasons for this situation, the principal one, in the author's opinion, is that there has been a lack of sustained research and development funding in this area. For example, we have yet to propose a set of reliable design guidelines to improve fatigue life of blades. A statistical approach was discussed more than a decade ago but progress has been lacking. This is in spite of Danforth's aforementioned dictum "suppression of vibratory fatigue is the design challenge" expressed three decades ago! Flutter analyses are still plagued by a variety of restrictive assumptions such as linearity, isolated rotor, two dimensionality, etc. Resonant stress prediction is limited by our current inability to predict flow defects and their deformation as they pass through multiple stages. In the same manner, in damping estimates there is virtually no effort to examine materials and manufacturing processes that may enhance material damping. In the research efforts pertaining to friction-induced damping, almost every effort assumes the law of friction to be of the Coulomb type. There is a real need to find methods to measure dynamic friction forces at interfaces and relate them to corresponding motions.

There is a general acceptance that linear unsteady aerodynamic analyses are adequate for practical purposes. At the same time, linear analyses are known to be inadequate when shocks and large flow defects are predominant in the flow. Two-dimensional modeling and use of strip theory are known to lead to unreliable prediction of aerodynamic damping. As remarked earlier, aeroelastic calculations that couple eigenmodes of an assembly of blades predict a 30 percent drop in aerodynamic damping compared to considerations of individual modes only. Similarly, calculations that use coupling among blade rows have shown marked influence on both resonance and flutter. These are admittedly preliminary observations based on limited analy-

ses. However, they raise important issues that need to be resolved in a systematic manner.

As the primary goal of analyses is to model the physical phenomena as completely as possible, the level of modeling needed can be driven only by data taken under carefully controlled test conditions in laboratories *and* rigs *and* in the real environment of engines. Reliable data are sorely needed in every aspect covered in this paper and such data must be obtained at each level indicated. The goals of these levels are different and equally important and it is in the interest of industry to promote each deliberately. Any attempt to skip these systematic steps will fail because a properly planned program aimed at solving a problem in a cost-effective, scientific manner would demand that the objectives of rig testing be set by results of laboratory testing and in a similar way the objectives of engine testing must be driven by results from rig testing.

Thus, the principal gap in all the areas discussed above is a conspicuous lack of good test data. In addition to its intrinsic value, experimental data provide the needed stimulus toward more realistic modeling efforts. Nearly 25 years ago, Dr. Whitehead remarked during a panel discussion that he was "struck rather forcibly by the almost complete absence of experimental data on these things" (Fleeter, 1972). Today, after a quarter century we could use essentially the same words to describe the situation. There just aren't any short cuts to develop mathematical models that withstand the scrutiny of the designer community.

One important scientific element that is conspicuously absent in our pursuit to improve structural integrity is similitude. As blades operate in a harsh thermal and centrifugal environment, successful laboratory modeling would imply that we can develop scaling laws that can be used to interpret data. There is an opportunity here for academia to assess the scope of needed research and provide guidelines.

Flutter measurements made about a quarter century ago showed vibration amplitudes of about $\frac{1}{8}$ in. for a blade thickness of 0.15. in. This is clearly in the nonlinear range and yet most of our analyses do not consider this level of vibration. Engine data show that flutter may develop and progress through the cascade. None of the procedures allow this feature in the formulations, and perhaps time domain approaches may be the preferred route here. Isolated pieces of data will not be taken seriously, but when data from *sustained* research efforts at all three levels noted before indicate the same trend, then the analyst may be persuaded to configure the analyses accordingly.

Nevertheless, the jet engine community can truly be proud of its accomplishments over the decades. For example: Jet engine life, which was a mere 25 engine hours for the JUMO-004, rose to a phenomenal failure rate of a mere 1 in 3 million engine hours (Danforth, 1967). Currently engine companies use in-flight shutdowns as a guide and issue warranties that assure 1 in-flight shutdown in 50,000 hours of flight *due to any cause.* The reasons for this spectacular achievement are obvious enough: vastly superior materials and manufacturing techniques; a better understanding of material behavior under a complex environment of loads, temperatures, and vibration; and a better grasp of structural analytical procedures leading to the design of parts.

Clearly there is a dilemma here. We appear to have a perfect product. Why not stop there? We cannot, because products are never considered perfect as long as innovative ideas flow from the research community that can yet enhance the product and its performance. And the product itself has changed so much over six decades that there is little resemblance between the JUMO-004 and a PW 4000 or a Trent or a GE-90. A close examination and comparison of the modal density in a first or second high compressor blade of the '50s with that of the '90s will show the changes that have occurred in the interim. The "product" will change again in ways that we cannot now predict as newer material systems, manufacturing techniques, measurement tools, diagnostics, aerodynamic profiles, and control ideas evolve. The list is as interesting as it is interdisciplinary and promises vast opportunities for innovation. We need better understanding of the physical phenomena we observe, a better grasp of the nature of steady and unsteady aerodynamic pressures, new modeling methods that bear down on observed behavior, strategies to exploit inevitable phenomena such as, for example, mistuning, stall, and separation, new ideas of structural design to prevent crack propagation, better representation of interfacial dynamics at joints, and more developmental efforts toward concepts such as blisks and blings.

Preventing failure of blades due either to flutter or resonance requires a multidisciplinary approach. Unless a dialogue is promoted and maintained among experts in analyses and testing in the fields of structures, aerodynamics, materials, fatigue and fracture, statistics, controls and diagnostics, the design goals cannot be adequately met. The problem should be viewed as a whole in which complex interactions take place between aerodynamic inputs and the resulting deformation. The interactions are not limited to a single blade, nor to a single blade row, but to the entire series of rotors. Thus considerations of single isolated rotors that have been the primary targets of analyses should now be replaced by multiple rows.

In the past two decades, innovations in the basic technologies, i.e., aerodynamic, structural, materials, and measurement technologies, have led to vastly increased thrust levels that have served as the basis for introducing to the market large-capacity passenger jets as well as superior fighter aircraft. Future demands to expand the operating envelope in terms of range, altitude, and speed of aircraft will have to be met by new advances in the basic technologies referred to above, under the time-honored constraints of improved thrust/weight ratio, satisfactory life, and costs. Additionally, component designers of the future will need to exploit "smartness" in material and structural characteristics in order to sense, acquire, process, and control the vibratory characteristics of engine components. Advances in aerodynamic and structural theories in the past have resulted in complex blade profiles, as evidenced by the current trend to introduce wide chord fan blades. The latter possess a rich variety of modal characteristics and therefore new aeromechanical characteristics. This trend will continue and pose yet a new set of challenges to the designer of gas turbine engines, and therefore provides an unusual set of opportunities for research and development.

Many of the problems discussed here and the approaches to solve them apply equally to the development of large-capacity industrial turbines. Similar challenges and opportunities exist, and shut-downs of these machines due to blade failure are known to have far-reaching consequences for a modern community whose lifestyle (at home, at work, at leisure) is now inconceivable without a dependable source of energy.

Finally, there is a real need to stimulate young minds toward setting and reaching new goals. An excellent beginning can be made at the laboratory level to obtain good data. We need accurate measurements of aerodynamic and structural characteristics through nonintervening measurement tools. We need basic studies, experimental as well as analytical, in the area of dynamic friction. We need to develop mistuning ideas further and develop a design approach based on statistical considerations. The responsibility to allocate resources and to set new directions in gas turbine aeroelastics has never been heavier and the stakes and potential benefits have never been higher. As a reminder "*I am going to make a gas turbine before I quit and . . . it is going to run without vibration. . .*" (Glen Warren, 1914). The capacity to dream and reach for the impossible is the hallmark of every technological breakthrough.

Acknowledgments

It is a pleasure to acknowledge several sources that made this contribution possible. I am grateful to the management at

United Technologies Research Center for allowing me to use their library and receive assistance in putting the document together. The enthusiastic assistance rendered by Florence Wendell and Sue Cebula deserves special mention. Special thanks to my wife Kamla and several of my colleagues who read through drafts and offered constructive criticisms: Dr. R. A. Arnoldi, Dr. Michael McFarland, Dr. Marc Mignolet, Dr. Milind Bakhle, and Dr. Joseph Verdon. Finally I thank the members of the IGTI Scholar Committee for selecting my proposal, providing useful suggestions to improve the manuscript, and giving me an opportunity to share my views and experience in this vital technology area.

References

Allen, R. E., and Sidenstick, J. W., 1980, "Turbine Blade Technology: Present and Future," ASME Paper No. 80-C2 Aero-10.

Annigeri, B. S., 1976, "Finite Element Analysis of Planar Elastic Contact With Friction." ME Thesis, Illinois School of Technology.

Antoniou, S. S., Cameron, A., and Gentle, C. R., 1976, "The Friction Speed Relation From Stick-Slip Data," *Wear,* Vol. 36, pp. 235–254.

Armstrong, E. K., 1967, "Recent Blade Vibration Techniques," ASME JOURNAL OF ENGINEERING FOR POWER, Vol. 89, pp. 437–444.

Aviation Week & Space Technology, 1994, Vol. 141, Issue 21 (Nov. 21), p. 32.

Ayer, T. C., and Verdon, J. M., 1996, "Validation of Nonlinear Unsteady Aerodynamic Simulator for Vibrating Blade Rows," ASME Paper No. 96-GT-340, to appear in the ASME *Journal of Turbomachinery.*

Bakhle, M. A., Reddy, T. S. R., and Keith, T. G., 1992, "Time Domain Flutter Analysis of Cascades Using a Full-Potential Solver," *AIAA Journal,* Vol. 30, No. 1, p. 163.

Bakhle, M. A., 1996, private communication.

Ball, C. L., and Reid, L., 1993, "NASA/Industry/University Fan and Compressor Research Accomplishments—An Overview," presented at the Hartman Memorial Session, IGTI EXPO.

Basu, P., and Griffin, J. H., 1986, "The Effects of Limiting Aerodynamic and Structural Coupling in Models of Mistuned Bladed Disk Vibration," ASME *Journal of Vibration, Acoustics, Stress, and Reliability in Design,* Vol. 108, pp. 132–139.

Beards, C. F., 1981, "The Damping of Structural Vibration by Controlled Interfacial Slip in Joints," ASME Paper No. 81-DET-86.

Bielawa, R. L., 1977, "An Analytical Study of the Energy Dissipation of Turbo-Machinery Bladed Disk Assemblies Due to Inter-shroud Segment Rubbing," ASME Paper No. 77-DET-73.

Bölcs, A., and Fransson, T. H., 1986, "Aeroelasticity in Turbomachines: Comparison of Theoretical and Experimental Cascade Results," Laboratoire de thermique appliquée et de turbomachines de l'Ecole Polytechnique Féderale de Lausanne, Communication No. 13.

Bowden, F. P., and Tabor, D., 1964, *Friction and Lubrication of Solids,* Oxford University Press, London (Part I, 1954; Part II, 1964).

Buffum, D. H., 1995, "Blade Row Interaction Effects on Flutter and Forced Response," *Journal of Propulsion and Power,* Vol. 11, No. 2, pp. 205–212.

Cardinale, V. M., Bankhead, H. R., and McKay, R. A., 1980, "Experimental Verification of Turboloading Aeromechanics," Turbine Engine Testing AGARD Conf. Proc., CP 293.

Chapman, G. M., and Wang, X., 1987, "Interpretation of Experimental and Theoretical Data for Prediction of Mode Shapes of Vibrating Turbocharger Blades," *Bladed Disk Assemblies,* Kielb, R. E., Crawley, E., and Simonis, J. C., eds., ASME, pp. 81–86.

Chiang, H. D., and Kielb, R. E., 1993, "An Analysis System for Blade Forced Response," ASME *Journal of Turbomachinery,* Vol. 115, pp. 762–770.

Constant, Hayne, 1947, *Development of the British Gas Turbine Unit,* ASME.

Danforth, C. E., 1967, "Designing to Avoid Fatigue in Long Life Engines," *Trans. Society of Automotive Engineers,* Vol. 75, Sec. 2, pp. 248–262.

Den Hartog, J. P., 1931, "Forced Vibrations With Combined Coulomb and Viscous Friction," *Transactions of ASME,* Vol. 53, pp. 107–115.

Deutch, J., 1995, presentation at the AFOSR Workshop on Jet Engine High Cycle Fatigue (HCF), Oct. 10–11.

Dowell, E. H., and Schwartz, H. B., 1983, "Forced Response of a Cantilever Beam with a Dry Friction Damper Attached, Part 1: Theory," *Journal of Sound and Vibration,* Vol. 91, No. 2, pp. 255–267.

Earles, S. W. E., and Williams, E. J., 1972, "A Linearized Analysis for Frictionally Damped Systems," *Journal of Sound and Vibration,* Vol. 24, No. 4, pp. 445–458.

El-Aini, Y. M., et al., 1996, "Friction Damping of Hollow Airfoils, Parts I and II," ASME Paper No. 96-GT-109/110.

El-Bayoumy, L. E., and Srinivasan, A. V., 1975, "Influence of Mistuning on Rotor-Blade Vibrations," *AIAA Journal,* Vol. 13, No. 4, pp. 460–464.

Ewins, D. J., 1969, "The Effects of Detuning Upon the Forced Vibrations of Bladed Disks," *Journal of Sound and Vibration,* Vol. 9, pp. 65–79.

Ewins, D. J., and Srinivasan, A. V., eds., 1983, *Vibration of Bladed Disk Assemblies,* ASME.

Financial Times, 1996, Sept. 2, 1996.

Flight International, 1994, "Resonance Problem Hits Gripen Engine," report in Feb. 2 issue, Reed Business Publishing.

Fleeter, S., ed., 1972, "Aeroelasticity in Turbomachines," panel session, ONR.

Forsching, H. W., 1989, "A Parametric Study of the Flutter Stability of Two-Dimensional Turbine and Compressor Cascades in Incompressible Flow," *Z. Flugwiss,* Weltraumforsch, 13, pp. 351–364.

Forsching, H. W., 1994, "Aeroelastic Stability of Cascade Turbomachinery," *Progress in Aerospace Sci.,* pp. 213–266.

Fransson, T. H., 1987, "Aeroelasticity in Turbomachines—Comparison of Theoretical and Experimental Cascade Results," *Proc. 4th International Symposium on Unsteady Aerodynamics, Aeroacoustics and Aeroelasticity in Turbomachines and Propellors,* Aachen, pp 788–789.

Fransson, T. H., and Verdon, J. M., 1991, "Standard Configurations on Unsteady Flow Through Vibrating Turbomachine Cascades," *Proc. 6th International Symposium on Unsteady Aerodynamics, Aeroacoustics and Aeroelasticity of Turbomachines and Propellors,* Notre Dame.

Fransson, T. H., and Verdon, J. M., 1992, "Standard Configurations on Unsteady Flow Through Vibrating Turbomachine Cascades," KTH.

Frischbier, J., Schulze, G., Zielinski, M. and Ziller, G., 1996, "Blade Vibrations of a High Speed Compressor Blisk-Rotor. . . ," ASME Paper No. 96-GT-24.

Gerolymos, G. A., 1993, "Coupled Three-dimensional Aeroelastic Stability Analysis of Bladed Disks," ASME *Journal of Turbomachinery,* Vol. 115, pp. 791–799.

Goodman, L. E., 1960, "A Review of Progress in Analysis of Interfacial Slip Damping," in: *Structural Damping Colloquium Papers,* Ruzicka, J. E., ed., Pergamon Press.

Greenwood, J. A., and Williamson, J. B. P., 1964, "The Contact of Nominally Flat Surfaces," *Proc. 2nd International Conference on Electric Contacts,* Graz, Austria.

Griffin, J. H., 1980, "Friction Damping of Resonant Stresses in Gas Turbine Engine Airfoils," ASME JOURNAL OF ENGINEERING FOR POWER, Vol. 102, pp. 329–333.

Griffin, J. H., and Sinha, A., 1985, "The Interaction Between Mistuning and Friction in the Forced Response of Bladed Disk Assemblies," ASME JOURNAL OF ENGINEERING FOR GAS TURBINES AND POWER, Vol. 107, pp. 205–211.

Griffin, J. H., 1988, "On Predicting the Resonant Response of Bladed Disk Assemblies," ASME JOURNAL OF ENGINEERING FOR GAS TURBINES AND POWER, Vol. 110, pp. 45–50.

Griffin, J. H., and Menq, C. H. 1991, "Friction Damping of Circular Motion and its Application to Vibration Control," ASME *Journal of Vibration and Acoustics,* Vol. 113, pp. 225–229.

Hall, R. M., and Armstrong, E. K., 1976, "The Vibration Characteristics of an Assembly of Interlock Shrouded Turbine Blades," *Structural Dynamic Aspects of Bladed Disk Assemblies,* Srinivasan, A. V., ed., ASME.

Hall, K. C., and Lorence, C. B., 1993, "Calculation of Three-Dimensional Unsteady Flows in Turbomachinery Using the Linearized Harmonic Euler Equations," ASME *Journal of Turbomachinery,* Vol. 115, pp. 800–809.

Holmes, D. G., Lamson, S. H., and Connell, S. D., 1988, "Quasi-3D Solutions for Transonic Inviscid Flows by Adaptive Triangulation," ASME Paper No. 88-GT-83.

Hoyniak, D., and Fleeter, S., 1986, "The Effect of Circumferential Aerodynamic Detuning on Coupled Bending-Torsion Unstalled Supersonic Flutter," ASME *Journal of Turbomachinery,* Vol. 108, pp. 253–260.

Huang, W. H., 1982, "Vibration of Some Structures With Periodic Random Parameters," *AIAA Journal,* Vol. 20, No. 7, pp. 1001–1008.

Irretier, H. D., and Rzadkowski, R., 1994, "Forced Vibration of Mistuned Bladed Discs in Stationary Operations," presented at the 4th IFToMM International Conference on Rotor Dynamics, Chicago.

Irretier, H. D., 1997, "The Maximum Transient Resonance Response of Rotating Blades With Regard to Centrifugal Force and Non-linear Damping Effects," ASME Paper No. 97-GT-116.

Jacobsen, L. S., 1930, "Steady Forced Vibration as Influenced by Damping," *Trans. ASME,* Vol. 52, pp. 169–181.

Jeffers, J. D., and Meece, C. E., 1975, "F100 Fan Stall Flutter Problem. Review and Solution," *AIAA Journal of Aircraft,* Vol. 12, No. 4, pp. 350–356.

Kandebo, S. W., 1994, "Pratt, USAF Resolve F119 Turbine Problem," *Aviation Week and Space Technology,* Nov. 21, p. 32.

Kielb, R. E., and Kaza, K. R. V., 1983, "Aeroelastic Characteristics of a Cascade of Mistuned Blades in Subsonic and Supersonic Flows," ASME *Journal of Vibration, Acoustics, Stress, and Reliability in Design,* Vol. 103, pp. 425–433.

Kielb, R. E., Leissa, A., MacBain, J., and Carney, K. S., 1985, "Joint Research Efforts on Vibration of Twisted Plates," NASA RP1150.

Kielb, R. E., and Rieger, N. F, eds., 1985, *Vibration of Blades and Bladed Disk Assemblies,* ASME.

Kielb, R. E., Crawley, E., and Simonis, J. C., eds., 1987, *Bladed Disk Assemblies,* ASME.

Kielb, R. E., and Chiang, H. D., 1992, "Recent Advancements in Turbomachinery Forced Response Analyses," *AIAA Joint Propulsion Conference Proc.* No. 28.

Kragelsky, I. V., and Ailsin, V. V., eds., 1981, *Friction Wear Lubrication; Tribology Handbook,* Mir Publishers, Moscow.

Kragelsky, I. V., Dobychin, M. N., and Kombalov, V. S., 1982, *Friction and Wear; Calculation Methods,* Pergamon Press.

Ku, P. M., ed., 1968, "Interdisciplinary Approach to Friction and Wear," NASA SP-181.

Kurkov, A., 1984, "Flutter of F100 Derivative 2 Engine," ASME JOURNAL OF ENGINEERING FOR GAS TURBINES AND POWER, Vol. 106, pp. 44–49.

Leyes, R., and Fleming, W., eds., 1997, *The History of North American Small Gas Turbine Aircraft Engines,* National Air and Space Museum, Smithsonian Institute, Washington, DC., to be published.

Lin, C.-C., and Mignolet, M. P., 1997, "An Adaptive Perturbation Scheme for the Analysis of Mistuned Bladed Disks," ASME JOURNAL OF ENGINEERING FOR GAS TURBINES AND POWER, Vol. 119, pp. 153–160.

Los Angeles Times, 1991, Business section, Fri., Jan. 4, Part D, column 1, p. 2.

Lubomski, J. F., 1980, "Status of NASA Full-Scale Engine Aeroelasticity Research," NASA TM 81500.

MacBain, J. C., Horner, J. E., Stange, W. A., and Ogg, J. S., 1979, "Vibration Analysis of a Spinning Disk Using Image-Derotated Holographic Interferometry," *Experimental Mechanics,* Vol. 19, No. 1, pp. 17–22.

Majjigi, R. K., and Gliebe, P. R., 1984, "Development of a Rotor Wake/Vortex Model," NASA Contract NAS3-23681, NASA-CR-174849.

Manwaring, S. R., and Wisler, D. C., 1993, "Unsteady Aerodynamics and Gust Response in Compressors and Turbines," ASME *Journal of Turbomachinery,* Vol. 115, pp. 724–740.

Mayer, R. L., and Mowbray, N. A., 1975, "The Effect of Coulomb Damping on Multidegree of Freedom Elastic Structures," *Earthquake Engineering and Structural Dynamics,* Vol. 3, pp. 275–286.

Mehalic, C. M., Dicus, J. H., and Kurkov, A. P., 1977, "Effect of Pressure and Temperature on the Subsonic Stall Flutter Region of a YF100 Engine," NASA TMS-73785.

Menq, C.-H., Chidamparam, P., and Griffin, J. H., 1991, "Friction Damping of Two-Dimensional Motion and its Application in Vibration Control," *Journal of Sound and Vibration,* Vol. 144, pp. 427–447.

Mignolet, M. P., and Christensen, K. R., 1990, "Probabilistic Analysis of Mistuned Bladed Disks: A Combined Closed Form Perturbation Approach," ASME Paper No. 90-GT-191.

Mignolet, M. P., and Lin. C. C., 1993, "The Combined Closed Form–Perturbation Approach to the Analysis of Mistuned Bladed Disks," ASME *Journal of Turbomachinery,* Vol. 115, pp. 771–780.

Mignolet, M. P., 1996, private communication.

Mignolet, M. P., and Lin, C. C., 1997, "Identification of Structural Parameters in Mistuned Bladed Disks," ASME *Journal of Vibration and Acoustics,* in press.

Mikolajczak, A. A., Snyder, L. E., Arnoldi, R. A., and Stargardter, H., 1975, "Advances in Fan and Compressor Blade Flutter Analysis and Predictions," *AIAA Journal of Aircraft,* Vol. 12, No. 4, pp. 325–332.

Namba, M., 1987, "Three-Dimensional Flows," AGARD *Manual on Aeroelasticity in Axial-Flow Turbomachines, Vol. 1—Unsteady Turbomachinery Aerodynamics,* Platzer, M. F., and Carta, F. O., eds., Chap. 4.

Oden, J. T., and Pires, E. B., 1983, "Nonlocal and Nonlinear Friction Laws and Variational Principles for Contact Problems in Elasticity," ASME *Journal of Applied Mechanics,* Vol. 50, pp. XXX–000.

Ottarson, G., and Pierre, C., 1993, "A Transfer Matrix Approach to Vibration Localization in Mistuned Blade Assemblies," ASME Paper No. 93-GT-115.

Ottarson, G., Castanier, M. P., and Pierre, C., 1994, "A Reduced-Order Modeling Technique for Mistuned Bladed Disks," Paper No. AIAA-94-1640-CP.

Ottarson, G., and Pierre, C., 1995, "On the Effects of Interblade Coupling on the Statistics of Maximum Forced Response Amplitudes in Mistuned Bladed Disks," Paper No. AIAA-95-1494-CP.

Panovko, Y. G., and Gubanova, I. I., 1965, *Stability and Oscillations of Elastic Systems,* Consultants Bureau, New York.

Petricone, R., and Sisto, F., 1971, "Vibration Characteristics of Low Aspect Ratio Compressor Blades," ASME JOURNAL OF ENGINEERING FOR POWER, Vol. 93, pp. 103–112.

Pfeiffer, R., 1985, "Blade Vibrations of Continuously Coupled and Packed Steam Turbine LP Stages," *Vibrations of Blades and Bladed Disk Assemblies,* Kielb, R. E., and Rieger, N. F., eds., ASME.

Pian, T. H. H., 1957, "Structural Damping of a Simple Built-Up Beam With Riveted Joints in Bending," ASME *Journal of Applied Mechanics,* Vol. 24, pp. 35–38.

Platzer, M. F., and Carta, F. O., eds., 1987, AGARD *Manual on Aeroelasticity in Axial-Flow Turbomachines, Vol. 1—Unsteady Turbomachinery Aerodynamics.*

Platzer, M. F., and Carta, F. O., eds., 1988, AGARD *Manual on Aeroelasticity in Axial-Flow Turbomachines, Vol. 2—Structural Dynamics and Aeroelasticity.*

Pratt, T. K., and Williams, R., 1981, "Non-linear Analysis of Stick/Slip Motion," *Journal of Sound and Vibration,* Vol. 74, No. 4, pp. 531–542. 1981

Rimkunas, D. A., and Frye, H. M., 1979, "Investigation of Fan Blade Shroud Mechanical Damping," Wright-Patterson AFB, Aero Propulsion Lab, Report No. FR-11065.

Sanliturk, K. Y., and Ewins, D. J., 1996, "Modelling Two-Dimensional Friction Contact and Its Application Using Harmonic Balance Method," *Journal of Sound and Vibration,* Vol. 193, No. 2, pp. 511–523.

Sinha, A., 1986, "Calculating the Statistics of Forced Response of a Mistuned Bladed Disk Assembly," *AIAA Journal,* Vol. 24, No. 11, pp. 1797–1801.

Sinha, A., and Chen, S., 1988, "Probabilistic Analysis of Forced Response of a Bladed Disk Assembly with Various Mistuning Distributions," AIAA Paper No. 88–2399.

Sinha, A., and Chen, S., 1989, "A Higher Order Technique to Compute the Statistics of Forced Response of a Mistuned Bladed Disk," *Journal of Sound and Vibration,* Vol. 130, pp. 207–221.

Sinha, A., and Griffin, J. H., 1984, "Effects of Static Friction on the Forced Response of Frictionally Damped Turbine Blades," ASME JOURNAL OF ENGINEERING FOR GAS TURBINES AND POWER, Vol. 106, pp. 65–69.

Smith, S. N., 1973, "Discrete Frequency Sound Generation in Axial Flow Turbomachines," British Aeronautical Research Council, ARC R&M. 3709.

Sogliero, G., and Srinivasan, A. V., 1980, "Fatigue Life Estimates of Mistuned Blades via a Stochastic Approach," *AIAA Journal,* Vol. 18, No. 1, pp. 318–323.

Srinivasan, A. V., ed., 1976, *Structural Dynamic Aspects of Bladed Disk Assemblies,* ASME.

Srinivasan, A. V., Lionberger, S. R., and Brown, K. W., 1978, "Dynamic Analysis of an Assembly of Shrouded Blades Using Component Modes," ASME *Journal of Mechanical Design,* Vol. 100, pp. 520–527.

Srinivasan, A. V., and Kurkov, A. P., 1981, "Effects of Mistuning on Blade Torsional Flutter," presented at the Fifth International Symposium on Air Breathing Engines, Bangalore, IN.

Srinivasan, A. V., Cutts, D. G., and Sridhar, S., 1981, "Turbojet Engine Blade Damping," NASA Contractor Report, No. 165406.

Srinivasan, A. V., and Cutts, D. G., 1983a, "Basic Study of Bladed Disk Structural Response," Final Report, Wright-Patterson Air Force Base.

Srinivasan, A. V., and Cutts, D. G., 1983b, "Dry Friction Damping Mechanisms in Engine Blades," ASME JOURNAL OF ENGINEERING FOR POWER, Vol. 105, pp. 332–341.

Srinivasan, A. V., and Fabunmi, J. A., 1984, "Cascade Flutter of Cantilevered Blades," JOURNAL OF ENGINEERING FOR GAS TURBINE AND POWER, Vol. 106, No. 34.

Srinivasan, A. V., and Cutts, D. G., 1984a, "Measurement of Relative Vibratory Motion at the Shroud Interfaces of a Fan," ASME *Journal of Vibration, Acoustics, Stress, and Reliability in Design,* Vol. 106, pp. 189–197.

Srinivasan, A. V., and Cutts, D. G., 1984b, "Aerodynamically Excited Vibrations of a Part-Span Shrouded Fan," ASME JOURNAL OF ENGINEERING FOR GAS TURBINES AND POWER, Vol. 107, pp. 399–407.

Srinivasan, A. V., and Cassenti, B. N., 1986, "A Nonlinear Theory of Dynamic Systems With Dry Friction Forces," ASME JOURNAL OF ENGINEERING FOR GAS TURBINES AND POWER, Vol. 108, pp. 525–530.

Srinivasan, A. V., and Tavares, G. G., 1995, "Direct Use of Unsteady Aerodynamic Pressures in the Flutter Analysis of Mistuned Blades," *J. Phys.* (France), Vol. III, No. 5, pp. 1587–1597.

Srinivasan, A. V., and McFarland, D. M., 1996, "Characterization of Laws of Friction in the Context of Engine Blade Dynamics," ASME Paper No. 96-GT-379; to appear in the ASME JOURNAL OF ENGINEERING FOR POWER.

Srinivasan, A. V., ed., 1976, *Structural Dynamic Aspects of Bladed Disk Assemblies,* ASME.

Stargardter, H., 1966, "Dynamic Models of Vibrating Rotor Stages," ASME Paper No. 66-WA/GT-8.

Stargardter, H., 1979, "Subsonic/Transonic Stall Flutter Study," Final Report, NASA CR-165256.

Tramm, P., 1972, Comments at a panel session, "Aeroelasticity in Turbomachines," Fleeter, S., ed., ONR.

Verdon, J. M., 1993, "Review of Unsteady Aerodynamic Methods for Turbomachinery Aeroelastic and Aeroacoustic Applications," *AIAA Journal,* Vol. 31, No. 2, pp. 235–250.

Warren, Glenn, 1914, in: *Seven Decades of Progress, A Heritage of Aircraft Turbine Technology,* GE Aircraft Engines, Aero Publishers Inc., 1979.

Wei, S. T., and Pierre, C., 1988a, "Localization Phenomena in Mistuned Assemblies With Cyclic Symmetry, Part I: Free Vibrations," ASME *Journal of Vibration, Acoustics, Stress, and Reliability in Design,* Vol. 110, No. 4, pp. 429–438.

Wei, S. T., and Pierre, C., 1988b, "Localization Phenomena in Mistuned Assemblies With Cyclic Symmetry, Part II: Forced Vibrations," ASME *Journal of Vibration, Acoustics, Stress, and Reliability in Design,* Vol. 110, No. 4, pp. 439–449.

Wei, S. T., and Pierre, C., 1990, "Statistical Analysis of the Forced Response of Mistuned Cyclic Assemblies," *AIAA Journal,* Vol. 28, No. 5, pp. 861–868.

Whitehead, D. S., 1962, "Force and Moment Coefficients for Vibrating Aerofoils in Cascade," A. R. C. R&M., 3254.

Whitehead, D. S., 1965, "Torsional Flutter of Unstalled Cascade Blades at Zero Deflection," Aeronautical Research Council, London, Reports & Memoranda No. 3429, 195–197.

Whitehead, D. S., 1966, "Effect of Mistuning on the Vibration of Turbomachine Blades Induced by Wakes," *Journal of Mechanical Engineering Science,* Vol. 8, No. 1, pp. 15–21.

Yeh, G. C. K., 1966, "Forced Vibrations of a Two-Degree-of-Freedom System With Combined Coulomb and Viscous Damping," *Journal of the Acoustical Society of America,* Vol. 39, pp. 14–24.

Zhuralev, V. A., 1940, "On the Physical Basis of the Amontons-Coulomb Law of Friction," *Journal of Tech. Phys.* (USSR), Vol. 10, p. 1447.

APPENDIX

In-Context Definitions

Resonance refers to a structure's response to forced vibration at a natural frequency. Blade resonance is caused by unsteady forces acting on a blade row. The forces may arise primarily due to any defects in flow. Resonant vibration occurs at natural frequencies and the amplitude of motion is limited by damping available in the system.

Flutter is aeroelastic instability caused by aerodynamic forces induced by vibration of a cascade of blades even when the flow is uniform. During flutter, energy may be added to

the blades during each cycle of vibration and the extent of escalation of stresses is controlled by damping.

Damping refers to the ability of the system to absorb energy due to vibration. The principal sources of damping are material damping, damping due to friction at rubbing interfaces, and aerodynamic damping.

Flap motion is vibration perpendicular to blade chord.

Membrane modes are modes in which the predominant motion is in-plane.

Stripe modes are modes in which more than one nodal line appears radially along the blade profile from root to tip.

Nodal diameter refers to any diameter in a circular structural component along which vibratory displacement is zero. See for example modes of vibration for a circularly symmetric disk shown in Fig. 8, which shows 1, 2, 3, 4, and 5 nodal diameter patterns. In addition the last pattern in the figure depicts a higher mode of vibration.

Mistuning refers to nonuniformities in structural or aerodynamic parameters around a fan, compressor or turbine stage.

Modes of vibration are vibratory shapes of structures. In general, modes consist of a combination of translation and rotational motions and therefore modes are referred to as coupled modes.

Dynamic flexibility pertains to motion (translation and rotation) at a selected point on a blade surface due to a unit forcing function (force or moment) acting at another location.

A Test Device for Premixed Gas Turbine Combustion Oscillations

G. A. Richards

R. S. Gemmen

M. J. Yip

U.S. Department of Energy,
Federal Energy Technology Center,
Morgantown, WV 26505

We report the design and operation of a test device suitable for studying combustion oscillations produced by commercial-scale gas turbine fuel nozzles. Unlike conventional test stands, this test combustor uses a Helmholtz acoustic geometry to replicate the acoustic response that would otherwise be observed only during complete engine testing. We suggest that successful simulation of engine oscillations requires that the flame geometry and resonant frequency of the test device should match the complete engine environment. Instrumentation for measuring both pressure and heat release variation is described. Preliminary tests suggest the importance of characterizing the oscillating behavior in terms of a nozzle reference velocity and inlet air temperature. Initial tests also demonstrate that the stabilizing effect of a pilot flame depends on the operating conditions.

Introduction

This report discusses the design and operation of a test combustor suitable for studying combustion oscillations from commercial-scale gas turbine fuel nozzles. To meet stringent NO_x emission goals, most stationary gas turbine vendors have adopted some form of lean, premixed (LPM) combustion (Lefebvre, 1995; Beer, 1995). The low flame temperatures associated with lean combustion produce low NO_x levels, but LPM combustion is often accompanied by undesirable pressure oscillations. Because of the resulting vibration, even small-amplitude pressure oscillations can damage engine hardware, and must therefore be eliminated during the development of new fuel nozzles and combustors. Unfortunately, the oscillations themselves are linked to the acoustic modes and acoustic gain (or loss) of a specific combustor geometry. Thus, tests of a single fuel nozzle in a conventional test stand usually do not reproduce the oscillating behavior that is found during complete engine testing. This increases the cost and time of new engine development because remedial modifications must be performed on the multinozzle, full-scale combustor.

As part of the U.S. Department of Energy's Advanced Turbine Systems Program (Alsup et al., 1995), the Federal Energy Technology Center (FETC) has developed a single-nozzle combustor that can be used to study the oscillating behavior of individual gas turbine fuel nozzles. This test combustor differs from conventional single-nozzle test rigs because it is designed to produce an acoustic environment suitable for studying combustion instabilities. The emphasis of the present work is natural gas combustion for stationary gas turbines, although the techniques described here may be useful for investigating liquid fuel nozzles as well. In this report, we describe the combustor design, capabilities, and relevant instrumentation. Initial operating experience is also presented, along with preliminary data suggesting the important role of the nozzle reference velocity and air temperature on combustion oscillations.

Background and Design Requirements

Dynamic pressure oscillations occur when heat release variations couple with the acoustic modes of a given combustor geometry. The variation in heat release can come from many different mechanisms, including vortex shedding, mixing variations, acoustic feedback to the fuel or air system, and other processes. Putnam (1971) describes many of the relevant processes in industrial burners. Yang and Anderson (1995) and Harrje and Reardon (1972) describe oscillating processes occurring in liquid fuel rockets. Kentfield and co-workers (1985, 1988, 1990) describe how oscillations may be deliberately created in a novel gas turbine application. Review articles by Candel (1992) and McManus et al. (1993) describe the oscillating mechanism in a variety of burner applications.

Whatever the specific mechanism, the basic features of all oscillations are the same: Pressure waves in the combustor must couple with the heat release variation via a feedback mechanism. The situation is shown schematically in Fig. 1 as a closed-loop system. A variation in the heat release rate, $\dot{Q}(t)$, produces a momentary disturbance in the acoustic field inside the combustor. The combination of acoustic reflections in the combustor and acoustic losses determines the resulting pressure disturbance, $P(t)$. If this pressure provides properly timed feedback to the combustion process (i.e., a change in fuel flow rate or mixing), an oscillation can occur. The mathematical statement of the requirement for oscillations is the well-known Rayleigh criterion (Rayleigh, 1945):

$$\frac{1}{T}\int_0^T \int_V P(\vec{x}, t)\dot{Q}(\vec{x}, t)dVdt > \text{acoustic losses.} \quad (1)$$

The term on the left is the product of heat release and pressure fluctuations integrated throughout the combustor volume, and averaged over a time T, which is the oscillation period. This integral must exceed the acoustic losses for oscillations to grow. A limit cycle oscillation will exist when the losses balance the driving by the heat release fluctuation. Thus, to mimic gas turbine combustion oscillations in a test device (as opposed to a full engine), one should use a test environment having comparable acoustic gain or losses. Likewise, the feedback between the pressure and heat release fluctuation must be the same between engine and test device.

For many instability mechanisms, the feedback between pressure and heat release is determined by the fuel nozzle and the flame geometry. We use the term flame geometry to describe the location and shape of the flame front relative to the fuel nozzle. The flame geometry is important because the timing of the feedback will be different if the flame is lifted off the nozzle, versus closely attached. Thus, where possible, in the design of single-nozzle tests, the flame geometry should be that which exists in the final engine. By testing the actual fuel nozzle hardware, most of the nozzle feedback can be replicated in a single-nozzle test. However, a careful evaluation of the acoustic boundary conditions on both the fuel and air supplies should

Contributed by the Advanced Energy Systems Division for publication in the ASME JOURNAL OF ENGINEERING FOR GAS TURBINES AND POWER. Manuscript received by the Advanced Energy Systems Division September 3, 1996; revision received February 14, 1997. Associate Technical Editor: M. J. Moran.

be performed. It may be necessary to duplicate some aspects of these boundary conditions to ensure that the fuel and air response is representative of the final hardware. Even with these precautions, it is not certain that the test device will mimic every aspect of the feedback that will occur on an engine. For example, when nozzle-to-nozzle interactions occur on an engine, a single-nozzle test will obviously not duplicate the feedback. In spite of this limitation, there is still an incentive to eliminate instability mechanisms associated with single nozzles before tackling the problem of multiple nozzles.

While some aspects of the feedback can be simulated in a test stand, the acoustic gain or loss occurring on the engine cannot be easily copied on a test device. The acoustic properties of the engine combustor are affected by the presence of the downstream hardware, such as the turbine nozzle. This is the reason combustor tests performed in isolation do not typically replicate the oscillating behavior that may (or may not) exist during final testing of the assembled engine. Single-nozzle development is often conducted in a can or tubular combustor, having a very large exhaust opening terminated by spray quench water. The large exhaust opening provides an easy exit passage for acoustic waves, and the water quench produces significant acoustic damping. These features make it difficult to observe oscillations in traditional can-type test rigs.

As an alternative to replicating the acoustic environment of a full combustor, it is possible to build a test device having very low acoustic losses at frequencies that have been observed on the full engine design. This allows subsequent development to occur on just a single nozzle. With some exceptions (discussed later), a nozzle that is stable in a test combustor having very low losses should also be stable in the final engine application where greater acoustic losses are present. This report describes a test combustor with low acoustic losses and a natural frequency that can be changed with minor modifications. To date, the combustor has shown comparable oscillations between single-nozzle results and oscillations observed in a full engine test.

Preliminary Experimental Design Considerations

To keep the design simple, we considered just two possible acoustic geometries (Fig. 2). To produce a flame geometry similar to what existed in the engine application, our first design requirement was that the combustion chamber diameter approximately match the diameter found in the engine combustor (or annular height); in this case, that was 19.8 cm (7.8 in.). Starting with Fig. 2, the so-called $\frac{1}{4}$-wave geometry will produce resonant frequencies inversely proportional to the length L. This assumes that the combustor exit does not interact acoustically with the pressure vessel and spray quench system further downstream. Because the pressure vessel inner diameter was only slightly larger than the combustion chamber (25.6 cm [10.1 in.]), it

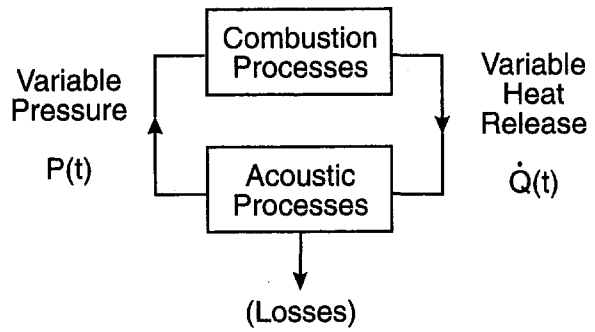

Fig. 1 A schematic of the processes occurring during combustion oscillations. Feedback between the acoustic pressure $P(t)$ and combustion heat release variation $Q(t)$ sustains oscillations.

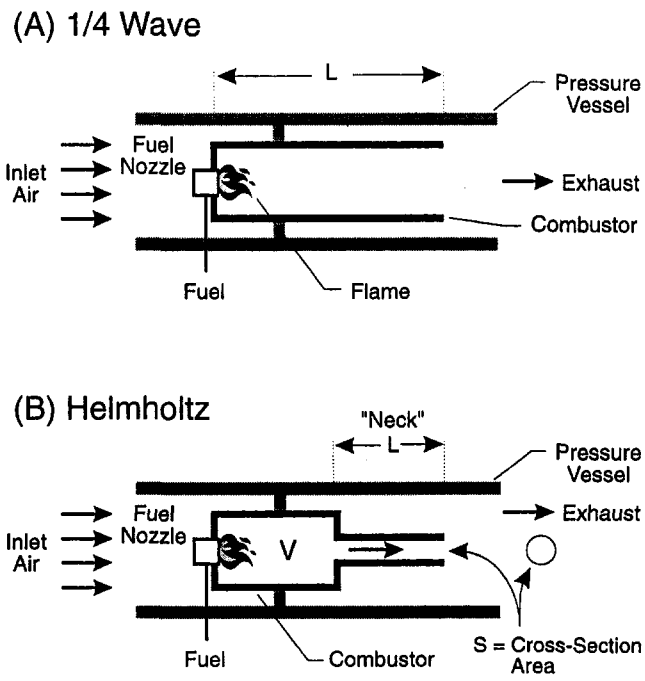

Fig. 2 Comparison of acoustic geometries considered for combustor design. The $\frac{1}{4}$ wave resonator (A) is a tube of length L. The Helmholtz geometry (B) is defined by the combustion volume V, and an exit neck with cross-sectional area S and length L.

was likely that some coupling would exist between the $\frac{1}{4}$-wave tube and the pressure vessel plenum.

To avoid this complication, we considered a Helmholtz geometry (Fig. 2). In this geometry, the acoustic pressure in the combustion chamber drives the slug of gas in the resonator neck, so that the natural frequency is established by the mass of gas oscillating in the neck and the "compliance" of the gas in the combustion chamber. At the exhaust of the neck, the area expansion (larger than Fig. 2) reduces the acoustic interaction with the downstream pressure vessel and the spray quench. A further advantage of the Helmholtz design is that the neck region of the combustor can be modified or relocated to excite different natural frequencies. The $\frac{1}{4}$-wave geometry would require changes to the length of the quarter-wave tube, meaning that the spray quench in the downstream exhaust duct (not shown) would need to be moved.

Experiment Description

Having established that a Helmholtz resonator provides an advantageous acoustic design, we now describe the combustor in detail. Figure 3 shows a cut-away and cross-sectional view of the combustor and pressure vessel. Air is supplied to the combustor from an inlet plenum. FETC's combustion facilities can supply up to 1.4 kg/s (3 lbm/s) of unvitiated air at inlet temperatures up to 840 K (1050°F) and pressures up to 30 atm. The experiment described here is limited to pressures up to 11 atm by certain components in the pressure vessel design. The facilities include gas sampling capabilities for major species such as NO_x, CO, and UHC. For a complete description of the facility capabilities, see Halow et al. (1994).

Early operating experience with this combustor showed that the combustor air supply should be diffused where it enters the inlet plenum. Our initial design supplied air to the inlet plenum via two 2.54-cm (1.0-in.) lines, with no precaution to diffuse the entering jets. This led to irregular combustion behavior at lean operating conditions because vortex shedding from the jet entry would cause fluctuations at the fuel nozzle. This problem

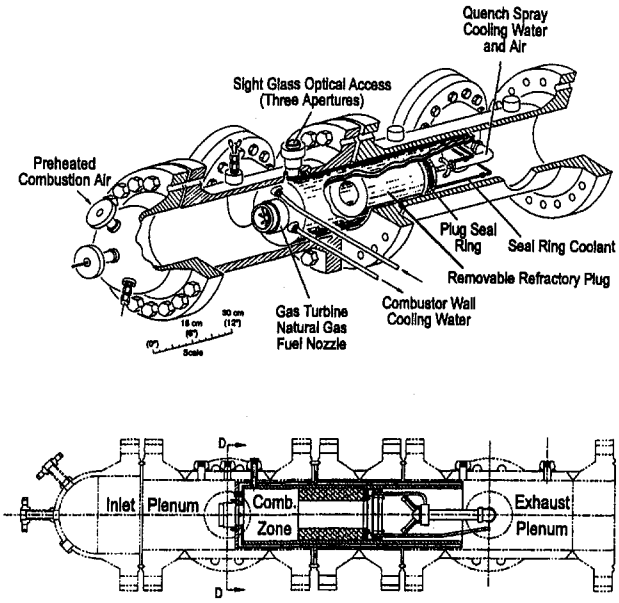

Fig. 3 Cut-away and cross-sectional views of the test combustor (note the scale on the upper figure)

was solved by redirecting the entry jets against the wall of the inlet plenum, thus diffusing the flow.

The fuel nozzle is mounted between the inlet plenum and the combustion zone. Fuel and air mix in the nozzle, and the flame is attached downstream of the nozzle. The nozzle used here was a commercial prototype that produced oscillations during full engine combustor testing, but not during conventional single-nozzle tests. The nozzle was typical of current gas turbine nozzle design, using swirl stabilization and a central pilot flame. The control valves on this experiment allow natural gas fuel flow rates up to 0.0263 kg/s (208 lbm/h), with a separately controlled pilot fuel flow rate of up to 0.0053 kg/s (41.6 lbm/h).

The combustor walls are formed by a water-cooled liner fabricated from 20.3 cm (8 in.) Schedule 80 pipe (304 stainless steel). The pipe is fitted with a rolled sheet metal jacket, forming a passage for water cooling. Likewise, the front of the combustor is formed from two metal plates, with water circulating between the plates for cooling. A central hole in the water-cooled plates will accept nozzles with an external diameter up to 8.9 cm (3.5 in.). The interior of the combustion chamber (i.e., the Schedule 80 pipe) was machined to an inside diameter of 19.8 cm (7.8 in.) with an eccentricity of less than 0.038 cm (0.015 in.). Precise tolerances were needed to allow the refractory plug and seal (described below) to be easily relocated.

The use of water-cooled combustor walls represents a compromise. The cold combustor walls will obviously lead to higher CO emissions than would occur in an engine application. However, the alternative of building a conventional air-cooled liner presents an acoustic problem: One cannot easily determine the acoustic losses occurring at the liner walls. Because we wanted to produce a combustor having very low acoustic losses, we decided to use acoustically hard, water-cooled walls. This will have two effects on the data. First, as noted already, we can expect the CO emissions to be higher than in the engine. Because our goal was to study the instabilities, we decided to accept this compromise. Second, we can expect the root mean square (rms) pressures to be higher than in an engine because the acoustic losses are low compared to the engine combustor. As explained previously, this was a desirable effect since lower acoustic losses would permit verification testing of stable nozzle designs.

To achieve oscillations, it is necessary to excite some acoustic mode associated with the Helmholtz combustor geometry. The Helmholtz geometry is determined by the cylindrical combustion zone and the resonator neck (Fig. 3). The neck of the resonator is an annular refractory plug mounted on a water-cooled ring (like a donut), attached to the back of the plug. The water-cooled ring carries a graphite packing seal that is compressed by a metal ring. The metal ring is forced out against the combustor walls by set screws, thereby locking the entire plug at one axial position. The resonator neck dimensions (S and L, Fig. 2) can be easily modified by simply re-casting a different plug. Likewise, the resonator volume (V, Fig. 2) can be changed by relocating the plug along the axis of the combustor. These dimensions are established by the desired resonant frequencies (explained later).

Spray quench water is atomized downstream of the refractory plug and sealing ring by a pair of air assist atomizers. These atomizers were developed at FETC to provide air blast atomization at low water flow rates, and pressure atomization at higher water flow rates. During testing, the nozzles operate at a fixed air blast air flow rate of 0.12 kg/s (0.26 lbm/s) air. The water flow rate is adjusted to establish an exhaust temperature above the dewpoint at the operating condition of interest. Thus, the quantity of quench water is not constant, but depends on the operating condition. As might be expected, the quantity of water affects the acoustic boundary at the exit of the Helmholtz neck. In some marginal cases, we observed that adding too much water[1] could silence an oscillation, although the water did not appear to modify resonant frequencies.

The Helmholtz resonator dimensions, V, S, and L, are used to determine the natural frequency of the resonator. The fuel nozzle inlet also plays a role, but we neglected the nozzle in design calculations. The inlet area is much smaller than the exit area, and the colder inlet gas is more dense than the exhaust, such that the inlet is a "hard" acoustic boundary relative to the exhaust. Janardan (1973) has measured the acoustic admittance of (rocket) nozzles/combustors having similar dimensions to the fuel nozzle and combustor studied here. Janardan showed that the nozzle acoustic admittance is almost zero, meaning the nozzle behaves acoustically like a solid wall. Notice this assumption depends on the relative size of the combustor and nozzle, and is not a general result. Neglecting the inlet area, the natural frequency (f_n) of the Helmholtz resonator is given by

$$f_n = \frac{c}{2\pi}\sqrt{\frac{S}{V(L+\Delta L)}}, \tag{2}$$

where the variables are identified:

c = the speed of sound in the burned combustion products,
L = the length of the combustion plug,
ΔL = the "end" correction to the neck length (zero here, see below),
S = the cross section area of the neck opening,
V = the volume of the combustion zone.

For design purposes, the speed of sound can be calculated at the expected combustion temperature using properties of combustion gases. The end correction, ΔL, is an effective extension of the neck length due to the gas that oscillates downstream of the plug. The end correction must be accounted for in classic acoustic analysis of Helmholtz resonators where there is no mean flow moving through the resonator neck. In that situation, ΔL has a value of 85 percent of the neck diameter, which for our case is a relatively small correction. However, large pressure oscillations (as expected here) and the presence of mean flow through the resonator tend to reduce the length of this correction

[1] Generally, as long as the exhaust temperature was above the dewpoint, the water did not have an obvious effect. Excess water, producing exhaust temperatures below the dewpoint, produced a significant damping effect.

factor; see the discussion by Laudien et al. (1995) and Janardan et al. (1976). In the FETC combustor, the presence of the air assist spray quench disrupts the flow in the neck exhaust region, effectively removing the oscillating mass that contributes to the end correction. Thus, for design purposes, it is acceptable to neglect this correction so that we set $\Delta L = 0$.

We mention that Eq. (2) will predict the *natural* acoustic frequency of the Helmholtz resonator. This frequency will not precisely match the oscillating frequency when combustion driving is present. It is well known that oscillating combustors will not operate at the natural frequency predicted by linear acoustics. The discrepancy depends on the phase relation between heat addition and the pressure waves, along with other factors; see Keller et al. (1989) for an example. Thus, Eq. (2) is a starting point for design; some adjustment after operation may be needed if precise frequencies are required.

The initial plug geometry and location were designed to produce a natural frequency of 300 Hz. As explained previously, the combustion chamber diameter is set to match the engine application chamber diameter or annular height. The combustion chamber length was selected to provide approximately the same residence time as would exist in the engine configuration. Having established the diameter and length, the combustor volume is fixed, and Eq. (2) can be used to select the neck length L and cross-sectional area S. The tradeoff between S and L was based on fabrication considerations of the refractory plug. From earlier experience with castable refractory, we expected reasonable durability if the annular wall of the plug was (at least) 3.8 cm (1.5 in.) thick. Based on these criteria, the following dimensions were used in the results reported here:

Combustion zone diameter:	19.8 cm (7.80 in.)
Combustion zone length:	19.8 cm (7.80 in.)
Plug inside diameter:	10.4 cm (4.10 in.)
Plug length:	22.9 cm (9.00 in.)

We expected that we would need to adjust the location and dimensions of the refractory plug to activate various acoustic modes, and the initial plan was to design the rig so that the plug could be moved (with a screw-jack) while the rig was operating. As explained below, this adjustment was not necessary.

Combustor Instrumentation

The combustor was equipped with dynamic pressure transducers connected to the inlet plenum, the exhaust plenum, and the combustion zone. The transducer attached to the combustion zone was mounted outside the pressure vessel, but connected via a 4.6-mm (0.18-in.) ID stainless steel tube. The direct connection of a dynamic pressure transducer to a transmitting tube can record artificially large pressure signals because the wave traveling down the tube stagnates at the transducer face, and thus converts both the pressure and kinetic energy of the wave into a measured pressure signal. Also, spurious signals in the measured wave can originate from "organ pipe" excitation occurring at the $\frac{1}{4}$-wave frequency of the tube. One method to avoid these complications is described by Mahan and Karchmer (1991). The transducer is mounted on a tee connection at a right angle to the transmitting tube with the remaining leg of the tee connected to a long length (8 m [25 ft]) of tubing. The additional tubing acts as a termination damper, preventing reflected waves from distorting both the amplitude and waveform that is recorded. In a separate study, we considered the effect of transducer connection arrangements on dynamic pressure measurements, showing that measurement without the termination damper is generally not a problem, unless the measurement is made near the resonant point of the transducer tube (Richards et al., 1994). For simplicity, we did not use the termination damper in preliminary testing reported here, but its use is recommended where precise measurement of oscillating amplitude is needed.

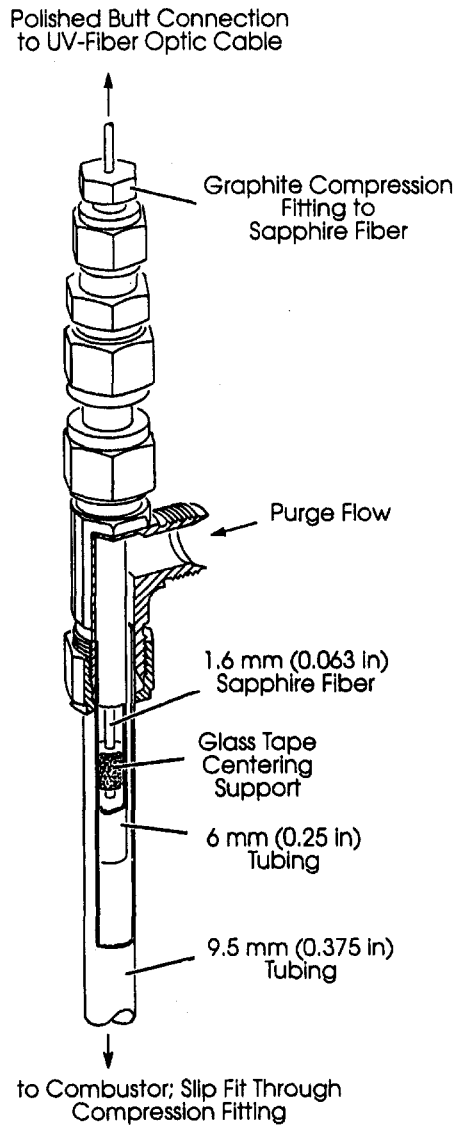

Fig. 4 Fiber optic probe for viewing OH* chemiluminescence. The OH* signal is proportional to the combustion heat release. The probe used on the experiment described here used a slightly different tubing arrangement (19 mm [0.75 in.]) for mounting on the pressure vessel, and did not require air purge.

In addition to the pressure transducer, we used one fiber optic probe to record the chemiluminescence signal from the combustor. Light emission from the excited-state hydroxyl radical (OH*) is proportional to the instantaneous value of the heat release (Mehta et al., 1981; Keller and Saito, 1987). Thus, the OH* measurement is a representation of the term $\dot{Q}(t)$ in Eq. (1). The pressure term, $P(t)$, comes from the pressure transducer. Together, these measurements can provide some insight into how the heat release and pressure are coupled together. One example of the use of the OH* measure is provided later.

Figure 4 is a cutaway view of the fiber optic OH* probe. The heart of the probe is a 1.6-mm (0.0625-in.) sapphire fiber, pressure-sealed using conventional compression fittings (with a graphite ferrule on the sapphire fiber). The viewing angle of the probe is determined by the geometry of the probe interior (or, at most, by the acceptance angle of the fiber that is 30 deg included). Other tubing arrangements are easily envisioned, allowing installations on operating engines. As shown, the probe

Table 1 Test conditions corresponding to cases P1 throughout P4

Case	Combustor Pressure (atm)	Inlet Temp. (K)	Reference Velocity (m/s)	Overall Equivalence Ratio	% Pilot
P1	6.7	289	24.3	0.66	0.0
P2	7.3	290	21.9	0.70	3.8
P3	4.8	396	38.6	0.79	5.8
P4	6.1	538	74	0.55	3.1

is fitted with a tee connection to allow purge flow. This is not essential for natural gas operation, but would be necessary for testing on fuel oil combustion. The external side of the fiber was attached to a UV-transmissive fiber optic cable, with the resulting signal detected by a standard photomultiplier tube (PMT). The PMT detector was fitted with an optical line filter, centered at the (optical) wavelength of interest for OH* emission (315 nm). This probe was installed through a fitting in the pressure vessel and combustor liner, viewing across the combustor diameter at an axial station 2.54 cm (1.00 in.) downstream of the fuel nozzle. The probe essentially replaced the sight glass optical access shown in Fig. 3.

Preliminary Operating Experience

We began testing the combustor by surveying various combinations of flow rate, operating pressure, and inlet air temperature. Table 1 lists four test cases (P1 through P4) that were selected as representative of the behavior observed during the survey of operating conditions. The pressure and OH* signals corresponding to these cases are shown in Figs. 5(a–d). In Table 1, we show the combustion air flow rate in terms of the reference velocity, which is the bulk velocity of air moving through the premixing nozzle. The reference velocity is calculated by dividing the nozzle air flow (mass per second) by the product of air density and nozzle cross-sectional area.

Cases P1 through P4 demonstrate that several different acoustic modes were easily excited, including the natural frequency of 300 Hz. Starting with case P1 (Fig. 5(a)), note that the pressure spectra and OH* spectra are dominated by a 150-Hz component, with a smaller component at 300 Hz. This was typical of combustor operation with ambient inlet air temperatures. Comparison of the time history between pressure and OH* reveals that the pressure signals include a smaller, but appreciable, perturbation leading the dominant pressure peak. The OH* signal shows only an occasional perturbation prior to peak heat release. This observation suggests that the dominance of the 150-Hz mode is the result of the combustion responding to every other natural acoustic cycle. Case P2 (Fig. 5(b)) is a slight variation of this situation, where the 300-Hz mode is evident in the pressure signal, but the heat release continues to oscillate at $\frac{1}{2}$ of the pressure cycle. We emphasize that the dominance of 150 Hz in the pressure spectra was not the result of acoustic coupling between the combustion zone and the large inlet plenum volume.[2] As is especially evident in case P2, the combustion heat release is "forcing" every other cycle of the natural acoustic period, producing a strong pressure signal in the combustor at $\frac{1}{2}$ of the natural frequency. This type of behavior was very common during testing with ambient inlet air temperature.

We reasoned that the frequency of the heat release variation was limited by the low inlet air temperatures and low reference velocities. Low inlet air velocities produce a lengthy time lag between processes in the fuel nozzle and events occurring at the flame. Likewise, low inlet air temperatures will produce a lower flame speed, meaning the flame may stand off the nozzle. This will also lengthen the time required for feedback between the nozzle and flame. Thus, case P3 included air preheat and a higher reference velocity (Fig. 5(c)). The OH* spectra and the pressure spectra are now both dominated by a 230 to 260 Hz signal. In contrast to cases P1 and P2, the time histories now show a correspondence between every pressure and OH* peak, rather than every other peak. Many of the test cases run to date have included signals in the range of 230 to 260 Hz, depending on the operating conditions. Note that this is slightly lower than the natural frequency of 300 Hz. Part of this discrepancy may be due to the approximate nature of the natural frequency calculation from Eq. (2), but also because oscillations will not necessarily occur at the natural acoustic frequency. As discussed previously, the phase between heat release and pressure will shift the operating frequency away from the natural frequency (Keller et al., 1989).

Finally, in case P4, we present results at a higher inlet air temperature and reference velocity (Fig. 5(d)). Here, a 410-Hz mode is excited, appearing in both the pressure and OH* spectra. This higher-frequency oscillation was generally observed only at higher inlet air temperatures (greater than 530 K [495°F]), and with larger reference velocities. Depending on operating conditions, we observed similar oscillations over a range of frequencies typically from 410 to 450 Hz. Again, the oscillating frequency is not necessarily the natural acoustic frequency of 300 Hz. It is interesting that these higher frequencies were activated without any changes in the geometry of the resonator. These higher frequencies are not explained by an increase in the speed of sound due to greater combustion temperatures associated with hotter inlet air. Notice the equivalence ratio is much lower in case P4 versus P3 (Table 1). We did not modify or move the resonator neck, as we thought would be necessary to activate various frequencies. At select conditions, we did identify some even higher frequencies (shown below).

The fuel nozzle used in these preliminary studies was also tested as a prototype on a commercial gas turbine engine. The same prototype nozzle was developed in a traditional single-nozzle test combustor, and appeared to be free of oscillations. Oscillations were observed in the engine application and the single-nozzle test device described in this paper. Below, the observed oscillating frequencies are compared between the engine and the single-nozzle test device:

	Frequencies in cycles per second (Hz)			
Engine:	—	295	475	—
Test device:	150	230–260	410–450	2300–2500

The very high frequencies (2300 to 2500 Hz) observed in the test device were the expected frequency for a transverse acoustic mode in the combustion zone volume. The low-frequency, 150-Hz mode was routinely observed in the test device when the inlet air temperature was ambient. This condition cannot be realized on an engine, which explains why no similar frequency was evident on engine tests. The middle-frequency ranges were comparable between test stand and engine. On the engine, the choice of the 295-Hz or 475-Hz mode depended on the operating conditions, and the same was true in the test device at approximately the same conditions. The complex geometry of the engine combustor will allow multiple acoustic modes, but aside from the transverse mode, it is not obvious how the Helmholtz resonator produces both the central acoustic frequency ranges (230 to 260; 410 to 450). At this point, we propose that the bandwidth of the resonator is large enough that the combustion can generate an appreciable acoustic response over a range of frequencies, providing feedback between the heat release and acoustic pressure.

[2] Measured pressures in the inlet plenum were $\frac{1}{4}$ of those in the combustion chamber, and occurred at 300 Hz. Thus, the inlet plenum was responding to the combustion chamber acoustics, but was not responding directly to the strong combustion fluctuations occurring every other acoustic cycle.

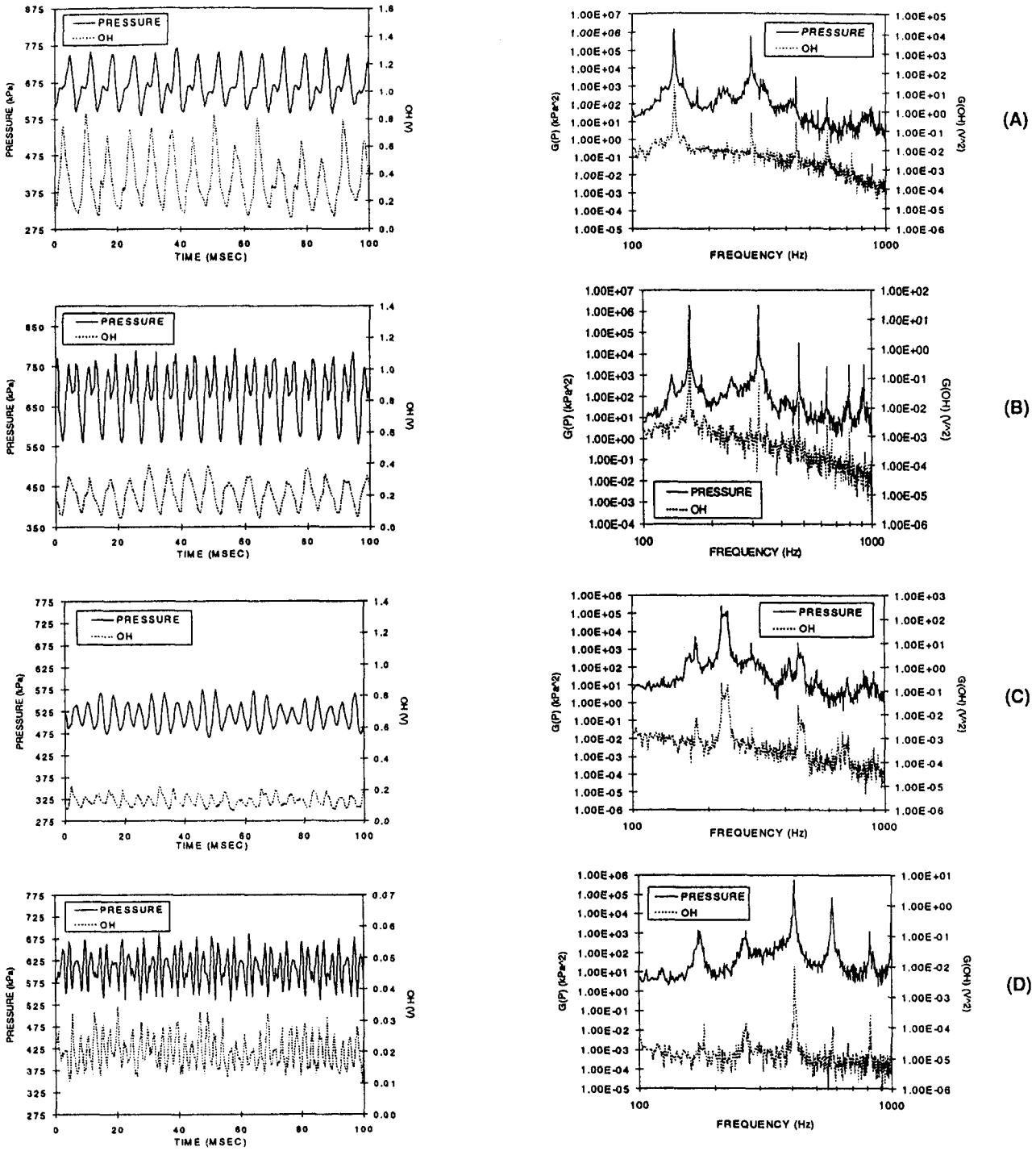

Fig. 5 Pressure and OH* signals for cases *P1–P4* listed in Table 1. Time histories for the pressure and OH* signals are shown in the left figure, with pressure and OH* spectra shown at the right.

A complete investigation of oscillating combustion requires mapping the combustor performance over a wide range of operating conditions. Relevant parameters include the mass flow, the operating pressure, the inlet air temperature, the equivalence ratio, and, if applicable, the amount of pilot fuel. It may be possible to reduce the number of independent parameters by examining data in terms of the reference velocity. For many instability mechanisms, the reference velocity determines the time lag in the feedback between processes inside the fuel nozzle and at the flame front. For example, rich or lean pockets of fuel are transported down the nozzle at the reference velocity. Thus, the reference velocity may be more significant than the value of the mass flow, because the reference velocity accounts for the effect of changes in inlet density (i.e., temperature and pressure), which would otherwise be overlooked by comparing the mass flow alone.

To demonstrate the significant role of the nozzle reference velocity, Fig. 6 shows the measured rms pressure as a function of reference velocity. The figure includes data at two different pressures (6.4 and 7.8 atm) and with or without pilot fuel. When present, the pilot fuel was set at 0.54 g/s (4.3 lbm/h), which is less than 3.5 percent of the lean premix fuel flow at any of the conditions shown. The dominant frequency is shown near each of the operating points. The qualitative response of the

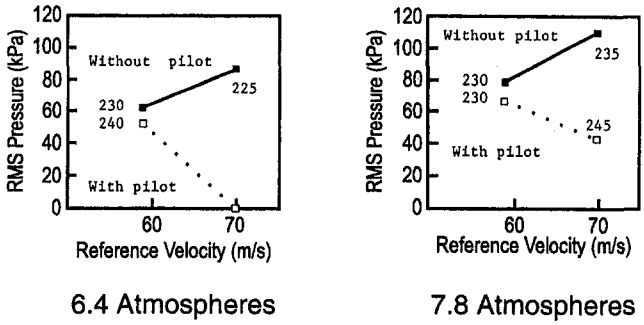

Fig. 6 Effect of reference velocity on the rms pressure at different pressures, and with or without pilot fuel. Operating conditions: 533 K (550°F) inlet air temperature, 0.56 equivalence ratio.

combustor to the presence of pilot is the same at the two pressure levels, in spite of the appreciable difference in nozzle mass flow and operating pressure. Notice that the pilot has little effect at the 60 m/s reference velocity, but has a significant effect at 70 m/s. It is sometimes assumed that a pilot is a certain method to silence an oscillation, but these results suggest that the effectiveness of a pilot can depend on other operating conditions. In general, we found that the reference velocity and temperature were critical parameters, and the pressure was less critical. *However, a slight change in pressure at a given mass flow would change the reference velocity.* At conditions near the onset of oscillation, the pulsations could begin by a slight change in rig back pressure because of the change in the reference velocity. Because of this behavior, we found it was essential to replicate and maintain operating conditions closely, including the operating pressure. Additional testing is now in progress to quantify these preliminary observations better.

Summary and Conclusions

This report discusses the development of a single-nozzle test device for studying premixed combustion oscillations. Combustion oscillations occurring in complete gas turbine engines are often difficult to reproduce during single-nozzle development because of differences in flame geometry and acoustic boundary conditions. In this paper, we suggest that some aspects of engine oscillations can be observed using a single fuel nozzle by taking the following steps: (1) The flame geometry should be maintained relative to engine testing, and (2) the acoustic losses in the test device should be minimized with a natural frequency corresponding to the oscillating frequency observed (or expected) on the complete engine. This approach was tested on a prototype fuel nozzle that produced oscillations during testing in a commercial engine. Similar oscillations were recorded in the single-nozzle test device as had occurred on the engine at comparable operating conditions. Although these results are encouraging, we noted that the single-nozzle test device will not reproduce arbitrary oscillations that occur on a complete engine test. Nozzle/nozzle interactions may complicate the response that exists on an engine and obviously cannot be reproduced with just a single nozzle. Likewise, oscillations that are controlled by acoustic velocities transverse to the nozzle axis will not be reproduced in a test device that relies on a bulk, Helmholtz mode. Although these complications should be recognized, the simplicity of single-nozzle testing makes the approach outlined here very attractive for a preliminary assessment of how changes to individual fuel nozzles will affect combustor stability.

A brief survey of operating conditions suggests that it may be helpful to characterize oscillating behavior in terms of the reference velocity and inlet air temperature, with the rig back pressure playing a smaller role. Preliminary operating experience showed that it was essential to replicate closely and maintain all operating parameters that could affect the reference velocity. For example, although the back pressure was less critical than the reference velocity, a modest change in back pressure could produce a different reference velocity (at constant mass flow) and thereby change the oscillating behavior. We also showed that the stabilizing effective of a pilot flame depends on the operating conditions and is not guaranteed to silence an oscillation at all conditions. These conclusions are based on preliminary experience. Work now in progress is aimed at studying these effects in more detail to provide a general approach to solving oscillation problems in premix turbine combustors.

References

Alsup, C. T., Zeh, C. M., and Blazewicz, S., eds. 1995, *Proc. of the Advanced Turbine Systems Annual Program Review Meeting,* 2 vols., DOE/METC-96/1023, NTIS/DE96000561 and NTIS/DE96000562, National Technical Information Service, Springfield, VA.

Beer, J. M., 1995, "Clean Combustion in Gas Turbines: Challenges and Technical Responses—A Review," *Journal of Institute of Energy,* Vol. 68, pp. 2–10.

Candel, S. M., 1992, "Combustion Instabilities Coupled by Pressure Waves and Their Active Control," *Twenty-Fourth (International) Symposium on Combustion,* pp. 1277–1296.

Halow, J. S., Maloney, D. J., and Richards, G. A., 1994, "METC Combustion Research Facility." *Proc. Advanced Turbine Systems Annual Program Review Meeting,* DOE/OR-2025.

Harrje, D. T., and Reardon, F. H., 1972, *Liquid Propellant Rocket Combustion Instability,* NASA SP-194.

Janardan, B. A., 1973, "Damping of Axial Instabilities by Solid Propellant Rocket Exhaust Nozzles," Ph.D. Thesis, Georgia Institute of Technology.

Janardan, B. A., Daniel, B. R., and Zinn, B. T., 1976, "Measurements of Acoustic Responses of Gaseous Propellant Injectors," *Journal of Sound and Vibration,* Vol. 47(4), pp. 559–569.

Keller, J. O., and Saito, K., 1987, "Measurement of the Combusting Flow in a Pulse Combustor," *Combustion Science and Technology,* Vol. 53, pp. 137–163.

Keller, J. O., Bramlette, T. T., Dec, J. E., and Westbrook, C. K., 1989, "Pulse Combustion: The Importance of Characteristic Times," *Combustion and Flame,* Vol. 73, pp. 33–44.

Kentfield, J. A. C., and Yerneni, P., 1985, "Pulsating Combustion Applied to a Small Gas Turbine," ASME Paper No. 85-GT-52.

Kentfield, J. A. C., and O'Blenes, M., 1988, "Methods for Achieving a Combustion-Driven Pressure-Gain in Gas Turbines," ASME JOURNAL OF ENGINEERING FOR GAS TURBINES AND POWER, Vol. 110, pp. 704–711.

Kentfield, J. A. C., and Fernandes, L. C. V., 1990, "Improvements to the Performance of a Prototype Pulse, Pressure-Gain, Gas Turbine Combustor," ASME JOURNAL OF ENGINEERING FOR GAS TURBINES AND POWER, Vol. 112, pp. 67–72.

Laudien, E., Pongratz, R., Pierro, P., and Preclik, D., 1995, "Experimental Procedures Aiding the Design of Acoustic Cavities," in: *Liquid Rocket Combustion Instability,* American Institute of Aeronautics and Astronautics, Cambridge, MA, pp. 377–399.

Lefebvre, A. H., 1995, "The Role of Fuel Preparation in Low Emission Combustion," ASME JOURNAL OF ENGINEERING FOR GAS TURBINES AND POWER, Vol. 117, pp. 617–654.

Mahan, J. R., and Karchmer, A., 1991, "Combustion and Core Noise," in: *Aeroacoustics of Flight Vehicles: Theory and Practice. Vol. 1: Noise Sources,* NASA Langley Research Center; available from AIAA Technical Library.

McManus, K. R., Poinsot, T., and Candel, S. M., 1993, "A Review of Active Control of Combustion Instabilities," *Progress in Energy and Combustion Science,* Vol. 19, pp. 1–29.

Mehta, G. K., Ramachandra, M. K., and Strahle, W. C., 1981, "Correlations Between Light Emission, Acoustic Emission, and Ion Density in Premixed Turbulent Flames," *The Eighteenth (International) Symposium on Combustion,* The Combustion Institute, Pittsburgh, PA; pp. 1051–1059.

Putnam, A. A., 1971, *Combustion Driven Oscillations in Industry.* American Elsevier Publishers, New York.

Rayleigh, J. S. W., 1945, *The Theory of Sound,* Dover, New York, Vol. 2, p. 226.

Richards, G. A., Gemmen, R. S., and Narayanswami, L., 1994, *Aerovalve Pulse Combustion,* Technical Note, DOE/METC-94/1009, NTIS/DE94012262, National Technical Information Service, Springfield, VA.

Yang, V., and Anderson, W., eds., 1995, *Liquid Rocket Combustion Instability,* American Institute of Aeronautics and Astronautics, Cambridge, MA.

The Development of the Junkers Jumo 004B—The World's First Production Turbojet

C. B. Meher-Homji
Bechtel Corporation,
Houston, TX 77252

This paper describes the pioneering work of Anselm Franz who, while working for the Junkers Engine company in Germany, designed and made operational the world's first production jet engine, the Junkers Jumo 004, which was the powerplant for the formidable Messerschmitt ME 262 fighter. The paper covers the historical background of jet engine development in Germany during the Second World War and discusses design details of this remarkable axial flow, 1980 lb (900 kg) thrust engine. The development represented a historic achievement for Anselm Franz and his design team at Junkers. Approximately 6000 engines were built at the end of the Second World War in the face of acute shortages and damage to German industry. The Jumo was brought from conceptual design to production in a span of four years. Franz joined Avco Lycoming in 1952 and worked for 16 years. He retired as Vice President in 1968 after making prolific contributions to the development of several Lycoming engines including the T53, the T55, and the AGT-1500. Anselm Franz passed away at the age of 94 in Stratford, Connecticut. This paper is a modest tribute to a jet engine pioneer who, in spite of his extensive contributions to gas turbine technology, will always be remembered as the man who designed the world's first production turbojet.

1.0 Introduction

On July 18th, 1942, a small group of people gathered at the airport in Leipheim in Germany to witness the first flight of the revolutionary Messerschmitt ME 262, powered by two Junkers Jumo 004 engines. Included in this group were Willy Messerschmitt and Anselm Franz, the chief designer of the jet engine. As recounted by Franz (1979), the aircraft with Fritz Wendel at the controls was standing at the beginning of the runway ready for take-off. The engines were turned on and carefully brought to full power. Releasing the brakes, Wendel rolled forward and accelerated right to the end of the runway. Suddenly, the aircraft climbed almost vertically with unprecedented speed until it disappeared in the clouds. Franz states that it was at this climactic moment that it became clear to him that the jet age had begun.

An account of Franz's achievement is presented here along with technical details on this 1980 lb thrust axial turbojet. The Junkers Jumo 004 was the world's first production jet engine and powered the advanced ME 262, which would have presented a serious threat to Allied air superiority had it been deployed expeditiously. The ME 262 with the Jumo 004 engine is shown in Fig. 1.

2.0 Evolution of the Jet Engine Industry in Germany

In order to put the development of the Junkers Jumo 004 into historical context, it is necessary to trace the development of the jet engine industry in Germany shortly before and during the Second World War.

The invention and development of the jet engine was a profound achievement in man's quest for higher speed. Along with the introduction of low wing monoplanes (circa 1935), jet propulsion allowed a quantum leap in fighter aircraft speeds. Pioneering the turbojet revolution were Sir Frank Whittle in England and Hans von Ohain in Germany, their work being extensively documented by Constant (1980), Schlaifer (1950), von Ohain (1979), Scott (1995), and Jones (1989). Both these pioneers, who envisioned flight speeds in excess of 500 mph, at altitudes of 30,000 feet and above, had their revolutionary ideas as students, and developed their engines without the help of the traditional aeroengine companies.

Von Ohain developed the idea of his jet engine while he was a doctoral student at the University of Göttingen. By 1934, he had completed rudimentary design calculations that indicated speeds of 500 mph were possible. He initiated patent procedures and decided to build a working model of the engine. Working with Max Hahn, an expert mechanic machinist and a natural engineer, he built his first model engine, which was plagued by combustion problems. Von Ohain's advisor, Professor R.W. Pohl, introduced Ohain to Ernst Heinkel, the legendary aircraft manufacturer, who, Pohl knew, was obsessed with high-speed flight. As a result, the 25-year-old Ohain was summoned to Heinkel's house on the Baltic Coast, and after a grueling one-day interview with Heinkel and his leading engineers, succeeded in convincing Heinkel to take a risk in hiring him.[1]

Von Ohain and Max Hahn started work under a shroud of secrecy in a special hut in Marienehe and were given instructions to develop a jet engine as rapidly as possible, with the stipulation that ground tests were to begin within a year. Heinkel kept this work secret from the German Air Ministry (RLM), the Luftwaffe, and engine manufacturers. The first engine, designated the HeS1, operated on hydrogen fuel and was successfully test run in March 1937. In about six months, the HeS2a operating on liquid fuel developed 1100 lb of thrust. The HeS3A ran in March 1938. The historic first pure jet-powered flight of the He 178 powered by a HeS3B turbojet occurred on August 27th, 1939, a few days before the start of World War II. Heinkel immediately informed high air ministry officials of this momen-

Contributed by the International Gas Turbine Institute and presented at the 41st International Gas Turbine and Aeroengine Congress and Exhibition, Birmingham, United Kingdom, June 10–13, 1996. Manuscript received at ASME Headquarters February 1996. Paper No. 96-GT-457. Associate Technical Editor: J. N. Shinn.

[1] Part of the reason for Heinkel hiring von Ohain was to prevent him from going to his archrival, Messerschmitt. This rivalry continued throughout the war in the race to produce the first jet fighter. For example, in 1940/41, Messerschmitt delayed for months by political means, Heinkel's acquisition of Hirth Moteren Gmbh (Schlaifer, 1950).

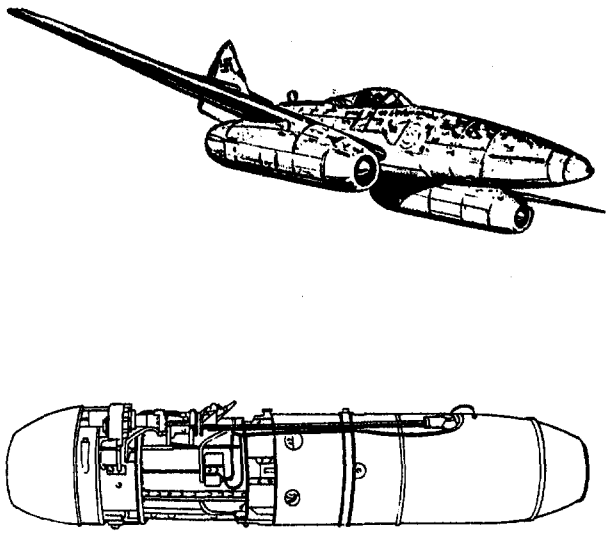

Fig. 1 The Messerschmitt ME 262 "Swallow" powered by two Junkers Jumo 004B turbojets. This formidable fighter was capable of speeds in excess of 550 mph.

tous event but was met with indifference. The German Air Ministry ordered Heinkel to cease all research on jet engines but Heinkel, convinced that his political connections would ultimately result in a lucrative contract, kept von Ohain's team working on turbojets. A few months later, Heinkel's proposal for a jet fighter (the He 280) was accepted by the air ministry. This aircraft was to be powered by two HeS8A engines designed by von Ohain.[2] The RLM canceled the He 280 on March 27, 1943, and development of the HeS8A was curtailed by the RLM in mid-1942 in favor of the Jumo 004 and BMW 003 engines. Von Ohain (1979) traces the evolution of engines from the HeS 1 to the advanced HeS 011.

During 1938 and 1939, engineers at yet another aircraft manufacturer, Junkers aeroplane company, were working on jet engines under the guidance of Hurbert Wagner. Wagner, a brilliant airframe designer, was well versed in steam turbine design and wanted to develop turboprop engines, which he felt would make Junkers a pre-eminent aircraft company. In 1938, Junkers had 30 designers and draftsmen working on the project and were in the process of developing an engine with a five-stage axial compressor, single combustor, and two-stage turbine.

At that time, two enterprising engineers, Helmut Schelp and his senior Hans Mauch in the German Air Ministry, who both had ambitious jet engine development programs in mind, were trying to work with the traditional aeroengine manufacturers and interest them in jet engine development. Schelp was educated in Germany and the USA (Stevens Institute of Technology) and had, in 1936, taken an advanced course at the German Research Institute for Aeronautics (DLV) in Berlin. He was aware of the limitations of piston engines for higher speeds and had concluded that jet propulsion was the solution.[3] Schelp worked on jet engine concepts, unaware of the ongoing research at Heinkel Aeroplane, or Junkers Airframe Company. The prevailing feeling at that time was that compressor and combustor efficiencies were too low to allow jet engine development. Schelp, however, knew of three leading compressor engineers, Professors Prandtl, Betz, and Encke, who worked at the Aerodynamic Research Establishment (AVA) at Göttingen, who had been successful in designing compressors based on aerodynamic airfoil theory and recognized that their work could provide the impetus required in developing a practical engine.

In 1938, Schelp and Mauch visited four dominant aeroengine manufacturers: BMW, Junkers Aeroengine Company, Daimler Benz, and Bramo. The head of Junkers Aeroengine, Otto Mader, reluctantly accepted a small development engineering contract. He was not aware of the ongoing program at Junkers Aeroplane Company. Daimler Benz refused Schelp's offer for funding. Bramo, fearful that they were soon to face severe competition in piston engine orders to their rivals BMW, agreed to perform a study. BMW took on a contract as they were searching for a use for a water-cooled turbine that BMW had already developed.

Frustrated by the inaction of the aeroengine companies, Schelp and Mauch, during the early part of 1939, made several visits to the companies trying to stimulate some activity. On his third or fourth visit to Junkers, Schelp was told by Otto Mader that even if there was something in "this jet idea," he had no one to put in charge of such a complex project. At this, Schelp suggested that Anselm Franz who was in charge of internal aerodynamics and turbo supercharger development be assigned to this project.[4] This was, as the project unfolded, a correct choice as Franz went on to develop the world's first production jet engine. It was Franz's engineering and management skills and his perceptive and deliberate choice of a conservative but achievable design target that resulted in the success of the Jumo 004 turbojet.

Wagner of Junkers Aeroplane Company handed over their existing design to Junkers Engine company but Dr. Max Mueller, who worked for Wagner, disliked Otto Mader and, not wanting to give up control of his engine, secretly approached Heinkel and offered to work for him. In May 1939, Mueller and most of his staff resigned from Junkers to go and work for Heinkel. Franz, having surveyed Mueller's work, decided against using it and started work on a brand new axial flow design that would finally become the Junkers Jumo 004—the world's first production jet engine.

At the end of the war, the German jet engine program was highly advanced. The BMW company (which had absorbed Bramo) produced the 002 and 003 engines in competition with the 004 engine of Junkers.

Clearly, the most advanced engine was the 011 engine developed by Ohain and Bentele at Heinkel Hirth.[5] The technical specifications for this were developed by Schelp who wanted a replacement for the BMW 003 and Jumo 004 engines. The design goals for the 011 engine included a 5:1 compressor pressure ratio, a thrust of 3000 lb and the utilization of no strategic materials, which called for a completely air-cooled turbine. Development of the 011 engine started in May 1943. Designed by von Ohain, this 3000 lb thrust engine utilized a completely air-cooled turbine developed by Dr. Max Bentele.

3.0 Design and Development of the Junkers Jumo 004 Engine

From the outset, Anselm Franz made a deliberate decision that his design would not aim at the maximum achievable but would focus on a very conservative goal that had the greatest chance of success. The reason that Franz did not aim high was that he recognized the need for rapid engine development and that failure may have caused Junkers or the Air Ministry to drop the entire program. This choice was the fundamental reason why

[2] Nine prototypes of the He-280 were built and in the spring of 1942 the prospects for this aircraft were favorable as the Jumo 004 was, at that time, plagued by problems. Once Franz resolved these problems, the ME 262 proved to be superior to the He-280 and was thus chosen for production.

[3] Schelp was aware of the work of Armengaud and Lemale published before 1910.

[4] It should be mentioned that Junkers had began, in 1938, a general survey of the field of gas turbines and jet engines under the charge of Anslem Franz.

[5] At Schelp's insistence, Heinkel had bought out the Hirth aeroengine company in August 1939, which provided them with excellent shops and facilities but also with the talents of people such as Dr. Max Bentele a renowned expert in blading vibration.

the Jumo 004 was the first jet engine to reach production. Franz was initially given a few people from his supercharger department, but his group grew steadily to about 500 people in 1944. According to Franz, there were never any constraints in terms of funding or test facilities. His facilities were well equipped with test rigs and stands and even had an altitude chamber test cell (Franz, 1979).

3.1 Development of the 004A Experimental Engine. As Franz had no opportunity to design individual engine components, a decision was made to design an experimental engine, the 004A, which would be thermodynamically and aerodynamically similar to the final production engine. The goal in developing the 004A was to have an operating engine in the shortest time frame without consideration for engine weight, manufacturing considerations, or minimizing the use of strategic materials. Based on the results of the 004A engine, the production 004B engine was to be built.

Even though Franz was familiar with centrifugal compressors because of his supercharger work, he chose an axial compressor design because he was convinced that frontal area was of fundamental importance and that gains could be achieved in efficiency with an axial design. The design of the 004 compressor was based on the work done by the AVA[6] in Göttingen, the compressor being designed by Encke with a peak efficiency of 82 percent and an operating efficiency of 75-78 percent. The compressor utilized pure reaction blading, which resulted in a pressure ratio of 3.14:1 in eight compression stages. The engine airflow rate was 46.6 lb/sec (21.2 kg/s). The turbine was based on steam turbine experience of AEG , Berlin, and blades were not of the vortex design as proposed by Whittle.

Franz recognized the superiority of an annular combustor design, but opted for a 6-can-type combustor, as he knew that these would present less of a problem and permit bench testing with a single can. When Schelp reviewed the design of the Jumo 004, he was critical of the conservative design in comparison to the BMW 003 but did not try to make Junkers institute any changes.

By the spring of 1940, the 004A had made its first test run and by January 1941 the engine was brought to full speed of 9000 rpm and a thrust of 946 lb (430 kg). At this juncture, the engine was plagued by compressor blade vibration failures. The sheet metal stator vanes, which were originally cantilevered from the outside, suffered from vibration difficulties, and renowned blade vibration specialist Max Bentele was asked to help in solving the vibration problems. The stator design was changed and by August 1941, a thrust of 1320 lb (600 kg) was attained. In December 1941, a ten-hour run at a thrust of 2200 lb (1000 kg) was demonstrated. On March 15, 1942, the engine was flown in a ME 110 test bed and later that year, on July 18th, the first flight of the ME 262 powered by two Jumo 004 jets took place and lasted for 12 minutes.

3.2 Development of the 004B Production Engine. Based on the excellent flight results, the air ministry issued a contract for 80 engines, These engines, rated at a thrust of 1850 lb, were used for further engine development and airframe testing. The 004A engine was unsuitable for production because of its considerable weight and its high utilization of strategic materials (Ni, Co, Mo), which were not available to Germany at that time. Because of this, the 004B engine was designed to use a minimum amount of strategic materials. All the hot metal parts, including the combustion chamber, were changed to mild steel (SAE 1010) and were protected against oxidation by aluminum coating. Extensive air-cooling was used throughout the engine. The later version of the 004B engine had hollow air-cooled stator vanes. Compressor discharge air was used to cool the blades. With the hollow Cromandur sheet metal blade, the complete 004B engine had less that 5 lb of chromium. A discussion of the materials used is provided in section 3.3.

Table 1 Leading particulars of the Junkers Jumo 004 B-1 production engine

Airflow	46.6 lb/sec (21.2 kg/s)
Pressure ratio	3.1:1
Turbine inlet temperature	1427°F (775°C)
Thrust	1980 lb (900 kg)
SFC	1.4 lb/lb-hr
Engine weight	1650 lb (750 kg)
Thrust/weight ratio	1.21
Engines diameter	30 in. (760 mm)
Engine length	152 in. (3860 mm)
Compressor blading reaction	100 percent
Turbine reaction	20 percent
$\eta_{compressor}$	78 percent
$\eta_{combustor}$	95 percent
$\eta_{turbine}$	79.5 percent

The first production model of the 004B-0 exhibited a weight reduction of 220 lb (100 kg) from the 004A engine. Additional modifications were made to the first compressor stages. A series of 100 hour tests were completed on several engines and a time between overhaul of 50 hours was achieved.

During the summer of 1943, several turbine blade failures were experienced due to a sixth-order excitation (6 × No. of combustors) when operating at full speed. The Junkers team worked diligently to resolve the problems. Franz recalls that he used the unconventional method of determining blade natural frequency by asking a professional musician to stroke the blades with a violin bow and then use his trained musical ear to determine the ringing natural frequency. The Air Ministry was, however, getting increasingly impatient and scheduled a conference in December, 1943, at the Junkers Dessau plant, to be attended by turbine experts from government, industry, and academia. Max Bentele, who was instrumental in solving the problem, attended this conference and listened to the numerous arguments pertaining to material defects, grain size, and manufacturing tolerances. As recounted by Bentele in his autobiography (Bentele, 1991), these were only secondary factors. When his turn came, he stated clearly, to the assembled group, the underlying cause of the problem, namely that the six combustor cans and the three struts of the jet nozzle housing after the turbine were the culprits. These induced forced excitation on the turbine rotor blades where a sixth-order resonance occurred with the blade bending frequency in the upper speed range. The predominance of the sixth-order excitation was due to the six combustor cans (undisturbed by the 36 nozzles) and the second harmonic of the three struts downstream of the rotor. In the 004A engine, this resonance was above the operating speed range, but in the 004B it had slipped because of the slightly higher turbine speed and the higher turbine temperatures. The problem was solved by increasing the blade natural frequency by increasing blade taper, shortening blades by 1 mm, and reducing the operating speed of the engine from 9000 to 8700 rpm.

The leading particulars of the production engine are shown in Table 1. Volume production of the 004B-1 started in early 1944. In spite of difficult conditions, the engine was manufactured in increasing quantities. Approximately 6000 engines were built by the end of the war.

According to Franz (1979) the 004E version was equipped with an afterburner. With turbine inlet gas temperature raised to 1600°F (870°C), the thrust increased to 2640 lb (1200 kg). The 004E was the first turbojet with an afterburner.

3.3 Hot Section Materials. In 1936, when development work on the Jumo 004 started, a high-temperature Krupp steel known as P-193 was available. This material, which contained Ni, Cr, and Ti, could be given good high-temperature strength by means of solution treating and precipitation hardening.

[6] Aerodynamische Versuchs Anstalt.

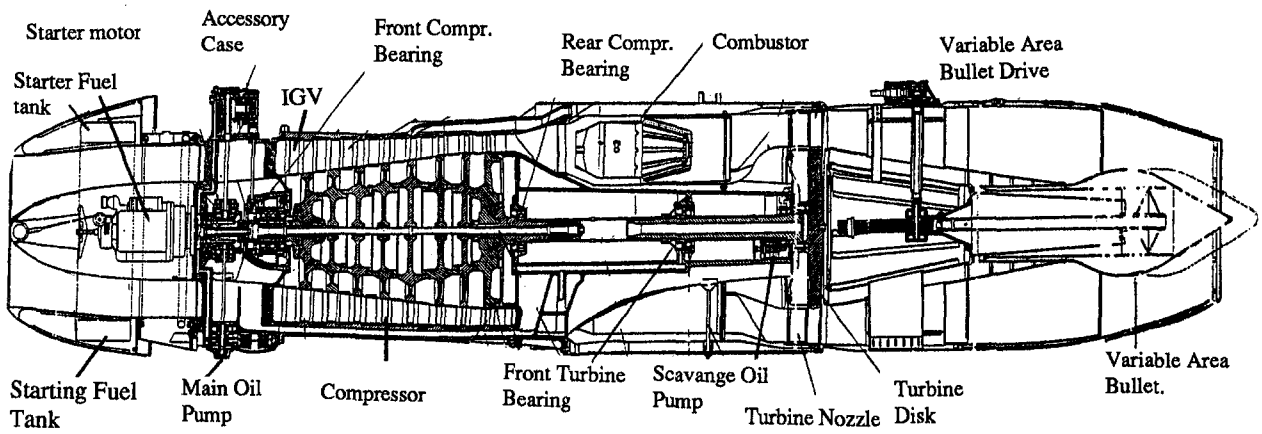

Fig. 2 Cross section of the Junkers Jumo 004 Turbojet (Neville and Silsbee, 1948)

Krupp developed an improved version of P-193 known as Tinidur.[7] It was of the same type as Nimonic 80, which was used in British Gas turbines from 1942 but contained over 50 percent iron (which was replaced by Ni in Nimonic 80) and this caused a rapid drop in creep strength at 1080°F (compared to 1260°F for Nimonic 80). While Krupp knew that Tinidur could be improved by increasing the Ni content from 30 to 60 percent, there was a recognition that Ni would not be available. The Ni content was therefore left at 30 percent. Similarly, work on cobalt-based alloys was also shelved due to a shortage of cobalt.

Junkers had investigated several materials, and by the summer of 1939, had concluded that Krupp's Tinidur was the material that would have to be accepted. The first turbine blades of the 004A version were solid. Early tests showed that even supposedly identical blades would have a large scatter life. By 1944, Junkers had solved the problem and obtained uniform quality of the blade by close control of the manufacturing process, especially of the critical forging process. When the hollow blades were employed, attempts were made to produce them by folding flat sheets of Tinidur and welding down the trailing edge. This resulted in failure as Tinidur was not weldable. Eventually, a deep drawing process was utilized where the stock used for the blade was a flat circular blank. Blades could be manufactured by this process faster than the solid blades.

Considerably before 1944, work was initiated to search for a new material that would not have a 30 percent Ni content. Krupp developed another alloy material called Cromadur.[8] Cromadur proved easy to weld and the process of folding the blade flat and welding turned out to be superior to deep drawing, so that the Cromadur blades turned out to be more reliable than the Tinidur blading despite the lower creep strength of Cromadur.

4.0 Design and Construction of the Jumo 004 Engine

Figure 2 shows a cross-sectional drawing of the Junkers Jumo 004 turbojet (Neville and Silsbee, 1948). The total engine represented a design compromise to minimize the use of strategic materials and to simplify manufacture. Evidence of this is the high usage (approximately 7 percent) of compressor air bleed for cooling. In practice, time between overhaul was only 10 hours versus a design life of 25 to 35 hours.[9] The Jumo 004 was a large engine, 152 in. (3860 mm) in length and with a 30 in. (760 mm) diameter at the skin around the six combustion chambers.

4.1 Inlet Section. The diameter of the intake was 20 in. The circular nose cowling contained two annular gas tanks. The upper 0.75 gallon gas tank contained fuel for the two-cylinder two-stroke horizontally opposed gasoline engine (made by Riedel). This engine produced 10 HP at 6000 rpm. The Riedel starter engine had its own electric starter motor but for emergency purposes, also had a cable "pull starter" located in the nose cone as is seen in Fig. 3. The lower 3.75 gallon capacity tank was used to feed starting fuel to the combustion chambers. Details of the starter motor, auxiliary drive, and main compressor bearing are shown in Fig. 4.

The starter engine was bolted to the six struts in the bevel gear casing, which contained gears to drive the accessories. Two drive shafts were used; one extended down to the main oil pumps, which were located inside the lower part of the casing. The rear part of the casing housed the front compressor bearing mounted in steel liners set in a light hemispherical housing, which was kept in contact with the female portion of the intake housing by the pressure of ten springs held in place by a plate bolted to the intake casting. The outer bearing races were mounted in separate sleeves that fit on the compressor shaft. This design allowed preloading of the bearings to ensure an even distribution of thrust. The other advantage was that the bearing assembly could be left intact during disassembly by withdrawing the compressor shaft from the inner sleeve.

4.2 Compressor Section. The Jumo 004 compressor was an eight-stage unit (air flow rate 46.6 lb/sec) with an outer casing of uniform diameter. The compressor rotor was made of

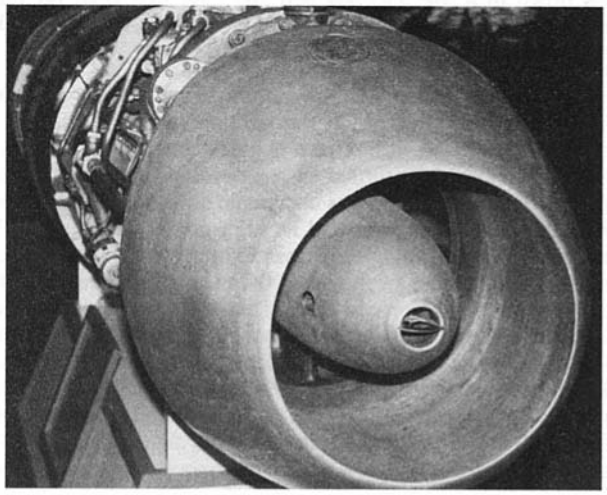

Fig. 3 Intake nose cowling of the Jumo 004. Intake diameter was 20 in. The cable "pull starter" handle can be seen in the nose cone.

[7] Tinidur composition: 15% Cr, 30% Ni, 2% Ti, 0.8% Si, 0.7% Mn, 0.15% C, balance Fe.

[8] Cromadur composition: 18% Mn, 12% Cr, 0.65% V, 0.5% Si, 0.2% Ni, 0.12% C, balance Fe.

[9] At the end of the war a heat-resistant alloy had been developed that gave 150 hours in test flights.

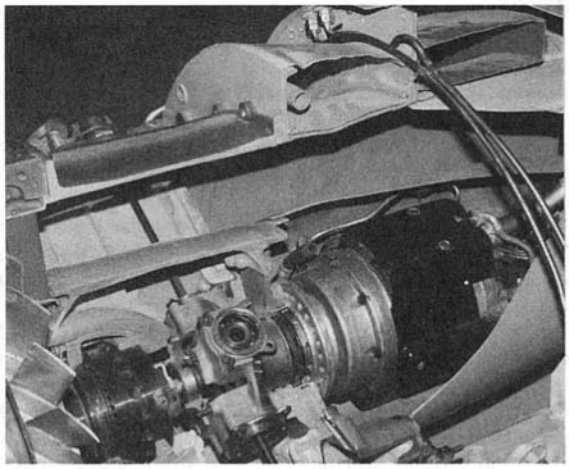

Fig. 4 Inlet section showing the Riedel starter motor, the auxiliary drive, and front compressor bearing. The annular fuel tank for the starter motor can be seen within the nose cowling.

eight aluminum disks held together by 12 bolts and located by spigots. The entire assembly was pulled together by a 38.75 in. long (0.75 in. diameter) tie rod, estimated to have a stress of 40,000 psi with a pull force on the assembly of 16,000 pounds. The compressor section is shown in Fig. 5. This figure depicts how each of the compressor sections was bolted together on shoulders of individual disks.

There were 27 stamped aluminum blades in the first two rows and 28 blades in the rest of the stages. All had machined roots that fitted into the pyramid-shaped slots in the rotor disk. A small screw was attached to the blade and extended into the disk. The stagger of the blades increased and the chord decreased in successive stages. The rotor turned on two steel shafts attached to the outside faces of the first and last disks. The compressor front bearing was made up of three ball races, each capable of taking end thrust. The rear bearing consisted of a single roller race.

Cooling air flows were derived from between the fourth and fifth compressor stages and led to the double skin around the combustion chamber assembly. Most of the air passed down one of the exhaust cone struts to circulate inside the cone and passed through small holes to cool the downstream face of the turbine disk. Air was also taken through three tunnels in two of the ribs of the casting and into the space between the two

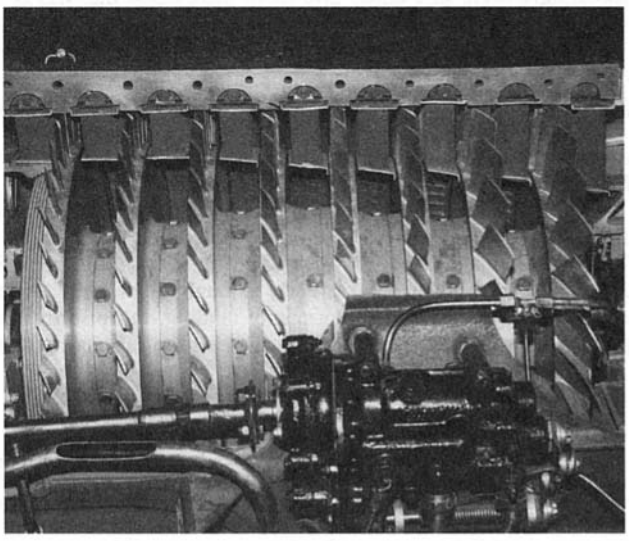

Fig. 5 Compressor section of the Jumo 004

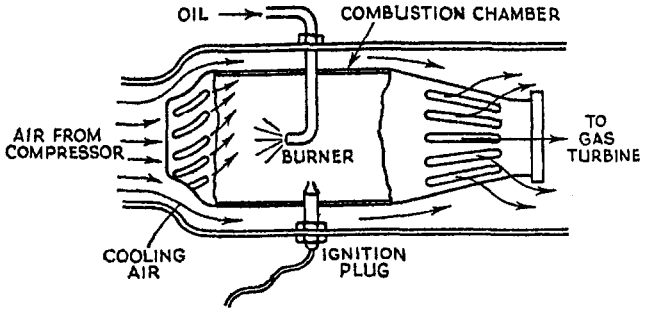

Fig. 6 Combustor can arrangement of the Jumo 004. Helical slots were provided for combustion air to provide a swirl. The burner injected fuel upstream. Hot gases passed out of the slots shown to the right and mixed with cooling air.

plate diaphragms in front of the turbine disk. Most of this air passed through the hollow turbine nozzle guide vanes, emerging through slits in the trailing edges.

4.3 Combustor. The Jumo 004 had six combustor cans arranged around the central casting carrying the rear compressor bearing and the turbine shaft bearing. Three of the cans carried spark plugs. The engine was designed to run on diesel fuel. Figure 6 (Judge, 1950) shows an individual Jumo 004 can. The approach to the combustor design was to derive a flame chamber region in the combustor for primary combustion at close to stoichiometric ratio. To obtain good mixing, and a short flame length, the primary combustion air was introduced in this chamber with swirl and fuel was injected with a swirl against the airflow. Spark plugs were located in three cans and interconnectors were provided. The combustion chambers were made of aluminized sheet steel.

4.4 Turbine. The turbine, designed in collaboration with AEG, had a degree of reaction of 20 percent, which represented a compromise between AEG who wanted less and Junkers who wanted more (afterburner considerations). The single-stage turbine had 61 blades that were fixed to the turbine disk by a formed root and kept in position by rivets. Figure 7 shows the turbine disk and blading. The production version had air-cooled

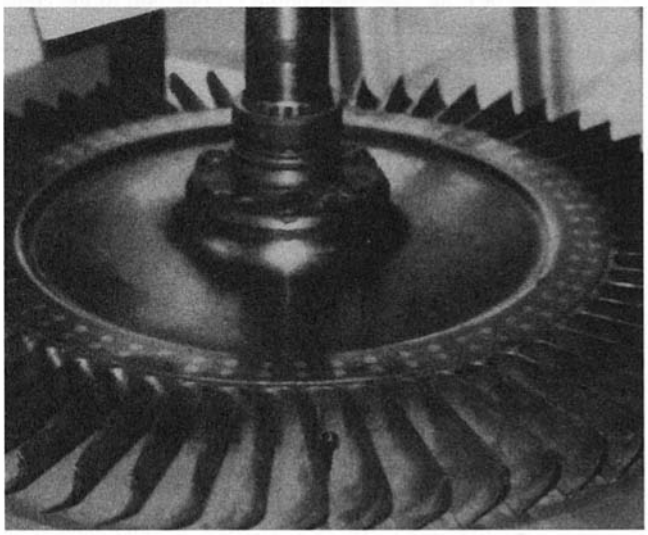

Fig. 7 Uncooled turbine blades held by pins and brazed to disk. A special supply of cooling air was directed to the blade roots to maintain the strength of the soldered joint. The splined shaft coupling can also be seen. Each blade weighed 12.25 oz. Rivet diameter was 11 mm. Estimated maximum centrifugal stress ≈18,000 psi and gas bending stress ≈3000 psi. Later models had air-cooled hollow blades.

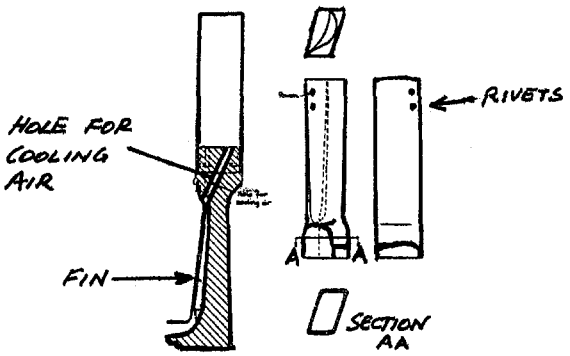

Fig. 8 Hollow air-cooled turbine blade. The disks for the hollow blade had a thin sheet across the front face flared out near the center. This picked up cooling air and whirled it toward the disk roots, where it entered two small holes drilled in the disk rim and then flowed up through the blade. Later production models had two small rivets at the blade trailing edge near the tips, which were needed to avoid a vibration cracking problem (Shepherd, 1949).

hollow blades as shown in Fig. 8 (Shepherd, 1949). The absolute discharge velocity is 663 ft/sec. The enthalpy drop across the turbine was approximately 64 Btu/lb.

4.5 Exhaust Nozzle. A movable "bullet" was mounted in the tailpipe operated by a servo-motor through the throttle lever. A rack and pinion device moved the bullet longitudinally, varying the nozzle area. On the ground, the bullet was fully forward under 50 percent of maximum rpm and fully back between 50 percent and 90 percent maximum rpm. At the beginning of take-off, the bullet was near the end of its backward travel. In flight above 20,000 feet, at a speed of 400 mph, the bullet was moved even farther back to provide maximum thrust. The servo-motor controlling the bullet was interlinked with a capsule surrounded by atmospheric pressure and having ram pressure inside it. This allowed the bullet position to be adjusted according to the ram pressure (i.e., the aircraft speed).

4.6 Other Engine Systems

4.6.1 Lubrication System. Lubricating oil was carried in an annular nose tank. Two pressure pumps were provided, one supplying oil to the rpm regulator, oil servo-motor, and compressor front bearing. The other pump supplied oil to the compressor rear bearing, and the two turbine rotor bearings. These oil pumps were located below the engine and driven by bevel gears through a nose casing strut.

4.6.2 Auxiliary Drive Case. The auxiliary casing was located above the engine and driven from the front compressor shaft. The casing drove the fuel injection pump, and the rpm governor drove the pump for the thrust regulator and the bullet servo-motor.

4.6.3 Instrumentation. The instrumentation consisted of the several gages indicating the fuel injection pressure gage, rpm,[10] exhaust gas temperature, exhaust gas pressure, and oil pressure.

5.0 The Me 262 Jet Fighter

5.1 Aircraft/Powerplant Development. In 1938,[11] the German Air Ministry awarded a design contract to Messerschmitt for the design of a radical jet fighter, the power plants of which were to be the BMW 003. The ME 262 was developed under Project No. 1065 and was conceived to be an interceptor fighter with swept back wings. After building a mockup in January 1940, a contract was awarded of three prototypes for flight testing.[12]

Messerschmitt encouraged his designers to work in teams and created a climate that encouraged innovation. The design team settled for two engines and a tail wheel undercarriage. Because the wing was too thin to accommodate the landing wheels, they were designed to retract into the fuselage, giving the aircraft its characteristic shark-like triangular cross section.

By 1941, Franz had developed the Jumo 004 to a point where it could be flown on the ME 262. During taxiing trials, Wendel found that in order to raise the tail wheel, he had to touch the brakes at approximately 112 mph. The cause of this problem was the attitude of the aircraft (tail wheel configuration) and the ground turbulence caused by the jet engines, which caused the elevator to be ineffective. At 8:40 am on July 18th, 1942, Wendel completed a successful test flight and described in section 1 of this paper and reported that the engines "ran like clockwork." Later, the fourth prototype ME 262 was also flown by a distinguished fighter pilot ace Adolf Galland. After the flight, Galland was most enthusiastic and even recommended that all fighter production be restricted only to ME 262s and Focke Wulf 190s.

5.2 Deployment of the ME 262. The deployment of the ME 262 was delayed by bureaucratic problems and Hitler's insistence that it be retrofitted as a bomber. A few days after the Normandy landings, he issued an order permitting *testing* of the ME 262 as a fighter but insisting that the bomber deployment not be delayed. Galland's vehement and vocal opposition to this finally resulted in his dismissal, though he was later recalled to form and lead a group of fighters (Fighter Group JV44)[13] as the war drew to a close.

From mid-1944, both fighter and bomber versions rolled off the production line. The supply of Jumo 004 engines really started in quantity in spring 1944. On July 25th, 1944, a RAF reconnaissance Mosquito flying at 29,000 ft near Munich encountered, for the first time in history, a jet-powered interceptor.

5.3 ME 262 Operation. The ME 262 is widely acknowledged to be superior (at least in terms of performance) compared to any fighter that the Allies had during 1946 and 1947. The ME 262 had a maximum speed of 524 mph (at 20,000 ft), a service ceiling of 37,565 feet, and a rate of climb of 3.937 ft per minute at sea level. It had an endurance of one and a quarter hours. The aircraft had a high wing load (66 lb/sq ft) and had a take-off speed of 190 mph requiring a long take-off run of 3200 feet into a 15 mph wind. The landing speed was correspondingly high, just under 200 mph. This made the ME 262 vulnerable to attack during take-off and landing.

Two versions of the aircraft were built: the ME 262 Schwalbe (Swallow), a fighter, and a fighter bomber called the Sturmvogel (Stormbird). The standard fighter was fitted with four Mk 108, 30 mm nose cannon. The fighter bomber was designed to carry two 550 lb bombs under the wings. Specifications of the Messerschmitt ME 262B are presented in Table 2.

The first pure turbojet flight of the ME 262 took place on July 18th, 1942, using two pre-production Jumo 004 engines. Testing continued through 1942 and 1943. Potentially the ME 262 could have seen service early enough to prevent allied air superiority prior to the Normandy landing, but priority for production was placed on bombers. During the fall and winter

[10] This gage had an inner (0–3000 rpm) scale for startup and outer scale (2000–14,000 rpm) for flight.

[11] Almost one year before the outbreak of WW II.

[12] This was approximately the same time when Heinkel obtained his contract for the HE 280.

[13] The JV44 Unit was based at Munich from March 31st, 1945. Galland choose an elite group of 50 pilots. Galland was shot down on August 26th, 1945, and his squadron fought on using the Autobahns to avoid strafed airfields. The squadron was then transferred to Salzburg where, on May 3rd, 1945, it was overrun by US forces. Adolf Galland died in Oberwinter, Germany, at the age of 83 on February 26th, 1996.

Table 2 Specifications of the Messerschmitt ME 262B

Engines	Two, Junker Jumo 004B, each rated at 1984 lb (900 kg) thrust
Span	40 ft, 11.5 in. (12.48 m)
Length	34 ft, 11.25 in. (10.65 m)
Wing area	233.8 sq. ft (21.72 sq. m)
Take-off weight	15,432 lb (7000 kg)
Maximum speed	503–530 mph (810 km/h+)
Service ceiling	34,450 ft (10,500 m)
Range	559 miles (900 km)
Climb to 26,000 ft	11 min

of 1944 and 1945, a substantial number of ME 262s were put into operational use. There is no doubt that, had the ME 262 been deployed quickly and in quantity, it would have seriously hampered the Allied campaign.

5.4 Other Applications of the Junkers Jumo 004 Engine. The Junkers Jumo engines also propelled the world's first jet bomber, the Arado 234. The Arado was designed in 1941 and went into production in 1944. Several variants were built, the most common being the Arado 234 B, which was an all-metal single-seat high wing aircraft powered by two Jumo 004 turbojets.[14] The Arado was a high wing, all-metal aircraft. This aircraft had a maximum speed of 421 mph at 20,000 ft, a range of 1000 miles, and a payload of 3300 lb. The Jumo 004 was also used in the experimental forward swept wing Junkers Ju 287 four engine bomber. After the war, the Jumo, designated the RD-10, was used in early Russian jets and powered the Yak-15, Yak-17, and the Sukhoi SU-9 (Morgan, 1994).

6.0 Anselm Franz: Distinguished Jet Engine Pioneer (1900-1994)

Anselm Franz was born in Schladming, Austria, in 1900. He studied mechanical engineering at the Technical University of Graz in his native Austria and received his bachelor's degree and master's degree. He obtained a Doctoral degree from the University of Berlin. He was later awarded honorary doctorates from the University of Graz and the University of Bridgeport.

Before World War II, Mr. Franz was a design engineer at Schwarzkopff Werke in Berlin where he developed hydraulic torque converters. He joined the Junkers Engine Company (Dessau, Germany) in 1936 where he finally became Chief Engineer. He was head of supercharger development when, in 1939, he was put in charge of the design of the Jumo 004 turbojet. This engine was a success due to his brilliant leadership and astute choices in terms of design compromise.

Following the war, he came to the USA where he first worked for the U.S. Air Force and then, in 1951, joined Avco Lycoming where he was responsible for setting up the gas turbine department and was responsible for several successful engine development programs including the T53 (which powers the US Military's AH-1S Cobra, Grumman OV-1 Mohawk, and Bell UH-1 helicopters) and the T55 series of turboshaft engines as well as the T55 high bypass turbofan (named the ALF502). In the 1960s, Anselm Franz led a team to design the 3 spool, 1500 SHP, AGT-1500 gas turbine, which is the power plant for the US M1 Abrams Main Battle Tank. He retired as Vice President of Lycoming in 1968. Dr. Franz was a Fellow of the ASME and of the AIAA and received numerous awards including the 1967 Dr. Alexander Klemlin award from the American Helicopter Society, the U.S Army Outstanding Civilian Service medal, the ASME R. Tom Sawyer Award, and the Grand Decoration of Honor, in Gold with Star from the Austrian Republic in 1991.

He passed away at the age of 94 in Stratford, Connecticut. Anselm Franz will forever be remembered as a jet engine pioneer and member of a select group of individuals who were responsible for the turbojet revolution.

[14] Later versions of the Arado 234 Bs were fitted with BMW 003 jet engines.

7.0 Conclusion

This paper has covered the background, design philosophy, and development of the world's first production jet engine, the Junkers Jumo 004 turbojet. The development represented a historic achievement of Anselm Franz and his design team at Junkers. Approximately 6000 engines were built at the end of the Second World War in the face of acute shortages of materials and damage to German industry. The Jumo was brought from conceptual design to production in a span of four years under the leadership of Anselm Franz, a pioneering achievement in the dawn of the jet age.

Acknowledgments

Obviously, in a historical report of this kind, considerable use has been made of historical texts and technical reports and these have been referenced to the extent possible. A major source was, of course, Franz's paper (1979) presented at the 40th Anniversary of the Jet Engine as well as the excellent work of Jones (1989), Schlaifer (1950), Constant (1980), Boyne (1980), and Gunston (1995), which are highly recommended to those wishing to pursue this topic further. A good reference on the ME 262 may be found in Morgan (1994).

References

Bentele, M., 1991, *Engine Revolutions: The Autobiography of Max Bentele,* SAE Publications.

Boyne, W., 1980, *Messerschmitt 262: Arrow to the Future*, Smithsonian Institute, Washington.

Boyne, W., and Lopez, D., eds., 1979, *The Jet Age: 40 Years of Jet Aviation,* Smithsonion Institute, Washington.

Constant, E. W., II, 1980, *The Origins of the Turbojet Revolution,* Johns Hopkins Univ. Press.

Foster, J., Jr., 1945, "Design Analysis of the Messerschmitt ME 262," *Aviation*, Vol. 44, No. 11.

Franz, A., 1979, "The Development of the Jumo 004 Turbojet Engine," *40 Years of Jet Engine Progress*, W. J. Boyne and D. S. Lopez, eds., National Air and Space Museum, Smithsonian, Washington, DC.

Gunston, B., 1995, *The Development of Jet and Turbine Aero Engines,* Patrick Stephens, Ltd., UK.

Gunston, B., 1995, *World Encyclopedia of Aero Engines*, Patrick Stephens, Ltd., UK.

Jones, G., 1989, *The Birth of Jet Powered Flight,* Methuen, London.

Judge, A. W., 1950, *Modern Gas Turbines*, Chapman and Hall Ltd., UK.

Morgan, H., 1994, *ME 262 Stormbird Rising,* Motorbooks International.

Neville, L. E., and Silsbee, N. F., 1948, *Jet Propulsion Progress,* McGraw-Hill Inc., 1948.

Schlaifer, R., 1950, *Development of Aircraft Engines,* Graduate School of Business Administration, Harvard University, Boston.

Scott, P., 1995, "Birth of the Jet Engine," *Mechanical Engineering*, Jan., pp. 66-71.

Shepherd, D. G., 1949, *Introduction to the Gas Turbine,* Constable & Company Ltd.

Smith, J. R., and Kay, A., 1972, *German Aircraft of the Second World War*, Putnam, London.

Von Ohain, H., 1979, "The Evolution and Future of Aeropropulsion Systems," *40 Years of Jet Engine Progress*, W. J. Boyne and D. S. Lopez, National Air and Space Museum, Smithsonian, Washington, DC.

Ceramic Matrix Composites Application in Automotive Gas Turbines

Takao Izumi[1]
Japan Automobile Research Institute,
Tsukuba, Japan

Hiroshi Kaya
Petroleum Energy Center,
Tokyo, Japan

We are conducting the development of ceramic matrix composites (CMC) and components made of CMC for a 100 kW automotive ceramic gas turbine (CGT) as shown in Fig. 1. When compared to monolithic ceramics (MC), CMC that we have developed demonstrate superior strength characteristics in terms of resistance to particle impact and thermal shock. We have conducted evaluation tests on the strength of CMC components in which MC such as silicon nitride and silicon carbide were used as a reference for comparison with CMC in the same testing process as employed for components made of MC such as silicon nitride and silicon carbide. It was confirmed that actual components made of CMC realized approximately the same strength as the test pieces. Furthermore, some CMC components have already passed screening tests that evaluated the strength of the components. It was therefore confirmed that the potential exists for the possibility of testing these components in high-temperature assembly tests and engine tests.

Introduction

The 100 kW Automotive CGT Development Project started in June of 1990 with assistance from the Ministry of International Trade and Industry's Agency of Natural Resources and Energy. The project is being carried out under the direction of the Petroleum Energy Center and with the aggressive cooperation of companies in the petroleum, automotive, ceramics, and other related industries [1, 2].

The project's objectives are to prove the excellent potential of a CGT in terms of multifuel capability, emission characteristics, and the attainment of a thermal efficiency of more than 40 percent. In order to achieve the extremely high target of more than 40 percent for thermal efficiency in a small size gas turbine, it is necessary to raise the turbine inlet temperature (TIT) to 1350°C (1623 K). This necessitates the use of ceramics for most of the components. The structure of our CGT engine and its components made of CMC are shown in Fig. 1.

The most important problem of silicon nitride and other MC for the use of structural components is their reliability. MC are brittle materials and any localized damage can lead to catastrophic failure in use. In order to overcome this weak point in MC and realize the full potential of our CGT, in this project we have taken up the challenge of developing CMC materials and components.

The first part of this paper will report on the CMC materials that we have developed and on the mechanical strength characteristics of these materials. The latter part will report on methods of evaluating the strength reliability of combustor and stationary components made of CMC and MC that have been used as a reference and on the results of evaluation tests.

Target Life

The design reliability goals for ceramic components were set at the levels necessary to satisfy the requirements for high reliability that are demanded of automotive components. The objective was to achieve a failure probability rate of not more than 10 ppm after ten years of operation (including 10,000 starts and stops) over a distance of 100,000 km.

In the CGT engine that has been equipped with high-efficiency heat exchangers, large thermal stresses are not generated since the changes in gas temperature when the engine is stopped are moderate due to the high thermal capacities of the cores in the heat exchangers. This being the case, we conducted analyses of the thermal stress on the primary stationary components under the following two conditions only: (1) the starting mode and (2) the continuous rated condition mode. In the starting mode, thermal stress changes over time. The time involved in these changes in thermal stress is extremely moderate and is approximately 10 to 100 seconds. It was concluded that the acceleration in the deterioration of the fatigue strength due to repetitions could be ignored. For this reason, in the design stage, the mechanism adopted for strength deterioration during the life of components was assumed to depend on slow crack growth. Strength reliability was examined on that basis, and it was confirmed that the designed reliability objectives for all components had been satisfied. Deteriorations in strength due to oxidation and creep and deteriorations in the special characteristics of CMC materials were not considered in the design stage.

Evaluation of Strength Reliability

In order to confirm the strength of the ceramic components, we followed the flow chart that we proposed for the evaluation of MC, shown in Fig. 2, to evaluate the strength reliability up to the stage of the engine tests [3]. We referred to this chart and conducted evaluations as identical as possible to those conducted for the MC components. It was decided to conduct separate investigations on subjects such as size effects. Furthermore, in connection with CMC materials being developed for use in our CGT, not only the basic strength characteristics but also the new characteristics that have been proved during their developments. Our report on the results of tests conducted in accordance with the evaluation flow chart is given below.

Tests on Materials

Evaluations of bending strength, static fatigue, fracture toughness, resistance to particle impacts, resistance to oxidation, etc., were carried out. This section of our paper will explain in particular detail the remarkably improved results demonstrated by

[1] Present Address: Nissan Motor Co., Ltd.

Contributed by the International Gas Turbine Institute and presented at the 41st International Gas Turbine and Aeroengine Congress and Exhibition, Birmingham, United Kingdom, June 10–13, 1996. Manuscript received at ASME Headquarters February 1996. Paper No. 96-GT-348. Associate Technical Editor: J. N. Shinn.

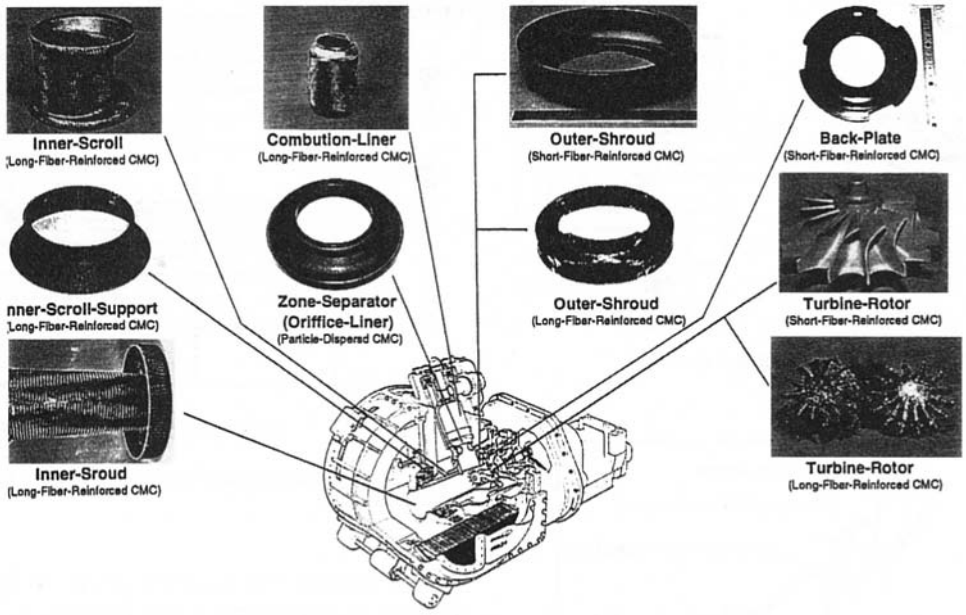

Fig. 1 Structure of 100 kW CGT engine and CMC components

CMC when compared to MC in terms of resistance to particle impacts.

Foreign Object Damage Tests. Foreign object damage (FOD) to turbine rotors made of MC results in a typical damage pattern that is caused by brittleness. Additionally, from the standpoint of engine reliability, FOD can be said to be a very serious problem. For this reason, we conducted FOD tests on rotors made of MC by employing spin tests (refer to Fig. 3) in order to understand the damage of turbine rotors. Rotor diameter is 127 mm. The impact particles were made of carbon, which is most likely to fly into and collide with the turbine rotor in a CGT. In the tests, the turbine rotor was suspended in a vacuum chamber and operated at its rated design speed of 100,000 rpm. A carbon particle was then forced to collide against the inlet blade of the rotor. The weight of the carbon particles was increased until damage developed in the turbine rotor. At the rotational speed mentioned above, it was verified beforehand that the carbon particles would collide in a section up to 2 mm from the tips of the blades. As a result of tests conducted on turbine rotors made of three different types of monolithic silicon nitride, chipping damage occurred in all of them upon collisions with carbon particles weighing as little as 2 to 6 mg. A typical damage pattern on the inlet blade is shown in Fig. 4. As a result of these tests, the importance of improving the FOD strength of MC was once again confirmed.

Particle Impact Tests. The development of turbine rotors made of CMC has not yet proceeded to the point at which they can subjected to the same FOD tests as MC. Because of this, we conducted particle impact tests in which bar test pieces were used in order to compare CMC and MC in terms of resistance to FOD and damage patterns. The equipment used in these impact tests is shown in Fig. 5. The particles used in all of these tests were made of spherical zirconia and had a diameter

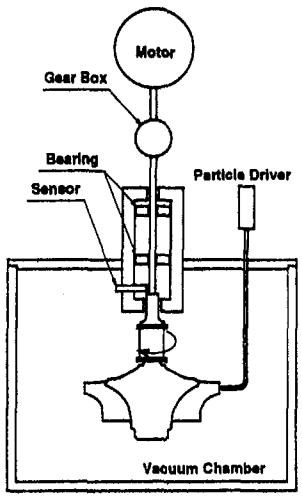

Fig. 3 Schematic of FOD test apparatus

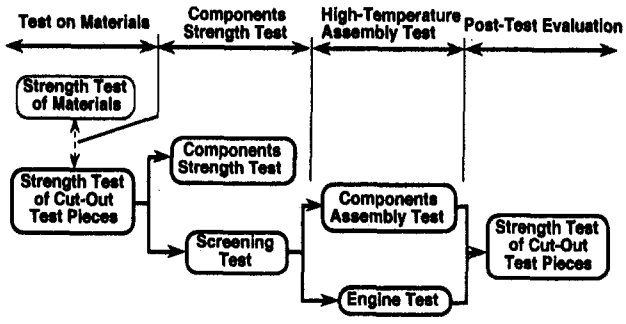

Fig. 2 Flow chart of the strength reliability evaluation

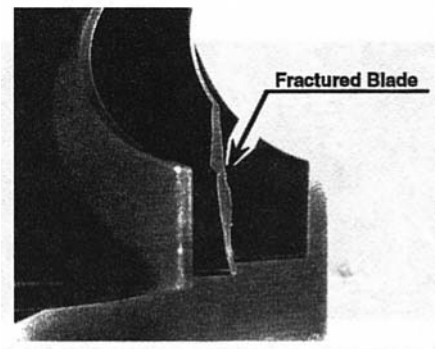

Fig. 4 Typical FOD damage on MC turbine rotor

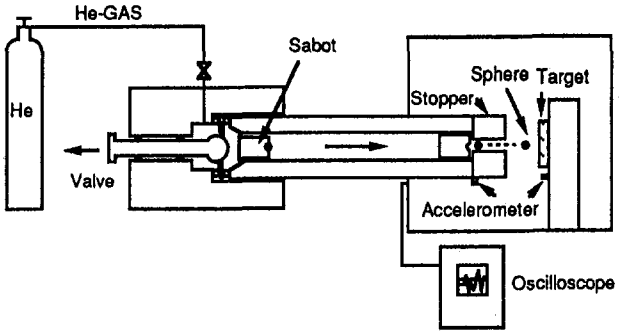

Fig. 5 Schematic of impact test apparatus

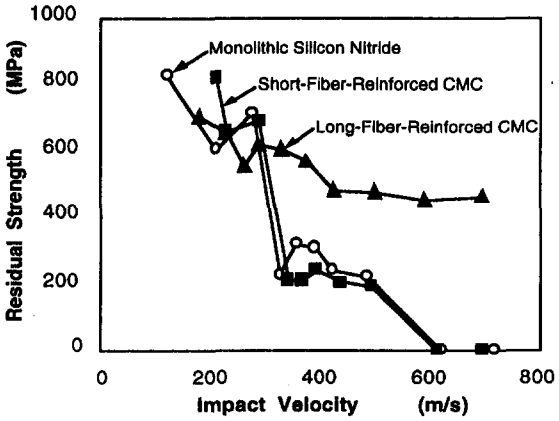

Fig. 6 Residual strength after impact test

of 1 mm. The test piece configuration had dimensions of 8 mm × 1.5 mm × 40 mm.

After the impact tests, the damage in the impacted surfaces was observed with a microscope, and the residual strength of the test pieces was measured made by a three-point bending test. The residual strengths after the tests are shown in Fig. 6. The SEM photographs in Fig. 7 show the fracture surfaces after the three-point bending tests. As shown in Fig. 6, critical velocities exist at which sudden deteriorations occur in the residual strength of MC and short-fiber-reinforced CMC. Fractures during the bending test advanced the Hertzian cracks caused by the particle impacts toward their starting points, and this became the cause of these deteriorations in strength. From the recognition of the positive correlation between critical velocity and fracture toughness shown in Fig. 8, it can be understood that an improvement in fracture toughness will contribute to resistance to FOD. Figure 6, on the other hand, indicates that critical velocities for the strength of long-fiber-reinforced CMC could not be clearly observed. As is suggested by Fig. 7, however, the deterioration in the strength of long-fiber-reinforced

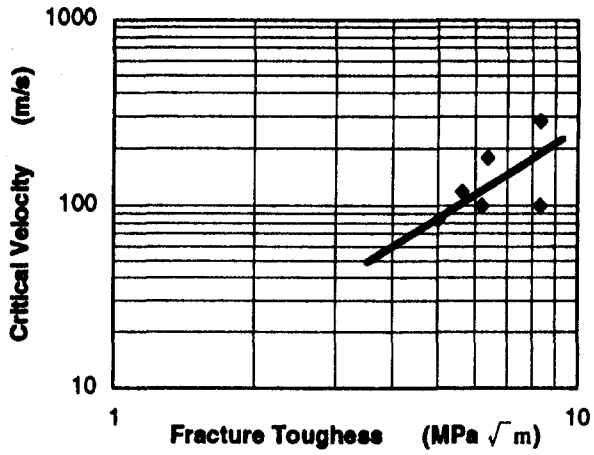

Fig. 8 Fracture toughness versus critical velocity (MC and short-fiber-reinforced CMC)

CMC is thought to be primarily influenced by delamination at the back surfaces of test pieces impacted by particles as well as by the reduction of the sectional area of the test pieces caused by particle penetration.

It was recognized that the results for CMC represented a clear improvement over those for MC in terms of resistance to FOD. In addition, although this will not be discussed in this paper, cyclic thermal-shock tests were conducted on ring-shaped test pieces that were exposed to high-temperature gas and an especially marked difference in terms of superior resistance to thermal shock was indicated for long-fiber-reinforced CMC [4]. It thus became clear that CMC has a sufficient potential for CGT components.

Strength Tests on Test Pieces Cut From Components

The probability of major defects in MC or short-fiber-reinforced CMC becomes larger and more complex depending on its size and configuration. At the same time, it is difficult to increase the density of components made of long-fiber-reinforced CMC. Consequently, the strength of small-size test pieces with simple shapes cannot always be realized in actual components. Moreover, it cannot be denied that there is always the possibility that regions of unexpectedly low strength may develop in a component during forming or sintering processes.

For these reasons, test pieces were cut from manufactured components, and bending tests and diametral ring compression tests were performed in order to evaluate the strength of the actual components. Figure 9 shows the sections cut out of an inner-scroll, the shapes of the cut-out test pieces, and the test methods that were used. The bar test pieces (c and d) were subjected to bending strength tests that comply to Japan Industrial Standard (JIS) R1601. The diametral ring test pieces (a and b) were subjected to compression strength tests. Table 1

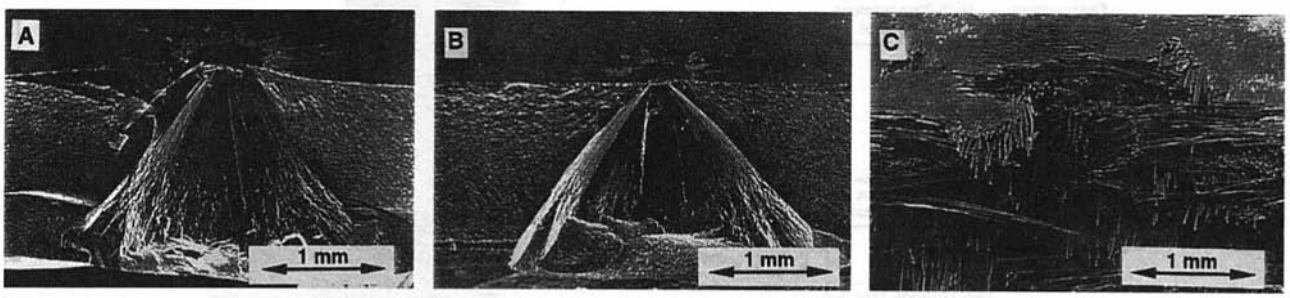

Fig. 7 SEM photographs of fractured surfaces after the bend tests (*A:* monolithic silicon nitride, *B:* short-fiber-reinforced CMC, *C:* long-fiber-reinforced CMC)

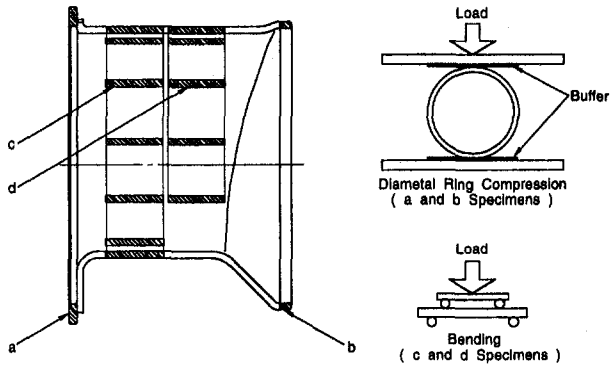

Fig. 9 Cut-out strength test of inner-scroll

gives the strength of the cut-out test pieces and the standard test pieces, i.e., the initial strength of the materials. The results confirmed that the strength of the cut-out test pieces for all of the components attained the same strength levels as the standard test pieces.

It thus became clear that forming, sintering, and other manufacturing processes posed no problems for those components, so the component strength tests to confirm the strength of the actual components in their various configurations were conducted.

Component Strength Tests

In component strength tests, the strength of a component is evaluated by mechanical loading on the part of the component in which the maximum thermal stress is assumed to be generated. In these tests, a pressure-loading method or a static-loading method was selected for each component after taking into consideration the shape and the maximum thermal stress of the component. Table 2 shows the test methods for all of the components.

A pressure-loading method was selected for the inner-scroll-support, which is axisymmetric and almost cylindrical in shape. Figure 10 shows the equipment used in the component strength test on the inner-scroll-support. Figure 11 shows the stress distribution in the component strength test on the inner-scroll-support. From Fig. 12, it can be understood that the distribution of the maximum thermal stress generated by the engine (100 s after starting) has been closely simulated.

Figure 13 shows the static-loading test method that was adopted for the back-plate during the course of the CGT development. As will be discussed below, this new method has modifications that reflect the results of assembly tests that were conducted on the back-plate. Figure 14 shows that the distribution of the stress generated in the component strength test on the back-plate. Figure 15 shows that the distribution of the maximum thermal stress generated by the engine on the back-plate has been almost perfectly simulated.

Table 2 Component strength tests

Parts	Test Methods
Outer-Scroll	Pressure-Loading
Inner-Scroll	Pressure-Loading
Back-Plate	Static-Loading
Inner-Scroll-Support	Pressure-Loading
Inner-Shroud	Static-Loading
Outer-Shroud	Not-Tested
Turbine-Nozzle	Termal-Shock
Dilution-Liner	Not-Tested
Combustion-Liner	Not-Tested
Zone-Separator	Not-Tested

Pass-or-fail-type screening tests, which apply the results of the component strength tests, were then conducted as a prerequisite to the next evaluation step, i.e., the stationary-component assembly tests. Screening tests are conducted by loading in the same way as in component strength tests, but the screening stress is not less than 120 percent of the maximum thermal stress that has been determined by stress analyses. All CMC and MC components must pass these screening tests before they can be tested in the stationary-component assembly tests. Several components made of MC that were trial manufactured in the past initially failed to pass their screening tests. Following additional trial-manufacturing efforts, however, all of these components have subsequently been improved and have reached the levels required to pass the tests. Since the back-plate made of CMC (in-situ silicon nitride and SiC whisker-reinforced-sialon) has already passed its screening test, it will be tested next in a stationary-component assembly test. In addition, preparations are now in progress for a screening test on an inner-scroll-support made of long-fiber-reinforced CMC. Provided that the CMC (continuous carbon-fiber-reinforced SiC) inner-scroll-support passes its forthcoming screening test, it will then be tested in a stationary-component assembly test in combination with MC components.

Combustor Assembly Tests

Prior to the engine tests, two types of high-temperature assembly test to evaluate strength reliability were conducted in a

Table 1 Results of cut-out strength tests

Materials		Parts	Standard Flexural Strength MPa (JIS R 1601)	Initial Cutout Strength MPa (JIS R 1601 Equivalent)		Cutout Strength after Structure Thermal Test MPa (JIS R 1601 Equivalent)	
				Flexural Strength (Weibull Modulus)	Diametral Ring Compression	Flexural Strength (Weibull Modulus)	Diametral Ring Compression
Monolithic	SN252	Outer-Scroll	615	644 (18.6)	417 ~ 643	671 (12.7)	578
	SN252	Inner-Scroll	615	626 (35.7)	543 ~ 688	635 (31.7)	654 ~ 770
	EC152	Back-Plate	1020	914 (34.9)	549 ~ 892	920 (16.4)	588 ~ 970
	EC152	Inner-Scroll-Support	1020	946 (17.2)	696 ~ 1028	806 (15.2)	717 ~ 793
	SN88	Inner-Shroud	790	762 (15)	521 ~ 561	---	---
	SN88	Outer-Shroud	790	731 (28)	637 ~ 729	---	---
	SN252	Dilution-Liner	615	---	481 (9.1)	---	472 (21.1)
	C600A	Combustion-Liner	537	---	467 (9.2)	---	---
	C600H	Zone-Separator	657	---	344 ~ 503	---	---
CMC	In-situ	Back-Plate	1016	1095 (17.3)	---	---	---
	Short-Fiber	Back-Plate	990	1031 (18.3)	---	---	---
	Particle	Zone-Separator	700	---	315 ~ 363	---	---

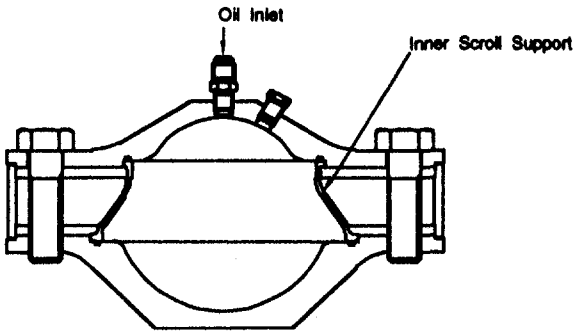

Fig. 10 Component strength test equipment of inner-scroll-support

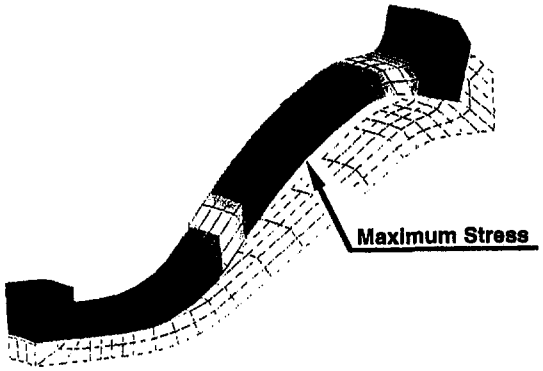

Fig. 11 Stress distribution of inner-scroll-support (component strength test: pressure loading)

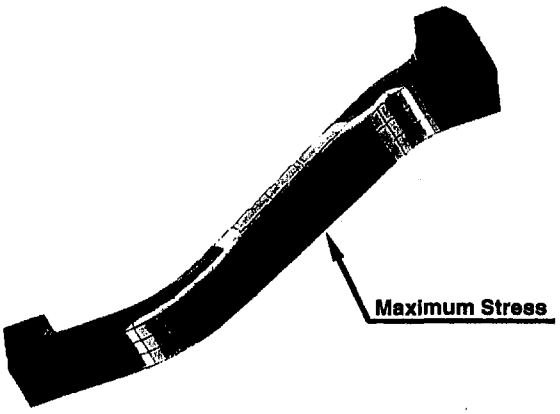

Fig. 12 Maximum thermal stress distribution of inner-scroll-support (starting mode)

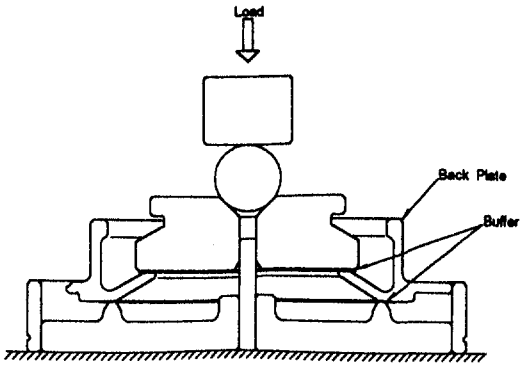

Fig. 13 Component strength test equipment of back-plate

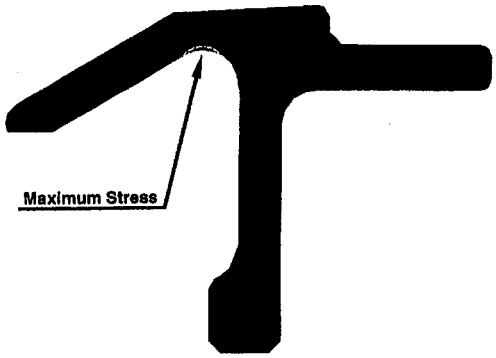

Fig. 14 Stress distribution of back-plate (component strength test: static loading)

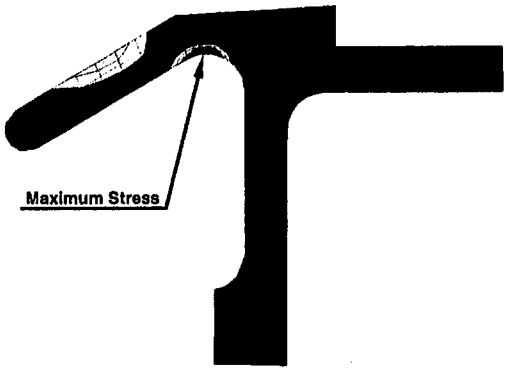

Fig. 15 Maximum thermal stress distribution of back-plate (rated condition mode)

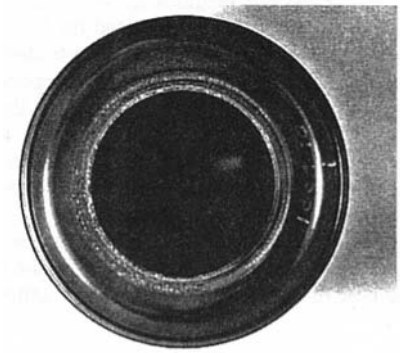

Fig. 16 Oxidation on monolithic SiC zone-separator

high-temperature environment that is equivalent to that in the CGT engine. The first was a combustor assembly test and the second was a stationary-component assembly test. In these assembly tests, the first step was to conduct the tests at a temperature of 1200°C (1473 K), which is lower than the target temperature of 1350°C (1623 K).

Since the levels of stress on the combustor components during operation are low and the major problem is oxidation, testing criterion were judged only by the strength tests on cut-out test pieces. In tests on the combustor performance in which the zone-separator made of monolithic SiC was tested, conspicuous oxidation developed on the surfaces of the zone separator. The surface condition of zone-separator on which oxidation formed is shown in Fig. 16. In order to improve resistance to oxidation, SiC CVD coating was provided on the surfaces of the SiC zone-separator. As a result, although small amounts of chipping sometimes occurred in the layers of the CVD coating, a remark-

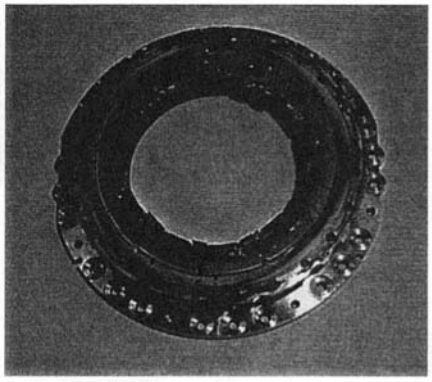

Fig. 17 Damaged monolithic SiC seal-plate

able improvement was noted in the resistance to oxidation. Since delamination of the layers of the CVD coating can cause FOD damage to the turbine rotor, however, it is necessary to conduct further improvements and evaluations in regard to the adhesive strength of the CVD layers.

A 50-hour test on combustor durability was conducted in which CMC zone-separator, which had been provided with SiC CVD coating, was tested. In this durability test, rated engine operation conditions at a turbine inlet temperature (TIT) of 1200°C were simulated. After the 50-hour test, close observation of the zone-separator surfaces revealed no damage. The condition of the surfaces was sound, and there were no significant changes in the weight of the zone-separator before and after the test. Consequently, the CMC (TiB2 particle-dispersed SiC) zone-separator provided with SiC CVD coating will be tested next at a gas temperature of 1350°C in a stationary-component assembly test in combination with combustor components made of MC.

Stationary-Component Assembly Tests at 1200°C

In stationary-component assembly tests, all of the peripheral stationary components for the turbine (without the turbine rotor) and the combustor components are assembled and exposed to a flow of high-temperature, high-pressure combustion gas that corresponds to the gas flow in the CGT engine. Only stationary components, shown in Fig. 17, that have passed the aforementioned screening tests are tested in these stationary-component assembly tests.

Seal-plates made from monolithic SiC that are incorporated in the seal-support-structure were damaged on three consecutive occasions during tests of short duration at a gas temperature of 1200°C and at the normal pressure. Figure 17 shows a photograph of a damaged seal-plate. Measurements of the deformation in the seal-support structure, observation of the damage in the seal-plates, temperature-measuring experiments conducted on seal-plates made of metal, and other investigations made clear that the cause of the damage to the SiC seal-plates was thermal stress generated by the temperature distribution within the seal-plates themselves. In order to reduce the thermal stress generated in the seal-plates, the material used for the plates was changed to silicon nitride, which can lower the generation of thermal stress since it has a lower Young's modulus and thermal expansion coefficient than silicon carbide. In subsequent experiments no damage was observed in seal-plates made of monolithic silicon nitride.

Following tests at the normal pressure, stationary-component assembly tests were conducted at a gas temperature of 1200°C and at pressures that correspond to the CGT engine conditions. Two types of condition were established for these tests. In the first type, rapid-heating tests were conducted by simulating the most severe thermal stress, which occurs under starting conditions. In the second type, continuous-rated-condition tests were conducted under the conditions in which the most severe thermal load occurs. Prior to the evaluation of CMC components, only components made of MC were first used in the durability tests that were conducted under both types of the aforementioned conditions. The continuous-rated-condition tests were conducted for 101 cumulative hours and the rapid-heating tests for a total of 200 cycles. The test conditions are shown in Table 3 and the structure of stationary components are shown in Fig. 18. During and after the tests, inspections were conducted a total of seven times. In addition, following the completion of all of the tests, strength tests were conducted on cut-out test pieces from all of the major stationary components. Figure 19 shows the various types of damage caused during the stationary-component assembly tests. In the 42nd hour of the continuous-rated-condition test, chipping and cracks were confirmed in the flanged area that forms in the contact seal for the inner-shroud. This damage was subsequently prevented by chamfering the edges to provide a curvature with a large radius. After the completion of the 101-hour continuous-rated-condition test, the cause of the damage observed on the outer-scroll could not be identified. Oxidation (whitening) in the outer-scroll had previously been observed in the inspection at 42nd hour of the test, however, and it was concluded that there was the possibility that this oxidation had been a factor in the initial stage of the damage. Oxidation in the inner-scroll-support advanced with each additional hour of the test, and the entire surface had whitened by the time the test had been completed. In the rapid-heating test, it was assumed that cyclic thermal stress had caused the chipping and cracks observed in the trailing edge of a nozzle vanes. The thermal stress has since been lowered by enlarging the fillet radius in the trailing edges.

Table 3 Test conditions

	1200℃		1350℃
	Rapid-Heating	Continuous-Rated-Condition	
Nozzle Inlet Temp.	R.T. - 1200℃	1200℃	1350℃
Combustor Inlet Temp.	R.T.	800℃	900℃
Combustor Inlet Pressure	0 - 0.13 MPa	0.37MPa	0.37MPa
Air Flow Rate	0 - 200 g/sec	380 - 420 g/sec	380 - 420 g/sec
Equiv. Turbine Speed	0 - 70%	100%	100%
Cycles or Hours	200 cycles	101 hours	over 50 hours

Table 1 (also referred to above) shows the results of the strength tests on cut-out test pieces from the primary stationary components after the completion of the assembly tests at 1200°C. Although oxidation had obviously occurred in some

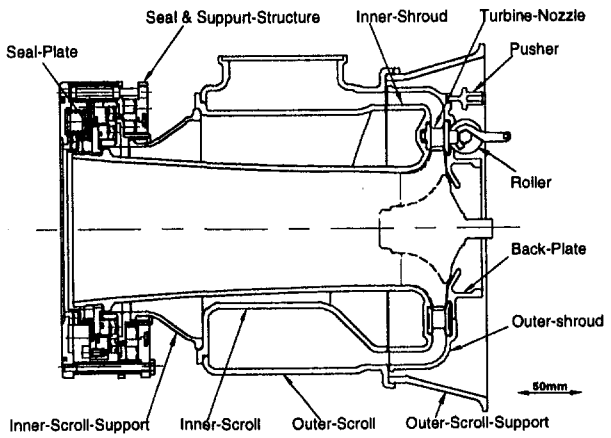

Fig. 18 Structure of stationary components

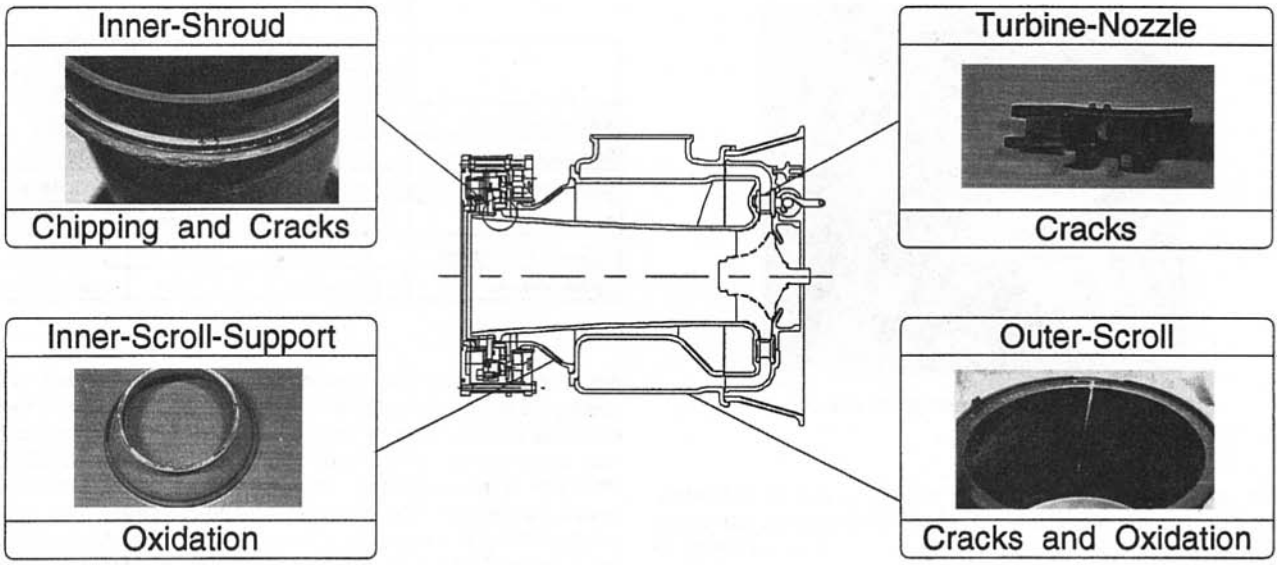

Fig. 19 Damages caused during the stationary-component assembly test at 1200°C

components, such as the inner-scroll-support, no significant deterioration in the strength of the components was noted. Since the various problems involved when the gas temperature is at a level of 1200°C, such as the problems of the high-temperature strength of the stationary components and oxidation, have been virtually solved, it was concluded that a level had been reached at which it was possible to test the high-temperature strength of stationary components in engine tests, and stationary components made of MC were subsequently tested in such tests. At present, these tests are being conducted while the engine is operating at a TIT of 1200°C and no damage to the MC components has been noted.

Stationary-Component Assembly Tests at 1350°C

Since the stationary-component assembly tests are conducted without the turbine rotor, the temperature conditions downstream from the nozzle are not the same as those in an actual engine because the temperatures in the turbine area do not drop, but instead become higher than those in an engine. For this reason, we modified the testing equipment used in stationary-component assembly tests in order to conduct the tests under conditions in which the final target temperature is 1350°C. A sectional drawing of the modified equipment for the stationary-component assembly tests is shown in Fig. 20. This equipment includes a mixing cooling nozzle for the cooling air that is introduced into the turbine area from an external source. The gas temperature downstream from the nozzle can therefore be adjusted to be identical to the temperature in an actual engine by controlling the flow rate of the cooling air. The test conditions are shown in Table 3. The use of this modified equipment for stationary-component tests enabled us to conduct numerous tests while the gas temperature was 1350°C at the nozzle inlet and 900 to 1000°C at the diffuser outlet. The duration of these tests was on the order of 10 hours and the longest was 25 hours. Cumulative testing time at a gas temperature of 1350°C has now reached a total of 50 hours.

Back-Plate. During these stationary-component assembly tests in which the temperature at the nozzle inlet was 1350°C, back-plates made of monolithic silicon nitride were damaged on many occasions. Figure 21 shows a photograph of one of these damaged back-plates. The results of investigations of these damaged components revealed that the starting point of the damage was in the radius area of the downward sloping surface where the back plate and the back face of the turbine rotor face

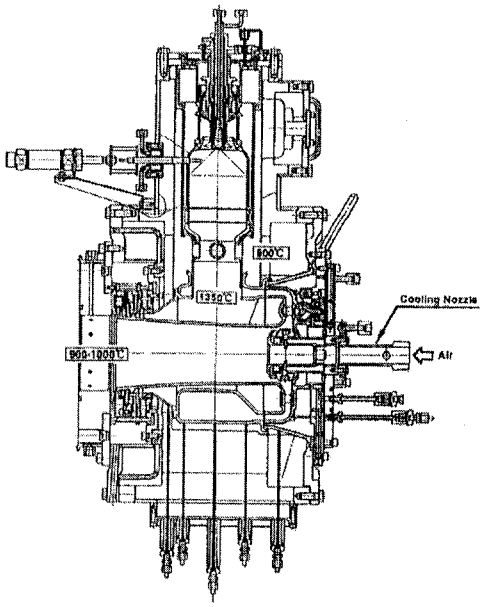

Fig. 20 Modified equipment for stationary-component assembly test

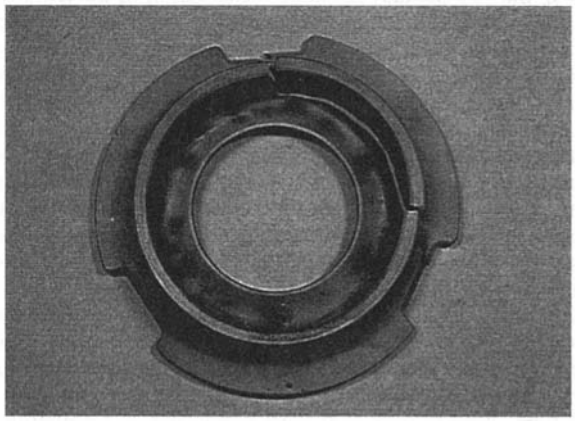

Fig. 21 Damaged back-plate

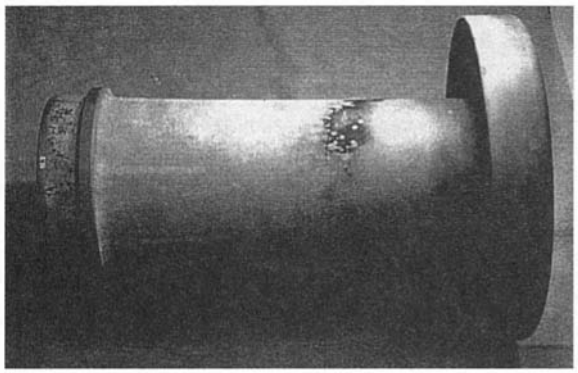

Fig. 22 Oxidation on inner-shroud

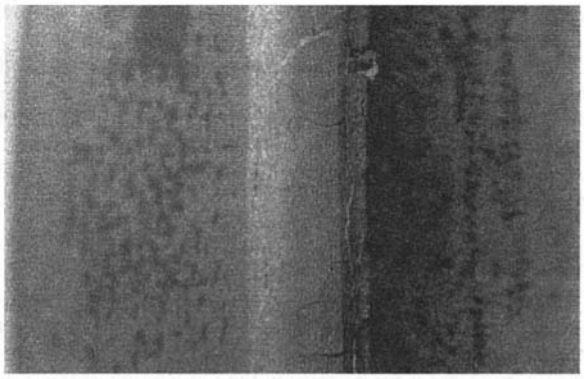

Fig. 23 Cracks on the flanged area of inner-shroud

each other (refer to Fig. 14). In many cases, large defects of more than 0.1 mm in size were found to exist at this starting point, and the damage advanced from this point. In response to this, we measured the temperature distribution in back plates after drilling six holes into the back-plates and inserting thermocouples with spherical platinum tips into the holes. Two sets of testing equipment were used in these temperature-measuring tests. One set was made up of the equipment used in the stationary-components assembly test. The second employed a compressor-turbine assembly test, which used an engine housing that provided an environment for the back-plate that can be said to be identical to that of an engine. The patterns of temperature distribution measured by each of these two sets of testing equipment were approximately the same, but it became clear that there were large differences between the actually measured temperature distribution and the original design estimates of temperature distribution. We then provided the thermal boundary conditions that had realized the actually measured temperature distribution and conducted an analysis of the thermal stress. It was learned that the maximum thermal stress was more than two times higher than the value in the original design estimates and that the section in which the maximum thermal stress was generated matched the starting point of the damage in the back plates. Since the cause of the damage to the back plates had now been identified, we studied the component strength test method in an attempt to focus its target to the radius area of the downward sloping surface in which the maximum thermal stress is generated. As a result, the method was changed to the one that is shown in the aforementioned Fig. 13. Moreover, a design modification was made that resulted in a reduction of approximately 40 percent in the thermal stress in the radius area of the downward sloping surface.

Inner-Shroud. One of the inner-shrouds among those tested developed oxidation that was limited to the as-fired surface. This oxidation is shown in Fig. 22. Moreover, as shown in Figs. 23 and 24, numerous cracks developed in the vicinity of the boundary of the ground surface and the as-fired surface, and three cracks that exceeded 30 mm in length occurred in the axial direction at the edge of the gas outlet. The cause of the damage has not yet been identified since this phenomenon did not recur, and the investigation of the cause is still in progress. However, since the region of damage matches that in which damage to the flanged area occurred during the 1200°C assembly tests and since the damage pattern is similar, there is the strong possibility that the cause is also the same. For this reason, the corrective measure that was previously performed was performed again on a larger scale as an interim countermeasure. Grinding to a depth of 0.5 to 1.0 mm was performed along a distance of approximately 5.0 mm on the flanged area and the adjacent cylindrical section. This grinding operation shifted the boundary of the ground surface and the as-fired surface to the cylindrical section and away from the outer diameter of the flanged area, which is subjected to tensile stress as well as thermal stress.

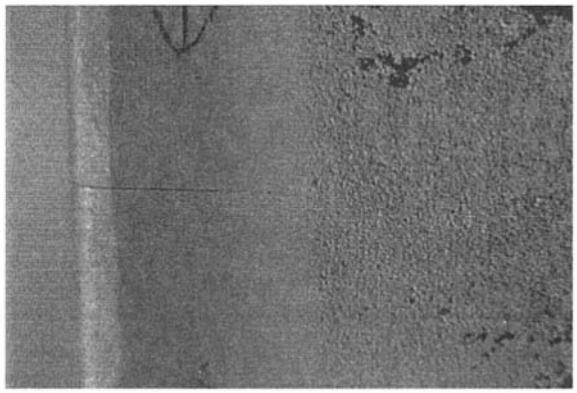

Fig. 24 Axial direction crack at edge of inner-shroud

At present, prior to the scheduled start of engine operations at a TIT of 1350°C in February of next year, we are conducting tests to confirm the results of the measures that have been taken to prevent damage to the back plate and the inner-shroud. Following these verification tests, stationary-component assembly tests will start in December of this year on three CMC components under testing conditions that correspond to the rated operation of an engine at a TIT of 1350°C. The three CMC components are a zone-separator, a back-plate that has already passed its screening test, and an inner-scroll-support, provided that it passes the screening test for it that will be conducted soon.

Conclusion

Evaluations of strength reliability were conducted on CMC materials and components that have been developed with the objective of using them in applications to a 100 kW automotive CGT. Similar evaluations were also conducted in which components made of MC were used as a reference for comparisons with CMC. The conclusions reached as a result of these evaluations may be summarized as follows:

1 CMC that has been developed exhibited superior strength to MC in resistance to particle impacts. This resistance strength to particle impacts can be attributed to reductions in the brittleness of the materials.

2 Components in various configurations made of the CMC that has been developed reached levels of strength that were the same as those of the test pieces. Additionally, some CMC components have passed screening tests in which loading of 120 percent of the maximum thermal stress generated in an engine has been applied. It has thus been confirmed that these

components have the potential that enables them to be tested in high-temperature assembly tests and engine tests.

3 It was confirmed that the components made of MC that were used as a reference had the high-temperature strength reliability necessary for them to adequately withstand 100 hours of use at a gas temperature of 1200°C. Furthermore, the problems with respect to strength at a gas temperature of 1350°C were clarified.

Acknowledgments

The authors deeply appreciate the Agency of Natural Resources and Energy of the Ministry of International Trade and Industry for supporting this research, and are grateful to Petroleum Energy Center for permitting the publication of this paper. The authors would also like to express thanks to the cooperative companies for supporting the program.

References

1 Petroleum Energy Center, "Report on Technical Development of the Automotive Ceramic Gas Turbine," Paper No. PEC-94C01.

2 Nishiyama, T., Iwai, M., Nakazawa, N., Sasaki, M., Katagiri, H., and Handa, N., "Status of the Automotive Ceramic Gas Turbine Development Program—Four Year Progress," ASME Paper No. 95-GT-447, 1995.

3 Izumi, T., Munekiyo, M., Nakazawa, N., Inaba, S., Sasaki, S., Akai, W., and Kondoh, S., "The Turbine Component Development for the 100 kW Automotive Ceramic Gas Turbine (Stationary Parts)," *Proc. 9th GTSJ Autumn Meeting,* Oct. 1994, pp. 39–46.

4 Watanabe, M., and Okano, H., "Recent Advances in the Development of Ceramic Stationary Components for Automotive CGT," *Proc. International Symposium on Ceramics for Structural and Tribological Applications,* Aug. 1995, pp. 333–342.

Creep Performance of Candidate SiC and Si_3N_4 Materials for Land-Based, Gas Turbine Engine Components

A. A. Wereszczak

T. P. Kirkland

High Temperature Materials Laboratory,
Oak Ridge National Laboratory,
Oak Ridge, TN 37831

The tensile creep-rupture performance of a commercially available gas pressure sintered silicon nitride (Si_3N_4) and a sintered silicon carbide (SiC) is examined at 1038, 1150, and 1350°C. These two ceramic materials are candidates for nozzles and combustor tiles that are to be retrofitted in land-based gas turbine engines, and interest exists to investigate their high-temperature mechanical performance over service times up to, and in excess of, 10,000 hours (≈14 months). To achieve lifetimes approaching 10,000 hours for the candidate Si_3N_4 ceramic, it was found (or it was estimated based on ongoing test data) that a static tensile stress of 300 MPa at 1038 and 1150°C, and a stress of 125 MPa at 1350°C cannot be exceeded. For the SiC ceramic, it was estimated from ongoing test data that a static tensile stress of 300 MPa at 1038°C, 250 MPa at 1150°C, and 180 MPa at 1350°C cannot be exceeded. The creep-stress exponents for this Si_3N_4 were determined to be 33, 17, and 8 for 1038, 1150, and 1350°C, respectively. The fatigue-stress exponents for the Si_3N_4 were found to be equivalent to the creep exponents, suggesting that the fatigue mechanism that ultimately causes fracture is controlled and related to the creep mechanisms. Little success was experienced at generating failures in the SiC after several decades of time through exposure to appropriate tensile stress; it was typically observed that if failure did not occur on loading, then the SiC specimens most often did not creep-rupture. However, creep-stress exponents for the SiC were determined to be 57, 27, and 11 for 1038, 1150, and 1350°C, respectively. For SiC, the fatigue-stress exponents did not correlate as well with creep-stress exponents. Failures that occurred in the SiC were a result of slow crack growth that was initiated from the specimen's surface.

Introduction

Silicon nitride (Si_3N_4) and silicon carbide (SiC) ceramics are leading candidates for use as structural components, e.g., nozzles and combustor tiles (Parthasarathy et al., 1995), in advanced industrial gas turbine engines. The utilization of Si_3N_4 or SiC over more traditional alloys offers several advantages, such as higher temperature capability (and an associated increased operating efficiency), reduced weight and inertia effects, and the potential design and use of noncooled components. In addition, both Si_3N_4 and SiC are candidates for these applications because they have good thermal shock resistance and high thermal conductivity, are relatively corrosion resistant, and possess good high-temperature tensile strength.

The utilization of Si_3N_4 and SiC at elevated temperatures has been inhibited by the lack of a database that describes their long-term stress-rupture (SR) behavior. Existing data for many high-performance structural ceramics such as Si_3N_4 and SiC are limited to exposure times less than the 1000–5000 hour range. The extension of these data to times of the order of 10,000 hours is required for the confident and reliable insertion of Si_3N_4 or SiC components into industrial gas turbines; see Fig. 1. One concern of interest is the possible transition from slow crack growth (SCG) dominated failure to creep-dominated failure. The SCG dominated failure tends to be prevalent at relatively high stresses and/or relatively low temperatures. However, as the temperature increases and/or the stress decreases, the generation and accumulation of creep damage may become more prevalent and control the lifetime. Because the creep process generally exhibits a larger stress sensitivity compared to SCG, the lifetime measured at low applied stresses will be significantly lower than those expected from SCG.

In the present study, the candidate Si_3N_4 and SiC materials were tensile creep-ruptured in ambient air as a function of temperature (1038, 1150, and 1350°C) and stress. These temperatures bracketed the service temperature of prospective structural ceramic, gas turbine engine components (Roode et al., 1993). The SR data were evaluated by continuing each creep test to failure. Tensile creep data were generated as well by measuring the tensile creep strain throughout the duration of each SR test. The applied stresses in the test matrix were chosen to obtain failure times ranging up to 10,000 h for these two materials. Last, the creep and SR data were used to generate mechanical reliability maps that describe the time to failure as a function of stress and temperature for both materials.

Material Description and Experimental Procedures

Materials and Specimens. Commercially available Si_3N_4[1] and SiC[2] were tested. Following green-state injection molding, the Si_3N_4 was densified by gas-pressure-sintering and the SiC was reaction sintered. Aluminum and ytterbium were identified by energy dispersive spectroscopy (EDS), and were located in the grain boundaries of the as-received Si_3N_4. Trace amounts of carbon and boron were used to assist the densification of the

Contributed by the International Gas Turbine Institute and presented at the 41st International Gas Turbine and Aeroengine Congress and Exhibition, Birmingham, United Kingdom, June 10–13, 1996. Manuscript received at ASME Headquarters February 1996. Paper No. 96-GT-385. Associate Technical Editor: J. N. Shinn.

[1] SN88, NGK Insulators, LTD., Nagoya, Japan.
[2] Hexoloy SA, Carborundum Co., Niagara Falls, NY.

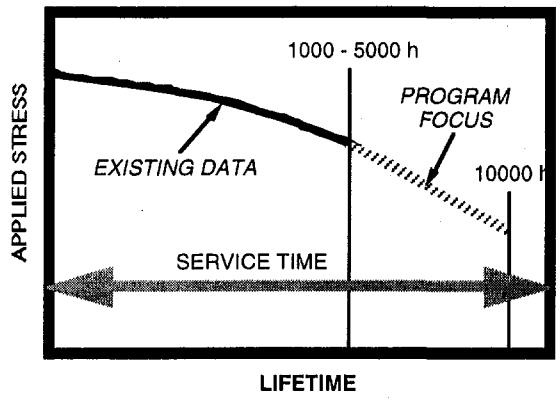

Fig. 1 The motivation for the present study was to generate engineering creep data for lifetimes in excess of 1000–5000 h.

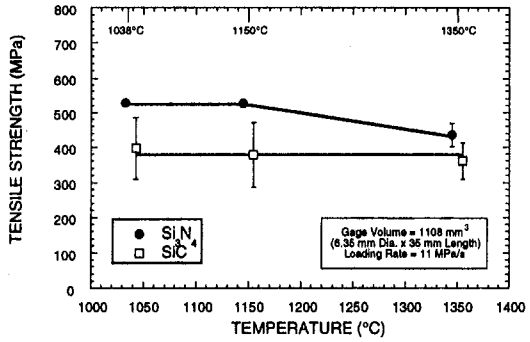

Fig. 2 Average tensile strength as a function of temperature for the Si_3N_4 and SiC ceramics examined. Vertical bars represent standard deviations.

α-SiC during reaction sintering. The sintered SiC was subjected to a post-sintering treatment of hot isostatic pressing to further improve densification.

Buttonhead tensile specimens were used for all testing. The specimen geometry had a characteristic gage diameter of 6.35 mm and a gage length of 35 mm, for a total gage volume of 1108 mm^3.

Mechanical Testing. Stress rupture tests were conducted either on electromechanical tensile testing machines[3] or actuator-driven, lever-arm tensile testing machines.[4] These systems possess either passive or active self-alignment fixturing in their load trains. Any imposed axial bending was less than 5 percent during all the stress rupture tests. Compact, two-zone, resistance-heated furnaces were used for heating the gage section of the buttonhead tensile specimens. These furnaces provided a hot-zone height of 50 mm, which overlapped the 35 mm gage length of the specimens. The buttonhead specimens were "cold-gripped" outside the hot zone of the furnace. A constant-temperature water chiller maintained a water supply to the upper and lower grips. High-temperature contact extensometers having a gage length of 25 mm were used to measure specimen elongation during the SR tests. Computers were used for test control and to collect load, temperature, and specimen elongation data as a function of time. Tests were conducted at 1038, 1150, or 1350°C and tensile stresses were varied with the intent to generate specimen lifetimes out to 10,000 h.

In addition to the SR tests, the tensile strengths of both the Si_3N_4 and the SiC were measured at 1038, 1150, and 1350°C. Specimens were loaded to failure using a loading rate of 11 MPa/s. Extensometry was employed during the early part of the strength tests yielding strain information needed for Young's Modulus determinations; however, the extensometers were manually removed during the latter stages of specimen loading to prevent their damage from the fracture event.

Post-Testing Characterization. Optical microscopy was used to determine the original fracture surfaces of all stress-ruptured specimens. Evidence for SCG, failure causing flaws, or creep damage was sought. X-ray diffraction (XRD) was conducted to determine if phase changes occurred in the Si_3N_4 as a result of the creep testing.

Results and Discussion

Tensile Strength of Si_3N_4 and SiC. The average tensile strengths of the Si_3N_4 and the SiC as a function of temperature are shown in Fig. 2. A minimum of two specimens was tested at each of the three temperatures. The vertical bars shown in Fig. 2 represent standard deviations. The average tensile strength for the Si_3N_4 was approximately 527 MPa at both 1038 and 1150°C, but dropped to about 435 MPa at 1350°C. The Si_3N_4 tensile specimens typically failed from abnormally large Si_3N_4 grains, an example of which is shown in Fig. 3. The tensile strengths of the SiC exhibited more scatter, and it is arguable that its value of 370 MPa was independent of temperature. Several SiC SR specimens broke during loading, so their ultimate loads (or strengths) are included in the average strength values. The failure of SiC tensile specimens was typically initiated at the surface, although identifiable flaws in the SiC were not detected during fractography.

Young's Modulus of Si_3N_4 and SiC. Showing the same trends as tensile strength, the average Young's Modulus of the Si_3N_4 decreased as temperature increased, while the average Young's Modulus of the SiC appeared to be independent of temperature up to 1350°C. The average Young's Modulus values shown in Fig. 4 were determined from a minimum of two samples for each temperature. Prior to specimen heating, every strength-test specimen was first subjected to a room temperature loading to approximately 200 MPa to measure their stress-strain. The Young's Modulus could be determined as well. As a consequence, the average room temperature Young's Modulus for both materials represents more than two samples.

The average room temperature Young's Modulus of the Si_3N_4 was determined to be 308 GPa. It decreased to 280 GPa at 1038 and 1150°C and further decreased to 246 GPa at 1350°C. During

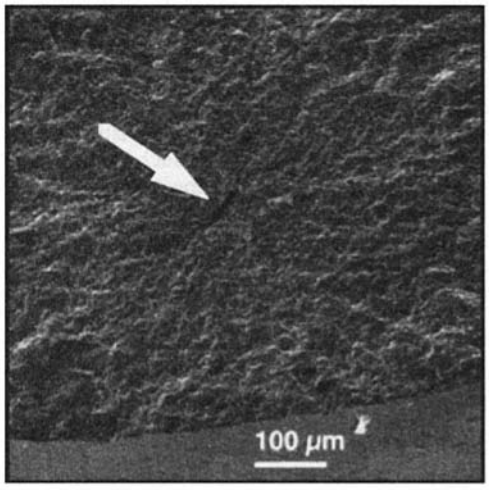

Fig. 3 Abnormally large Si_3N_4 grains were the typical flaw where fracture was initiated during tensile strength testing.

[3] Model 1380, Instron Corp., Canton, MA.
[4] Series 2300, Applied Test Systems, Butler, PA.

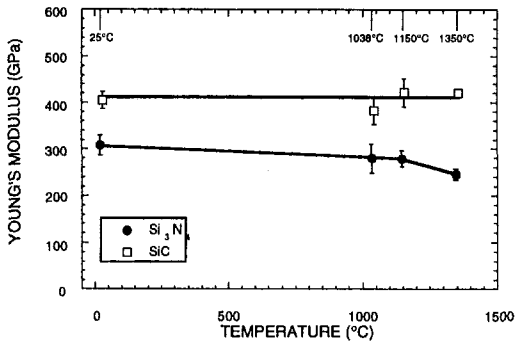

Fig. 4 Young's Modulus as a function of temperature for the Si_3N_4 and SiC ceramics examined. Vertical bars represent standard deviations.

the tensile strength testing of the Si_3N_4, nonlinearity in the stress-strain response was not observed up to 300 MPa at a stressing rate of 11 MPa/s for any of the test temperatures. This observation does not imply that nonlinearity may not be present above 300 MPa, as the extensometers were removed from the specimen surface at a tensile stress of approximately 300 MPa to prevent damage to them. Lending further credence to this observation, the authors did not observe nonlinearity when this material was stressed to 414 MPa at 1300°C using the same stressing rate (Wereszczak et al., 1995a). The gradual decrease of the Si_3N_4 Young's Modulus as test temperature increased is believed to be a consequence of the ytterbium–silicon–oxynitride grain boundary phase undergoing some softening. This phenomenon has been reported for this material in flexure loading at 1350°C (Osborne and Graves, 1997).

The average Young's Modulus of the SiC was determined to be 410 GPa at room temperature and remained essentially constant up to 1350°C, as seen in Fig. 4. Essentially no grain boundary phase is present in this material, and the observation that the Young's Modulus does not decrease with increasing temperature is consistent with this.

Tensile Creep-Rupture Behavior

Tensile Creep Histories. Transient creep strain histories were typical of Si_3N_4 and SiC specimens creep tested at 1038, 1150, and 1350°C. Depending on the tensile stress, the accumulated creep strains for the Si_3N_4 specimens ranged up to 0.2, 0.7, and 2.6 percent for creep tests at 1038, 1150, and 1350°C, respectively, as shown in Figs. 5(*a–c*). Typical failure creep strains of 1.5 to 2.0 percent at 1300°C and 250 MPa and 2.5 to 3.0 percent at 1400°C and 150 MPa have been reported for this material (French and Wiederhorn, 1995). The accumulated creep strains for the SiC specimens only ranged up to 0.05, 0.08, and 0.14 percent for creep tests at 1038, 1150, and 1350°C, respectively, as shown in Figs. 6(*a–c*). The measured engineering creep data for all the static creep tests for Si_3N_4 and SiC are shown in Table I. The amounts of accumulated creep strains for the SiC creep tests were so small that the creep strain-time profiles illustrate the ultimate resolution of the extensometer, as evidenced by the scatter in the measured creep strains shown in Fig. 6(*a–c*).

The creep strain-time profiles in Figs. 5(*a–c*) and 6(*a–c*) show that for equivalent stresses that the SiC is more creep resistant than the Si_3N_4; however, Si_3N_4 was able to withstand higher static creep stresses than the SiC. The variability in the strength of the SiC, as shown in Fig. 2, revealed itself in the static creep testing in that several of the SiC specimens broke during loading to the desired stress setpoint. Specimens of SiC broke during loading as low as 300 MPa (at 1150°C), while at the same temperature, the Si_3N_4 was able to withstand a static stress as high as 450 MPa for over 39 hours before rupturing.

The generated creep-rupture data on the Si_3N_4 show (or suggest based on ongoing test data) that to achieve lifetimes approaching 10,000 hours, a static tensile stress of 300 MPa at 1038 and 1150°C, and a static tensile stress of 125 MPa at 1350°C cannot be exceeded. These stress limits for the Si_3N_4 are not limited by its high temperature tensile strength. For the SiC ceramic, a static tensile stress of 300 MPa at 1038°C, 250 MPa at 1150°C, and 180 MPa at 1350°C cannot be exceeded. However, unlike the Si_3N_4, these limiting stresses for the SiC are closer to its variable high-temperature tensile strength, and in fact may overlap. For example, some SiC tensile strength specimens failed below 350 MPa at 1038°C; however, some SiC SR specimens have exhibited lives in excess of 800 hours at stresses above 350 MPa at this same temperature, as shown in Fig. 6(*a*).

Post-Testing Analysis. For the stress ranges examined, SCG typically was the cause of failure in the Si_3N_4 at 1038 and 1150°C, while a transition to creep damage-induced failure occurred at 1350°C. Fracture surfaces of representative specimens tested at 1038, 1150, and 1350°C are shown in Figs. 7(*a–d*).

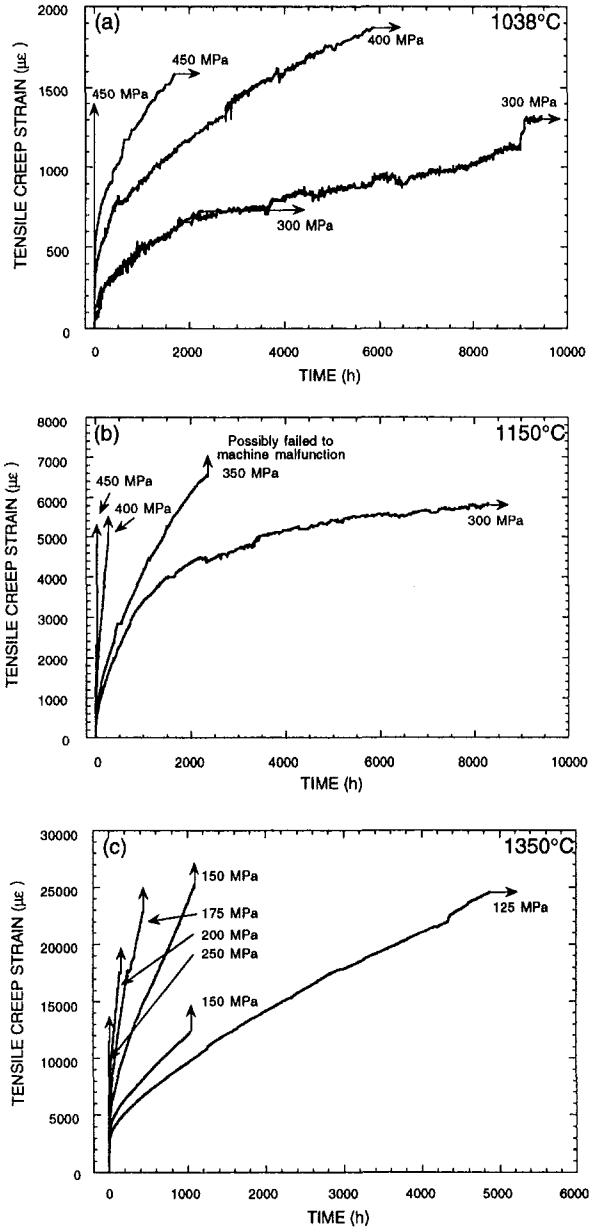

Fig. 5 Creep histories of the Si_3N_4 at (*a*) 1038°C, (*b*) 1150°C, and (*c*) 1350°C. Vertical arrows represent specimen failures, while horizontal arrows represent ongoing tests.

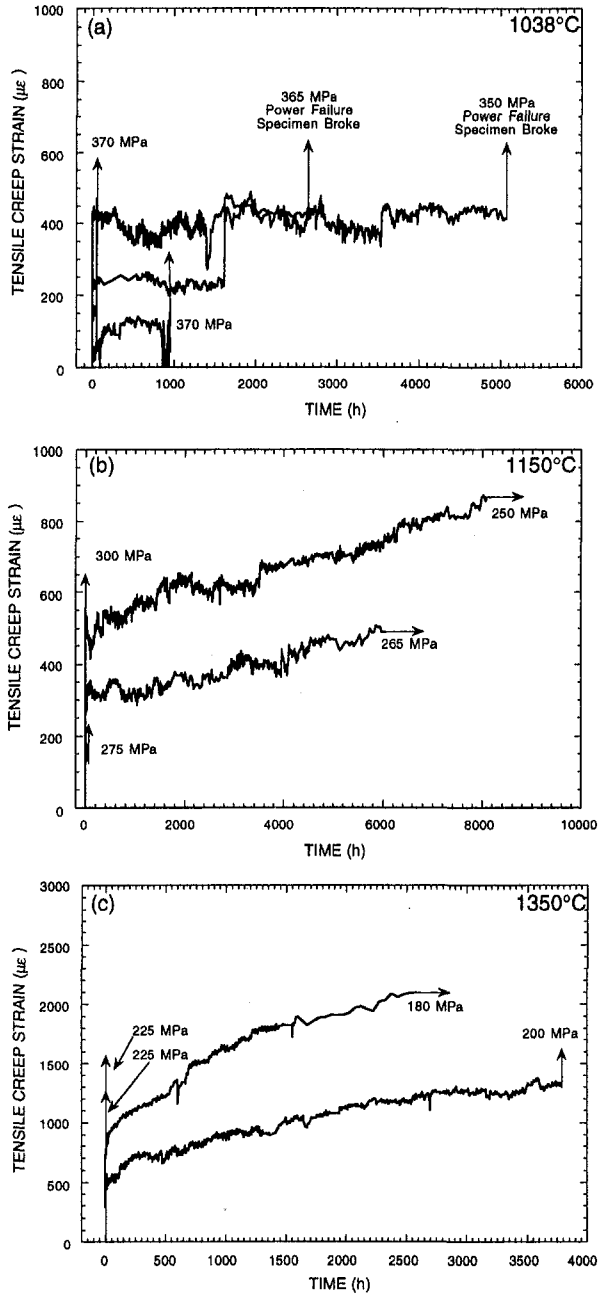

Fig. 6 Creep histories of the SiC at (*a*) 1038°C, (*b*) 1150°C, and (*c*) 1350°C. Vertical arrows represent specimen failures, while horizontal arrows represent ongoing tests.

The high stresses required to cause creep rupture at 1038 and 1150°C resulted in the creation of correspondingly small fracture mirrors, which are somewhat difficult to discern in Figs. 7(*a*–*b*). The creep damage zones that caused failure at 1350°C are positioned at the 6 o'clock positions in Figs. 7(*c*–*d*) at the surface of specimens tested at 200 and 250 MPa. The authors have previously found (Wereszczak et al., 1995b, 1995c) that the growth of analogous damage zones in another Si_3N_4 is affected by environmental, oxidation, and microscopic creep-damage. The transition from SCG-induced failure at 1038 and 1150°C to one of creep-damage-induced failure at 1350°C also is reflected in the magnitudes of the strains-to-failure for these temperatures; creep strains to failure were typically low for tests conducted at 1038 and 1150°C (up to ≈0.7%), while those creep strains to failure at 1350°C were significantly greater (up to ≈2.6 percent). It is interesting to note that the change in the Si_3N_4 material between 1150 and 1350°C was accompanied by the changes in its tensile strength and Young's Modulus that were respectively shown in Figs. 2 and 4. Analysis from XRD results showed that the grain boundary phase(s) in the Si_3N_4 changed during creep testing at 1350°C, as shown in Fig. 8; however, it is not known whether these phase changes are a cause or consequence of the mechanical performance change in the material observed between 1150 or 1350°C, but they are further reflective of this change.

Slow crack growth was the cause of failure in SiC at all three test temperatures. No specimens creep fractured at 1038°C, as shown in Table 1. One creep failure occurred at 1150°C and three at 1350°C. The fracture surface of the specimen tested at 1150°C and two at 1350°C, indicating consistent initiation of fracture at the specimen surfaces, are shown in Figs. 9(*a*–*c*). A small reaction zone (an oxidation-induced reaction pit?) is evident at the surface of the two specimens tested at 1350°C (Figs. 9(*b*–*c*)). Slow-crack-growth-induced fracture at all three temperatures is consistent with the lack of a tensile strength or modulus change in SiC at these three temperatures as well. The as-received SiC was a single phase material (i.e., 100 percent α-SiC), unlike the Si_3N_4, so that no change in the phase or content was expected as a consequence of the creep testing.

Representation of Creep and Fatigue Performance. The steady-state or minimum creep rate ($\dot{\epsilon}$) may be represented as a function of the applied static creep stress (σ) using the temperature-independent Norton–Bailey equation,

$$\dot{\epsilon} = A_0 \sigma^n, \tag{1}$$

where A_0 is a pre-exponential factor and n is the creep-stress exponent. The temperature-*dependent* version of this equation includes an Arrhenius-like term containing an activation energy and a temperature term. Due to the change in the dominant creep mechanism in the Si_3N_4, the temperature-*independent* relation was chosen to avoid the temperature-dependent analysis of the activation energy; that will be a focus of a future study. The minimum creep rates as a function of stress results for the Si_3N_4 and SiC are shown in Fig. 10(*a*–*b*), respectively, for all three temperatures. The determined creep-stress exponents were 33, 17, and 8 for the Si_3N_4, and 57, 27, and 11 for the SiC at 1038, 1150, and 1350°C, respectively. The creep rates are faster for the Si_3N_4 than the SiC for equivalent stresses, while the creep-stress exponents are consistently less for the Si_3N_4 compared to the SiC for the same temperatures. The large-valued creep-stress exponents for the Si_3N_4 at 1038 and 1150°C, as well as those for the SiC at all three temperatures, are indicative of the potentiality of SCG-dominated failures at these temperatures. The effective softening or phase changes in the grain boundaries of the Si_3N_4 at 1350°C was associated with the greater amounts of accumulation of creep damage (e.g., cavitation, grain boundary separation by viscous flow, etc.), and a lower creep-stress exponent resulted as a consequence.

The time to failure (t_f) may be represented as a function of the applied static creep stress using

$$t_f = B_0 \sigma^{-N}, \tag{2}$$

where B_0 is a pre-exponential factor and N is the fatigue-stress exponent. The temperature-independent version of this empirical equation was chosen using the same rationale used for the choice of Eq. (1). The graphic representations of Eq. (2) for the Si_3N_4 and SiC are shown in Figs. 11(*a*–*b*), respectively. The determined fatigue-stress exponents were 51, 13, and 7 for the Si_3N_4, and 79, 67, and 33 for the SiC at 1038, 1150, and 1350°C, respectively. The large-valued fatigue exponents that were determined for the Si_3N_4 at 1038 and 1150°C and for the SiC are typically indicative of the SCG-dominated failures. This mode of failure was exhibited by Si_3N_4 at 1038 and 1150°C

Table 1 Test matrix and experimentally measured creep data

Specimen ID	Temp (°C)	Stress (MPa)	Minimum Creep Rate x 10^{-12} (/s)	Time to Failure (h)	Failure Strain (με)	Comments
Si_3N_4						
SN 45907	1038	300	14*	10159*	1400*	ongoing
SN 44807	1038	300	53*	2226*	730*	ongoing
SN 32805	1038	400	36*	5880*	1870*	ongoing
SN 56609	1038	450	2400	9.6	80	
SN 45207	1038	450				Broke on loading
SN 33205	1038	450	95*	1585*	1660*	ongoing
SN 45807	1150	300	27*	9021*	6000*	ongoing
SN 33105	1150	350	290	2379	6570	Failure - Eqpt malfunction?
SN 57609	1150	375	1525*	569*	4800*	ongoing
SN 44507	1150	400	3800	279.8	5070	
SN 44707	1150	450	18000	39.3	3180	
SN 57409	1350	125	972*	5599*	27100*	ongoing
SN 56509	1350	150	1900	1047	12300	Failed from power outage
SN 44307	1350	150	4100	1090	25120	
SN 33905	1350	175	8900	443	22860	
SN 44607	1350	200	20000	142	17540	
SN 45507	1350	250	?	17.9	?	Extensometer malfunction
SiC						
SiC 289	1038	350	1.7	5062	420	Failed from power outage
SiC 291	1038	350				Broke on loading
SiC 241	1038	365	6.5	2595	240	Failed from power outage
SiC 272	1038	365				Broke on loading
SiC 242	1038	370	150	54.3	170	Failed from power outage
SiC 292	1038	370	6	957	≈120	
SiC 327	1038	375				Broke on loading
SiC 247	1150	250	13.4*	8050*	860*	ongoing
SiC 243	1150	265	8.3*	5987*	490*	ongoing
SiC 333	1150	275	160	47	130	
SiC 273	1150	300				Broke on loading
SiC 234	1150	300				Broke on loading
SiC 232	1350	180	70*	2569*	2100*	ongoing
SiC 266	1350	200	84	3784	1330	
SiC 290	1350	225	1400	8.5	760	
SiC 246	1350	225	840	18.5	520	
SiC 326	1350	250				Broke on loading
SiC 244	1350	365		0.001		

* Ongoing test - reported value will change as test continues.

and by SiC at 1150 and 1350°C, and can be expected for SiC at 1038°C as well. The stress–t_f relationships determined in the present study at 1038, 1150, and 1350°C, are consistent with what has been generated on this material previously (Watanabe et al., 1992) at 1200, 1300, and 1400°C, as illustrated in Fig. 12. Referring to Figs. 10 and 11, the creep-stress and fatigue-stress exponents are numerically equivalent for all three respective temperatures for both materials; this observation suggests that whatever mechanism dominated the creep process also dictated fatigue life. The graphic representations in Figs. 11(a–b) are useful for life prediction, for they suggest that if a component is subjected to a stress at any of the three temperatures in their respective domains below the shown stress–t_f functions, then failure of the component would not be expected.

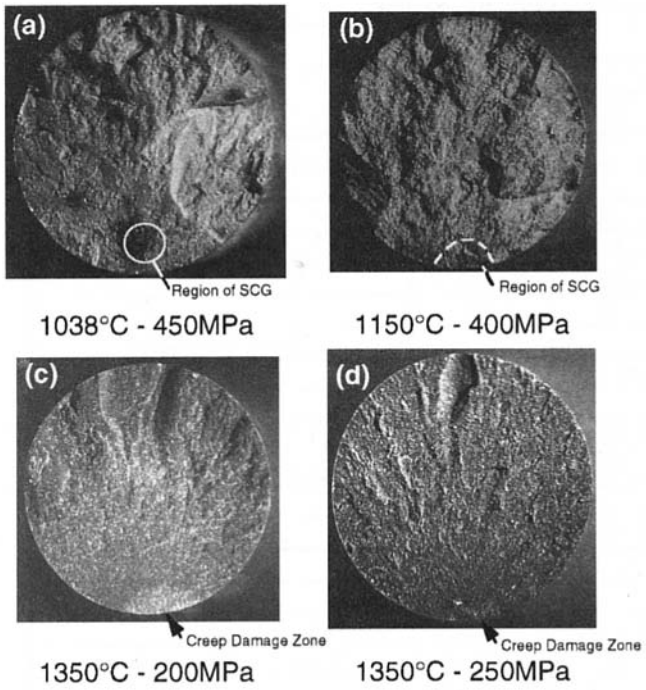

Fig. 7 Fracture surfaces of creep-ruptured Si_3N_4 Specimens at (*a*) 1038°C and 450 MPa, (*b*) 1150°C and 400 MPa, (*c*) 1350°C and 200 MPa, and (*d*) 1350°C and 250 MPa.

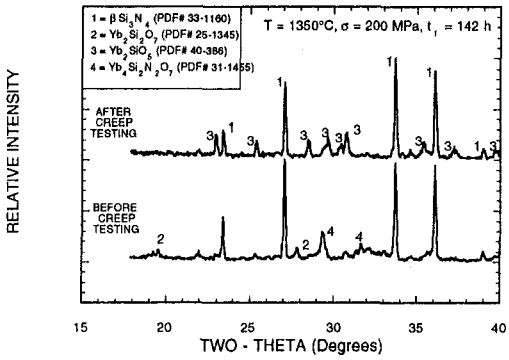

Fig. 8 X-ray diffraction profiles of the as-received and creep tested Si_3N_4

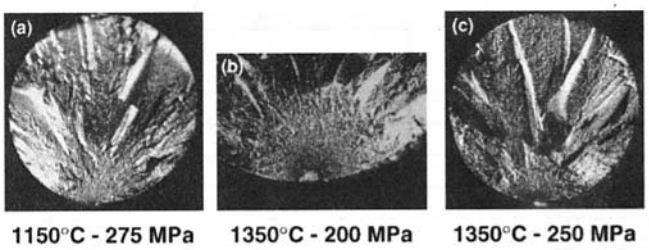

Fig. 9 Fracture surfaces of creep-ruptured SiC specimens at (*a*) 1150°C and 275 MPa, (*b*) 1350°C and 200 MPa, and (*c*) 1350°C and 250 MPa.

Finally, the applicability of the Monkman–Grant relationship (minimum creep rate as a function of time to failure) to the generated engineering creep data was explored. The Monkman–Grant relationship (Monkman and Grant, 1956) is represented by

$$t_f = C\dot{\epsilon}^{-m}, \tag{3}$$

where C and m are constants. From Eqs. (1) and (2), it is

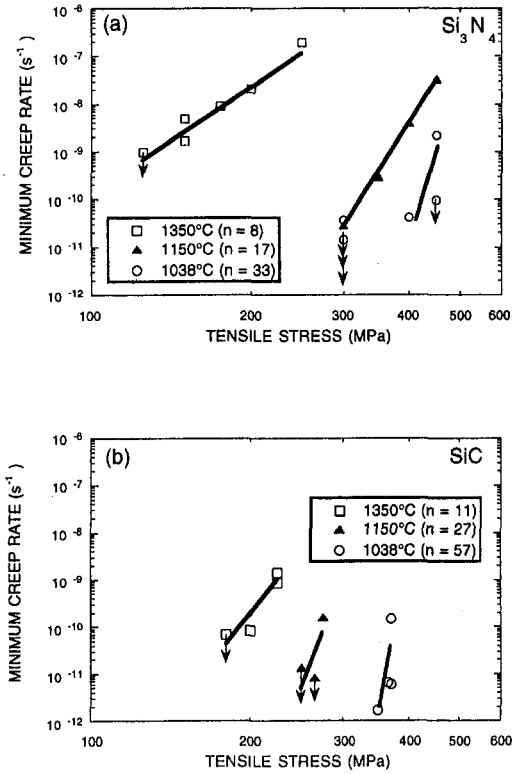

Fig. 10 Minimum creep rate as a function of applied tensile stress at 1038, 1150, and 1350°C for the (*a*) Si_3N_4, and (*b*) SiC. Creep-stress exponent values for each temperature are shown in the legend. Arrows represent ongoing tests.

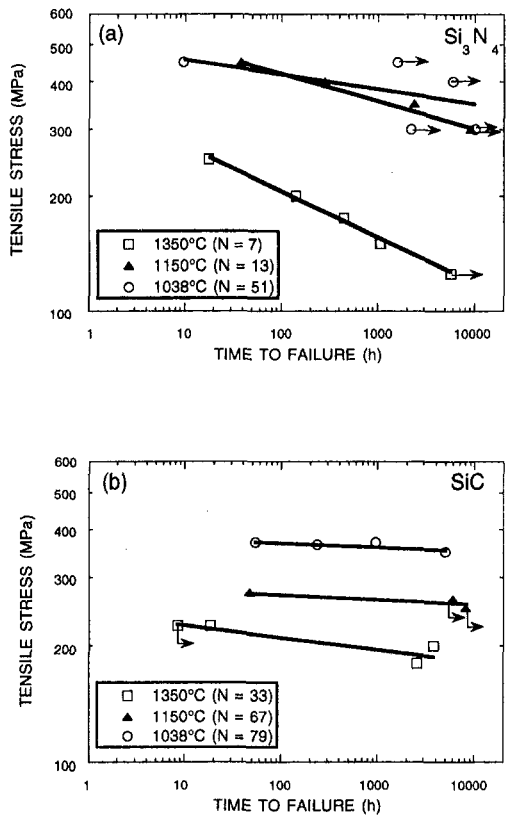

Fig. 11 Applied tensile stress as a function of the time to failure at 1038, 1150, and 1350°C for the (*a*) Si_3N_4, and (*b*) SiC. Fatigue-stress exponent values for each temperature are shown in the legend. Arrows represent ongoing tests.

observed that $N = n \cdot m$; this relationship has been previously explored and discussed (Cranmer et al., 1991; Ferber and Jenkins, 1992; Menon et al., 1994). In particular, when N and n are equivalent in value (i.e., the creep-stress and fatigue-stress dependencies are equivalent) and the activation energies for both creep and fatigue are equivalent, then the value of m should be approximately equal to one (which has been shown to be the case by Ferber and Jenkins, 1992, and Ding et al., 1994) and all the minimum creep rate as a function of time to failure data should collapse to, or be approximated by, the function shown in Eq. (3).

The Monkman–Grant relationship does not satisfactorily represent the creep data generated in this study for either the Si_3N_4 or the SiC, as evidenced by the lack data convergence in Figs. 13(a–b) for each respective ceramic material. It is arguable that the engineering data generated on the Si_3N_4 at 1150 and 1350°C exhibit convergence using the Monkman–Grant relationship; however, differences between these two temperatures were already shown in the creep-stress and fatigue-stress exponents in Figs. 10(a) and 11(a). This suggests that there is an activation energy difference as well (i.e., temperature dependence of the minimum creep rate, and of fatigue life stress relation), and in this instance, this difference results in a net effect that the Monkman–Grant relationship represented by Eq. (3) is *apparently* obeyed between 1150 and 1350°C. If the activation energy differences are acknowledged in Eqs. (1) and (2), along with the recognition of dominant-failure-mechanism changes, then the Monkman–Grant relationship may be modified to make it more applicable to represent all the engineering data generated in the present study.

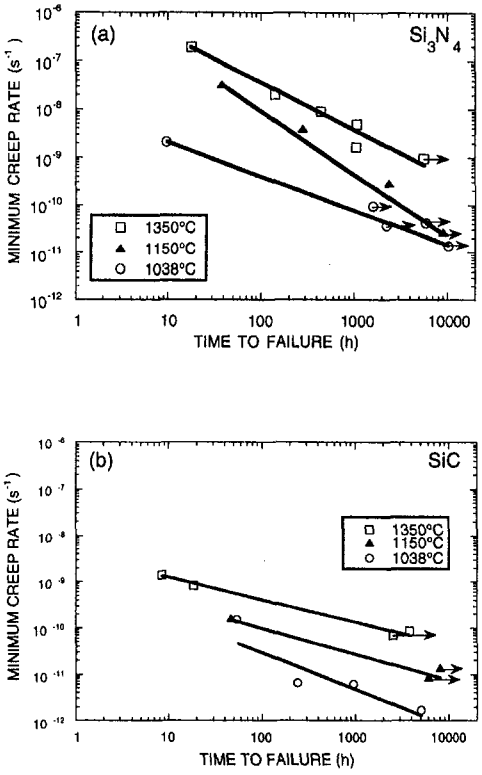

Fig. 13 Minimum creep rate as a function of the time to failure (i.e., Monkman–Grant relationship) at 1038, 1150, and 1350°C for the (a) Si_3N_4, and (b) SiC. Arrows represent ongoing tests.

Conclusions

To achieve lifetimes approaching 10,000 hours for the candidate Si_3N_4 ceramic examined in this study, it was found (or estimated based on data from ongoing tests) that a static tensile stress of 300 MPa at 1038 and 1150°C, and a stress of 125 MPa at 1350°C cannot be exceeded. For the SiC ceramic, it was estimated based on data from ongoing tests that a static tensile stress of 300 MPa at 1038°C, 250 MPa at 1150°C, and 180 MPa at 1350°C cannot be exceeded. The creep-stress exponents for this Si_3N_4 were determined to be 33, 17, and 8 for 1038, 1150, and 1350°C, respectively. The fatigue-stress exponents for the Si_3N_4 were found to be equivalent to the creep-stress exponents, suggesting that the fatigue mechanism that ultimately causes fracture is controlled and related to creep processes. It was observed that if failure did not occur on loading, then the SiC most often did not creep-rupture. Creep-stress exponents for the SiC were determined to be 57, 27, and 11 for 1038°C, 1150°C, and 1350°C, respectively. For SiC, the fatigue-stress exponents did not correlate to the creep-stress exponents as closely as they did for the Si_3N_4. Failures that occurred in the SiC were a result of SCG that initiated from the specimen's surface.

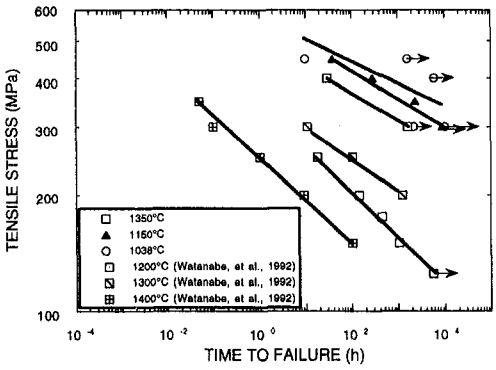

Fig. 12 Comparison of the applied tensile stress as a function of the time to failure between this and reported literature values. Arrows represent ongoing tests.

Acknowledgments

Research sponsored by the U.S. Department of Energy, Assistant Secretary for Energy Efficiency and Renewable Energy, Office of Industrial Technologies, Industrial Energy Efficiency Division and Advanced Turbine Systems Program, under Contract DE-AC05-96OR22464 managed by Lockheed Martin Energy Research Corporation.

The authors wish to thank Drs. K. C. Liu and E. Sun for reviewing the manuscript and for their helpful suggestions and comments.

References

Cranmer, D. C., Hockey, B. J., Wiederhorn, S. M., and Yeckley, R. L., 1991, "Creep and Creep-Rupture of HIP-ed Si_3N_4," *Cer. Eng. Sci. Proc.*, Vol. 12, pp. 1862–1872.

Ding, J.-L., Liu, K. C., More, K. L., and Brinkman, C. R., 1994, "Creep and Creep Rupture of an Advanced Silicon Nitride Ceramic," *J. Am. Cer. Soc.*, Vol. 77, pp. 867–74.

Ferber, M. K., and Jenkins, M. G., 1992, "Evaluation of the Strength and Creep-Fatigue Behavior of Hot Isostatically Pressed Silicon Nitride," *J. Am. Cer. Soc.*, Vol. 75, pp. 2453–62.

French, J. D., and Wiederhorn, S. M., 1995, "Tensile Specimens From Ceramic Components," submitted to *J. Am. Cer. Soc.*

Menon, M. N., Fang, H. T., Wu, D. C., Jenkins, M. G., and Ferber, M. K., 1994, "Creep and Stress Rupture Behavior of an Advanced Silicon Nitride: Part III, Stress Rupture and the Monkman–Grant Relationship," *J. Am. Cer. Soc.*, Vol. 77, pp. 1235–41.

Monkman, F. C., and Grant, N. J., 1956, "An Empirical Relationship Between Rupture Life and Minimum Creep Rate in Creep-Rupture Tests," *Proc. Am. Soc. Test. Mater.*, Vol. 56, pp. 593–620.

Osborne, N. R., and Graves, G. A., 1997, "Dynamic Fatigue Testing of Candidate Ceramic Materials for Turbine Engines to Determine Slow-Crack-Growth Parameters," ASME JOURNAL OF ENGINEERING FOR GAS TURBINES AND POWER, Vol. 119, pp. 273–278.

Parthasarathy, V. M., Price, J. R., Brentnall, W. D., Graves, G. A., and Goodrich, S., 1995, "Material Characterization of Candidate Silicon Based Ceramics for Stationary Gas Turbine Applications," ASME Paper No. 95-GT-249.

Roode, M. van Brentnal, W. D., Norton, P. F., and Pytanowski, G. P., 1993, "Ceramic Stationary Gas Turbine Development," ASME Paper No. 93-GT-309.

Watanabe, K., Masuda, M., Ozawa, T., Matsui, M., and Matsuhiro, K., 1993, "Research and Development of Ceramic Turbine Wheels," ASME JOURNAL OF ENGINEERING FOR GAS TURBINES AND POWER, Vol. 115, pp. 36–41.

Wereszczak, A. A., Ferber, M. K., Kirkland, T. P., Lara-Curzio, E., Parthasarathy, V., and Gribb, T. T., 1995a, "Stress Relaxation of Silicon Nitride at Elevated Temperatures," *Cer. Eng. Sci. Proc.,* Vol. 16, pp. 519–528.

Wereszczak, A. A., Ferber, M. K., Kirkland, T. P., More, K. L., Foley, M. R., and Yeckley, R. L., 1995b, "Evolution of Stress Failure Resulting From High-Temperature Stress-Corrosion Cracking in a Hot Isostatically Pressed Silicon Nitride," *J. Am. Cer. Soc.,* Vol. 78, pp. 2129–2140.

Wereszczak, A. A., Kirkland, T. P., and Ferber, M. K., 1995c, "Differences in Creep Performance of a HIPed Silicon Nitride in Ambient Air and Inert Environments," *Cer. Eng. Sci. Proc.,* Vol. 16, pp. 901–909.

Experimental Studies of Air Extraction for Cooling and/or Gasification in Gas Turbine Applications

J. S. Kapat[1]

T. Wang

Gas Turbine Research Laboratory,
Department of Mechanical Engineering,
Clemson University,
Clemson, SC 29634

W. R. Ryan

I. S. Diakunchak

R. L. Bannister

Power Generation Business Unit,
Westinghouse Electric Corporation,
Orlando, FL 32826

This paper describes an experimental study on how the flow field inside the dump diffuser of an industrial gas turbine is affected by air extraction through a single port on the shell around the dump diffuser. A subscale, 360 deg model of the diffuser-combustor section of an advanced developmental industrial gas turbine was used in this study. The experiments were performed under cold flow conditions, which can be scaled to actual machine operation. Three different conditions were experimentally studied: 0, 5, and 20 percent air extraction. It was found that air extraction, especially extraction at the 20 percent rate, introduced flow asymmetry inside the dump diffuser and, in some locations, increased the local flow recirculations. This indicated that when air was extracted through a single port on the shell, the performance of the dump diffuser was adversely affected with an approximate 7.6 percent increase of the total pressure loss, and the air flow into the combustors did not remain uniform. The global flow distribution was shown to be approximately 35 percent nonuniform diametrically across the dump diffuser. Although a specific geometry was selected, the results provide sufficient generality for improving understanding of the complex flow behavior in the reverse flow diffuser-combustor sections of gas turbines under the influence of various air extractions.

Introduction

Integrated Gasification Combined Cycle (IGCC) systems are of specific interest to the governments and utility companies of many countries as well as to gasifier and gas turbine manufacturers. The United States government is especially interested in developing reliable and cost-competitive IGCC systems for generating power using its abundant coal reserves for the following reasons: (*a*) to reduce U.S. dependency on foreign energy sources, (*b*) to have a matured and cost-effective IGCC technology in place when the natural gas supply diminishes in the future, (*c*) to provide a clean coal technology, and (*d*) to help U.S. industries achieve and maintain leadership in advanced IGCC technologies, which will also play an important role in future power generation in countries with limited natural gas resources, like China and India. To emphasize the U.S. government's interest in using coal gas as a fuel for future gas turbines, the U.S. Department of Energy (DOE) specifically required that new gas turbines developed under the support of its Advanced Turbine Systems (ATS) program be adaptable to coal gas (DOE/Clemson Workshops I and II, 1991 and 1992, and DOE Congressional Report, 1993).

One of the most important technical challenges for an IGCC system is how to integrate the gasifier and the gas turbine systems to achieve cost reduction and enhanced efficiency. The critical aspect of this integration is the removal of the compressor from the original gasifier system and supplying the gasifier with compressed air from the gas turbine. Following this integration process, the next technical question is how and where to extract the compressed air from the gas turbine. To investigate this issue, a collaborative research program between Clemson University and Westinghouse Electric Corporation, under the support of the Morgantown Energy Technology Center (METC) of DOE, was initiated at Clemson University.

In addition to extracting air for IGCC, air is extracted to cool the rotor. Extracting air from the compressor to cool vanes and blades in the turbine has been a common practice. The locations of the air extraction ports are mostly dictated by two considerations: (*a*) the convenience and accessibility of the sites and (*b*) for matching the pressures at the sites of the cooling components.

In view of the gasification requirement for the highest pressure at which air can possibly be extracted, the section between the compressor exit and the turbine inlet, i.e., the diffuser-combustor section, has become the focus of the search for adequate sites for air extraction.

The diffuser-combustor section has two major functions: (*a*) to decelerate the high velocity air coming from the compressor (Wilson, 1984) and (*b*) to distribute air uniformly to the combustors (Lyons, 1981).

A typical heavy-frame industrial gas turbine uses a two-part diffuser-combustion section to decelerate the air exiting the compressor. Air from the compressor first flows through an annular prediffuser and recovers some of its kinetic energy before being discharged into a comparatively large chamber called the dump diffuser or the dump chamber. Different from the in-line annular combustor geometry in aircraft engines and small industrial gas turbines, heavy-frame industrial gas turbines employ reverse flow, can-annular combustors (Lefebvre, 1983) to reduce the overall system length and to make the combustion process relatively insensitive to inlet flow conditions. In these gas turbines, air from the annular prediffuser turns approximately 150 deg before entering the combustors and must maneuver around combustors and transition pieces as it travels to the inlet of the combustor. As a result, the flow characteristics in these diffusers are extremely complex and entirely different from those of in-line diffusers. Because of

[1] Current address: Department of Mechanical and Aerospace Engineering, University of Central Florida, Orlando, FL 32816-2450.

Contributed by the International Gas Turbine Institute and presented at Turbo Asia '96, Jakarta, Indonesia, November 5–7, 1996. Manuscript received at ASME Headquarters July 1996. Associate Technical Editor: J. W. Shinn. Paper No. 96-TA-10.

these complex flow fields, the irreversible losses in the diffuser-combustor sections generated from separation eddies in the dump diffuser and friction losses on the wall are significant. These losses manifest themselves as total pressure loss. Typically, one percentage point reduction in the total pressure loss (expressed as a fraction of the total pressure at the annular pre-diffuser inlet) translates to a 0.09 to 0.13 percentage point reduction in combined cycle efficiency (please note the distinction between percentage point and percentage). In addition, due to the nonaxisymmetric component arrangement in the dump diffuser, the flow entering the combustors is not ideal and may adversely affect the uniformity of combustion in the combustor. As a result, the emission levels may be compromised. Consequently, it is of vital importance to investigate the effects of air extraction on the flow pattern, the aerodynamic losses, and the uniformity of flow entering the combustors.

To the authors' knowledge, few experimental studies have been performed regarding air extraction for IGCC. Kapat (1997) have reported the effect of air extraction on diffuser performance for another manufacturer's industrial gas turbine; however, only global performance has been studied. They reported that use of a single port for extracting air adversely affects the cooling of the transition pieces of the gas turbine. It was discovered that some cooling air is sucked outward from the transition piece cooling holes by the extraction force instead of impinging on the transition pieces as originally designed. These studies called our attention to the importance of improving our understanding of flow behavior under the influence of air extraction.

With the knowledge gained from the previous research, the current program was conducted through a series of studies with the overall objectives of (*a*) identifying potential locations for placing the air extraction ports, (*b*) assessing the advantages/disadvantages of various locations for extracting air, and (*c*) investigating the effects of air extraction on the aerodynamics, total pressure losses, and flow fields that affect the uniformity of combustion in the combustor.

First, a baseline study without air extraction was conducted computationally by Zhou et al. (1996). The computational results were then used to guide the design and instrumentation of an experimental study of the baseline case without air extraction by Kapat et al. (1996). For the air extraction study, the potential locations for the air extraction ports were identified at various locations on the walls of the prediffuser and the dump diffuser, taking into consideration the issues of accessibility and structural soundness. Objectives (*a*) and (*b*) were achieved through a numerical study (to be published at a later date) to compare the diffuser effectiveness under the conditions of applying air extraction at the inlet, in the middle, and at the exit of the annular prediffuser, respectively.

To achieve objective (*c*), a very complex experimental study for investigating the effects of air extraction on the detailed flow field inside the dump diffuser was conducted. This paper focuses on presenting the experimental results in the dump diffuser.

Two different air extraction rates, 20 and 5 percent of the flow at the dump diffuser outer wall (sometimes referred to as the combustor shell), were considered. The larger extraction simulates the conditions when air was extracted for gasification, and the smaller extraction simulates the conditions when air was extracted for cooling.

Although a specific geometry was selected for the present study, the results should provide sufficient generality for improving understanding of the complex flow behaviors in the reverse-flow-type diffuser-combustor sections of industrial gas turbines under the influence of air extraction.

Experimental Facility

The desired air flow through the test model was provided by an open-circuit, suction-type wind tunnel. The overall layout is shown in Fig. 1. Air from the test section went into a plenum box, which was maintained at $-40''$ H_2O gage pressure by a suction fan rated at 33,000 cfm (15.6 m^3/s) at 1.4 psi (9.65 kPa) and driven by a 220 hp motor. The plenum box isolated the test section from vibrations or oscillations of the fan and provided the necessary work space for installing a probe traversing system and changing the instrumentation. A detailed description of the experimental facility is provided by Kapat et al. (1996).

Test Section

Figure 2 shows a sectional view of the test section. A 48 percent subscale, 360 deg model of the diffuser-combustor section of a developmental heavy-frame gas turbine was constructed. The selection of a 360 deg model was necessary to investigate the effect of asymmetric air extraction (for cooling or IGCC) on the flow patterns in this study.

Before entering the model, the flow traveled through a straight annular section to condition the flow. At the end of the developing section, the flow entered the annular prediffuser, where it decelerated before being discharged into the dump diffuser.

After entering the dump diffuser, the air turned approximately 150 deg, maneuvered around the transition pieces and combustors, and entered the annular passage between the combustor and the top hat (Fig. 2). The annular passage in the top hat helped to distribute the flow before it turned approximately 180 deg and entered the combustor. After passing through the combustor and the transition piece, the flow was exhausted into the plenum.

The dump diffuser in this test model contained all of the components in the actual engine, including the cooling pipes and support struts. The annular passages in the top hats around the combustors contained the combustor cross-flame tubes with their complex angles to the flow maintained. In the actual engine, the cross-flame tubes are used sequentially to ignite the combustors by circumferentially conducting flame through the tubes. The transition pieces were vacuum-formed to match the outer contours of the actual engine transition pieces. Cooling holes were drilled in the transition pieces such that the fraction of cooling air flow entering the transition piece lining was identical to that expected in the actual engine. Geometric similarity

Nomenclature

1, 2, 3 = longitudinal measurement planes (Fig. 2)
$B, \ldots, G$ = streamwise measurement locations (Fig. 2)
D_h = hydraulic diameter at the annular prediffuser inlet
IGCC = Integrated Gasification Combined Cycle
r = radial distance measured from the centerline of the test section
U = average axial velocity at the test section inlet
V = velocity
x = axial distance from the annular prediffuser inlet
$X1, X2, X3$ = extraction sites (Fig. 3)

Subscripts

a = axial component
c = circumferential component (positive for clockwise motion when looking in the direction of the flow at the annular prediffuser inlet)
r = radial component

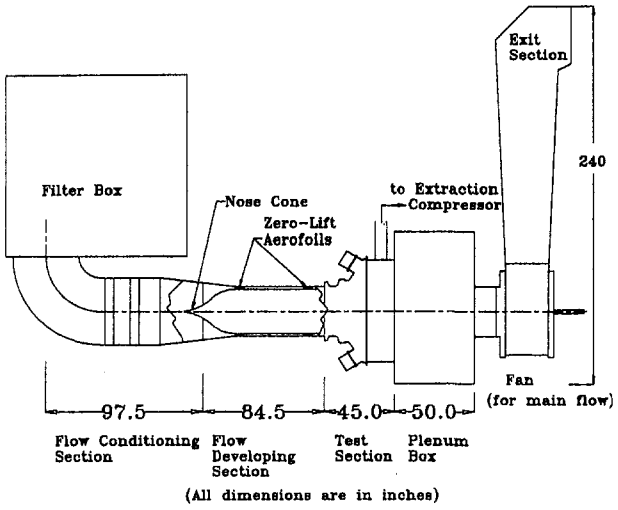

Fig. 1 Layout of test facility

between the prototype and the model was maintained everywhere. Detailed information on the test section and calibration of the combustor pressure loss coefficient is described by Kapat et al. (1996).

Air Extraction

In the test section, all profile measurements were made around combustor 2 (Fig. 3). In order to study the circumferential nonuniformity due to air extraction, three different extraction ports ($X1$, $X2$, and $X3$), situated 90 deg apart circumferentially, were built into the test section (Fig. 3). Only one of these ports was used at a time for extraction. Thus by extracting air at different circumferential locations but taking measurements at the same locations, the study of circumferential variation of the effects of extraction was achieved. In this way, the number of instrumented sites was minimized.

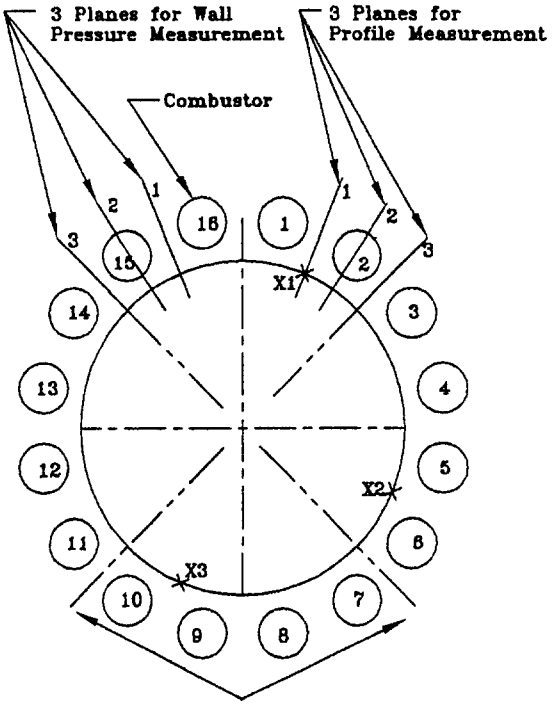

NOTE:
1. In this view, flow is into the paper at the Pre-Diffuser Inlet.
2. Plane 1 is the mid-plane between combustors 1 and 2 or between combustors 15 and 16.
3. Plane 2 is the mid-plane of combustor 2 or 15.
4. Plane 3 is the mid-plane of a rotor cooling pipe and in between two combustors.
5. X1, X2 and X3 are three extraction sites; only one is used at a time.

Fig. 3 Circumferential layout of measurements

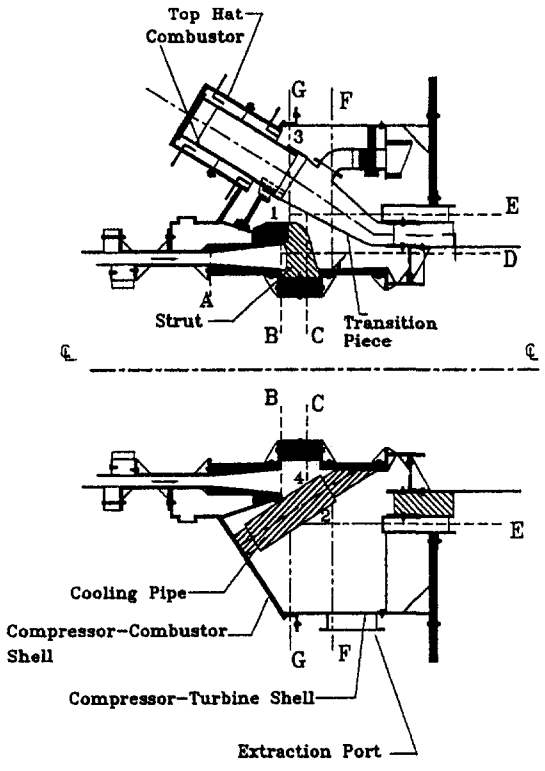

Fig. 2 Subscale test model and measurement locations

The extraction duct was equipped with a pitot-static probe which was used to monitor the air flow rate through the extraction duct (Fig. 4). The desired flow rate through the extraction duct was achieved by using both the extraction and the bypass ducts. Small adjustments in the flow rate were performed by using the extraction valve. However, for large variations, the bypass valve was used so as to maintain the total flow rate through the extraction compressor within the operating range. The extraction compressor comprised six stages and was rated at 5000 cfm (2.36 m^3/s) at 5 psia (0.34 bars).

For different combinations of openings of the extraction and/or bypass valves, the pitot-static probe was traversed inside the duct and velocity profiles were obtained. By integrating the profiles, the corresponding flow rates were calculated.

During the main experiments with 5 or 20 percent extraction, one of the three extraction ports, $X1$, $X2$, and $X3$, was connected to the extraction duct. First, the main flow through the test section was adjusted with the extraction valve closed. Then, the extraction flow rate was obtained by adjusting the extraction and/or bypass valves. Since the adjustment of the extraction flow rate affected the main flow rate, the main flow needed adjustment again, and the process was repeated until both main and extraction flow rates were at the desired values.

After the velocity profiles were measured by traversing the five-hole probe at different locations (as described in the following section), the whole process was repeated for each of the other two extraction ports.

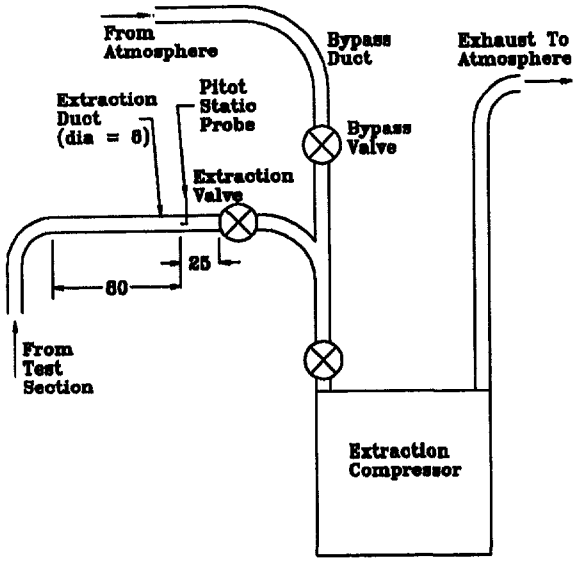

Fig. 4 Air extraction ducting and flow control

Instrumentation and Measurements

In the developing section, a pitot-static probe was placed 6 D_h upstream of the inlet to the annular prediffuser at four circumferential locations, 90 deg apart. By moving the probe radially at each of these four locations, the radial profiles of the axial velocity and the total pressure were obtained.

An angle-type five-hole probe was traversed at 15 different locations or ports to measure three-dimensional velocity profiles at those locations. These 15 measurement ports were located on three longitudinal planes; the circumferential locations of these planes, numbered 1 through 3, are shown in Fig. 3. The ports were located at six different streamwise locations along the flow path. The streamwise locations, named B through G, are shown in Fig. 2. Out of the possible total of 18 ports, $B1$ through $G3$, no measurement was made at $C2$, $D3$, or $E2$ because of geometric obstructions. In total, 49 traverses were performed to measure the three-dimensional velocity profiles in the dump diffuser.

The calibration indicated that the five-hole probe used has an acceptance angle of ±30 deg in the pitch plane and an acceptance angle of ±35 deg in the yaw plane. Outside these acceptance angles, flow separation occurred for the air velocities used, and the five-hole probe became ineffective. If the pressure coefficients calculated from the measured data were outside the range of the pressure coefficients obtained during the calibration process, the corresponding measurement point was discarded. This could happen for one of two reasons: (a) either the air was stagnant at the point of measurement or (b) the local velocity vector was outside the acceptance angle of the probe. After the experiments were completed, it was found that the three-dimensional flow was very complex, so only the results from the B, C, and E ports have been used as representatives for discussion in this paper.

The pressure readings of the five-hole probe were measured by a scanning module from Scanivalve. The transducer used in the experiments has a range of ±2.5, with a calibrated precision of ±0.007 psi (at 95 percent confidence). The detailed calibration process is described by Kapat et al. (1996).

The overall mass flow rate entering each combustor was obtained by integrating the velocity distributions measured by a commercial tungsten hot wire 2.5 μm in diameter.

Results and Discussion

The results are presented in nondimensional form. Radial distances were measured from the centerline unless otherwise specified and were normalized by the hydraulic diameter (D_h) of the annular inlet to the test section. All axial distances were measured from the annular pre-diffuser inlet (location A in Fig. 2) and were normalized by D_h. All velocities were normalized with U, the average (axial) velocity at the annular prediffuser inlet. All of the experiments were performed for a fixed flow rate at the inlet to the prediffuser. This flow rate was monitored by the pitot-static probe in the development section.

The flow field for the baseline (no extraction) has been discussed in detail by Kapat et al. (1996), and hence the corresponding velocity profiles are presented only for reference and for comparison with the velocity profiles for the extraction cases. The velocity results at three locations (B, C, and E, see Fig. 2) are grouped for each port ($X1$, $X2$, or $X3$, see Fig. 3) for a specific extraction rate at 5 or 20 percent. The figure for each location includes three planes: Plane 1 cuts through the midplane between two can-type combustors, Plane 2 cuts through the centerplane of the combustor, and Plane 3 cuts through the midplane between two combustors and the centerplane of a cooling pipe (Fig. 3). There were sixteen combustors and only four cooling pipes, so while Plane 3 cuts through a cooling pipe, Plane 1 does not. The results for the $X1$ port indicate the maximum effects of nearby extraction. The $X2$ port is located 90 deg away from the measurement planes, and the $X3$ port is located diametrically from the $X1$ port as well as from Plane 1. Hence, the results of the $X3$ port extraction should indicate the effects from the air extraction directly opposite the other side of the dump diffuser. The following discussion of the results is conducted by fixing a specific location, say the B location first, and then comparing the results from port to port and between two extraction rates.

Figure 5 shows the results of the velocity profiles at locations B, C, and E for the baseline case, i.e., without air extraction. For 5 percent air extraction, only the results for extraction at the $X1$ port are shown (see Fig. 6). Comparison of the velocity profiles between Figs. 5 and 6 at $B1$ (location B and Plane 1), which is at the prediffuser exit, shows that there was no qualitative change in the shape of the axial velocity profiles due to 5 percent extraction at $X1$. Plane 1 is located between the combustors with no flow obstructions between the combustors. Increasing the extraction to 20 percent did not change the trend of the axial velocity profiles very much at $B1$ (Va in Figs. 7(a), 8(a), and 9(a)), except that the profile became broader with a slightly reduced axial velocity. A greater reduction of the axial velocity occurred for extraction at $X2$ and $X3$ (Va in Figs. 8(a) and 9(a)) than at $X1$ (Va in Fig. 7(a)). This is because both $X2$ and $X3$ are located at different quadrants; $X2$ is 90 deg away and $X3$ is diametrically across the dump diffuser, respectively. Extraction at $X3$ increased the radial momentum on Plane $B1$ toward the other side of the dump diffuser where $X3$ is located (negative Vr) and made the flow exiting the prediffuser bend less radially toward the outer dump diffuser of the same side (positive Vr). Extraction at $X2$ would have increased the circumferential velocity (Vc) as well as the negative radial velocity. Indeed, the results of the radial and circumferential velocity components (Vr and Vc) at $B1$ in Figs. 7(a), 8(a), and 9(a) support these facts. As can be seen in these figures, the radial component for 20 percent extraction actually became negative for a small section of the profile at $B1$ for all ports (Vr in Figs. 7(a), 8(a), and 9(a)), and more regions of negative values occurred at port $X3$. The increase in the circumferential velocity components (Vc) can be also seen in these figures. The increased values of both Vr and Vc are thought to contribute to the reduction of the axial velocity components (Va).

Plane 3 is similar to Plane 1 in that both cut through the midplane between two combustors; however, a rotor cooling air supply pipe is located on Plane 3. This rotor cooling air

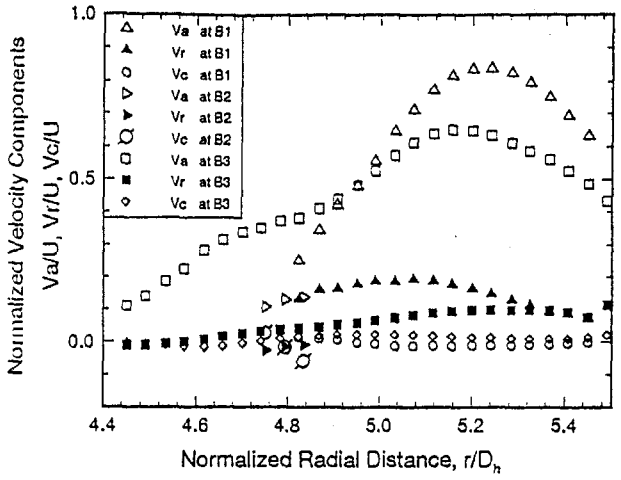

(a) At location B (exit of the pre-diffuser, see Figure 2)

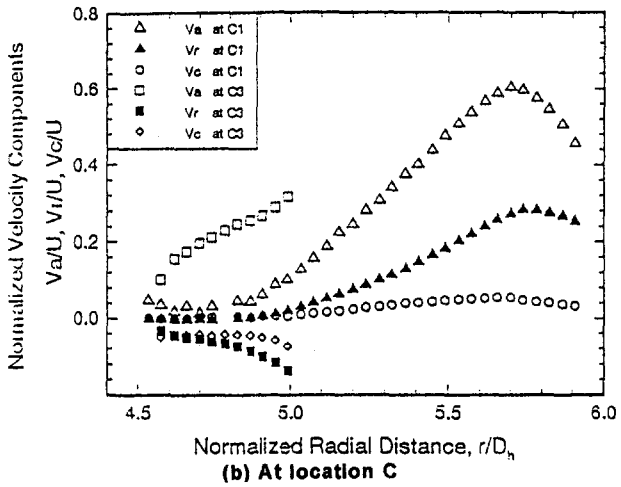

(b) At location C

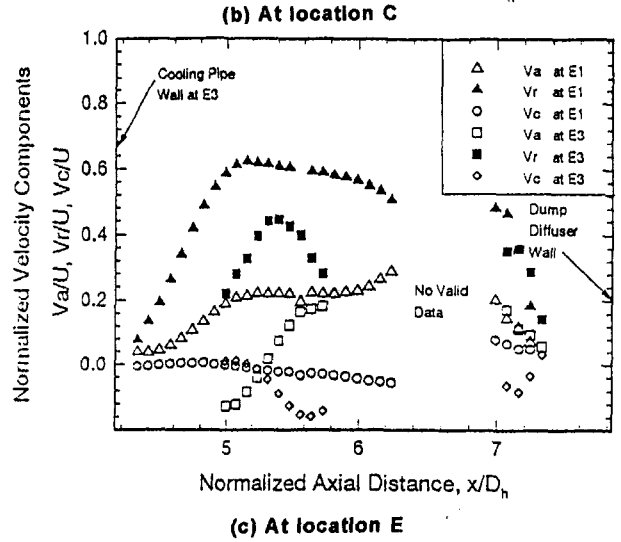

(c) At location E

Fig. 5 Velocity profiles without air extraction (baseline)

pipe forced the flow to become more uniform at the annular prediffuser exit (see *Va* at *B*3 in Fig. 5(*a*)) and reduced the radial momentum (see *Vr* at *B*3 in Fig. 5(*a*)). Extractions did not strongly affect the velocity profiles at *B*3 at any of the three ports, except that the circumferential component increases in magnitude (*Vc* at *B*3 in Figs. 4(*a*)–9(*a*)) and some of the radial velocities become negative at *X* 3 (*Vr* at *B*3 in Fig. 9(*a*)). This happens because extraction at any of these ports disturbs the circumferential uniformity of the flow field around *B*3.

Just downstream of Plane *B*2, the flow was obstructed by a support strut (Fig. 2). As a result, there was not much flow through this section for the baseline case (*B*2 in Fig. 5), and measurements were difficult. Five percent extraction did not strongly affect the velocity profile; however, 20 percent extraction significantly changed the flow pattern in all aspects on Plane 2. The axial velocity at *B*2, which was low and had only a few points within the measuring range of the five-hole probe, increased considerably in the presence of extraction at all extraction ports (*Va* at *B*2 in Figs. 7(*a*), 8(*a*), and 9(*a*)). The circumferential and radial velocity components, small as they were, were measurable by the five-hole probe. As on Plane *B*1, nega-

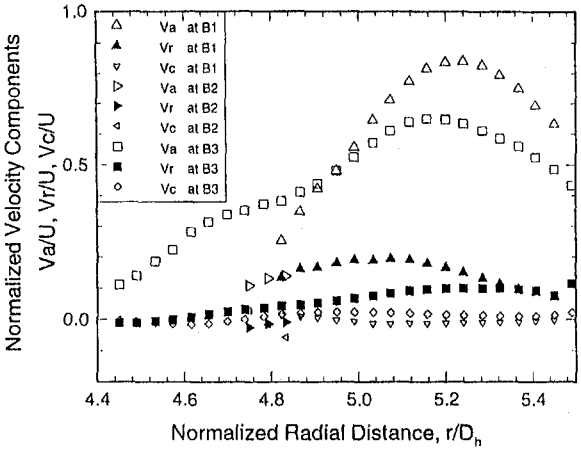

(a) At location B (exit of the pre-diffuser, see Figure 2)

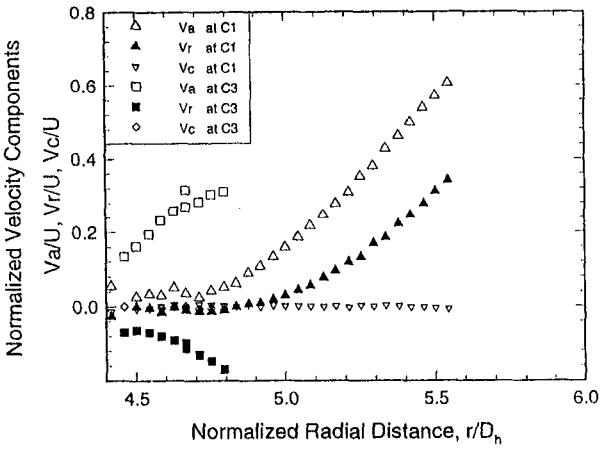

(b) At location C

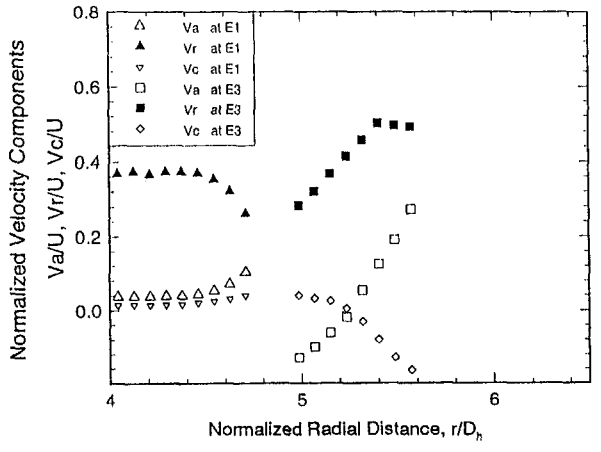

(c) At location E

Fig. 6 Velocity profiles with 5 percent air extraction at *X* 1

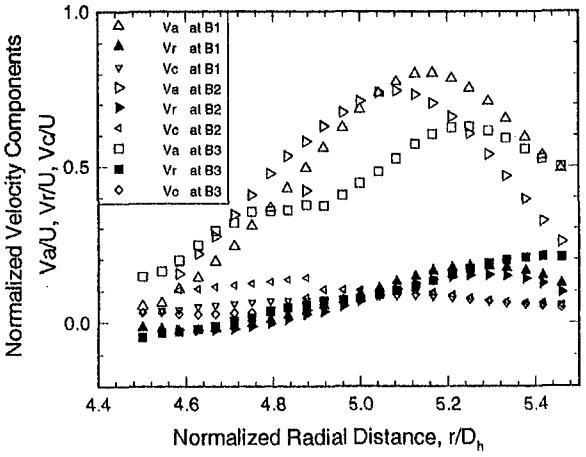

(a) At location B (exit of the pre-diffuser, see Figure 2)

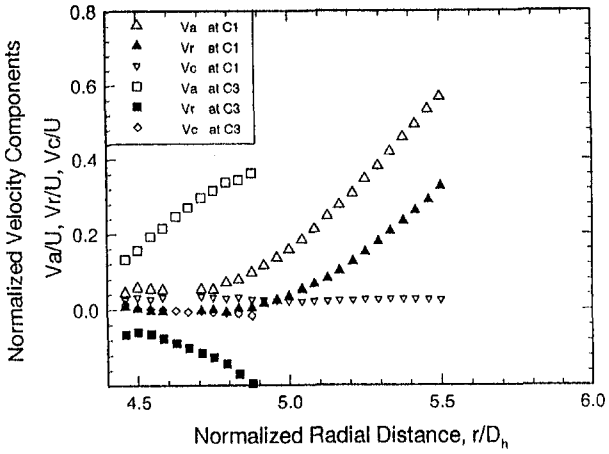

(b) At location C

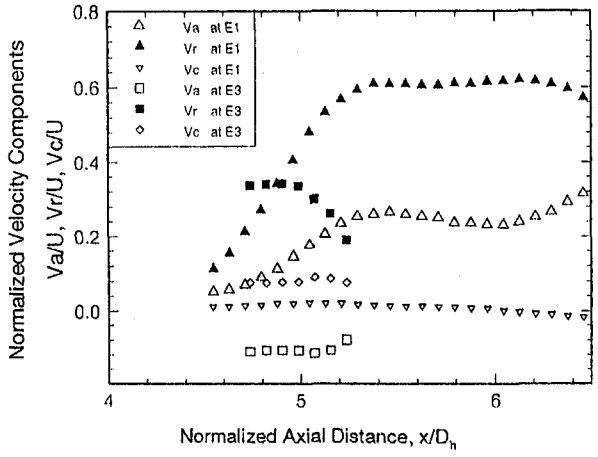

(c) At location E

Fig. 7 Velocity profiles with 20 percent air extraction at *X*1

tive *Vr* appeared at *B*2 (Figs. 8(*a*) and 9(*a*)) as the result of extraction. These increases in *Va* and *Vc* were probably related to the increase in the circumferential component at *B*1 or *B*3.

Location *C* is situated downstream of location *B*. Plane 2 at location *C* (or *C*2) is blocked by the support strut, so no flow was available for *C*2. Only *C*1 and *C*2 are shown in Fig. 5(*b*) for the baseline cases. The nonsymmetric, nonuniform velocity profile at *B*1 continued at *C*1 (see *Va* at *C*1 in Fig. 5(*b*)) as the air flowed through the space between two combustors toward the outer dump diffuser. Because of the cooling pipe, the air at *C*3 had a radially inward motion (with negative *Vr* values at *C*1 in Fig. 5(*b*)), possibly caused by impingement on the cooling pipe. This radially inward motion suggests the existence of a recirculation zone in the region between the cooling pipe and the inner surface of the dump diffuser (region 4 in Fig. 2). It is hypothesized that air from the annular prediffuser, which flowed toward the rotor cooling pipe, was deflected to either side of the pipe, flowed around the pipe, ultimately joined together on the other side of the pipe (region 2 in Fig. 2), and

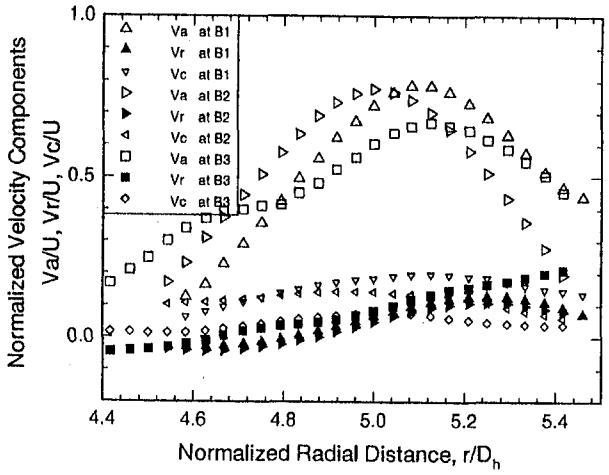

(a) At location B (exit of the pre-diffuser, see Figure 2)

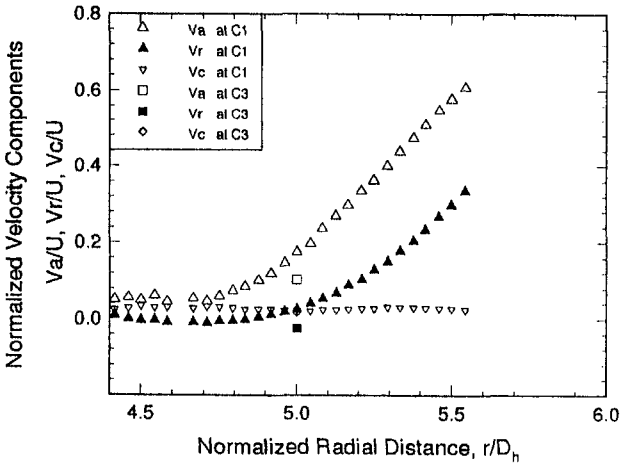

(b) At location C

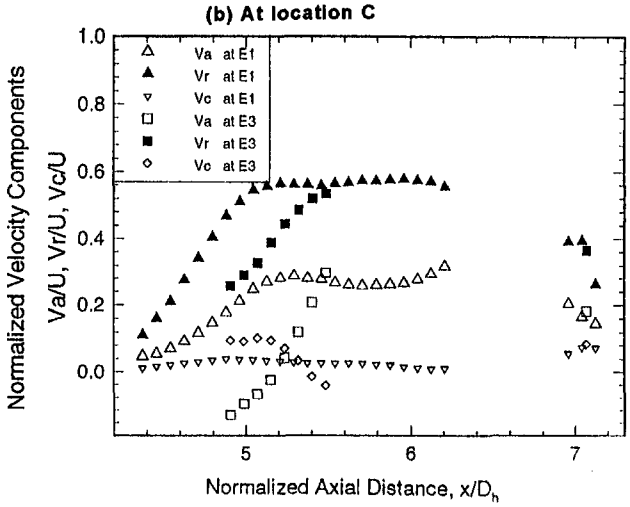

(c) At location E

Fig. 8 Velocity profiles with 20 percent air extraction at *X*2

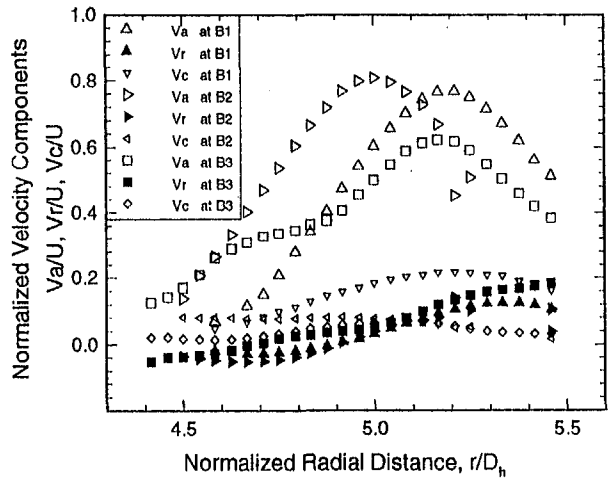

(a) At location B (exit of the pre-diffuser, see Figure 2)

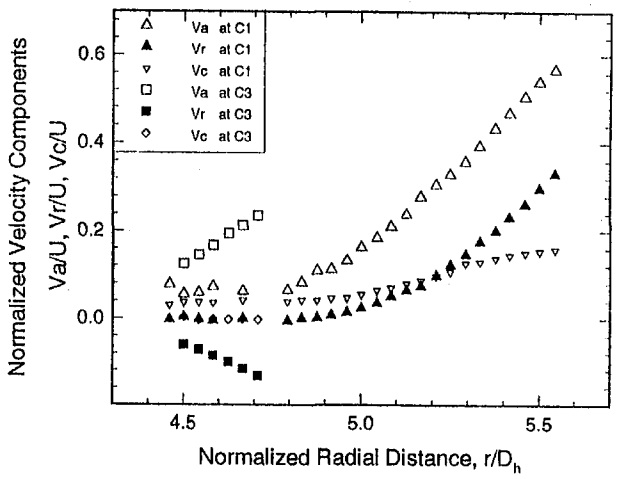

(b) At location C

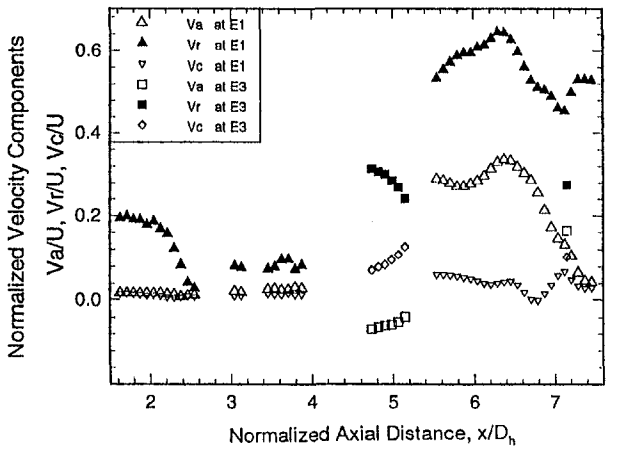

(c) At location E

Fig. 9 Velocity profiles with 20 percent air extraction at $X3$

then flowed outward to the outer dump diffuser. This presumed flow pattern would have created wakes and recirculation eddies on the downstream side (region 2 in Fig. 2) of the cooling pipes. Further testing is required to verify this presumption; however, its existence is supported by the Vr profile at $E3$ in Fig. $5(c)$, to be discussed later. Extraction seems to have a negligible effect on the above-mentioned flow pattern for the baseline cases except that the circumferential component at $C1$ had a noticeable increase with 20 percent extraction at $X3$ (see Vc at $C1$ in Fig. $9(b)$). Otherwise, extraction at this port or at the other two ports caused only a minor increase in the axial velocity near the outer wall (see Va at $C1$ in part b of Figs. 5–9). At plane $C3$, extraction seems to have reduced the negative circumferential velocity for all ports (see Vc at $C3$ in part b of Figs. 5–9).

Of all the profiles studied here, the profiles at the E locations are most affected by extraction. The velocity profiles at the E planes indicate the major flow activity in the dump diffuser; the flow field mostly consisted of radial flow moving from the inner dump diffuser to the outer dump diffuser. Due to the complex three-dimensional flow in various planes at location E and the strong effects of extraction on the flow pattern, it is very difficult to piece together the limited information available from the data. For the baseline cases, the air at plane $E1$ moved outward and forward without any obstruction with dominant radial velocities, as indicated by the Va profiles in Fig. $5(c)$. With 20 percent extraction, the qualitative nature of the profiles of all three components of velocity at $E1$ did not seem to be affected by extraction at $X1$ or $X2$, although the flow did increase with more uniform distribution of the radial components (Vr), as can be seen at $E1$ in Figs. $7(c)$ and $8(c)$.

For the baseline cases, the axial velocity profile at $E3$ in Fig. $5(c)$ indicates that Va became negative at around $x/D_h = 5.3$ and that the air started reversing its axial motion to flow toward the combustor inlets. The radial velocity at $E3$ flowed radially outward only over a limited region. Between this region and the cooling pipe, no valid data were available, as marked in Fig. $5(c)$. One possible reason for this lack of valid data was the existence of a recirculation zone(s) next to the cooling pipe. The recirculation flow was obviously outside the effective measuring range of the five-hole probe. The existence of this recirculation zone also supports the previous speculation that circulation eddies may have occurred behind the cooling pipes. It should be noted that the center of the extraction port is at $x/D_h = 5.2$.

Extraction significantly changed the flow pattern at $E3$. The region of flow reversal, indicated by the change in sign of Va at $E3$ in Fig. 5, became all negative with 20 percent suction at $X1$ and $X3$ (Fig. $7(c)$ and $9(c)$). It is not clear what the actual mechanism was that caused the negative Va. One possible explanation is that the suction on the wall at $X/D_h = 5.2$ generated a low pressure center at the suction ports, which reduced the region of flow moving forward (positive Va) and outward (positive Vr); hence the portion of reversed flow that moved toward the combustor inlet expanded, and Va became all negative. This trend did not occur with suction at $X2$, so Va at $E3$ in Fig. $8(c)$ still shows evidence of changing sign. The circumferential velocity components (Vc) became all positive with extraction at $X1$ and $X3$ (Figs. 7 and 9), which indicates flow toward the suction port. Extraction at $X3$ caused complex flow patterns around $E1$ or $E3$, as can be seen by the corresponding profiles in Fig. $9(c)$. It is interesting to see that Vr at $E1$ was measurable in the region with $X/D_h < 4.0$ (Fig. $9(c)$), where no data were available for the baseline and all other cases.

Table 1 Total pressure losses (normalized by the velocity head at the the inlet of pre-diffuser) at 20 percent suction from location A to the top hat inlet (or dump diffuser outlet)

20% Suction	Average of 3 Planes	Difference %
Baseline	0.58	
Port 1	0.624	7.6 %
Port 3	0.581	0 %

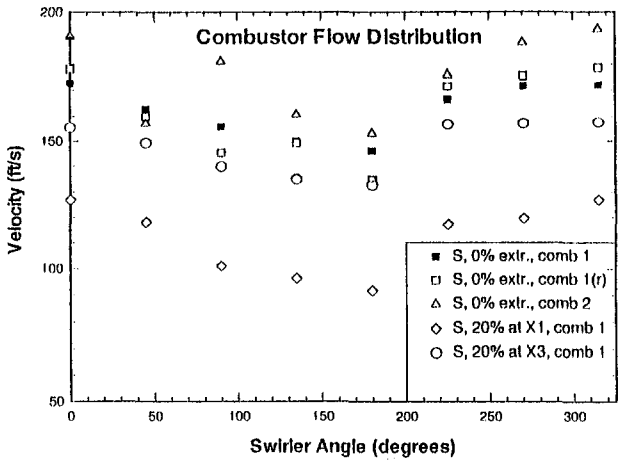

Fig. 10 Combustion flow distribution for baseline and extraction cases

The total pressure losses at 20 percent suction are compared to the baseline case in Table 1. Near extraction port 3, the effect of suction on the total pressure losses is negligible, whereas the total pressure losses increased 7.6 percent near port 1. The velocity distributions at every 45 deg interval surrounding the inlet of the combustor for various conditions were measured by a hot wire sensor and are shown in Fig. 10. Generally, this figure shows that the flow rate near the region between 130 and 180 deg (the inner side of the ombustor in Fig. 2) is about 20 percent less than the flow rate at the outer part of the combustor. This is consistent with the CFD prediction conducted by Zhou et al. (1996). The differences between the two baseline cases for combustor 1 indicate a maximum measurement uncertainty of approximately ±5 percent. The flow rate in combustor 2, which was located closer to the rotor cooling pipe (see Fig. 3), was greater than the flow rate in combustor 1. Figure 10 also shows that air extraction did not cause the flow distribution of the baseline case near port 1 to vary, although the flow rate did decrease. Near port 3, 20 percent air extraction significantly reduced the flow rate about 20 percent on top of the combustor (near 0 deg) and about 50 percent on the bottom of the combustor (near 180 deg). The difference between port 1 and port 3 implies that the global flow distribution was approximately 35 percent nonuniform diametrically across from the dump diffuser.

Conclusions

An experimental study was performed in a 48 percent scale, 360 deg model of the diffuser-combustor section of a developmental industrial gas turbine to investigate the effects of various air extractions for cooling (5 percent) and gasification (20 percent) on flow fields in the dump diffuser. Detailed wall pressures and three-dimensional flow fields were measured. The results for 5 percent air extraction did not show a significant effect on the flow fields in the dump diffuser. However, the results for 20 percent air extraction from a single port on the shell indicated that strong circumferential motion, up to 10 percent of the mean flow velocity, was induced and significant distortion of the flow fields was produced in various parts of the dump diffuser. The distortion of the flow field adversely affected the uniformity of the air flow to the combustor, and hence the combustor performance. The global flow distribution was approximately 35 percent nonuniform diametrically across from the dump diffuser. The circumferential motion through the dump diffuser resulted in an approximate 7.6 percent increase of the total pressure losses near the suction port in the dump diffuser. This test demonstrated the adverse effects of single-port air extraction on total pressure losses and on the uniformity of the flow distribution to each combustor. The results of this experiment strongly suggest that single-port air extraction should be avoided and that axisymmetric multiport extraction should be considered.

Acknowledgments

The authors wish to thank Mr. Michael Thom for his help in fabricating the experimental facility and the test model. This work was supported by the Morgantown Energy Technology Center of the U.S. Department of Energy through DOE/METC contract No. DE-AC21-93MC30247. The authors also wish to thank Dr. Richard A. Johnson at the Morgantown Energy Technology Center for his guidance in this program.

References

DOE/Clemson Workshop, 1991, *Proceedings, Workshop to Define Gas Turbine System Research Needs,* Part I, Apr. 8–10.

DOE/Clemson Workshop, 1992, *Proceedings, Workshop to Define Gas Turbine System Research Needs,* Part II, Jan. 7–8.

DOE, 1993, "Comprehensive Program Plan for Advanced Turbine Systems," Congressional Report, DOE/FE-0279.

Kapat, J. S., Agrawal, A. K., and Yang, T. T., 1997, "Air Extraction in a Gas Turbine for Integrated Gasification Combined Cycle (IGCC): Experiments and Analysis," ASME JOURNAL OF ENGINEERING FOR GAS TURBINES AND POWER, Vol. 119, pp. 20–26.

Kapat, J. S., Wang, T., Ryan, W. R., Diakunchak, I. S., and Bannister, R. L., 1996, "Cold Flow Experiments in a Sub-Scale Model of the Diffuser Combustor Section of an Industrial Gas Turbine," ASME Paper No. 96-GT-518.

Lefebvre, A. H., 1983, *Gas Turbine Combustion,* Hemisphere Pub. Corp., Washington, DC.

Lyons, 1981, "Effect of Fuel-Air-Ratio Nonuniformity on Emissions of Nitrogen Oxides," NASA TP 1798.

Welz, J. P., 1986, "An Algorithm for Using the Five-Hole Probe in the Non-nulled Mode," AIAA/ASME 4th Fluid Mechanics, Plasma Dynamics and Lasers Conference, Atlanta, GA, May 11–14.

Wilson, D. G., 1984, *The Design of High-Efficiency Turbomachinery and Gas Turbines,* MIT Press, Cambridge, MA.

Zhou, D., Wang, T., and Ryan, W. R., 1996, "Cold Flow Computations in a Sub-scale Model of the Diffuser-Combustor Section of an Industrial Gas Turbine," ASME Paper No. 96-GT-513.

Experimental Investigation of the Liquid Fuel Evaporation in a Premix Duct for Lean Premixed and Prevaporized Combustion

M. Brandt

K. O. Gugel

C. Hassa

Institute for Propulsion Technology,
German Aerospace Research Establishment,
D-51140 Köln, Federal Republic
of Germany

Liquid fuel evaporation was investigated in a premix duct, operating at conditions expected for lean premixed and prevaporized combustion. Results from a flat prefilming airblast atomizer are presented. Kerosine Jet A was used in all experiments. Air pressure, air temperature, and liquid fuel flow rate were varied separately; their relative influences on atomization, evaporation, and fuel dispersion are discussed. The results show that at pressures up to 15 bars and temperatures up to 850 K, nearly complete evaporation of the fuel was achieved, without autoignition of the fuel. For the configuration tested, the fuel distributions of the liquid and evaporated fuel show very little difference in their dispersion characteristics and were not much affected by a variation of the operating conditions.

Introduction

Lean premixed and prevaporized combustion is a concept designed to decrease nitric oxide emissions of gas turbines significantly (Tacina, 1990). As low combustion temperatures reduce the thermal NO_x formation, a lean homogeneous air–fuel mixture has to be achieved at the combustor inlet. If liquid fuel is used, it has to be atomized, evaporated, and mixed homogeneously with the air in a premix duct before autoignition of the fuel occurs. For typical engine operating conditions, this means a few milliseconds (Spadaccini and TeVelde, 1982). Since both atomization and evaporation depend on the operating conditions, an experiment was designed that allows the study of liquid fuel evaporation at conditions corresponding to cruise conditions of aircraft engines (Dunker, 1993) or full load of industrial gas turbines (Schulenberg, 1990). Optical access into the premix duct enables the use of nonintrusive measurement techniques. Particle size distributions and liquid fuel concentrations are measured with Phase-Doppler Anemometry. The distribution of the evaporated fuel is described by extinction measurements of infrared and visible light along the line of sight of two laser beams.

Test Facility

All experiments were carried out in a test cell allowing three-way optical access into the rectangular premix duct. Inside the premix duct, a quartz glass channel with a cross section of 25 × 40 mm, pressures up to 15 bars, and temperatures up to 850 K could be achieved at air velocities above 120 m/s. A sketch of the test cell is shown in Fig. 1. The duct is surrounded by a cooling air flow. Operating conditions in the duct were adjusted by a variation of the mass fluxes of main and cooling air and the use of different throttles at the air exit of the test cell. The air was heated by a 520-kW electrical air heater. Atomizers could be mounted at two axial positions inside the duct. In previous studies (Eickhoff et al., 1983; Brandt et al., 1994), a flat prefilming airblast atomizer showed excellent atomizing qualities at operating conditions expected in a premix duct. In this type of atomizer the fuel is admitted to the free surface by a thin slit, where the liquid spreads out as a thin film and is atomized behind the atomizer edge by the forces of the high-velocity air flow.

In the present investigation two flat prefilming atomizers were used. The small atomizer (Fig. 2(*a*)) was mounted horizontally in the duct, allowing a good spatial resolution perpendicular to the atomizer plane for the line-of-sight measurements. During the tests, it turned out that the fuel temperature on the atomizer surface seemed to be strongly influenced by the operating conditions. Hence, after the first experimental phase, a thermocouple was mounted on the surface of atomizer 1. The pearl ($\varnothing$ = 100 μm) was embedded in a ceramic insulator, so that heat conduction from the atomizer housing to the thermocouple could be ignored. It was set up that the thermocouple was completely covered by the liquid film.

The large atomizer (Fig. 2(*b*)) was a better approximation of a two-dimensional atomizer with a more practical slit height. It had to be mounted vertically in the duct.

Measurement Techniques

A sketch of the optical setup is shown in Fig. 3. The evaporation of the liquid fuel was recorded by Phase-Doppler Anemometry (PDA) (DANTEC, 1992). The instrument measures particle size distributions, particle velocities, and liquid volume fluxes. To minimize drop sizing errors caused by the temperature dependence of the refractive index of the heating droplets, a scattering angle near the brewsters angle is preferable (Pitcher et al., 1990). However, as optical access was limited by the test cell, a scattering angle of 52 deg was chosen, resulting in a systematic drop sizing error below 5 percent at investigated conditions. Other error sources like the nonlinearity of the phase–drop size correlation resulted in drop sizing uncertainties of about 1 μm, the maximum error due to misalignement was about 3 percent (Gugel, 1995).

As the evaporation rates of the spray had to be determined by the liquid volume flux measurements, the related uncertainties were studied in detail. The liquid volume flux density is calculated using the total droplet volume passing the cross section of the measurement volume over a certain time.

One important source of error is the correct determination of the number of droplets passing the measurement volume. As the PDA allows only one particle to be in the measurement

Contributed by the International Gas Turbine Institute and presented at the 41st International Gas Turbine and Aeroengine Congress and Exhibition, Birmingham, United Kingdom, June 10–13, 1996. Manuscript received at ASME Headquarters February 1996. Paper No. 96-GT-383. Associate Technical Editor: J. N. Shinn.

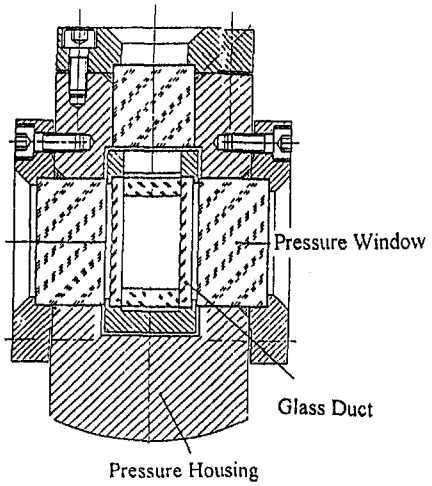

a) cross section

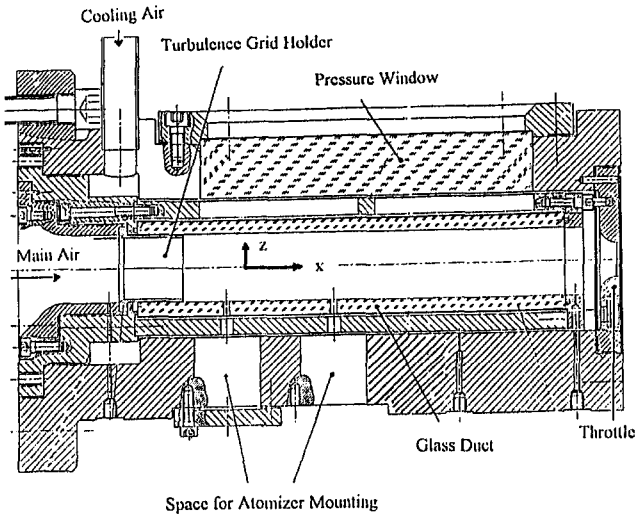

b) longitudinal section

Fig. 1 Test cell

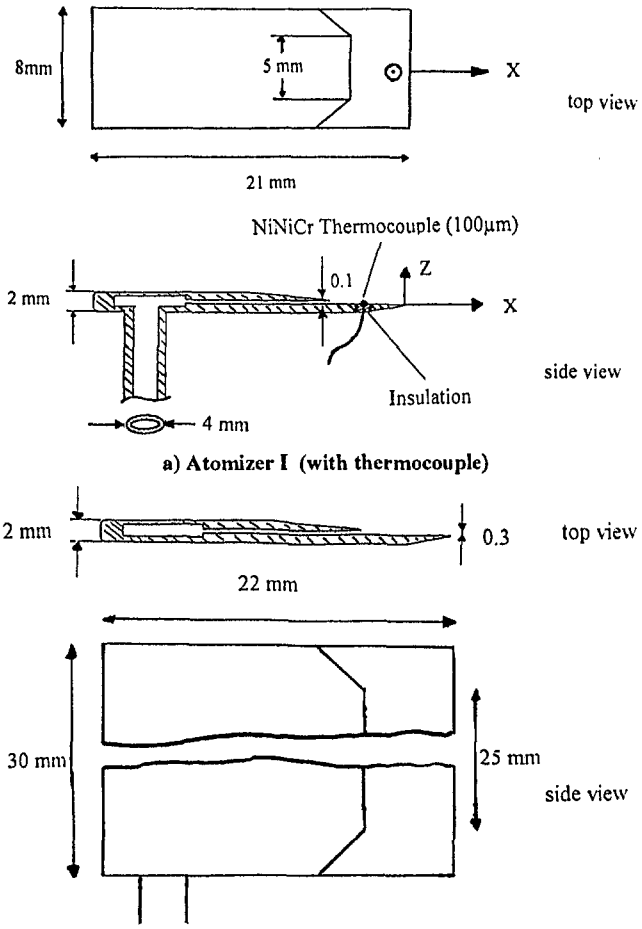

Fig. 2 Flat prefilming airblast atomizer

volume at the same time, signals of more than one particle in the measurement volume will be rejected and not counted in the liquid flux measurements. The measured liquid volume fluxes were corrected with an algorithm suggested by Edwards and Marx (1991). Based on Poisson statistics, they gave the probability of particle rejection. The probe volume of the PDA with a gaussian measurement volume diameter of about 70 μm was limited by a slit in the receiving optics, which was set to 100 μm at high particle concentrations and 520 μm at locations where particle concentrations were low. It turned out that, due to extraordinary high particle concentrations at some conditions, mainly close to the atomizer lip, the limits of this measurement instrument were exceeded (data rates above 150 kHz and concentrations above 5×10^7 particles per cubic centimeter), making correct volume flux measurements impossible. Edwards and Marx (1991) found that the rejection of particles is reasonably free of a particle size bias up to rejection rates of 90 percent, such that for the measurements shown, an influence on the SMD measurements can be neglected.

Another problem in the accurate measurement of the liquid volume flux is the correct determination of the measurement volume size, which is done by PDA with a method first suggested by Saffman (1987), for one-dimensional flow. As optical limitations and the orientation of the main flow direction forced

Nomenclature

90 percent Volume Undersize Diameter = diameter such that 90 percent of the total liquid volume of the spray is in drops below this diameter, μm

IR = infrared light, here: 3.14 μm wavelength

P = air pressure, bar

SMD = Sauter Mean Diameter = $\Sigma D_i^3/\Sigma D_i^2$, μm

T = air temperature, K

VIS = visible light, here: 632 nm wavelength

lr = liquid loading ratio, g/s/m; liquid mass flux per atomizer width

w = mean axial bulk air velocity, m/s

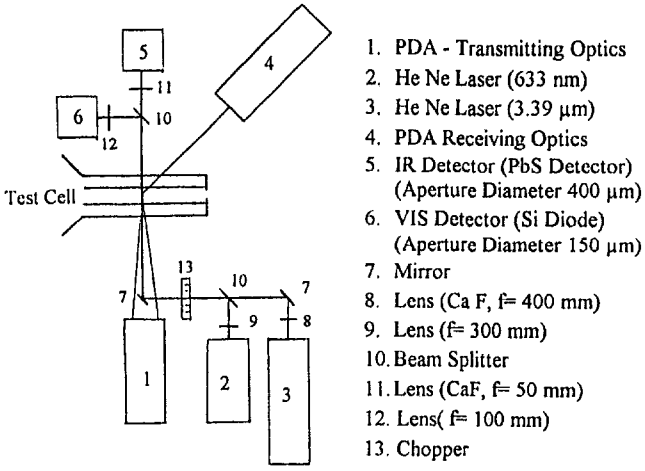

Fig. 3 Sketch of the optical setup

a nonstandard optical setup, post-processing of the liquid volume fluxes became necessary. This post-processing took into account the special form of the measurement volume, limited by the slit in the receiving optics and the orientation of the main flow direction. In a previous publication (Brandt et al., 1995), this post-processing is described in detail. The error of the volume flux measurement was determined at comparable operating conditions and found to be below ±15 percent of the total liquid flux, if the particle concentrations are not too high. This is the error margin of the liquid volume flux measurements presented here.

Measurements on the evaporating fuel were made at four axial (x) positions downstream of the atomizer lip. Typically between 50 and 80 PDA measurements were made per measurement plane. Mean diameters of the total spray were obtained from an addition of all single point values, weighted with the local liquid mass fluxes. Relative liquid mass fluxes of the total spray were obtained from an integration over all measurement points, normalized with the inlet liquid mass flux.

Usually 20,000 particles were collected in one single point measurement at acceptance rates above 90 percent. At conditions of high evaporation rates, where data rates of only a few Hertz were measured, sometimes only a few hundred particles were collected. But, with the exception of the last measurement plane at 15 bars, 850 K, the condition with the highest evaporation rate where only 4000 particles have been collected, at least 10,000 particles have been used for the computation of the mean values of one measurement plane.

The distribution of the evaporated fuel was determined by the extinction measurement of an infrared laser beam, as first described by Chraplywy (1981). The infrared light extinction is based upon strong absorption bands of most of the hydrocarbon fuels near 3.4 μm wavelength. In an evaporating fuel spray, the extinction of the laser beam is mainly a superposition of light scattered by droplets, light absorbed by droplets, and absorption of the gaseous fuel. If the amount of the gaseous fuel is to be measured, light absorption and scattering by particles have to be removed from the IR-extinction measurements.

The amount of light scattered by particles was evaluated by a method described by Winklhofer and Plimon (1990): The light scattering is measured in the visible range, where light absorption can be ignored. If the light detection apertures are adjusted according to the different Mie parameter for the infrared and visible wavelengths, the light scattered in the infrared can be measured with light scattered in the visible range. The amount of light absorbed by particles was neglected.

The technique was used with the aim of seeing relative values in the gaseous fuel distribution. Absorption coefficients depend on the ambient pressure and temperature. Kerosine is a multi-component fuel with varying absorption coefficients and line-of-sight measurements have a limited spatial resolution. Hence, to get absolute values at the present state of the work was judged impractical and no attempt was made to get vapor phase concentrations from these measurements.

Results and Discussion

Kerosine Jet A was used in all experiments. If not explicitly mentioned otherwise, all measurements were made at a constant air velocity of 120 m/s, which was computed by the measured air mass fluxes at operating conditions and the cross section of the duct. The turbulence of the air in the duct, measured with Laser-Doppler Anemometry at atmospheric pressure and ambient temperature, was about 5–7 percent.

With respect to the autoignition limit of the fuel, the most challenging operating conditions investigated were 15 bars, 750 K and 9 bars, 850 K. The autoignition times for kerosine Jet A calculated with the correlation of Spadaccini and TeVelde (1982) are about 7 ms (at 15 bars, 750 K) and 1.1 ms (9 bars, 850 K). Although the observable pathlength of 150 mm resulted in residence times of the fuel of 1.25 ms (computed with the mean air velocity), no autoignition was observed.

In Fig. 4 the Sauter Mean Diameter of the total spray and the relative liquid mass flux are presented for a variation of the

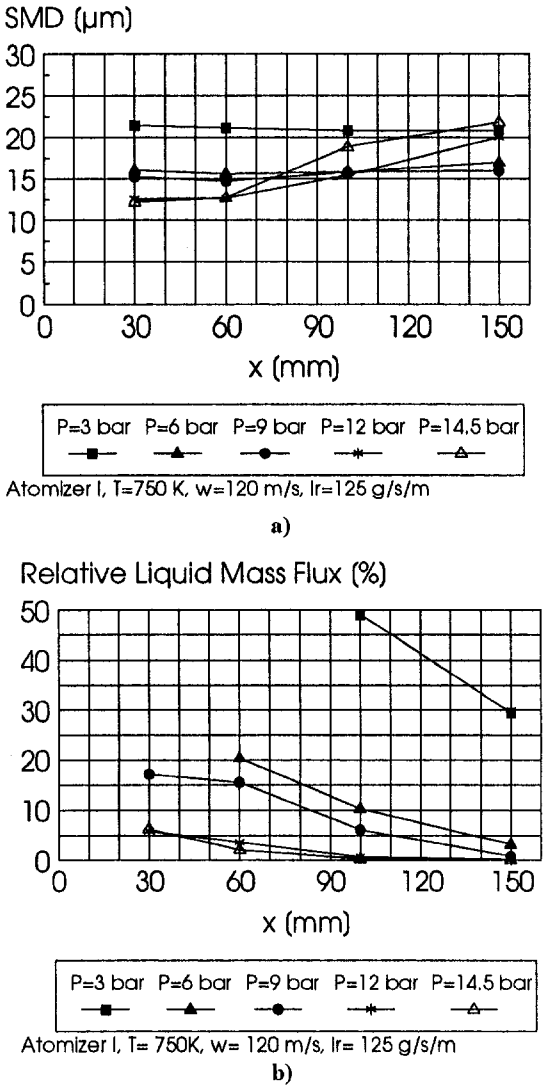

Fig. 4 Sauter Mean Diameter (a) and relative liquid volume flux (b) at different air pressures

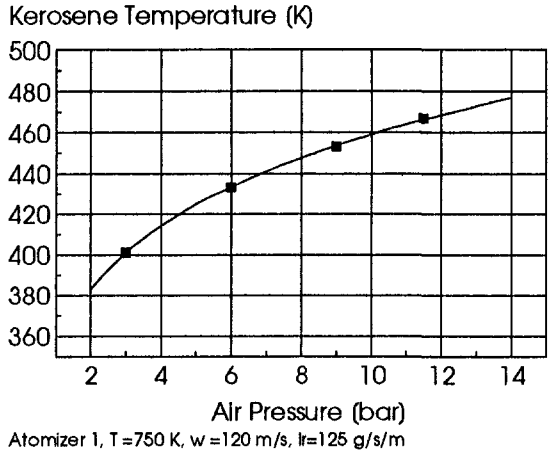

Fig. 5 Fuel temperature on the surface of atomizer 1 at different air pressures

ambient air pressure at a constant air temperature of 750 K. Atomizer 1 was used. The fuel loading ratio per atomizer width was $lr = 125$ g/s/m.

An increase of the ambient air pressure leads to a decreasing Sauter Mean Diameter of the spray. The finer initial drop-size distribution at higher pressures leads to a distinct increase of the evaporation rates of the fuel (Fig. 4(*b*)). While 150 mm behind the atomizer lip at 3 bars only 70 percent of the liquid fuel was evaporated, at 15 bars evaporation rates of more than 99 percent were measured.

As the air temperature is held constant, the increase of the air pressure increases the pressure head of the atomizing air. The influence found is about SMD $\sim P^{-0.3}$, which agrees with results obtained from other prefilming airblast atomizers, as reviewed by Lefebvre (1989), or Mellor (1990).

However, this decrease of the SMD is also caused by a decrease of the surface tension of the fuel. For airblast atomizers and low-viscosity fuels, the SMD of the spray is roughly proportional to the square root of the surface tension of the liquid (Lefebvre, 1989; Mellor, 1990). The fuel was fed with ambient temperature into the test cell, but heats up when it flows through the atomizer surrounded by the hot air. The fuel temperature measured on the atomizer surface (Fig. 5) increases with the ambient air pressure, because heat transfer from the air to the fuel is improved. This higher temperature reduces the surface tension of the fuel (Vargaftik, 1975). The surface tension itself could not be measured in this experiment.

However, the influence of the air density on atomization seems to minimize at least at increased air pressures. This is possible when atomization approaches "prompt" atomization for high-momentum airstreams (Lefebvre, 1991), where no influence of the air density on atomization is predicted.

A variation of the air temperature at a constant air pressure of 9 bar is shown in Fig. 6. With respect to the decrease of the air density and thus the atomizing pressure head, an increase of the SMD should be expected with increasing air temperature, but the contrary is found. The fuel temperature measured on the surface of atomizer 1 is shown in Fig. 7. The increase of the fuel temperature reduces the surface tension of the fuel and leads to finer atomization.

Both the higher temperature and the better atomization at higher air temperatures lead to an increase of the evaporation rates of the spray. At an air temperature of 850 K more than 99 percent of the fuel was evaporated as early as 100 mm behind the atomizer. The boiling range of kerosine Jet A is about 450–530 K (at 1 bar), hence at an air temperature of 550 K 150 mm behind the atomizer lip an evaporation rate of only 20 percent was found (for better comparison with other figures it is not shown in Fig. 6(*b*). Further increased air temperatures then produce the dramatic rise of evaporation rates.

A variation of the fuel flow rate at a constant air pressure of 9 bar and an air temperature of 750 K was made with atomizer 2 (Fig. 8). For both atomizers the fuel velocities leaving the slit were about 2 m/s, so the relative velocity between the liquid

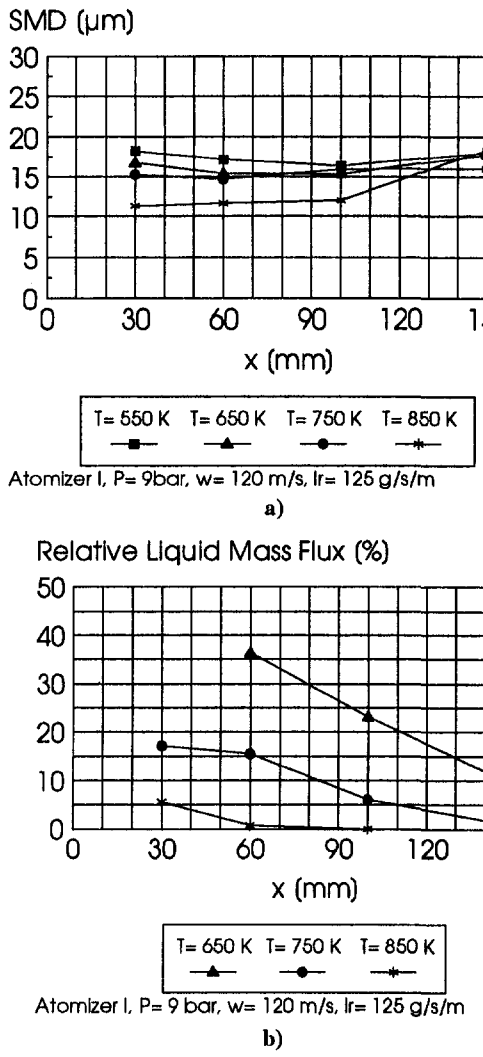

Fig. 6 Sauter Mean Diameter (*a*) and relative liquid volume flux (*b*) at different air temperatures

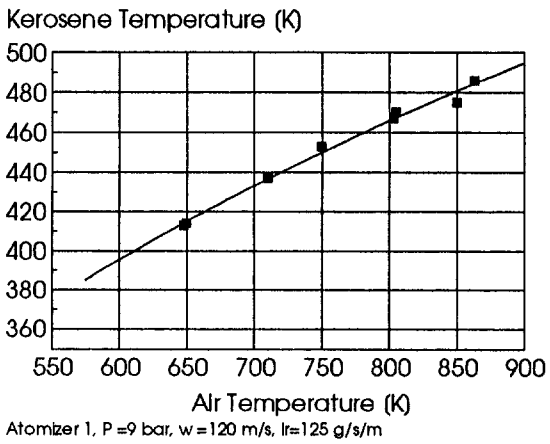

Fig. 7 Fuel temperature on the surface of atomizer 1 at different air temperatures

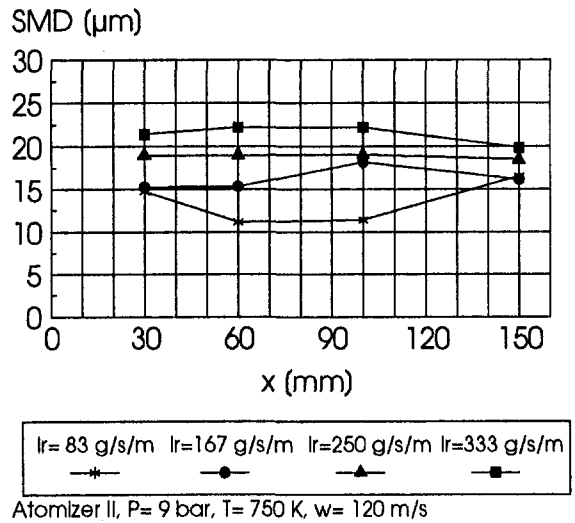

a)

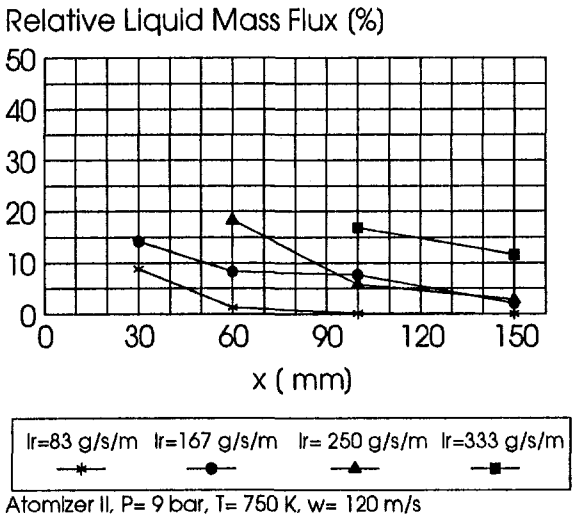

b)

Fig. 8 Sauter Mean Diameter (*a*) and relative liquid volume flux (*b*) at different fuel loadings

and the air was nearly equal to the bulk air velocity of 120 m/s. A comparison with the results from atomizer 1 shows that at comparable fuel loadings per atomizer width, the same initial dropsize diameters were measured; for this type of atomizer at the investigated operating conditions the different heights of the slits don't have a dominant role on atomization. Furthermore, since nearly the same evaporation rates were measured in both cases, the absolute liquid mass flux doesn't seem to have a dominant effect on evaporation, if the initial drop size distribution remains unchanged.

However, an increase of the liquid mass flux per atomizer width leads to an increase of the SMD of the spray and thus to a reduction of the evaporation rates. To a certain extent this increase of the SMD is again caused by the surface tension of the fuel, because at increased fuel flow rates a lower fuel temperature and a higher surface tension are expected. Measurements of the fuel temperature were only made with atomizer 1, but they revealed only a relatively small reduction of the fuel temperature from 430 K to 390 K, when the liquid loading ratio is increased from 167 to 333 g/s/m.

The increase of the SMD of the drop size distribution might also be an effect of the high local fuel concentration in the gas field. In Fig. 9 mean velocities of the 6 μm (interval from 5 to

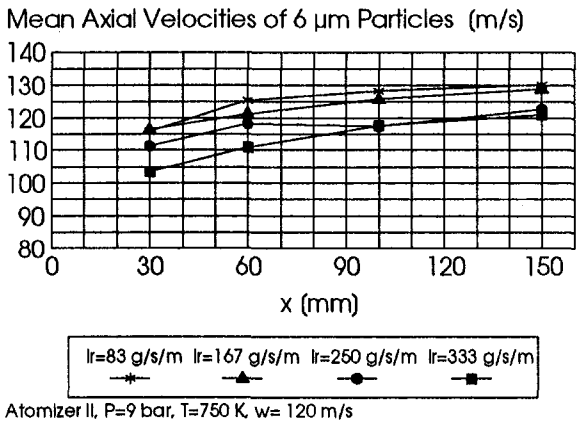

Fig. 9 Mean axial velocities of 6 μm particles at different fuel loadings

7 μm) particles are shown. These mean velocities were obtained for the total spray by weighting the mean velocities with the liquid mass fluxes measured at each point. In a first approximation, they can be taken as a measure for the gas velocity inside the spray. Caused by the higher momentum loss of the air, accelerating and atomizing a higher amount of fuel, the mean gas velocities are reduced inside the spray. This results in a drastic increase of the 90 percent Volume Undersize Diameter as seen in Fig. 10, which might also be an effect of hindered secondary breakup of the large particles. The effects of the higher fuel flow rate lead to a decrease of the fuel evaporation, which is mainly caused by the larger initial drop size diameter, but is not as drastic as the increase of the 90 percent Volume Undersize Diameter of the spray might suggest.

Whereas, with the exception of very high evaporation rates, for a given operating condition the measured SMD of the spray remains nearly constant (see Figs. 4, 6, and 8), the 90 percent Volume Undersize Diameter in Fig. 10 exhibits distinct differences. In the beginning of the spray evaporation, all droplet diameters start to diminish (a possible increase of the diameter during heat-up is neglected), leading to a decrease of the diameter of the biggest particles. This can be seen in Fig. 10 for the 90 percent Volume Undersize Diameter of the highest fuel flow rates, where evaporation rates are relatively small. On the other side, the smallest particles evaporate completely very soon. Thus, depending also on the initial drop size distribution of the spray, the SMD of the spray remains nearly constant. When the

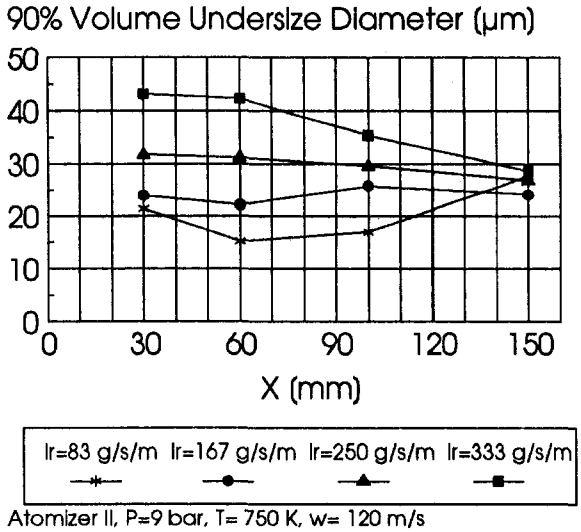

Fig. 10 90 percent Volume Undersize Diameter at different fuel loadings

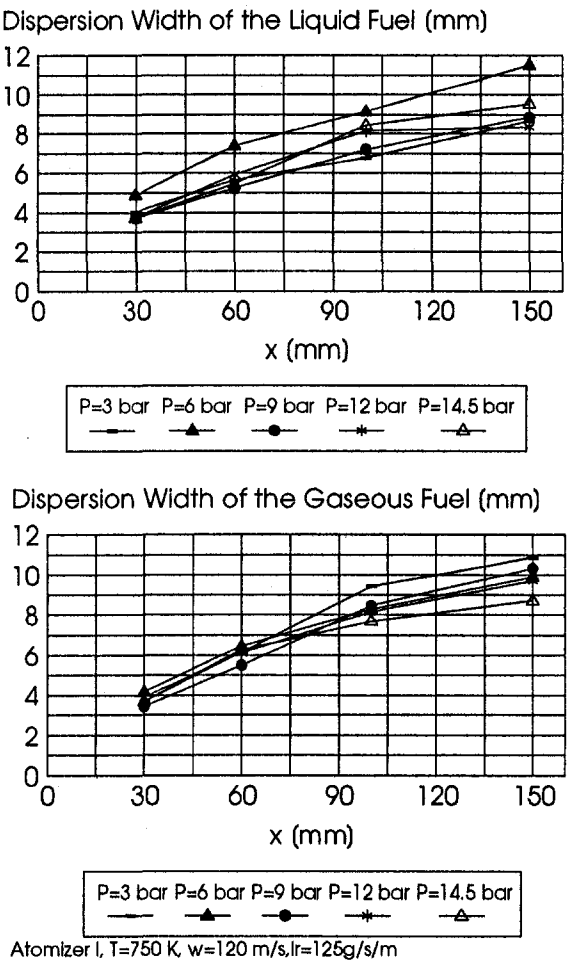

Fig. 11 Comparison of the 68 percent dispersion width of liquid and gaseous fuel at different air pressures

evaporation of the spray is very high (here typically above 98%) only a few of the initially biggest particles "survived" resulting in an increase of both the SMD and the 90 percent Volume Undersize Diameter of the spray.

From the results presented so far, it should be noted that the high evaporation rates of the kerosene are caused to a large extent by the good fuel atomization, which in turn is caused by the high air velocity of 120 m/s.

It turns out that the relative velocity is the dominant factor for airblast atomization in this operating range: A measurement was made at $P = 9$ bar, $T = 750$ K and an air velocity of 80 m/s and exhibited an initial SMD of the spray of about 25 μm and evaporation of about 50 percent of the fuel at the last measurement plane 150 mm behind the atomizer lip. Compared with the evaporation of more than 95 percent at an air velocity of 120 m/s, fuel evaporation rate is drastically decreased, although the residence time of the fuel (computed with the mean air velocity) increased by a factor of 1.5.

With respect to lean premixed and prevaporized combustion, not only complete evaporation, but also the homogeneity of the air fuel mixture at the combustor inlet are important factors for a reduction of the nitric oxide emissions. Measurements of the optical thickness of the gaseous fuel, which is proportional to the integration of the fuel concentration along the line of sight of the laser beams, are shown in Fig. 11 for a variation of the ambient air pressure. Presented are the limits of the fuel distribution perpendicular to the atomizer plane, containing 68.3 percent of the totally measured fuel. As early as 30 mm behind the atomizer lip, the measured profiles exhibited a reasonable Gaussian distribution. Hence the 68.3 percent width equals twice the standard deviation. These measurements are compared with the fuel distribution of the liquid phase. For comparison, the point measurements of the liquid mass fluxes were integrated over the line of sight of the laser of the extinction measurements.

The differences between the evaporated and liquid fuel distributions are small. Due to the good atomization, the spray produced is very fine and follows the streamlines of the gas flow quite well. Measurements show that 30 mm behind the atomizer edge even particles with a mean diameter of 30 μm (interval from 25–35 μm) have reached more than 80 percent of the mean gas velocity. This means, as for the most part of the spray the acceleration is nearly finished 30 mm behind the atomizer, the mixing and penetration of the particles are dominated by the velocity fluctuations of the main flow. In the present air flow, which was not modified by, i.e., turbulence generators, the turbulent length and time scales of the gas flow allow a good response of the spray to the gas motion.

There is only a weak influence of the ambient air pressure, air temperature, and the fuel flow rate on the penetration and mixing of the liquid, as well as the gaseous fuel. A very slight tendency of a weaker fuel penetration for higher air densities was found. The mixing of the liquid with the air is relatively poor and leads to the next step in further investigations: a modification of the main air flow by turbulence generators upstream the atomizer, allowing the study of the effects of an increased air turbulence on fuel mixing and evaporation.

Conclusion

Evaporation rates and mixing qualities of liquid fuel have been investigated for a flat prefilming airblast atomizer, at conditions expected in a premix duct for lean premixed and prevaporized combustion. The results show that at high atomizing air velocities, complete evaporation of the fuel can be achieved without autoignition of the fuel.

Evaporation rates are strongly influenced by the initial drop-size distribution, which is dominated by the air velocity. For the investigated atomizer, the fuel temperature was found to have an important effect on atomization and evaporation.

Differences found between the distributions of the liquid and the evaporated fuel are small. The mixing of the fuel with the air is not much affected by ambient air pressure, air temperature, or the fuel flow rate.

Acknowledgments

This work was sponsored by the CEC BRITE/EURAM "Low Emissions Combustor Technology—Phase II," Contract No. AERO-CT92-0036.

References

Brandt, M., Hassa, C., Kallergis, K., and Eickhoff, H., 1994, "An Experimental Study of Fuel Injectors for Premixing Ducts," presented at ICLASS-94 Rouen, France.

Brandt, M., 1995, "Liquid and Gaseous Fuel Measurements in a Premix Duct," presented at ILASS-95 Nurnberg, Germany.

Chraplywy, A., 1981, "Nonintrusive Measurements of Vapor Concentration Inside Sprays," *Applied Optics*, Vol. 20, No. 15.

DANTEC, 1992, *PDA User's Manual,* Tonsbakken 18, DK-2470 Skovlunde, Denmark.

Dunker, R., 1993, *Advances in Engine Technology,* Wiley, EC Aeronautics Research.

Edwards, C. F., and Marx, K. D., 1991, "Application of Poisson Statistics to the Problem of Size and Volume Flux Measurements by Phase Doppler Anemometry," presented at ICLASS-91, Gaithersburg, MD.

Eickhoff, H., Granser, D., and Krockow, W., 1983, "Liquid Fuel Atomization and Mixing in a High Velocity Airstream," AGARD-CP-353, Paper No. 14.

Gugel, K. O., 1995, "Experimentelle Untersuchung der Zwei-Phasen-Strömung in einer Vormischstrecke fur die magere vorgemischte und vorverdampfte Verbrennung," Thesis, University of Karlsruhe, Germany.

Lefebvre, A. H., 1989, *Atomization and Sprays,* Hemisphere Publishing Corporation, Washington, DC.

Lefebvre, A. H., 1991, "Twin Fluid Atomization—Factors Influencing Mean Drop Size," presented at ICLASS-91, Gaithersburg, MD.

Mellor, A. M., 1990, *Design of Modern Turbine Combustors,* Academic Press, ISBN 0-12-490055-0.

Pitcher, G., Wigley, G., and Saffman, M., 1990, "Sensitivity of Dropsize Measurements by Phase Doppler Anemometry to Refractive Index Changes in Combusting Fuel Sprays," presented at the 5th Int. Symp. Application of Laser Techniques to Fluid Mechanics, Lisbon.

Saffman, M., 1987, "Automatic Calibration of LDA Measurement Volume Size," *Applied Optics,* Vol. 26, No. 13.

Schulenberg, T., 1990, "Übersichtsvortrag zum 2. Statusseminar der Arbeitsgemeinschaft Hochtemperatur-Gasturbine," Nov. 20–23, DLR Köln-Porz, published by Sekretariat AG TURBO, DLR, D-51140 Koln.

Spadaccini, L. J., and TeVelde, J. A., 1982, "Autoignition Characteristics of Aircraft-Type Fuels," *Combustion and Flame,* Vol. 46, pp. 283–300.

Tacina, R. R., 1990, "Combustor Technology for Future Aircraft," Paper No. AIAA-90-2400.

Vargaftik, N. B., 1975, *Tables on the Thermophysical Properties of Liquids and Gases,* Hemisphere Publishing Corporation, ISBN 0-470-90310-4, p. 692.

Winklhofer, E., and Plimon, A., 1990, "Monitoring of Hydrocarbon Fuel–Air Mixtures by Means of a Light Extinction Technique in Optically Accessed Research Engines," *Optical Engineering.*

The Effects of Dissolved Oxygen Concentration, Fractional Oxygen Consumption, and Additives on JP-8 Thermal Stability

J. S. Ervin

T. F. Williams

S. P. Heneghan

S. Zabarnick

University of Dayton,
Dayton, OH 45469-0210

Since dissolved oxygen participates in fuel deposit formation, knowledge of the effects of dissolved oxygen concentration on fuel thermal stability is critical for fuel system design. In this work, the combined effects of dissolved oxygen availability and additives on jet fuel thermal stability are studied. Experiments with JP-8 jet fuel were conducted in a three-part heat exchanger that simulated a complex thermal and flow environment. The dissolved oxygen content at the flow inlet was varied, and deposition was studied under conditions of either fractional or complete oxygen consumption. The effects of a thermal stability additive package were also studied. An intriguing result found with JP-8 fuels is an increase in deposits formed in heated regions for decreased oxygen consumption, but inverse behavior with the additive package.

Introduction

Most high-performance aircraft rely on jet fuel circulation for cooling. Unfortunately, heated fuel reacts with small concentrations of dissolved oxygen gas to form oxidized products and deposits that can block fuel lines, foul close-tolerance valves, and deteriorate sealing materials (Hazlett, 1991; Ervin et al., 1996). On certain military jets, the fuel tanks are vented to the ambient air. At high altitudes, the ambient pressure and temperature are reduced significantly, resulting in a diminished concentration of dissolved oxygen. In addition, as a fire-preventative measure, an on-board inert gas generating system (OBIGGS) may be used to reduce the oxygen level in the fuel tank ullage space and, ultimately, in the liquid fuel. A fundamental understanding of the effect of low dissolved oxygen concentration and oxygen consumption on thermal stability (thermal stability refers to the deposit forming tendency of the fuel) is essential for aircraft design.

There is a general concensus that reducing the dissolved oxygen decreases the resulting deposition (Baker et al., 1983; Taylor, 1979). This has been observed in the case of complete oxygen consumption (Zabarnick et al., 1996; Heneghan et al., 1995) for both static and flowing tests. Few studies have considered the effects of fractional oxygen consumption on deposition. In previous works (Bradley et al., 1974; Taylor, 1974, 1976; Taylor and Frankenfeld, 1978; Frankenfeld and Taylor, 1980), the effects of intermediate levels of dissolved oxygen (20 to 40 ppm, mass basis) on surface fouling were not studied in detail. This regime of available oxygen is particularly important for aircraft that make use of OBIGGS or have vented fuel tanks. Further, the flow conditions and temperature fields were not well defined. More recent works (Heneghan et al., 1995; Jones et al., 1995) have studied the formation of jet fuel deposits under conditions of complete consumption of the dissolved oxygen at relatively high temperatures. Under these conditions, the mass of deposits increased as the mass of oxygen consumed increased. In contrast, under conditions of incomplete consumption of the available oxygen, Ervin et al. (1996) in a flowing test and Zabarnick et al. (1996) in a static test have found that decreasing the oxygen availability does not necessarily result in reduced deposition. Moreover, in aircraft, high fuel flow rates often result in circumstances in which the dissolved oxygen is not completely consumed (Harrison et al., 1993).

Additives can sometimes be used in small quantities to improve the deposition characteristics of the jet fuel (Zabarnick and Grinstead, 1994). However, additives are not always effective in reducing fouling. The relationship between fuel oxidation and deposit formation is extremely complex, and the ways in which additives affect this relationship are unclear. Moreover, the effects of thermal stability additives on deposition for fuel oxygen concentrations below that of normal air saturation are unknown.

In this work, experiments were conducted using a three-part heat exchanger, which simulated a complex thermal and flow environment approaching that of an aircraft. Different dissolved oxygen concentrations at the flow inlet determined the amount of available dissolved oxygen within the bulk flow. The objectives of these experiments were:

1. To study fouling produced by JP-8 jet fuel under conditions of partial oxygen consumption.
2. To study the effect of a thermal stability additive package on deposition under conditions of partial oxygen consumption.
3. To study deposition produced by JP-8 fuel with different inlet dissolved oxygen concentrations under conditions in which the available bulk oxygen is entirely depleted.

Experimental

In the experimental apparatus described in detail in Heneghan et al. (1993) (Fig. 1), fuel at ambient temperature is pumped from a preconditioning tank into the heated sections, which are at a pressure of 2.48 MPa. At this pressure level, the fuel remains as a liquid everywhere within the system. In the preconditioning tank, nitrogen and oxygen are bubbled through the fuel to control the amount of dissolved oxygen which enters the test section. Dissolved oxygen concentrations at the inlet can be varied from the air-saturation concentration of 70 ppm to as

Contributed by the International Gas Turbine Institute and presented at the 41st International Gas Turbine and Aeroengine Congress and Exhibition, Birmingham, United Kingdom, June 10–13, 1996. Manuscript received at ASME Headquarters February 1996. Paper No. 96-GT-132. Associate Technical Editor: J. N. Shinn.

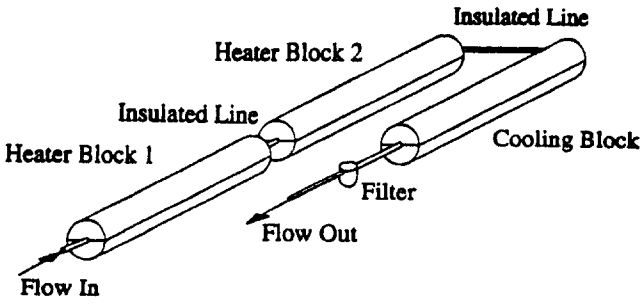

Fig. 1 Flow rig

low as 1 ppm. Bulk dissolved oxygen levels are measured online at the flow inlet and at a location within each insulated tube section by means of a Hewlett Packard 5890 Series II gas chromatograph (Rubey et al., 1992). After passing through two heated sections, the fuel flows into the cooled section, then is collected in a waste reservoir.

Two heated copper blocks (46 cm long with a 7.6 cm diameter) envelop the 316 stainless-steel tubing (180 cm long by 2.16 mm ID by 3.18 mm OD) through which the fuel passes. In the experiments performed here, the deposits remained thin (on the order of microns) and, as a result, did not appreciably affect the heat transfer or fluid motion. Thus, the temperatures were essentially steady. The tubing between the heated blocks is insulated. A third copper block (46 cm long with a 7.6 cm diameter), which has internal passages through which chilled water flows, provided cooling of the tube. Calibrated type K thermocouples (20 gage) are welded to the outer surface of the stainless-steel tubing to provide the outer tube wall temperatures with an uncertainty of ±2°C. The stainless-steel tubes (ASTM grade A269/A213) have a surface roughness (arithmetic average) of 8 to 15 μin. and are cleaned with Blue Gold alkaline solution in an ultrasonic bath, rinsed with deionized water, and dried with flowing laboratory-grade nitrogen gas prior to use.

Table 1 lists characteristics of neat F2980, F2827, and F3119, the straight-run base fuels used in this study. These Jet A fuels were acquired from different sources to avoid biasing the results. Jet A base fuels that contain compounds in the amounts (military specification MIL-T-83133) listed in Table 2 are referred to as JP-8 fuels. Table 3 lists additives that comprise the thermal stability additive package used, which is also being considered for use by the U.S. Air Force (Anderson et al., 1994). Here, JP-8 fuel containing the additive package is referred to as JP-8A.

In the present experiments, the volumetric flow rate was selected to be either 16 ml/min or 62 ml/min. The flow was laminar at the entrance of the first heated block for both flow rates, and Reynolds numbers (Re_D) based on the tube diameter and bulk temperature are listed in Table 4 for the exit of the second heated block. Steady temperature and velocity distributions within the fuel were obtained by the finite difference solution of the Navier–Stokes, turbulent energy, and enthalpy equations. Fluid motion inside the tube was assumed to be axisymmetric, and a cylindrical coordinate system was used (Katta and Roquemore, 1993). The density of the fuel changes significantly with temperature, which gives rise to considerable buoyancy force on the fuel near the tube wall. It is believed that the buoyancy forces normal to the forced flow direction increased the heat and mass transport, rendering the flow turbulent (Katta et al., 1995). Thus, turbulent simulations yielded bulk temperatures that approximated the measured values more accurately than did the laminar computations. Turbulent flow is normally encountered in the fuel systems of military aircraft.

The extent of oxidation depends on both the residence time and the temperature field. Dissolved oxygen is more readily consumed under conditions of high temperature and long residence times. Although the available dissolved oxygen is not completely consumed in aircraft fuel systems (Harrison et al., 1993), thermal stability studies of flowing jet fuel are generally performed under conditions of complete oxygen consumption (Heneghan et al., 1993; Jones et al., 1995). Thus, two categories of experiment were performed for purposes of comparison. In the first, the available dissolved oxygen was partially consumed. In the second, it was entirely depleted. For the first category, a block temperature of 270°C and a volumetric flow rate of 62 ml/min were used since these conditions resulted in little oxidation. The partial oxidation tests were conducted in 24 hour periods to obtain sufficient accumulation of deposits. In experiments performed with fractional oxygen consumption, both JP-8 and JP-8A fuel were used. In the experiments in which the dissolved oxygen was entirely consumed, the flow rate was 16 ml/min, the block temperature was either 300°C or 270°C, and the test period was six hours. In addition, JP-8 fuel alone was used. The dissolved oxygen concentrations provided at the flow rig inlet for all experiments are listed in Table 4. (The nominal dissolved oxygen concentration for air-saturated fuels here is 70 ppm; 30 ppm is representative of conditions that may be produced by an OBIGGS.)

At the termination of an experiment, the tubes were removed from the system, drained, and rinsed with hexane. They were then dried by flowing filtered nitrogen gas through them. Finally, they were sliced into 50 mm segments and heated in a vacuum oven at 120°C for one hour. Since the deposits are comprised largely of carbon, carbon measurements provide an indication of the axially distributed mass of deposits. A Leco (RC-412) multiphase carbon analyzer determined the mass of carbon in each tube segment; the reproducibility in the determination of the carbon mass is on the order of ±5 percent, determined by sequential tests performed within one week using fuel from the same batch.

Results and Discussion

In subsequent figures, the mass of carbon obtained from carbon burnoff measurements is ratioed by the inner surface area of the tube. The wall temperature distribution, given by polyno-

Nomenclature

$A^\cdot$ = antioxidant radical
AH = antioxidant species
$AO_2^\cdot$ = antioxidant peroxy radical
ASTM = American Society for Testing and Materials
BHT = butylated-hydroxy-toluene
D = tube diameter, m
FXXXX = U.S. Air Force naming scheme for neat Jet A fuels
JP-8A = JP-8 with BHT, MDA, and 8Q405
JP-8 = Jet A fuel with additives given by military specification MIL-T-83133
MDA = proprietary metal deactivator
OBIGGS = on-board inert gas generation system
O_2 = dissolved oxygen
PH = phenol molecule
$R^\cdot$ = hydrocarbon alkyl radical species
Re_D = Reynolds number = VD/ν
$RO_2^\cdot$ = peroxy radical
RH = hydrocarbon compound representing bulk fuel
RO_2H = hydroperoxide
V = mean velocity, m/s
8Q405 = Betz Corporation proprietary dispersant
ν = kinematic viscosity, m^2/s

Table 1 Neat fuel properties

fuel (Jet A)	sulfur mass %	aromatics volume %	JFTOT breakpoint (C)
F2980	0.1	17.0	288
F3119	0.1	18.0	285
F2827	<0.05	19.0	282

mial fits of the measured values, and the computed bulk temperature distribution are provided for reference. As the test section is horizontal, Taylor instabilities (Katta et al., 1995) yield an essentially turbulent flow at a flow rate of 16 ml/min. At 62 ml/min, the buoyancy force is less significant, and the flow undergoes a reverse transition to laminar flow (Katta et al., 1995). The complex dynamics of the flow at 62 ml/min are believed to be highly three dimensional and, hence, were not captured by the numerical simulation since the mathematical formulation was based on the assumption that the flow is axisymmetric. Thus, the bulk temperatures computed for 16 ml/min agree well with the measured values, but those computed for 62 ml/min lie above the measured temperatures within the heated sections and are used to show qualitative trends. As the fuel passes through the cooling block at 62 ml/min, the flow becomes more turbulent, and the computed and measured bulk temperatures become closer in agreement.

Partial Consumption of Dissolved Oxygen. In Fig. 2, the surface density of carbon deposited on the inner surface of the tube is expressed as a function of the axial distance through the two heated tube segments and the cooling block. Figure 2 shows three peaks, labeled A, B, and C, in the carbon deposit profiles obtained for both (F2980) JP-8 and JP-8A fuels under conditions of partial consumption of the bulk oxygen. Within the unheated segment between *A* and *B*, the deposition declines as the wall temperature decreases. Deposition then increases near 50 cm as the wall temperature approaches 270°C. Between *B* and *C*, near 100 cm, another decline occurs in the deposition profiles due to the fuel entering the unheated tube segment between the second heated block and the cooled block. Although the measured bulk temperature (200°C) at 100 cm is greater than that (160°C) at 50 cm, the deposition still falls to low levels. Figure 2 shows that the deposition in heated sections more closely follows the wall temperature than the bulk fuel temperature. The dependence of the deposition on wall temperature within heated sections was also observed in experiments with F2827 (Fig. 3) and F3119 (not shown). This dependence is plausible because in heated regions the stainless-steel wall is the location of maximum radial temperature and, thus, fuel oxidation rate. In addition, the wall is the location of minimum velocity and greater residence time than at the center of the tube. Further, the stainless-steel may be responsible for potential catalytic activity, such as the decomposition of hydroperoxides formed in the fuel autoxidation process.

At location C of Fig. 2, the wall temperature is a minimum, yet the level of deposition for JP-8 (and JP-8A) is of the same order as that at *A* and *B* where the temperature is greater. Increased deposition in cooled regions downstream of heated sections has been previously observed (Heneghan et al., 1995). The deposition mechanisms within the cooled tube are believed to be different from those in heated locations for several reasons. Chemical differences between fouling with JP-8 in the heated and cooled sections have been measured by means of X-ray photoelectron spectroscopy, and morphological differences have been detected by scanning electron microscopy (Ervin et al., 1996). Furthermore, the oxygen consumption within the cooled tube was immeasurably small, in contrast to that measured in the heated sections (Tables 5 and 6), which contain locations *A* and *B*. Lastly, experiments (Ervin et al., 1996) have shown that significantly more deposits are formed in the cooled section with higher cooling rates. Thus, deposits are believed to accumulate within the cooled section as a result of oxidized fuel products becoming less soluble at lower temperatures. The formation of deposits in cooled regions has particular import to the development of recirculating fuel systems. Recirculation systems will use ram air heat exchangers to cool the fuel prior to returning it to the fuel tanks. These heat exchangers would

Table 2 Properties of JP-8 additives

additive name	additive classification	type of compound	concn (mg/L)
DiEGME	icing inhibitor	diethylene-glycol -monomethyl-ether	25
DuPont Stadis 450	static dissipator	proprietary	2
DCI-4A	corrosion inhibitor/ lubricity enhancer	proprietary	9

Table 3 Properties of thermal stability additives

additive name	additive classification	type of compound	concn (mg/L)
BHT	antioxidant	butylated-hydroxy-toluene	25
8Q405	detergent-dispersant	proprietary	100
MDA	metal deactivator	N,N'-disalicylidene-1,2-propanediamine	2

Table 4 Experiments performed

JP-8 fuel	thermal stability additives	flow rate (ml/min)	testing period (hrs)	heated block temp. (C)	inlet O_2 concn. (ppm)	Re_D exit heated block 2
partial O_2 consumption						
F2980	no	62	24	270	70,30, 6,1	2500
F2980	yes	62	24	270	70,30	2500
F2827	no	62	24	270	70,30	2500
F2827	yes	62	24	270	70,30	2500
F3119	no	62	24	270	70,30	2500
F3119	yes	62	24	270	70,30	2500
complete O_2 consumption						
F3119	no	16	6	300	70,30, 19	950
F3119	no	16	6	270	70,30, 19	850

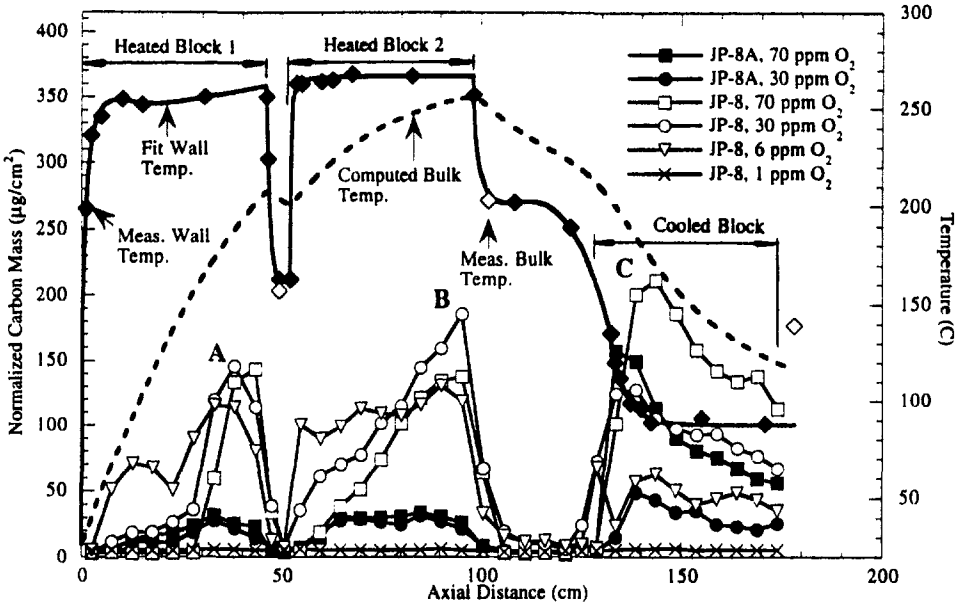

Fig. 2 Tube deposit and temperature profiles: partial O_2 consumption for fuel F2980, 62 ml/min, and 24 h

likely collect deposits similar to those found here in the cooled tube.

Figure 2 shows that the deposit profiles formed from JP-8 fuel are influenced by the inlet dissolved oxygen concentration. At locations *A* and *B*, the measured deposition for JP-8 fuel is greater for a dissolved oxygen concentration of 30 ppm than that obtained with air-saturated fuel. Similarly, greater deposition was observed with a dissolved oxygen concentration of 30 ppm rather than with 70 ppm for both F2827 (Fig. 3) and F3119 (not shown). Figure 2 shows that at a dissolved oxygen concentration of six ppm, the JP-8 fuel deposits at locations *A* and *B* are even greater than those that occur with higher dissolved oxygen concentrations and occur earlier in the tube. In Fig. 2, when the dissolved inlet oxygen is further lowered to 1 ppm, there is little deposition. Likewise, Tables 5 and 6 show that, with decreasing inlet oxygen concentrations for JP-8 (F2980 and F2827), the total mass of deposits formed in the heated sections approaches a maximum and then falls with lower oxygen concentrations.

The JP-8 deposit profiles of F2980 (Fig. 2), F2827 (Fig. 3), and F3119 (not shown) in the first heated section (between 0 and 49 cm) for dissolved oxygen concentrations less than 70 ppm rise above background levels near the tube entrance, well upstream of that for air-saturated conditions. In this region of the tube, as the initially thin thermal boundary layer develops near the heated wall, the radial temperature gradient is large at the wall but decreases with increasing axial distance. In the second heated section (between 55 and 99 cm) following the insulated tube, the thermal boundary layer again develops. The deposit profiles for initial dissolved oxygen concentrations below 70 ppm again rise at locations upstream of the point where the deposit profile for initially air-saturated fuel rises. In a flow-

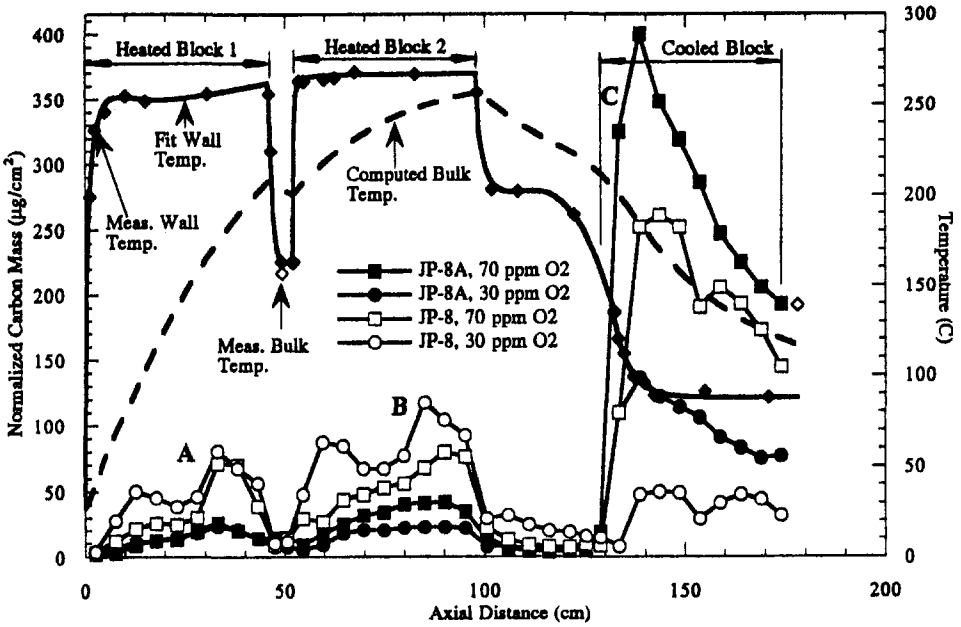

Fig. 3 Tube deposit and temperature profiles: partial O_2 consumption for fuel F2827, 62 ml/min, and 24 h

Table 5 Carbon deposits and consumed dissolved O_2 for partial consumption conditions and fuel F2980

inlet O_2 concn. (ppm)	O_2 consumed heated block 1 (ppm)	O_2 consumed heated block 2 (ppm)	total O_2 consumed (ppm)	deposits-heated blocks (μg)	deposits-cooled block (μg)
JP-8					
70	5	11	16	4057	4774
30	4	6	10	5800	2976
6	1	3	4	6007	1400
1	0.7	0.3	1	482	183
JP-8A					
70	5	6	11	1366	2909
30	5	6	11	1177	923

ing system, the oxygen consumption is controlled by both the kinetics of oxidation and the species transport. The fuel near the wall is heated at a faster rate and for a greater residence time than fuel passing through the center of the tube. In experiments using a quartz crystal microbalance, Zabarnick et al. (1996) observed an increasing fuel oxidation rate occurring at low dissolved oxygen concentrations. However, this observation is not consistent with the consumed oxygen values given in Tables 5 and 6.

At location *C* of Fig. 2, deposition for the JP-8 fuel is greatest for the inlet oxygen concentration of 70 ppm. Lower inlet levels of dissolved oxygen resulted in lower levels of deposits in the cooled tube (between 95 cm and the exit). The relationship between inlet oxygen concentration and the mass of deposits formed in the cooled section is quite different from that in the heated sections; that is, the deposition in the cooled section declines with decreasing inlet oxygen concentrations. Similar trends in deposition for JP-8 without additives are also observed for F-2827 (Fig. 3) and F-3119 (not shown). In addition, these observations support the previously described concept of a mechanism different from that of the heated sections, acting in the cooled section.

Additives and Partial Consumption of Dissolved Oxygen. Figure 2 shows deposit distributions resulting from stressed JP-8A (F-2980). Within the heated sections, the magnitude of deposit accumulation is significantly reduced in comparison to that formed from JP-8 for all inlet dissolved oxygen concentrations. Further, the level of deposition in the heated sections resulting from JP-8A now seems to follow the inlet oxygen concentration. Similar results were obtained with F2827 (Fig. 3) and F3119 (not shown). In addition as the inlet dissolved oxygen concentrations increased, Figs. 2 and 3 show that JP-8A, like JP-8, yielded more deposits in the cooled tube. In contrast to the deposition behavior of the JP-8 fuels described previously, Figs. 2 and 3 show that the deposit profiles of the JP-8A fuels rise above background levels at the entrance of the first and second heated blocks at nearly the same location, regardless of inlet dissolved oxygen concentration. Previous work (Zabarnick and Grinstead, 1994) has demonstrated that the additive package can significantly delay the oxidation process.

The addition of thermal stability additives complicates the understanding of the relation between deposition and oxidation for JP-8A because the thermal stability additives can change the chemical mechanisms of deposit formation. For example, Table 5 for fuel F2980 shows that for an inlet dissolved oxygen concentration of 30 ppm, JP-8 and JP-8A consumed similar amounts of oxygen. However, JP-8A formed significantly less deposits. These trends in oxidation and deposition were also found with F3119. Although (F2827) JP-8 and JP-8A consumed nearly the same mass of oxygen for each inlet dissolved oxygen concentration (Table 6), JP-8A formed more deposits in the cooled section than did JP-8. Thus, the thermal stability additive package affected deposition in the cooled tube with F2827 differently from that observed with F2890 and F3119.

Complete Consumption of Dissolved Oxygen. In military aircraft, jet fuel is recirculated through the fuel system and exposed to a variety of temperatures. These temperatures change continuously during a mission while the aircraft manuevers. Thus, an understanding of the effect of temperature on jet fuel thermal stability is essential to the design of jet fuels systems. In experiments performed under conditions of complete consumption of the bulk dissolved oxygen, the heated block temperature was varied while monitoring deposition and oxidation.

Figures 4(*a*) and 4(*b*) show deposition profiles for JP-8 fuel (F3119) resulting from different heated block temperatures, and the measured tube wall temperatures and computed bulk temperatures are given for reference. Within the heated or insulated tube, the deposition may fall to very low levels for two reasons. The first is that the dissolved oxygen is fully consumed and, thus, there is no more fuel oxidation. The second reason is that the temperature is low, and oxidation proceeds at a very slow rate (as shown in Figs. 2 and 3 between locations *A* and *B*). In Fig. 4(*a*), at a nominal block temperature of 300°C, the oxygen is fully consumed within the first heated block (Table 7). Thus, there is little deposition in the insulated tube and the second heated block. In the first heated block, deposition and oxidation follow each other except near the entrance of the first heated block (before 10 cm), where an inlet dissolved oxygen concentration of 19 ppm produces the greatest mass of deposits. In the cooled block there is little deposition. Figure 4(*b*) shows that a dissolved oxygen concentration of 19 ppm, the lowest level of dissolved oxygen, results in the greatest mass of deposits within the first heated section for block temperatures of 270°C. Interestingly, the dissolved oxygen is completely consumed within the first heated block for oxygen concentrations of 70 and 30 ppm. However, for an inlet dissolved oxygen concentration of 19 ppm, the bulk dissolved oxygen is not entirely consumed there (Table 7). Thus, Fig. 4 shows that even under conditions of partial oxygen consumption, greater deposition may occur with dissolved oxygen concentrations below that of normal air saturation. Similar to the fouling observed under conditions of partial oxygen consumption (Figs. 2 and 3), there are now obvious peaks in the deposition occurring in

Table 6 Carbon deposits and consumed dissolved O_2 for partial consumption conditions and fuel F2827

inlet O_2 concn. (ppm)	O_2 consumed heated block 1 (ppm)	O_2 consumed heated block 2 (ppm)	total O_2 consumed (ppm)	deposits-heated blocks (μg)	deposits-cooled block (μg)
JP-8					
70	4	7	11	2986	6179
30	1	5	6	5727	2407
JP-8A					
70	5	6	11	1357	8827
30	3	5	8	976	3161

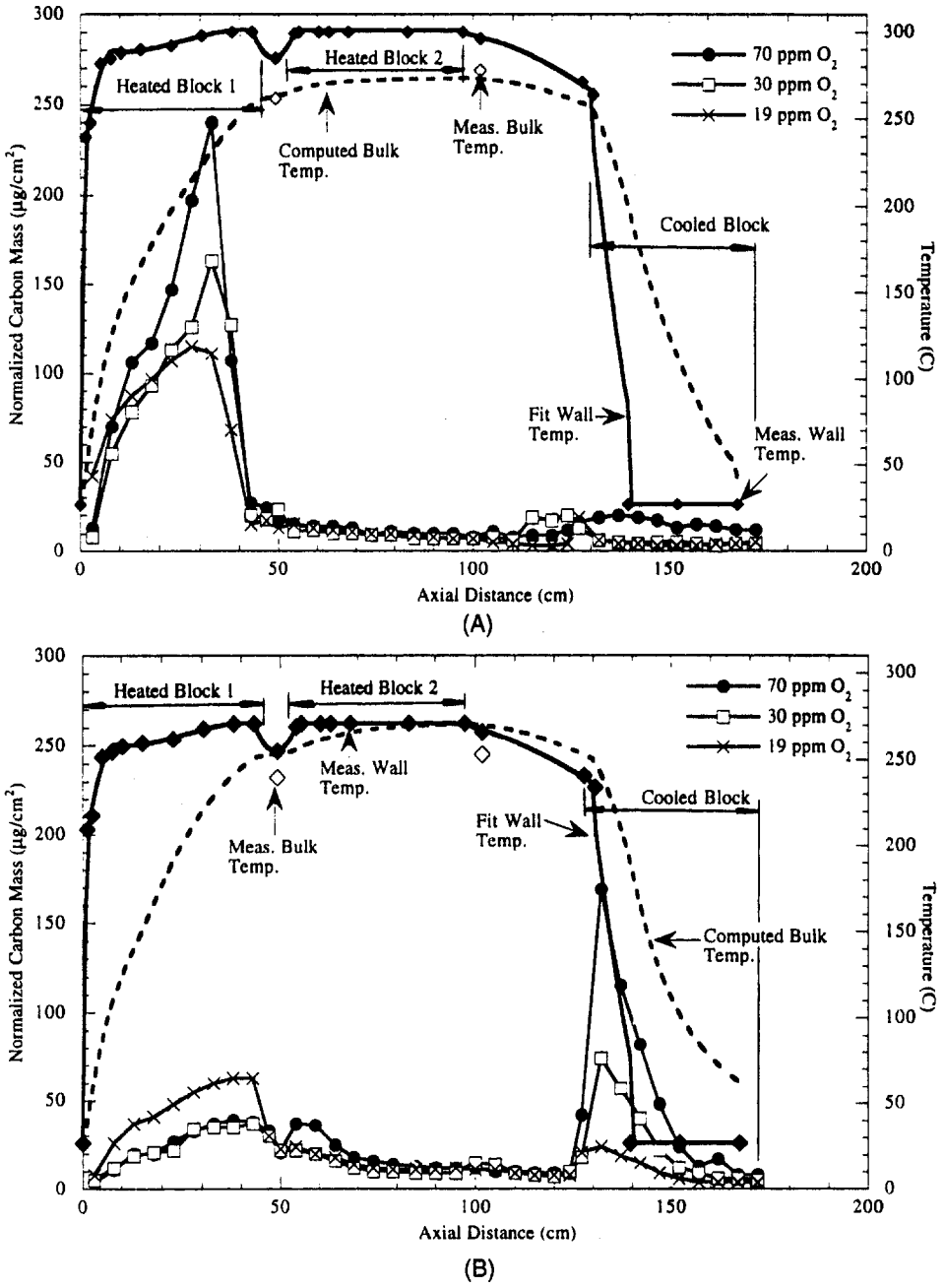

Fig. 4 Tube deposit and temperature profiles for complete O_2 consumption, JP-8 (F3119), and 16 ml/min: (*A*) 300°C block temperature; (*B*) 270°C block temperature

the cooled tube, and these peaks follow the inlet dissolved oxygen concentration.

Figure 4 shows that the heated block temperature affects the kind of oxidation products that are produced. The dissolved oxygen is consumed at a greater rate at the heated block temperature of 300°C than at the heated block temperature of 270°C. For example, Table 7 with 19 ppm dissolved oxygen and a block temperature of 300°C shows all dissolved oxygen is consumed within the first heated block. However at 270°C, 9 ppm is consumed within the second block. Although Table 7 does not show differences in oxidation rates between 270 and 300°C for the other dissolved oxygen concentrations, Heneghan et al. (1995) have observed that under conditions of complete oxygen consumption, greater temperatures result in greater rates of oxygen consumption. Furthermore, fewer solubles that deposit in cooled regions (Ervin et al., 1996) are produced with relatively high block temperatures. This has been observed previously (Heneghan et al., 1995) under conditions of complete oxygen consumption and different heated block temperatures.

An intriguing result found with JP-8 fuel is that increases in deposits in the heated sections may coincide with decreased oxygen consumption (Figs. 2–4). This observation is seemingly contrary to nearly all prior observations concerning the relation between deposit formation and oxygen consumption (Heneghan et al., 1995; Jones et al., 1995). Further, it conflicts with theories concerning the formation of deposits (Heneghan and Zabarnick, 1994; Hazlett, 1991). The mechanism proposed by Heneghan and Zabarnick (1994) for the autoxidation and antioxidant chemistry of jet fuels is:

Initiation Production of $R^{\bullet}$ (1)

Propagation $R^{\bullet} + O_2 \rightarrow RO_2^{\bullet}$ (2)

Table 7 Carbon deposits and dissolved O_2 consumption for complete consumption conditions, JP-8 (F3119)

inlet O_2 concn. (ppm)	O_2 consumed heated block 1 (ppm)	O_2 consumed heated block 2 (ppm)	total O_2 consumed (ppm)	deposits-heated blocks (μg)	deposits-cooled block (μg)
300 C					
70	70	0	70	3893	482
30	30	0	30	2974	139
19	19	0	19	2792	124
270 C					
70	70	0	70	1420	1673
30	30	0	30	1163	795
19	10	9	19	1837	302

$$RO_2^{\cdot} + RH \rightarrow RO_2H + R^{\cdot} \quad (3)$$

Termination $RO_2^{\cdot} + RO_2^{\cdot} \rightarrow$ Termination Products (4)

Transfer $RO_2^{\cdot} + AH \rightarrow RO_2H + A^{\cdot}$ (5)

$$AO_2^{\cdot} + RH \rightarrow AO_2H + R^{\cdot} \quad (6)$$

$$A^{\cdot} + O_2 \rightarrow AO_2^{\cdot} \quad (7)$$

$$AO_2^{\cdot} + AH \rightarrow AO_2H + A^{\cdot} \quad (8)$$

Deposition $AO_2^{\cdot} + AO_2^{\cdot} \rightarrow$ Deposit (9)

This mechanism is reconsidered in an attempt to explain the behavior observed here. Jet fuels are composed of hundreds of compounds. Thus, it is impractical to model the chemical changes of all components in the mixture. Here, the bulk fuel is modeled as a single hydrocarbon compound, *RH*. AH represents an antioxidant species, $R^{\cdot}$ is a hydrocarbon alkyl radical species, RO_2H is a hydroperoxide. O_2 represents the dissolved oxygen present in the fuel. In addition, $RO_2\cdot$ is a peroxy radical, $A\cdot$ is an antioxidant radical, and $AO_2\cdot$ is an antioxidant peroxy radical. The first four reactions constitute a simplified autoxidation mechanism for hydrocarbons in the liquid phase, and the remaining reactions include the chemistry of an antioxidant molecule. Reaction (9) is responsible for the production of insoluble deposits. From the results of the current work, it is desirable for a mechanism to account for increases in deposits in heated sections that occur with decreased oxygen consumption. It should also account for the presence of soluble deposits which form in cooled regions. Hence, reactions (6)–(9) are replaced with the following reactions:

Equilibrium $A^{\cdot} + O_2 \leftrightarrow AO_2^{\cdot} \rightarrow$ Soluble Products (6′)

Deposition $A^{\cdot} + PH \rightarrow$ Deposit (7′)

Thus, it is proposed that reaction (6′) is an equilibrium reaction that leads to soluble products, and a competiting reaction, (7′), leads to the formation of deposits in the heated regions. *PH* represents an unidentified molecule, but may be a phenol as Heneghan and Kauffman (1994) have shown a strong correlation between the formation of deposits in jet fuels and the presence of phenols. The equilibrium in reaction (6′) would be shifted to the right under large initial O_2 concentrations resulting in decreased deposits for each oxygen molecule consumed as shown in the heated regions of Figs. 2 and 3 and by Zabarnick et al. (1996). In addition, the equilibrium would be shifted to the left at high temperatures, causing increased deposition with temperature, a well-established trend (Hazlett, 1991). In future work, detailed computational kinetic modeling will be performed to verify the predicted behavior and establish values for the equilibrium constant in reaction (6′).

Conclusions

An understanding of the effect of the dissolved oxygen concentration on thermal stability is essential for the design of jet fuel systems. For this purpose, the dissolved oxygen concentration within the fuel at the inlet of a flowing system was varied. It was found that with JP-8 fuel under conditions of either partial or complete dissolved oxygen consumption there may be an increase in deposition for decreased inlet dissolved oxygen concentration. In addition, it was found that the thermal stability additive package improved the deposition characteristics of JP-8 fuel in the heated tube, but not necessarily in the cooled tube. From the results of this work, the following conclusions may be drawn:

- Deposit formation can be significantly affected by the upstream availability of the dissolved oxygen. Under certain conditions, more deposits can be produced with less dissolved oxygen. This is important for fuel system devices such as OBIGGS.
- Global chemistry models used in computational fluid dynamics computer codes to simulate jet fuel fouling do not presently account for the effects of dissolved oxygen availability observed here. A better understanding of the underlying chemical kinetics is needed for improved numerical simulation.
- Thermal stability tests are often conducted under conditions of high temperature and long residence time such that the influence of bulk dissolved oxygen availability on deposition is not observed. Thus, the testing of jet fuel thermal stability should be performed over a range of dissolved oxygen concentrations, residence times, and temperatures.

Acknowledgments

This work was supported by the U.S. Air Force, Fuels and Lubrication Division, Aero Propulsion and Power Directorate, Wright Laboratory, WPAFB, under Contract No. F33615-92-C-2207 (Technical Monitor: C. W. Frayne).

References

Anderson, S., Harrison, W., III, and Roquemore, W., 1994, "Development of Thermal Stability Additive Package for JP-8," *Proc. Fifth International Conference on the Handling and Stability of Liquid Fuels,* Rotterdam, Netherlands.

Baker, C. E., Bittker, D. A., Cohen, S. M. and Seng, G. T., 1983, NASA Tech Memorandum 83420.

Bradley, R., Bankhead, R., and Bucher, W., 1974, *High Temperature Hydrocarbon Fuels Research in an Advanced Aircraft Fuel System Simulator on Fuel AFFB-14-70* (AFAPL-TR-73-95), Air Force Aero Propulsion Laboratory, Wright-Patterson Air Force Base, Ohio.

Ervin, J. S., Heneghan, S. P., Martel, C. R., and Williams, T. F., 1996, "Surface Effects on Deposits From Jet Fuels," ASME JOURNAL OF ENGINEERING FOR GAS TURBINES AND POWER, Vol. 118, pp. 278–285.

Frankenfeld, J., and Taylor, W., 1980, "Deposit Formation From Deoxygenated Hydrocarbons. 4. Studies in Pure Compound Systems," *Ind. Eng. Chem. Prod. Res. Dev.,* Vol. 19, p. 65.

Harrison, W., Binns, K., Anderson, S., and Morris, R., 1993, "High Heat Sink Fuels for Improved Aircraft Thermal Management," SAE Paper No. 11E525.

Hazlett, R., 1991, *Thermal Oxidation Stability of Aviation Turbine Fuels,* American Society for Testing and Materials, Philadelphia, PA.

Heneghan, S., Martel, C., Williams, T., and Ballal, D., 1993, "Studies of Jet Fuel Thermal Stability in a Flowing System," ASME JOURNAL OF ENGINEERING FOR GAS TURBINES AND POWER, Vol. 115, p. 480.

Heneghan, S. P., and Zabarnick, S., 1994, "Oxidation of Jet Fuels and the Formation of Deposits," *Fuel,* Vol. 73, p. 35.

Heneghan, S. P., and Kauffman, R. E., 1994, "Analytic Tests and Their Relation to Jet Fuel Thermal Stability," *Proc. Fifth International Conference on the Stability and Handling of Liquid Fuels,* Rotterdam, Netherlands.

Heneghan, S., Martel, C., Williams, T., and Ballal, D., 1995, "Effects of Oxygen and Additives on the Thermal Stability of Jet Fuels," ASME JOURNAL OF ENGINEERING FOR GAS TURBINES AND POWER, Vol. 117, p. 120.

Jones, E. G., Balster, W. J., and Post, M. E., 1995, "Degradation of a Jet-A Fuel in a Single Pass Heat Exchanger," ASME JOURNAL OF ENGINEERING FOR GAS TURBINES AND POWER, Vol. 117, p. 125.

Katta, V. R., and Roquemore, W. M., 1993, "Numerical Method for Simulating Fluid Dynamic and Heat Transfer Changes in Jet Engine Injector Feed-Arm Due to Fouling," *J. of Thermophysics and Heat Transfer,* Vol. 7, p. 651.

Katta, V. R., Blust, J., Williams, T. F., and Martel, C. R., 1995, "Role of Buoyancy in Fuel-Thermal Stability Studies," *J. of Thermophysics and Heat Transfer,* Vol. 9, p. 159.

Rubey, W., Striebich, R., Anderson, S., Tissandier, M., and Tirey, D., 1992, "In Line Gas Chromatographic Measurement of Trace Oxygen and Other Dissolved Gases in Flowing High Pressure Thermally Stressed Jet Fuel," *Symposium on Structure of Jet Fuels III,* American Chemical Society, Div. Petr. Chem., San Francisco, California.

Taylor, W., 1974, "Deposit Formation from Deoxygenated Hydrocarbons. I. General Features," *Ind. Eng. Chem. Prod. Res. Dev.,* Vol. 13, p. 133.

Taylor, W., 1976, "Deposit Formation From Deoxygenated Hydrocarbons. II. Effect of Trace Sulfur Compounds," *Ind. Eng. Chem. Prod. Res. Dev.,* Vol. 15, p. 64.

Taylor, W., and Frankenfeld, J., 1978, "Deposit Formation From Deoxygenated Hydrocarbons. 3. Effects of Trace Nitrogen and Oxygen Compounds," *Ind. Eng. Chem. Prod. Res. Dev.,* Vol. 17, p. 87.

Taylor, W. F., 1979, "Jet Fuel Thermal Stability," NASA TM-79231.

Zabarnick, S., and Grinstead, R., 1994, "Studies of Jet Fuel Additives Using the Quartz Crystal Microbalance and Pressure Monitoring at 140°C," *Ind. Eng. Chem. Res.,* Vol. 33, p. 2771.

Zabarnick, S., Zelesnik, P., and Grinstead, R., 1996, "Jet Fuel Deposition and Oxidation: Dilution, Materials, Oxygen, and Temperature Effects," ASME JOURNAL OF ENGINEERING FOR GAS TURBINES AND POWER, Vol. 118, pp. 271–277.

Evaluation of the Effectiveness of a Metal Deactivator and Other Additives in Reducing Insolubles in Aviation Fuels

E. G. Jones

W. J. Balster

L. M. Balster

Innovative Scientific Solutions, Inc.,
2786 Indian Ripple Road,
Dayton, OH 45440-3638

Surface fouling in aircraft fuel lines resulting from autoxidation of aviation fuel leads to reduced efficiency as deposits collect on heat exchangers, nozzles, and servocontrols and may ultimately lead to system failure. Metal surfaces and trace quantities of metals dissolved in the fuel exacerbate the surface-fouling problem because they can catalyze free-radical initiation, thereby accelerating autoxidation. Additives and additive packages containing antioxidants, dispersants, and metal deactivators (MDA) have been shown to reduce insolubles in some fuels. Because of metal chelation and possible metal-surface passivation, MDA has been proposed as an additive component to be included in all fuels, even those without dissolved metals. The goal of the present study was to obtain fundamental information on the behavior of MDA under conditions where surface-passivation effects are minimal. Experiments have been conducted to (1) study the effects of adding MDA to fuels containing a significant concentration of dissolved metals (i.e., chelation) and to those containing minor concentrations of dissolved metals and (2) investigate interactions when MDA is used in conjunction with an antioxidant and a dispersant. Simple fuel-line-fouling simulations with a single-pass tubular heat exchanger operated under near-isothermal conditions have been conducted to study the thermal behavior at 185°C of several neat and MDA-treated jet fuels as well as fuels treated with MDA plus other additives. Comparison of neat and treated fuels is based on several criteria: (1) dependence of autoxidation on stress duration, (2) dependence of surface deposition on stress duration, and (3) quantity of total insolubles (bulk filterables and surface deposits). Potential advantages and disadvantages of using MDA alone and in combination are discussed.

Introduction

Fouling of aircraft fuel lines that results from autoxidative and pyrolytic degradation of jet fuel is a significant problem for current aircraft and is projected to become more serious in the future, particularly for military aircraft (Edwards et al., 1992; Edwards, 1993). Approaches taken to mitigate fouling include (1) additional refining techniques such as hydrotreatment to remove trace polar components, (2) innovative onboard fuel management to utilize the additional fuel-sink capacity of the fuel, and (3) introduction of individual additives and additive packages, including antioxidants to slow autoxidation, metal deactivators to reduce the rate of initiation and possibly passivate metal surfaces, and dispersants/detergents to prevent agglomeration of insolubles. The use of these and other specific additives to inhibit corrosion, fuel icing, and static charge has been summarized by Martel (1987). As part of the USAF JP-8 + 100 program to improve fuel operating stability by 100°F (Edwards et al., 1993), the use of a generic additive package containing the antioxidant BHT, dispersant 8Q405, and metal deactivator MDA has been proposed.

Dispersants and, to a lesser extent, antioxidants have been shown to improve thermal stability in USAF fuels (Zabarnick and Grinstead, 1994; Jones et al., 1995); however, the use of MDA is still under consideration. Experimental studies on the use of MDA in aviation fuels are extensive and have been reviewed and summarized by Hazlett (1991). Metal deactivators have been reported (Clark, 1988) to operate via two distinct mechanisms: (1) chelation of metal ions and (2) surface passivation. Many reports in the literature support the role of chelation (Morris and Turner, 1990; Mills and Kendall, 1986); however, the role of surface passivation is less clear (Morris and Turner, 1990; Schreifels et al., 1991).

The goal of the current study was to use a very simple laboratory simulation of fuel-line fouling for (1) obtaining quantitative data for autoxidation and deposition at a fixed temperature (185°C) from several neat and MDA-treated aviation fuels, (2) making a comparison with similar data obtained from antioxidant- and dispersant-treated fuels, and (3) investigating possible benefits of using MDA, antioxidants, and dispersants in combination. The experimental conditions were specifically selected to discriminate against any metal-surface passivation mechanism by MDA and focus on the homogeneous function of MDA and other additives within the bulk fuel. In order to minimize possible complications from surface effects, autoxidation was studied for fuel reacting in tubing having inner surfaces passivated by the Silcosteel process. Also, deposition was studied using tests of long duration (72 h) in which inner wall surfaces became passivated by deposition early in the course of testing. The selection of 185°C for additive evaluation is predicated on the need for achieving isothermal reaction conditions in the absence of fluid-dynamic complications in order to simplify data interpretation. However, it should be noted that MDA may function quite differently if evaluated at higher temperatures under nonisothermal conditions of fast fuel flow.

Experimental Arrangement

The physical properties of the six fuels studied in this program are summarized in Table 1. Neat and additized fuels were

Contributed by the International Gas Turbine Institute and presented at the 41st International Gas Turbine and Aeroengine Congress and Exhibition, Birmingham, United Kingdom, June 10–13, 1996. Manuscript received at ASME Headquarters February 1996. Paper No. 96-GT-204. Associate Technical Editor: J. N. Shinn.

Table 1 Properties of aviation fuels

Fuel No.	Class	JFTOT Breakpoint Temp., K	Total S ppm	Dissolved Metals, ppb*
2827	Jet-A, Straight Run	539	790	Cu, <5; Fe, 8
2980	Jet-A, Merox-Treated	561	614	Cu, <5; Fe,<5
2962	JP-5		438	Cu, 10; Fe,<5
2934	JP-8	539	755	Cu, 34; Fe,<5
3084	Jet-A	541	527	Cu, 35; Fe,<5
3119	Jet-A	516	1000	Cu, 7; Fe, 26

*Measurements made for USAF using graphite Zeeman/5000 System Atomic Absorption Spectrometer by United Technologies, Pratt and Whitney.

Table 2 Additives studied

Class	Name	Chemical Name	Source	Conc. (mg/L)
Antioxidant	BHT	2,6-di-tert-butyl-p-cresol	DuPont	25
Metal Deactivator	MDA	N,N'-disalicylidene-1,2,-propanediamine	DuPont	2, 6
Dispersant	8Q405	roprietary	Betz	100

initially saturated with respect to air at room temperature and were passed through a 15-μm filter before use. Information on MDA and the other additives is given in Table 2. Reaction occurred as fuel was pumped through 0.318-cm- (0.125-in.-) o.d., 0.216-cm- (0.085-in.-) i.d. tubing, clamped tightly within a Cu-block heat exchanger at 185°C. System pressure was maintained at 2.3 MPa to ensure a single reaction phase. Two experimental arrangements were utilized, differing only in the length of the heat exchanger.

The concentration of dissolved oxygen, O_2, was measured using the first or standard setup with the NIFTR, which has been described in detail elsewhere (Jones et al., 1993) and will be reviewed here only briefly. For these experiments a fixed reaction pathlength of 81.3 cm (32 in.) was used; stress duration or residence time was varied by changing the fuel flow rate and was calculated based on plug flow, with a 15 percent correction to accommodate fuel expansion at 185°C. Dissolved oxygen was measured in-line at system pressure using a GC technique developed by Rubey and co-workers (1995). Based on the difference between O_2 readings for the unstressed and stressed fuel, the percentage of residual O_2 was determined as a function of the calculated reaction time. The tubing selected for O_2 experiments was passivated by the Silcosteel process (Restek Corp.) in order to minimize possible surface catalytic effects. Reproducibility in oxidation data is estimated to be ±5 percent.

Deposition experiments were conducted using the second experimental arrangement with an extended-length heat exchanger (NIFTR-2). Under fixed flow rates of 0.25 and 0.20 ml/min, this unit has a continuous, isothermal 183-cm heated pathlength that provides 23 and 28 min, respectively, of stressing to accommodate the complete deposition profile of all fuels and most additized fuels used in this study. Deposits were collected over a relatively long test duration (72 h), resulting in the passage of 864–1080 ml of air-saturated fuel during the course of each experiment. Commercial stainless-steel (304) tubing was used for all deposition experiments; during the first few hours of each test, the original stainless-steel surfaces became covered with deposits and were passivated with respect to autoxidation (Jones and Balster, 1995). Thus, deposition and autoxidation experiments were conducted under very similar test conditions, with minimal interaction of metal surfaces.

Because of the slow fixed flow rate used in deposition experiments, isothermal conditions prevail after fuel has passed ~5 cm into the block; thus, the reaction time is proportional to the distance along the heated tube. Reaction time is calculated from tubing dimensions and flow rate, with corrections being made for fuel expansion. At test completion, the tube was cut into a total of 36 segments, each 5.1 cm long. Following heptane rinse and vacuum drying (130°C for 12 h), the carbon associated with the surface deposit was quantified by conventional surface-carbon-burnoff techniques (LECO RC-412). The surface-deposition rate on each tubing segment was calculated from the amount of carbon measured in burnoff, the fuel residence time within that tubing segment, and the total amount of fuel passed. Rate is expressed in units of micrograms of carbon/hour per milliliter of fuel, representing an average over the entire 72-h test period, and is plotted as a function of stress duration. The total surface carbon (μg/ml) was obtained by integrating the differential-rate data. Reproducibility in deposition data is estimated to be ±20 percent.

Bulk insolubles were collected over the entire 72-h test period on two sets of in-line Ag-membrane filters (0.45 and 0.2 μm). The quantity of bulk insolubles from the two filter sets was summed and expressed in units of micrograms per milliliter, representing an average over complete oxygen conversion. Filter housings located ~10 cm from the heat exchanger remained near room temperature; thus, measured filterables include additional contributions resulting from fuel cooling.

Results and Discussion

Effect on Autoxidation and Deposition of Using MDA at a Concentration of 2 mg/L. The impact of adding MDA at a concentration of 2 mg/L to six fuels is shown in Fig. 1. Autoxidation in plots *a–c* for fuels that contain low concentrations of dissolved metals is only slightly delayed by MDA. On the other hand, autoxidation in plots *d–f* for fuels that contain greater concentrations of dissolved metals is significantly slowed by the chelating effects of MDA, as evidenced by the observed delays. The sensitivity of autoxidation, as measured in passivated tubing, to dissolved metals and to treatment with MDA makes comparisons such as those in Fig. 1 definitive in detecting the presence of metals.

The corresponding deposition rates are given in Fig. 2. For brevity, consideration has been limited to only two fuels of each category. Deposition in POSF-2827 shows no effect from introduction of MDA, while POSF-2980 with MDA shows some slight delay but virtually the same deposition profile. The response to MDA in the two metal-containing fuels is more pronounced. The deposition profiles broaden and are shifted to longer stress times. Such changes are anticipated from the slowed autoxidation that arises when chelation of the dissolved

Nomenclature

BHT = Hindered-Phenol Antioxidant, see Table 2
GC = Gas Chromatograph
JFTOT = Jet-Fuel Thermal-Oxidation Test
MDA = Metal Deactivator, see Table 2
NIFTR = Near-Isothermal Flowing Test Rig
POSF- = Jet-Fuel Designation, see Table 1
USAF = United States Air Force
8Q405 = Dispersant, see Table 2

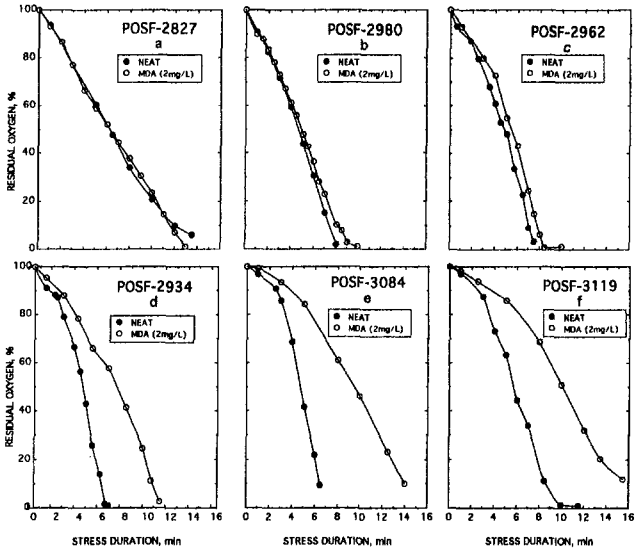

Fig. 1 Effect of MDA (2 mg/L) on autoxidation of fuels without dissolved metals (*a*, *b*, *c*) and with dissolved metals (*d*, *e*, *f*)

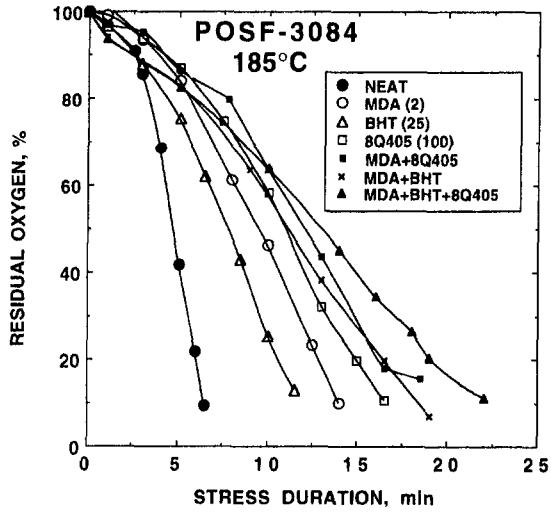

Fig. 3 Autoxidation of POSF-3084: effect of additives singly and in combination with MDA

copper eliminates metal-initiated autoxidation (Scott, 1965). The beneficial reduction in fouling related to the autoxidation delay is noticeable; however, after deposition processes have been completed, more total deposits (area under profiles) have been produced in the MDA-treated fuels. Since fuels are rarely stressed to complete oxygen conversion, this latter point may be moot; however, it does raise questions as to what chemical or physical changes may be occurring in the MDA-treated fuels, leading to the observed increase in total deposits.

Effects on Deposition of Using MDA at a Concentration of 6 mg/L. A maximum of 5.8 mg/L of MDA is allowed in JP-8 aviation fuel, according to specification Mil-T-83133D; however, a concentration of 2 mg/L represents an excess of chelating agent for the current concentrations of dissolved metals. Thus, introduction of MDA at higher concentrations should not significantly alter either the autoxidation or surface-fouling behavior. This view is supported by the deposition data in Fig. 2 for POSF-3084. More significant changes are apparent with

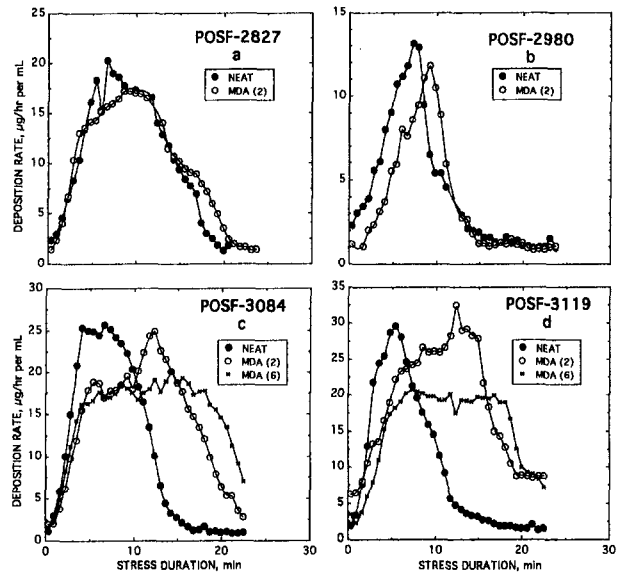

Fig. 2 Effect of MDA (2 mg/L) on surface deposition in fuels without dissolved metals (*a*, *b*) and of MDA (2 and 6 mg/L) in fuels with dissolved metals (*c*, *d*)

higher MDA concentrations in POSF-3119, although it is not clear whether the observed differences fall outside experimental reproducibility.

Autoxidation in POSF-3084 and -3119; MDA, Antioxidant, and Dispersant Used Singly and in Combination. Two candidate additives that have been identified as effective in reducing surface fouling in fuels are the antioxidant BHT (25 mg/L) and the proprietary dispersant 8Q405 (100 mg/L). In the following sections the effect of additives is assessed only for the two metal-containing fuels POSF-3084 and -3119. The impact of the three additives used singly and in all combinations containing MDA is considered, maintaining fixed individual concentrations.

The autoxidation data for POSF-3084 are given in Fig. 3. When used singly, all three additives slow autoxidation relative to the neat fuel. As discussed above, MDA introduces a delay due to metal chelation; similar delays can arise from an antioxidant because the free-radical chain-breaking mechanism of hindered phenols slows the chain-propagation rate. However, the role of a dispersant in slowing autoxidation is unknown. In a previous report (Jones et al., 1995), we noted that the dispersant 8Q405 does not slow autoxidation in fuels such as POSF-2827 and -2980 that do not contain dissolved metals but does slow autoxidation in another Cu-containing fuel, POSF-2934. This suggests that the dispersant is operating to offset the free-radical initiating effect of the dissolved copper. Interestingly, autoxidation is slowed more by the dispersant than by either the antioxidant or MDA.

Additive pairs containing MDA inhibit autoxidation more than any individual additive. Incorporation of all three additives provides the optimum slowing of autoxidation. The current data are best explained by accumulating delays in autoxidation, which are less than their summed effects.

Similar to these observations, in POSF-3119 (Fig. 4) when all three additive types are introduced singly, autoxidation is slowed relative to the neat fuel. Use of BHT in conjunction with MDA slows autoxidation relative to that in the MDA-treated fuel. As was noted for POSF-3084, incorporation of all three additives provides an antioxidant effect that is greater than any individual or pair combination but not greater than the sum of the three individual effects. The two fuels when treated with the three-additive combination behave similarly, requiring ~21–23 min for total oxygen conversion. Again, benefits accrue from the use of multicomponent additives, but the absence of overall effects greater than the sum of the individual effects indicates antagonism or overlap of additive function rather than

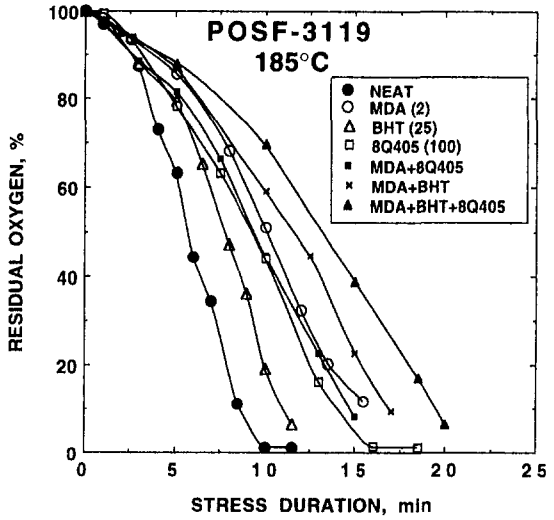

Fig. 4 Autoxidation of POSF-3119: effect of additives singly and in combination with MDA

synergism. For example, if the dispersant is functioning to cancel some of the catalytic initiation of dissolved metals, then its application with MDA will result in a competitive rather than a cooperative interaction.

Surface Deposition in POSF-3084 and -3119: MDA, Antioxidant, and Dispersant Used Singly. In order to better visualize differences resulting from the incorporation of additives and reduce overlap in the differential-rate data such as shown in Fig. 2, the deposition data are presented in the following format. The total surface carbon in each additized fuel is summed along the tube (integration under curves such as in Fig. 2) and is corrected by subtracting the corresponding sum obtained with the neat fuel. This results in the total surface carbon for each additive relative to the neat fuel; positive and negative values indicate, respectively, increased and decreased surface fouling caused by additive introduction. For example, the relative behavior upon introduction of the three individual additives is given in Figs. 5(a) and 5(b).

The two fuels behave similarly. BHT causes negligible reduction in fouling (<0.2 μg/mL) at short stress times and a pronounced increase (~2 μg/mL) for longer times. Despite the effectiveness of BHT in slowing autoxidation, its introduction does not correspondingly reduce surface deposition. Contrast the introduction of MDA, which does effectively reduce fouling for short stress times, reflecting delays in autoxidation. However, for longer stress times the situation reverses, and MDA causes the total deposition to increase relative to the neat fuels. The reasons for such reversals in surface fouling using MDA are not apparent; this is a topic of current investigation in our laboratory. Finally, the dispersant provides the greatest reduction in surface fouling for all stress times. Based upon Figs. 5(a) and 5(b), the order of the individual additives with respect to their ability to reduce surface fouling in metal-containing fuels is 8Q405 > MDA ≫ BHT.

Surface Deposition in POSF-3084 and -3119: Antioxidant and Dispersant Used in Combination With MDA. The impact of the three additives used in combination for the same two fuels is given in Figs. 5(c) and 5(d). It was previously noted that all additive combinations delay autoxidation (see Figs. 3 and 4) relative to the neat fuels. All combinations similarly reduce surface fouling relative to the neat fuels for the first 10 min of stressing. When used in pairs, MDA + 8Q405 causes the greatest reduction in surface fouling, and MDA + BHT causes the least reduction. The behavior of MDA + BHT is approximately equal to the average of the individual additive effects in improving thermal stability for short times, but the benefits disappear at higher conversion. This combination of antioxidant and MDA has been reported to improve long-term storage stability in Cu-containing diesel fuels (Golubeva et al., 1994), and it has recently been postulated that MDA is effective only when introduced at the refinery, i.e., prior to Cu exposure (Pande and Hardy, 1995). The impact of the dispersant is greater than that of the antioxidant and MDA. The combination of the three additives provides the greatest reduction in surface fouling, and this finding is consistent with the observed delays in autoxidation shown in Figs. 3 and 4. The relative order of the additive and additive combinations in their ability to reduce fouling in metal-containing fuels is MDA + BHT + 8Q405 > 8Q405 > MDA + 8Q405 > MDA ≈ MDA + BHT ≫ BHT.

Quantification of Surface and Bulk Insolubles for Complete Conversion: Additive Combinations With MDA. Additives also impact the quantity of bulk insolubles collected on in-line filters. Filtration occurs following 23–28 min of stressing; thus, quantification relates only to the condition of complete oxygen conversion. The total quantities of surface and bulk insolubles evaluated at 185°C are given in Fig. 6. Used singly, the dispersant 8Q405 exerts the greatest effect in reducing bulk and total insolubles, while neither BHT nor MDA has significant impact. Both BHT and MDA operate to slow autoxidation, the former by slowing free-radical propagation and the latter by slowing metal-catalyzed initiation; however, when fuels are evaluated based on long-term stressing, which permits all oxygen to react, i.e., completion of autoxidation and deposition, the impact of delays is negated. Dispersants operate by reducing agglomeration to keep particle size small; the current data indicate that this is an essential step for reducing bulk insolubles. Since the two filters (0.45 and 0.20 μm) are in series, the partitioning of insolubles on them provides some quantitative information concerning the dimensions of the bulk particles. The histogram in Fig. 7, giving the percentage of insolubles transmitted by the 0.45-μm filter for each additive combination, clearly indicates the impact of the dispersant in reducing particle size. POSF-3084 and -3119 exhibit the same patterns in Figs. 6 and 7, indicating that cases where surface and bulk insolubles are mitigated are coincident

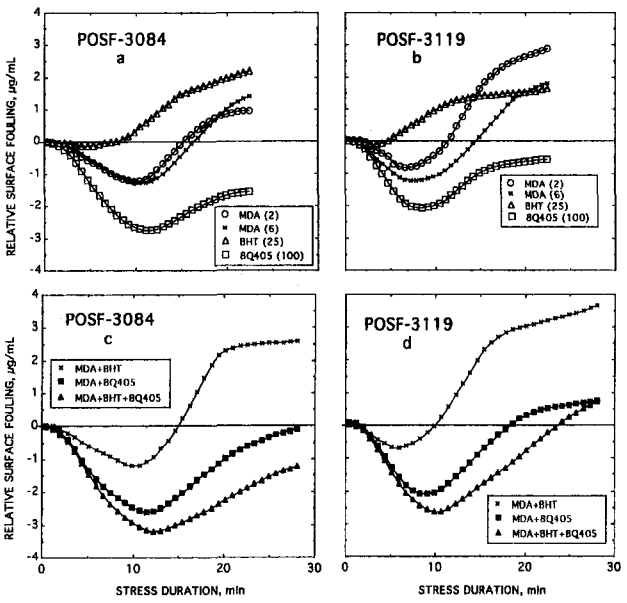

Fig. 5 Relative surface fouling in fuels with dissolved metals for additives used singly (a, b) and in combination with MDA (c, d)

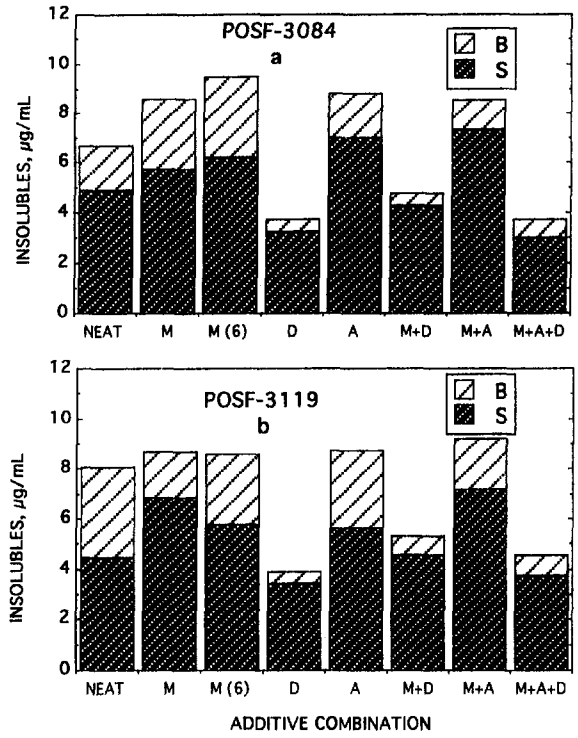

Fig. 6 Histogram of quantity of surface and bulk insolubles formed in neat and additized POSF-3084 (*a*) and -3119 (*b*) fuels evaluated for complete oxygen conversion. *M*: MDA, *D*: dispersant, *A*: antioxidant.

with cases where the size of bulk particles has been reduced. The benefit of the dispersant is apparent for both limited and complete oxygen conversion.

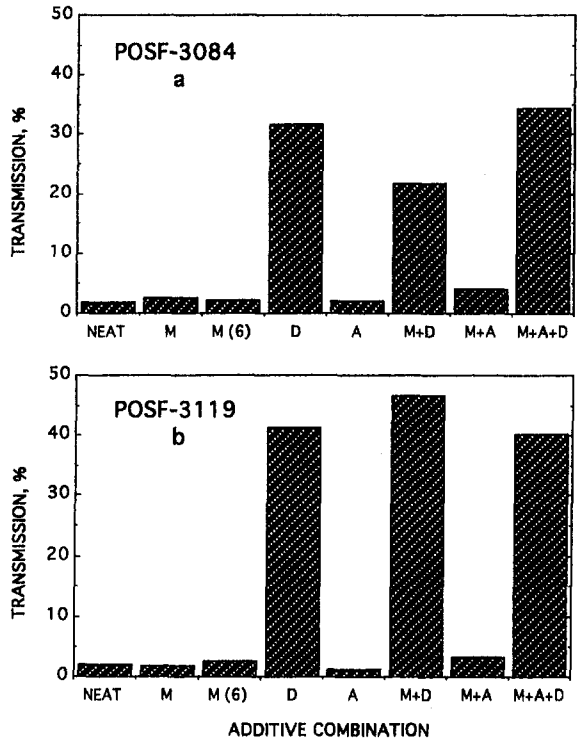

Fig. 7 Histogram showing percentage of bulk insolubles having diameters less than 0.45 μm (percent transmission through 0.45-μm filter) in neat and additized POSF-3084 (*a*) and -3119 (*b*) fuels. *M*: MDA, *D*: dispersant, *A*: antioxidant.

Summary and Conclusions

A series of experiments has been conducted using MDA along with an antioxidant and a dispersant to study their effects on the thermal stability of aviation fuels when used singly and in combination at fixed concentrations. Thermal-stability evaluation was based on dissolved-oxygen measurements to monitor autoxidation and on surface-carbon measurements to monitor the rate of surface fouling. Autoxidation occurring in three fuels containing negligible concentrations of dissolved metals is minimally altered by MDA, whereas for three fuels containing metals, autoxidation is slowed significantly; this observation is consistent with dissolved-metal chelation by MDA. Similarly, MDA causes minor changes in surface-deposition rates in two fuels without dissolved metals but delays deposition in two fuels containing dissolved metals.

In autoxidation experiments using the two metal-containing fuels POSF-3084 and -3119, it was found that (1) each additive used singly inhibited autoxidation, (2) each additive used in conjunction with MDA exerted a more pronounced effect in POSF-3084, whereas delays were less obvious in POSF-3119, and (3) the three additives used together caused the greatest inhibition of autoxidation. Dispersants are known to prevent agglomeration, but the impact of 8Q405 in slowing autoxidation suggests a second—and, possibly, more important—role of dispersants, i.e., reducing metal-catalyzed free-radical initiation.

In deposition experiments with the same fuels, differences in the total additive effect are found to be dependent on whether the evaluation is made after short or long stress times. For conditions of short stress times, with the exception of BHT, all single and multiple additive combinations reduced surface fouling. The major improvement could be traced to the dispersant and, to a lesser extent, to MDA; but the three-additive combination caused the greatest reduction. Under conditions where the fuel is stressed for long times, surface deposits are not significantly reduced; however, the quantity of bulk insolubles drops for all additive combinations containing the dispersant. These benefits are attributed to reduced agglomeration based upon partitioning of bulk insolubles on the in-line filters.

Overall, the dispersant is the dominant additive, and all combinations containing it exhibit the greatest improvement in thermal stability based on autoxidation or surface-fouling criteria. The greatest improvement in autoxidation (slowing) and in deposition (reduction) occurred with the use of the three-additive combination. This finding is ascribed not to synergism, but to a nonlinear addition of individual effects.

The current results indicate that the introduction of MDA into metal-containing fuels slows autoxidation and reduces surface fouling over short stress times at 185°C; however, reversals in surface fouling for longer stress times raise concerns for its use as a single additive. When MDA is used in conjunction with an antioxidant and dispersant, additional benefits are obtained that are attributable primarily to the dispersant.

Acknowledgments

This work was funded by Wright Laboratory, Aero Propulsion and Power Directorate, Wright-Patterson AFB, Ohio, under USAF Contract Nos. F33615-90-C-2033 (with SRL) and F33615-95-C-2507 (with ISSI). The current work was performed with the cooperation and encouragement of Mr. Steve Anderson (USAF) in his role as monitor of the JP−8 + 100 program. The authors would like to thank Mr. Tim Gootee for performing the surface-carbon analyses and Mrs. Marian Whitaker for lending editorial assistance.

References

Clark, R. H., 1988, "The Role of a Metal Deactivator in Improving the Thermal Stability of Aviation Kerosines," *Proc. 3rd International Conference on the Stability and Handling of Liquid Fuels,* Institute of Petroleum, London, U. K., pp. 283–293.

Edwards, T., Anderson, S. D., Pearce, J. A., and Harrison, W. E., III, 1992, "High Temperature Fuels—An Overview," AIAA Paper No. 92-0683.

Edwards, T., 1993, "USAF Supercritical Hydrocarbon Fuels Interests," AIAA Paper No. 93-0807.

Edwards, T., Roquemore, W. M., Harrison, W. E., III, and Anderson, S. D., 1993, "Research and Development in High Thermal Stability Fuels," Paper No. PEP-18, *AGARD Conference Proceedings 536, Fuels and Combustion Technology for Advanced Aircraft Engines,* Advisory Group for Aerospace Research and Development, Neuilly sur Seine, France.

Golubeva, I. A., Klinaeva, E. V., and Yakoviev, V. S., 1994, "Stabilization of Blended Diesel Fuels by Combinations of Antioxidants and Metal Deactivators," *Chemistry and Technology of Fuels and Oils,* Vol. 30, pp. 119–122.

Hazlett, R. N., 1991, *Thermal Oxidation Stability of Aviation Turbine Fuels,* ASTM Monograph 1, American Society for Testing and Materials, Philadelphia, Chaps. VIII and IX.

Jones, E. G., and Balster, W. J., 1993, "Phenomenological Study of Formation of Insolubles in a Jet-A Fuel," *Energy and Fuels,* Vol. 7, pp. 968–977.

Jones, E. G., and Balster, W. J., 1995, "Surface Fouling in Aviation Fuel: Short- vs. Long-Term Isothermal Tests," *Energy and Fuels,* Vol. 9, pp. 610–615.

Jones, E. G., Balster, L. M., and Balster, W. J., 1995, "Quantitative Evaluation of Jet-Fuel Fouling and the Effect of Additives," *Energy and Fuels,* Vol. 9, pp. 906–912.

Martel, C. R., 1987, "Military Jet Fuels, 1944–1987," Technical Report AFWAL-TR-87-2062, Air Force Wright Aeronautical Laboratories, Wright-Patterson Air Force Base, OH.

Mills, J. S., and Kendall, D. R., 1986, "The Quantification and Improvement of the Thermal Stability of Aviation Turbine Fuel," ASME JOURNAL OF ENGINEERING FOR GAS TURBINES AND POWER, Vol. 108, p. 381.

Morris, R. E., and Turner, N. H., 1990, "Influences Exerted by Metal Deactivator on the Thermal Stability of Aviation Fuels in the Presence of Copper," *Fuel Science and Technology International,* Vol. 8, p. 327.

Pande, S. G., and Hardy, D. G., 1995, "Effect of Copper, MDA, and Accelerated Aging on Jet Fuel Thermal Stability as Measured by the Gravimetric JFTOT," *Energy and Fuels,* Vol. 9, pp. 177–182.

Rubey, W. A., Striebich, R. C., Tissandier, M. D., Tirey, D. A., and Anderson, S. D., 1995, "Gas Chromatographic Measurement of Trace Oxygen and Other Dissolved Gases in Thermally Stressed Jet fuel," *Journal of Chromatographic Science,* Vol. 33, pp. 433–437.

Schreifels, J. A., Morris, R. E., Turner, N. H., Mowery, R. L., and Hues, S. M., 1991, "Adsorption of a Metal Deactivator Additive Onto Metal Surfaces," *Energy and Fuels,* Vol. 5, pp. 263–268.

Scott, G., 1965, *Atmospheric Oxidation and Antioxidants,* Elsevier, New York, p. 17.

Zabarnick, S., and Grinstead, R. R., 1994, "Studies of Jet Fuel Additives Using the Quartz Crystal Microbalance and Pressure Monitoring at 140°C," *Industrial and Engineering Chemistry Research,* Vol. 33, pp. 2771–2777.

Reduction of NO_x Formation by Water Sprays in Strained Two-Stage Flames

S. C. Li

N. Ilincic

F. A. Williams

Center for Energy and Combustion Research, Department of Applied Mechanics and Engineering Sciences, University of California, San Diego, La Jolla, CA 92093-0411

Staged combustion can be employed to reduce the formation of CO and NO_x, stabilize the flame, decrease the flame temperature, and create better working conditions in gas turbine combustors. To help understand influences of partial premixing and addition of water on NO_x formation, we study two-stage flames in a counterflow spray burner. This paper reports experimental and theoretical results concerning two-stage combustion in which one feed stream is composed of a fuel-rich mixture of methane and air and the other is air. Water sprays are added to the air stream. This two-phase laminar counterflow configuration exhibits a green premixed flame, a blue diffusion flame, and a vaporization plane. All three are flat and parallel. The separation distances between them decrease with increasing equivalence ratio and strain rate. Flow visualization is provided through illumination by an argon ion laser sheet, velocity fields and spray structure are measured by a phase-doppler particle analyzer, concentration fields of major stable species are measured by gas chromatography of samples withdrawn from the flame, and temperature fields are measured by a thermocouple. Numerical integrations that employ a recent chemical-kinetic data base are performed to model the flame structure and NO_x formation. Comparisons of experimental results with numerical predictions are made to test agreement. This work provides information on hydrocarbon combustion in both premixed flames and diffusion flames, indicates how NO_x is formed in fuel-rich flames, and suggests how the pollutants can be reduced.

Introduction

Staged combustion is employed in many practical applications. In some cases, staged burners are designed to reduce the emissions of CO and NO_x [1]. There are many attractive concepts for reduction of NO_x emissions from gas turbines [2]. In one promising design for aircraft gas turbines, the combustor employs a two-stage combustion mechanism [3]; there is a fuel-rich combustion stage with equivalence ratio between 1.2 and 1.8, in which abundant hydrocarbon fuel rapidly consumes oxygen, and a fuel-lean combustion stage with equivalence ratio around 0.5, in which partially burned fuel from the previous stage burns practically completely after it mixes with newly introduced hot air. The formation of pollutants can be minimized in this design, and the turbine combustor can work under less harsh conditions, since the flame temperatures are relatively low.

In order to understand combustion processes in such flames and to identify the dominant reactions that lead to NO_x formation, experiments and numerical computations are performed here for a two-stage methane flame. To provide simple boundary conditions for the numerical modeling and to study the influences of sprays on the two-stage combustion, the present study employs an axisymmetric counterflow burner in which a rich fuel–air stream from one circular duct flow against an air stream from another circular duct. The boundary conditions at the exit of each duct are well defined, and therefore comparisons between experiment and theory can be made more easily. The influences of sprays on the formation of NO_x can be studied by adding sprays to either one of the two streams without difficulty. Further advantages of the present configuration are that it affords ready access for instrumentation, that the experiments are relatively easy to perform, and that comparisons between theory and experiment are facilitated because the conservation equations are reduced to ordinary differential equations whose numerical analysis is thereby simplified.

A few experimental and computational studies of partially premixed diffusion flames for purely gaseous fuels have been performed for counterflowing streams, one fuel rich and the other fuel lean [4–6]. Because the equivalence ratio was larger than 10 in the fuel-rich stream and smaller than 0.5 in the fuel-lean stream, all reactions occured in a relatively narrow zone, so that the flame was essentially a diffusion flame. In contrast to those studies, the present study is focused on two-stage combustion in which a fuel-rich stream with equivalence ratio between 1.3 and 3.0 is directed against a spray–air stream.

In a series of experimental studies, Yamaoka and Tsuji [7–9] have investigated the structure of a rich fuel–air flame in the forward stagnation region of a porous cylinder. Their work improves understanding of two-stage combustion. Yamaoka and Tsuji indicated that, as the equivalence ratio decreases, the premixed flame approaches the porous cylinder, which results in considerable heat loss from the flame through heat conduction to the burner and radiation from it. This heat loss complicates the boundary conditions for numerical simulation. In addition, because of the porous cylinder, it is difficult to add sprays into the Tsuji burner. Therefore, this attractive geometry is not employed here.

The NO_x emission characteristics of methane–air combustion in two-stage flames of Yamaoka and Tsuji [7–9] were studied numerically by Nishioka et al. [10] who used a chemical-kinetic data base given by Miller and Bowman [11] in 1989, which included 235 steps and 52 species. The results of their numerical integrations showed that the maximum NO emission index was smaller than 1 g/kg CH_4 when the equivalence ratio was in the range of 1.5 to 3.0 with strain rates less than 50 s^{-1}. They also found that the prompt NO and thermal NO contributed almost equally to the NO emission index. Since an improved chemical-

Contributed by the International Gas Turbine Institute and presented at the 41st International Gas Turbine and Aeroengine Congress and Exhibition, Birmingham, United Kingdom, June 10–13, 1996. Manuscript received at ASME Headquarters February 1996. Paper No. 96-GT-545. Associate Technical Editor: J. N. Shinn.

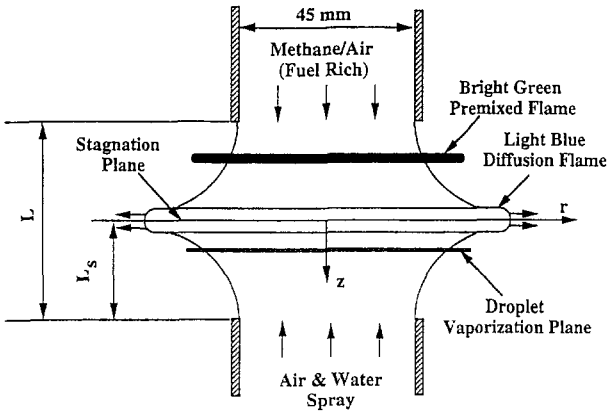

Fig. 1(*a*) Sketch of a two-stage methane–air flame in water-spray counterflowing streams

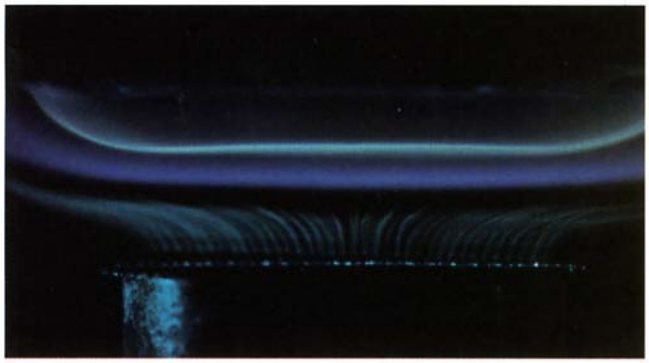

Fig. 1(*b*) A photograph of the flame sketched above

kinetic data base is now available, it is useful to see how different the results can be by using different chemical-kinetic data bases.

Experiment

Experimental Arrangement. A two-phase laminar counterflow burner is employed in the present study. As shown in Fig. 1, fuel-rich methane–air mixtures flow through the upper duct and the water spray, produced by a pressure atomizer, is carried by air through the lower duct. Both ducts have the same exit radius of 22.5 mm. The separation distance between the upper and lower ducts is $L = 18$ mm. The other details of the experimental arrangement have been described earlier [12, 13]. With this burner, a well-defined laminar two-stage flame can be obtained, as shown in the photograph in Fig. 1. Gas chromatographic analysis shows that methane is consumed in the premixed flame and produces hydrogen and carbon monoxide that burn in the diffusion flame, which is stabilized near the stagnation plane, as illustrated in the figure.

In the present experiment, the flame structure is controlled by the equivalence ratio of the methane–air mixture in the top stream and by the strain rate of the counterflowing streams. The former is determined by the ratio of Q_F, the volumetric flow rate of methane, to Q_+, the total volumetric flow rate of the methane–air mixture, while the latter is determined by both Q_+ and Q_-, the total flow rate of the air stream directed against the methane–air stream. The ratio Q_+/Q_- controls the location of the flame between the two duct exits. There are only three experimentally adjustable parameters, Q_+, Q_F, and Q_-, because the volumetric flow rate of the water spray is a function of Q_-, as discussed previously [12]. Three flowmeters are used in the present study to measure Q_+, Q_F, and Q_-. In our experiment, the ratio of Q_F/Q_+ is adjusted so that the equivalence ratio is in the range from 1.3 to 3.0. The strain rate is established in the range from 50 to 250 s^{-1} by adjusting Q_+ and Q_-. It is found experimentally that when $Q_+/Q_- \approx 1$, the light blue diffusion flame can be stabilized at a position approximately equidistant from the two duct exits, and this is the condition selected for the experiments, to minimize flame interactions with the ducts.

Experimental Diagnostics. The species H_2, O_2, N_2, CH_4, CO, CO_2, C_2H_2, C_2H_4, and C_2H_6 are measured by a Varian 3600 gas chromatograph (Varian Instrument Group) that has molecular sieve and porapak-Q columns with a thermal conductivity detector. A Varian DS-651 data system (Varian Instrument Group) is used to control the gas chromatograph and to perform the data analysis. High-purity helium is employed as the carrier gas flowing in the columns and as the reference gas. The quartz microsampling probe employed was a standard type, as described by Fristrom and Westernberg [14] and by Saito et al. [15], and it is mounted on an $r-z$ positioner to fix the probe at the desired location. The inner diameter of the probe tip is smaller than 0.1 mm. Samples are withdrawn from the flame continuously at a line pressure of 0.6 atm, monitored by an electronic pressure transducer. Since this transducer does not have room to accumulate gas, the sample volume needed in the measurement is significantly reduced, compared with a mechanical vacuum pressure gage. In the measurement, as long as the sampling line pressure is the same, the values of peak area are very repeatable for all the species except H_2O. The well-known difficulty with H_2O is due to water condensation in the sampling system and to interaction of water vapor with the material in the columns. The problem is greatest when samples are taken from the flame zone where water concentrations are high. In the data analysis, we assume that the water concentration in the flame zone is a known parameter, given by the numerical computation. Since air contains 0.932 percent argon, which elutes with oxygen, the results for oxygen are corrected to account for argon by use of the measured concentration of nitrogen.

Centerline temperature profiles in the present two-stage flame are measured by a Pt–6%Rh versus Pt–30%Rh thermocouple with a bead diameter of 135 μm. Corrections for radiation are made based on available literature [16]. Although the two-stage

Nomenclature

a = strain rate, s^{-1}
D_{23} = Sauter mean diameter
L = distance between the jet exits
L_s = separation distance between the air duct exit and the stagnation plane
M_i = molecular weight of ith species
Q_F = volumetric flow rate of methane in fuel–air stream
Q_+ = total volumetric flow rate of fuel-air stream
Q_- = total volumetric flow rate of air stream
r = radial coordinate
T = gas temperature
t = time
u = radial gas velocity
w = axial gas velocity
w_p = axial droplet velocity
X_i = mole fraction of ith species
Y_i = mass fraction of ith species
Y_W = mass fraction of water added in the air stream
z = axial coordinate
Φ = equivalence ratio of the fuel–air mixture
ρ = gas density
$\dot{\omega}_i$ = molar production rate of species i

flame is very flat over a circle with diameter equal to the diameter of the duct exit, the flame curves up at the edges because of the exhaust ventilation (see Fig. 1). When the thermocouple is positioned between the upper duct exit and the premixed flame, the curved flame outside of the duct heats the thermocouple extension, and heat conduction from the extension to the bead is not negligible so that the temperature measurement in that region becomes inaccurate. In the present paper, we therefore do not report the results of temperature measurements in that region.

Velocity fields and spray structure are measured by a two-component fiber-optical phase-doppler particle analyzer (PDPA) that has been discussed previously [13]. The probe volume formed by the laser beams of the PDPA is positioned at the desired point by moving the burner assembly axially and radially. Data on the arrival time, velocity, and diameter of droplets passing through the probe volume are then recorded by collecting about 4000 samples at each probe position.

The flame configurations are recorded by a camera, and the separation distance between the premixed and diffusion flames is measured on the photograph. A thin laser sheet is constructed by directing a 2 W argon-ion laser beam (wavelength 488 nm) through cylindrical lenses to observe the relative position of the vaporization plane of the water spray, with respect to the flame location. Trajectories of the water droplets in the spray stream, illuminated by the laser sheet, are recorded by a camera. These photographs provide useful information in interpreting the experimental results obtained by the PDPA.

Analysis of the flow-visualization and PDPA data gives droplet trajectories, droplet number densities, and evaporation rates. These experimental results, along with the measured profiles of temperature and species concentrations, can be compared with results of numerical computations.

Numerical Integrations

The numerical integrations apply to laminar flames with potential flow in the outer streams. Only the radiation from CO, CO_2, and H_2O is taken into account in the energy equation. In accounting for water addition, single-phase flow was assumed throughout the computational domain for simplicity, but the heat of vaporization of water is taken into account in the energy equation. With these assumptions, the equations of continuity, r-direction momentum, energy, and chemical species essentially reduce to those given previously [5, 6], with the air-side external strain rate a as a constant parameter. For the present problem, the boundary conditions are

$$Y_{CH_4} = Y_{CH_{4-\infty}}, \quad Y_{O_2} = Y_{O_{2-\infty}} = 4Y_{CH_{4-\infty}}/\Phi,$$

$$Y_{N_2} = Y_{N_{2-\infty}} = 3.3Y_{O_{2-\infty}}, \quad Y_i = 0, \quad \text{otherwise}$$

$$T = 298 \text{ K}, \quad \rho w = \rho_{-\infty} w_{-\infty} \quad \text{at} \quad z = -L_s;$$

$$Y_{O_2} = Y_{O_{2\infty}}, \quad Y_{N_2} = Y_{N_{2\infty}} = 3.3Y_{O_{2\infty}},$$

$$Y_{H_2O} = Y_W, \quad Y_i = 0, \quad \text{otherwise}$$

$$T = 298 \text{ K}, \quad \rho w = \rho_\infty w_\infty \quad \text{at} \quad z = L_s.$$

The present reaction mechanism consists of 140 elementary steps most of which are reversible. The rate coefficients of 55 reactions related to the C_1 and C_2 chemistry come from a recent publication (namely, reactions 1–18, 21–24, and 29–61 in Table 1 of [17]). The rate data for the other 85 reactions, related to CH, $^3CH_2$, $^1CH_2$, and NO_x formation, are essentially the same as those given in [18] but updated by Hewson and Bollig [19]. The following 38 species are involved in the chemical scheme: CH_4, O_2, CO, CO_2, H_2, H_2O, H, OH, O, HO_2, H_2O_2, CH, CHO, CHCO, $^1CH_2$, $^3CH_2$, CH_2O, CH_3, C_2H, C_2H_2, C_2H_3, C_2H_4, C_2H_5, C_2H_6, N, NH, NH_2, NH_3, NO, HNO, HCN, HNCO, NCO, CN, NO_2, N_2, N_2H, and N_2O.

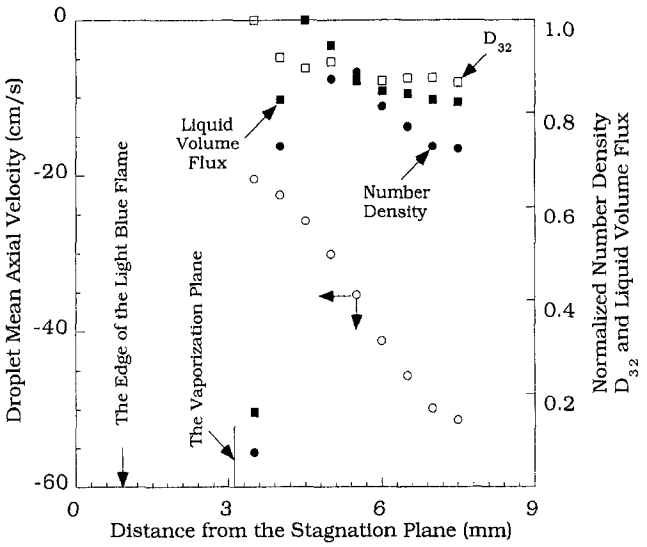

Fig. 2 Measured droplet axial velocity, number density, Sauter mean diameter, and liquid volume flux on the burner axis (the last three variables are normalized by their maximum values)

The present numerical computations are performed employing a numerical code developed at RWTH, Aachen, Germany [20]. The method of solution implemented in the code is essentially the same as in an older code [5, 6, 21]. This code was modified locally to include the effects of droplet vaporization in the energy equation. In the present paper, we report results for a strain rate of 100 s^{-1} at atmospheric pressure. The equivalence ratio is varied from $\Phi = 1.3$ to $\Phi = 3.0$. For each value of Φ, the water mass fraction Y_W in the air stream is changed from 0 to 15 percent in the calculations.

Results

Droplet Velocity and Spray Structure. Experimentally, the stagnation plane is always located in the light blue region of the diffusion flame when Φ is in the range from 1.3 to 3.0 and the strain rate is in the range from 50 to 250 s^{-1}, although the stagnation plane may not completely coincide with the center of the blue region. For convenience, the light blue diffusion flame is set in the center plane between two exits by adjusting Q_- and the stagnation plane can be assumed to be nearly midway between the duct exits. As shown in Fig. 1, the origin of the $z - r$ coordinates is at the center of the stagnation plane, with $z = L_s$ at the air-spray exit and $z = -L_s$ at the methane–air exit. In this coordinate system, particles moving upward have negative velocity and vice versa.

Different initial flow conditions are studied to obtain different strain rates in the counterflow streams, but in the present paper the main condition discussed has $Q_+ = 870$ cm^3/s and $Q_- = 850$ cm^3/s. The local strain rates on the burner axis are determined based on the PDPA measurement. We first plot the measured axial velocity as a function of the coordinate z and fit a curve to the data to define the air-side strain rates as $a = -dw/dz$. With the flow condition given here, $a = 100$ s^{-1}.

Figure 2 shows the spray structure for an equivalence ratio of 1.4. For convenience, the number density, Sauter mean diameter and liquid volume flux are normalized by 18800 cm^{-3}, 38 μm, and 0.0035 cm^3/cm^2-s, respectively. The axial velocity w_p is shown as open circles, while other symbols represent normalized number density, Sauter mean diameter, and liquid volume flux. The results in this figure are what one would expect for counterflow streams with the flame present. The Sauter mean diameter becomes larger in the neighborhood of the vaporization plane because smaller droplets move away from the stagna-

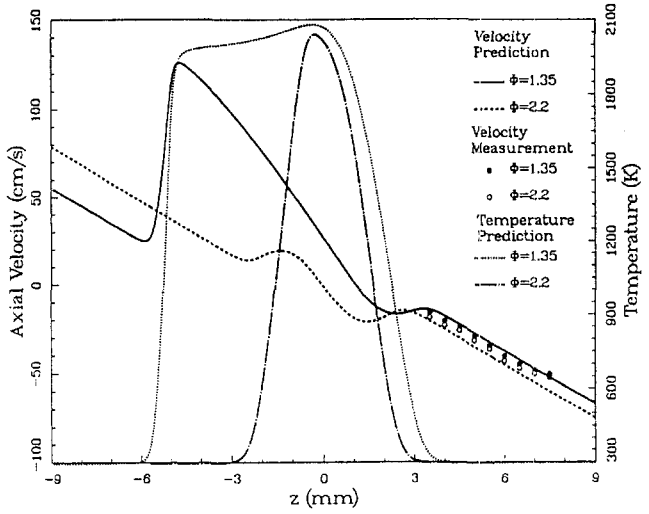

Fig. 3 Comparison between measurement and prediction of profiles of axial velocity

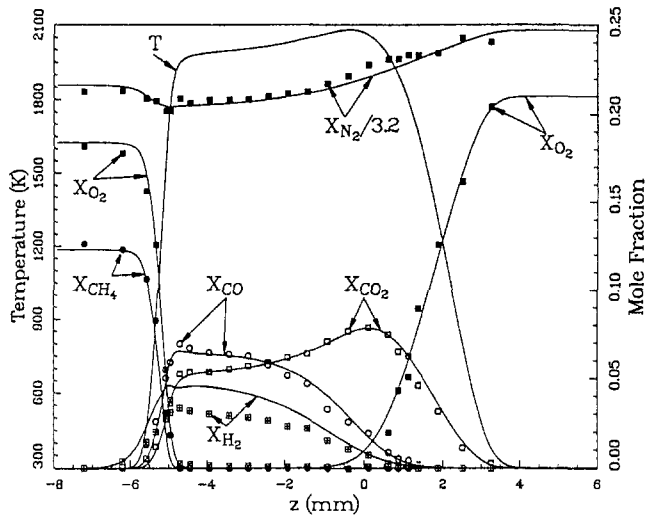

Fig. 5(a) Comparison between measurement and prediction for concentration profiles for Φ = 1.35 without water

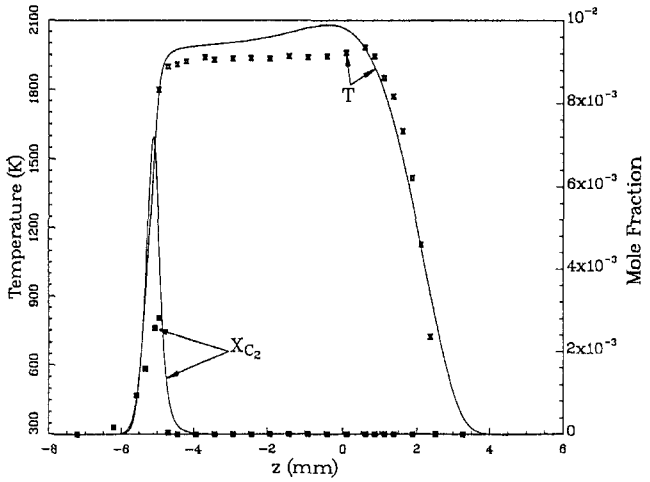

Fig. 5(b) Comparison between measurement and prediction for profiles of temperature and of the sum of the mole fractions of C_2H_2, C_2H_4, and C_2H_6 for Φ = 1.35 without water

tion streamline in the radial direction more easily and vaporize faster.

Figure 3 compares the profiles of axial velocity for a strain rate of 100 s^{-1}. The points are measured mean axial velocities of droplets smaller than 5 μm, which we take as a measure of the gas velocity, since small droplets are expected to follow the gas. To assist in understanding how the flame affects the velocity field, the predicted temperature profiles are plotted in the figure as well. Agreement is good where data exist. Where droplets are absent, the computed velocity profiles differ considerably for the two values of Φ.

Flame Structure. The separation distance between the premixed flame and the diffusion flame at a given strain rate depends strongly on Φ. Figure 4 illustrates how the measured distance between the two flames changes with changing equivalence ratio. It indicates that the separation distance increases with decreasing Φ. Figure 4 also indicates the predicted distances between the concentration peaks of OH and C_2H_4 and those of OH and CH. It shows that the former is larger than the latter although they become nearly equal for $\Phi < 1.5$. The measured distance is closer to the predicted distance between

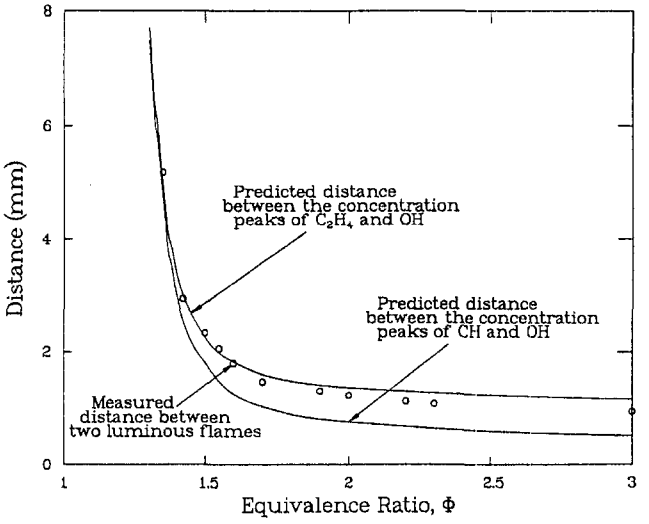

Fig. 4 Comparison of measured distance between two luminous flames with predicted distances between the concentration peaks of CH and OH and of C_2H_4 and OH

the concentration peaks of OH and C_2H_4, suggesting that the green emissions come not from CH but rather from species involved in C_2H_4 formation.

Figures 5(*a*) and 5(*b*) for Φ = 1.35 and Figs. 6(*a*) and 6(*b*) for Φ = 2.20 show profiles of temperature measured by thermocouple and concentrations measured by gas chromatography. The agreement between experiment and numerical computation is very good for temperature and for most of the species measured. There is some quantitative disagreement between experiment and theoretical prediction for X_{H_2} in Fig. 5(*a*), but even these agree within better than a factor of two.

We see from Fig. 5 that methane and oxygen in the rich mixture react very rapidly to form CO and H_2, and X_{CO} and X_{H_2} reach maxima as X_{CH_4} becomes zero. The further oxidation of CO and H_2 to form CO_2 and H_2O occurs in the diffusion flame. The C_2 species, such as C_2H_2, C_2H_4, and C_2H_6 are produced rapidly as CH_4 disappears. However, these species have very short lives, and they cannot be found experimentally in the diffusion flame in Fig. 5. Figures 5(*b*) and 6(*b*) clearly show that the concentrations of C_2 species strongly depend on the equivalence ratio; the richer the flame is, the higher is the concentration of C_2 species, consistent with observed soot emissions in fuel-rich methane–air flames. Since the computations here overpredict X_{C_2}, the reaction mechanism needs some revision to be consistent with the experimental results.

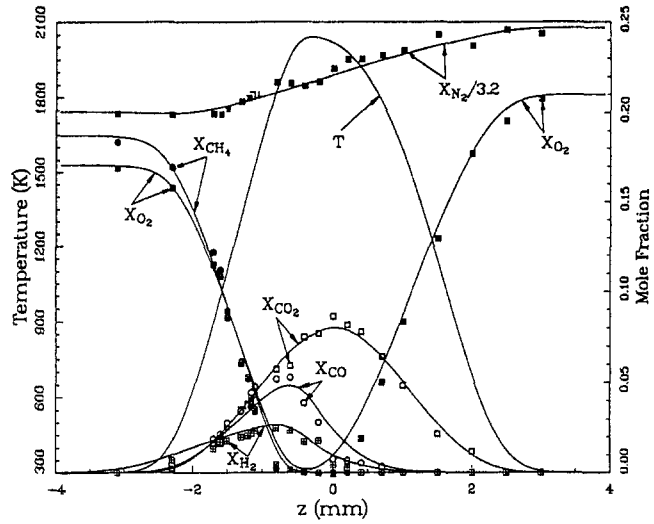

Fig. 6(*a*) Comparison between measurement and prediction for concentration profiles for $\Phi = 2.20$ without water

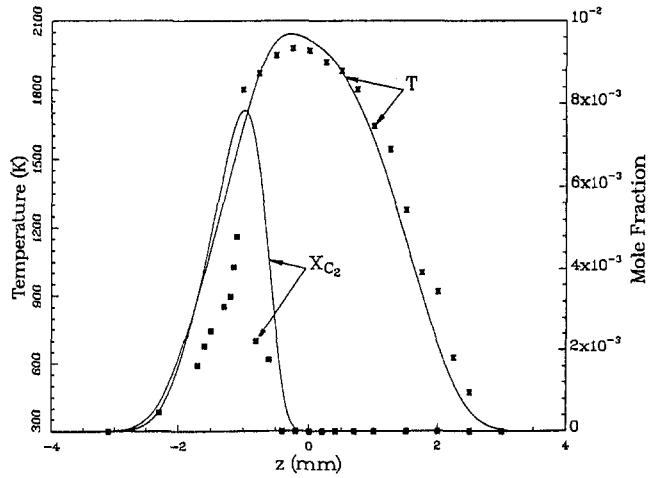

Fig. 6(*b*) Comparison between measurement and prediction for profiles of temperature and of the sum of the mole fractions of C_2H_2, C_2H_4, and C_2H_6 for $\Phi = 2.20$ without water

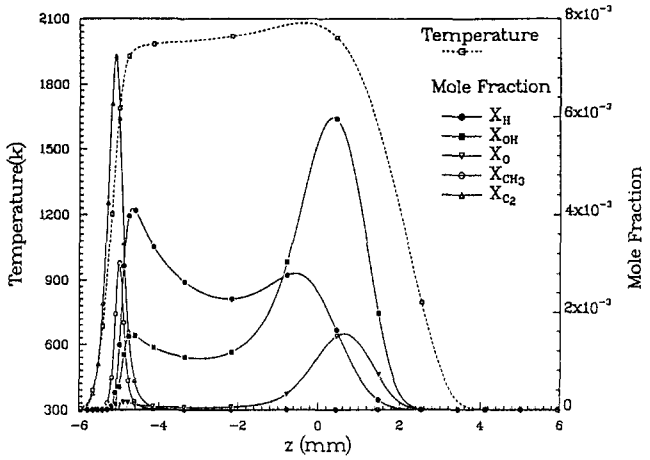

Fig. 7(*a*) Predicted profiles of temperature and radical concentration for $\Phi = 1.35$

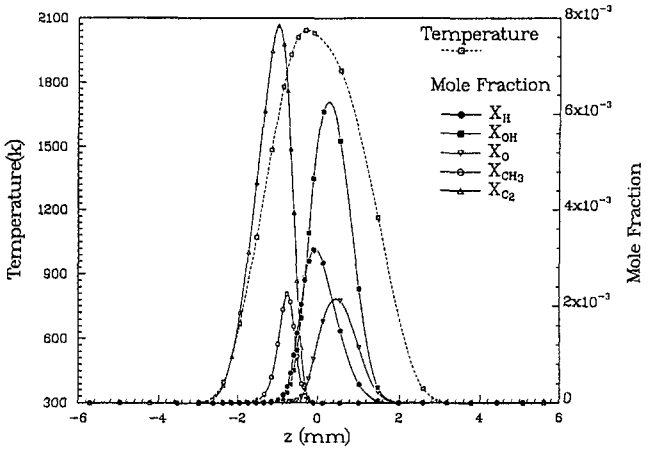

Fig. 7(*b*) Predicted profiles of temperature and radical concentration for $\Phi = 2.20$

Since radicals such as H, OH, and O play dominant roles in hydrocarbon flames, knowledge of their distributions in the flame should help in understanding flame structure and NO_x formation. Figures 7(*a*) and 7(*b*) show predicted profiles of concentrations of H, OH, and O, for $\Phi = 1.35$ and 2.20, respectively. The separation of peaks for $\Phi = 1.35$ means that two flames are present, while for $\Phi = 2.20$ they have merged into one. To give further information on minor fuel species, X_{CH_3} and and X_{C_2}, which includes C_2H_2, C_2H_4 and C_2H_6, are also plotted. Both peak in the premixed flame. It is found that the maximum concentrations of CH_3, $^3CH_2$, $^1CH_2$, and CH are of order 10^{-3}, 10^{-5}, 10^{-6} and 10^{-6}, respectively, while those of C_2H_2, C_2H_4, C_2H_6, C_2H_5, C_2H_3, and C_2H are of order 5×10^{-3}, 2×10^{-3}, 2×10^{-3}, 10^{-5}, 10^{-5}, and 10^{-6}, respectively.

Influence of Water Addition on NO_x Formation

Influence of Water Addition on the Prompt Mechanism. Since the prompt NO formation begins with the reaction $CH + N_2 \rightleftharpoons HCN + N$ as found by Fenimore [22], it is helpful to understand how the species in this reaction are distributed in the flame zone and how the temperature and water concentration affect them. Figures 8(*a*), 9(*a*), and 10(*a*) show concentration profiles of CH, N, and HCN without water added, respectively, while Figs. 8(*b*), 9(*b*), and 10(*b*) show distributions of these species with $Y_W = 10$ percent water added in the air stream. In these figures, Φ changes from 1.35 to 3.00, and profiles of temperature corresponding to each Φ are also plotted for reference.

According to Fig. 8(*a*), without water, the peak concentration of CH is high at $\Phi = 1.35$, decreases to its lowest value at $\Phi = 1.5$, then increases to a large value at $\Phi = 3.0$. As shown in Fig. 8(*b*), the water addition in the air stream significantly reduces the CH concentration when Φ is larger than 1.7 but has little influence on CH when Φ is smaller than 1.55. It is found that the concentrations of CH are directly controlled by the reactions

$$1 \quad CH + H_2O \rightleftharpoons CH_2O + H$$

$$2 \quad CH + O_2 \rightleftharpoons CHO + O$$

$$3 \quad CH + CO_2 \rightleftharpoons CHO + CO$$

$$4 \quad {}^3CH_2 + H \rightleftharpoons CH + H_2$$

$$5 \quad {}^3CH_2 + OH \rightleftharpoons CH + H_2O$$

where the first three consume CH and the last two produce it. It is clear that when the premixed flame is close to the diffusion flame ($\Phi \geq 1.7$), the CH production can be slowed significantly by increasing water concentration in the air stream. When the premixed flame is far from the stagnation plane, the water added in the air stream cannot reach the region where CH is produced. As expected, the reaction $CH + N_2 \rightleftharpoons HCN + N$ is unimportant

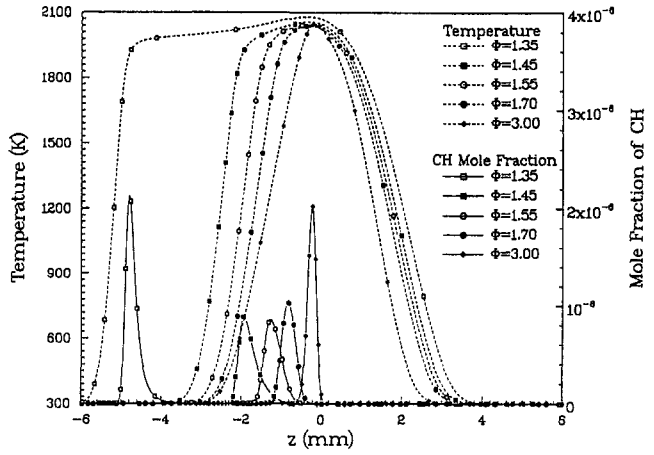

Fig. 8(*a*) Predicted profiles of temperature and CH concentration without water

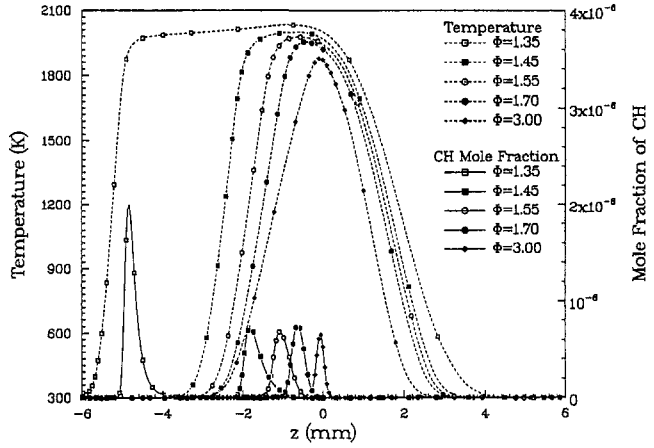

Fig. 8(*b*) Predicted profiles of temperature and CH concentration with 10 percent water added in air stream

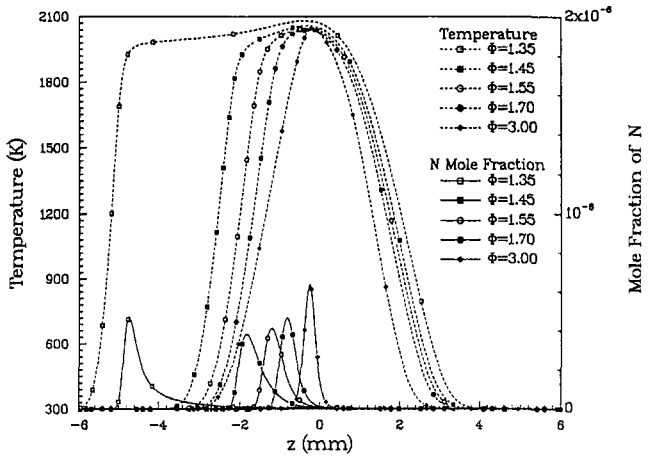

Fig. 9(*a*) Computed profiles of temperature and N concentration without water

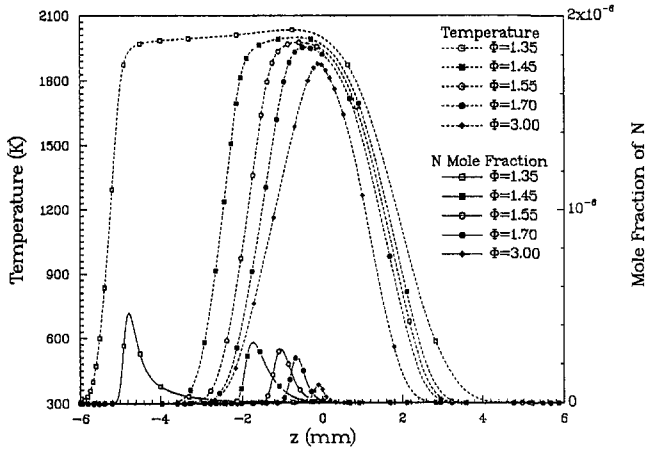

Fig. 9(*b*) Computed profiles of temperature and N concentration with 10 percent water added in air stream

for the CH concentration because it is much slower than reactions 1 to 3.

When Φ is relatively high, water addition in the air stream seems to greatly reduce the concentration of the radical N, as illustrated in Figs. 9(*a*) and 9(*b*). For example, with $\Phi = 3.0$, the maximum value of X_N is about 10^{-7} with water addition, while it is about 6×10^{-7} without water addition. Of importance for N are

$$6 \quad N_2 + CH \rightleftharpoons N + HCN$$

$$7 \quad NH + H \rightleftharpoons N + H_2$$

$$8 \quad NH + OH \rightleftharpoons N + H_2O$$

$$9 \quad NCO + M \rightleftharpoons N + CO + M$$

$$10 \quad N + OH \rightleftharpoons NO + H$$

$$11 \quad N + O_2 \rightleftharpoons NO + O$$

where reactions 6 through 9 produce N, while 10 and 11 consume it. The calculations show that reaction 6 contributes most to the production of N, while reaction 10 is much faster than reactions 11 in consuming N. Reaction 6 slows down when X_{CH} decreases. From these discussions, we can see that most of the N produced here comes from the prompt mechanism.

The species HCN is an important intermediate in NO_x production. As indicated in Figs. 10(*a*) and 10(*b*), its concentration strongly depends on the flame structure and water addition in the air stream. Reactions for X_{HCN} are

$$6 \quad N_2 + CH \rightleftharpoons N + HCN$$

$$12 \quad NO + CH \rightleftharpoons O + HCN$$

$$13 \quad HCN + O \rightleftharpoons NCO + H$$

$$14 \quad HCN + H \rightleftharpoons CN + H_2.$$

The HCN is produced by the first two reactions and is consumed by the last two. At lower equivalence ratios, reaction 6 plays a more important role in the production of HCN, while 12 is more important at high equivalence ratios. Water addition reduces HCN by reducing CH concentrations in both reactions 6 and 12. Whether HCN yields NO or N_2 depends on the oxidation of NCO and CN.

Influence of Water Addition on the Emission Index. The NO emission index by reaction j is defined as

$$E_j = \frac{\int_{-L_s}^{L_s} M_{NO}\dot{\omega}_{NO_j} dz}{-\int_{-L_s}^{L_s} M_{CH_4}\dot{\omega}_{CH_4} dz},$$

where $-\dot{\omega}_{CH_4}$ is the total consumption rate of methane. The total NO emission index is defined by

$$E = \Sigma_j E_j.$$

According to these definitions, some of the E_j are negative, describing "reburn" of NO.

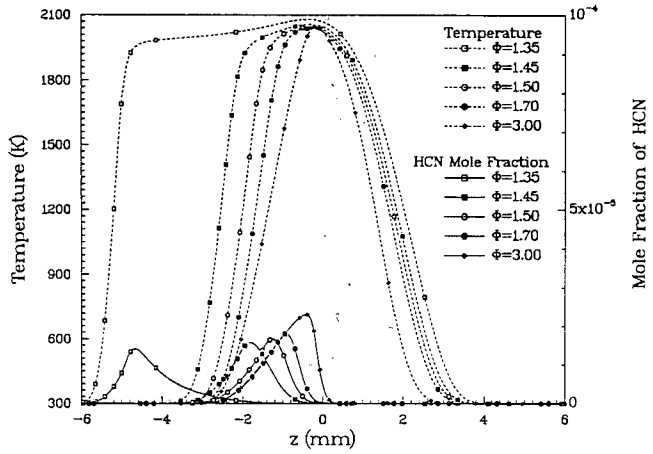

Fig. 10(*a*) Computed profiles of temperature and HCN concentration without water

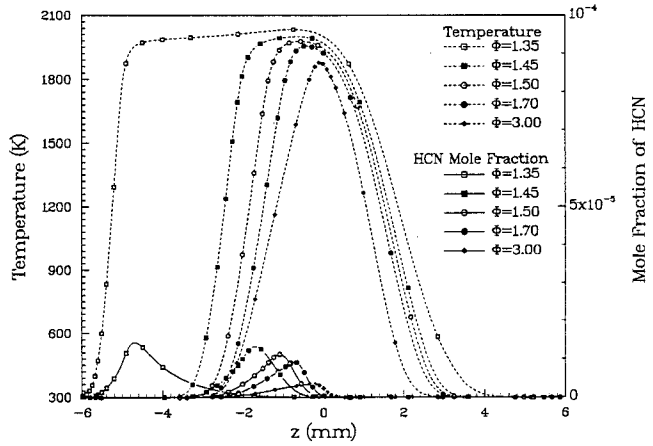

Fig. 10(*b*) Computed profiles of temperature and HCN concentration with 10 percent water added in air stream

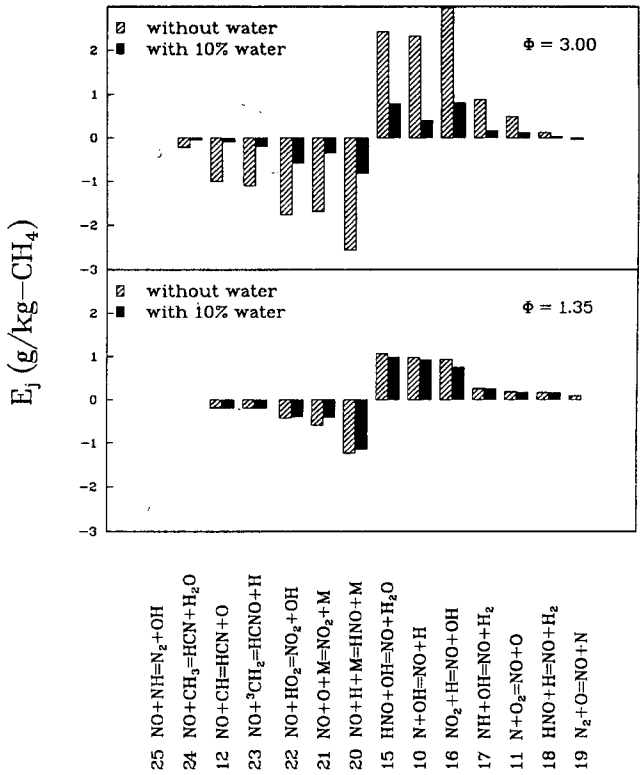

Fig. 11 Contributions to NO emission index from various reactions

Figure 11 illustrates the emission index E_j contributed by various reactions. Several conclusions are suggested from this figure. First, NO formation is dominated by the prompt mechanism, since the thermal NO reactions 11 and 19 are not important and since the N atom in reaction 10 is mainly produced by the reaction CH + N_2 ⇌ HCN + N, as discussed previously. Second, E_j for a specific reaction j may be much higher than E because of NO consumption. For instance, E_{16}, is about 3 g/kg CH_4, while E is only 1.8 g/kg CH_4 for $\Phi = 3.0$ without water addition. This suggests strategies for reducing the NO_x formation by slowing down the reactions that contribute most to NO formation. Third, water addition in the air stream can greatly affect E at large Φ.

The role of water addition in reducing the emission index can be understood by studying Figs. 12(*a*) and 12(*b*). Comparison can be made between profiles of X_{NO} without water added, as shown in Fig. 12(*a*), and those with water added in the air streams, as shown in Fig. 12(*b*). We see that concentrations of NO increase with increasing Φ without added water, and the concentration peaks become substantially smaller when water is added. Results in these two figures indicate that the NO formation strongly depends on the flame structure and on the water concentration in the flame.

Figure 13 plots the predicted E as a function of Φ and Y_W at a strain rate of 100 s^{-1}. It can be seen that when $Y_W = 0$, E decreases slightly and then increases as Φ increases from 1.36 to 3.00. As Y_W increases, E decreases, and the water addition is always more effective in reducing NO_x when Φ is large.

The NO_x emission index is very sensitive to the rate parameters for the reaction CH + N_2 → HCN + N. The most direct determination of those parameters is the shock-tube study of Dean et al. [23] and from the experimental results, the rate constant is found to be $k = 4.4 \times 10^{12} \exp(-11072/T)$ cm^3/mole-s. With this rate, the NO_x emission predicted by the present study is higher than that predicted by Nishioka et al. [10], who used a lower rate constant. Measurements of NO_x in these flames would be desirable to test these predictions.

Conclusions

Well-defined two-stage flames in counterflowing streams have been employed in testing a chemical-kinetic data base for H-C-N-O combustion systems recently published. Agreement between measured and predicted profiles of temperature and CO, CO_2, CH_4, and O_2 is very good. The present computation overpredicts the concentrations profiles of C_2H_2, C_2H_4 and C_2H_6 and thus suggests that the reaction mechanism needs to be revised in the future. Flame visualization and PDPA measurements indicate that water droplets in the air-spray stream very rapidly disappear through vaporization at the vaporization plane, which is close to the diffusion flame. The water vapor from the spray helps to increase the water concentration in flame zone. Numerical computations reveal that prompt NO in the present two-stage counterflow combustion plays a dominant role in NO_x formation and that the NO_x emission index strongly depends on the flame structure and on the mass fraction of water added in the air stream. The NO_x emission index can be substantially reduced by adding water to remove CH.

Acknowledgments

We are indebted to R. X. Zang and W. Willemse of UCSD for helping with experimental measurement and to M. Bollig of RWTH, Aachen, Germany, for helping with numerical computation. This research was supported by the Department of

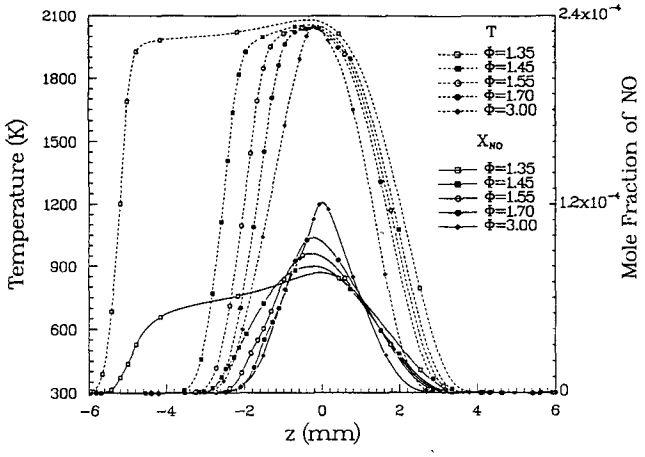

Fig. 12(*a*) Computed profiles of temperature and NO concentration without water

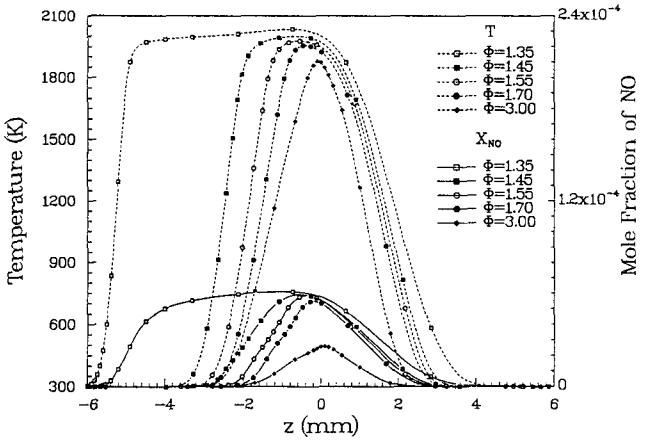

Fig. 12(*b*) Computed profiles of temperature and NO concentration with 10 percent water added in air stream

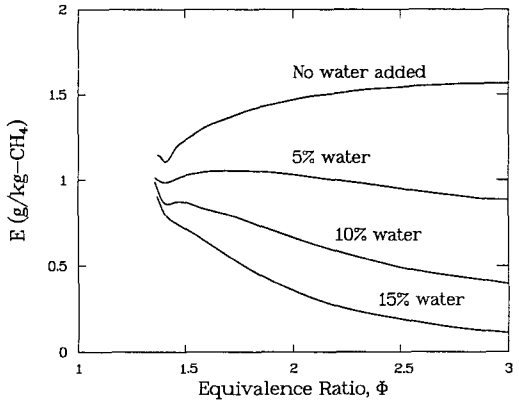

Fig. 13 Predicted NO emission index as a function of equivalence ratio and mass percentage of water added to the air stream

Energy, Office of Basic Energy Sciences, Division of Engineering and Geosciences under contract No. DE-F003-87ER13685.

References

1 Yamagishi, K., Nozawa, M., Yoshie, T., Tokumoto, T., and Kakegawa, Y., "A Study of NO_x Emission Characteristics in Two Stage Combustion," *Fifteenth Symposium (International) on Combustion,* The Combustion Institute, Pittsburgh, 1975, pp. 1157–1166.

2 Becker, B., Berenbrink, P., and Brandner, H., "Premixing Gas and Air to Reduce NO_x Emissions With Existing Proven Gas Turbine Combustion Chambers," Paper No. B-9, presented at the International Gas Turbine Conference and Exhibit, Dusseldorf, West Germany, June 8–12, 1986.

3 Howe, G. W., Li, Z., Shih, T. I-P., and Nguyen, H. L., "Simulation of Mixing in the Quick Quench Region of a Rich Burn-Quick Quench Mix-Lean Burn Combustor," AIAA Paper No. 91-0410, Jan. 1991.

4 Seshadri, K., Puri, I. K., and Peters, N., "Experimental and Theoretical Investigation of Partially Premixed Diffusion Flames at Extinction," *Combustion and Flame,* Vol. 61, 1985, pp. 237–249.

5 Smooke, M. D., Seshadri, K., and Puri, I. K., "The Structure and Extinction of Partially Premixed Flames Burning Methane in Air," *Twenty-Second Symposium (International) on Combustion,* The Combustion Institute, Pittsburgh, 1988, pp. 1555–1563.

6 Smooke, M. D., Crump, J., Seshadri, K., and Giovangigli, V., "Comparison Between Experimental Measurements and Numerical Calculations of the Structure of Counterflow, Diluted, Methane–Air, Premixed Flames," *Twenty-Third Symposium (International) on Combustion,* The Combustion Institute, Pittsburgh, 1990, pp. 463–470.

7 Yamaoka, I., and Tsuji, H., "The Structure of Rich Fuel-Air Flames in the Forward Stagnation Region of a Porous Cylinder," *Fifteenth Symposium (International) on Combustion,* The Combustion Institute, Pittsburgh, 1975, pp. 637–644.

8 Yamaoka, I., and Tsuji, H., "Structure Analysis of Rich Fuel–Air Flames in the Forward Stagnation Region of a Porous Cylinder," *Sixteenth Symposium (International) on Combustion,* The Combustion Institute, Pittsburgh, 1977, pp. 1145–1154.

9 Yamaoka, I., and Tsuji, H., "An Experimental Study of Flammability Limits Using Counterflow Flames," *Seventeenth Symposium (International) on Combustion,* The Combustion Institute, Pittsburgh, 1979, pp. 843–855.

10 Nishioka, M., Nakagawa, S., Ishikawa, Y., and Takeno, T., "NO Emission Characteristics of Methane–Air Double Flame," *Combustion and Flame,* Vol. 98, 1994, pp. 127–138.

11 Miller, J. A., and Bowman, C. T., "Mechanism and Modeling of Nitrogen Chemistry in Combustion," *Prog. Energy Combust. Sci.,* Vol. 15, 1989, pp. 287–338.

12 Li, S. C., Libby, P. A., and Williams, F. A., "Experimental and Theoretical Studies of Counterflow Spray Diffusion Flames," *Twenty-Fifth Symposium (International) on Combustion,* The Combustion Institute, Pittsburgh, 1992, pp. 1503–1512.

13 Li, S. C., Libby, P. A., and Williams, F. A., "Spray Structure in Counterflowing Streams With and Without a Flame," *Combustion and Flame,* Vol. 94, pp. 1993, 161–177.

14 Fristrom, R. M., and Westernberg, A. A., *Flame Structure,* McGraw-Hill, New York, 1965.

15 Saito, K., Williams, F. A., and Gordon, A. S., "Structure of Laminar Coflow Methane–Air Diffusion Flames," ASME *Journal of Heat Transfer,* Vol. 108, 1986, p. 640.

16 Sato, A., Hashiba, K., Hasatani, M., Sugiyama, S., and Kimura, J., "A Correctional Calculation Method for Thermocouple Measurements of Temperatures in Flames," *Combustion and Flame,* Vol. 24, 1975, pp. 35–41.

17 Peters, N., "Flame Calculations With Reduced Mechanism—an Outline," in: *Reduced Kinetic Mechanisms for Applications in Combustion Systems,* N. Peters and B. Rogg, eds., Spinger-Verlag, Berlin, 1993, pp. 3–13.

18 Bockhorn, H., Chevalier, C., Warnatz, J., and Weyrauch, V., "Experimental Investigation and Modeling of Prompt-NO Formation in Hydrocarbon Flames," in: *Heat Transfer in Fire and Combustion Systems,* ASME HTD-Vol. 166, 1991, pp. 11–16.

19 Hewson, J. C., and Bollig, M., "Reduced Mechanisms for NO_x Emissions From Hydrocarbon Diffusion Flames," *Twenty-Sixth Symposium (International) on Combustion,* The Combustion Institute, Pittsburgh, 1996, pp. 2171–2179.

20 Pitsch, H., "Entwicklug eines Programmpaketes zur Berechnung eindimensionaler Flammen am Beispiel einer Gegenstomdiffusionsflamme," Master's thesis, RWTH Aachen, Germany, 1993.

21 Smooke, M. D., Miller, J. A., and Kee, R. J., "Solution of Premixed and Counterflow Diffusion Flame Problems by Adaptive Boundary Value Methods," *Numerical Boundary Value ODEs,* U. M. Ascher and R. D. Russel, eds., Birkhöuser Boston, Inc., 1985, pp. 303–317.

22 Fenimore, C. P., "Formation of Nitric Oxide in Premixed Hydrocarbon Flames," *Thirteenth International Symposium on Combustion,* The Combustion Institute, Pittsburgh, 1971, pp. 373–379.

23 Dean, A. J., Davidson, D. F., Hanson, R. K., and Bowman, C. T., "Development and Application of CH Laser Absorption Diagnostic for Shock Tube Kinetic Studies," presented at the Western States Section/Combustion Institute Meeting, Paper No. 88-91, 1988.

Development of a Catalytic Combustor for a Heavy-Duty Utility Gas Turbine

R. A. Dalla Betta

J. C. Schlatter

S. G. Nickolas

Catalytica Inc.,
Mountain View, CA 94043

M. B. Cutrone

K. W. Beebe

General Electric Co.,
Schenectady, NY 12345

Y. Furuse

T. Tsuchiya

Tokyo Electric Power Co.,
Yokohama, Japan

The most effective technologies currently available for controlling NO_x emissions from heavy-duty industrial gas turbines are diluent injection in the combustor reaction zone, and lean premixed Dry Low NO_x (DLN) combustion. For ultralow emissions requirements, these must be combined with selective catalytic reduction (SCR) $DeNO_x$ systems in the gas turbine exhaust. An alternative technology for achieving comparable emissions levels with the potential for lower capital investment and operating cost is catalytic combustion of lean premixed fuel and air within the gas turbine. The design of a catalytic combustion system using natural gas fuel has been prepared for the GE model MS9OOIE gas turbine. This machine has a turbine inlet temperature to the first rotating stage of over 1100°C and produces approximately 105 MW electrical output in simple cycle operation. The 508-mm-dia catalytic combustor designed for this gas turbine was operated at full-scale conditions in tests conducted in 1992 and 1994. The combustor was operated for twelve hours during the 1994 test and demonstrated very low NO_x emissions from the catalytic reactor. The total exhaust NO_x level was approximately 12–15 ppmv and was produced almost entirely in the preburner ahead of the reactor. A small quantity of steam injected into the preburner reduced the NO_x emissions to 5–6 ppmv. Development of the combustion system has continued with the objectives of reducing CO and UHC emissions, understanding the parameters affecting reactor stability and spatial nonuniformities that were observed at low inlet temperature, and improving the structural integrity of the reactor system to a level required for commercial operation of gas turbines. Design modifications were completed and combustion hardware was fabricated for additional full-scale tests of the catalytic combustion system in March 1995 and January 1996. This paper presents a discussion of the combustor design, the catalytic reactor design, and the results of full-scale testing of the improved combustor at MS9OO1E cycle conditions in the March 1995 and January 1996 tests. Major improvements in performance were achieved with CO and UHC emissions of 10 ppmv and 0 ppmv at baseload conditions. This ongoing program will lead to two additional full-scale combustion system tests in 1996. The results of these tests will be available for discussion at the June 1996 Conference in Birmingham.

Introduction

Trends in environmental regulations are necessitating use of clean burning fuels (particularly natural gas), advanced gas turbine combustion systems, which reduce the amount of NO_x formed during the combustion process and, where emissions regulations are at the single-digit NO_x levels, use of Selective Catalytic Reduction (SCR) of the NO_x in the gas turbine exhaust. An example is California, where NO_x levels of newly constructed combined cycle plants are regulated to as low as 5 ppm (at 15 percent O2).

Consequently, the incentive now exists for development of a new generation of combustion systems capable of meeting NO_x emissions levels of approximately 3–5 ppm, directly within the turbine, without recourse to downstream denitrification by SCR in the turbine exhaust. This new generation of combustion systems should be suitable for turbines firing at today's turbine inlet temperatures of approximately 1290°C (at the inlet of the first-stage rotor), with growth potential to the next generation of turbines expected to fire at approximately 1427°C. The costs associated with heat rate deterioration due to diluent injection, combined with capital and operating costs required for SCR systems, provide substantial economic incentive to develop ultralow NO_x combustion systems for application to combined cycle and cogeneration power plants incorporating gas turbines.

Direct catalytic combustion has significant potential, as demonstrated by tests performed at GE for natural gas fuel with very low emissions of NO_x, CO, and UHC. A promising concept for the catalytic combustion of natural gas has been developed by Catalytica/Tanaka Kikinzoku Kogyo K.K. In general terms, the design involves partially reacting the fuel–air mixture within the catalytic reactor to generate a gas temperature of about 800–1000°C at the reactor exit. The full adiabatic flame temperature is reached downstream of the reactor exit via homogeneous gas phase reactions. Due to the relatively low temperatures maintained in the reactor (<1000°C), the catalyst can include precious metals, and the substrate may be cordierite or metal. Low emissions (i.e., high combustion efficiency) have resulted when the temperature of the gas exiting the reactor was above ~980°C and the peak combustor discharge temperature was above ~1180°C. The concept has successfully demonstrated meeting emissions goals by both GE and Catalytica at reactor subscale sizes up to 75 mm (3 in.) in diameter. Most recently, GE has developed a full-scale catalytic combustor system for its MS9001E gas turbine (firing at 1105°C turbine inlet temperature). The combustor incorporates a 508 mm (20 in.) diameter catalytic reactor designed and manufactured by Catalytica.

Contributed by the International Gas Turbine Institute and presented at the 41st International Gas Turbine and Aeroengine Congress and Exhibition, Birmingham, United Kingdom, June 10–13, 1996. Manuscript received at ASME Headquarters February 1996. Paper No. 96-GT-485. Associate Technical Editor: J. N. Shinn.

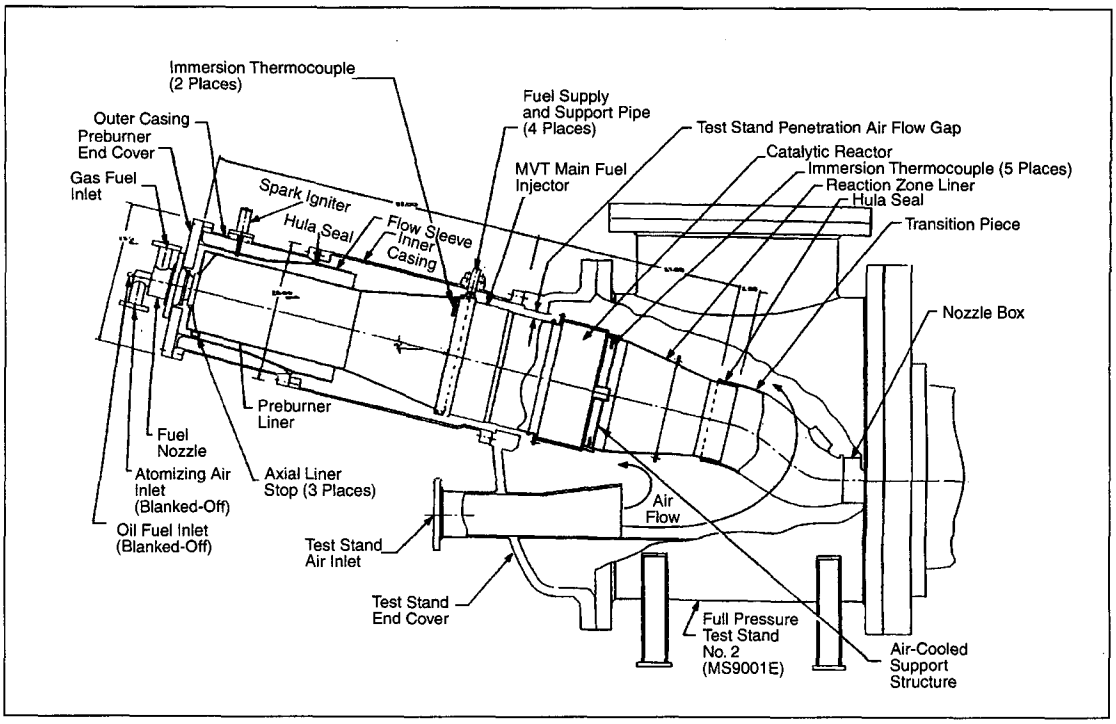

Fig. 1 Catalytic combustion test rig for full-pressure Test 1 in March 1995

Combustor Design for Test 1 in March 1995

The catalytic combustion system design for the March 1995 Test 1 is shown in Fig. 1. There are four major subassemblies in the total combustion system: the preburner, the fuel–air preparation system, the catalytic reactor, and the post reactor combustion liner.

The purpose of the preburner is to carry the machine load at operating conditions that yield catalytic reactor inlet temperature and temperature rise too low for satisfactory catalytic combustion. The preburner also provides the necessary preheat to achieve catalytic reactor ignition and to sustain catalytic combustion at full-load, design point conditions. The preburner is designed to operate from machine ignition up to a firing temperature (turbine inlet temperature) of approximately 700°C, which is designed as the start of catalytic staging. At this operating condition, the main fuel injector is fueled and ignition occurs in the catalytic reactor bed. From a machine firing temperature of 700°C to full-load firing temperature of 1105°C (combustor exit temperature 1180°C), fuel flow to the main fuel injector is continuously ramped up while fuel flow to the preburner is ramped down. In order to minimize NO_x emissions, the preburner will be operated at the minimum temperature rise necessary to maintain a fully active catalytic reactor. Prior investigations by Dalla Betta et al. (1994) at reduced scale have indicated that the minimum catalyst inlet temperature required at baseload conditions is 450°C, which would be obtained at a preburner temperature rise under 150°C.

The purpose of the fuel–air preparation system is to provide a mixture of fuel and air, or fuel and preburner products of combustion, to the catalytic reactor bed inlet with uniform distribution of mixture strength, pressure, velocity and temperature. A multi-venturi tube (MVT) fuel injection system was developed for this purpose.

Catalytic Reactor Design

The major challenge in designing a workable catalytic combustor for a gas turbine is the high gas temperatures required at the turbine inlet. For example, the GE Model MS9001E requires that the combustors generate an exit gas temperature of about 1193°C (2180°F), and other models require still higher temperatures. An example is GE's FA class of gas turbines with turbine rotor inlet temperatures of approximately 1290°C (2350°F), and combustor reaction zone temperatures of nominally 1500°C (2732°F). Such temperatures are well beyond the maximum tolerable for most catalytic materials, and this requirement has in the past prevented application of catalytic combustion technology to gas turbines.

The catalytic reactor promotes the oxidation of hydrocarbons and carbon monoxide for lean mixtures at adiabatic flame temperatures below the threshold for thermal NO_x formation. The combustion process is initiated by the catalyst and is completed by homogeneous combustion in the postcatalyst region where the highest temperatures are obtained. Catalytic reactor technology development has produced a bed that can operate with the full fuel and air flow required to operate the gas turbine, while avoiding exposure of the catalyst to high temperatures, which could cause deactivation and damage to the supporting substrate.

Nomenclature

CO = carbon monoxide emissions
DLN = Dry Low NO_x
FSNL = Full Speed No Load
ISO = International Standards Organization
MVT = Multiple Venturi Tube-type fuel injector
MWe = megawatts electrical output
NO_x = oxides of nitrogen emissions
ppm = parts per million by volume
SCR = Selective Catalytic Reduction
UHC = Unburned Hydrocarbon emissions

The catalyst must be designed to: (1) burn enough of the fuel to attain an outlet gas temperature sufficient to achieve low emissions via the downstream homogeneous combustion, and (2) burn the fuel in a manner that maintains the catalyst temperature below the maximum limit of the constituent materials. Some of the catalyst design issues have been discussed previously (Dalla Betta et al., 1994). The primary challenge is to maintain the catalyst surfaces at temperature well below the adiabatic combustion temperature. Traditional catalyst designs do not achieve this, so the choices of catalytic materials for such designs have been limited to ceramics, which are a durability concern in heavy-duty turbine applications.

The present design takes advantage of the unique thermodynamics of palladium oxidation and reduction to control surface temperatures. Palladium oxide is highly active in catalyzing methane oxidation, while metallic palladium is appreciably less active (McCarty, 1994). The oxide decomposes to the metal at temperatures between 780°C and 920°C (1440°F to 1690°F), depending upon the pressure. This transition between palladium oxide and palladium metal can be used to limit the catalyst temperature, and this allows the option of using metal catalyst supports rather than ceramics.

The testing reported here was done using catalysts designed like those used in previous full-scale tests (Beebe et al., 1995). The reactor consisted of three separate catalyst stages, each designed to deliver gas at the appropriate temperature to the subsequent stage or to the downstream homogeneous combustion section. Each stage was formed by corrugating a strip of oxidation-resistant metal foil 0.05 mm (0.002 in.) thick, and coiling the strip in such a way as to form a channeled monolithic structure. The active catalytic material was deposited as a coating on the foils. The stages were separated and supported in the reactor container by large-cell honeycomb structures, 13 mm (0.42 in.) thick, made of Hastelloy X for full-scale Test 1 and Cabot 214 for full-scale Test 2. For Test 1, the overall length of the catalytic reactor was 200 mm (8 in.), and the flow path diameter was 508 mm (20 in.). The reactor for Test 2 had the same flow path diameter but the overall length was increased to 305 mm (12 in.). Figure 2 is a photograph of the instrumented reactor ready for insertion into the test stand combustor for Test 1.

Full-Scale Test Rig and Instrumentation

The full-scale testing discussed in this paper was conducted at the GE Power Generation Engineering Laboratory located in Schenectady, New York. The single-burner test stand used for full-scale (reactor diameter of 508 mm), full-pressure testing (pressure ratio of 11.7) of the catalytic combustion system duplicates a sector of the internal geometry of the MS9001E gas turbine containing one combustor of a machine set of 14. Figure 1 is a drawing of the full-scale catalytic combustion system test rig for Test 1 installed in the MS9001E full pressure combustion development test stand. The fuel used for all fired testing was natural gas supplied by a local utility company.

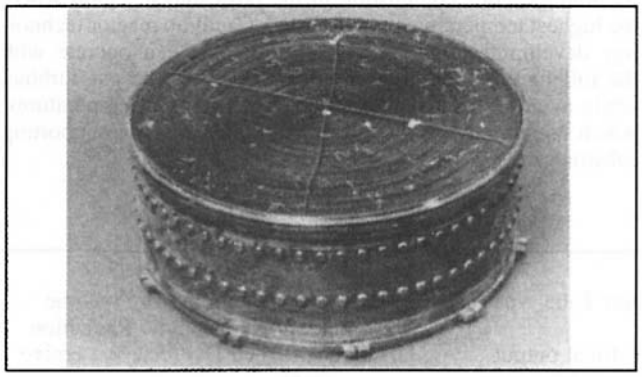

Fig. 2 Catalytic reactor in containment can

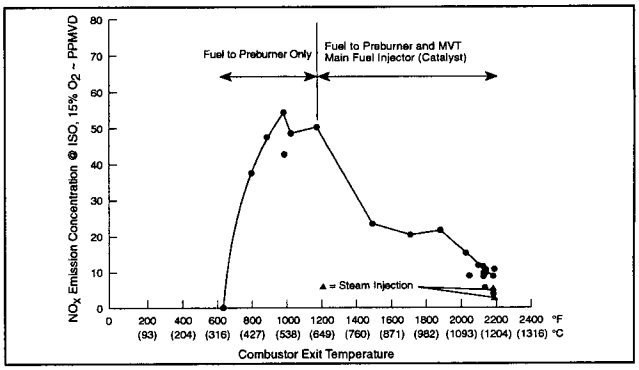

Fig. 3 Test 1, TEPCO/GE catalytic combustor, NO_x versus combustor exit temperature

Gas sampling for emissions concentration measurements was done continuously. The gas sample was forced through the sample probe by the pressure differential between the test stand and ambient. The gas sample was cooled to room temperature and the condensate was removed. The sample gas then flowed through a "hot box" to the emissions console via a heated Teflon sample line. The sample was maintained at a constant pressure at the emissions console. The gas sample flow rate was much higher than needed for measurement in order to minimize residence time in the sample train. The excess sample was vented to atmosphere. All materials in contact with the sample gas were stainless steel glass or Teflon.

Test Results and Discussion for Test 1

Experimental data were obtained over a range of test conditions from full-speed no-load (FSNL) simulation to base load simulation for the GE model MS9001EA gas turbine. The combustor discharge temperature at the entrance to the first-stage nozzles (T3.95) ranged from 543°C (1009°F) at the FSNL simulation to 1195°C (2184°F) at the base load simulation. The data included inlet and exit temperatures and pressures, dynamic pressures, and emissions. Additional temperature data and flame visualization were obtained using a video camera system looking at the rear face of the reactor through a viewing window in the transition piece. Reactor operation was started by first heating the system with the preburner and then initiating the main fuel flow through the reactor. This procedure resulted in a smooth lightoff of the reactor with a uniform temperature profile across the face of the reactor. The reactor could be completely extinguished simply by turning off the fuel supply to the MVT main fuel injector, and could be restarted by repeating the startup sequence. One shutdown/restart cycle was performed during the full-scale test.

NO_x Emissions. Figure 3 presents NO_x measurements corrected to ISO ambient and 15 percent oxygen concentration as measured at the test stand exit, versus average combustor exit temperature measured at the nozzle box. The data show a peak NO_x value of 55 ppmv at a combustor exit temperature 519°C. The data presented in Fig. 3 for combustor exit temperatures 519°C and below were taken at a constant pressure of 12.2 atma, the base load operating pressure of the MS9001EA gas turbine. Data for higher combustor exit temperatures were taken at design cycle conditions.

The highest level of NO_x measured under simulated machine cycle conditions is the 51 ppmvd point at 626°C combustor exit temperature. This relatively high NO_x level results from the diffusion flame in the preburner. Up to this point only the pre-

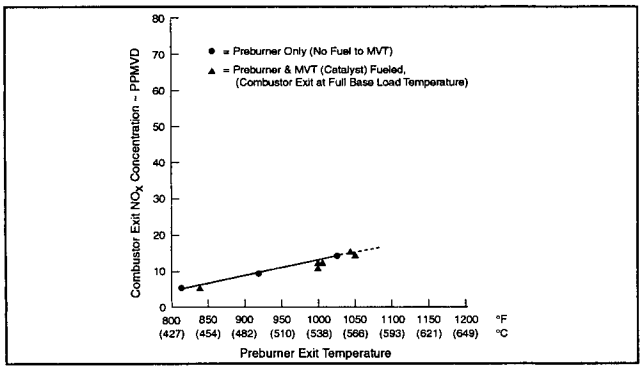

Fig. 4 Test 1, TEPCO/GE catalytic combustor, NO_x emissions versus preburner exit temperature at base load operating conditions

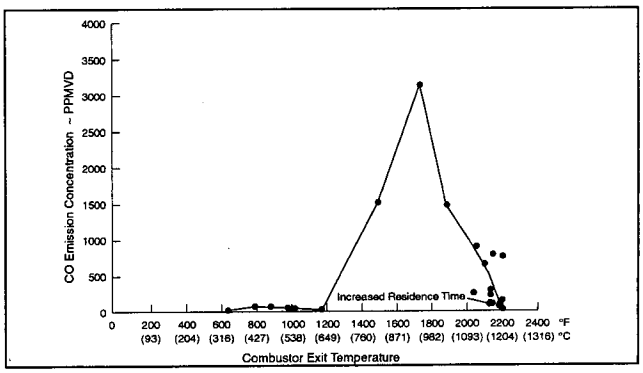

Fig. 5 Test 1, TEPCO/GE catalytic combustor, CO versus combustor exit temperature

burner was fueled with no fuel delivery to the MVT main fuel injector and catalyst. At 626°C exit temperature, the combustion system temperature rise occurs in the preburner, and as a result, NO_x levels are maximum for machine cycle conditions. As the combustor was taken to higher combustor exit temperatures, the temperature rise across the preburner decreased as fuel was shifted to the MVT main fuel injector, while temperature rise in the catalytic reactor and post-catalyst combustion zone increased. The data show that during this transition, NO_x emissions drop to a level of approximately 11 ppmvd, dry. The higher than desired NO_x was caused by the level of preburner exit temperature required to keep the catalytic reactor fully active. To demonstrate that the total NO_x observed was generated almost entirely by the preburner, a small amount of steam was injected into the preburner reaction zone via the preburner fuel nozzle atomizing air passages. Results are shown in Fig. 3 as the two points labeled "steam injection." These points correspond to steam to preburner fuel mass ratios of 1.02 and 1.17. NO_x emissions were 5 and 3 ppmvd, respectively, which is consistent with existing data for NO_x suppression by steam injection for diffusion flame combustors burning natural gas (Touchton, 1984), and confirmed that all measured NO_x was generated in the preburner. This was further demonstrated during the initial test points when fuel was supplied to the preburner but not the catalyst. These points were designed to quantify the relationship between the preburner temperature rise and the resulting NO_x production. The total NO_x emissions from the combustor are the sum of the NO_x produced by the preburner and NO_x produced by the catalyst. The contribution of the catalyst to NO_x production was estimated by subtracting the preburner NO_x from the total measured NO_x at each test point. This showed that the overall NO_x emissions with fuel supplied to the catalyst and preburner were approximately the same as the levels generated by the preburner alone at the same operating conditions. The correspondence of NO_x emission levels versus preburner exit temperature for the two cases is shown in Fig. 4. At base load operating condition, the catalytic reactor fuel flow was approximately 80 percent of the total combustor fuel flow. The data show that the catalytic reactor produced essentially no NO_x.

CO Emissions. Carbon monoxide emissions, shown in Fig. 5, are initially below 100 ppmvd during preburner-only operation, then peak at approximately 3200 ppmvd when combustor exit temperature reaches 930°C during catalyst staging. Catalyst staging is a transient condition that occurs between FSNL and base load (100 percent rated load at turbine rotor inlet temperature of 1124°C). During this process, combustion system temperature rise was transferred from entirely within the preburner to primarily within the catalytic reactor and post-catalyst reaction zone. At the start of catalyst staging, fuel was introduced through the MVT main fuel injector and into the catalytic reactor at a low-load simulation condition while combustor discharge temperature was held constant. Approximately constant combustor discharge temperature is maintained by lowering the preburner exit temperature to compensate for the additional energy released by the additional fuel introduced through the MVT main fuel injector and reacted in the catalyst and post-catalyst reaction zone. At the end of catalyst stating, nearly all of the combustion system temperature rise has been transferred to the catalytic combustor. At the base load point, which occurs at a combustor exit temperature of 1196°C (1124°C machine firing temperature), approximately 80 percent of the total fuel is delivered to the MVT main fuel injector.

The 3200 ppmvd peak, shown in Fig. 5, results from the post-catalyst reaction zone temperature being too low for complete reaction of CO in the available residence time. As the reaction zone temperature increases, CO emissions fall to a minimum value of 10 ppmvd at the base load operating condition, provided preburner exit temperature is maintained at a high enough level to keep the catalytic reactor fully active. Figure 6 shows the very sensitive effect of reactor exit temperature on CO emissions.

Figure 5 shows considerable scatter in the CO emissions levels near base load combustor operating conditions. This is due to experimentation with different preburner exit temperature levels for a given combustor exit temperature. CO and UHC emissions were found to be very sensitive to preburner exit temperature. It was necessary to maintain preburner exit temperature above 538°C in order to obtain good CO and UHC burnout at the base load operating condition.

UHC Emissions. Unburned hydrocarbon emissions are shown in Fig. 7. These data exhibit two distinct peaks. The first peak occurs near 427°C and results from preburner combustion

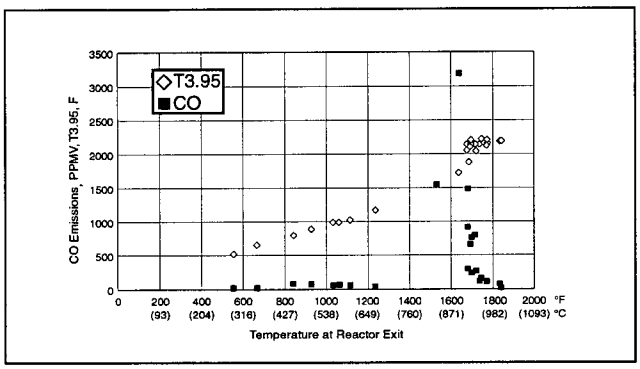

Fig. 6 Effect of reactor discharge temperature on CO emissions for 11 ms residence time

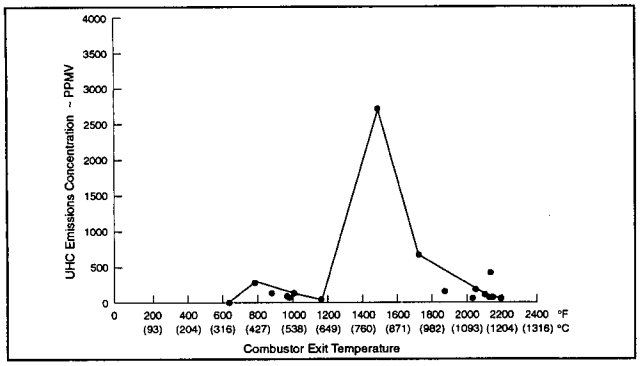

Fig. 7 Test 1, TEPCO/GE catalytic combustor, UHC versus combustor exit temperature

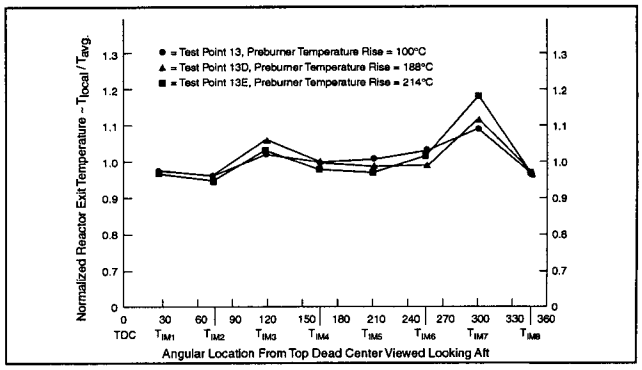

Fig. 8 Test 1, TEPCO/GE catalytic combustor, normalized reactor exit temperature distribution, base load

inefficiency at low temperature rise. The major peak occurs near 800°C and is the result of incomplete combustion as the preburner fuel is being reduced during catalyst staging. As more fuel is added to the MVT main fuel injector, combustor exit temperature increases and UHC emissions decrease to none at the simulated base load operating point. A data point was taken with combustor exit temperature of 1196°C and preburner exit temperature reduced to 448°C. At this point, CO rose to 731 ppmvd and UHC to 1922 ppmv. The reason for this emissions performance is that the preheat was insufficient to keep the catalytic reactor fully lit. Partial extinction of the reactor was observed in the video image and could also be detected in the combustor exit temperature distribution.

At the simulated base load operating point with preburner exit temperature at 563°C, the overall conversion of fuel to equilibrium combustion products was greater than 99.99 percent, based on the measured CO and UHC levels at the combustor exit. On the basis of the temperatures measured at several axial stations along the test rig, the fuel conversions were approximately as follows: 23 percent in the preburner, 52 percent in the catalytic reactor, and 25 percent in the post-catalyst reaction zone. Thus, with catalytic reactor exit gas temperature (bulk average) of approximately 1000°C, the homogeneous reactions after the catalyst were responsible for burning the remaining 25 percent of the main fuel flow to equilibrium in a residence time of approximately 11 milliseconds.

Dynamic Pressures and Pattern Factors. Dynamic pressure activity measurements showed that the catalytic combustor system had dynamic pressures lower than production combustion systems currently being supplied with heavy-duty industrial gas turbines. The highest discrete peak had a magnitude of 0.00173 MPa, at a frequency of 252 Hz, and was measured during a test point with steam injection into the preburner to determine the NO_x abatement effectiveness of steam injection into the preburner, which uses a conventional diffusion flame burning zone. The maximum overall rms noise level of 0.00836 MPa was also measured during the preburner steam injection experiment. The steam was injected through the atomizing air passages of the preburner fuel nozzle at a mass flow rate approximately equal to the preburner fuel flow rate. Without steam injection, dynamic pressures were approximately 0.00139 MPa.

Combustor exit gas temperature distributions were measured using an array of fixed thermocouples located in the test stand nozzle box. The nozzle box is located at the downstream end of the transition piece, which would be just forward of the turbine inlet on an actual machine installation. Exit gas temperature data were reduced to a pattern factor number at each fired test point. Pattern factor is the ratio of the maximum temperature variation from the mean divided by the overall combustor temperature rise.

The pattern factor goal for the catalytic combustor system was 0.10 or less at simulated base load conditions. Data at the simulated MS9001E base load operating point showed a pattern factor of 0.138. Insight into the cause of nonuniformity in the combustor exit gas temperature distribution may be gained by study of the gas temperature distribution measurements made at the catalytic reactor exit. Reactor exit hot gas temperature distribution was measured by eight type B immersion thermocouples spaced evenly on a circle about 203 mm (8 in.) from the centerline of the reactor and about 25 mm (1 in.) downstream from the exit face of the catalyst. Figure 8 shows the circumferential distribution of reactor exit temperature measured by the eight type B thermocouples as a function of preburner temperature rise. The data for these plots were all taken at simulated base load operating conditions, and the data were normalized for plotting by dividing the local temperature measured by each thermocouple by the average value for all eight. It can be seen that the level of the highest temperature peak, which is located 300 deg clockwise from top dead center when viewed looking aft, increases with increasing preburner temperature rise.

Figure 9 presents data on circumferential temperature distribution from the same eight thermocouples with only the preburner fired. These data are normalized in the same manner as used for Fig. 8 and presented as functions of preburner temperature rise. Some observations based on the data in Fig. 8 and 9 follow:

1 The highest peak in the catalyst exit temperature distribution occurs in a region where preburner exit temperature is high.
2 The magnitude of the highest peak in catalyst exit temperature distribution increases with increasing preburner temperature rise.

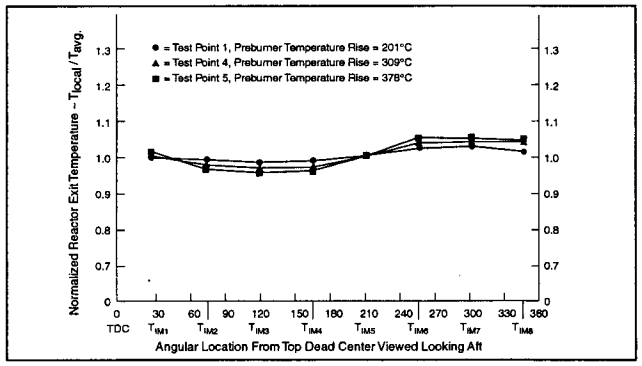

Fig. 9 Test 1, TEPCO/GE catalytic combustor, normalized reactor exit temperature distribution, preburner only fueled

3 The magnitude of preburner discharge gas temperature variation increases with increasing preburner temperature rise.

From these data, it was inferred that preburner exit gas temperature nonuniformity was a contributing factor to catalytic reactor exit gas temperature nonuniformity. However, the observed preburner exit temperature nonuniformity was reasonably small, as can be seen by the data in Fig. 9, with only a range of approximately 4 percent or 22°C; and so the very large spread in reactor exit temperature (refer to Fig. 8) appeared to be inconsistent with the preburner distribution. This was, in fact, confirmed by a subsequent test in which a static mixer was introduced in the diffusing section of the preburner before the MVT fuel injector system. The mixer produced a slight improvement in the preburner exit temperature distribution, but resulted in a major degradation of the reactor exit temperature distribution uniformity. These data were the basis for suspecting that the nonuniform reactor exit temperature distributions were likely caused, not by preburner temperature nonuniformity, but by the nonuniformity of the fuel–air distribution inlet to the reactor face. The latter was affected negatively by nonuniformity of the hot gas mass flux distribution exiting the preburner and entering the MVT fuel system, which provides the fuel to the reactor. This predominant effect of preburner exit mass flux distribution on the reactor inlet fuel–air distribution was confirmed by the diagnostic instrumentation included in the next test, Test 2, which is described below.

With this as a backdrop, the relatively cool center section of the reactor seen in Fig. 10 was reasoned to be due to low fuel–air ratio at the center of the reactor caused by higher than average mass flux at the center of the preburner discharge, assuming uniform fuel injection by each of the venturis in the MVT. Additional information on reactor exit temperature distribution during the test was obtained using a combustion video system developed by GE. This system monitored reactor exit surface temperature distributions in real time and uses computer image analysis to produce color plots of the temperatures from the digitized video input. Figure 10 shows an example of the reactor exit temperature distribution with the preburner and catalytic reactor fired. A nonuniform temperature distribution is evident over the cross section.

Any particular catalyst system is designed to have a range of conditions over which it will achieve stable operation with low emissions. This operating window is bounded by the following constraints:

1 The inlet gas temperature must be high enough to sustain the requisite catalytic activity.
2 The gas temperature leaving the catalyst must be high enough to promote homogeneous combustion and CO burnout within the available residence time.

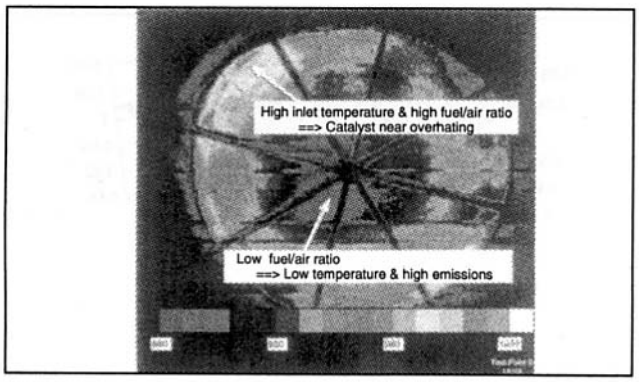

Fig. 10 Test 1, video image of the reactor exit temperature distribution

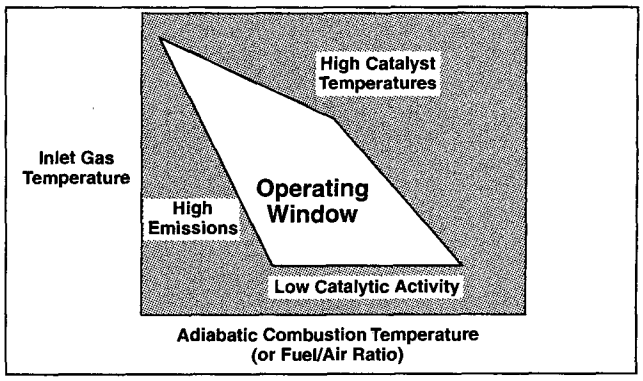

Fig. 11 Test 1, boundaries of catalytic reactor operating window

3 The temperatures within the catalyst stages must be low enough to provide stable, long-term reactor operation.

Figure 11 shows how these three factors constrain the operable combinations of inlet gas temperature and adiabatic combustion temperature (or fuel–air ratio) over which the catalytic combustor can meet the performance targets. It also shows how the inlet gas temperature and adiabatic combustion temperature interact. For example, a decrease in adiabatic combustion temperature can be compensated by an increase in inlet gas temperature to keep the operating point within the window.

Figure 11 indicates that, for any particular inlet gas temperature, a fuel–air ratio below the operating window results in low catalyst temperatures and high emissions of CO and UHC. On the other hand, a fuel–air ratio above the operating window causes the catalyst to overheat. If there are variations in the local temperature and fuel–air ratio across the inlet face of the reactor, some regions of the catalyst can be exposed to conditions at the "high emissions" side of the window diagram while at the same time other regions are near the "catalyst overheating" boundary. The thermal images of the reactor in operation suggest that such variations in inlet existed during the Test 1. Nonuniformities make it more difficult to assure that conditions in all portions of the reactor are within the operating window; so nonuniformities in the combustor limit the degree of flexibility in responding to the fuel–air ratios at changing load conditions.

As can be seen in Figs. 5 and 6, CO emissions were very low at the base load high firing temperature points, but increased rapidly as combustor exit temperature was decreased. Although the overall solution to this CO dependence is to include air staging into the combustor design to control fuel–air ratio, which will be a part of actual turbine applications, the very narrow operating window in Test 1 has been found to be due to spatial variations across the reactor inlet face of both preburner exit temperature and, more importantly, fuel–air ratio. Figure 12 presents reactor exit gas and foil metal temperature data for test points 13D and 13E plotted against reactor inlet gas temperature. Both are base load operating points with very similar combustor discharge temperatures, but with preburner exit (thus, reactor inlet) temperatures differing by approximately 50°F (26°C). Also shown as dashed lines on Fig. 12 are the maximum allowable foil wall temperature (limit set for foil endurance), the minimum outlet gas temperature required for CO/UHC emissions burnout to less than 10 ppmv, and the corresponding minimum outlet wall temperature necessary to achieve the required outlet gas temperature. For test point 13D, it can be seen that the average exit gas temperature just equals the required minimum for low CO emissions (consequently, there are regions of the reactor below the required minimum exit gas temperature), and one of the foil wall temperature TC's is in fact below the minimum wall temperature. Emissions for

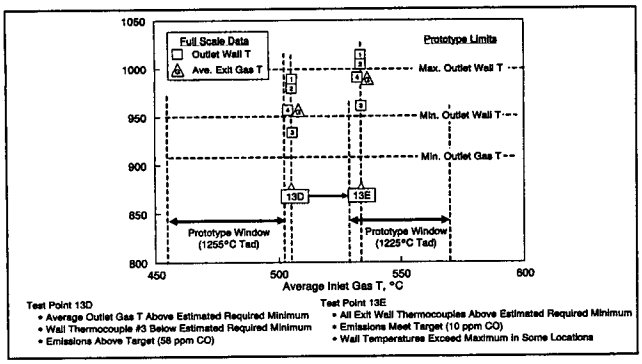

Fig. 12 Test 1, reactor exit foil and gas temperature at two different inlet gas temperatures

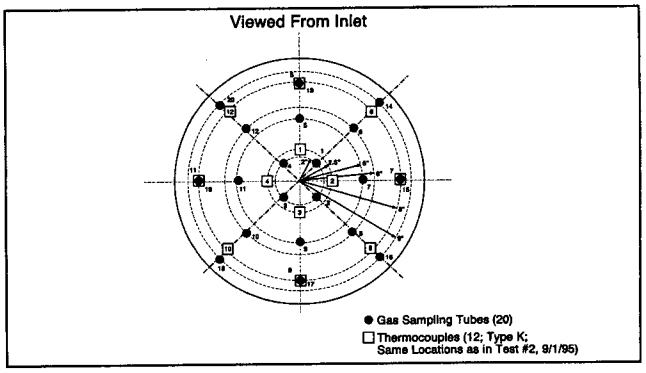

Fig. 13 Test 2, instrumentation locations at reactor inlet

this point are shown in Table 1 and are 58 ppmv CO and 2 ppmv UHC. When the reactor inlet temperature was increased by approximately 50°F (26°C) to reach test point 13E, the average outlet gas temperature now exceeded the required minimum by close to 75°F (40°C), indicating that the bulk of the reactor was likely now operating above this temperature and the emissions, as seen in Table 1, were reduced to 10 ppmv CO and no detectable UHC.

Modified Combustor Design for Test 2—January 1996

A number of changes were incorporated into the full-scale test rig and instrumentation for the second full pressure development test of the series, Test 2, in order to improve performance and provide more diagnostic data to increase understanding of operational characteristics observed during the first full-pressure test. A brief description of the changes incorporated into the test rig for Test 2 and the objectives of these changes follows:

1 The size of the post catalyst reaction zone was increased to approximately double the original length and volume. The purpose of this change was to increase post catalyst residence time in order to reduce CO and UHC emissions, improve turndown performance, and permit operation at lower catalyst inlet temperature for lower NO_x.

2 The length and volume of the catalytic reactor were increased to approximately 1.5 times the size of the original design. The purpose of this change was to accommodate interstage supports made of structural metal honeycombs and increase the active length/volume of the catalytic reactor for lower emissions and increased turndown capability.

3 A perforated plate was added in the hot gas flow path near the preburner combustion liner exit plane. The purpose of this change was to obtain a more uniform velocity distribution (i.e., mass flux distribution), at the inlet to the MVT main fuel injector which is expected to result in a more uniform fuel air mixture strength distribution at the catalytic reactor inlet.

Table 1 Emissions at base load conditions

Test Point	13D	13E	17A *
Combustor Exit T, °C	1193	1197	1194
Preburner Exit T, °C	537	563	569
Catalyst Exit T, °C	965	1003	1000
NOx, ppm @ISO, 15% O_2	9	11	5
CO, ppm	58	10	34
UHC, ppm	2	0	1

* Steam injected at 0.21 lb/lb total fuel

4 An array of 12 hot gas immersion thermocouples was added to the inlet face of the MVT main fuel injector. The objective of this addition was to obtain data on preburner exit temperature distribution.

5 An array of 12 hot gas immersion thermocouples was added to the catalytic reactor inlet face to obtain data on reactor inlet temperature distribution.

6 An array of 20 hot gas sample probes was added to the catalytic reactor inlet face to obtain data on fuel air mixture strength distribution at the catalytic reactor inlet.

Test Results and Discussion for Test 2

Test 2 has been completed and the available portion of these results are presented here. A perforated plate was introduced at the discharge of the preburner, upstream of the MVT fuel injector, in an attempt to reduce the preburner exit temperature variations and, most importantly, to make the mass flux distribution exiting the preburner and entering the MVT injector more uniform, leading to an expected reduction in fuel–air ratio variations inlet to the reactor. Figure 13 shows the location of the thermocouples and gas sampling tubes at the inlet to the reactor.

Figure 14 shows the measured methane concentration measured at the reactor inlet face for the base case without a perforated rate. Figure 15 shows the measured methane concentration distribution with a perforated plate in place having a 1.5 psi pressure drop. The fuel–air ratio (or methane concentration) distribution is somewhat more uniform, but still shows areas with significantly lower fuel–air ratios, and some areas with high fuel–air. These nonuniformities will be resolved before further combustion testing. This is necessary for truly effective reactor operation with a reasonable operating window with acceptable low CO/UHC emissions, and lower foil temperatures. The data show the significantly lower fuel–air ratios in the center third of the reactor compared with the higher fuel–air

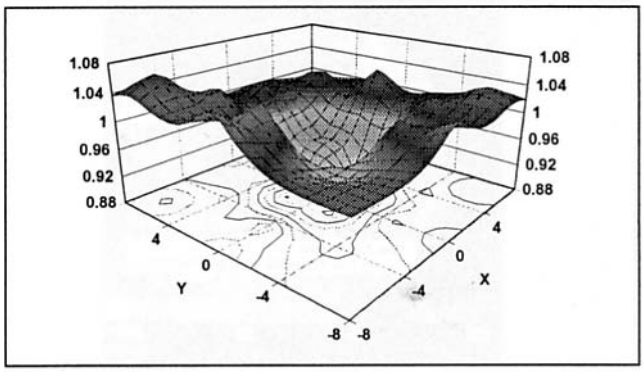

Fig. 14 Normalized methane concentration (without perforated plate)

ratios in the surrounding annular two thirds of the reactor. These data are consistent with the temperature map shown in Fig. 10, which presents the reactor exit temperature distribution measured by the video system. The rapid increase in CO emissions seen in Fig. 5 as the combustor discharge temperature is reduced below base load conditions can now be understood on the basis of the reactor operating map of Fig. 11 and the data of Fig. 14. As can be seen from the data, a large portion of the reactor is operating with low fuel–air ratio at its inlet, which will lead to lower than average exit gas temperatures and higher than average CO emissions. To achieve very low CO/UHC emissions, it was necessary to operate the reactor with the outer portion near foil temperature limits in order to increase the exit gas temperature emanating from the center third of the reactor to a level high enough for complete CO burnout.

However, overall performance was improved over the Test 1 results discussed above. A major reduction in NO_x emissions at full-load operating conditions was achieved, with NO_x levels of the order of 3–5 ppmv without steam injection. These low NO_x emissions resulted from being able to operate the reactor at significantly lower preburner exit temperatures. CO and UHC emissions were approximately 40 and 80 ppmv, respectively. Table 2 compares the March 1995 and January 1996 overall performance results.

Table 2 Combustor performance data

Test 1 (March 1995) vs. Test 2 (January 1996)		
Parameter	**Test 1**	**Test 2**
T3.95 (°C)	1195	1191
Tpbexit (°C)	563	433
MCP (psig)	188	188
Tinlet CD (°C)	349	338
Air Flow (pps)	53	53
NOx @ 15% O2 (ppmv)	11	3.5
CO (ppmv)	10	82
UHC (ppmv)	0	43
Tgas reactor exit (°C)	1003	908

Summary and Conclusions

Since 1990, GE, Catalytica, and TEPCO have collaborated in the development of a catalytic combustion system for the MS9001E gas turbine, rated at 104 MWe at a turbine inlet temperature of 1105°C (E conditions). The system utilizes partial combustion of fuel in the reactor section, with completion of reactions in a post-reactor homogeneous combustion zone before entering the turbine first stage nozzle. Tests at subscale (5–7.6 cm diameter reactors) have demonstrated single-digit NO_x, CO, and UHC at E conditions.

A full-scale test of the MS9001E catalytic combustor was completed in March 1994 and reported earlier (Beebe et al., 1995), which demonstrated the potential for achieving program goals. After redesign and hardware fabrication, the catalytic combustor was tested again in March 1995. The results discussed in this paper show significant advances over previous full-scale tests in this program and over other reported work in the field of catalytic combustion applied to actual gas turbines. Among the major accomplishments of this latest test are the following:

1 First full-scale test to achieve full MS9001E turbine cycle conditions (1105°C turbine inlet temperature).
2 Major improvement in reactor mechanical integrity as measured by minimal distortion of the 508 mm (20 in.) diameter reactor at the exit of Stage 3 after several hours of operation.
3 Less than 1 ppmvd NO_x generated by the catalytic reactor, approximately 9 ppmvd NO_x (ISO, 15 percent O_2, dry) generated by the preburner. NO_x was reduced to 3–5 ppmvd by the addition of a small quantity of steam (steam-to-fuel mass ratio ~ 0.25).
4 CO and UHC emissions were significantly reduced from earlier test results (several hundred ppmv), to as low as 10 ppmv CO/0 ppmv UHC at base load conditions.
5 Stable operation of the reactor at base load flow, temperature, and pressure, with very low combustion-driven dynamic pressure oscillations.

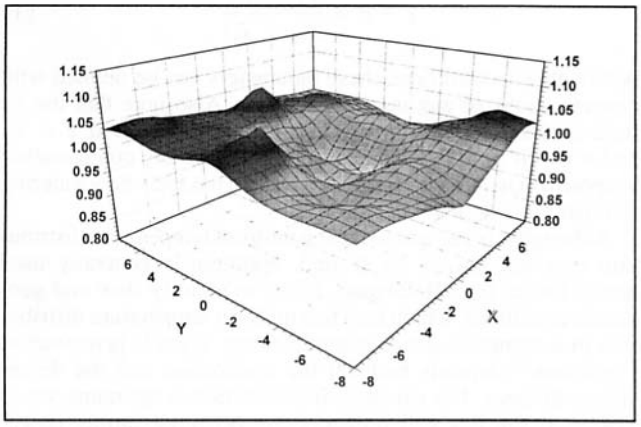

Fig. 15 Normalized methane concentration (with perforated plate)

After redesign of the system, Test 2 was performed in January 1996 with a system designed to increase the post-reactor residence time, the fuel–air distribution inlet to the reactor, and the mechanical reactor support system. Initial results show improvement and have provided detailed reactor inlet fuel–air distributions, which are the basis for further improvements to the fuel–air uniformity.

Acknowledgments

The authors wish to recognize and express thanks for the efforts of the GE Power Generation Laboratory personnel, especially Mr. F. Belisle and Mr. J. Johnson, test engineers; and the assistance of Mr. M. B. Hilt, former program manager, who continues to act as a strong advocate of catalytic combustion, helping to keep this important new technology development moving forward. The authors also wish to recognize and express thanks to Mr. Itoh of TEPCO, whose guidance and leadership have been a key contribution to this work.

References

Beebe, K., Ohlcoshi A., Radalc, L., and Weir, A., Jr., 1987, "Design and Test of Catalytic Combustor Fuel–Air Preparation System," Paper 51, presented at Tokyo, Japan.

Beebe, K., Cutrone, M., Matthews, R., Dalla Betta, R., Schlatter, J., FDe, Y., and Tsuchiya, T, 1995, "Design and Test of a Catalytic Combustor for a Heavy-Duty Industrial Gas Turbine," ASME Paper No. 95-GT-137.

Dalla Betta, R. A., Schlatter, J. C., Nickolas, S. G., Yee, D. K., and Shoji, T., 1994, "New Catalytic Combustion Technology for Very Low Emissions Gas Turbines," ASME Paper No. 94-GT-260.

McCarty, J. G., 1994, "Kinetics of PdO Combustion Catalysis," in: *Proc. International Workshop on Catalytic Combustion*, H. Arai, ed., p. 108.

Touchton, G. L., 1984, "Influence of Gas Turbine Combustor Design and Operating Parameters on Effectiveness of NO_x Suppression by Injected Steam or Water," ASME Paper No. 84-1PGC-GT-3.

Mixing of Multiple Jets With a Confined Subsonic Crossflow: Part I—Cylindrical Duct

J. D. Holdeman
NASA Lewis Research Center,
Cleveland, OH 44135

D. S. Liscinsky
United Technologies Research Center,
E. Hartford, CT 06108

V. L. Oechsle
Allison Engine Company,
Indianapolis, IN 46206

G. S. Samuelsen
University of California,
Irvine, CA 92717

C. E. Smith
CFD Research Corporation,
Huntsville, AL 35805

This paper summarizes NASA-supported experimental and computational results on the mixing of a row of jets with a confined subsonic crossflow in a cylindrical duct. The studies from which these results were excerpted investigated flow and geometric variations typical of the complex three-dimensional flowfield in the combustion chambers in gas turbine engines. The principal observations were that the momentum-flux ratio and the number of orifices were significant variables. Jet penetration was critical, and jet penetration decreased as either the number of orifices increased or the momentum-flux ratio decreased. It also appeared that jet penetration remained similar with variations in orifice size, shape, spacing, and momentum-flux ratio when the number of orifices was proportional to the square root of the momentum-flux ratio. In the cylindrical geometry, planar variances are very sensitive to events in the near-wall region, so planar averages must be considered in context with the distributions. The mass-flow ratios and orifices investigated were often very large (mass-flow ratio >1 and ratio of orifice area-to-mainstream cross-sectional area up to 0.5), and the axial planes of interest were sometimes near the orifice trailing edge. Three-dimensional flow was a key part of efficient mixing and was observed for all configurations. The results shown also seem to indicate that nonreacting dimensionless scalar profiles can emulate the reacting flow equivalence ratio distribution reasonably well. The results cited suggest that further study may not necessarily lead to a universal "rule of thumb" for mixer design for lowest emissions, because optimization will likely require an assessment for a specific application.

1 Introduction

Jets-in-crossflow have been extensively treated in the literature. Flows in which this is an integral constituent occur in a number of areas important in combustion and energy science and technology. In a gas turbine combustor for example, fuel and air mixing is important to combustor performance and emissions. Also, the mixing associated with arrays of jets in crossflow can play a critical role as in the dilution zone of a conventional combustor, and the mixing zone of a staged combustor such as the Rich-Burn/Quick-Mix/Lean-Burn (RQL) combustor. Although results reported to date have all contributed additional understanding of the general problem, the information obtained in them may not satisfy the specific needs of different applications.

One characteristic of jet-in-crossflow applications in gas turbine combustion chambers is that they are often confined mixing problems, with up to 80 percent of the total flow entering through the jets. The result is that the equilibrium mixing pattern and composition of the exiting flow may differ significantly from that of the entering mainstream flow.

A summary of NASA-supported research in the 1980s is given in Holdeman (1993). Several reports and papers have been published since the previous summary was presented that address cylindrical configurations. These include Cline et al. (1995), Hatch et al. (1995a, b), Holdeman et al. (1992), Holdeman (1993), Howe et al. (1991), Kroll et al. (1993), Leong et al. (1995), Liscinsky et al. (1993), Oechsle et al. (1992–1994), Oechsle and Holdeman (1995), Richards and Samuelsen (1992), Smith et al. (1991), Sowa et al. (1994), Talpallikar et al. (1992), Winowich et al. (1991), Yang et al. (1992), Zhu and Lai (1995).

2 Description of the Flowfield

Figure 1 shows a schematic of the flow in a cylindrical duct with injection from a row of jets at the wall. The scalar field results are often presented as plots of the temperature difference ratio, θ, where

$$\theta = \frac{(T_m - T)}{(T_m - T_j)}$$

or,

$$1 - \theta = \frac{(T - T_j)}{(T_m - T_j)} \tag{1}$$

Although T is used here, these parameters can be defined with concentrations or any conserved scalar. Also note that the jet fluid is identified by larger values of θ (i.e., $\theta = 1$ if $T = T_j$, and $\theta = 0$ if $T = T_m$). The equilibrium θ for any configuration is approximately equal to the fraction of the total flow entering through the jets, w_j/w_T.

Although it is recognized that a uniform temperature distribution may not always be desired, optimum is generally used herein (as in, e.g., Holdeman, 1993) to identify flow and geometric conditions, which lead to a uniform temperature distribution in a minimum downstream distance. What is perceived as "optimum" depends both on the application and the downstream distance. For example, if penetration is optimum, say at $x/R = 1$, the jets will probably overpenetrate farther downstream and underpenetrate upstream of this location.

The primary independent geometric variables are the spacing between adjacent orifices, S, the orifice diameter, d; the orifice aspect ratio, (L/W), and the orifice angle (with respect to the

Contributed by the International Gas Turbine Institute and presented at the 41st International Gas Turbine and Aeroengine Congress and Exhibition, Birmingham, United Kingdom, June 10–13, 1996. Manuscript received at ASME Headquarters February 1996. Paper No. 96-GT-482. Associate Technical Editor: J. N. Shinn.

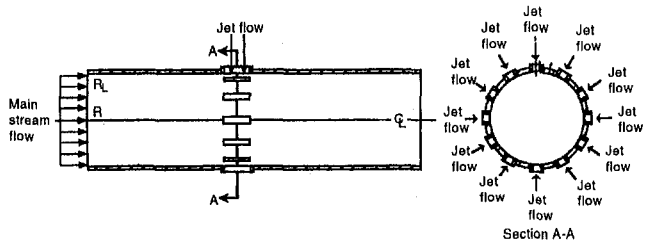

Fig. 1 Schematic of typical configuration

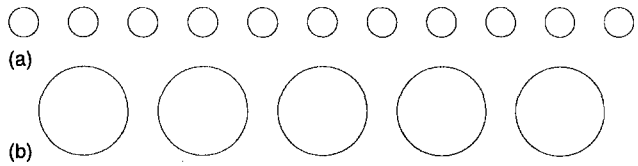

Fig. 2 Sample orifice geometry: (*a*) previous dilution jet mixing, (*b*) current investigations

axial direction). Because the objective in combustor applications is to identify configurations to provide a desired mixing pattern within a given downstream distance, locations of interest are identified in intervals of the duct height (radius) rather than the orifice diameter, d. The primary independent flow variables are the jet-to-mainstream mass-flow (MR = w_j/w_m) and momentum-flux (J) ratios. These can be expressed as:

$$J = \frac{\mathrm{MR}^2}{(\mathrm{DR})(C_d)^2(A_j/A_m)^2} \tag{2}$$

It was reported in Holdeman (1993) that jet penetration and centerplane profiles were similar when the orifice spacing and the square root of the momentum-flux ratio were inversely proportional, i.e.:

$$C = (S/H)\sqrt{J} \tag{3}$$

In a cylindrical duct, the radius, R, corresponds to the channel height, H, for one-side injection in a rectangular duct. For single-sided injection the centerplane profiles are approximately centered across the duct height and approach an isothermal distribution in the minimum downstream distance when C = 2.5. This appeared to be independent of orifice diameter, as shown in both calculated and experimental profiles. The similarity of the profiles with the same orifice spacing but with different orifice diameters was also shown by Holdeman et al. (1973). Values of C in Eq. (3) that are a factor of 2 or more smaller or larger than the optimum correspond to underpenetration or overpenetration, respectively.

For a can the optimum orifice spacing was specified at the radius, which divides the can into equal areas. That is, the relationship of the spacing between jet centerlines to the number of holes around the circumference of the can would be

$$S = \frac{2\pi R_{1/2}}{n} \tag{4}$$

where

$$R_{1/2} = \frac{H}{\sqrt{2}} \tag{5}$$

Substituting Eq. (5) into Eq. (4), and the resulting S/H into the spacing and momentum-flux relationship for a rectangular duct (Eq. (3)) gives the appropriate number of round holes as:

$$n = \frac{\pi\sqrt{2J}}{C} \tag{6}$$

It follows that the sector for each orifice would be $360/n$ deg.

3 Results and Discussion

The following paragraphs describe the results from recent investigations in the context of the effects of the primary independent variables. Both experimental and computational studies were performed, but are interspersed here. The work cited was performed by Allison Engine Company, CFD Research Corporation, United Technologies Research Center, and the University of California, Irvine. Sources are identified when results are discussed, and specifics of the calculations or experiments, as appropriate, are given in the corresponding references.

All planar nonuniformity values are expressed as a variance from the mean values. Although the definitions used in the original papers differ slightly, they are essentially rms values. All orifices considered in this paper are thin (thickness/diameter < 0.25, and are plenum-fed with no bypass air.

Investigations published prior to 1991 were primarily in a rectangular duct, and at significantly lower mass-flow ratios than in more recent studies. A schematic showing the relative orifice size is given in Fig. 2. Effects investigated in recent studies included: (1) variation in momentum-flux ratio (J) at constant geometry; (2) variation of number of orifices at constant J; (3) comparison of slots and holes; (4) variation of slot aspect ratio; (5) variation of slanted slot angle; (6) results of orifice optimization; (7) effect of mixing duct size; (8) relation of mixing and emissions; and (9) effect of reaction. These are discussed in the following sections. Results from previous stud-

Nomenclature

A_j/A_m = jet-to-mainstream area ratio
$AC_d = (A_j)(C_d)$
$C = (S/H)\sqrt{J}$
C_d = orifice discharge coefficient
D = diameter of cylindrical duct
d = orifice diameter
DR = jet-to-mainstream density ratio
H = duct height (rectangular)
J = jet-to-mainstream momentum-flux ratio
$= (\mathrm{DR})(V_j/U_m)^2$
$= (\mathrm{MR})^2/((\mathrm{DR})(C_d)^2(A_j/A_m)^2)$
L = long dimension of orifice
L/W = orifice aspect ratio
MR = jet-to mainstream mass-flow ratio
$= w_j/w_m$
n = number of holes around can
r = radial coordinate
R = can radius
S = lateral (circumferential) spacing between orifice centers
T = temperature
T_j = jet exit temperature
T_m = mainstream temperature
U = axial velocity
U_m = mainstream velocity
V_j = jet velocity
$w_j/w_m = (\sqrt{\mathrm{DR}})(\sqrt{J})(C_d)(A_j/A_m)$
w_j/w_T = jet-to-total mass flow ratio
$= \mathrm{MR}/(\mathrm{MR} + 1)$
W = short dimension of orifice
x = downstream coordinate
= 0 at leading edge of orifice
y = cross-stream (radial) coordinate
= 0 at wall
z = lateral (circumferential) coordinate
= 0 at centerplane
$\theta = (T_m - T)/(T_m - T_j)$

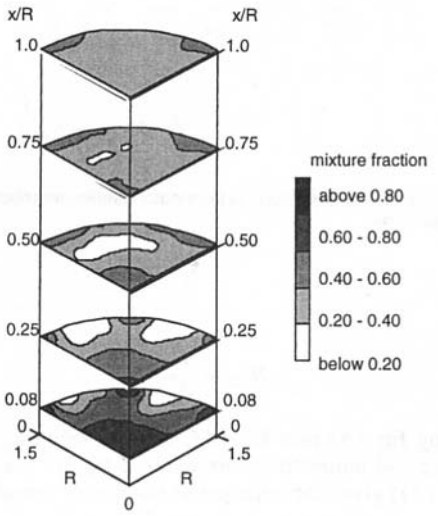

Fig. 3 Mixture fraction, eight round hole configuration, J = 26.7 (data from Hatch et al., 1995a)

ies showed that the density ratio (DR) was not a significant variable at constant momentum-flux ratio (J).

3.1 Momentum-Flux Ratio. Based on previous studies, which reported that the most important flow variable influencing the extent of jet mixing in a crossflow was the momentum-flux ratio, Hatch et al. (1995a) performed a series of tests with eight orifices at three representative J values. The results reaffirmed the importance of the momentum-flux ratio in determining the downstream flowfield.

A representative flowfield evolution for a baseline case of eight round orifices at J near 25 (Hatch et al., 1995a), is shown in Fig. 3. In the first plane (bottom), the absence of jet fluid is noted by the limited near-zero mixture fraction values, while the presence of unmixed mainstream flow is apparent by the high mixture fraction values approaching 1 (unmixed jet fluid = 0 and unmixed mainstream fluid = 1). By the fifth plane downstream (up in Fig. 3), the jet and mainstream flow have mixed and have created a band of mixture fraction values that approach the equilibrium value. Mixture uniformity values calculated per plane provide the basis for the planar trend shown in Fig. 4.

A similar effect is apparent in the results of Talpallikar et al. (1990) as shown in Fig. 5. The planar mixture nonuniformity for this case is shown in Fig. 6 with a clearly defined optimum

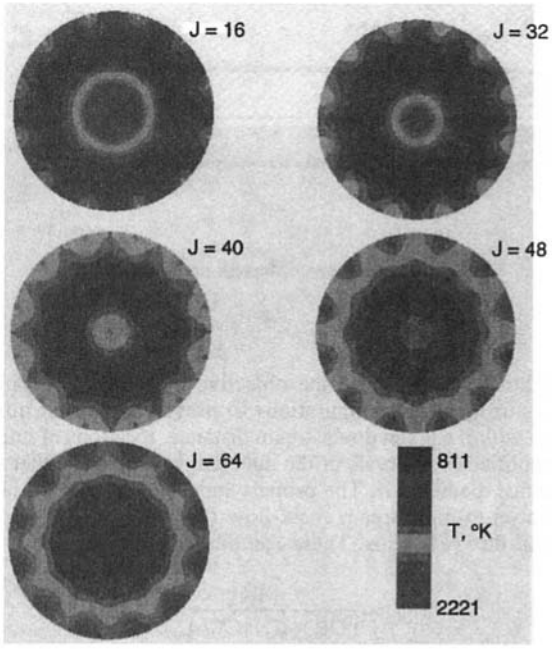

Fig. 5 Temperature contour maps for reacting conditions: x/R = 2.0 (data from Talpallikar et al., 1990)

J for the configurations examined, with underpenetration to the left and overpenetration to the right.

The effect of momentum-flux ratio can also be seen in the experimental results of Vranos et al. (1991) as seen in Fig. 7. A planar distribution from this study for slanted slots in shown in Fig. 8. Differences in the J value of the minimum in these studies (for example Vranos et al. (1991) and Talpallikar et al. (1990) are due to slight differences in the conditions examined, and are unimportant.

The data shown in Figs. 7 and 8 are for slanted slots. The slant angle for slots is the angle between the long dimension and the axial direction. Note that slanted slots induce swirl although none is present in the main flow (Vranos et al., 1991). It is also apparent in the results that although a local minimum is identified, it is possible to achieve low values of mixture nonuniformity at higher J values corresponding to overpenetration. This emphasizes that although planar-averaged values are very useful and can provide insight, one cannot rely on them alone, and must also assess the flowfield distributions as shown in Figs. 3, 5, and 7.

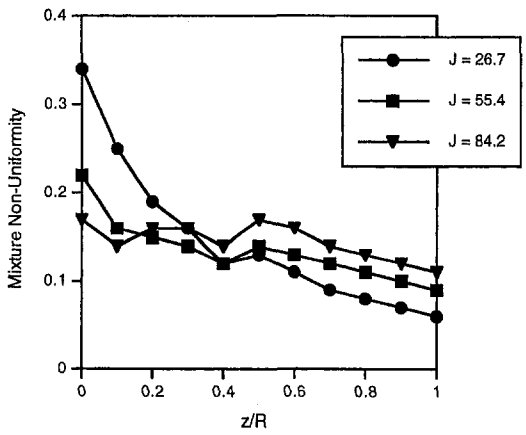

Fig. 4 Mixture nonuniformity, eight round hole configuration (data from Hatch et al., 1995a)

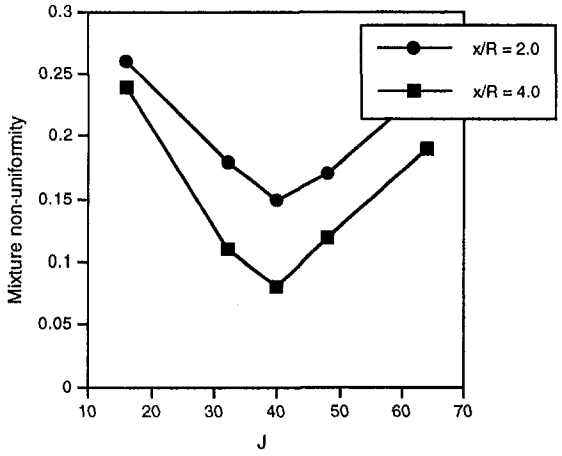

Fig. 6 Mixture nonuniformity: reacting flow (data from Talpallikar et al., 1990)

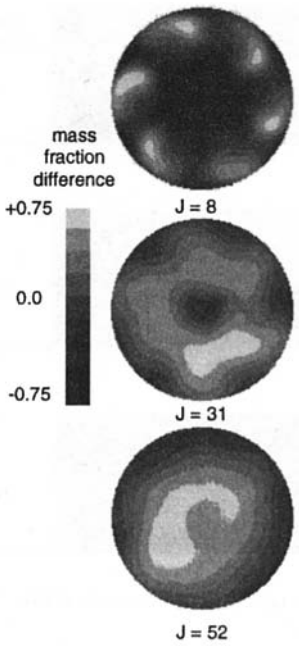

Fig. 7 Effect of momentum-flux ratio on mixing from 6 slanted slots at x/R = 1.2 and DR = 1.0 (data from Vranos et al., 1991)

3.2 Number of Orifices. In general, the effect of increasing the number of orifices around the perimeter of a can is similar to the effect of decreasing the momentum-flux ratio (see Eq. (6)). Although this was also evident in previous results, the optimum was recently shown in the computational study by Smith et al. (1991). Since the optimum number relation, Eq. (6), was originally developed from computational results and round-hole data obtained in rectangular ducts at low mass-flow ratios, its applicability to other shapes and at higher mass-flow ratios was unknown.

Figure 9 shows isotherms of the centerplane (radial-axial plane through the geometric center of the orifice) for a different number of 4:1 aligned slots for J = 36. The jet penetration increases as an inverse function of the number of orifices. It is obvious that the flow from 14 slots is underpenetrated, whereas that for 10 is overpenetrated. Furthermore, the latter case can lead to upstream flow near the duct center, and can cause both poor mixing and high NO_x emissions (Talpallikar et al., 1990). For this configuration, 12 orifices seem to give optimum mixing whereas 11 would be predicted from Eq. (6).

The optimum number of round orifices was found experimentally for J = 52 to be between 12 and 15. This is shown in Fig. 10 from Kroll et al. (1993). These distributions are radial-axial planes through the orifice center that were constructed from 100 thermocouple measurements in each of five planes. Here the jets enter from the can wall at the top, and proceed toward the can centerline at the bottom. The mainstream flow is from left to right. The mean jet trajectory can be traced by following the lowest values of mixture fraction downstream from the orifice.

3.3 Slots and Holes. Representative still frames from movies of low-speed flows from Vranos et al. (1991) are shown in Fig. 11. These indicate significant differences in the jet/jet and jet/mainstream interactions between slanted slots and round hole injectors. The jet exiting a round hole forms two counterrotating vortices of equal strength. The jet penetrates directly toward the center of the duct, and the jet cross section is stretched as J increases. The connecting sheet moves closer to the duct axis, but the vortices tend to remain near the wall.

The tendency of the vortices to stay near the wall is attributed, in part, to interaction between neighboring vortices, which act to translate adjacent vortices toward the duct wall. An additional influence of neighboring jets is to constrain the lateral spreading of the jet, and to spread it along its centerplane. This is particularly evident in the can as the lateral spread is increasingly restricted as the duct centerline is approached from the wall.

In contrast to the round jet, the slanted slot initially forms a pair of counterrotating vortices, which are of unequal size and strength. Larger vortices form downstream of the orifice leading edge and move toward the duct wall, while the smaller vortex moves away from the wall. There is considerable interaction between neighboring jets early in the injection process. In this case, unlike the round jet system, the induced velocity field is such that the vortex pair rotates about an axis connecting the vortex centers.

The bulk of the jet fluid identifies the location of the leading edge, thereby showing the direction that the slot is slanted (in Fig. 7 the upstream edge of the slot is on the clockwise side). Furthermore, the slanted slot jet experiences a lateral force that causes it to rotate about the duct axis. The greatest circumferential velocity is due to the large vortex, and is near the wall. At the same time, the flow near the center is of the opposite sense so the net angular momentum is zero.

Planar nonuniformity for round holes and 45 deg slanted slots at x/R = 1.2 is shown in Fig. 12. At this distance the two systems exhibit roughly the same average mixing, although the optimum J for round holes is less than that for slanted slots. It follows from the discussion in the previous section that the optimum spacing for slanted slots would be greater than for round holes for the same momentum-flux ratio.

3.4 Slot Aspect Ratio. The slot aspect ratio affects (1) the amount of jet mass injected per unit length, and (2) the axial domain over which the mass is injected. Generally, increasing the aspect ratio (long:short dimension) of slanted slots decreases jet penetration. This is seen in Fig. 13 from the computational results reported by Oechsle et al. (1992).

This effect can also be seen experimentally in the slanted slot results of Hatch et al. (1995a). For a given momentum-flux ratio and number of orifices, the smaller aspect ratio 45-deg slots penetrate farther into the crosstream. The larger aspect ratio slots, although penetrating less, create a stronger swirl component that enhances circumferential mixing. Figure 14 compares the mixture uniformity for 8:1 and 4:1 slanted slots. At the lowest and intermediate J values, the 4:1 geometry is a better mixer at all axial locations. At the highest J values tested, however, the 8:1 slot is competitive, and is the better mixer beyond x/R = 0.5. This is because of overpenetration of the jets at J = 84.2 for the 4:1 slots, which improves mixing at the initial planes, but produces unmixed regions near the wall at downstream locations.

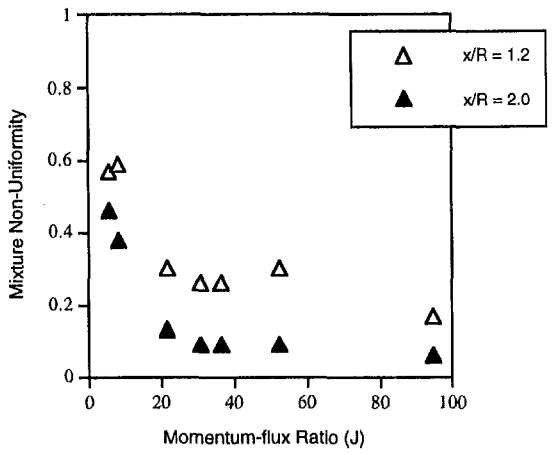

Fig. 8 Mixture nonuniformity of slanted slots (data from Vranos et al., 1991)

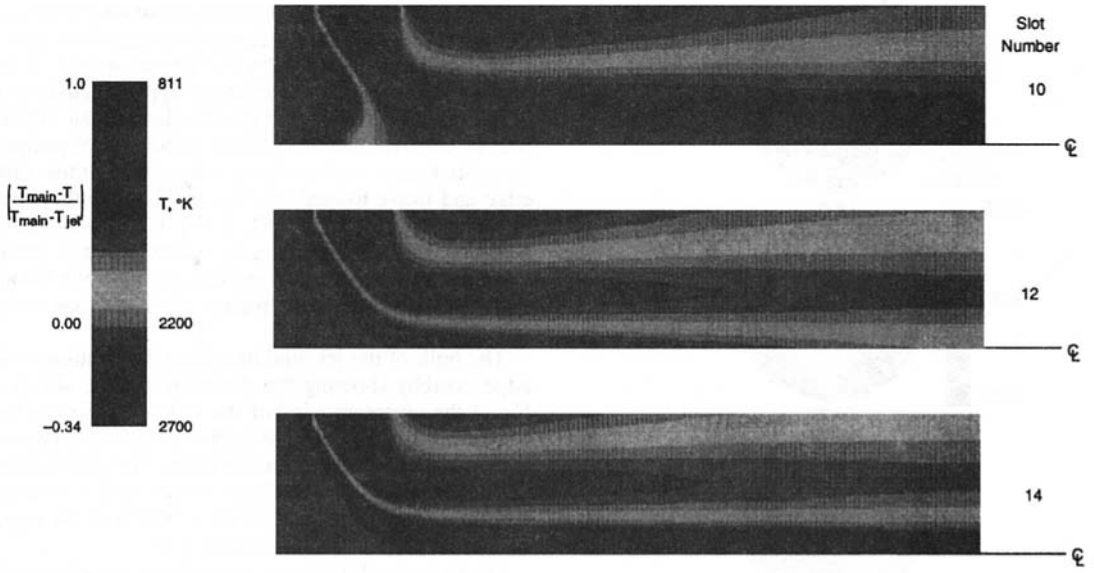

Fig. 9 Predicted isothermal maps for $J = 36$; variation in number of slots (data from Smith et al., 1991)

3.5 Slanted Slot Angle. The computational results in Fig. 15 from Oechsle et al. (1992) indicate a significant decrease in jet penetration as slot slant angle is increased. Note that the slant angle is the angular deviation from the axial direction. This effect is also shown in the experimental results of Hatch et al. (1995a) that are shown in Fig. 16.

3.6 Orifice Optimization. Sowa et al. (1994) engaged in a more comprehensive optimization scheme incorporating parameters such as the number of orifices, orifice aspect ratio, and orifice angle at a fixed momentum-flux ratio. Optimum mixing occurred when the mean trajectory lay between a radial distance of 50–65 percent from the mixer centerline at one duct radius downstream from the leading edge of the orifices. A numerical regression performed on the data yielded a nonlinear relationship between the orifice configurations and the mixture uniformity. At the optimum number of orifices, both a round hole and a 5:1 22 degree slanted slot had minima in mixing uniformity. These distributions are shown in Fig. 17.

3.7 Mixing Duct Size. Three duct sizes were reported in Smith et al. (1991) using a previously optimized 12-slot geometry as a baseline case. The three mixing section diameters were 6, 5, and 4 in. (15.24, 12.70, and 10.16 cm). As the area was reduced, the velocity of the mainstream flow in the mixing section increased proportional to the area reduction. The re-

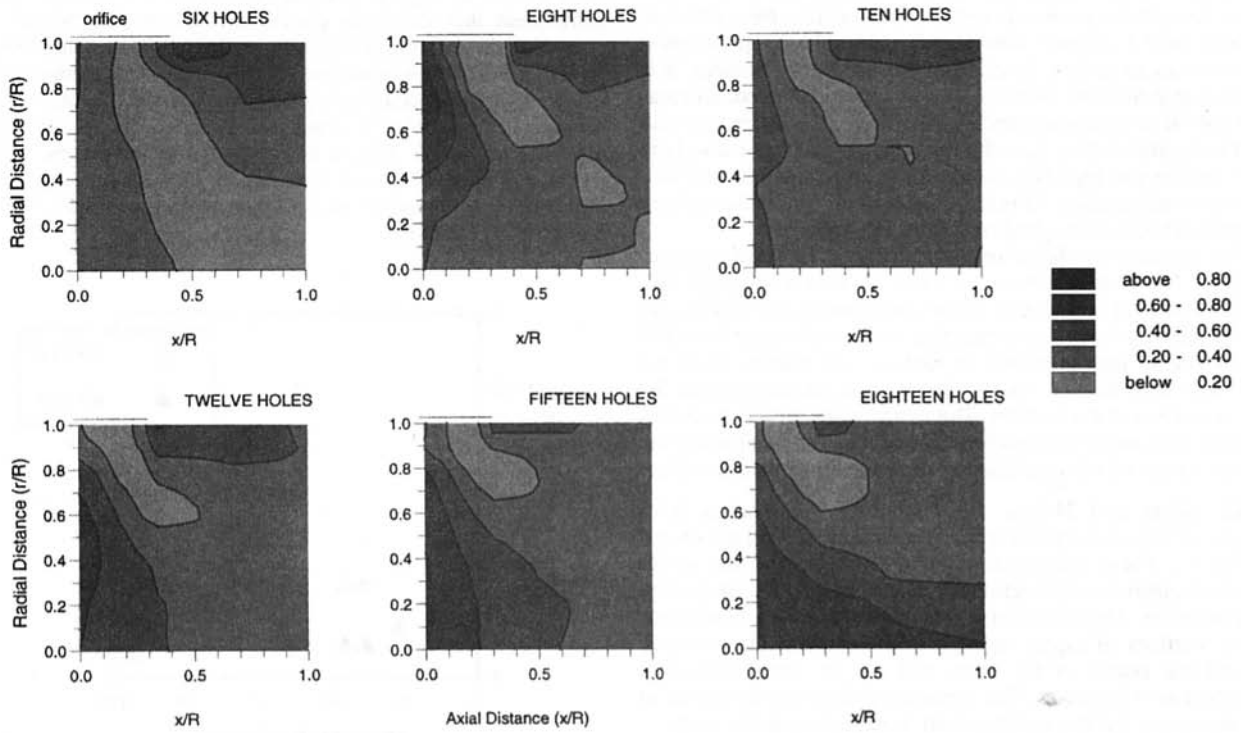

Fig. 10 Local mixture fraction contours as the number of orifices are varied at $J = 52$. Radial distance ranges from the module centerline ($r = 0''$) to the wall ($r = 1.5''$). Axial distance ranges from the orifice leading edge ($z = 0''$) to one duct radius downstream ($z = 1.5''$) (data from Kroll et al., 1993).

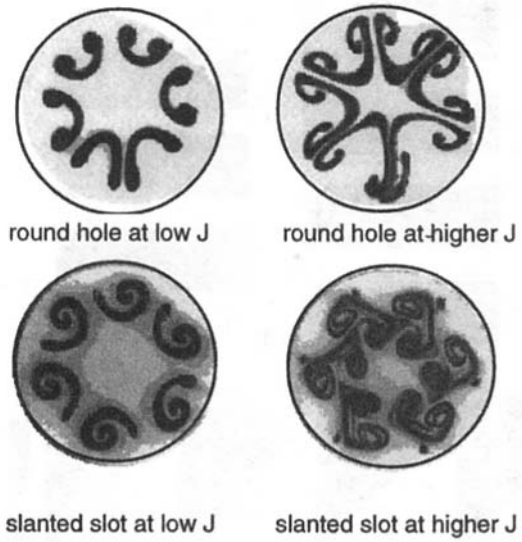

Fig. 11 Frames from movies at low Reynolds number (data from Vranos et al., 1991)

sulting reduction in static pressure in the mixing section increases the pressure drop across the orifices, thus increasing the jet velocity. Both the jet and mainstream velocities increase, and these counterbalance such that the momentum-flux ratio remains constant as the mixing flow area is reduced.

The resultant mixing is shown in Figs. 18 and 19 from Smith et al. (1991). The slot size was adjusted according to the variation in diameter of the mixing section to ensure a constant mass-flow ratio.

Figure 18 shows the temperature distributions in radial-axial planes through the orifice centerline for all three diameters. Figure 19 shows the corresponding distributions in a radial-transverse plane at one mixing section diameter downstream of the jet inlet. In this figure a full circle is shown, although the computations were performed for a 15 deg pie section. The similarity of the plots suggests that the flow was nondimensionally identical for these cases.

However, the corresponding NO_x results (Smith et al., 1991) are not identical, as shown in Fig. 20. In this figure, NO_x production is plotted as a function of axial location for each of the three mixing section diameters. The NO_x Emission Index (EI (as defined by ARP 1256A)) at $x/R = 2$ for the 4″ section is 70 percent less than that for the 6″ section. For these cases, CO was completely depleted by $x/R = 2$.

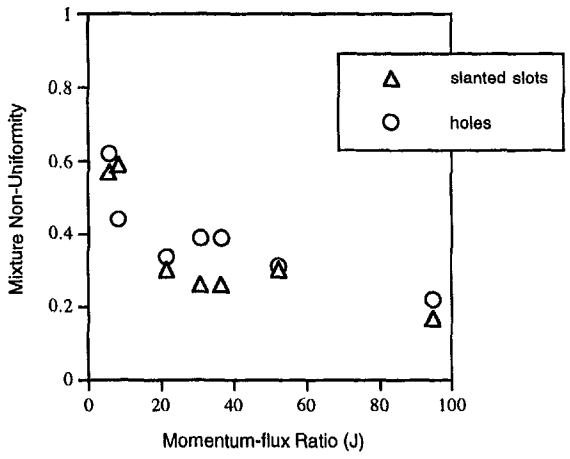

Fig. 12 Mixture nonuniformity of equal area slanted slots and holes at $x/R = 1.2$ (data from Vranos et al., 1991)

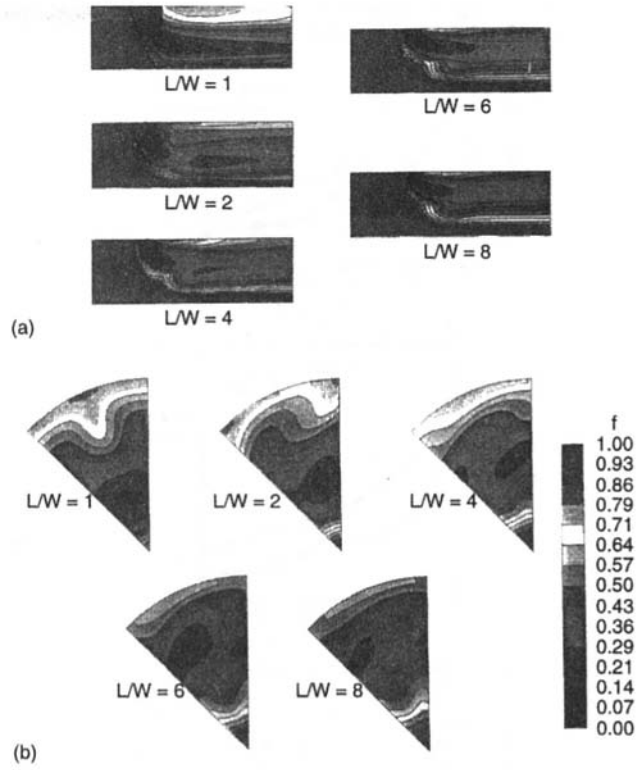

Fig. 13 Effect of slot aspect ratio (L/W) on mixing for $J = 20.5$, (a) axial-radial plane through orifice center, (b) radial-tangential plane at $x/R = 1$ (data from Oechsle et al., 1992)

The formation of NO_x is controlled by temperature, oxygen concentration, and residence time. Since mixing was identical, temperatures and oxygen concentrations must be identical, leaving only residence time to account for the difference. The NO_x reduction apparent in Fig. 20 is related to the decrease in residence time that occurs in smaller sections both through increased velocities and shorter mixing lengths. This is discussed in Smith et al. (1991).

3.8 Mixing and Emissions. The relation between mixing and NO_x was investigated in Hatch et al. (1995b) using a procedure to infer NO_x signatures from nonreacting experimental data. The NO formation rate corresponding to the mixing flow field in Fig. 3 is shown in Fig. 21. The mixing and NO production field for the same configuration (eight round holes) at a higher momentum-flux ratio ($J = 84.2$) are shown in Fig. 22. The Mixing Uniformity, NO Production Rate, and the Accumulated NO Produced for these configurations plus an intermediate J are shown in Fig. 23.

The majority of nitric oxide is formed early in the injection. As a result the mixing processes in the initial region are critical in the overall emissions performance of the mixer. However, as can be seen in Fig. 23, rapid early mixing due to overpenetrating jets (e.g. at $J = 84.2$ in Figs. 22 and 23), does not necessarily lead to a minimum production of NO.

For the range of momentum-flux ratios and orifice geometries examined in Hatch et al. (1995b) the round holes and 45 deg 4:1 slanted slots at $J \sim 55$ yielded the best mixers from a NO perspective.

The relation between NO_x and mixing, for a fixed number of orifices, was also examined in the computations reported in Oechsle and Holdeman (1995). It was shown that, in general, statistical mixing parameters do not correlate with NO_x production rates at downstream axial locations (e.g., $x/R = 1$), as the planar variances lack historical information from throughout the mixing region.

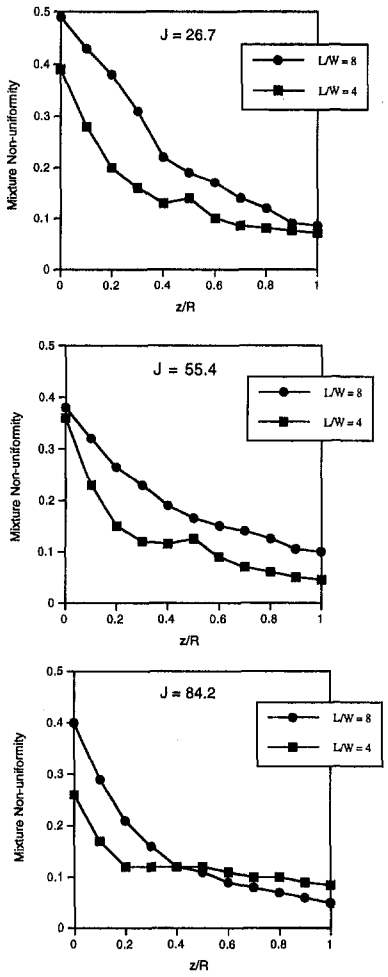

Fig. 14 Effect of slot aspect ratio on mixture nonuniformity (data from Hatch et al., 1995a)

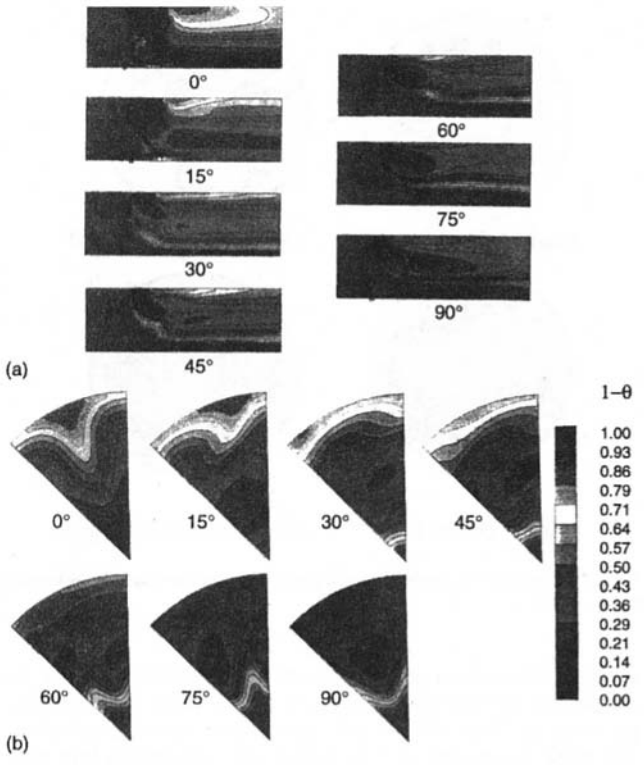

Fig. 15 Effect of slot slant angle on mixing for $J = 20.5$, (*a*) axial-radial plane through orifice center, (*b*) radial-tangential plane at $x/R = 1$ (data from Oechsle et al., 1992)

NO_x production is shown to be highly related to the jet penetration. Overpenetrating configurations show increased NO_x production, as do underpenetrating cases. For example, at low J conditions, optimum penetration is achieved with round holes, and NO_x is minimum. At higher J's the jets overpenetrate and NO_x increases primarily due to its formation near the combustor walls. Similarly, jet penetration is optimum at higher momentum-flux ratios with large aspect ratios and slant angles, and NO_x is minimum for these configurations. At lower J's the jets severely underpenetrate, and NO_x increases due to its formation near the combustor centerline.

Although planar parameters don't seem to correlate with NO_x, one can infer relative NO_x production from the radial-axial and radial-transverse distributions, namely optimum penetration will generally yield minimum NO_x. One caveat is important here though: What one calls optimum depends on the axial location observed, that is, "optimum" penetration near the orifice will result in overpenetration farther downstream; and conversely "optimum" downstream penetration will look like underpenetration upstream of that location.

3.9 Reaction. The computational results reported by Oechsle et al. (1994) show that reacting flow distributions are very similar to nonreacting ones, provided that a conserved scalar is compared (which dimensionless temperature is not in a reacting flow as sources and sinks exist for this).

The dimensionless temperature distributions for the nonreacting cases are compared with normalized equivalence ratio distributions for the reacting flow cases. Radial-axial planes appear in Fig. 24, while the corresponding radial-tangential planes at $x/R = 1$ are shown in Fig. 25. These results suggest that the nonreacting temperature profiles can emulate the reacting flow equivalence ratio distribution reasonably well.

It is worth noting, however, that the nonreacting jets appear to interact more near the center of the mixer as compared to the corresponding reacting flow results. This is usually spotted by the upstream swirling flow production near where opposing jets merge. This was not observed in the 12-orifice cases investigated due to the much shallower penetration for these compared to the 8-orifice cases.

Reacting flow studies by Leong et al. (1995) were the first experimental characterization of jet mixing in a rich reacting cylindrical crossflow. Species concentration measurements were obtained for four round hole orifice configurations at a predetermined J. Jet penetration, as indicated by the maximum O_2 trajectory, was observed to affect reaction and mixing processes.

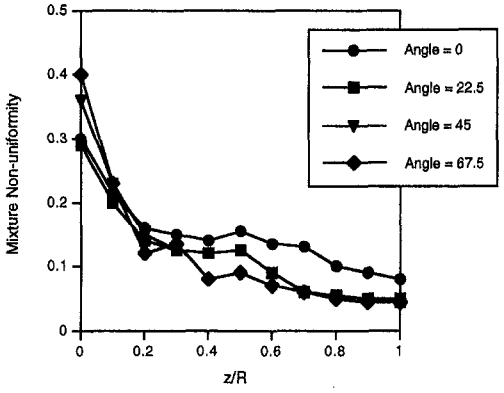

Fig. 16 Effect of slot angle on mixture nonuniformity (data from Hatch et al., 1995a)

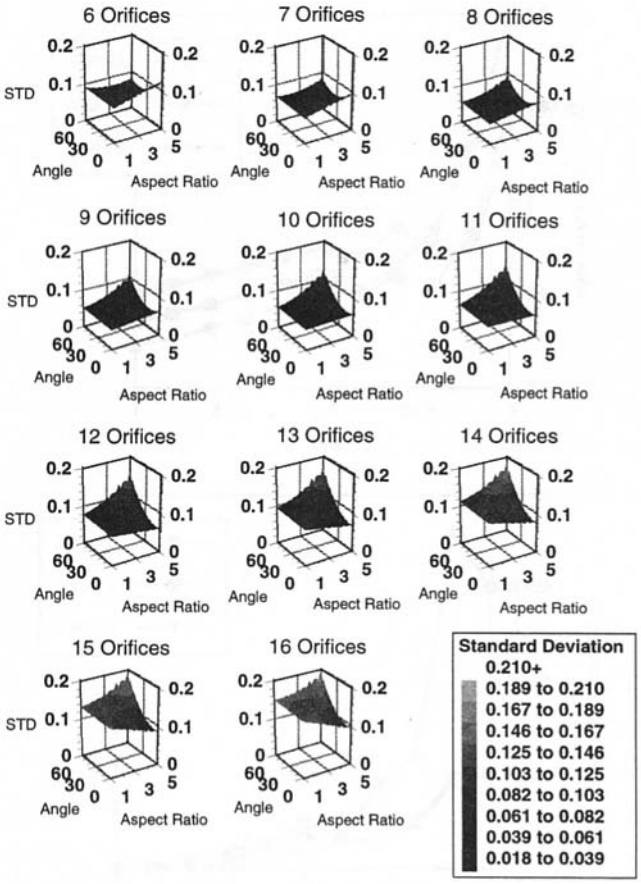

Fig. 17 Predicted values of area weighted standard deviation "STD" for different orifice numbers as orifice aspect ratio and orifice angle are changed (data from Sowa et al., 1994)

Jet penetration toward the midradius by $x/R = 1$ resulted in more lateral spreading of jet fluid, which made available more fluid volume to react with the rich crossflow to produce CO_2. Figures 26 and 27 show that the 12-hole case produced an optimal jet (O_2 trajectory, which gave a more evenly dispersed CO_2 distribution that most closely matches the concentration expected for the equilibrium equivalence ratio.

4 Design Procedure

These results suggest that for a given momentum-flux ratio and downstream distance, combustor design procedure should first identify the circumferential orifice spacing required to obtain the desired penetration and profile shape. The orifice size

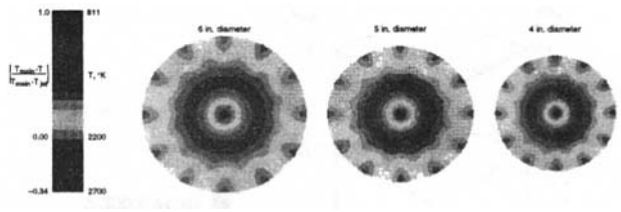

Fig. 19 Predicted radial-tangential plane isothermal maps (x/R = 2.0) for J = 36; variation in mixing diameter (data from Smith et al., 1991)

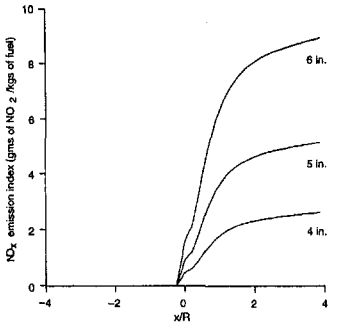

Fig. 20 NO_x emission index for mixing diameters of 6″, 5″, and 4″ (data from Smith et al., 1991)

would then be chosen to provide the required jet-to-mainstream mass-flow ratio. Some adjustments, including noncircular orifices or multiple rows, may be needed to arrive at the final design because the penetration varies slightly with orifice size and shape, and other parameters such as the combustor pressure loss; and the ratio of the orifice spacing to diameter must be monitored to insure that the suggested configuration is physically realistic.

Based on these results, the suggested procedure is, given mass-flow ratio, pressure drop, and channel height:

1 Choose desired orifice shape and C_d
2 Identify needed total orifice area
3 Calculate momentum-flux ratio (J)
5 Select number of orifices for optimum penetration
4 Calculate individual orifice size
6 Determine blockage, fit, etc.
7 Iterate to solution

Summary of Results

(A) Several results from recent studies in a cylindrical duct are consistent with previous results from investigations in rectangular ducts. These include:

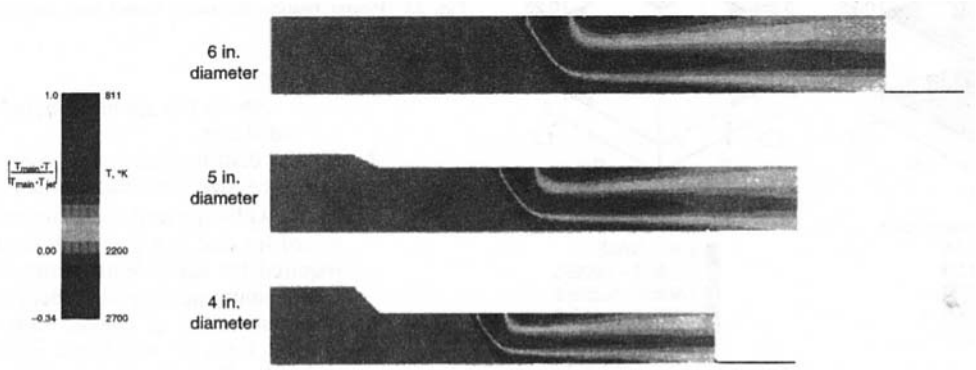

Fig. 18 Predicted radial-axial plane isothermal maps (data from Smith et al., 1991)

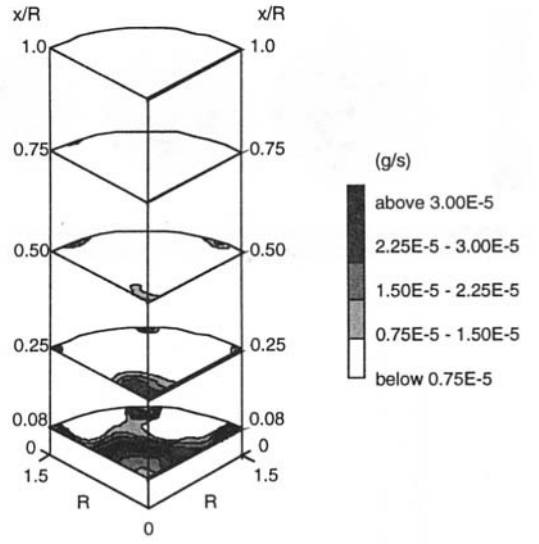

Fig. 21 NO production, eight round hole configuration, J = 26.7 (data from Hatch et al., 1995b)

1 Variations in momentum-flux ratio and number of orifices have a significant effect on the flow distribution.
2 Optimum configurations may depend on given momentum-flux ratio, number of orifices, and orifice shape.
   (a) Optimum spacing may vary with orifice shape.
   (b) The optimum number of orifices (n) increases with increasing momentum-flux ratio (J). For most orifice shapes, n is proportional to $\sqrt{J}$.
   (c) The same orifice shape may not be best for all momentum-flux ratios.
   (d) What is perceived as "optimum" depends both on the application and the downstream distance.
3 Similar distributions can be obtained, independent of orifice size and shape, when n is proportional to $\sqrt{J}$. Although orifice configurations can be optimized for any J, a greater downstream distance is required for equivalent mixing if either J and/or the optimum number of orifices is small.
4 The penetration of slanted slots is less than for aligned slots, or equal-area circular holes. Also, scalar distributions for slanted slots are rotated with respect to the injection centerplane.

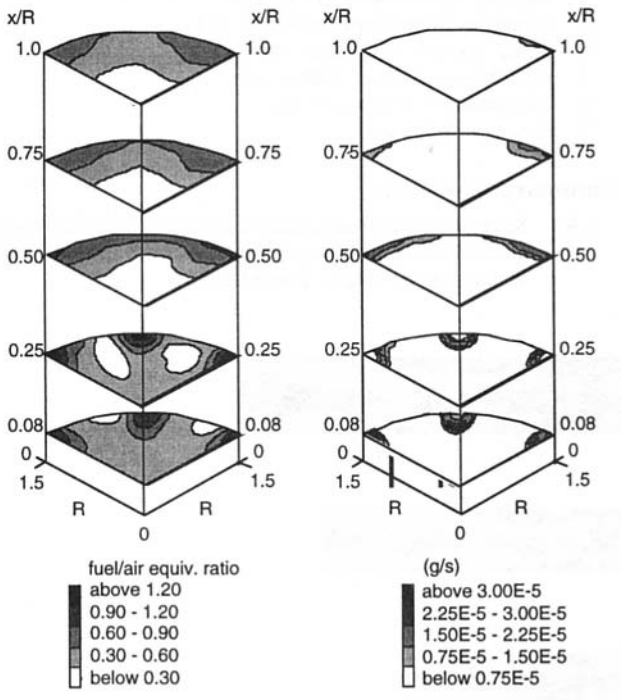

Fig. 22 Equivalence ratio and NO production, eight round hole configuration, J = 84.2 (data from Hatch et al., 1995b)

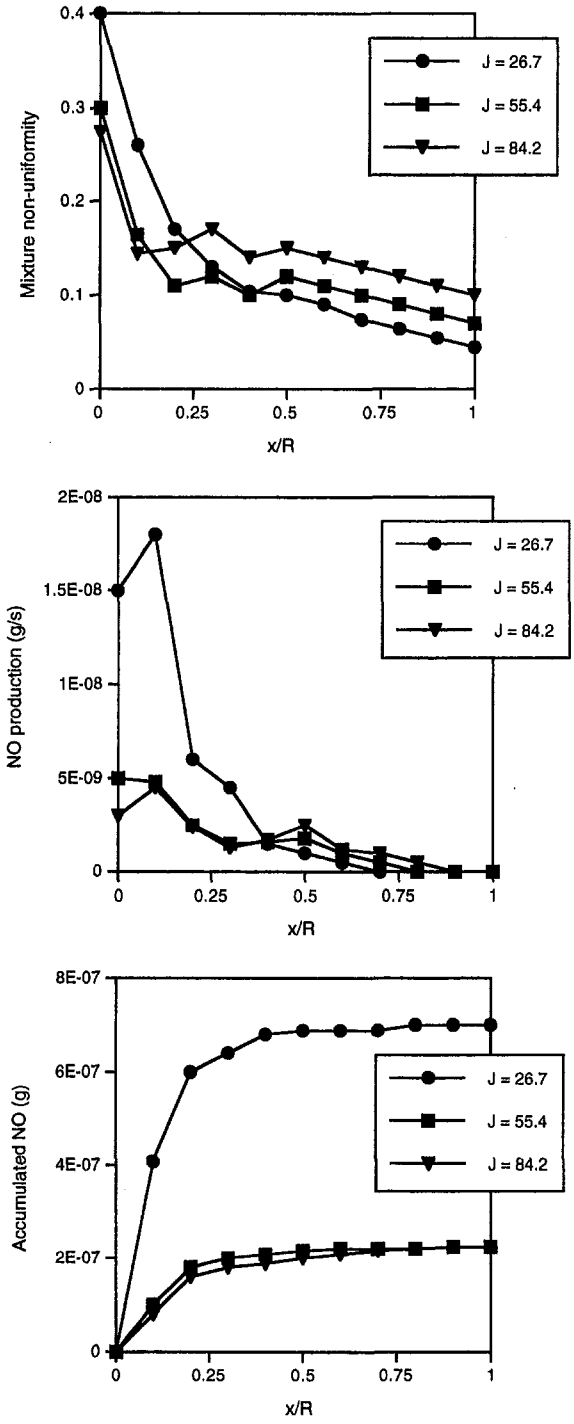

Fig. 23 Planar results for eight round hole configuration (data from Hatch et al., 1995b)

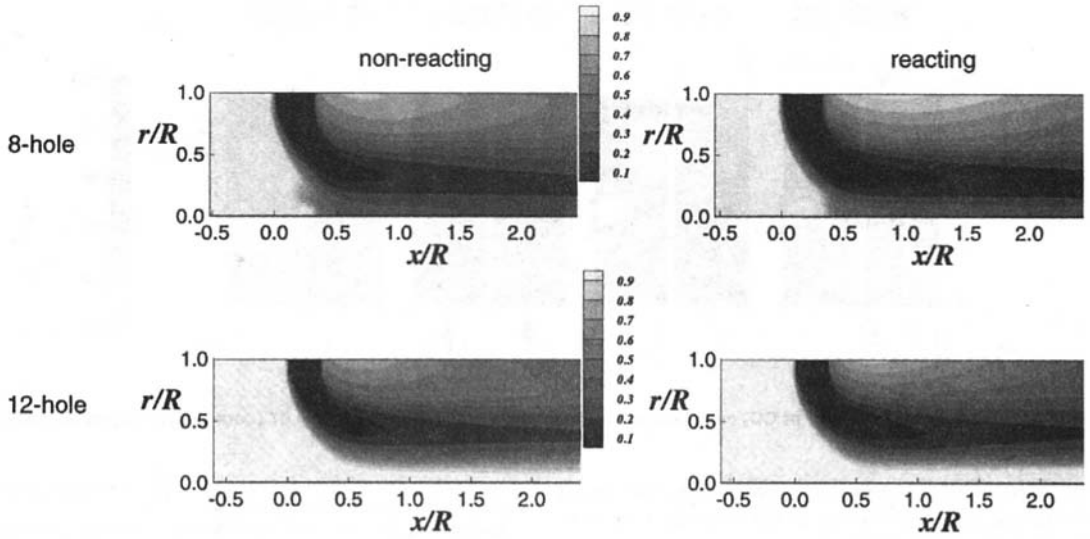

Fig. 24 Normalized temperature distribution for nonreacting flow compared to the normalized equivalence ratio distribution for reacting flow (plane through the center of the jet) (data from Oechsle et al., 1994)

5 For orifices that are symmetric with respect to the main flow direction, the effects of shape appear to be significant mostly in the region near the injection plane. Beyond, e.g., $x/R = 1$, scalar distributions are expected to be similar to those observed from equally spaced equal-area circular orifices.

(B) The minimization of NO production in a quick mixer

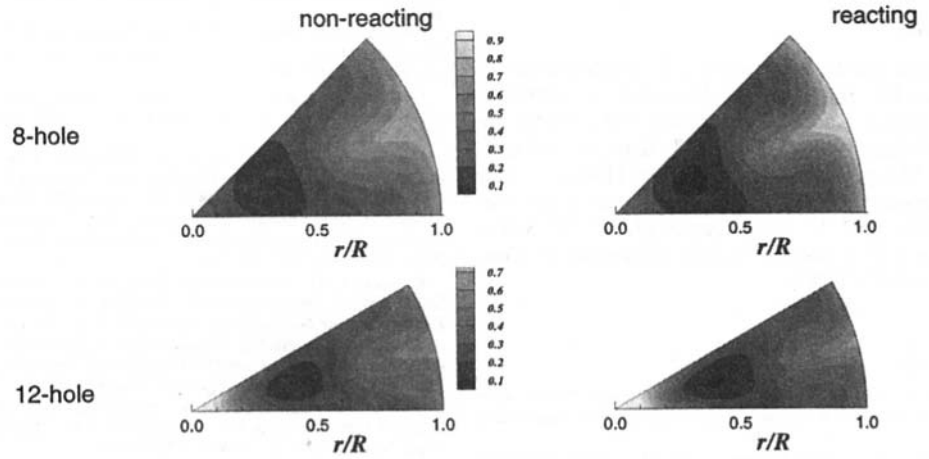

Fig. 25 Normalized temperature distribution for nonreacting flow compared to the normalized equivalence ratio distribution for the reacting flow for radial-tangential plane at $x/R = 1$ (data from Oechsle et al., 1994)

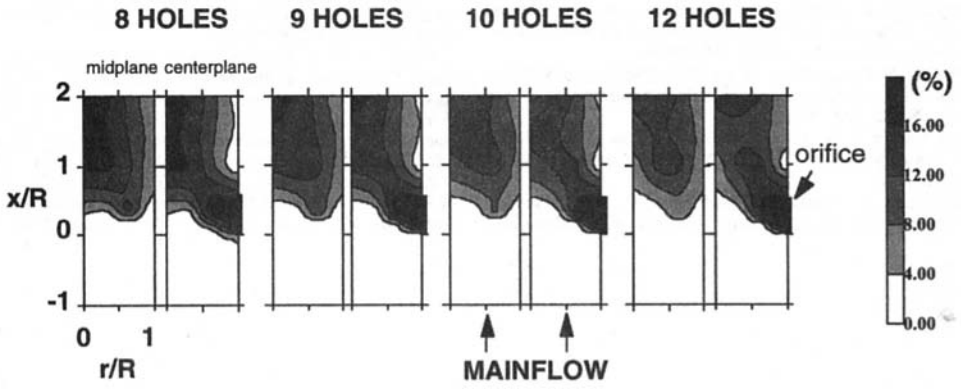

Fig. 26 Averaged axial history of O_2 evolution at two radial-axial cross sections at $J = 57$ (data from Leong et al., 1995)

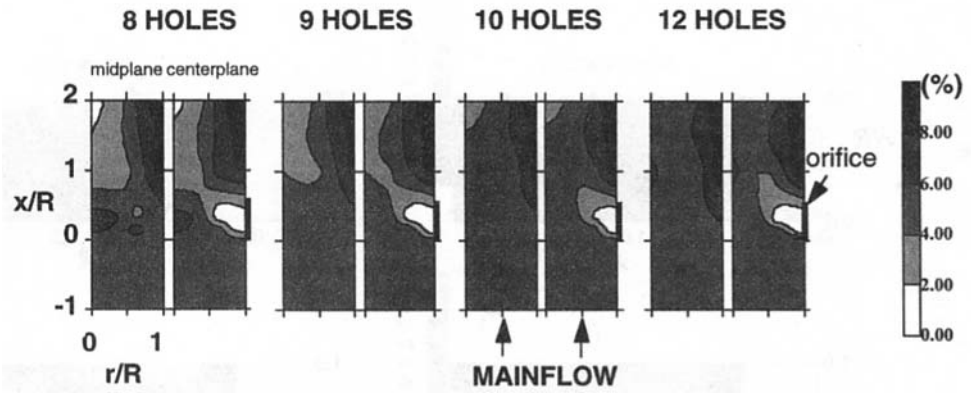

Fig. 27 Averaged axial history of CO_2 evolution at two radial-axial cross sections at $J = 57$ (data from Leong et al., 1995)

will often require a tradeoff between effective initial mixing and effective mixing in the wall region downstream of the plane of injection.

(C) The results cited suggest that further study may not necessarily lead to a universal "rule of thumb" for mixer design for lowest emissions, because optimization will likely require an assessment for a specific application.

(D) The results shown seem to indicate that nonreacting dimensionless scalar profiles can emulate the reacting flow equivalence ratio distribution reasonably well.

Acknowledgments

The authors would like to acknowledge the contributions of the following: D. B. Bain, CFD Research Corporation (CFDRC); M. S. Hatch, Radian Corporation (formerly at the University of California, Irvine (UCI)); J. T. Kroll, UCI; M. Y. Leong, UCI; H. C. Mongia, GE Aircraft Engines (formerly with Allison Engine Company); B. True, United Technologies Research Center (UTRC); M. V. Talpallikar, CFDRC: W. Sowa, UTRC (formerly at UCI); and A. Vranos, University of Connecticut (formerly with UTRC).

References

ARP 1256A, 1980, *Procedure for the Continuous Sampling and Measurement of Gaseous Emissions From Aircraft Turbine Engines,* Society of Automotive Engineers, Inc.

Cline, M. C., Micklow, G. J., Yang, S. L., and Nguyen, H. L., 1995, "Numerical Analysis of the Flowfield in a Staged Gas Turbine Combustor," *Journal of Propulsion and Power,* Vol. 11, No. 5, pp. 894–898.

Hatch, M. S., Sowa, W. A., Samuelsen, G. S., and Holdeman, J. D., 1995a, "Jet Mixing Into a Heated Cross Flow in a Cylindrical Duct: Influence of Geometry and Flow Variations," *Journal of Propulsion and Power,* Vol. 11, No. 3, pp. 393–402, see also AIAA-92-0773 & NASA TM 105390.

Hatch, M. S., Sowa, W. A., Samuelsen, G. S., and Holdeman, J. D., 1995b, "Influence of Geometry and Flow Variation on NO Formation in the Quick Mixer of a Staged Combustor," to be published in ASME JOURNAL OF ENGINEERING FOR GAS TURBINES AND POWER; see also NASA TM 105639.

Holdeman, J. D., Walker, R. E., and Kors, D. L., 1973, "Mixing of Multiple Dilution Jets With a Hot Primary Airstream for Gas Turbine Applications," Paper No. AIAA-73-1249; also NASA TM-71426.

Holdeman, J. D., and Walker, R. E., 1977, "Mixing of a Row of Jets With a Confined Crossflow," *AIAA Journal,* Vol. 15, No. 2, pp. 243ff; see also AIAA-76-48 and NASA TM-71821.

Holdeman, J. D., Srinivasan, R., Reynolds, R., and White, C., 1992, "Studies of the Effects of Curvature on Dilution Jet Mixing," *Journal of Propulsion and Power,* Vol. 8, No. 1, pp. 209–218; see also AIAA-87-1953 (NASA TM 84878) and AIAA-88-3180 (NASA TM-100896).

Holdeman, J. D., 1993, "Mixing of Multiple Jets With a Subsonic Crossflow," *Prog. Energy Combust. Sci.,* Vol. 19, pp. 31–70; see also AIAA-91-2458 and NASA TM 104412.

Howe, G. W., Li, Z., Shih, T. I.-P., and Nguyen, H. L., 1991, "Simulation of Mixing in the Quench Zone of a Rich Burn-Quick Quench Mix-Lean Burn Combustor," AIAA Paper No. 91-0410.

Kroll, J. T., Sowa, W. A., Samuelsen, G. S., and Holdeman, J. D., 1993, "Optimization of Circular Orifice Jets Mixing Into a Heated Crossflow in a Cylindrical Duct," AIAA Paper No. 93-0249; also NASA TM 105934.

Leong, M. Y., Samuelsen, G. S., and Holdeman, J. D., 1995, "Jet Mixing in a Reacting Cylindrical Crossflow," AIAA Paper No. 95-3109; also NASA TM 106975.

Liscinsky, D. S., Vranos, A., and Lohmann, R. P., 1993, "Experimental Study of Cross-Stream Mixing in Cylindrical and Rectangular Ducts," NASA CR 187141.

Oechsle, V. L., Mongia, H. C., and Holdeman, J. D., 1992, "A Parametric Numerical Study of Mixing in a Cylindrical Duct," AIAA Paper No. 92-3088; also NASA TM 105695.

Oechsle, V. L., Mongia, H. C., and Holdeman, J. D., 1993, "An Analytical Study of Jet Mixing in a Cylindrical Duct," AIAA Paper No. 93-2043; also NASA TM 106181.

Oechsle, V. L., Mongia, H. C., and Holdeman, J. D., 1994, "Comparison of the Mixing Calculations of Reacting and Non-reacting Flows in a Cylindrical Duct," AIAA Paper No. 94-0865; also NASA TM 106435.

Oechsle, V. L., and Holdeman, J. D., 1995, "Numerical Mixing Calculations of Confined Reacting Jet Flows in a Cylindrical Duct," AIAA Paper No. 95-0733; also NASA TM 106736.

Richards, C. D., and Samuelsen, G. S., 1992, "The Role of Primary Jets in the Dome Region Aerodynamics of a Model Can Combustor," ASME *Journal of Engineering for Gas Turbines and Power,* Vol. 114, pp. 20–26.

Sowa, W. A., Kroll, J. T., Samuelsen, G. S., and Holdeman, J. D., 1994, "Optimization of Orifice Geometry for Crossflow Mixing in a Cylindrical Duct," AIAA Paper No. 94-0219; also NASA TM 106436.

Smith, C. E., Talpallikar, M. V., and Holdeman, J. D., 1991, "Jet Mixing in Reduced Flow Areas for Lower Emissions in Gas Turbine Combustors," AIAA Paper No. 91-2460; also NASA TM 104411.

Talpallikar, Milind V., Smith, Clifford E., and Lai, Ming-Chia, 1990, "Rapid Mix Concepts for Low Emission Combustors in Gas Turbine Engines," NASA CR 185292.

Talpallikar, M. V., Smith, C. E., Lai, M.-C., and Holdeman, J. D., 1992, "CFD Analysis of Jet Mixing in Low NO_x Flametube Combustors," ASME *Journal of Engineering for Gas Turbines and Power,* Vol. 114, pp. 416–424; see also ASME Paper 91-GT-217, NASA TM 104466.

Vranos, A., Liscinsky, D. S., True, B., and Holdeman, J. D., 1991, "Experimental Study of Cross-Stream Mixing in a Cylindrical Duct," AIAA Paper No. 91-2459; also NASA TM 105180.

Winowich, N. S., Moeykens, S. A., and Nguyen, H. L., 1991, "Three-Dimensional Calculations of the Mixing of Radial Jets From Slanted Slots With a Reactive Cylindrical Crossflow," AIAA Paper No. 91-2081.

Yang, S. L., Cline, M. C., Chen, H., and Chang, Y.-L., 1992, "A Three-Dimensional Grid Generation Scheme for Gas Turbine Combustors With Inclined Slots," *ASME Computers in Engineering 1992,* Vol. 2, pp. 43–51.

Zhu, G., and Lai, M.-C., 1995, "A Parametric Study of Penetration and Mixing of Radial Jets in Necked-Down Cylindrical Cross-Flow," *Journal of Propulsion and Power,* Vol. 11, No. 2, pp. 252–260; see also Paper No. AIAA-92-3091.

M. Lukas

D. P. Anderson

Spectro Inc.,
Littleton, MA 01460

Lubricant Analysis for Gas Turbine Condition Monitoring

Introduction

Analysis of used lubricating oil is a fast-evolving technique for predictive maintenance with any closed-loop lubricating system such as those in gas and steam turbines, diesel and gasoline engines, transmissions, gearboxes, compressors, pumps, bearings, and hydraulic systems.

To be effective in monitoring both machine condition and lubricant condition, a modern oil analysis program takes the form shown in Fig. 1. Based on analysis of periodic oil samples, a laboratory diagnostic report is sent to the personnel responsible for the equipment to warn of any possible problem or to make a specific maintenance recommendation. The entire process, from sample taking to the diagnostic report, should take less than 48 hours to be effective. These reports, when combined with statistical analysis and trending, can provide an insight to management personnel on the effectiveness of the program, efficiency of the maintenance department, repair status of equipment, recurring problems, and even information on the performance of different lubricants.

Condition monitoring by oil analysis can be broken down into two categories: debris monitoring to measure the trace quantities of wear particles carried by the lubricant away from the wearing surfaces and lubricant condition monitoring to determine whether the lubricant itself is fit for service based on physical and chemical tests.

Debris Monitoring

Debris monitoring pertains primarily to the detection, and sometimes also the analysis, of metallic wear particles. The most common techniques and devices applied to this category of condition monitoring include atomic emission spectroscopy (AES), atomic absorption spectroscopy (AAS), X-ray fluorescence spectroscopy (XRF), ferrography, magnetic plugs, magnetic chip detectors, and microscopic examination of filter debris.

Debris monitoring is the backbone of oil analysis condition monitoring programs. It is effective in the sense that tests can be applied to determine that a system is nearing, or has reached, a failure mode. Further damage can thus be contained or avoided through immediate shutdown and repair.

Spectroscopy is the most widely applied technique for debris monitoring. It provides a quantitative, multi-elemental analysis of wear debris in lubricating oil. The elemental concentration of as many as 20 elements are reported in parts per million (ppm). Wear metals such as iron, aluminum, chromium, copper, tin, lead, silver, titanium and nickel are detectable, as well as lubricant additives such as calcium, barium, zinc, phosphorus, magnesium, boron and molybdenum. Certain contaminants such as silicon, sodium and potassium are also routinely detected. Trends are used to determine the mechanical health of a system. Concentration trends are established through routine monitoring to indicate if a continuing wear condition exists, the rate of wear, and as a consequence, the immediacy of the wear problem.

There are several types of spectrometers used for debris monitoring. These include rotating disk arc emission (RDE), atomic absorption (AAS), X-ray fluorescence (XRF), and inductively coupled plasma (ICP) emission spectrometers. Each has its own advantages and disadvantages; however, the RDE technique is preferred for applications with large numbers of oil samples and is the most popular due to its ease of use in all types of environments.

An effective spectrometric oil analysis program is dependent upon interpretation of the analytical data. The interpretation is an evaluation of the maintenance status of an oil wetted system and consists of the laboratory's recommended maintenance action.

The evaluation process can be manual or computer assisted. It is based on wear metal guidelines for a particular piece of equipment, but must also take into account a combination of variables. Equipment operating conditions are a prime factor. The environment is also important; for example, an arid location will cause an increase in silicon readings accompanied by a corresponding increase of wear. Time since last oil change and oil consumption will affect readings and possibly disguise a wear trend. The length of time the equipment is in service is extremely important. During the engine break-in period, either when new or after overhaul, wear metal concentrations are abnormally high and are no cause for alarm. If equipment is left to stand idle for long periods of time, rust can form and iron readings will increase. Older systems will also generate more wear metals than fairly new ones of the same model. Load on the engine is also a factor, particularly changes in load; increases in wear may be due to an additional load placed on the engine. The chemical composition of the oil and coolant are also important. Metals present may not be due to wear at all, but rather due to an oil additive or coolant leak.

Since the spectrometer is able to differentiate between metals, it is able to determine which metals make up the total wear-metal content of the oil. For example, if only iron and aluminum are present in abnormal amounts, the analyst's job is much simpler. The entire system does not have to be torn down and inspected; the inspection can be restricted to those components made up of iron and aluminum. Knowing the relative concentrations of the elements will further narrow down their possible source. For example:

1 An increase in silver and nickel in a certain type of railroad diesel is indicative of bearing wear. If detected early enough, a relatively simple bearing replacement can be made, rather than a $30,000–$50,000 overhaul and crankshaft replacement.

2 An increase in the amount of silicon in conjunction with a corresponding increase in iron, aluminum, and chromium is probably caused by dirt ingestion, Fig. 2. Air filter replacement and oil change may be the only maintenance action required. An increase of silicon alone may mean the oil type was changed to one containing a silicon-based antifoaming agent and no maintenance action is required. The trend without an increase of silicon could mean piston wear.

Contributed by the International Gas Turbine Institute and presented at Turbo Asia '96, Jakarta, Indonesia, November 5–7, 1996. Manuscript received at ASME Headquarters July 1996. Associate Technical Editor: J. W. Shinn. Paper No. 96-TA-54.

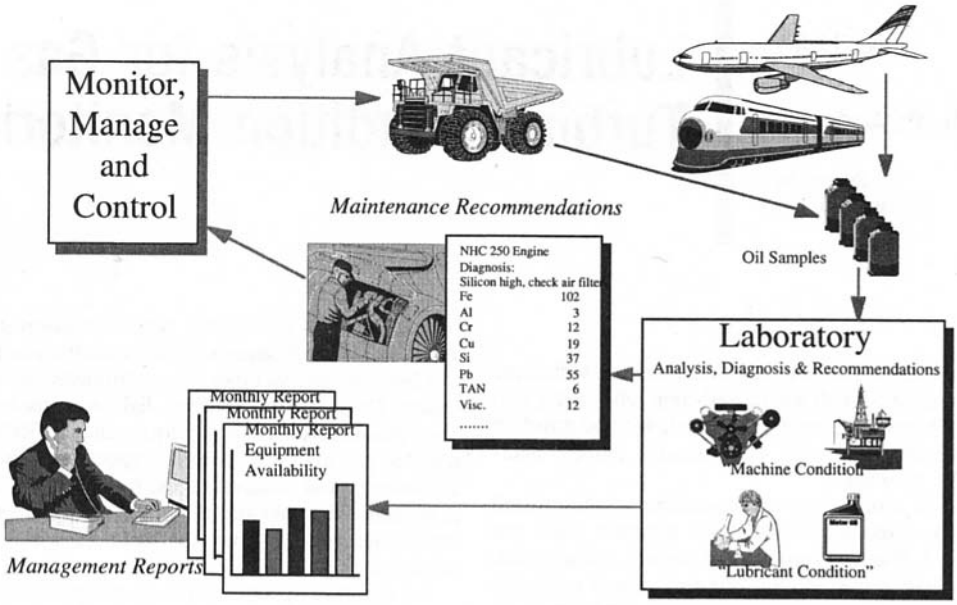

Fig. 1 Oil analysis program, flow diagram

3 Sometimes even the slightest increase or presence of an element can be cause for alarm. The bearing shown in Fig. 3 was removed from the gearbox of an aircraft. The presence of only 2 ppm (parts-per-million) of copper was sufficient to warrant maintenance action. The source of the copper was the bronze bearing cage.

4 A trend showing the presence of boron in most water-cooled systems would indicate a coolant leak. If left unchecked, the coolant combines with combustion products and forms harmful acids, which attack metal.

Oil analysis by itself or in conjunction with additional simple tests can be used to extend oil change intervals. This is accomplished by monitoring the oil's additives package and contamination, an added capability that makes oil analysis even more cost effective and popular in today's unpredictable oil market.

Lubricant Condition Monitoring

The second part of an effective oil analysis program is lubricant condition monitoring to determine the effectiveness and remaining life of the lubricant based on degradation and contamination analysis. The number and type of tests performed on a used oil sample vary with the type of oil and the type of machine being monitored. Physical property tests performed by the typical used oil analysis laboratory, often using modifications of ASTM procedures to reduce analysis time, include the following: viscosity, TBN (Total Base Number), TAN (Total Acid Number), water content (Karl Fischer), fuel dilution, and insolubles.

Physical property analysis has been a "must" product of the commercial laboratories and is becoming a serious consideration of the military programs. It consists of a series of related tests, which determine the contamination and degradation of a lubricant. Physical property analysis is synonymous with extended oil change interval, which is, of course, at today's prices, the same as money in the bank to users of larger quantities of lubricants. Oil change intervals are generally based on mileage or time on a system. Physical property analysis, on the other hand, allows retention of the oil in a system as long as it holds its beneficial properties.

The extended oil change program is what makes oil analysis appealing and sellable to the owner of large fleets of vehicles. The typical program consists of wear metal analysis and the six tests shown in Table 1. The first four tests monitor oil degradation and the remainder, contamination.

Oxidation is a term used to describe degradation of a lubricant caused by chemical reaction between the oil and oxygen at the elevated temperatures of operation. The result is an acidic condition and sludge, which cause component wear and oil thickening. Oxidation reduces a system's service life and impairs oil circulation.

Nitration in some aspects is similar to oxidation, but in this instance, nitrogen-containing compounds combine with used oil to form oxides, mostly at the top of the cylinders. Nitration is an indication of blow-by and is characterized by oil thickening and an offensive odor.

The flow rate of a lubricant in relation to time is referred to as viscosity and it is one of the most important properties of a lubricant. An abnormally low viscosity reduces oil film strength, which is its ability to prevent metal to metal contact. Its ability to carry contaminants away from moving parts and sealing ability will also be degraded. An abnormally high viscosity reduces the effectiveness of the lubricant and the contaminants that are the cause of it will increase wear of components and could create harmful deposits.

The use of chemical additives in lubricants has become extremely important in modern machinery. As mentioned earlier, an additive may be in the lubricant to combat an adverse condition or enhance lubricating properties. Some additives are required for efficient operation. In some cases, the presence of an incorrect additive can be detrimental to the equipment. For these reasons, the quantity and type must be continuously monitored. Additive depletion testing has, therefore, become very important in oil analysis programs.

Water in the oil is a result of coolant or anti-freeze leaks, or, in the case of marine applications, can be caused by sea water. Excessive amounts of water will cause wear, attack bearing metal, and affect the lubricating qualities of the oil. Excessive water could be an indication of inadequate head torquing, a cracked head, or broken lining.

Small amounts of fuel in the lubricant do not present a problem. At engine operating temperatures, small amounts evaporate and an equilibrium is reached. Large amounts of fuel dilution result in the same detrimental effects as experienced with water dilution.

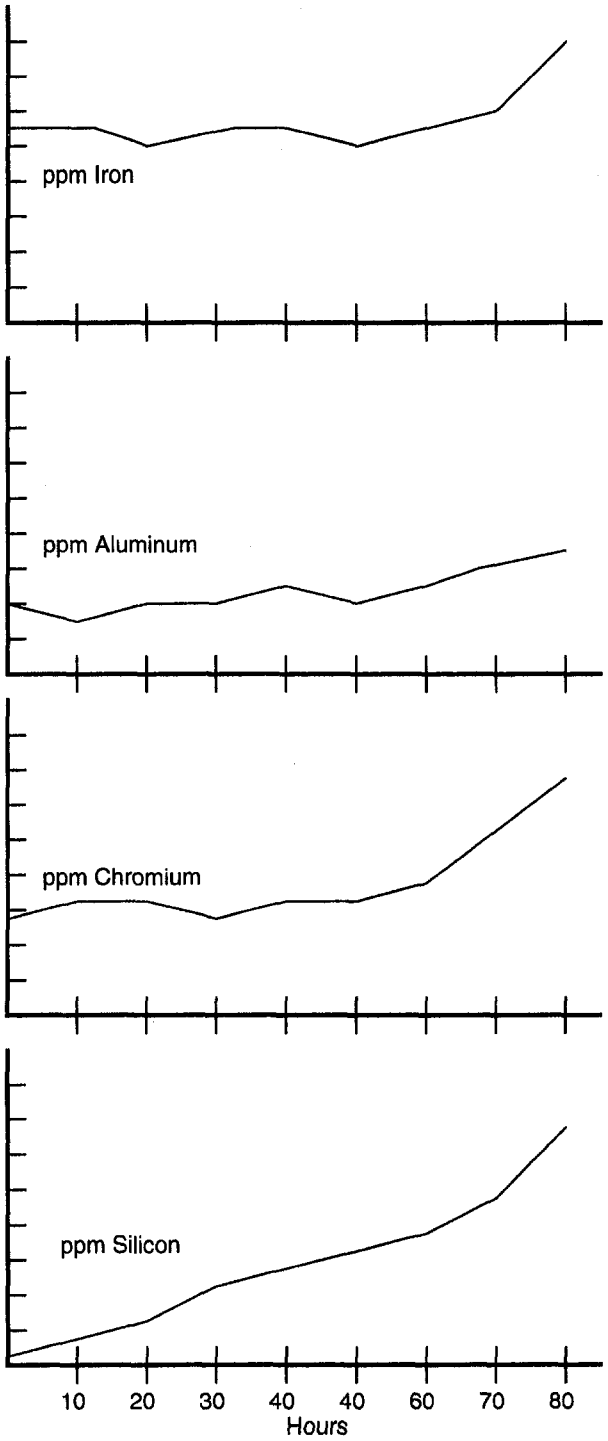

Fig. 2 Spectrometric trend showing dirt ingestion

Solids in a lubricant may be due to ingested dirt, wear metals, or byproducts of an incomplete combustion process. They are indicative of carburetor problems, oil filter saturation, and an indication of the efficiency of the air intake system. Excessive solids will cause wear.

Turnkey Used Oil Analysis Laboratories

The configuration and required instrumentation of a laboratory will vary based on the machines being monitored and the sample work load. A full-service laboratory is shown in Fig. 4. In a modern oil analysis program, the basic minimum components consist of an emission spectrometer, a Fourier Transform-Infrared spectrometer (FT-IR), and a viscometer. Each instrument sends its results to a data-based laboratory information management system for data storage, evaluation, and reporting.

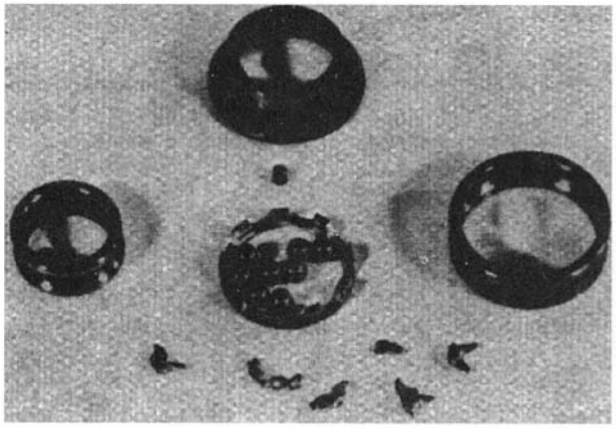

Fig. 3 Example of a bearing failure

A rotating disk emission (RDE) spectrometer is the basic instrument recommended for routine measurement of the elemental concentration of wear metals, contaminants, and additives. It provides simplicity of operation, sensitivity to larger particles, freedom from diluting samples, and requires no gas or cooling water while completing analysis of approximately 20 elements in less than a minute. An atomic absorption spectrometer (AAS) is seldom used unless the sample volume is extremely low and cost per sample is not a consideration. An inductively coupled plasma (ICP) spectrometer is recommended only where absolute accuracy of results is important, such as quantification of additive elements in a lubricating-blending plant.

FT-IR spectrometers for used oil analysis have dedicated programs that extract lubricant degradation and contamination parameters from the measured spectrum of the used oil sample. The technique is fast, less than a minute per sample, and provides data on oxidation, nitration, sulfation, soot, fuel dilution, water and glycol contamination, and in some cases, additive depletion. As a fast trending technique, it has become a standard instrument in many high sample volume used oil analysis laboratories.

A viscometer is the third required instrument in the basic turnkey used oil analysis system. Viscosity is the single most important physical characteristic of a lubricant since it determines load carrying ability as well as flow and heat flow characteristics. Manual viscometers are inexpensive and work well in low sample volume requirements. Automatic viscometers are readily available for various degrees of automation and unattended operation.

In the basic system, measurements from each analytical instrument are sent to a central computer file where the results are incorporated into a history file for each unit (specific machine or sampling point on a machine). When tests are complete, the computer calls up the file of each unit and compares the results

Table 1 Lubricant physical properties

Oxidation
Nitration
Viscosity
Additive Depletion
Water Dilution
Fuel Dilution
Solids

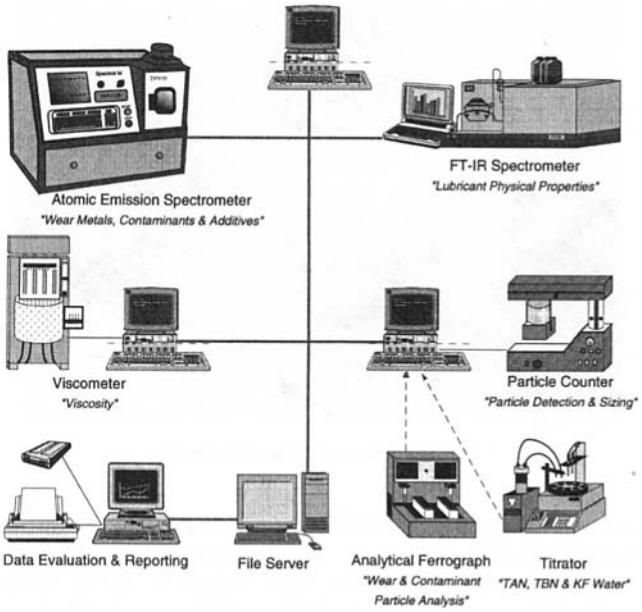

Fig. 4 Full-service turnkey used oil analysis laboratory

to a criteria matrix with allowable limits and to past analyses. In an automatic evaluation mode, records for samples with all data within limits are passed directly to the history file and a report with no recommended action is sent to the maintenance personnel. Samples with "out of limit readings" are flagged for review by the laboratory expert, who can then send a report with a maintenance recommendation to the maintenance personnel via telephone, telefax, or printed copy.

This basic used oil analysis laboratory can be expanded as the analytical requirements of the laboratory or the sample work load increase. Ferrography, which magnetically separates the wear particles in an oil sample and arranges them according to size on a microscope substrate, gives important supplemental information on ferrous particles too large to be measured by routine spectrometric methods.

Total Acid Number (TAN), Total Base Number (TBN), and Karl Fischer water determination are three frequently performed ASTM tests for oil degradation and contamination. An automatic titrator is sometimes supplied with a turnkey system if more definitive information than that supplied by the FT-IR spectrometer is required.

Particle count measurement is sometimes recommended, primarily for use with hydraulic systems or other clean lubricating oil systems such as those for turbines and compressors.

With this added equipment, the used oil analysis laboratory combines the analytical speed required for large sample volumes with the additional capabilities of providing specialized ASTM based tests. It contains instruments and operating software designed specifically for used oil analysis with turnaround times of 24 to 48 hours to provide data trends used for effective machine condition monitoring. With expanding needs, a local area network (LAN) can be used to share information and additional tests can be added to match specific machinery monitoring needs.

Case Histories

The following are a selection of predictive maintenance examples. They show the effectiveness and versatility of well-managed and properly applied condition monitoring programs based on oil analysis.

Aircraft Turbines. Several case histories documented at Nellis Air Force Base, Nevada, are good examples of oil analysis as applied to aircraft components.

Case 1. Table 2 shows the last seven spectrometric oil analysis results of the lubricant taken from an F100-100 engine out of an F15 aircraft. Note from the spectrometric readings that initially there was no trend; however, after 430 hours of operation, the iron content jumped from 4 to 11 parts-per-million from one flight to the next. A check sample and ground run gave the laboratory sufficient cause to request a teardown. The cause for the increase in iron is shown in Fig. 5. The number 4 bearing case was found to be broken and pieces were found in the sump. This is an ideal example of the SOAP program's capability of predicting an imminent malfunction and preventing catastrophic failure.

Case 2. The spectrometric analysis results for a J79 engine out of an F4C Phantom aircraft are shown in Table 3. The laboratory requested a resample when an increase in the sample aluminum content from 3 to 10 ppm was noted. A teardown revealed that the inlet gearbox vertical drive shaft shims had torn loose and metal particles were found in the screen. Note the particles and cracked housing in Fig. 6. Obviously, JOAP did not detect the large particles shown, but enough smaller ones were present to indicate the increasing aluminum trend.

Case 3. A TF30P3 engine out of a F111 Aircraft did not show a drastic increase in the wear metal trend. The iron content increased very gradually with operation and oscillated back and forth near the upper allowable iron threshold. When the iron level reached the threshold for the second time over several hours of operation, the engine was recommended for teardown. Upon disassembly for overhaul, the discrepancy found by the depot facility was a loose outer case in the tower shaft bearing (Fig. 7), causing it to turn in its housing.

Lubricant Mix-Up. A serious recurring problem in maintenance procedures is the use of an incorrect lubricant. A condition monitoring program can readily identify such problems through the analysis of the lubricant additive package and lubricant physical property analysis.

The most common lubricant mix-ups occur when an oil system is "topped off" to replace the oil that has been lost due to use or leakage. Usually a small amount of incorrect oil in a large closed loop system presents few immediate problems. This is, however, not the case in certain diesel engines, as illustrated by this example.

Table 4 is a summary of the last four oil analyses for a medium speed diesel engine from a locomotive. Only the most significant analytical data is shown.

The data clearly shows that after the first two samples, an incorrect oil was used to top off the reservoir. The three additive metals magnesium (Mg), phosphorus (P), and zinc (Zn) appear in the third analysis and increase in the fourth, a clear indication that the oil formulation has changed. In this type of engine, an incorrect oil that contains a zinc-based additive package can result in severe wear problems. Several components such as bearings and wrist pins have silver coatings, which corrode and wear in the presence of zinc. The early stages of the corrosive action caused by the zinc additive are indicated by the increase in the iron, copper and silver wear metals. A recommendation based on the analysis was made to drain and flush the system and to observe correct top-off oil requirements. Without oil analysis, the wear problem could have resulted in a bearing failure and a major overhaul costing over $150,000.

Contamination Example on a Pump Turbine. Pump turbines are used in many parts of the world to generate electrical power. Water is pumped to an elevated reservoir at night when power is relatively inexpensive. During peak power requirement periods, the water is allowed to flow downhill to turn a turbine coupled to a generator. These are reliable systems. However, condition monitoring based on oil analysis can be very effective at predicting a possible failure in the very early stages of the problem and prior to secondary damage or catastrophic failure.

Table 2 SOAP trend on F100-100 aircraft engine, end item F15

OVHL	Reason for Sample	Fe	Ag	Al	Cr	Ni	Ti	Lab Recommendation
				Elements				
424	R	4	0	0	0	1	1	A
426	R	4	0	0	1	1	1	A
427	R	4	0	2	1	1	1	A
428	R	4	0	2	1	1	1	A
430	R	3	0	2	1	1	1	B
430	R	12	0	2	1	1	1	G
430	L	12	0	2	1	1	1	T

R = Routine; L = Lab Requested; B = Submit Special Sample ASAP;
A = No Recommendation, Continue Routine Sampling
G = Sample After Each Flight - DO NOT FLY UNTIL RESULTS ARE KNOWN;
T = GROUND UNIT, Examine for Discrepancy, Advise Lab

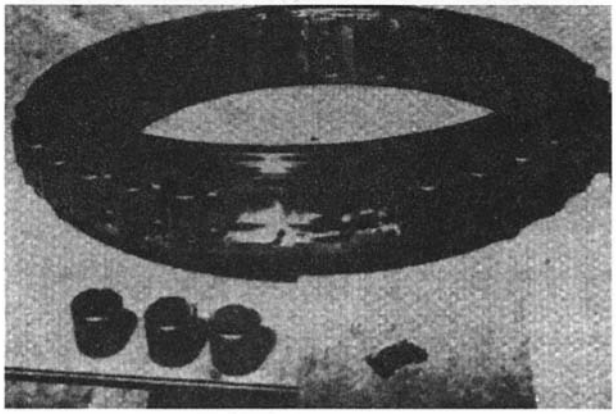

Fig. 5 No. 4 bearing from F100-100 engine

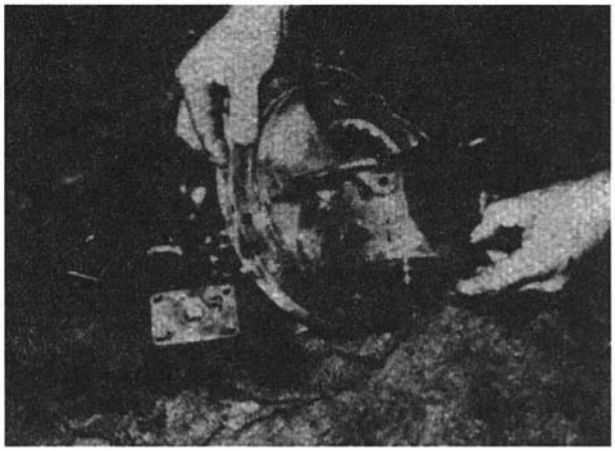

Fig. 6 Gearbox from J79-GE-15 engine

A pump storage system of an electric utility was part of a condition monitoring program when the laboratory detected an increase in "coarse" wear particles in the upper guide bearing assembly of the turbine. Although the normal analysis using an emission spectrometer was acceptable, the laboratory requested more frequent sampling based on the data for iron and babbit metals obtained with a large particle detection system option to the emission spectrometer. The original and the next three analyses using the standard emission spectrometer and the large particle detection (Rotrode Filter Spectroscopy, RFS) technique are shown in Fig. 8. Although the normal emission spectrometric analysis does not show a trend, the RFS analysis definitely does.

Ferrographic analysis on the last two samples verified the presence of large cutting wear particles, Fig. 9, causing the laboratory to issue an ALERT.

However, the presence of spheres on the ferrogram was the eventual indicator that led to the source of the wear problem. Tilting pad bearings such as those used on the turbine do not generate spheres in a wear mode. Weld beads were suspect and it was eventually verified that the turbine had not been protected during overhead construction work. Weld debris including weld beads, and not a defective component, was the cause of the wear trend.

Table 3 JOAP trend on a J79 aircraft engine, end item F4C

OVHL	Reason for Sample	Fe	Ag	Al	Cr	Mg	Ni	Lab Recommendation
				Elements				
181	R	23	0	0	0	11	1	A
196	R	26	0	4	1	10	1	B
196	L	24	0	4	1	10	1	G
196	R	26	0	3	1	11	1	A
197	R	26	0	5	1	12	1	A
198	R	28	0	7	1	13	1	A
202	R	31	0	10		14	1	F
202	L	34	0	11	1	18	1	T

R = Routine; L = Lab Requested; B = Submit Special Sample ASAP;
A = No Recommendation, Continue Routine Sampling
F = Submit Special Sample After Each Flying Day
G = Sample After Each Flight - DO NOT FLY UNTIL RESULTS ARE KNOWN;
T = GROUND UNIT, Examine for Discrepancy, Advise Lab

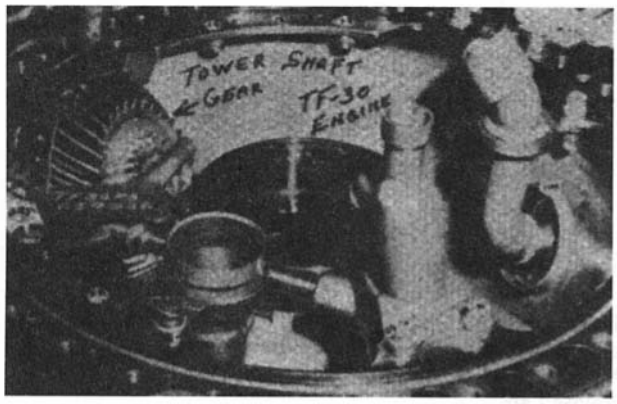

Fig. 7 Tower shaft bearing TF30P3 engine

Table 4 Spectrometric results for an EMD medium speed diesel locomotive

Date	Fe	Cu	Ag	Mg	P	Zn
9/30	19	10	0	0	0	3
12/23	21	10	0	0	9	3
3/23	27	13	2	107	75	90
6/11	25	30	10	220	110	123

Although the wear was not critical, the oil was cleaned as a precaution and more frequent oil analysis monitoring was recommended. The wear trend, if undetected by oil analysis, may or may not have led to a catastrophic failure. The thought of failure is not a pleasant one, especially in view that such a failure can require a multimillon dollar overhaul.

Conclusion

It is never too late to implement a machine condition monitoring program. The benefits of the program can be realized in a very short period of time. Figure 10 is a typical summary of the types of problems that will be encountered in most instances. A number of serious or critical problems will be identified almost immediately. These will require immediate attention to avoid secondary damage, unexpected downtime, or a major overhaul. A surprising number of imminent problems will also be identified. These are the future unplanned failures and should be scheduled for action and/or repair during the next scheduled maintenance shutdown.

The objective of a predictive maintenance program based on condition monitoring through oil analysis is to identify potential

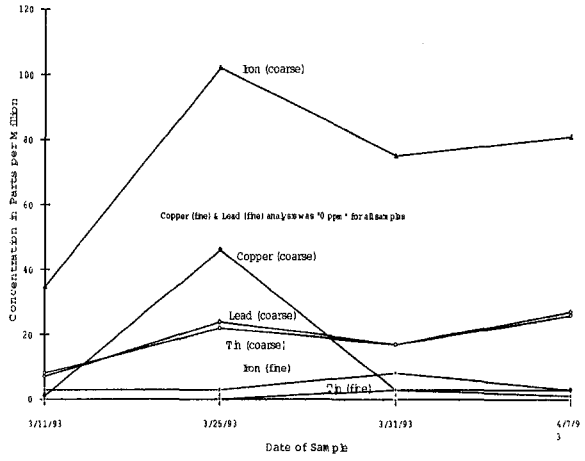

Fig. 8 Pump turbine guide bearing wear trend

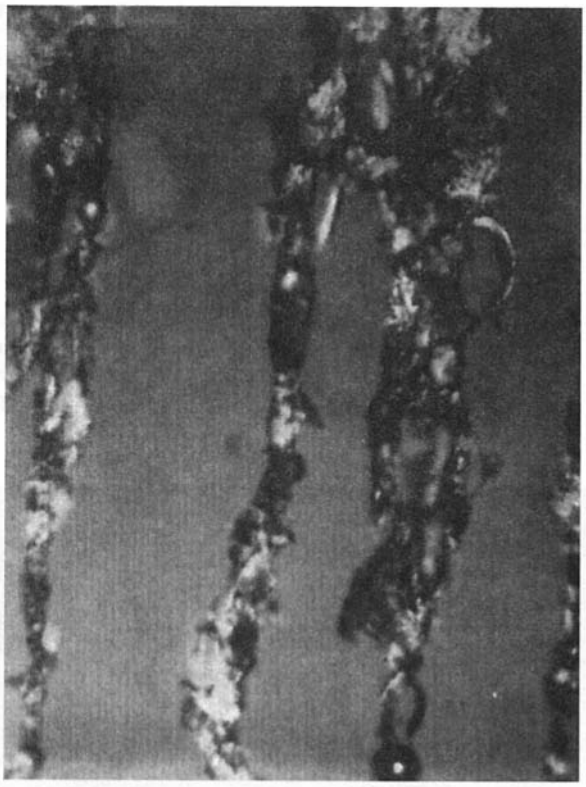

Fig. 9 Ferrogram showing cutting wear and weld beads

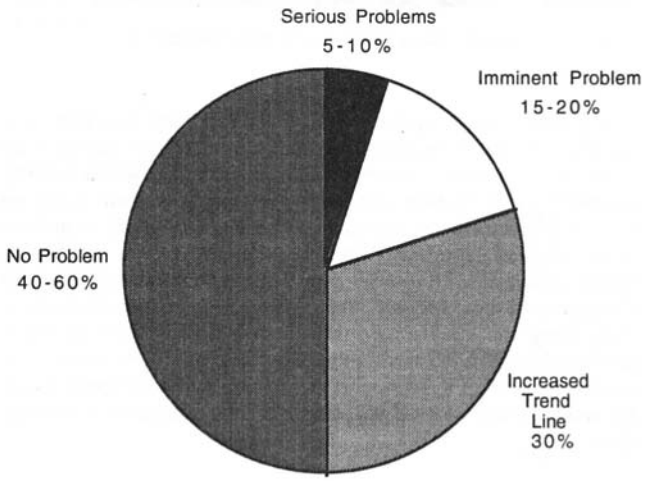

Fig. 10 Summary of problems in a maintenance program

failures in their early stages when repairs can still be initiated and costly secondary damage is avoided. A second objective is to monitor the quality of lubricants and to reduce lubricant usage through extended oil change intervals. The net benefits are reduced maintenance costs, increased equipment availability and life, reduced lubricant usage, and improve safety. They can be summarized as follows:

1 Reduced Maintenance Costs: This is the most apparent advantage, but sometimes the most difficult to document. Several problems can be avoided through an oil analysis program:

(a) Total equipment loss. A serious mechanical failure can result in the total destruction of that piece of equipment. An obvious example could be the failure of the main bearing in a turbine.

(b) Secondary damage. The failure of a minor component can often result in much more extensive damage to the equipment. For example, if detected early enough, the replacement of a defective bearing can prevent the catastrophic damage and cost associated with a crankshaft replacement.

(c) Over-maintenance. A system of routine, scheduled maintenance will inevitably result in work that is performed before it is necessary. An on-condition maintenance system based on oil analysis can prevent this.

(d) Maintenance-generated failures. The potential for human error exists whenever a piece of equipment is overhauled. A mistake such as the failure to tighten a bolt can result in equipment damage and failure when, in many cases, the equipment need not have been overhauled in the first place.

2 *Increased Equipment Availability:* A mining company must make effective use of its equipment in order to fulfill its function. Profitability or effectiveness is lost every time a piece of equipment is in the shop due to secondary damage or unnecessary maintenance.

3 *Reduced Lubricant Usage:* The analysis of oil for degradation and contamination provides an indicator of its ability to lubricate. If the reserve alkalinity, detergent, and extreme pressure qualities have not degraded and the contamination is low, the oil change interval can be extended, conserving both money and natural resources.

4 *Improved Safety:* When considering aviation, not much more need be said, especially in the case of single engine aircraft. Other equipment, such as diesels, compressors, or generators, may also pose potential safety hazards in the event of a major destructive failure.

It is almost impossible in today's competitive environment to operate a mine without some kind of predictive maintenance program. Condition monitoring based on oil analysis is a proven technique, which leads to more efficient use of equipment and maintenance savings. Some basic principles that must be followed in implementing such a program to fully realize its benefits are:

1 *Well-Defined Purpose:* You must clearly state what is to be accomplished. In most cases it is to save maintenance costs and improve equipment availability.

2 *Appropriate Tests:* Testing takes time and costs money. Many tests are possible, but the proper mix provides the necessary data and a certain amount of double checking.

3 *Careful and Timely Sampling:* An oil analysis program creates reports based on the analysis of the oil taken to the laboratory. An improperly taken or contaminated sample results in poor and erroneous data. Samples taken too infrequently can miss a potential problem, and those taken too frequently add to operating cost.

4 *Commitment to Act on the Information:* Everyone from the individual who takes the sample, the laboratory personnel and maintenance and management personnel, must be committed to act on the information produced by the laboratory. It does no one any good, for example, if a mechanic ignores the information provided by the laboratory.

References

Hunt, T. M., 1993, *Handbook of Wear Debris Analysis and Particle Detection in Liquids,* Elsevier Applied Science Publishers Ltd., London, pp. 25, 263.

Lukas, M., 1980, "Lubricating Oil Analysis," J. W. Sayer, *Sawyer's Turbomachinery Maintenance Handbook, ed.,* Turbomachinery International Publications, Norwalk, CT, pp. 8-1 to 8-20.

Lukas, A., and Anderson, D. P., 1992, "Machine and Lubricant Condition Monitoring for Extended Equipment Lifetimes and Predictive Maintenance," presented at International Symposium on Mining, 15–17 Sept. Pretoria, South Africa.

Nadkarni, R. A., 1991, "A Review of Modern Instrumental Methods of Elemental Analysis of Petroleum Related Material," *Modern Instrumental Methods of Elemental Analysis of Petroleum Products and Lubricants,* ASTM STP 1109, American Society of Testing and Materials, Philadelphia, PA.

Rhine, W. E., Saba, C. S., and Kaufmann, R. E., 1986, "Metal Particle Detection Capabilities of Rotating Disc Emission Spectrometers," *Lubrication Engineering,* Vol. 42, No. 12, p. 755.

Sieber, J. R., and Salmon, S. G., 1994, "Elemental Analysis of Lubricating Oils and Greases," *Lubrication,* Vol. 80, No. 1.

Wavelet Analysis for Gas Turbine Fault Diagnostics

N. Aretakis
Research Assistant.

K. Mathioudakis
Assistant Professor.

Laboratory of Thermal Turbomachines,
National Technical University of Athens,
Athens, Greece

The application of wavelet analysis to diagnosing faults in gas turbines is examined in the present paper. Applying the wavelet transform to time signals obtained from sensors placed on an engine gives information in correspondence to their Fourier transform. Diagnostic techniques based on Fourier analysis of signals can therefore be transposed to the wavelet analysis. In the paper the basic properties of wavelets, in relation to the nature of turbomachinery signals, are discussed. The possibilities for extracting diagnostic information by means of wavelets are examined, by studying the applicability to existing data from vibration, unsteady pressure, and acoustic measurements. Advantages offered, with respect to existing methods based on harmonic analysis, are discussed as well as particular requirements related to practical application.

1 Introduction

It is well known today that techniques based upon fast response measurements can provide important information about the condition of gas turbine components. Vibration analysis, in particular, is a standard procedure for monitoring the condition of an engine, giving the possibility to detect the occurrence of faults and mechanical wear. Not only gross faults but also faults of minor extent are identifiable by related techniques, as for example described by Loukis et al. (1991).

Identification of the type of fault, once a fault has been detected, is mainly based on techniques employing Fourier analysis. The harmonic content of measured dynamic quantities can be used to identify mechanical malfunctions. Certain typical mechanical problems, as for example misalignment or unbalance, constitute routine cases, and harmonic signatures for them can be found in manuals or textbooks (e.g., Cempel, 1991, and Collacott, 1977). On the other hand, minor faults of gas turbines blades can be identified by appropriate processing of dynamic measurement data, on the basis of Fourier analysis, as for example was shown by Mathioudakis et al. (1991). Reviews of related techniques have been the subject of several recent publications, as for example by Simmons and Smalley (1989) and Meher-Homji (1995).

In recent years a new technique for signal analysis has emerged under the name of wavelet analysis. Wavelet analysis decomposes a given signal into components, which are not simple harmonic functions, as in Fourier analysis, but are functions of another type, called wavelets. Although the original idea for wavelet decomposition is more than fifty years old, it is only recently that systematic applications have been undertaken and the method has started being established. The original impetus for wavelets came from the analysis of earthquake records, but wavelet analysis has found important applications in speech and image processing and is becoming a new significant tool in signal analysis (Newland, 1993).

The technique of wavelet analysis possesses some features that make it attractive to applications of signal processing. The present authors have therefore decided to investigate its suitability for analyzing signals from measurements on gas turbines, with more particular aim the application to fault diagnosis. The purpose of this paper is to present different aspects of wavelet analysis of turbomachinery signals, including matters related to interpretation of results, choice of processing parameters, possibilities of establishing fault signatures, and possible advantages offered. To the authors' knowledge, it is the first time that such an investigation is presented.

Since the method is not widely known, we have included some elements of wavelet theory essential for understanding the discussion on the applications in this paper. These elements come not only from existing literature, but also from derivations of the present authors, particularly concerning the relation to Fourier analysis. Applications to experimental data that have been previously analyzed with techniques based on Fourier analysis are then considered, in order to have some reference for examining possible advantages over those techniques.

2 Some Fundamentals for Wavelet Analysis

Wavelet analysis provides a method for decomposing a signal into one of different possible families of orthogonal local basis functions called wavelets. For practical calculations, mainly two classes of wavelets have been used, the dilation and the harmonic wavelets. In this paper we are concerned only with dilation wavelets (also known as Daubechies wavelets). This choice is made because the dilation wavelets are more suitable for applications requiring detailed features to be identified precisely in the time domain, a property useful for application to fault diagnosis. Some information about the dilation wavelets and the corresponding signal decomposition is given in the appendix.

Applying the wavelet transform to $N = 2^n$ samples of a time signal, wavelet amplitudes α_i, $i = 1{:}N$, are derived and the signal is related to these amplitudes through the relation:

$$x_i = \alpha_1 + \sum_{j=0}^{n-1} \sum_{k=0}^{2^j-1} \alpha_{2^j+k+1} w\left(2^j \cdot \frac{i-1}{N-1} - k\right), \quad i = 1{:}N \quad (1)$$

where $w(\ )$ are the wavelet functions. The summations in this relation introduce a grouping of the coefficients into what is termed "levels." This expression shows that there are $n + 1$ "levels," running from -1 to $n - 1$, corresponding to the external summation of this equation. For each level j, there are 2^j wavelets and wavelet amplitudes, corresponding to the internal summation. For example, there are two wavelets in level 1, the wavelets $w(2t)$ and $w(2t - 1)$ with corresponding wavelet amplitudes α_3 and α_4.

The wavelet expansion presented above shows that a signal can be fully described by the values of the wavelet amplitudes α_i, in the same way that a time signal is fully described by the Fourier coefficients. One way to present the values of the

Contributed by the International Gas Turbine Institute and presented at the 41st International Gas Turbine and Aeroengine Congress and Exhibition, Birmingham, United Kingdom, June 10–13, 1996. Manuscript received at ASME Headquarters February 1996. Paper No. 96-GT-343. Associate Technical Editor: J. N. Shinn.

amplitudes is the so called wavelet map. This way of presentation is discussed in the appendix.

The present authors have found that for diagnostic applications, it is sufficient to present the amplitudes on a graph in a sequential manner, similar to power spectra. Even though this presentation loses some of the advantages of the wavelet map, it can be linked to the structure of the signal, as will be explained in the following sections. In order to explain this fact, we will attempt to establish the relation of wavelet amplitudes to Fourier coefficients.

2.1 Fourier and Wavelet Analysis. A key fact for the physical interpretation of the wavelet amplitudes is that amplitudes of one particular level are related to harmonic components of a specific frequency range. Therefore, looking at amplitudes of one level is equivalent to observing a part of a periodogram, between certain frequencies. The connection between wavelet level and frequency can be established by correlating the wavelet amplitudes with Fourier coefficients. The later have a direct physical meaning and represent the frequency content of a time signal. It can be proved that the Fourier coefficients are linear combinations of wavelet amplitudes and vice versa. These linear combinations are unique for specific dilation wavelets DM and specific number of samples N of the analyzed signal, as shown in the appendix.

Each wavelet amplitude contributes to a Fourier coefficient with a different weighting factor. This means that the values of wavelet amplitudes of a specific level are connected to the amplitudes of harmonics within a frequency band of the power spectrum. The frequency range affected the most is related directly to the wavelet amplitudes with the largest weighting factors. In order to make this statement clearer, consider the following example.

If we have a signal sampled at $N = 8$ points, with sampling frequency f_s, analyzed by using D20 wavelets, then the Fourier coefficient C2, which corresponds to frequency $f_s/8$, is related to wavelet amplitudes by the following equation:

$$|C_2|^2 \approx 32 \cdot \alpha_2^2 + 8 \cdot (\alpha_3^2 + \alpha_4^2) + 0.000468 \cdot (\alpha_5^2 + \alpha_6^2 + \alpha_7^2 + \alpha_8^2) \quad (2)$$

We see that the wavelet amplitude α_2, which corresponds to level 0, contributes to C_2 with the greatest weighting factor, so the central frequency of this level is $f_s/8$. This can be more clearly shown by solving the system of equations for all Fourier coefficients with respect to α_2. We get:

$$\alpha_2^2 \approx 0.01 \cdot |C_2|^2 + 2.25 \cdot 10^{-6} \cdot |C_4|^2 \quad (3)$$

The harmonic mostly contributing to amplitude α_2 is the one corresponding to Fourier coefficient C_2.

Similarly, it can be shown that the central frequency of level 1, with wavelet amplitudes α_3, α_4, is $2f_s/8 = f_s/4$, because these amplitudes contribute to the Fourier coefficient for this frequency with the greatest weighting factor. The central frequency of the last level of the 8 samples signal (level 2, with wavelet amplitudes α_5 through α_8), is the Nyquist frequency $4f_s/8 = f_s/2$.

Generally, it can be shown that the central frequency for each level increases in octaves with the wavelet level. The central frequency for level j can then be defined from the following equation:

$$f_j = 2^j \cdot \frac{f_s}{N} \quad (4)$$

Figures 1 and 2 give a more descriptive picture of wavelets and the relation between wavelet level and frequency. In Fig. 1, D20 wavelets of levels 3, 4, 5, 7 with $N = 256$ points are shown. The power spectra of these wavelets are illustrated in Fig. 2.

The form of these spectra substantiates the arguments given previously. The wavelet of one level contains information mainly from the frequencies corresponding to the maxima of the spectra. On the other hand, while the information in the lower levels is localized in narrow bands of the frequency range, higher levels tend to cover wider bands, and higher frequencies (compare for example level 3 to level 7 in this figure). As observed from the figure, the central frequency of the levels increases in octaves, as explained above. It should also be noticed that this figure contains only four out of the total of nine levels, just for reasons of clarity.

2.2 Reasoning for Applicability to Turbomachines. The main feature of wavelet analysis is that it provides information that describes a signal in time and frequency domains simultaneously. In this respect, it offers advantages over other techniques used for simultaneous time-frequency descriptions of signals, such as Wigner–Ville method or Short-Time Fourier Transform (STFT). The advantages offered have been discussed by Newland (1994a). The feature of interest to the present work, however, is the representation of the information contained in frequency bands, by the amplitudes of the different wavelet levels.

As mentioned above, each wavelet level has a constant percentage bandwidth, with the central frequency increasing in octaves from level to level. High resolution in the time domain is possible with higher levels, because of the wide frequency band that they cover. That's why wavelet analysis allows local features and hidden details of a signal to be identified. This particular feature makes it useful for condition monitoring in turbomachinery components, where the detection of small changes in dynamic quantities is important.

In order to demonstrate applicability of wavelet analysis to turbomachinery signals, results of application to experimental data will be presented below. These signals come from measurements on an engine in both healthy and faulty condition and have been previously analyzed with techniques based on Fourier analysis. Therefore, they provide good reference cases for demonstrating the capabilities offered by wavelet analysis. In particular, the possibility of fault signatures derivation is examined.

3 Wavelet Transforms of Turbomachinery Signals

3.1 Experimental Data. The data used for the following applications have been obtained from measurements on an in-

Nomenclature

C_i = Fourier coefficients
$Df = f_s/N$
DM = dilation wavelet, with M wavelet coefficients
$\mathcal{F}(\ )$ = Fourier transform
$I_{N\times N} = N \times N$ unity matrix
$N = 2^n$ = number of samples of a record
$W(\ )$ = wavelet transform
$W^{-1}(\ )$ = inverse wavelet transform
f = frequency
f_s = sampling frequency
$w(t)$ = wavelet function
x_r = samples of a time signal $x(t)$
α_i = wavelet amplitudes

Subscripts and Superscripts

f, h = condition with fault, healthy condition
r, i = index
j = index of wavelet level

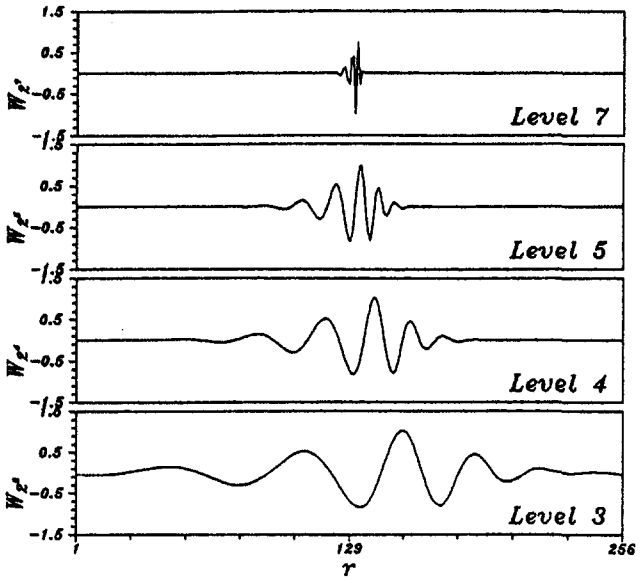

Fig. 1 Dilation wavelets D20 of different levels (N = 256 points)

dustrial gas turbine into which different faults were implanted. The experimental investigation has been documented by Mathioudakis et al. (1991) and Loukis et al. (1991).

Three quantities were measured. These measurements include: (1) unsteady pressure, measured with a fast response pressure transducer, fitted to the casing at the location of the first compressor stage, (2) compressor casing vibration, measured with accelerometers positioned at different locations, and (3) sound radiated from the compressor, measured with a microphone pair traversing upon a circular ring.

Experiments were performed testing the datum healthy engine and engine with the following faults: (a) two blades of rotor 1 fouled, (b) one twisted blade of rotor 1, (c) three vanes of stator 1 mistuned. The tests were performed at four different operating points, A, B, C, D, at the nominal rotational speed. The results presented in this paper were derived from data strings of 8192 samples per channel, acquired with sampling frequency 32,000 Hz.

3.2 Choice of Processing Parameters. Before we present the results of processing the data with wavelet analysis, comments on the reasoning for choosing specific processing parameters will be given. This is judged useful, since implementation to signals of the kind considered here is completely new and the parameters chosen have to conform with different requirements imposed by the nature of the signals.

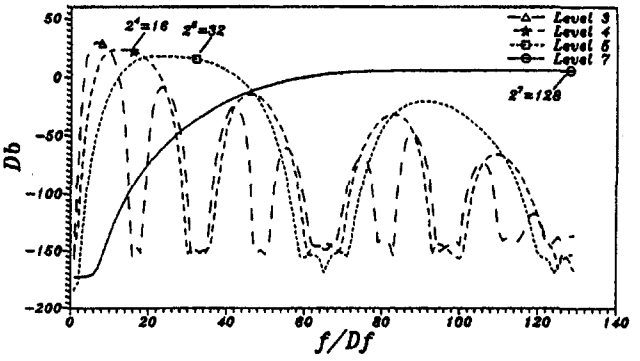

Fig. 2 Power spectra of D20 wavelets of different levels; definition of the corresponding central frequency for each level

First of all, we have to choose the kind of dilation wavelets to be used, or equivalently, the number of the wavelet coefficients which designate the wavelet's structure. By increasing the number of wavelet coefficients, the wavelet transform approximation converges toward to Gaussian-weighted harmonic signal. On the other hand, for the calculation of the wavelet transform with a large number of wavelet coefficients, longer computational times are required. Compromising these two requirements, the D20 wavelets were selected.

Another parameter that has to be chosen is the time duration of the examined signals. Considering the periodicity of the analyzed signals and the fact that only stationary faults are investigated, we apply phase averaging to the signals. The phase averaging is done with respect to a specific time point, provided by a key phasor signal. In this way the phase-averaged signals are synchronized. This is an essential feature of two signals that have to be compared, because of the time dependence of the wavelet amplitudes. In this way the influence of the random noise is reduced, whereas the periodic and stationary features of the signals are preserved. The derived signal covers more than one period of shaft rotation (to be exact, 256 points, 1.5 periods). This method should not be appropriate in the case of nonstationary signals where all the available time duration of the analyzed signal has to be processed.

3.3 Sample Results. Two typical examples of phase averaged signals are illustrated in Fig. 3. These are wall pressure signals for healthy condition and one rotor blade twisted.

The wavelet transforms of these signals have been calculated and the wavelet amplitudes, presented as wavelet maps, are shown in Fig. 4. The map for the healthy signal (Fig. 4(a)) exhibits peaks at level 5, whose central frequency is close to the Blade Passing Frequency (BPF). In order to facilitate discussion on the wavelet maps of Fig. 4, the spectral difference signature, that is the difference of power spectra of faulty and healthy signals, is shown in Fig. 5. This figure shows that differences appear mainly in frequency bands contained between the BPF and its harmonics. While at BPF, 2BPF, 3BPF the differences are small, they obtain large values at intermediate frequencies. For a more detailed discussion, see Mathioudakis et al. (1991). This is reflected on the wavelet maps by the appearance of differences at higher levels on the map, namely at level 4 (with 2000 Hz central frequency) and higher. Differences are indicated by the arrows on the twisted blade map and are more clearly shown in the difference of the wavelet maps (Fig. 4(c)). The location of differences along the x axis (''time'' axis) is the same as for the corresponding time signals (indicated by the circles on Fig. 3(b)).

A more distinct difference of the wavelet map can be observed for the data from a microphone and the case of 3 vanes of stator 1 mistuned. Wavelet maps for this case are shown in Fig. 6. It is observed that the difference is mainly located in level 5, which covers a wide frequency band with 4000 Hz central frequency. A clear displacement of the energy content of the signal from low levels to higher levels is also observed.

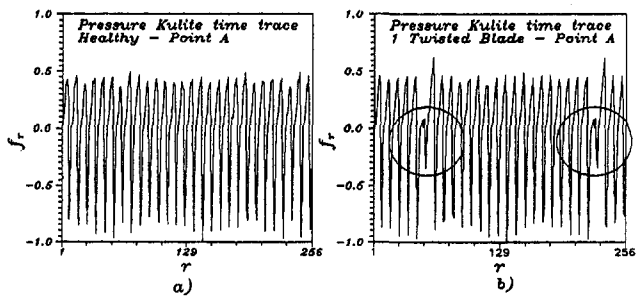

Fig. 3 Unsteady pressure phase-averaged signals: (a) healthy, (b) one rotor blade twisted

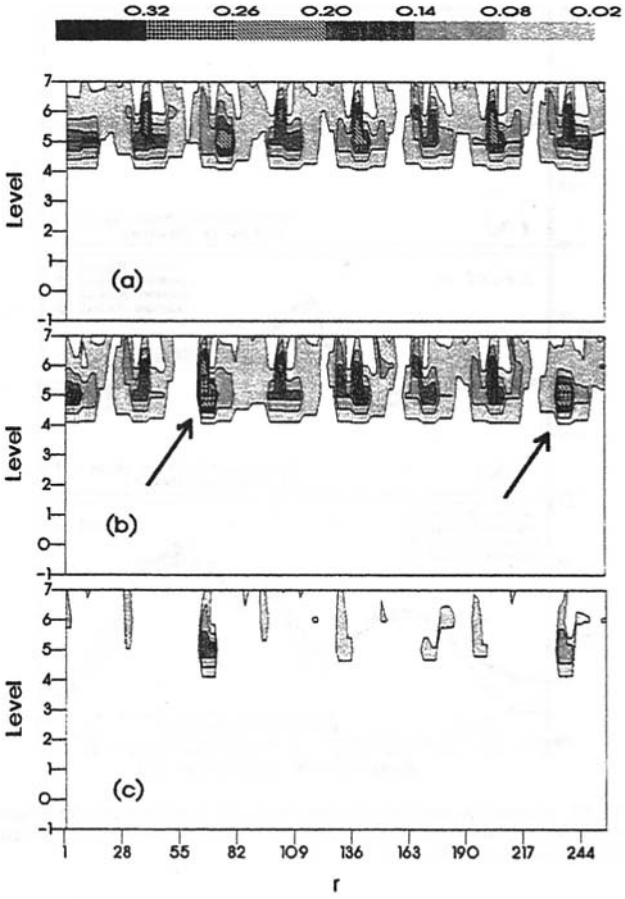

Fig. 4 Unsteady pressure wavelet maps: (*a*) healthy, (*b*) one rotor blade twisted, (*c*) difference of the wavelet maps (*b*) and (*a*)

This difference can also be interpreted from examination of the corresponding spectral differences in Fig. 7 (see also Loukis et al., 1991). It is seen that the difference of the two signals is mainly at the BPF, close to the central frequency of level 5.

Finally, Fig. 8 shows the wavelet amplitudes presented by the map of Fig. 6, plotted in a sequential manner.

So far in this paper, the representation of the wavelet information illustrates several drawbacks to this approach in real-time diagnostic applications. First of all, interpretation of the fault signature information is subjective. Moreover, automating the fault detection process will require significant computational resources. For example, classification of signatures in the form of maps would require a technique of pattern recognition of plane images.

For these reasons, the possibility of obtaining fault signatures of significantly reduced complexity has been investigated. At

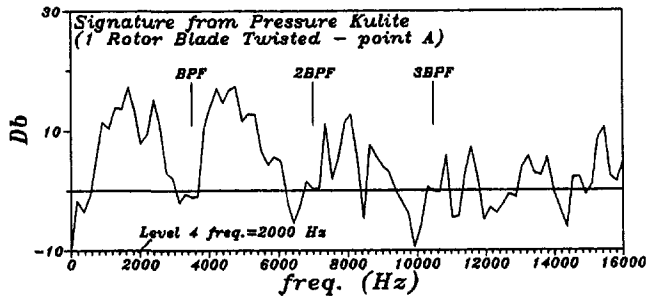

Fig. 5 Unsteady pressure signatures (spectral differences, one rotor blade twisted)

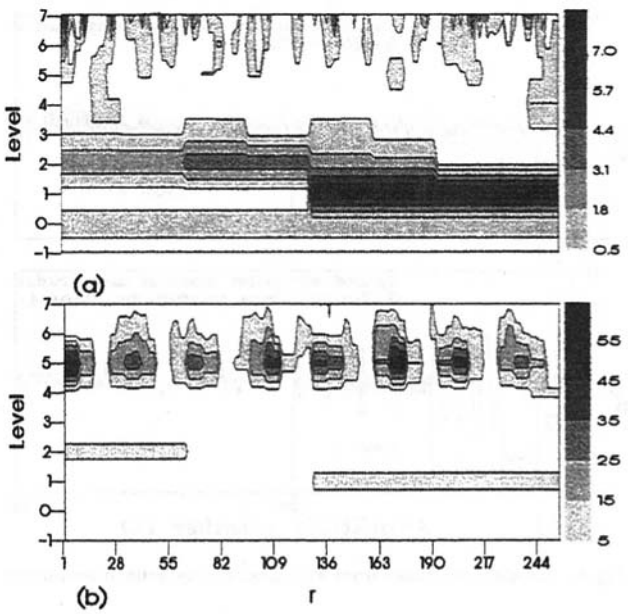

Fig. 6 Wavelet maps from microphone: (*a*) healthy, (*b*) three stator vanes restaggered

this point it should be mentioned that since satisfactory fault signatures have been produced by spectral analysis, it should be worthy to proceed with another method only if some advantage is offered in relation to existing techniques. The technique the authors have found to fulfill these purposes is described below.

4 Derivation of Fault Signatures

In order to derive fault signatures for all the examined cases, the differences $\alpha_{if} - \alpha_{ih}$ are calculated, where α_{ih} are the wavelet amplitudes for healthy and α_{if} the ones for faulty condition. If these differences are obtained for all the amplitudes, namely for $i = 1$ to N, then we still have to handle the same amount of information as for the wavelet map. We would like, therefore, to examine if a subset of the amplitudes can be examined.

Since Fourier analysis has shown that differences appear within specific frequency bands, one should expect that, if wavelet amplitudes representing these bands are examined, then they would provide the necessary information. Therefore, a method for examining a subset of the wavelet amplitudes is required.

As we have seen from the sample results presented above, each fault causes differences located mainly at one or more wavelet levels. Higher levels provide a higher degree of detail than the lower levels, due to the wider frequency band they cover. That's why, for the detection of faults that cause small differences, the higher levels should be used.

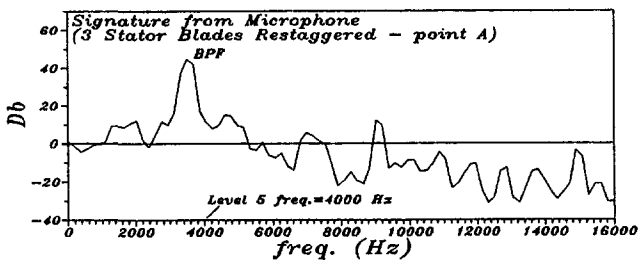

Fig. 7 Signature from microphone (spectral differences, three stator vanes restaggered)

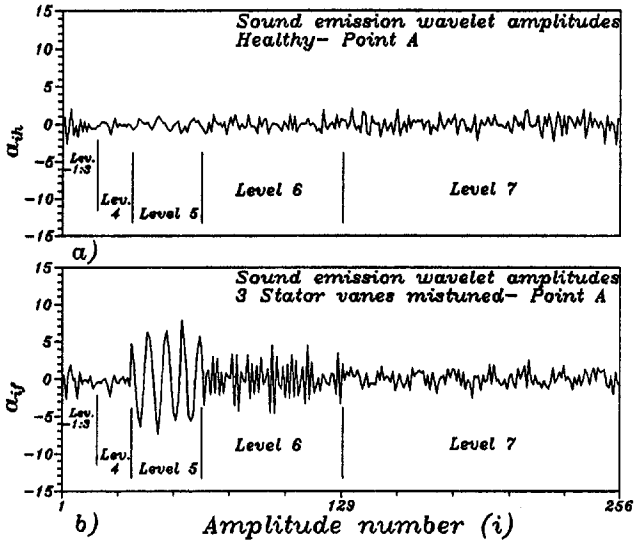

Fig. 8 Wavelet amplitudes from microphone: sequential presentation

The signatures for two rotor blades faults, evaluated from wavelet amplitudes of level 4, for unsteady pressure measurements are shown in Fig. 9. Signatures for four different operating points are shown, while a signature for the same fault but with smaller severity is included. Similar information but this time derived from casing vibration signals is shown in Fig. 10. In this figure the signatures of the two faults for one accelerometer are shown, while the signature of the twisted blade case is also shown for a second accelerometer. In Fig. 11, a signature of the mistuned vanes fault, for acoustic measurements is shown.

The patterns shown in all these figures exhibit two basic properties which make them suitable for fault signatures. These properties are: (1) operating condition independence and (2) each failure condition generates a unique failure signature, since different faults produce different patterns, as seen from Figs. 9 and 10.

Another interesting feature demonstrated by Fig. 9 is that the same fault with different severities produces the same form of pattern, but with a magnitude proportional to the fault's magnitude.

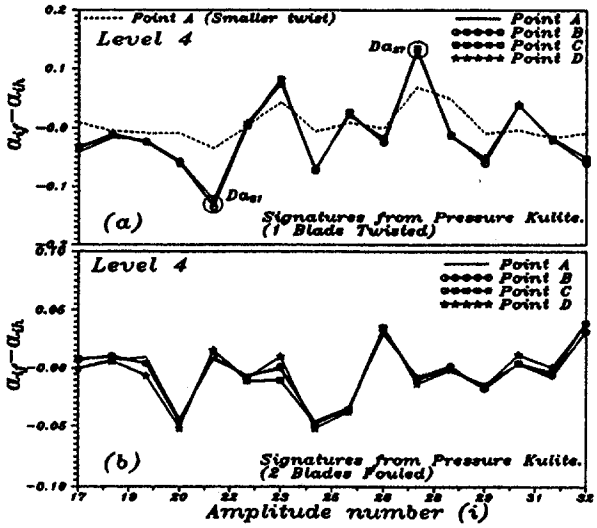

Fig. 9 Unsteady pressure signatures (level 4, wavelet amplitude differences): (*a*) one rotor blade twisted, (*b*) two rotor blades fouled

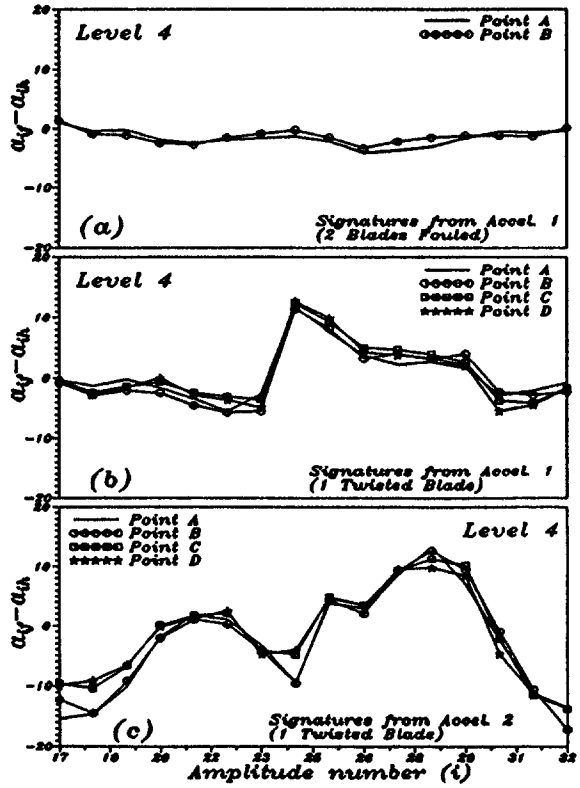

Fig. 10 Signatures from accelerometers (level 4, wavelet amplitude differences): (*a*) two rotor blades fouled, acc1, (*b*) one rotor blade twisted, acc1, (*c*) one rotor blade twisted, acc2

5 Discussion

Some features of wavelet signatures will now be discussed. The reason for the discussion is to comment on aspects related to application of the technique. In particular, we will examine dependence on the number of points used for the transform and will compare wavelet signatures to signatures from Fourier analysis.

One question that may arise is how the signatures depend on specific parameters used for the analysis. It will be very interesting to examine whether the signatures established above are independent from the number of samples of the analyzed signal. In order to answer this question, we process the first 128 samples of the signals of Fig. 3. The examined level in this case is level 3, which now has the same central frequency as level 4 in the case of 256 samples. The eight corresponding wavelet amplitudes differences are almost identical to the last eight of level 4 in the case of 256 samples, as shown in Fig. 12.

If 64 points are used, the signature, by examining level 2 this time, and the corresponding 4 wavelet amplitudes is also

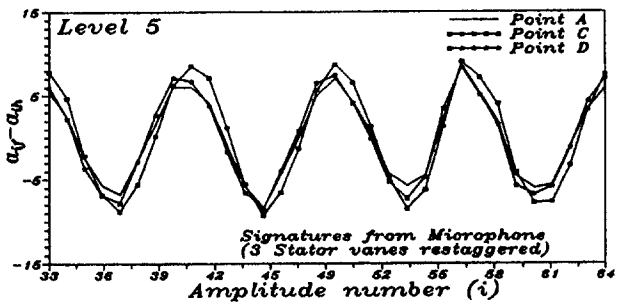

Fig. 11 Signature from microphone (level 5, wavelet amplitude differences, three stator vanes restaggered)

presented in Fig. 12. These four wavelet amplitude differences are the same as the first four differences of the second case.

The following observations can be made from inspection of Fig. 12.

- When half the points of a record are processed, the signature derived is almost identical to half of the initial signature. This implies that if the necessary features are covered by that half, then processing half the points of the record is sufficient. A further implication for turbomachinery signals is that, it should be essential but sufficient as well, to cover one period of rotation.
- Wavelet signatures have a different character from Fourier signatures. For the latter, reducing the points reduces the resolution and corresponds to a kind of smoothing of spectra. For wavelets, on the contrary, part of the information is lost, while the remaining information remains the same.

The results presented above have demonstrated that fault signatures can be established from wavelet amplitudes. At this point it is of interest to compare the features of such signatures with respect to corresponding signatures derived from power spectra differences. From the discussion above, it is concluded that signatures consisting of 16 values can be used and that reduction to a number of 8 values can still provide a signature of the fault. Spectral differences, on the other hand, need information on values covering at least the number of shaft harmonics contained in the bandwidth defined by the blade passing frequency, which in the present test case is 19. This fact has been established by Mathioudakis et al. (1991). Therefore, an advantage offered by the wavelet signatures is that fewer diagnostic parameters are essential. This fact may be exploited when pattern recognition algorithms are to be employed for fault classification.

Another advantage of wavelet analysis is that the wavelet signatures are more stable with the operating point. This can be proven if wavelet signatures of a fault for different engine operating points are compared to the corresponding ones from Fourier analysis. For example, signatures from data of accelerometer 1 from Fourier analysis, for one twisted rotor blade, are shown in Fig. 13. Comparison to Fig. 10(b) shows that the repeatability of wavelet signatures is far better than the corresponding Fourier ones.

Concerning implementation of wavelet analysis, it should be mentioned that rather simple computer programs are required and PCs offer sufficient computing power for practical implementation. Routines performing wavelet analysis are already available in some commercial signal processing packages.

Finally, it should be noted that results of wavelet analysis are not easily interpretable as compared to results of Fourier analysis. This is a fact that may be related to existing tradition and lack of familiarity with wavelets. Should they prove a powerful tool, however, the picture may change in the future!

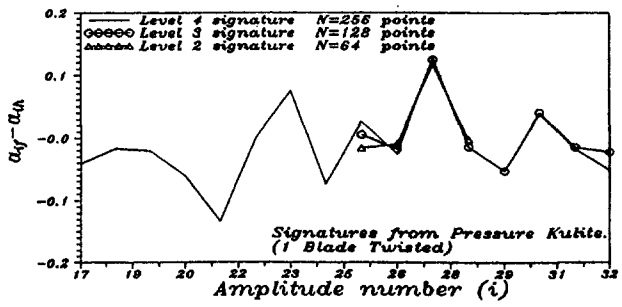

Fig. 12 Unsteady pressure signatures (wavelet amplitude differences, one rotor blade twisted, levels 2, 3, 4)

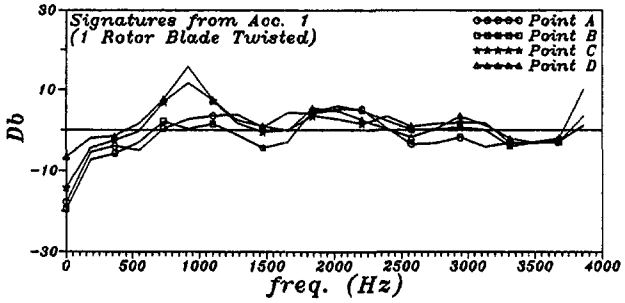

Fig. 13 Signatures from accelerometer and one rotor blade twisted (spectral differences, different operating points)

6 Conclusions

An investigation of wavelet analysis applicability to typical cases of turbomachinery signals has been presented. The possibilities that exist for generating fault signatures using this new technique have been examined.

A brief analysis was presented in order to establish a link of wavelet analysis results and the Fourier analysis more familiar today. Applications to turbomachinery signals and gas turbine fault diagnostics have been examined on an experimental set of measurement data.

It was demonstrated that wavelet amplitudes provide information about signal characteristics in frequency bands. This property proves to be useful for establishing fault signatures, usable for turbomachinery diagnostics. The fact that wavelets can be used for information compression is demonstrated by the properties of wavelet signatures, which can characterize faults using fewer parameters than corresponding techniques based on Fourier analysis. Moreover, wavelet signatures have shown a much better repeatability than spectral ones, for different operating conditions.

References

Cempell, C., 1991, *Vibroacoustical Condition Monitoring,* Ellis Horwood Limited, ISBN 0-13-931718-X.

Collacott, R. A., 1977, *Mechanical Fault Diagnosis and Condition Monitoring,* Chapman and Hall Ltd, ISBN 0-412-12930-2.

Loukis, E., Wetta, P., Mathioudakis, K., Papathanasiou, A., and Papailiou, K., 1991, "Combination of Different Unsteady Quantity measurements for Gas Turbine Blade Fault Diagnosis," ASME paper 91-GT-201.

Mathioudakis, K., Papathanasiou, A., Loukis, E., and Papailiou, K., 1991, "Fast Response Wall Pressure Measurement as a Means of Gas Turbine Blade Fault Identification," ASME JOURNAL OF ENGINEERING FOR GAS TURBINES AND POWER, Vol. 113, pp. 269–275.

Meyer, Y., 1993, *Wavelets: Algorithms & Applications,* SIAM, Philadelphia.

Meher-Homji, C. B., 1995, "Blading Vibration and Failures in Gas Turbines, Part C: Detection and Troubleshooting," ASME Paper No. 95-GT-420.

Newland, D. E., 1993, *An Introduction to Random Vibrations, Spectral & Wavelet Analysis,* Longman, Harlow; Wiley, New York.

Newland, D. E., 1994a, "Wavelet Analysis of Vibration, Part 1: Theory," ASME *Journal of Vibration and Acoustics,* Vol. 116, pp. 409–416.

Newland, D. E., 1994b, "Wavelet Analysis of Vibration, Part 2: Wavelet Maps," ASME *Journal of Vibration and Acoustics,* Vol. 116, pp. 417–425.

Simmons, H. R., and Smalley, A. J., 1989, "Effective Tools for Diagnosing Elusive Turbomachinery Dynamic Problems in the Field," ASME Paper No. 89-GT-71.

APPENDIX

A1 Dilation Wavelets

The dilation wavelets are defined by starting with a function $w(t)$, which is called a "mother wavelet," and which generates the other wavelets of the family. This function can't be expressed in analytical form, but is defined by an equation that has to be solved by iterative or recursive methods. This equation contains a set of coefficients called the wavelet coefficients. These coefficients are not chosen arbitrarily, but in such a way that they conform to particular properties, in order to achieve orthogonality and other convergence properties. The number of

the wavelet coefficients designates the wavelet's structure. A wavelet with M coefficients is usually called "DM wavelet." The dilation wavelet properties and the conditions that the wavelet coefficients must satisfy are described by Newland (1993). The wavelet $w(t)$ generates the other wavelets $w(2^j t - k)$ of the family by change of the scale and translation in time (the wavelet $w(t)$ is a wavelet of scale 1 and is centered around 0, while the wavelet $w(2^j t - k)$ is a wavelet of scale $\frac{1}{2}^j$ and is centred around $k/2^j$) (Meyer, 1993). The integer j is usually called "wavelet level."

The approach for dilation wavelet analysis is similar to that used for harmonic analysis except that, instead of breaking down a signal into harmonic functions of different frequencies, the signal is broken down into wavelets of different scale (or level) and different positions along the t axis. For example, consider a signal $x(t)$, which extends in the interval $0 \leq t < 1$. This signal can be expressed by its dilation wavelet expansion

$$\begin{aligned} x(t) &= \alpha_1 + \alpha_2 w(t) + [\alpha_3 w(2t) + \alpha_4 w(2t-1)] \\ &\quad + [\alpha_5 w(4t) + \alpha_6 w(4t-1) + \alpha_7 w(4t-2) \\ &\quad + \alpha_8 w(4t-3)] + \ldots \\ &= \alpha_1 + \sum_{j=0}^{\infty} \sum_{k=0}^{2^j-1} \alpha_{2^j+k+1} w(2^j t - k), \end{aligned}$$

$$\text{for} \quad 0 \leq t < 1 \qquad \text{(A.1)}$$

where α_i are the wavelet amplitudes. These amplitudes can be computed by using the discrete wavelet transform and Mallat's pyramid algorithm, which is described by Newland (1993). The remarkable feature of the algorithm is that the wavelet amplitudes can be computed without even finding the wavelets $w(2^j t - k)$ explicitly. The coefficient α_1 represents the average level (or level -1) of $x(t)$ and its introduction is necessary since all the wavelets have zero mean.

A2 Wavelet Map

A first way to present the values of the amplitudes is the so called wavelet map. This presentation is in direct analogy to Fourier analysis. In the case of Fourier analysis the Fourier coefficients squared are plotted along the frequency axis (power spectrum). Each coefficient corresponds to one harmonic component with particular frequency. The summation of these coefficients squared is equal to the mean square amplitude of the analyzed signal according to Parseval's theorem. Using similar logic the wavelet amplitudes are plotted in a three dimensional plot so that the volume below the established surface is equal to the mean square amplitude of the analyzed signal. The contour map of this surface erected on a horizontal plane with wavelet level plotted along one axis and time plotted along the other axis is called wavelet map.

Since the wavelet level is a measure of frequency, we can say that the wavelet map represents the distribution of the signal energy content along frequency and time. One of the features of the wavelet map is its ability to detect small details in the analyzed signals that may otherwise go unnoticed. This may be valuable for many applications, as for example in vibration monitoring, where it is important to detect small changes of vibration records (Newland, 1994b).

A3 Fourier Coefficients and Wavelet Amplitudes

When we have $N = 2^n$ samples of a time signal $x(t)$ (x_r, $r = 1 \ldots N$), then applying the wavelet transform to this signal, N wavelet amplitudes α_i ($i = 1 \ldots N$) will be derived. If we consider now that $x(t)$ is equal to one of the wavelets, for example:

$$x(t) = w(t) \qquad \text{(A.2)}$$

where $w(t)$ is the wavelet of level 0, then according to Eq. (1) this signal must have α_2 wavelet amplitude equal to one and all other amplitudes equal to zero. So, the inverse wavelet transform is defined and for a finite number of amplitudes we have:

$$w(t) = W^{-1} \begin{bmatrix} 0 \\ 1 \\ \cdot \\ 0 \end{bmatrix}_{N\times 1} \qquad \text{(A.3)}$$

where W^{-1} represents the inverse wavelet transform of an array written as a column matrix. If each one of the wavelets is expressed in this form (setting all the wavelet amplitudes equal to zero except the corresponding to the specific wavelet, which is set equal to 1) then substitution to Eq. (1) gives:

$$\begin{bmatrix} x_1 \\ x_2 \\ \cdot \\ x_N \end{bmatrix} = \alpha_1 \cdot W^{-1} \begin{bmatrix} 1 \\ 0 \\ \cdot \\ 0 \end{bmatrix}_{N\times 1} + \alpha_2 \cdot W^{-1} \begin{bmatrix} 0 \\ 1 \\ \cdot \\ 0 \end{bmatrix}_{N\times 1} + \ldots + \alpha_N \cdot W^{-1} \begin{bmatrix} 0 \\ 0 \\ \cdot \\ 1 \end{bmatrix}_{N\times 1} \qquad \text{(A.4)}$$

We extend the definition of W^{-1} to the case of a $N \times N$ matrix. The inverse wavelet transform of a $N \times N$ matrix is defined as another $N \times N$ matrix, whose each column is the inverse wavelet transform of the corresponding column of the initial matrix. Then Eq. (A.4) can be rewritten as:

$$\begin{bmatrix} x_1 \\ x_2 \\ \cdot \\ x_N \end{bmatrix} = W^{-1} \begin{bmatrix} 1 & 0 & 0 & \cdots & 0 \\ 0 & 1 & 0 & \cdots & 0 \\ \cdot & \cdot & \cdot & \cdots & \cdot \\ 0 & \cdot & \cdot & \cdots & 1 \end{bmatrix}_{N\times N} \cdot \begin{bmatrix} \alpha_1 \\ \alpha_2 \\ \cdot \\ \alpha_N \end{bmatrix}_{N\times 1} \qquad \text{(A.5)}$$

or

$$[x] = W^{-1}[I_{N\times N}] \cdot [\alpha]$$

where $I_{N\times N}$ is the $N \times N$ unity matrix. By applying the Fourier transform to both sides of Eq. (A.5), we have:

$$\mathcal{F}[x] = \mathcal{F}(W^{-1}[I_{N\times N}]) \cdot [\alpha] \qquad \text{(A.6)}$$

or

$$[C_F]_{N\times 1} = [C_W]_{N\times N} \cdot [\alpha]_{N\times 1}$$

where C_F are the Fourier coefficients and C_W is a matrix whose columns consist of the Fourier coefficients of the corresponding column of the $W^{-1}[I_{N\times N}]$ matrix. The elements of C_W are complex numbers, which, through this relationship, correlate the wavelet amplitudes with the Fourier coefficients. They are unique for a specific number N of samples and specific dilation wavelets DM. From Eq. (A.6) we can say that the Fourier coefficients are linear combinations of the wavelet amplitudes and vice versa.

D. Müller
BMW Rolls-Royce GmbH,
Dahlewitz, Germany

A. G. Sheard[1]
Techniche Group Ltd.,
Coventry, United Kingdom

S. Mozumdar[2]

E. Johann

BMW Rolls-Royce GmbH,
Dahlewitz, Germany

Capacitive Measurement of Compressor and Turbine Blade Tip to Casing Running Clearance

It is an established fact that the efficiency of a gas turbine engine has an inverse relationship with the clearance between the rotor blades and the casing (Tip Clearance, or TC). TC is an essential measurement during the testing of development engines. While commercial TC measurement systems are available, their applicability to an engine is dictated by engine size, geometry, physical accessibility, and temperature distribution around the measurement region. This paper describes the development of a TC measurement system, based on the capacitive measurement principle, which was undertaken to satisfy the application requirements of a specific class of gas turbine engines. The requirements included a relatively long and flexible cable to route the electrical signals out of the engine. The TC measurement system was successfully used during engine testing and valuable data were obtained.

1 Introduction

Rotor blade tip to casing clearance (Tip Clearance, or TC) has a significant effect on the flow field in the blade-tip region of gas turbine engines. In general, the larger the TC, the larger is the tip-leakage with an associated loss of high energy gas, and hence, the lower is the efficiency of the engine. While computer models are available to predict the TC for both compressors and turbines, such predictions have to be verified and fine-tuned with test data. TC is thus an essential measurement during the development program of a gas turbine engine.

During the development of the family of BR 700 engines in the 65 to 110 kN thrust class (Kappler et al., 1992), the design requirements called for a TC measurement system with a 2.5 to 3.0 m long flexible cable to measure clearances accurately in the 0.0 to 2.0 mm range. No commercially available system could meet the installation and performance requirements for this application. It was, therefore, decided to develop a new system based on the existing knowledge base of frequency modulated capacitive type TC measurement systems (Chivers, 1989). The Frequency Modulated (FM) system was chosen because it is, in contrast to a Direct Current (DC) capacitance probe system, insensitive to gas ionization effects and thus can be used in turbine application.

Development of the system comprised several separate, but carefully coordinated activities, which were pursued in parallel by four different organizations working as a team. Probe development, system integration, and calibration were performed by Techniche Group Ltd. Analogue electronic parts were developed by Fylde Electronic Laboratories Ltd. The mineral insulated cables and the flexible cables were developed by BICC Thermoheat Ltd. The development of calibration procedures, test planning, system testing on gas turbine engines, and data evaluation were performed by BMW Rolls-Royce GmbH. Finally, all four organizations participated in post-test analysis of the respective parts of the system.

The following sections describe the system concept and validation of the system by comparison with an alternate measurement system. Results obtained from tests on development engines are also presented.

2 System Concept

The capacitive TC measurement system is based on the measurement of the capacitance between a probe and the blade tip. The measured capacitance can be related to the clearance using a predetermined calibration.

A button probe fitted into the engine casing over the blade tips represents one plate of a capacitor, the blade tip the other plate. The resulting capacitance is a function of the geometry of the plates, the distance between the plates, and the material in between. If the geometry and material properties are assumed to remain constant, the value of the capacitor is a function only of distance between the plates, from which tip clearance can be derived.

The small overlap area between probe tip and blade of typically 5 mm^2, combined with the large distance between them of typically 1 mm, results in a very small capacitance of 0.04 pF. To measure this small capacitance accurately, the capacitor is integrated into an oscillator. A change in the value of the capacitor will result in a change in the oscillator natural frequency. This frequency shift can be measured and related to tip clearance using a calibration.

2.1 System Module Description. The structure of the system is shown in Fig. 1 as a schematic block diagram. Probe cable assembly and oscillator module are linked to a demodulator, which converts the change in frequency into a change in voltage. A linearizer is used to apply the system calibration, enabling it to output clearance in engineering units. In addition a speed meter is used to generate an analogue speed signal and a once-per-revolution (1/rev) trigger, which is used for the dynamic data analysis.

2.1.1 Probe-Cable-Assembly. The probe-cable-assembly comprises the probe head and the cable, Figs. 1 and 2.

The probe head was designed for a maximum temperature environment of 800°C and a maximum tip temperature of 1000°C.

The cable capacitance of typically 300 pF forms a shunt capacitance, which is approximately 1000 times greater than the capacitance to be measured at the probe tip. Very small changes in cable temperature and shape result in a change in its capacitance by more than the value of the capacitor at the probe tip. To eliminate the shunt capacitance the probe-cable-assembly is made to a tri-axial design with conductor, inner screen and outer screen, Fig. 1. The conductor connects the

[1] Current address: Allen Power Engineering Ltd., Bedford, United Kingdom.
[2] Current address: AlliedSignal Aerospace Co., Phoenix, AZ.

Contributed by the International Gas Turbine Institute and presented at the 41st International Gas Turbine and Aeroengine Congress and Exhibition, Birmingham, United Kingdom, June 10–13, 1996. Manuscript received at ASME Headquarters February 1996. Paper No. 96-GT-349. Associate Technical Editor: J. N. Shinn.

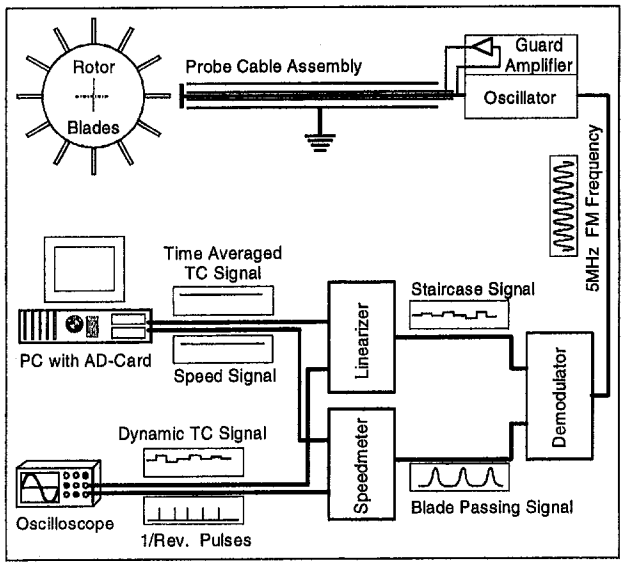

Fig. 1 Frequency modulated clearance measurement system schematic block diagram

oscillator electronics to the probe tip. The outer screen is connected to ground. The inner screen is driven by a guard amplifier to the same voltage as the conductor (Section 2.1.2). As there is no voltage difference between conductor and inner screen, the effect of cable capacitance is eliminated. This enables the oscillator to be connected to the probe tip without cable effects interfering with the system output.

To accommodate the application requirements for engine installations, two different kinds of cable were developed:

- A mineral insulated (MI) tri-axial cable for use in high-temperature applications. This cable type is made out of stainless steel with silicon oxide as insulator and is suitable for temperatures of up to 800°C. The materials used result in a cable that is relatively stiff and inflexible, thus making it difficult to negotiate bends and corners for routing in an engine application.
- A flexible tri-axial cable for use in applications where flexibility is required and the environment is relatively cool. It can withstand temperatures of up to 200°C. The cable is made out of copper with Poly-Tetra-Fluoro-Ethylene (PTFE) as insulator and is protected mechanically by an external nickel braiding.

Both cable types can be combined as needed up to a total cable length of 3 m.

2.1.2 Oscillator and Guard Amplifier. The function of the oscillator is to convert a change in capacitance that arises as a consequence of blade passing at the probe tip into a change in frequency. The oscillator frequency for the described system is 5 MHz. The change in frequency due to a passing blade is 150 kHz/pF or approximately 6 kHz for a 1-mm-thick blade and 1 mm clearance.

The guard amplifier drives the inner screen of the tri-axial probe cable. The voltage on the inner screen has to follow the oscillator in frequency, amplitude, and phase, to ensure a zero voltage difference between conductor and inner screen. The performance of the guard amplifier is a limiting factor in the maximum cable capacitance that can be driven. This, therefore, limits the maximum cable length. In the present case, the cable properties and the amplifier characteristics allowed a cable length of up to 3 m.

The oscillator and guard amplifier electronics size was reduced to a cylinder 25 mm in diameter and 44 mm in length, Fig. 2. The tri-axial probe plugs into one end of the oscillator. Power to, and signal from, the oscillator are carried over a standard 50 Ohm co-axial BNC cable. BNC cable lengths of up to 150 m have been used in engine installations.

2.1.3 Demodulator. The primary function of the demodulator is to convert a change in oscillator frequency into a change in output voltage. The demodulator unit comprises a Voltage Controlled Oscillator (VCO) and a Phase-Locked-Loop (PLL). The VCO control voltage is adjusted using the PLL to keep it in phase with the external oscillator to which the probe is connected. For this reason the VCO control voltage is proportional to the external oscillator frequency. This VCO control voltage is passed to an AC-coupled amplifier to yield the "blade passing signal," Fig. 3.

The amplifier, and hence the demodulator, is calibrated to give a 6 V peak-to-peak output for a 30 kHz change in the oscillator nominal operating frequency of 5 MHz. This corresponds to a typical clearance of 0.2 mm over a 1-mm-thick blade. Because of this electronic arrangement, all calibrated demodulators behave identically and hence are exchangeable. Probe and oscillator pairs can be calibrated with a single demodulator, and then used with any demodulator without affecting system calibration.

The demodulator also incorporates a "staircase" module. This module is a peak-to-trough picker and restores the blade passing output to a DC voltage. The voltage level corresponds to the height of the blade passing pulse, Fig. 3. This output is updated each time a new peak is registered.

The staircase signal offers two advantages:

- The staircase signal is insensitive to base line modulation of the blade passing signal. Base line modulation can occur when the probe cable is exposed to high vibrations.

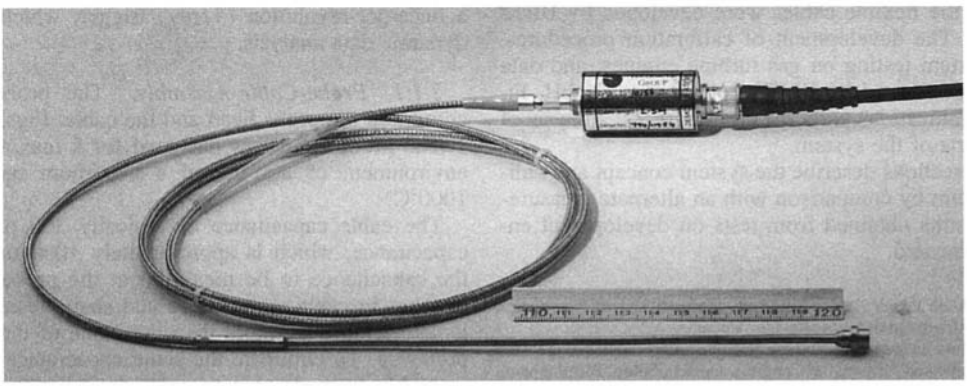

Fig. 2 Probe cable assembly and oscillator

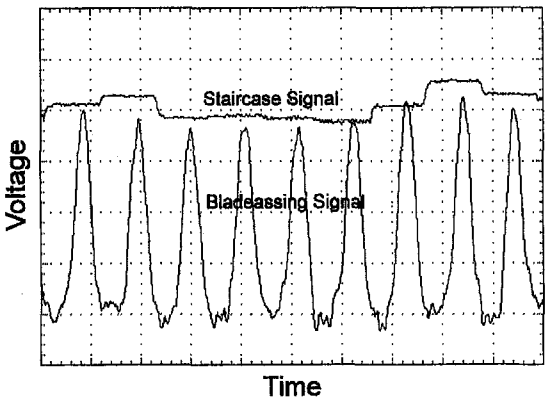

Fig. 3 Blade passing and staircase signal, blade thickness ≫ 1 mm, clearance ≪ 1 mm (hardcopy from the oscilloscope)

- The staircase signal offers direct dynamic investigations of the TC signal.

2.1.4 Linearizer. The last module in the signal processing chain is the linearizer. The linearizer uses as input the staircase voltage of the demodulator, Fig. 1. This staircase signal is converted into a linear tip clearance signal in engineering units. One volt of the TC signal is equivalent to 1 mm of tip clearance. The required calibration data for the conversion is stored as a look up table in an EPROM within the linearizer.

The outputs of the linearizer are:

- A dynamic linear staircase signal (1 V = 1 mm TC).
- A linear TC signal, which is time averaged over 1 s to eliminate the influence of system noise (1 V = 1 mm TC).

2.1.5 Speed Module. The blade passing signal from one channel of the system is fed into a speed module, Fig. 1. This module, with the prestored information about the number of blades against the channel, extracts the speed information from the frequency of the blade passing signal, and generates an output voltage proportional to the engine speed. This output voltage is logged by the data acquisition system together with the TC signals. The speed module also provides a 1/rev trigger, which is needed for the analysis of the dynamic TC data (Section 5.3).

2.2 System Performance and Specification. Performance of the system can be described by considering its resolution and signal to noise ratio. The measurement uncertainty depends on influences such as calibration, installation, etc., which will be discussed in section 3.

2.2.1 System Resolution. The system resolution is ultimately limited by the performance of the demodulator. The minimum shift in frequency, detectable by the demodulator, is 50 Hz. The oscillator has a sensitivity of 150 kHz/pF. Therefore, the minimum detectable change in capacitance is 0.0003 pF. This is equivalent to a resolution of 0.01 mm at a nominal clearance of 1 mm.

2.2.2 System Signal-to-Noise Ratio. The staircase module picks the voltage between pulse peak and trough, and therefore is susceptible to noise. The major origin of noise within the FM clearance measurement system is in the demodulator. The VCO control voltage hunts around the point at which the VCO and the external probe-oscillator frequencies are matched. This hunting takes the form of typically 250 mV of noise peak-to-peak on the blade passing output.

System signal to noise ratio can be best illustrated by a typical output; see Fig. 3. The system noise is a function of the amplification factor of the demodulator. The noise level is related to a signal height for a defined condition: A probe over 1-mm-thick blading with a 5-mm-dia probe tip and a clearance of 0.2 mm gives a signal output of approximately 6 V. The signal-to-noise ratio is, therefore, typically 25.

A second source of noise is the cross talk between channels in a multichannel installation. System tests have shown that the influence of this noise source has no visible effect on the system uncertainty, and is, therefore, not considered for this discussion.

To reduce the influence of noise, the staircase signal is time averaged in the linearizer. A small amount of noise manifests itself as an offset of approximately 30 mV on the averaged staircase signal. Due to the randomness of the noise this offset is not constant and may fluctuate ±10 mV over 30 mV.

2.2.3 System Specification. The clearance measurement system specification is summarized in Table 1.

In Table 1 the *minimum and the maximum blade tip velocities* define the minimum and the maximum velocities, respectively, below which or above which the system will not work correctly. The velocities are valid for a 5-mm-dia probe and a blade thickness of 1 mm. The *oscillator sensitivity* describes the shift in oscillator frequency for a change in probe to blade tip capacitance of 1 pF. The *demodulator sensitivity* describes the change in staircase signal output voltage for a frequency shift of 1 kHz. The *measurement range* is typically 2.5 mm for a 5 mm probe and a blade thickness of 1 mm. A thicker blade or a larger probe will lead to a higher measurement range. The *system resolution* is defined in section 2.2.1. The *signal-to-noise ratio* is defined in section 2.2.2.

3 Calibration and System Uncertainty

The calibration uncertainty is limited by the system performance, by the uncertainty of the calibration procedure, and by the representation of the engine blade-casing geometry.

3.1 Calibration Procedure. Due to the variations in electrical properties of the probe and the oscillator, it is necessary to calibrate a probe and oscillator as a pair. It is impractical in larger gas turbines to calibrate the probes directly over the actual rotor that they will be run with. To overcome this, a calibration rig, Fig. 5, is used. Calibration disks are manufactured that replicate the blade tip geometry for a specific engine stage. In practice, due to the production tolerances of the blades, the calibration disks will not represent the geometry exactly. To minimize the uncertainty introduced due to this difference, a method was developed to correct the calibration data.

To calibrate a probe, the probe is mounted in a replica of the engine casing, Fig. 6. The position of the probe relative to the engine casing can be adjusted, to set the immersion of the probe accurately in the engine casing.

During the calibration, the output voltages for a set of known distances between blade and casing is logged. This set of calibration data is corrected using the exact geometry of the blades the probes will be run with. The corrected calibration data is characterized using a least-squares curve fitting routine to calculate the coefficients of a polynomial, Fig. 4. This calibration curve is down loaded into the linearizer.

Table 1 Clearance measurement system specification

Operating Frequency	5 MHz
Min. Blade tip Velocity	1 m/s
Max. Blade tip Velocity	500 m/s
Oscillator Sensitivity	150 kHz per pF
Demodulator Sensitivity	200 mV per kHz
Measurement Range	2.5 mm typically
System Resolution	0.01 mm
Signal to Noise Ratio	25 typically

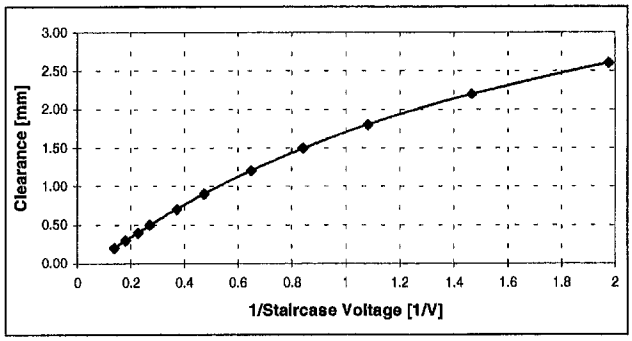

Fig. 4 Typical calibration curve (blade thickness = 1 mm)

3.2 Uncertainty Analysis. Most of the uncertainties associated with the TC measurement system may be classified into three broad categories. The first originates within the clearance measurement system itself (system uncertainty). The second category is associated with the calibration. The third includes all effects related to the installation and the operation of the system. Table 2 quantifies uncertainty sources, which are present in practice.

3.2.1 System Uncertainty. To determine the system uncertainty, the linearizer is programmed with a 1:1 calibration curve. The uncertainty is related to the staircase output voltage of the system.

System noise and cross talk, described in section 2.2.2, have major influences on system uncertainty. Minor uncertainties are thermal stability effects on the electronic components.

The uncertainty due to the analogue-to-digital and digital-to-analogue conversion within the linearizer is 10 mV.

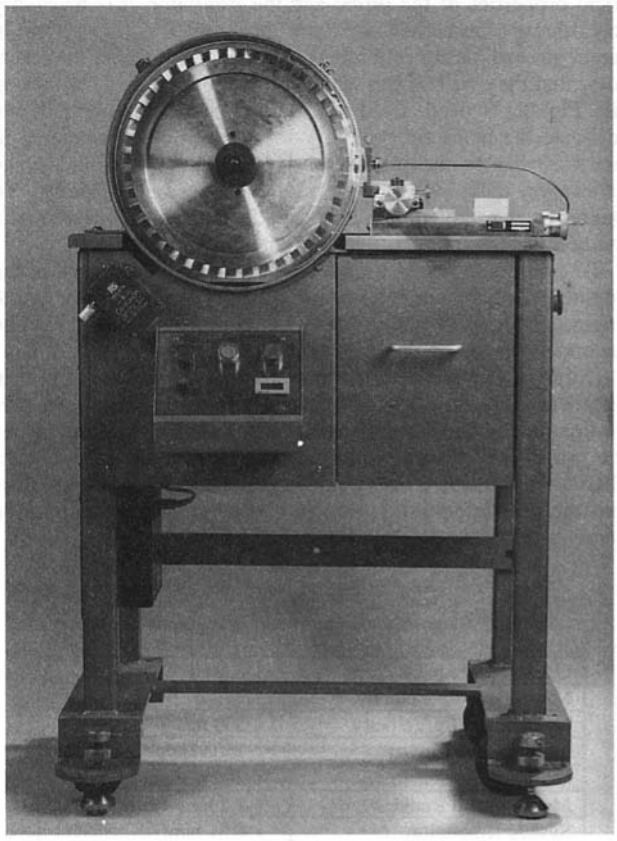

Fig. 5 Capacitance probe calibration rig

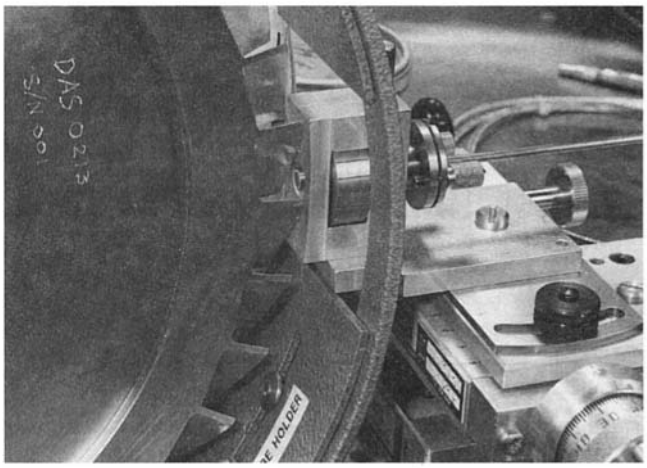

Fig. 6 Capacitance probe mounted in the calibration rig

The AD-card used for the data logging system has an uncertainty of 4 mV.

3.2.2 Calibration Uncertainty. The main uncertainty in the calibration process is the deviation between the real engine blade geometry and the calibration disk geometry. Due to the correction of the calibration data, this uncertainty is minimized. The demodulator is calibrated separately; therefore, a separate uncertainty source has to be considered. The zero position of the probe is adjustable to an uncertainty of 0.005 mm. The clearance relative to this zero position is measured with an uncertainty of 0.005 mm.

3.2.3 Installation and Operation Uncertainty. The main installation uncertainty is introduced in the measurement of the probe setback. It was found that this uncertainty can easily dominate the overall uncertainty. By the introduction of standard procedures within the engine build process, this uncertainty was reduced to a minimum of 0.02 mm.

During the operation of the system, uncertainties my be introduced by changes in the gas composition and changes in gas properties due to thermal effects. Uncertainties due to these effects have been found to be less than 1 percent of the measured capacitance in standard compressor and turbine applications (Chivers, 1989).

4 System Installation

The clearance measurement system was first installed in stage 4 of the high-pressure compressor (HPC) of a BR710 core engine. The data obtained from this test were used for system evaluation by direct comparison with an alternate measurement system.

The system was then installed and operated on two BR710 development engine. Probes were fitted to the HPC stages 6, 8, and 10 and the second stage of the high-pressure turbine (HPT). Four probes were fitted with approximately equal distribution around the circumference of the casing of each stage.

Using a similar arrangement, four probes were also fitted on the casing of the second stage of the HPT of a second development engine.

4.1 Probe. The probe head incorporates a flange against which it seats in the compressor casing. A retaining ring and a clamping plate are used to fix the probe in the casing. The compressor casing incorporated a deep chamfer in the abradable liner, which prevented the probe tip and casing forming a "stray" capacitor. To avoid damage to the probe in the event of a tip rub, the probe was fitted recessed approximately 0.5

mm (referred to as "set back") within the casing. The exact value of probe set back was measured during the engine build.

4.2 Cable. The probe tip to oscillator mineral insulated (MI) and flexible cable are fragile due to their tri-axial design. Care was taken to avoid damage to the cable during installation and operation. A cable routing scheme was designed to avoid high temperature and high vibration locations. The preferred cable was MI, with the change to flexible cable coming only when the flexibility was essential for routing purposes.

Total cable length for each probe was optimized, resulting in each probe being of the same total length for the HPC. This was to ensure that the cable just reached the oscillator enclosure on the outside of the engine casing. A similar arrangement was used to optimize the cable length for the HPT.

4.3 Oscillator. An oscillator enclosure was designed to contain 20 single oscillator modules. The oscillator enclosure was mounted on the outside of the engine bypass duct, adjacent to the exit port of the probe cables from the casing.

4.4 Ground Station. All signal conditioning electronics were located in a cabinet, referred to as a "ground station." The ground station contained five electronic racks, Fig. 7, with each rack containing the electronics needed for four channels. In this way each rack was configured for use with the four probes for a single stage.

The link between demodulators within the ground station and engine-mounted oscillators was made using 50 Ohm co-axial BNC cables. These cables were test bed cables that were a permanent fixture of the test bed. An important feature of the system was its ability to utilize existing test bed wiring, with no special additional cables.

Table 2 Clearance measurement system uncertainty analysis

System Uncertainty:	**Uncertainty**
System Noise/Cross Talk	10 mV
Oscillator Temperature Coefficient	1.0 % OR (1)
Demodulator Temperature Coefficient	0.5 % OR
Linearizer Uncertainty	10 mV
Data Logger A/D Card Uncertainty	4 mV
RSS (2) Uncertainty Typical at 1 mm Clearance	**< 0.02 mm**
Calibration Uncertainty:	
Zero Position Uncertainty	0.005 mm
Clearance Measurement Uncertainty	0.005 mm
Data Logger A/D Card Uncertainty	4 mV
Curve Fit Uncertainty	0.010 mm
Influence of Blade Thickness	0.020 mm
Calibration of Demodulator	0.005 mm
RSS Uncertainty Typical at 1 mm Clearance	**< 0.03 mm**
Installation and Operation Uncertainty:	
Set Back Measurement Uncertainty	0.020 mm
Uncertainty of Probe Head Length Measurement	0.020 mm
Uncertainty of Installation of the Probe Head	0.020 mm
Thermal Gas Effects	1% OR
RSS Uncertainty Typical at 1 mm Clearance	**< 0.04 mm**
Total RSS Uncertainty Typical at 1mm Clearance	**< ±0.06 mm**

(1): OR = Of Reading
(2): RSS = Root Sum Squared

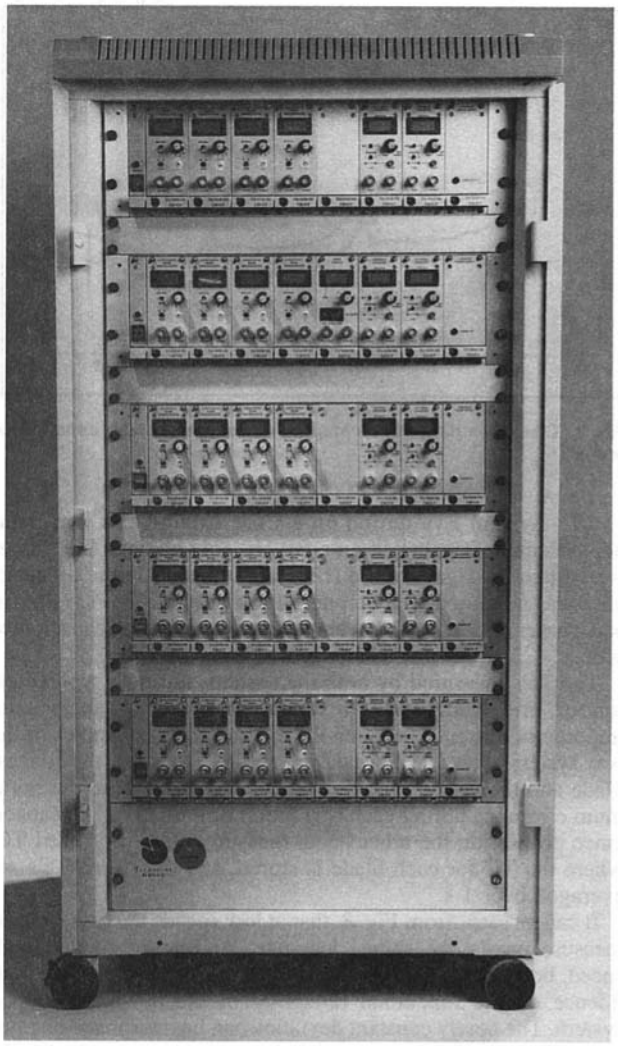

Fig. 7 A twenty-channel capacitance clearance measurement ground station

4.5 Data Logging. The primary output of the clearance measurement system is the Linearizer mean output (time-averaged TC). This output gives mean clearance in engineering units. This voltage can be logged by any data logging system.

For the described measurements a PC-based stand-alone data acquisition system was used to log tip clearance data. The data were scanned at 1 Hz and stored in an ASCII file format. In those instances where dynamic data were required, the system staircase output was recorded onto high bandwidth magnetic tape.

5 Operating Experience

Experience with the system is summarized by reporting results from three vehicles. On the first vehicle, i.e., a core engine, a two-channel system was evaluated by comparing the TC data with that from a second independent TC measurement system. On the second vehicle, a development engine, extensive measurement experience was gained with a 12 channel system on the HPC and a four channel system on the HPT. On the third vehicle, a second development engine, measurements were made with a four-channel system installed on the second stage of the HPT.

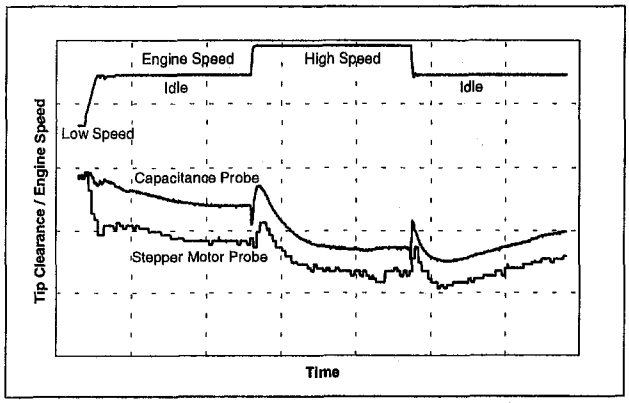

Fig. 8 Clearance data from a stepper motor probe and a capacitance probe

5.1 System Evaluation on a Core Engine. A two-channel system was evaluated on a BR710 core engine. The probes were fitted to stage 4 of the HPC. Simultaneously the tip clearance was measured with Stepper Motor Probes (SMPs) (Sheard and Turner, 1992), which were fitted adjacent to the capacitance probes.

The TCs measured by both the systems during a typical test run are presented in Fig. 8. It may be noted that there is an important difference between the measurement principles of the two systems. The SMPs measure the TC between the longest blade and the casing, and thus, they always measure the minimum clearance during each revolution of the rotor. The capacitance probes, on the other hand, measure a time-averaged TC, where the TC for each blade is stored, and the stored TCs are averaged over 1 s.

It can be seen, from Fig. 8, that at low speeds the two systems measure nearly the same clearance. At idle speed and high speed, both measurements show the same trend. This gave confidence on the functional reliability of the newly developed system. The nearly constant deviation can be interpreted as rotor eccentricity, which is not recorded or considered by the SMPs. Any rotor eccentricity, or difference between blade heights, is taken into account by the capacitance probes during the averaging process. A similar phenomenon was also observed during engine testing, as described in Section 5.3.

5.2 Measurement Experience on Engines. Since the core test results gave confidence in the operational reliability of the new system, a 16-channel system was installed in one of the development engines. On this engine the stages 6, 8, and 10 of the HPC were configured each with four capacitance probes. A set of four probes were also installed on stage 2 of the HPT of this engine. However, the data obtained from the HPT probes were not reliable. Hence, a second development engine was configured with four probes on stage 2 of the HPT.

The circumferential probe positions on each stage are labeled A to D clockwise, aft looking forward, as shown in Fig. 9.

The arithmetic mean of the four individual TCs on each stage will be called in the "Mean TC." Specific tests and results are described in the following sections.

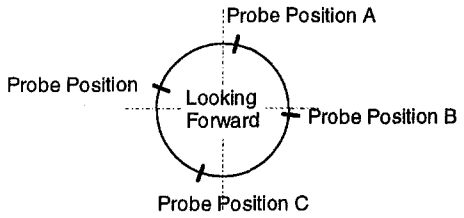

Fig. 9 Typical circumferential probe positions

Table 3 Comparison between cold crank clearance and measured clearance

Stage	Deviation between measured clearance and CBC
6	4%
8	4%
10	5%
Turbine, Rotor 2	3%

5.2.1 Engine Cranks. The first tests with a newly built engine are cranks under cold conditions. During the cranks, TC was measured and compared to the Cold Build Clearance (CBC) measured during engine build. Ideally, the cold crank TC and the CBC should match exactly.

Table 3 shows the deviation between measured TC and CBC related to the total CBC (i.e., CBC plus setback).

These initial measurements showed that the uncertainty of the installed system is within 5 percent of the total distance between probe and blade tip. This is within the measurement uncertainty (Section 3.2).

5.2.2 Running in Procedure. The engine running in procedure incorporates a planned blade-tip rub, resulting in a defined "running clearance."

The maneuver performed to create a tip rub involves stabilization of the engine at its maximum condition, followed by a fast deceleration to idle and re-stabilization for a few seconds, followed by a rapid acceleration back to the maximum condition. The corresponding engine speed curve is shown in Fig. 10. TC was logged throughout the manoeuvre. It may be seen, from Fig. 10, that for both the probes at location D on stages 8 and 10, the recorded TC went slightly negative, indicating a tip rub at these positions. This was further confirmed by an inspection of the engine parts following a tear-down after the test program was completed. The measured depth of tip-rub and that from the parts-inspection report were found to be within the uncertainty of the measurements.

A comparison of the measured TC at the thermally stabilized condition before and after the tip rub, as shown in Fig. 10, indicates an increase in the TC at both stages 8 and 10. This increase can be related to a blade-tip rub during which the tips suffer wear, but the abradable liner is not affected to the same extent.

5.2.3 Performance Curve. A test program was undertaken to characterize the engine performance. The engine speed was increased in steps from idle condition to maximum take off condition. The mean TC is presented in Fig. 11.

The data presented in Fig. 11 are typical of those logged, and enable the physical effects that influence TC to be extracted.

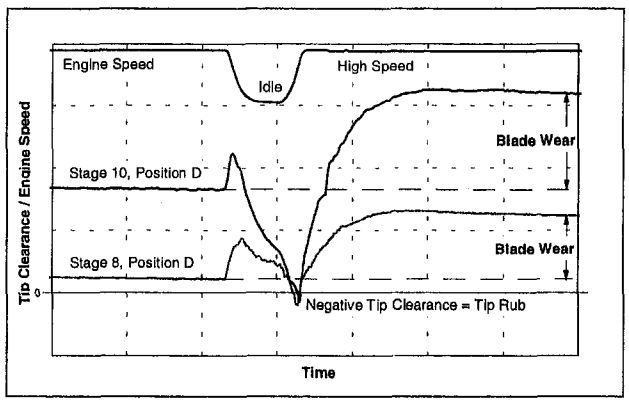

Fig. 10 Tip rub during running in procedure

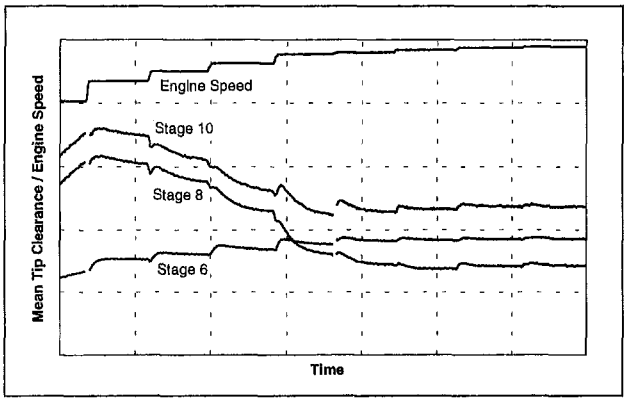

Fig. 11 Mean tip clearance data for a performance curve

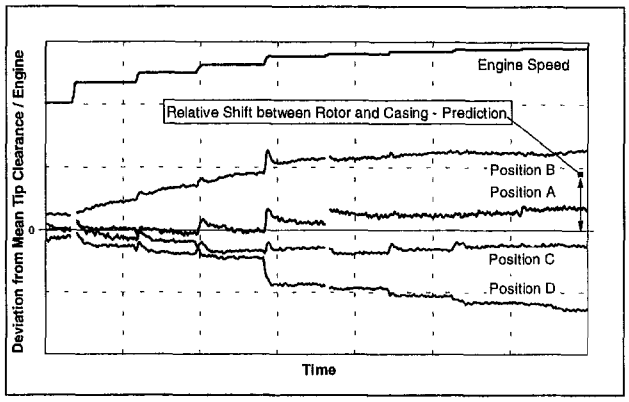

Fig. 13 Deviation from mean tip clearance for four circumferential probe positions on compressor Stage 6

For a typical engine acceleration the TC first reduces due to centrifugal load. The light casing heats more quickly than the heavy rotor, resulting in the TC increasing, and then slowly reducing as the rotor heats up. The difference in the trend for stage 6 can be explained by the difference of casing and rotor material combination for stage 6. This behavior of the individual stages was also predicted by an analytical thermal model.

The TCs measured by the probes on stage 6 are presented in Fig. 12. The four probes around stage 6 all show the same trends in clearance; however, it is clear that the TC characteristics at the four circumferential locations are different. A clearer understanding of this difference is obtained from Fig. 13, where the difference between the mean TC and the TC at each circumferential location is plotted. The difference is set to zero for a thermally stabilized idle condition.

It can be seen from Fig. 13 that the difference curves are diverging with speed. The highest and the lowest difference curves are given by probes positioned opposite to each other. A study of Fig. 13 indicates that there was a relative radial shift between the casing and the rotor so that the TC at position B was the largest, and that at position D was the smallest of the four circumferential positions. This effect was also predicted by an analytical engine performance model, and the difference between the prediction and the measurement was within the order of magnitude of measurement uncertainty. It may be noted that this conclusion also correlates with the observations of tip rub described in section 5.2.2. Tip rub was observed only at position D where the TC is was found to be the smallest.

5.2.4 Turbine Measurement. An example of TC data obtained from stage 2 of the HPT during cold stabilization test is presented in Fig. 14. This test is used to determine the transient thermal behavior of the engine during a typical take-off maneuver. The engine is stabilized at idle before a fast acceleration to maximum take-off condition is carried out.

During the operation of turbine probes, it was found that the high temperatures encountered around the turbine at high-speed conditions affect the electrical properties of the ceramic materials within the probe-head. This led to a change in system sensitivity and hence, to a deviation between indicated and actual TC at high speeds. A procedure was developed to partially correct for this deviation and a corrected data point is indicated in Fig. 14. Further analyses of the data and development work on the turbine probes are ongoing, and will be reported in a future publication.

5.2.5 Probe Durability and Long-Term Uncertainty. The vehicle configured with 12 compressor probes ran for approximately 100 hours. During this period intensive testing was carried out including several performance curves, cold stabilization tests, and fuel spiking tests. In the early phase of testing one probe failed due to a defective flexible cable. A second probe failed later in the test program, and the reason was found to be a broken conductor in the MI cable. All other probes gave reliable data. Post-test inspection showed that the probe-heads were in a good condition with no significant signs of mechanical fatigue.

Turbine probes were used over a period of 100 hours of rigorous testing. Post-test inspection of the probes showed no significant mechanical fatigue effects.

The long-term uncertainty of the system proved to be stable. The measured clearance for a defined engine condition (20 percent speed, cold engine) was constant throughout the

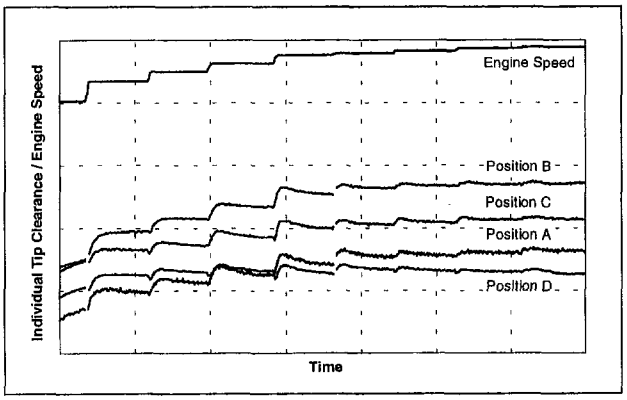

Fig. 12 Individual tip clearance from four circumferential positions around compressor stage 6

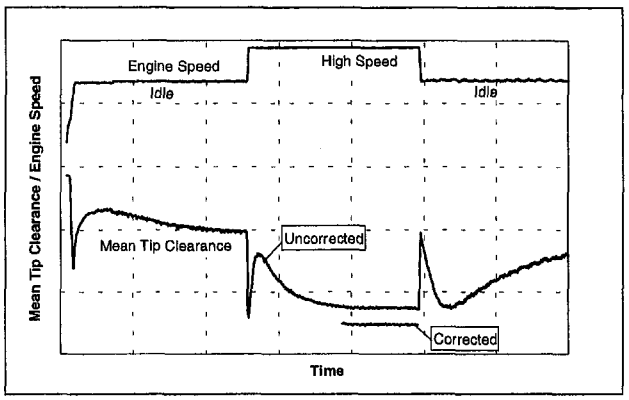

Fig. 14 HP turbine, Stage 2 mean tip clearance measured during a cold stabilization test

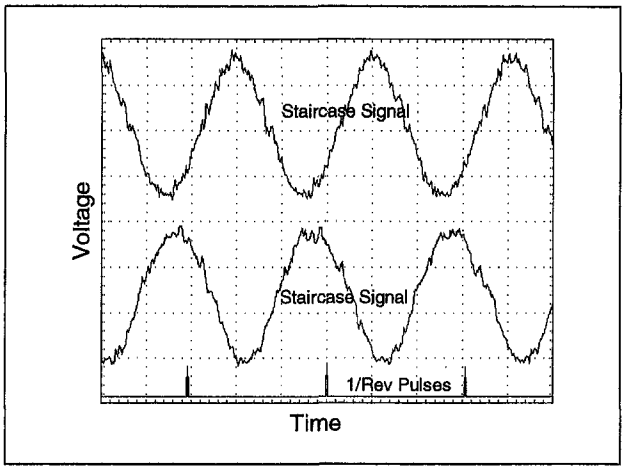

Fig. 15 Dynamic system output of two circumferentially opposed compressor probes

entire test with maximum deviations within the measurement uncertainty.

5.3 Dynamic Data Analysis. As described in section 2.1.3, the TC system incorporates a dynamic TC output, the staircase signal, which allows the study of rotordynamic effects.

The staircase output was logged on tape and analyzed using a digital storage oscilloscope. As described in section 2.2.2, the staircase signal is affected by system noise. To analyze the staircase signal, the noise had to be eliminated. To eliminate the noise the oscilloscope was operated in the "Average Mode" and triggered by the once-per-revolution pulse generated by the speed module. In this mode the oscilloscope keeps a defined number of data sets in the memory and overlays them. Since the oscilloscope was triggered by the once-per-revolution pulse, each dataset contains TC information of the same number of blades in the same order. By overlaying and averaging the datasets, the noise is canceled out. The noise filtered TC signals of two compressor probes positioned opposite to each other, locations B and D, recorded over approximately three revolutions of the rotor, is shown in Fig. 15. In addition the once-per-revolution trigger is also displayed.

Figure 15 clearly indicates that the TC is modulated with the first engine order, and that the phase shift between the two signals is approximately 180 deg. This indicates rotor eccentricity with reference to the casing. The magnitude of the eccentricity was found to be of the same order as that observed on the core, and can be related to analytically predicted effects within the rotor-shaft support structure of the engine. A similar effect was reported by Sheard and Killeen (1995).

6 Summary and Conclusions

A capacitance type frequency modulated TC measurement system has been developed to satisfy the measurement and installation design requirements of a family of gas turbine engines. The system has been successfully used to measure the TC in the compressor section and the turbine of an engine. The development program has significantly advanced the state of the art in TC measurement with the inclusion of a long (up to 3 m) flexible cable and a linearizer to acquire data directly in engineering units. The following summarizes the present work:

- An uncertainty analysis of the clearance measurement system predicted that clearance could be measured within the engine to an uncertainty better than ± 0.06 mm. Operational experience with the system gave confidence that this uncertainty was achieved in practice.
- The capacitance clearance measurement system has been demonstrated to measure TC, consistent with measurements of clearance made with a second system, utilizing a different operating principle.
- Measurements of TC during cold engine cranks matched cold build clearances measured during engine assembly to within 5 percent of reading.
- Tip rub was measured using the clearance measurement system and by inspection following an engine strip. The two measurements showed agreement within the measurement uncertainty.
- Clearance data from four probes around a stage showed a relative displacement of the casing with reference to the rotor. This displacement was found to increase with rotor speed. An analytical model also predicted this effect. The difference between the measured and predicted displacement was within the measurement uncertainty.
- The dynamic clearance data showed a modulation of the TC signal by a first engine order frequency. This modulation was related to rotor eccentricity, which can be explained by analytically predicted effects within the rotor-shaft support structure.
- During the entire test program the probes showed no significant signs of mechanical fatigue.

Acknowledgments

The authors acknowledge the assistance of John Stringfellow and Paul Wilson of Fylde Electronic Laboratories for developing the analogue components of the clearance measurement system. The assistance of Bernard Killeen is acknowledged for the development of the digital electronic components and programming systems. The authors acknowledge the assistance of Dr. Otto Fernholz, Les Donald, Ken Abbot, and others during the design, development, and manufacture of the clearance measurement system. The authors appreciate the clearance from BMW Rolls-Royce GmbH to publish the material in this paper.

References

Chivers, J. W. H., 1989, "A Technique for the Measurement of Blade Tip Clearance in a Gas Turbine," Ph.D. Thesis, Imperial College, London, United Kingdom; also Paper No. AIAA 89-2916.

Kappler, G., Moore, R., and Hourmouziadis, J., 1992, "Hochleistung-Turbo-Fan-Triebwerke ein Familienkonzept," DGLR Paper No. 92-03-043.

Sheard, A. G., and Turner, S. R., 1992, "Electromechanical Measurement of Turbomachinery Blade Tip to Casing Running Clearance," ASME Paper No. 92-GT-50.

Sheard, A. G., and Killeen, B., 1995, "A Blade-by-Blade Tip Clearance Measurement System for Gas Turbine Applications," ASME JOURNAL OF ENGINEERING FOR GAS TURBINES AND POWER, Vol. 117, pp. 326–331.

A Tool for Thermoeconomic Analysis and Optimization of Gas, Steam, and Combined Plants

A. Agazzani

A. F. Massardo
Mem. ASME

University of Genova,
Istituto di Macchine e Sistemi Energetici,
Genova, Italy

The aim of this work is to demonstrate the capability of an original "modular" simulator tool for the thermoeconomic analysis of thermal-energy systems. The approach employed is based on the Thermoeconomic Functional Analysis (T.F.A.), which, through definition of the "functional productive diagram" and the establishment of the capital cost function of each component, allows the marginal costs and the unit product costs, i.e., the "internal economy," of the functional exergy flows to be obtained in correspondence to the optimum point. The optimum design of the system is obtained utilizing a traditional optimization technique, which includes both physical structure of the energy system described in terms of thermodynamic variables and cost model (capital cost of the components, maintenance and amortization factors, unit fuel cost, unit electricity cost, etc.). As an application example to show the practicability of the tool, the thermoeconomic analysis of various complex multipressure combined cycles (with or without steam reheating) is carried out. The results are analyzed and discussed in depth.

Introduction

The design of an energy conversion process is a highly intensive task. Frequently, when the engineer has to devise an energy conversion system, different configurations have to be calculated before the "optimal" one is found. It is thus very convenient to have access to some simulation tool that allows a quick and reliable calculation of the relevant mass–energy balances, as well as an estimation of the cost of components and the evaluation of cost balances by means of a thermoeconomic study. There are several reasons that favor the choice of a modular structure: Flexibility and expandibility are the most important ones.

The approach looks at a generic process, and analyzes it, not as a whole system, but as an assembly of several elemental components interconnected in various ways. This allows the user to simulate any plant configuration without adapting the core of the "code" to it, making process simulation much easier. Obviously the plant can comprise only components included in the code's library: Each component is handled separately by a specific subroutine (Agazzani, 1996).

The code modularity built-in design knowledge is such that the user can quickly compare several different plant schemes and build a complete reference data base upon which a decision about the most convenient plant layout can be based.

The tool presented here has been aimed at the following targets:

(*i*) thermodynamic and exergy analysis
(*ii*) thermoeconomic analysis
(*iii*) optimization

The performances of an energy system can be calculated by mathematically describing its *physical structure* in terms of thermodynamic variables. Once such a structure is defined, the thermoeconomic method provides the cost of the components and the costs of the interconnection among components.

Essentially, there are two thermoeconomic techniques proposed in literature: the *Thermoeconomic Functional Analysis* (T.F.A.) and the *Exergetic Cost Theory.* The first, proposed by El-Sayed and Evans (1970) and El-Sayed and Tribus (1983) and subsequently developed by Frangopoulos (1983, 1991, 1992) and von Spakovsky and Evans (1990, 1993), is an optimization methodology that provides marginal costs. The second, introduced by Tsatsaronis and Winhold (1985) and then developed by Valero et al. (1986), is a cost accounting methodology, which provides average costs.

The approach here utilized and already presented by the authors for the study of steam plants (Lenti et al., 1989; Agazzani et al., 1995), is similar to T.F.A., but employs an original direct approach to carry out the optimization (D.T.O., *Direct Thermoeconomic Optimization*).

The productive relationships (called, in this paper, *functional exergy flows*) between the components, are expressed by the extensive variable exergy. In such cases it is useful to calculate the marginal and average unit costs of the products defining the global performances of the components (*internal economy*). Any thermoeconomic accounting and optimization methodology for an energy system is based upon a different definition of the productive purpose for each component. On the basis of this definition the *functional productive diagram* of the *Thermoeconomic Functional Analysis* (T.F.A.) (Frangopoulos, 1983, 1992) is utilized here in which each component has several inputs (fuels) and one output (product). It differs from the physical one because of the introduction of fictitious branches and junctions. The knowledge about the connectivity of the processes (i.e., how the functional fluxes connect the components to each other and with the environment) is assigned to the program by means of an interconnection functional matrix.

The Lagrangian formulation of the optimization problem allows the marginal costs of the functional exergy flows to be determined as Lagrangian multipliers, but the same equation can be obtained by direct inspection of the productive structure using the marginal cost definitions. A single equation per each

Contributed by the International Gas Turbine Institute and presented at the 41st International Gas Turbine and Aeroengine Congress and Exhibition, Birmingham, United Kingdom, June 10–13, 1996. Manuscript received at ASME Headquarters February 1996. Paper No. 96-GT-479. Associate Technical Editor: J. N. Shinn.

unit (component, junction) is obtained. In this way the D.T.O., coupled with the *Functional Analysis,* allows the internal economy to be easily carried out at the optimum point conditions already evaluated.

The present paper reports the philosophy of the simulation approach, describes the details of its mathematical representation and presents detailed results of some case studies: several multipressure level combined-cycle power stations for the generation of electricity.

Functional Productive Analysis

The plant analyzed is subdivided into a set of units, each one including one or more physical components, connected by material flows. The schematization of the plant in single units interconnected by material and mechanical work streams is called the *physical structure* of the system (Serra et al., 1995). Starting from this structure, a productive diagram (or structure) can be made by establishing the productive interconnections between the components on the basis of the definition of the exergetic productive purpose (or product) of each component. From this definition derives also the one of component input (fuel), i.e., of the functional exergy flows that contribute to the formation of the component product. The representation of the input/output functional exergy flows of a component requires in general the introduction of fictitious branches and junctions. As a consequence a new study of the system is introduced, called *Functional Productive Analysis.*

The Functional Productive Analysis can be considered from two different points of view: graphic and mathematical.

The Graphic Approach. The graphic representation, called the *functional productive diagram,* is composed of units described by geometric figures and lines connecting the units, which represent the relations (functional exergy flows y) between units or between the system and the environment. The complete distribution of functions y is obtained graphically by adding fictitious branches and junctions to the physical structure; in this way a single output (product) and one or more input (fuels) functional exergy flows are considered for each unit (see Fig. 3).

As an example, the compressor of Fig. 3 is considered (unit 2). In the physical structure it directly supplies exergy to the combustion chamber (unit 3). In the functional diagram only a part of the compressor functional exergy flow (flow 2) enters the combustion chamber to overcome the pressure losses (the flow 2, 3 represents the mechanical exergy spent by unit 3); the rest of the flow 2 is branched in order to overcome the pressure losses of the gas side heat exchangers (the flows 2, 6, 2, 7, etc., represent the mechanical exergy spent by unit 6, 7 etc.), supply mechanical exergy (flow 2, 4) to the gas turbine expander (unit 4) and thermal exergy (flow 2, 27) to the unit junction 27.

When introducing branches it is also necessary to introduce fictitious junctions, whose purpose is to join each component product (not exiting the system) to the rest of the system. Generally after a junction unit, a branch unit follows. In the example of Fig. 3, there are two junction units (see 27 and 28). Into the latter the main exergy productions of the various units (compressor, combustion chamber for the gas cycle; heat exchangers of the HRSG, pumps for the steam cycle) converge. The output functional exergy flow of these junctions (equal to the sum of inputs) is split into several functional flows, which correspond to the inputs of units where an exergy consumption is realized (turbines, exchangers), or to unused exergy flows transferred to the environment.

For cyclic processes such as steam power cycles, the exergy interactions are not sufficient to describe completely the functional productive diagram. The negentropy interactions (see dotted lines in Fig. 3) are then introduced to define the condenser product, which consists of generating and distributing negentropy to the other components of the steam cycle in order to compensate for the entropy they produce (Frangopoulos, 1983; Lenti et al., 1989; von Spakovsky and Evans, 1990).

The Mathematical Approach. The productive purpose of each component can be defined by introducing *functional exergy flows* (y) in addition to the physical exergy flows. The documented determination of these functions is achieved by a particular analysis. With the introduction of fictitious branches in the physical structure, each physical component (component unit) and each junction unit having several purposes is split into a unit having a single product plus a branch (this last is not numbered like the other units).

The mathematical description of the Functional Productive Analysis is the following:

$$\text{component unit products} \quad y_r = y_r(x_r) \quad r = 1, \ldots, \sigma \tag{1}$$

$$\text{component unit inputs} \quad y_{r',r} = f_{r',r}(x_r) \cdot y_r \quad r', r = 1, \ldots, \sigma \quad r \neq r' \tag{2}$$

$$\text{junction unit outputs} \quad y_r = \sum_{r'=0}^{\tau} y_{r',r} \quad r = \sigma + 1, \ldots, \tau \quad r' = 0, \ldots, r-1, r+1, \ldots, \tau \tag{3}$$

$$\text{branches} \quad \sum_{r'=0}^{\tau} y_{r,r'} = y_r \quad r = 1, \ldots, \tau \quad r' = 0, \ldots, r-1, r+1, \ldots, \tau \tag{4}$$

where y in the equations represents output or input functional exergy/negentropy flows. In the subscript (r', r) or (r, r') the second number indicates the unit which the function enters (i.e., the unit utilizing the function), while the first number indicates

Nomenclature

$c_{r,r'}$ = average unit cost of $y_{r,r'}$ \$/kJ
F = objective function
m = mass flow rate, kg/s
T = temperature, K
x = set of design decision variables
y = set of all functional exergy flows
y_r = output functional exergy flow of unit r
$y_{r,r'}$ = functional exergy flow going from unit r to r'
$y_{r,0}$ = functional exergy flow going from unit r to the environment
$y_{0j,r}$ = functional exergy flow supplied by the environment to the unit r
Z_r = capital cost of unit r (including investment, depreciation, maintenance, etc.), \$/s
β = pressure ratio
Γ = total cost rate entering the system (capital and operation expenses), \$/s
Γ_r = cost rate of the component r, \$/s
$\Gamma_{0j,r}$ = cost associated with the function $y_{0j,r}$ supplied by the environment to the unit r, \$/s
$\Gamma_{r,0}$ = revenue time from selling the product $y_{r,0}$ to the outside environment, \$/s
η = efficiency
$\lambda_{r,r'}$ = marginal cost of $y_{r,r'}$ \$/kJ
σ = number of component units
τ = number of units and junctions

Subscripts

c = compressor
is = isoentropic
t = turbine

the unit where the function comes from. If $r' = r$, $y_{r,r} = y_r$ represents the function output of unit r. Each $y_{r',r}$ entering a component r is a function of its product (y_r) and its independent variables x_r while each y_r associated with a component unit product is a function of the independent variables x_r alone.

Marginal and Average Unit Costs

In a general sense thermoeconomics is the science of energy saving (Serra et al., 1995). All thermoeconomic methodologies use the costs to solve problems. Generally the cost expresses the amount of resources consumed to obtain a product. There are two main groups of thermoeconomic costs (Tsatsaronis and Winhold, 1985): (a) average unit costs; (b) marginal costs.

The Functional Productive Analysis, described above allows the costs (average and marginal) of the $y_{r',r}$ functional flows to be directly calculated.

Average Unit Costs. An average cost c_r expresses the amount of resources (in monetary terms) consumed to obtain a product y_r. A cost balance is written for each unit, considering break-even operation:

$$c_r y_r = Z_r + \sum_{j=1}^{j_r} c_{0j,r} y_{0j,r} + \sum_{r'=1}^{\tau} c_{r,r'} y_{r,r'}$$

$$r = 1, \ldots, \tau \quad r' = 1, \ldots, r-1, \quad r+1, \ldots, \tau \qquad (5)$$

where

$Z_r = Z_r(x_r, y_r)$ capital cost of unit r (\$/s) including investment, depreciation, maintenance, etc. (Frangopoulos, 1983; Agazzani et al., 1995)

and

$$c_{r,r'} = c_r \qquad (6)$$

The latter are "branch equations" and represent equality conditions of unit costs of the functional flows and they are justified by considering that the unit costs of the functional flow splitting in branch cannot change because no losses or other phenomena occur. For $r = 0$ (goods and services coming from the environment) the unit cost $c_{0j,r}$ is considered a known constant (i.e., fuel price, electricity purchased price). The costs in which $r' = 0$ ($c_{r,0}$) represent costs for the products of the system.

Therefore the total set of equations is:

- input-output cost balance equations of the component units (Eq. (5) with $r = 1, \ldots, \sigma$),
- input-output cost balance equations of the junction units (Eq. (5) with $r = \sigma, \ldots, \tau$ and $Z_r = 0$),
- equality unit costs conditions for the functional exergy flows of branches (Eq. (6))

and can be solved for the unit costs c with no need of additional equations.

In the functional approach, costs carriers are not necessarily streams of matter or energy but the functions appearing in the functional diagram. The cost of each function is apportioned to its consumers. In this way, a more equitable allocation of the costs to the final products is achieved.

In short, the information obtainable from the above-introduced costs, can be summarized in this way: high value of $c_{r,r'}$ denotes a large monetary expenditure for each exergy unit carried by the functional flow $y_{r,r'}$.

Marginal Costs. The marginal cost λ_r of a component product y_r represents the variation of the total cost rate entering the system (Γ) associated with a unit increase of the product itself:

$$\lambda_r = \frac{\partial \Gamma}{\partial y_r} \qquad (7)$$

where

$$\Gamma = \sum_{r=1}^{\sigma} Z_r + \sum_{r=1}^{\tau} \sum_{j=1}^{j_r} \Gamma_{0j,r} - \sum_{r=1}^{\tau} \Gamma_{r,0} \qquad (8)$$

with

$\Gamma_{0j,r}$ = cost associated with the function $y_{0j,r}$ supplied by the environment to the unit r (\$/s); it will be assumed that $\Gamma_{0j,r} = c_{0,r} y_{0,r}$ (with $c_{0,r}$ constant)

$\Gamma_{r,0}$ = revenue from selling the function (product) $y_{r,0}$ to the outside environment (\$/s)

Since, in a fixed design point, the conditions (2) can be applied and y_r can be considered as an independent variable, by applying Eq. (7), it can be noticed that

$$\lambda_r = \frac{\partial \Gamma}{\partial y_r} = \frac{\partial \Gamma_r}{\partial y_r} = \frac{\partial (Z_r + \sum_{r=1}^{j_r} \lambda_{0j,r} y_{0j,r} + \sum_{r'=1}^{\tau} \lambda_{r',r} y_{r',r})}{\partial y_r}$$

$$r = 1, \ldots, \tau \qquad (9)$$

i.e., the marginal cost of unit product can be calculated as the variation of the cost rate of the component r (Γ_r) instead of as a variation of the system total cost. Also in this case, as the Eqs. (6), cost equality conditions in the branches are valid:

$$\lambda_{r,r'} = \lambda_r \qquad (10)$$

Therefore, by observing Eqs. (9), it can be concluded that the marginal and average unit costs of the unit outputs (i.e., component or junction products) are coincident when linear laws of the capital cost function Z_r with respect to the product y_r are used.

Marginal costs can be shown to be equal to Lagrange multipliers in the thermoeconomic analysis of the systems. The Lagrangian formulation of an optimization problem, in which equality constraints are made up of a thermoeconomic model of the system allows the marginal costs of the functional exergy flows "y" to be determined as Lagrange multipliers. Methods for determining them are presented in the literature (El-Sayed and Tribus, 1983; Frangopoulos, 1983).

Structure of TEMP (ThermoEconomic Modular Program)

When allocating costs to a plant, each thermoeconomic theory needs a productive model to add to the physical and economic models of the plant. The physical model consists of a group of equations that describe the thermodynamic behavior of the components. It allows parameters such as temperatures, pressures, efficiencies, powers, etc., to be calculated. The economic model consists of another group of equations that relates thermodynamic variables with the investment cost of the components. Finally the productive model consists of a group of equations that define the purpose of each component in the productive system.

The code here presented, called TEMP (*ThermoEconomic Modular Program*), considers each component as a black box, and scans in turn the appropriate set of thermodynamic and thermoeconomic equations that are known to apply to that component, attempting to solve only for those thermodynamic variables whose values are neither assigned as design data nor known as inputs or outputs of other components already calculated.

Figure 1 shows a general structure of the tool and the interconnections among the optimization program and the three analyses to be executed: thermodynamic, exergy, and thermoeconomic. The physical model of the plant is included in the thermodynamic/exergy analysis, which is directly connected with the thermodynamic/exergy modules library. Instead, the eco-

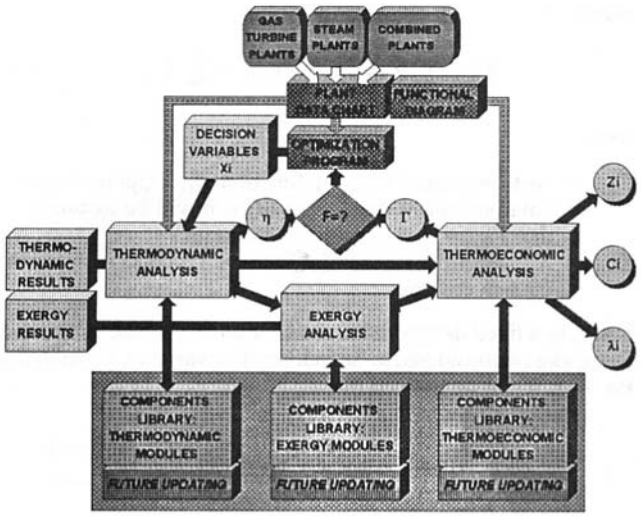

Fig. 1 General structure of the TEMP code

nomic model is inserted inside the thermoeconomic modules library, which is linked with the thermoeconomic analysis. The latter and the functional diagram allow the productive model to be performed.

Therefore, for each module included in the library, there are three subroutines: The first is utilized for the thermodynamic analysis, the second for the exergy analysis, the third for the thermoeconomic analysis. However, there are modules without cost or functional productive purpose, as for example a flow splitter, which does not have a thermoeconomic subroutine, or on the other hand, modules with a functional productive purpose but which are not utilized in the thermodynamic/exergy analysis, as for example junction modules or the "environment" module. The latter is used to define every functional exergy flow that enters inside the system from the environment.

The plant data chart contains: all the physical components; how they are physically interconnected among themselves; their fixed thermodynamic values and, in some cases, also economic data values (i.e., unit fuel price or unit electricity purchased); fictitious units, such as junctions or the "environment unit" utilized for the T.F.A.; functional productive diagram; data of some heat exchangers (geometry and metallurgy); setting of decision variables x and of inequality constraints.

The form chosen to store the functional diagram is that of a square matrix $N \times N$, where N is the sum of components utilized for the thermodynamic analysis (some of which are utilized also for the T.F.A.), junctions units, and environment unit. The matrix, called the Interconnection Functional Matrix (IFM), is defined as follows:

$\mathrm{IFM}(i, j) = 1$ if the functional exergy flow $y_{i,j}$ or y_i (if $i = j$) exists

$\mathrm{IFM}(i, j) = 0$ if the functional exergy flow $y_{i,j}$ or y_i (if $i = j$) does not exist

At the present time, the available library allows gas turbine plants, steam plants, combined plants, and cogeneration plants to be studied. Since methods to analyze, improve, and optimize energy systems have to deal not only with the energy consumption and economic aspects but also with the pollution of the environment, goods and services for the reduction of pollution will be taken into account and penalty policy will be considered in the future. Therefore the next library expansion will be realized with the introduction of new modules regarding the environmental aspects (i.e., components for NO_X or SO_X abatement) and advanced energy systems (Agazzani, 1996).

Thermodynamic and Exergy Analysis. The system to be calculated is defined as an ensemble of interconnected components, which allows a modular structure of the model to be used. All the modules utilized for the thermodynamic analysis of the plant are sequentially called several times. Therefore operating characteristics and mass/energy balances of each component are calculated sequentially until the thermodynamic conditions (pressure, temperature, mass flow, etc.) at all interconnections converge towards a stable value. Once the thermodynamic subroutine calls are concluded, the exergy modules are sequentially called to calculate the exergy of each point and the irreversibility of the components.

Thermoeconomic Analysis. Once the thermodynamic and exergy analysis are carried out, TEMP calls sequentially all the modules that have thermoeconomic purposes. By means of the matrix IFM and the sort of unit, each thermoeconomic module utilized calculates its one functional purpose y (or more if this is split into several outputs through a branch). In this way all the functional exergy flows of the functional diagram are analyzed and the functional productive analysis is performed. Besides each module estimates the capital cost Z by means of a "cost equation" function, written in terms of geometric and manufacturing variables, or a "costing equation" function, written in terms of performances and stream variables. Further information about the component cost functions are reported in Agazzani et al. (1995), Boehm (1987), Frangopoulos (1991), and Lazzaretto and Macor (1994). Instead, regarding costing equations of gas turbine components (compressor, combustor, and turbine), a short description that explains their updating in comparison to the old functions provided by the literature is provided in the appendix.

The calculation of the marginal and average unit costs is carried out only at the end of the optimization procedure, in correspondence to the optimum point (this allows the computer calculation time to be reduced). The former are calculated by solving the system of N equations made up of Eqs. (9) and (10), the latter by solving the system of N equations made up of Eqs. (5) and (6).

Optimization. The goal of the optimization tool is to minimize the rate of total cost entering the system or to maximize the thermal efficiency (or possibly a combination of both). In the first case the optimization problem is expressed as follows:

$$\min F = \Gamma = \Gamma(x, y) \tag{11}$$

where x is the set of decision variables. The equality constraints are imposed by the physical and economic model of the system. They consist of mathematical relations describing the thermodynamic performances as well as the costs of the components and the other economic parameters as a function of the independent variable set x. Also inequality constraints are taken into consideration (exhaust gas temperature, steam quality at the exit of the turbine, maximum steam temperature, etc.).

A nonlinear algorithm of optimization described in depth by Massardo et al. (1990) is directly applied to the objective function (Agazzani et al., 1995). Therefore the physical and cost models are used to describe the objective function of the system, while the mathematical formulation of the T.F.A. is not requested to find the optimum design conditions. In this way the introduction of many dependent variables related to the internal economy of the system is not necessary to locate the minimum, and therefore it can be avoided with a strong reduction in computation time. The calculation of the internal economy (marginal and average unit costs) is then performed at the optimum conditions.

Analysis of Multipressure Combined Plants

As an application example to show the practicability of the tool, the thermoeconomic analysis of various multipressure

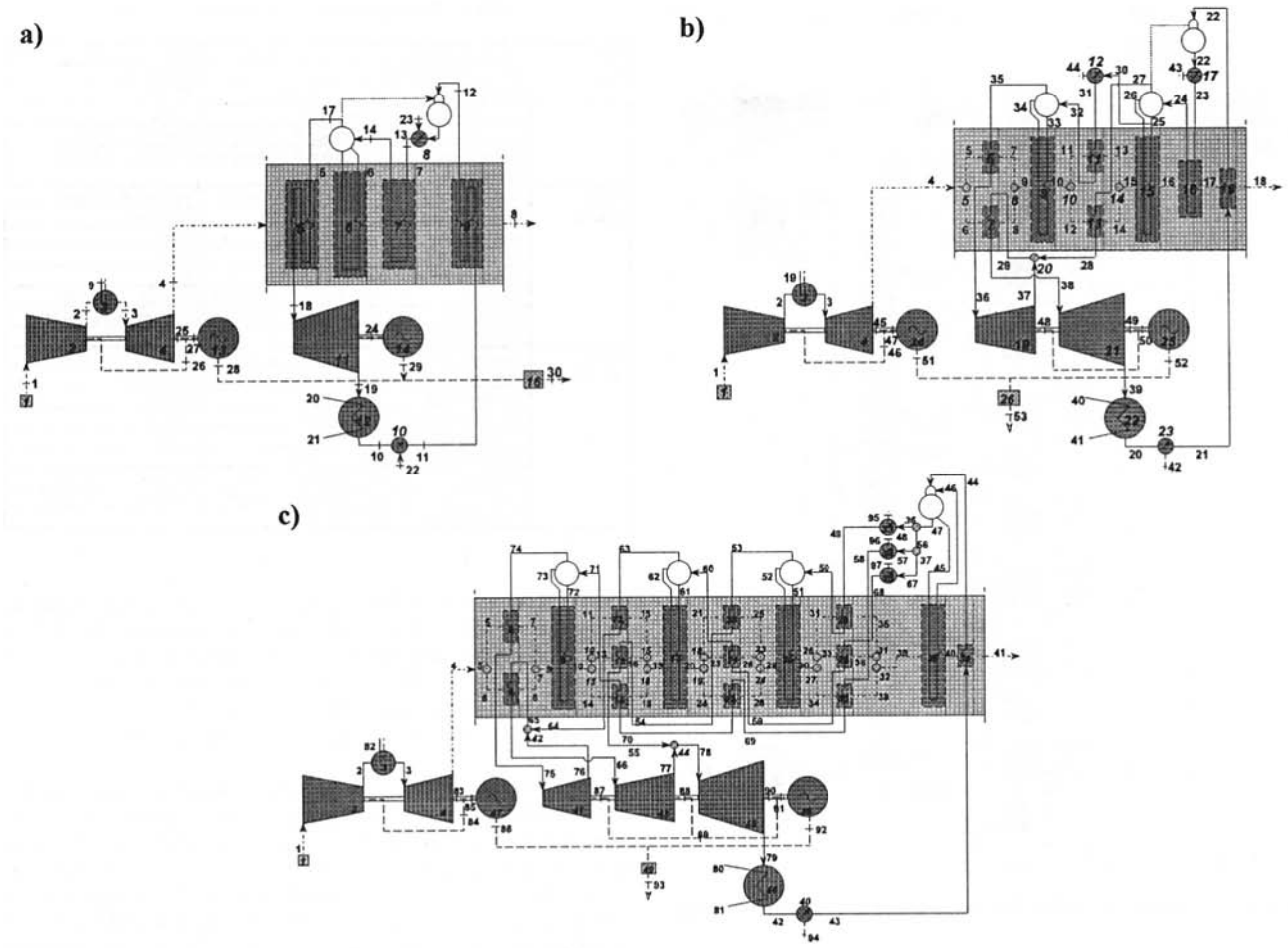

Fig. 2 Combined plant diagrams: (*a*) 1 pressure level (1PL); (*b*) 2 pressure levels with reheating (2PL + R); (*c*) 3 pressure levels with reheating (3PL + R)

combined cycles (with or without steam reheating) is carried out. The combined plants analyzed are the following: 1 pressure level (1PL), 2 pressure levels with reheating (2PL + R), 3 pressure levels with reheating (3PL + R).

Figure 2 shows the layouts of the plants. The italic numbers represent component modules utilized for the thermodynamic analysis. Some of them are also employed in the functional productive diagram (in such a case the numbering of units corresponds to the numbering utilized inside the layout of the plant). Only the functional productive diagram of the 2PL + R plant, is reported, as example, in the already mentioned Fig. 3 (the functional diagrams of the other two plants are rather similar). In these examples the gas turbine has been split into three components (compressor, combustion chamber, turbine); however the code gives also the opportunity to consider a single component, i.e., setting an existing gas turbine with a fixed price.

Values of optimization variables (decision variables) have been assumed known at the beginning of analysis and are opportunely modified during the iterative analysis of the optimization process. Other quantities are considered known and fixed once and for all at the beginning of calculation, as reported in Table 1. The electrical power considered for the three plants is 60 MWe. The fuel cost and the electricity cost utilized during the analysis are respectively 4.0×10^{-6} \$/kJ and 1.67×10^{-5} \$/kJ (0.06 \$/kWh). Besides Table 1 reports the inequality constraints taken into consideration during the optimization.

The selected decision variables are: maximum temperature of the gas turbine, pressure ratio, steam level pressures; but in any case the code allows any sort of decision variables to be selected. The main results of the three plants are reported in Table 2: objective function (i.e., total cost), design variables, thermal efficiency, electrical power, etc.

Only the internal economy of the 2PL + R combined plant is presented here, as an example; Table 3 reports the functional exergy flows (y) and their marginal and average unit costs obtained from the functional diagram (Fig. 3). The costs of the functional flows related to the compressor (unit 2), combustor (unit 3), and turbine (unit 4) are equal since their capital cost functions are here expressed linearly with respect to the products.

Figure 4(a), 4(b), and 4(c) show the total costs, and the owning and operating costs of the three optimized systems (with total cost as objective function), while Fig. 4(d) reports their thermal efficiencies. In the same figures, costs and efficiencies concerning plants with optimized efficiency are compared.

The plants with optimized efficiency have costs near the plants with optimized overall costs. Evidently the operating costs, equal to about four times the owning costs, depending on the thermal power entering into the plant and therefore depending on efficiency, affect the total costs very much.

Figure 5 reports the percentage distribution of the main components owning costs; the HRSG item includes superheaters, evaporators, economizers, preheater, pumps, etc. The gas turbine has a great influence of around 50–60 percent (35–45 percent the compressor, ~2 percent the combustion chamber, ~10 percent the turbine), while the HRSG costs have the following percentage values: ~8 percent for the 1PL plant, ~11 percent for the 2PL + R plant, ~17 percent for the 3PL + R plant.

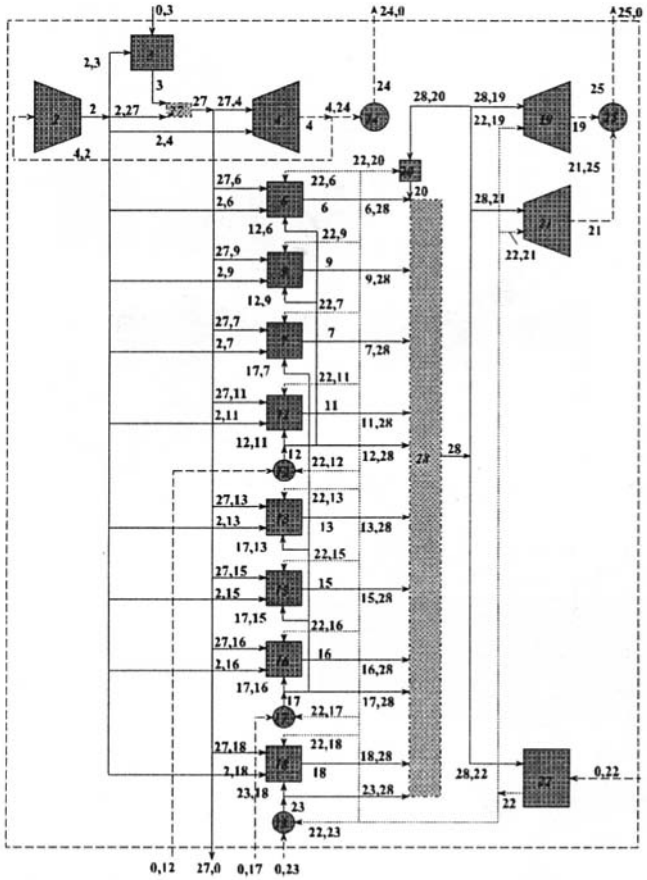

Fig. 3 Functional productive diagram of the 2PL + R combined plant

By observing Fig. 4, it can be noted that the three pressure levels combined plant has a total cost (3.475 c$/kWh) and an owning cost (0.701 c$/kWh) greater than the total and owning costs of the two pressure levels plant (3.426 c$/kWh and 0.632 c$/kWh respectively), while the operating cost is not much lower (2.774 c$/kWh against 2.794 c$/kWh).

Evidently the high cost estimated for the 3PL + R combined plant depends on the complex configuration chosen for the HRSG (see layout in Fig. 2) with many exchangers (economizers and superheaters) put in parallel among themselves. Besides the thermal efficiency, which has a great influence on the operating cost, has only a slight increase if a 3PL + R plant is selected instead of the 2PL + R plant. Therefore, the operating cost decrease is not great enough to compensate for the owning cost increase.

In order to examine this last aspect in depth, several calculations have been carried out varying the fuel cost (c_f) from 4.0

Table 1 Main assumptions

ΔT minimum between gas and evaporating steam (ΔTpp)	10°C	ΔT minimum between inlet evaporator and outlet economizer (ΔTsc)	10°C
ΔT minimum between gas and superheated steam or water (ΔTap)	25°C	ΔT between condensing steam and cooling water	5°C
condenser pressure	0.005 MPa	turbine mechanical efficiency	0.995
deaerator pressure	0.14 MPa	pump efficiency	0.83
alternator efficiency	0.985	steam turbine efficiency	0.85
pump electrical/mecha. efficiency	0.90	environment temperature	15°C
compressor efficiency	0.86	gas turbine expander efficiency	0.88
fuel LHV	50030 kJ/kg	net electrical power plant	60 MW
number of operating hours per year	8000 h/year	annual fixed charge rate	18.2%
wet steam quality	>0.86	max. steam temperature	<565°C
stack gas temperature	>100 °C		

Table 2 Thermoeconomic optimization results

Plant 1PL	Decision variable	Optimal value	Optimization range	
	max. gas temp. [°C]	1400	1200-1400	
	pressure ratio	26.85	12-30	
	1st pressure level [MPa]	7.2	6-10	
	total cost	3.492 c$/kWh	thermal efficiency	0.502
	owning cost	0.606 c$/kWh	steam cycle power	18.3 MW
	operating cost	2.889 c$/kWh		
Plant 2PL+R	Decision variable	Optimal value	Optimization range	
	max. gas temp. [°C]	1399.8	1200-1400	
	pressure ratio	26.62	12-30	
	1st pressure level [MPa]	1.384	1-3.5	
	2nd pressure level [MPa]	13.95	8-20	
	total cost	3.426 c$/kWh	thermal efficiency	0.522
	owning cost	0.632 c$/kWh	steam cycle power	20.04 MW
	operating cost	2.794 c$/kWh		
Plant 3PL+R	Decision variable	Optimal value	Optimization range	
	max. gas temp. [°C]	1372	1200-1400	
	pressure ratio	25.5	12-30	
	1st pressure level [MPa]	0.72	0.5-1.6	
	2nd pressure level [MPa]	3.5	2.5-5	
	3rd pressure level [MPa]	17.5	10-20	
	total cost	3.475 c$/kWh	thermal efficiency	0.525
	owning cost	0.701 c$/kWh	steam cycle power	21.7 MW
	operating cost	2.774 c$/kWh		

$\times 10^{-6}$ \$/kJ to 1.0×10^{-5} \$/kJ. In this way it is possible to verify the presence of a break-even point between the 2LP + R total cost plant and the 3LP + R total cost plant. Figure 6 reports this analysis. By varying the fuel cost, the total cost of the two plants show nearly linear curves; their difference becomes equal to zero with a fuel cost value near to 8.0×10^{-6} \$/kJ.

The economic results here presented must be considered not as an absolute solution, but they can be interpreted as a starting point for a thermoeconomic comparison of different plants. In fact, it is difficult to consider adequately every factor that contributes to estimate the final purchase cost of a component. A cost function must be related to thermodynamic parameters of the plant and factor covering every type of item cost. Besides, it must be possible to update it taking into account the progress about both performance improvement and market prices. However, for the two pressure levels combined plant, the results obtained are sufficiently in accordance with data reported by Bianchi (1995).

Conclusions

A computational, modular approach to the thermoeconomic simulation of energy conversion systems has been described in this paper. The code, called TEMP from the acronym of *ThermoEconomic Modular Program* is a robust, efficient, and

Table 3 Functional exergy flows (y) and internal economy (l and c) of the functional productive diagram in Fig. 3

Flow	y [kW]	λ·10⁶ [$/kJ]	c·10⁶ [$/kJ]	Flow	y [kW]	λ·10⁶ [$/kJ]	c·10⁶ [$/kJ]	Flow	y [kW]	λ·10⁶ [$/kJ]	c·10⁶ [$/kJ]
2	51457.3	9.29	9.29	13,28	381.613	11.9	12.1	22,21	2131.53	0.672	0.681
2,3	127.728	9.29	9.29	15	2664.17	9.31	9.41	22	34748.0	0.672	0.681
2,4	27205.6	9.29	9.29	15,28	2664.17	9.31	9.41	22,23	0.581	0.672	0.681
2,6	84.937	9.29	9.29	16	1781.12	10.5	10.6	23,18	0.238	29.1	31.3
2,7	84.937	9.29	9.29	16,28	1781.12	10.5	10.6	23	2.201	29.1	31.3
2,9	84.937	9.29	9.29	17,7	1.614	24.3	25.4	23,28	1.963	29.1	31.3
2,11	84.937	9.29	9.29	17,13	1.755	24.3	25.4	24	39961.3	7.97	7.98
2,13	84.937	9.29	9.29	17,15	0	24.3	25.4	24,0	39961.3	7.97	7.98
2,15	84.937	9.29	9.29	17,16	2.437	24.3	25.4	25	20038.7	11.7	12.2
2,16	84.937	9.29	9.29	17	22.975	24.3	25.4	25,0	20038.7	11.7	12.2
2,18	84.937	9.29	9.29	17,28	17.169	24.3	25.4	27,4	75693.9	6.36	6.36
2,27	23444.5	9.29	9.29	18	639.788	19.0	19.2	27,6	7567.99	6.36	6.36
3	83611.3	5.54	5.54	18,28	639.788	19.0	19.2	27,7	1146.49	6.36	6.36
3,27	83611.3	5.54	5.54	19	7668.12	11.2	11.8	27,9	10017.3	6.36	6.36
4,2	56458.8	7.69	7.69	19,25	7668.12	11.2	11.8	27,11	4279.47	6.36	6.36
4	97028.6	7.69	7.69	20	834.761	11.2	11.3	27,13	469.72	6.36	6.36
4,24	40569.8	7.69	7.69	20,28	834.761	11.2	11.3	27,15	3076.01	6.36	6.36
6	6615.46	8.24	8.31	21	12675.2	11.4	11.8	27,16	2174.97	6.36	6.36
6,28	6615.46	8.24	8.31	21,25	12675.1	11.4	11.8	27,18	1298.37	6.36	6.36
7	999.856	9.01	9.11	22,6	4939.73	0.672	0.681	27	107056	6.36	6.36
7,28	999.856	9.01	9.11	22,7	750.354	0.672	0.681	27,0	1331.56	6.36	6.36
9	8861.62	8.12	8.17	22,9	8203.90	0.672	0.681	28,19	8611.17	9.03	9.11
9,28	8861.62	8.12	8.17	22,11	4646.53	0.672	0.681	28,20	1023.69	9.03	9.11
11	3864.22	8.54	8.62	22,12	24.613	0.672	0.681	28,21	15085.9	9.03	9.11
11,28	3864.22	8.54	8.62	22,13	351.607	0.672	0.681	28,22	2115.83	9.03	9.11
12,6	15.648	22.2	22.8	22,15	4432.23	0.672	0.681	28	26833.5	9.03	9.11
12,9	0	22.2	22.8	22,16	4234.98	0.672	0.681	0,3	115118.	4.00	4.00
12,11	21.733	22.2	22.8	22,17	3.539	0.672	0.681	0,12	259.681	16.7	16.7
12	209.152	22.2	22.8	22,18	3831.01	0.672	0.681	0,17	29.462	16.7	16.7
12,28	171.771	22.2	22.8	22,19	786.498	0.672	0.681	0,22	21.752	16.7	16.7
13	381.613	11.9	12.1	22,20	188.934	0.672	0.681	0,23	3.092	16.7	16.7

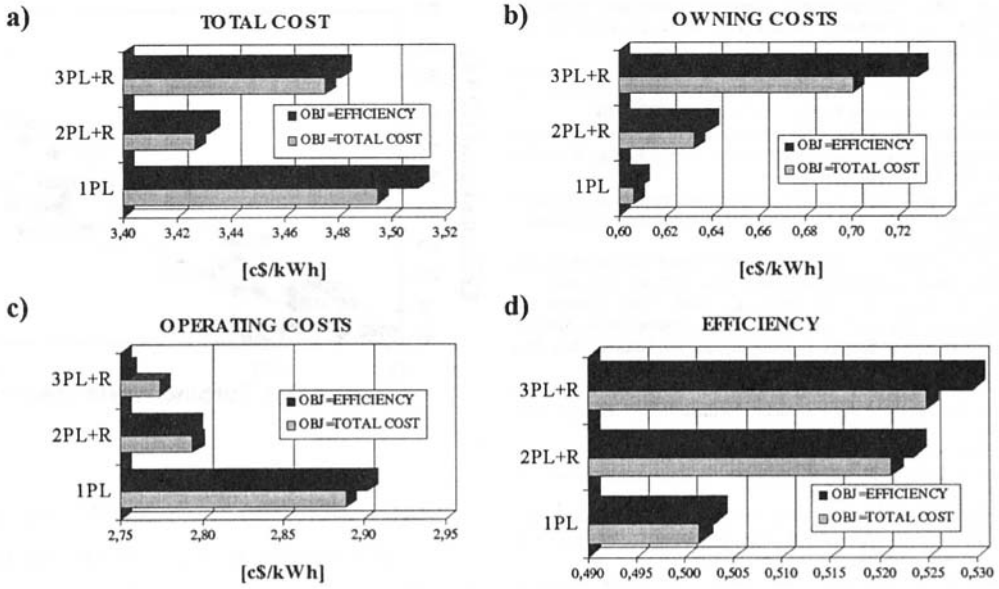

Fig. 4 Comparison among plants: (*a*) total costs; (*b*) owning costs; (*c*) operating costs; (*d*) efficiencies

reliable tool to use once the configuration of the system has been defined.

The *Thermoeconomic Functional Analysis* (T.F.A.) approach employed here, joined to a direct optimization (D.T.O., *Direct Thermoeconomic Optimization*), allows the component costs and the internal economy to be easily carried out at the optimum point conditions.

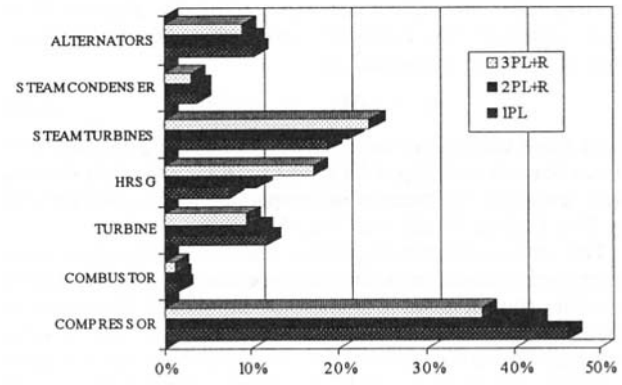

Fig. 5 Percentage distribution of the owning costs

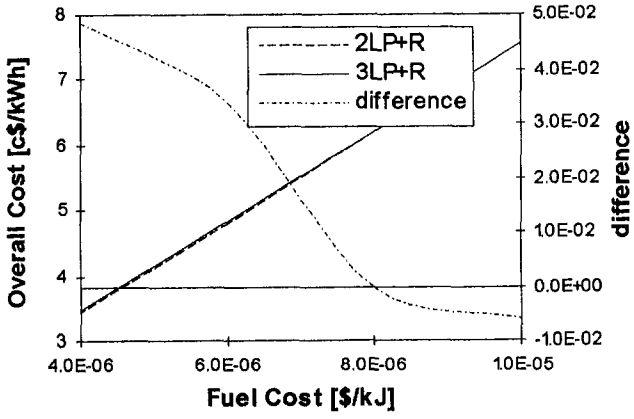

Fig. 6 Influence of the fuel cost on the total costs

The code, already tested with steam plants and gas turbine plants, has been improved here by analyzing simple and complex combined plants. The results have shown that the high costs of a complex combined plant (three pressure level with reheating configuration) become competitive in comparison to the costs of a two pressure level (with reheating) combined plant, only for a high fuel price. But the numerical examples presented here serve only to clarify the methodology; the results obtained are valid under the economic assumptions made in this example with no claim to general applicability. However, thanks to the modularity of the code, the updating of components cost functions can be readily carried out, once more information is available.

At this moment, the procedure is capable of accepting 25 component models, but in principle, and by means of its modularity, it can be expanded at will. The authors are working on a further extension of the code's capabilities, to include environmental aspects (pollution) and to study advanced energy systems (STIG, ISTIG, HAT, Kalina, etc.).

Besides, in the near future, unsteady-state conditions will be inserted inside the tool. In this new formulation, the kind of system will be considered known, but the system configuration, the design characteristic of the components and the point of operation at any time interval Δt which lead to an overall optimum, will be determined by the solution of an appropriately formulated problem (Agazzani, 1996).

References

Agazzani, A., Massardo, A., Satta, A., 1995, "Thermoeconomic Analysis of Complex Steam Plants," ASME Paper No. 95-CTP-38.

Agazzani, A., 1997, "Thermoeconomic Analysis of Energy Systems," Ph D. Thesis, University of Pisa, Italy.

Bianchi, S., 1995, "Ottimizzazione Tecnico-Economica degli Impianti a Ciclo Combinato 'Gas-Vapore' per le Centrali di Zaharani e Beddawi," Master's Thesis, University of Genoa, Italy.

Boehm, R. F., 1987, *Design Analysis of Thermal Systems,* Wiley, New York.

El-Sayed, Y. M., and Evans, R. B., 1970, "Thermoeconomics and the Design of Heat System," ASME JOURNAL OF ENGINEERING FOR POWER, Vol. 92, pp. 27–34.

El-Sayed, Y., and Tribus, M., 1983, "Strategic Use of Thermoeconomics for System Improvement," in *Efficiency and Costing: Second Law Analysis of Processes,* R. A. Gaggioli, ed., A.C.S. Symposium Series, No. 235, Washington, DC, pp. 215–239.

Frangopoulos, C. A., 1983, "Thermoeconomic Functional Analysis: a Method for Optimal Design or Improvement of Complex Thermal System," Ph.D. Thesis, Georgia Institute of Technology, Atlanta, GA.

Frangopoulos, C. A., 1991, "Comparison of Thermoeconomic and Thermodynamic Optimal Designs of a Combined-Cycle Plant," *Proc. of ATHENS '91*, Athens, June 3–6, pp. 305–318.

Frangopoulos, C. A., 1992, "Optimal Synthesis and Operation of Thermal Systems by the Thermoeconomic Functional Approach," ASME JOURNAL OF ENGINEERING FOR GAS TURBINES AND POWER, Vol. 114, pp. 707–714.

Lazzaretto, A., and Macor, A., 1994, "Marginal and Average Costs in Engineering Functional Analysis," presented at the Florence World Energy Research Symposium, FLOWERS '94, Florence, July 6–8.

Lenti, F., Massardo, A., and Satta, A., 1989, "Thermoeconomic Optimization of a Simple Thermal Power Plant Using Mathematical Minimization Algorithm," IECEC Paper No. 899341.

Massardo, A., Satta, A., and Marini, M., 1990, "Axial Flow Compressor Design Optimization," ASME *Journal of Turbomachinery*, Vol. 112, pp. 399–410.

Serra, L., Lozano, A., Valero, A., and Torres, C., 1995, "On Average and Marginal Costs in Thermoeconomics," *Efficiency, Costs, Optimization, Simulation and Environmental Impact of Energy Systems*, ECOS '95, Istanbul, July 11–15.

Tsatsaronis, G., Winhold, M., 1985, "Exergoeconomic Analysis and Evaluation of Energy Conversion Plants. I—A New General Methodology," *Energy*, Vol. 10, No. 1, pp. 69–80.

von Spakovsky, M. R., and Evans, R. B., 1990, "The Design and Performance Optimization of Thermal Systems," ASME JOURNAL OF ENGINEERING FOR GAS TURBINES AND POWER, Vol. 112, pp. 86–93.

von Spakovsky, M. R., and Evans, R. B., 1993, "Engineering Functional Analysis—Part I and Part II," ASME *Journal of Energy Resources Technology*, Vol. 115, pp. 86–99.

Valero, A., Lozano, M. A., and Munoz, M., 1986, "A General Theory of Exergy Savings," "Part I: On Exergetic Cost," "Part II: On the Thermoeconomic Cost," "Part III: Energy Savings and Thermoeconomics," ASME Book HO341A, WAM, AES, Vol. 2–3, pp. 1–21.

Gas Turbine World, 1995, "Gas Turbine World 1995 Handbook," Pequot Publishing Inc., Fairfield (USA), Vol. 16.

APPENDIX

Purchase Cost of Gas Turbine Components

The following cost functions for compressor, combustor, and turbine (expander) were introduced by El-Sayed and Tribus (1983) and then modified by Frangopoulos (1992):

$$\text{compressor} \quad \Xi = c_1 \cdot \frac{39.5 \cdot m_{\text{air}}}{0.9 - \eta_{is}} \cdot \beta_c \cdot \ln \beta_c \qquad \text{(A1)}$$

$$\text{combustor} \quad \Xi = c_1 \cdot \frac{25.6 \cdot m_{\text{air}}}{0.995 - \Delta p\%} \times [1 + \exp(0.018 \cdot T_{\max} - 26.4 \cdot c_2)] \qquad \text{(A2)}$$

$$\text{turbine} \quad \Xi = c_1 \cdot \frac{266.3 \cdot m_{\text{gas}}}{0.92 - \eta_{is}} \cdot \ln \beta_t \times [1 + \exp(0.036 \cdot T_{\max} - 54.4 \cdot c_2)] \qquad \text{(A3)}$$

with $c_1 = c_2 = 1$.

The highest temperature of gas turbine cycle ($T_{\max}$) affects the purchase cost of the combustor and the turbine by the temperature factors

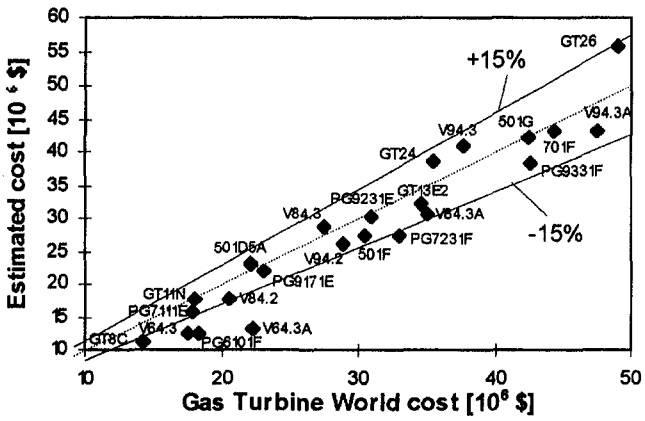

Fig. A1

$$[1 + \exp(0.018 \cdot T_{\max} - 26.4)] \quad \text{for combustor,}$$

$$[1 + \exp(0.036 \cdot T_{\max} - 54.4)] \quad \text{for turbine.}$$

These factors increase tremendously when $T_{\max}$ exceeds the values

$$26.4/0.018 = 1466.7 \text{ K} \quad \text{for combustor,}$$

$$54.4/0.036 = 1511.1 \text{ K} \quad \text{for turbine.}$$

However, these two old temperature limits have to be updated (current gas turbines reach temperatures near 1700 K).

In this work the authors utilized new cost functions for the compressor, combustor, and turbine as similar as possible to the functions employed by Frangopoulos. Therefore two new correction factors (c_1 and c_2) have been inserted into Eqs. (A1), (A2), (A3). Their values have been calculated by utilizing, as reference, the gas turbine costs reported by *Gas Turbine World 1995 Handbook*. The values of c_1 and c_2 that allow the reference costs to be better estimated are

$$c_1 = 1.051, \quad c_2 = 1.207 \qquad \text{(A4)}$$

With these values, the majority of gas turbine estimated costs (i.e., obtained with Eqs. (A1), (A2), (A3), and (A4) show an error less than ±15 percent in comparison to the costs reported by Gas Turbine World (see Fig. A1).

The subdivision of a gas turbine into three components could seem useless since, regarding thermoeconomic studies, it could be easily considered as a single fixed component. However, the authors have preferred to execute a subdivision since it could be useful for the thermoeconomic analysis of advanced complex gas plants (HAT cycle, STIG or ISTIG cycle, CAES systems, etc.).

J. De Ruyck

S. Bram

G. Allard

Dept. of Mechanical Engineering,
Vrije Universiteit Brussel,
Brussels, Belgium

REVAP® Cycle: A New Evaporative Cycle Without Saturation Tower

A new evaporative cycle layout is disclosed that is shown to have a performance similar to the HAT cycle, but where the saturation tower has been eliminated. This new cycle is a result of a combined exergetic and composite curve analysis discussed in a previous paper, assuming one intercooler and no reheat (De Ruyck et al., 1995). The new cycle uses two-phase flow heat exchange in the misty regime, which is a well-known process. Existing aeroderivative gas turbine equipment can be adapted for application of this cycle, which therefore needs a minimum of development.

Introduction

Efficient large-scale power production from natural gas can be achieved from gas turbines where the exhaust heat is recovered, either to make steam for a steam cycle (combined cycles), or to make steam that is expanded in the gas turbine (steam-injected gas turbine, full STIG), or to heat water that is evaporated in the compressor air (evaporative cycle, HAT). In steam-injected and evaporative cycles the steam turbine is eliminated: The steam is mixed with the compressed air, superheated in the combustor, and expanded in the gas turbine. There is no more steam turbine, feedwater heater, condenser, and cooling tower, the steam being condensed in the atmosphere. Evaporation at variable temperatures in dual or triple pressure combined cycles and in evaporative cycles reduces the irreversibilities during heat recovery and leads to the best efficiencies known so far.

Different studies can be found in the literature where the performances of the different cycles are compared (Chiesa et al., 1995; Rao et al., 1991; Frutschi and Plancherel, 1989; Macchi et al., 1995; Rosen, 1993; Mathisson, 1994). In general, the evaporative cycle is considered to have a better efficiency/cost ratio then the combined cycle, although this is still to be demonstrated. According to the same studies, the specific water consumption of an evaporative cycle is comparable to the consumption in an equivalent wet cooling tower (Cook and Rao, 1991; Day and Rao, 1993).

Although the HAT cycle is the best known evaporative cycle, it should be emphasized that alternative cycles are proposed in the literature (El Masri, 1988a, b; Takeya and Yasui, 1988; Nakamura et al., 1983; Drnevich, 1992; Basil, 1991). An evaporative cycle that is closer to realization and known as CHAT is discussed in Nakhamkin et al. (1995). Commercial availability of CHAT on a turnkey basis is announced for 1998.

The present paper discloses a new alternative evaporative cycle where no saturation tower is used. It is called REVAP, which stands for REgenerative EVAPoration cycle. The cycle has performances similar to HAT. The theoretical procedure that has been followed to find the new cycle layout is first summarized. The REVAP cycle is discussed next.

Cycle Development Procedure

In a general approach of gas turbine cycles for arbitrary working fluids, it has been decided to start from a cycle consisting of the following elementary components (Fig. 1, Bram and De Ruyck, 1995):

- compression
- expansion
- heat source
- heat sink
- heat regeneration

A two-step procedure results, where the heat recovery system is first considered as an adiabatic black-box, and where this black-box is next designed making use of composite curves (Linnhoff et al., 1982).

The concept is shown in Fig. 1. One intercooler in the compressor and no reheat during expansion are taken as technically sound options. The major design problem then resides in the heat regeneration, which in the case of mixed gas/steam cycles combines latent and sensible heat recovery (and in the future, chemical recovery). Second law violations inside the black box are watched by computing the exergy destruction inside and by assuming that about 5 percent of the system exergy input is a feasible minimum. At the hot side of the black box a temperature difference of 50°C between hot and cold stream is assumed as viable. In the case of dry cycles (no water injection), the stack temperature is computed from the adiabatic condition in the black box recovery system. In the case of water injection, the stack temperature is imposed and the amount of feedwater is computed from the adiabatic condition. The applied cooling model is discussed in the appendix. After optimization of the pressure ratio and limiting the black box destruction to 5 percent, cycle performances are found that are probably difficult to optimize further for given boundary conditions such as intercooling, turbine inlet temperature, engine efficiencies, and head losses.

Scenarios. Starting from a simple gas turbine cycle, the performance can be improved by:

- adding intercooling
- adding evaporation
- recovering the heat from the intercooler into the cycle

The following best scenarios with intercooling are reported:

- dry cycle with rejection of intercooler heat (I)
- evaporative cycle with rejection of intercooler heat (II)
- evaporative cycle with adiabatic recovery of intercooler heat through water evaporation (III)
- evaporative cycle with dry intercooling where the heat is recovered into the black box recovery system (IV)

The boundary conditions given in Table 1 are used for all four scenarios. For comparison, a dual pressure combined cycle is included as scenario V, where the same major boundary condi-

Contributed by the International Gas Turbine Institute and presented at the 41st International Gas Turbine and Aeroengine Congress and Exhibition, Birmingham, United Kingdom, June 10–13, 1996. Manuscript received at ASME Headquarters February 1996. Paper No. 96-GT-361. Associate Technical Editor: J. N. Shinn.

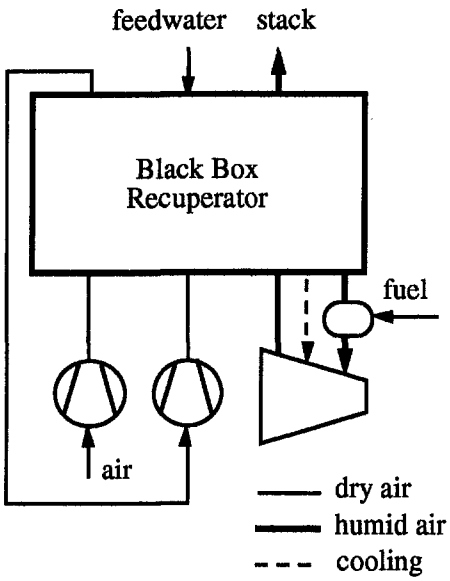

Fig. 1 Concept of an intercooled evaporative cycle

tions are used. Additional parameters for the combined cycle simulation are found in Table 2. According to the followed procedure, the potential of the five scenarios can be compared in a coherent way, even without knowing the exact layout of the cycles.

Scenario Results. Figure 2 summarizes the performances obtained from the concept as shown in Fig. 1 and Tables 1 and 2. Optimum performances fall within the 5 to 40 pressure ratio range. As expected, the dry cycle has the poorest performance with a peak around 44 percent efficiency. Rejecting the heat from the intercooler or recovering it through water evaporation surprisingly yields almost similar results, not exceeding 50 percent, which should discourage any cycle with intercooling through water injection. This nonadvantage of water injection is a result from the increased compressor work. The best performance is found when recovering the intercooler heat as sensible heat into the recovery system, giving a peak around 53 percent.

The specific power reaches 580 kW/kg at the pressure ratio of 35, which triples the base case gas turbine power output. A corresponding water injection of 15 percent of the compressor flow is obtained. When compared with the combined cycle (scenario V), similar thermal efficiencies are obtained in the best case scenario IV, but the specific power is significantly better due to the intercooling and due to the higher expansion temperature of the water vapor. Hence, in addition to the suppression of the steam turbine, a better use of the gas turbine is made in the evaporation cycle. Assuming triple instead of dual pressure in the combined cycle makes its efficiency superior, but at the expense of higher investment costs.

The optimum performance from Fig. 2 corresponds with the target 5 percent minimum exergy destruction in the black box, which should ensure the feasibility. As a test case, the HAT cycle as described in Rao et al. (1991) has been investigated by the same authors (De Ruyck et al., 1995) and was found to correspond with the found optimum.

From this analysis one can conclude that it is not possible to optimize the HAT evaporative cycle further, but also that any heat recovery system that satisfies the boundary conditions of the best case black box recovery system will yield the same optimal result.

Table 2 Combined cycle data

Gas turbine :	
Compressors polytropic efficiency	88%
Turbine polytropic efficiency	87%
Turbine back pressure :	30 mbar
Turbine inlet temperature ISO	1200°C
Dry cycle design cooling flow rate at 15 bar	9%
Combustor pressure drop	4%
Air temperature	15°C
Steam Cycle :	
High pressure	90 bar
Medium pressure	20 bar
Condenser pressure	0.04 bar
Deaerator pressure	1.5 bar
Turbine isentropic efficiencies	89%
Heat recovery system :	
Hot side pressure loss	30 mbar
Economizer pressure loss	0.1 bar
Superheater pressure loss	1 bar
Hot side temperature difference	min 10°C
Steam temperature	max 540°C
Stack temperature :	110°C
Overall mechanical efficiency	99%

Proposed New Evaporative Cycle

By application of composite curve theory, it is in principle possible to fill in the black box recovery system with the theoretical minimum amount of components. An alternative to the HAT has thus been found, which is disclosed in Fig. 3.

In this system, heat is simultaneously recovered from three streams: the intercooling (1), the aftercooling (2), and the economizer (3). The recovered heat is transferred to the air at the aftercooler exit (4). The lack in heat capacity is compensated by injecting liquid water (5), which evaporates as the temperature increases. The liquid volume is less than 0.2 percent of the total volume flow, and according to theory a misty two-

Table 1 Concept cycle data

Gas turbine :	
Compressors polytropic efficiency	88%
Turbine polytropic efficiency	87%
Turbine back pressure :	30 mbar
Turbine inlet temperature ISO	1200°C
Dry cycle design cooling flow rate at 15 bar	9%
Combustor pressure drop	4%
Heat recovery system :	
Cold side pressure loss	3%
Hot side pressure loss	30 mbar
Hot side temperature difference	50°C
Intercooler low temperature	40°C
Intercooler pressure drop	2%
Feed water and air temperature	15°C
Stack temperature :	110°C
Overall mechanical efficiency	99%

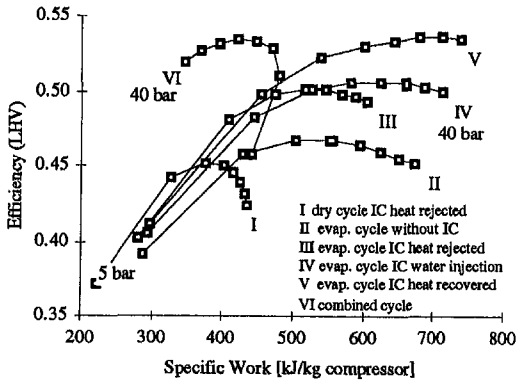

Fig. 2 Performance of the considered scenarios, with black box heat recovery system, pressure ratio varying from 5 to 40, step 5

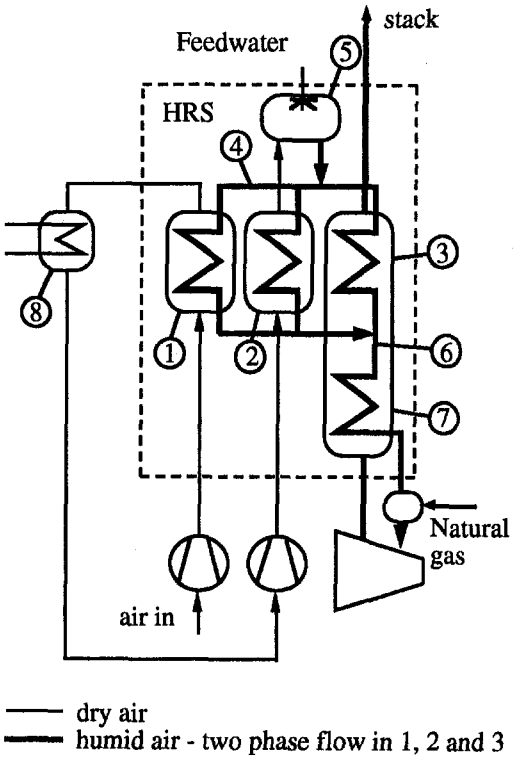

Fig. 3 REVAP® cycle

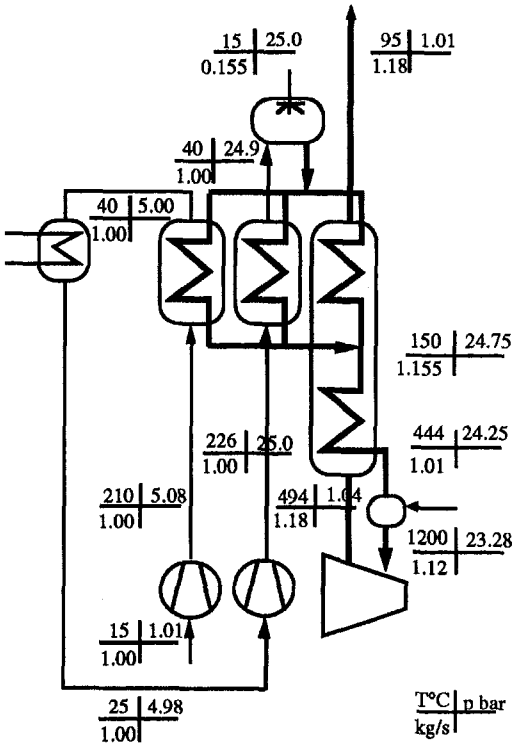

54 % efficiency
545 kJ/kg compressor flow

Fig. 4 REVAP example

phase flow regime is expected in the tubes. At exit of the triple heat recovery all water is evaporated (15 percent of the flow according to the previous analysis) and the air is not saturated (6). The high-temperature exhaust heat is utilized to further heat the moist compressed air prior to combustion (7). The feedwater can be preheated on top of the recovery system, in particular at intercooler and aftercooler exit (8). Very low temperatures are desirable and achievable at these exits, since the fluid is dry air.

As an example, the energy balance of the cycle as shown on Fig. 4 has been computed. The net resulting efficiency is 54 percent, where 1 percent has been gained with respect to the concept cycle through the addition of small heat sinks at intercooler and aftercooler exits and by reducing the stack temperature to 20°C above the dew point.

The corresponding composite heat recovery curves are shown in Fig. 5. The curves are not very different from the composite curves obtained from the HAT cycle as shown on Fig. 6 taken from De Ruyck et al. (1995). 10°C difference is found at the pinch point, which looks more like a pinch "area" located on top of the three heat recovery units. In this area a good evaporation is thus required, saturating the air and leading to a maximum heat capacity of the mixed air-water flow. This maximum capacity is the limiting factor in the heat recovery system leading to the lower limit in stack temperature. The apparent capacity is given by

apparent capacity

$$= \text{air capacity} + \text{evaporation heat} \times \text{evaporation rate}$$

This capacity is given in Fig. 7. According to this figure, the stream heat capacity is tripled at about 100°C, which is the requirement to absorb all the recovered heat. Lower temperatures can, however, be obtained since the air at inlet of the evaporators is dry and an extra temperature drop of about 30° is attainable. The cold curve curvature in the pinch area in Fig. 5 corresponds to the increasing heat capacity shown in Fig. 6. It is to be observed that the loop aftercooler + evaporator acts as a generator of low temperatures, in a way similar to some cooling cycles. Better matching of the hot and cold curves with evaporation is probably difficult to achieve.

Preliminary Design and Cost Figures

For demonstration purposes a 40 MWe REVAP plant design is being considered assuming a 20 MWe simple cycle gas turbine with intercooling and regeneration, which is now available. The sizing shown in Fig. 8 is based on the data shown in Table 3.

In order not to modify the toroidal water intercoolers that are considered on such engines, it is proposed to use the intercooler water as heat carrier to a separate air heater, as indicated on

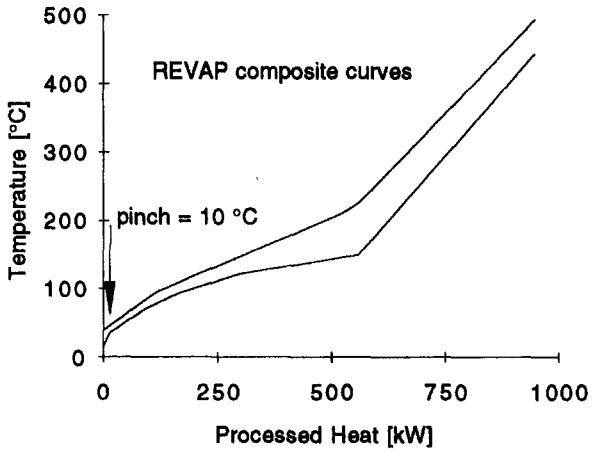

Fig. 5 REVAP composite curves

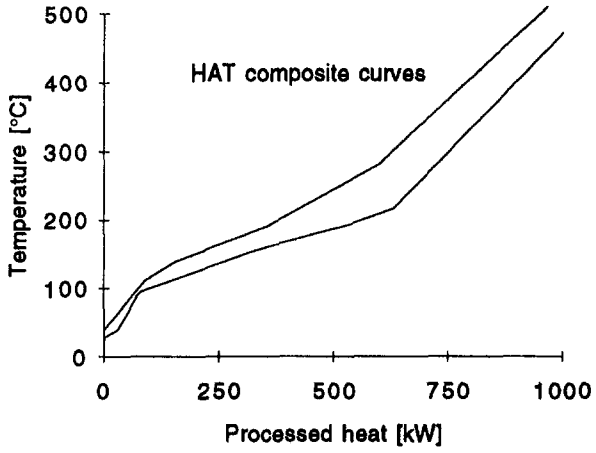

Fig. 6 HAT composite curves for similar boundary conditions, data obtained from Day and Rao, (1993)

Fig. 8. The intercooler heat sink can be included in this closed water circuit.

To control the pinch area (Fig. 5) it is necessary to tune finely the heat capacities at cold side of the three parallel exchangers (items 1, 2, and 3 on Fig. 3), which can be done by adjusting the water flow through three separate atomizers on top of the three components. The misty flow regime ensures good evaporation and air conditions close to saturation. Erosion problems may, however, be expected from droplet impacts in the tube bends, which is to be further investigated. A possible solution to this problem is the use of helicoidal heat exchanger tubes.

In the REVAP cycle gas/gas heat exchangers are used rather than a saturation tower in combination with water/gas exchangers. At first sight one might therefore expect much more heat exchange surface, but this is not the case. All evaporative cycles need to heat the compressor air from the low aftercooler exit temperature to the combustor inlet temperature, requiring gas-side heat exchange surface. In the REVAP cycle, exchange between the hot and cold gases occurs in fact more directly than in the HAT, where water is used as an intermediate heat carrier calling for extra surface and pumping. A limited gain in the HAT is the gas temperature increase due to direct contact heat exchange in the saturator, which for the reminder is mainly a latent heat exchanger. This direct contact latent heat exchange occurs in the REVAP cycle as well, but in a nonadiabatic way. A heat exchange surface reduction is finally found in the REVAP through the higher heat transfer coefficients, which can be expected in the misty two-phase flows. An increase of 20 percent

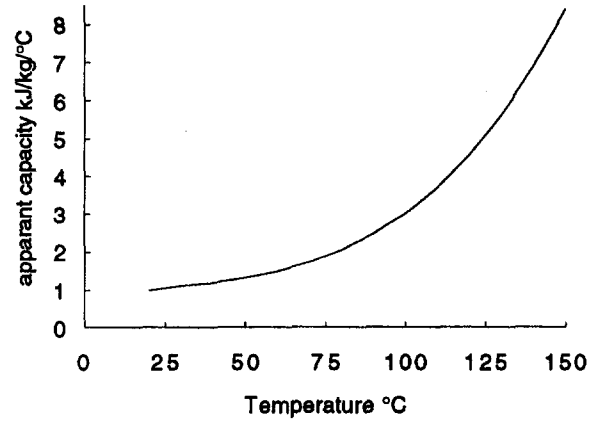

Fig. 7 Apparent heat capacity during evaporation at 25 bar

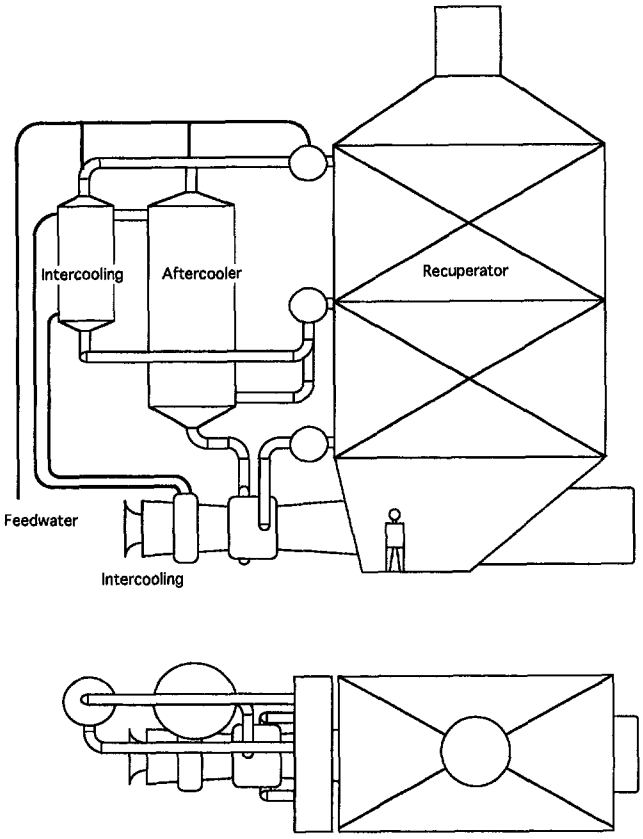

Fig. 8 40 MW/20 bar REVAP sizing, with exclusion of the water treatment plant

has been assumed tentatively, but according to literature this might be more. Tests to find out about correct heat transfer coefficients and potential erosion problems will be carried out before making final designs.

Based on these assumptions, a first specific cost estimation is made in Table 3 for the drawn 40 WMe demonstration plant. At comparable scale the considered costs would be about 25 percent less when compared with a dual pressure combined cycle, leading to a reduction of about 0.6 ct/kWh (20 years, 8 percent rate). This gain is reduced by about 0.2 ct/kWh variable cost due to the treatment of water.

Conclusions, Future Work

A new evaporative cycle is disclosed, which has performances similar to other evaporative cycles such as HAT or CHAT. When compared with a combined cycle, following in-

Table 3 Cost estimation for a 40 MWe REVAP cycle

Item	Cost USD/gross kWe	Comment/source
Turbomachinery	218.6	Turbine World Handbook[1]
Economizer	41.4	330 m2/kg/s Aisi 316
Gas/gas regenerator	36.7	292 m2/kg/s Aisi 316
Intercooler	48.0	385 m2/kg/s Aisi 316
Aftercooler	40.5	322 m2/kg/s Aisi 316
Flashing/sinks	15.1	
Water treatment	20.0	
Piping	10.0	
Capital Investment	430	USD/gross kWe
Contingency 20%	86	USD/net kWe
Total	**516**	**USD/net kWe**

[1]Base cost x 1.1 (for adaptations) x 0.7 (for increased specific power)

centives for the evaporation in general and REVAP in particular can be mentioned:

- Relatively small units with short construction time
- Very few components (less than HAT and CHAT)
- Relatively simple control is expected, automation should be possible
- The unit is expected to be low cost and low risk
- Broad range in applications going from pipeline pumping over distributed power stations to load following power plants consisting of two to four 100 MWe modules, based on the largest available aeroderivative engines.

If the availability of water is not a problem no disadvantages with respect to the combined cycle are to be reported so far.

The predesign of a 40 MWe demonstration plant is being considered based on available engines, which are intercooled and have a regenerator. Part-load and variable inlet conditions will be assessed after selection of a suitable aeroderivative engine, provided engine data can be obtained.

Acknowledgments

The present work is done with support from the Commission of European Communities, contract No. JOU2-92-0128

References

Basil, O. M., 1991, European patent No. 0 444 913 A1

Bram, S., and De Ruyck, J., 1995, "Exergy Analysis Tools for Aspen Applied to Evaporative Cycle Design," ECOS 96.

Chiesa, P., Lozza, G., Macchi, E., and Consonni, S., 1995, "An Assessment of the Thermodynamic Performance of Mixed Gas–Steam Cycles: Part B: Water-Injected and HAT Cycles," ASME JOURNAL OF ENGINEERING FOR GAS TURBINES AND POWER, Vol. 117, pp. 499–508.

Cook, T. C., and Rao, A. D., 1991, "HAT Cycle Simplifies Coal Gasification Power," *Modern Power Systems*, May, p. 19.

Day, W. H., and Rao, A. D., 1993, "FT4000 HAT With Natural Gas Fuel," *Turbomachinery Int.*, Jan.–Feb. pp. 22–29.

De Ruyck, J., Bram, S., and Allard, G., 1995, "Humid Air Cycle Development Based on Exergy Analysis and Composite Curve Theory," ASME Paper No. 95-CTP-039.

Drnevick, R. F., 1992, European patent No. 0 546 501 A2.

El Masri, M. A., 1988a, "A Flexible, Efficiency Gas-Turbine Cogeneration Cycle With Novel Dual-Mode Heat Recovery System," *ASME COGEN II Proc.*

El Masri, M. A., 1988b, "A Modified, High-Efficiency, Recuperated Gas Turbine Cycle," ASME JOURNAL OF ENGINEERING FOR GAS TURBINES AND POWER, Vol. 110, pp. 233–242.

Frutschi, H. U., and Plancherel, A., 1989, "Comparison of Combined Cycles With Steam Injection and Evaporation Cycles," *ASME COGEN II Proc.*

Linnhoff, B., Townsend, D. W., Boland, D., Hewitt, G. F., Thomas, B. E. A., Guy, A. R., and Marsland, R. H., 1982, *A User Guide on Process Integration for the Efficient Use of Energy*, The institute of chemical engineers, Rugby, Warks, England, ISBN 0 85295 156 6.

Macchi, E., Consonni, S., Lozza, G., and Chiesa, P., 1995, "An Assessment of the Thermodynamic Performance of Mixed Gas–Steam Cycles: Part A: Intercooled and Steam-Injected Cycles," ASME JOURNAL OF ENGINEERING FOR GAS TURBINES AND POWER, Vol. 117, pp. 489–498.

Mathisson, J. H., 1994, "Combined Gas and Steam Cycles—a Thermodynamic Analysis at Full Load and Part Load," rapport ISRN LUTMDN/TMVK-7015-SE, Dept. of Heat and Power Engineering, Lund Institute of Technology, Lund, Sweden.

Nakamura, H., Takahashi, T., Yamamoto, K., Sayama, N., and Nazaraki, N., 1983, European patent No. 0 081 995 A2.

Nakhamkin, M., Wilson, J. M., and Polsky, M., 1995, "The Cascaded Humidified Advanced Turbine," ASME Paper No. 95-CTP-5.

Nguyen, H. B., and den Otter, A., 1994, "Development of Gas Turbine Steam Injection Water Recovery (SIWR) System," ASME JOURNAL OF ENGINEERING FOR GAS TURBINES AND POWER, Vol. 116, pp. 68–74.

Rao, A. D., Francuz, V. J., Shen, J. C., and West, E. W., 1991, "A Comparison of Humid Air Turbine (HAT) Cycle and Combined-Cycle Power Plants," EPRI IE-7300, Project 2999-7, Final Report.

Rosén, P. M., 1993, "Evaporative Gas Turbine Cycles—a Thermodynamic Evaluation of Their Potential," Dept. of Heat and Power Engineering, Lund Institute of Technology, Lund, Sweden, March, ISRN LUTMDN/TMVK-7010-SE.

Takeya, K., Yasui, H., 1988, "Performance of the Integrated Gas and Steam Cycle (IGSC) for Reheat Gas Turbines," ASME JOURNAL OF ENGINEERING FOR GAS TURBINES AND POWER, Vol. 110, pp. 220–232.

APPENDIX

Cooling Model

Since 1200°C will be assumed at gas turbine inlet, blade cooling is to be considered. A simple model is used that consists in injecting the coolant flow at an intermediate point in the expansion. The temperature of the intermediate point in the expansion is set to 1000°C, assuming a maximum material temperature of 860°C.

$$\tilde{T} = \frac{(T_{in} + T_{\text{blade}})}{2} = \frac{(1200°\text{C} + 860°\text{C})}{2} \cong 1000°\text{C}$$

The heat balance is expressed through

$$\dot{m}_{\text{cool}} c_{p,\text{cool}} (T_{\text{blade}} - T_{\text{cool}}) = h \frac{K\dot{m}_{in}}{\tilde{p}\sqrt{\tilde{\gamma} R\tilde{T}}} (\tilde{T} - T_{\text{blade}})$$

This model assumes strong film cooling (h) by imposing the material temperature as ultimate temperature of the coolant flow. The cooling surface (second term in the right-hand side) is taken proportional (K) to the engine cross section, which itself is proportional to the volume flow divided by the nearly sonic speed. Kh can be assumed constant through construction and is calibrated to yield 9 percent cooling flow at 15 bar in dry turbine operation. The cooling flow is thus mainly affected by the changes in gas velocity and by the blending temperature. In dry cycles this temperature is the compressor discharge temperature. In mixed cycles this temperature can be lowered through compressor aftercooling, which decreases the required cooling flow by several points.

Efficient District Heat Production by Heat Extraction From Combined Cycle Plants

H. Haselbacher
Technical University of Vienna,
Vienna, Austria

H. U. Frutschi
Asea Brown Boveri,
Baden, Switzerland

Among cogeneration facilities, block heating stations and large combined cycle plants are two extreme examples of district heating technologies. In this paper, these two alternatives will be applied to one and the same representative district heating task. The thermodynamic differences will be made clear and the advantages of heating by extracting steam from a combined cycle plant will become evident. An important conclusion from an engineering point of view is that extracting heat from a combined cycle plant should be considered even if this plant is located at greater distances from the heat consumers.

1 Introduction

By combining the generation of electricity and useful heat, both together can be produced from fossil fuels at rather high fuel utilization rates of about 85 to 90 percent. Such systems are commonly and quite appropriately called cogeneration plants.

As an example, they can consist of gas engines with waste heat utilization. Plants comprising several such units with an electric capacity of a few megawatts each are considered for supplying space heating to city quarters or large housing developments. For this purpose, they are built in close vicinity to the consumers, and the "waste" heat is actually their main product. These plants are known as block heating stations.

Another possibility of practicing cogeneration is to extract heat from large thermal power stations, which are designed first and foremost for electricity production with an output of several hundred megawatts. The amount of heat extracted would usually be a relatively small portion of the maximum possible. If these plants are located at greater distances from the consumers (10 to 20 miles are practicable; see, for example, Piller, 1988), main transmission pipelines need to be installed to transport the heat over these distances. The hot water temperature normally needs to be higher than in the block heating station cases in order to operate the system at a higher energy density.

Evidently, these are two extreme possibilities for cogeneration of electricity and district heat. It is, therefore, of considerable interest to investigate which one of these two methods is more advantageous thermodynamically (i.e., with respect to fuel consumption) to perform a certain heating duty.

The following analysis will be done for a district heating system with a peak demand of 30 MW at −15°C ambient temperature. Other system parameters will be presented in Section 3. As a condition common to both types of power plant, it is stipulated that they are representative of their respective states of technology. This means that the large thermal power station is a modern combined cycle plant. In terms of electricity generation, the two types of plant need to be compared on the basis of the thermal efficiency referred to a common voltage level, which obviously is that of the medium voltage grid. Accordingly, it is assumed that the thermal efficiency of the gas engine block heating station is 32 percent while that of the combined cycle plant is 49 percent, equivalent to 54 percent (50 to 58 percent) at generator terminals (Frutschi, 1990; *Gas Turbine World,* 1993).

Contributed by the International Gas Turbine Institute and presented at the 41st International Gas Turbine and Aeroengine Congress and Exhibition, Birmingham, United Kingdom, June 10–13, 1996. Manuscript received at ASME Headquarters February 1996. Paper No. 96-GT-538. Associate Technical Editor: J. N. Shinn.

It should be mentioned here that between these two extreme plant configurations of gas engines and combined cycle stations, there is a whole spectrum of other power plant concepts (Stachel et al., 1995). They comprise Diesel engines and gas turbines (aeroderivatives) of up to 40 percent thermal efficiency at generator terminals, large steam power plants in excess of 40 percent thermal efficiency at generator terminals, as well as large two-stroke Diesel engines with supercharging, waste heat boilers, and steam turbines, the latter of which would be the counterparts of the gas turbine combined cycle plants.

The comparison of the two extreme cases to be presented here will be indicative of the range of results that may be expected. It is obvious that in every instance an optimization would need to be performed, the level of which would depend on the project stage.

2 Plant Schematic Diagrams and General Performance Considerations

2.1 Block Heating Station With Gas Engines. A simplified plant schematic diagram of a block heating station with a gas engine driving a generator is shown in Fig. 1. The waste heat of the gas engine cooling water is used in a heat exchanger CWHE, which is the first stage of raising the hot water temperature of the district heating network. The water is heated further by the exhaust gas in a second heat exchanger EHE.

The maximum heat output of the gas engine does not correspond to the maximum demand of the district heating system but covers only about two thirds of it. The peak energy demand, which is merely a small fraction of the total, is met by a peaking boiler. In this manner investments are avoided that would be used during brief periods of time only.

During low heat demand, the hot water will be prepared by intermittent operation of the gas engine. This allows full capacity operation of the gas engine at maximum efficiency, but, on the other hand, requires the installation of storage tanks not shown in Fig. 1. There is also the possibility of installing several gas engines, preferably of different capacities, running singly or in parallel.

Accordingly, the following analysis will be based on two gas engines always operating when needed at full capacity. The effect of ambient temperature variation will be taken care of by using corresponding mean values of output and efficiency.

2.2 Combined Cycle Plant. Figure 2 exhibits a simplified plant schematic diagram of a combined cycle power station. A gas turbine GT, a steam turbine ST, and a generator G form a single unit. The gas turbine exhaust gas gives off its heat in

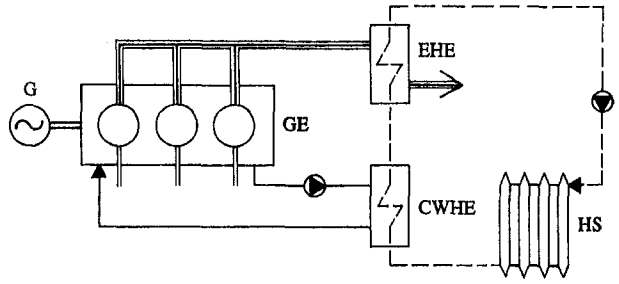

Fig. 1 Plant schematic diagram of block heating station with gas engine

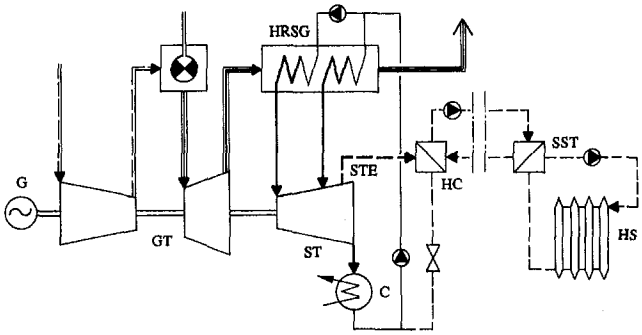

GT	gas turbine		
G	generator	STE	steam extraction
HRSG	heat recovery steam generator	HC	heating condenser
ST	steam turbine	SST	substation
C	condenser	HS	heating system

Fig. 2 Plant schematic diagram of combined cycle

a two or three pressure heat recovery steam generator HRSG. Steam raised there is used to drive the steam turbine where approximately 50 percent of the gas turbine output is produced without consuming any supplemental fuel (unfired steam generator).

There is also the possibility of reheating the steam, which further raises the thermal efficiency of combined cycle plants. By optimizing the gas and steam turbine cycles, thermal efficiencies of almost 60 percent are within reach (see also Stachel et al., 1995).

For maximum electricity production, the combined cycle plant is operated in condensing mode. The condenser C could be cooled by a wet cooling tower, which will be the basis of the analysis presented below.

Two-stage steam extraction is usually employed for the purpose of district heating. This will be assumed here as well. The latent heat of the steam is transferred in a heating condenser HC to the heating water, which is circulated to a district heating system HS. Extracting steam reduces the output of the low pressure section of the steam turbine, but it does not affect its high and medium pressure sections, and, evidently, the gas turbine is not affected either.

An important point is the fact that the electric output potential of a combined cycle plant increases significantly as the ambient

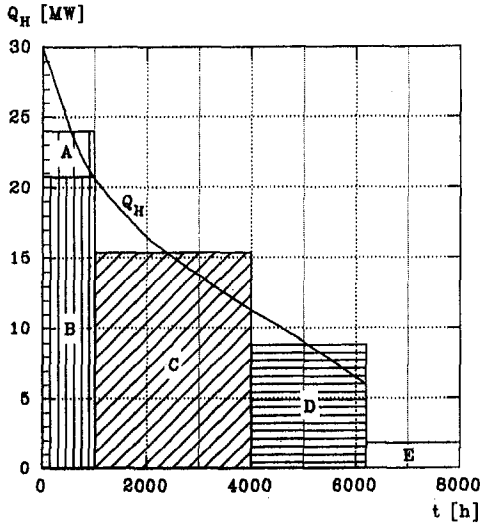

Fig. 3 Heat load duration curve

temperature drops. Actually, this effect is much stronger than the output reduction due to the extraction of steam required for heating. As will be shown later, it is therefore possible to produce correspondingly much more electricity at high efficiency by cogeneration in the combined cycle plant than by a gas engine. The thermal efficiency of the combined cycle is practically unaffected by the ambient temperature, and it will be considered to be constant in the following analysis.

Another significant point is the fact that the steam extraction can be adjusted at any time to the demand so that monovalent, i.e., thermodynamically optimal, cogeneration is possible, not requiring a peaking boiler or other supplemental investments. Also, domestic hot water supply during the summer, which will not be considered in this analysis, would be possible without negative consequences.

3 Specification of District Heating System and Power Plants

Figure 3 shows the district heat duration curve used in this study. The maximum heat demand is assumed to be

$$\dot{Q}_{H\max} = 30 \text{ MW at } -15°\text{C}$$

at block heating station terminals. The heating limit is 6 MW at 15°C. The resulting area is divided into five elements, A to E. Element E, corresponding to the domestic hot water demand outside of the heating period, is neglected here (see above). Element A, on top of element B, represents the heating demand above the two thirds limit mentioned earlier. It is assumed to be covered by a peaking boiler in case of the block heating station. In case of heat extraction from the combined cycle plant, monovalent operation is easily provided because, as explained earlier, this amount of heat can be supplied without difficulty. The network needs to be designed for this requirement, which

Nomenclature

E = electric energy
P = electric power
Q = heat or fuel energy
$\dot{Q}$ = output, load
t = time
Δ = difference
ϵ = coefficient of performance
η = thermal efficiency
ϑ = heat-to-power ratio
ν = fuel utilization rate

Subscripts

a = ambient
cc = combined cycle
F = fuel
f = flow
GE = gas engine
H = heat
max = maximum
r = return
0 = at cc plant site

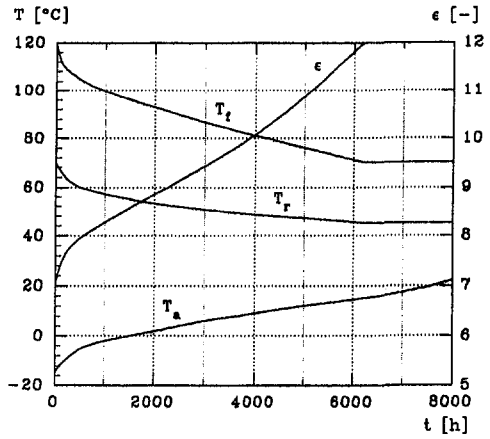

Fig. 4 Duration curves of temperatures and coefficient of performance

is, however, greatly relieved by operating the system with sliding water temperatures.

The main data of the gas engine to serve these requirements are as follows:

Total electrical output	$P_E = 12.09$ MW
Total heat output	$\dot{Q}_H = 20.4$ MW
Thermal efficiency	$\eta = 32$ percent
Fuel utilization rate	$\nu = 86$ percent

The combined cycle plant is rated at 300 MW and its thermal efficiency at generator terminals is 54 percent as indicated already in the Introduction. The analysis is performed with these values, independent of ambient temperature.

Figure 4 is a graph presenting the duration curves of the ambient temperature and the flow and return temperatures as well as the coefficient of performance for heat extraction from the combined cycle plant.[1]

These parameters are relevant only for this type of plant, while for the gas engine, a sensitive parameter could possibly be the return temperature because of the maximum allowable cooling water temperature of the engine. However, this influence may be neglected here because the local network operates in any case at a much lower temperature than that required for a long distance pipeline.

4 Power Plant Operating Data

Table 1 summarizes the operating data for the case of the block heating station. For each of the elements A to D the heating energy Q_H, the electricity produced E, the fuel utilization rate ν, and the fuel energy input Q_F are presented. To cover element A, a peaking boiler of 10 MW capacity and 90 percent efficiency is assumed.

When the electricity produced is viewed as having been generated with a thermal efficiency of 49 percent, which corresponds to the state of technology referred to the medium voltage grid, and the corresponding fuel credit is taken into account, then the fuel energy input for producing 100 percent heating energy is 66.2 percent. This is obtained from

$$\left.\frac{\Delta Q_F}{Q_H}\right|_{GE} = \frac{161.648 - \dfrac{50.447}{0.49}}{88.730} = 0.662.$$

Table 2 contains the main data for operation of the combined cycle plant.

[1] The coefficient of performance is defined as the ratio of usable heat and electricity lost by extraction.

Table 1 Main performance data of block heating station

	Q_H	E	ν	Q_F
	GWh	GWh	-	GWh
A	3.600	-	0.90	4.000
B	20.400	12.089	0.86	37.778
C	45.810	27.146	0.86	84.833
D	18.920	11.212	0.86	35.037
Σ	88.730	50.447	-	161.648

A: boiler, B to D: waste heat

The total quantity of heat to be extracted is $Q_{HO} = 98.589$ GWh, which results in a mean heating duty of 15.90 MW at site based on a total operating time of 6200 h. The weighted mean ambient temperature is 2.84°C, and the corresponding heating water temperatures are 91°C and 54°C. The coefficient of performance amounts to $\epsilon = 9.15$, which is 2.5 to 3 times higher than in the case of heat pumps. This would correspond to a deficit in electricity output of $\Delta P = 1.738$ MW; i.e., in order to maintain 300 MW at the generator terminals, the internal power of the combined cycle plant has to be increased corresponding to an output at generator terminals of 301.74 MW. Since the thermal efficiency of the combined cycle is 54 percent, the total amount of the additional fuel energy to produce the required heating energy of 88.730 GWh is $\Delta Q_F = 19.955$ GWh. Of some interest is the ratio

$$\left.\frac{\Delta Q_F}{Q_H}\right|_{cc} = \frac{19.955}{88.730} = 0.225,$$

i.e., for the case of extracting heat from the combined cycle plant, 100 percent heating energy requires only 22.5 percent fuel energy. Table 2 contains the corresponding numbers also for the individual elements A to D and for the maximum heat demand of 30 MW.

5 Performance Comparison

Table 3 compares the most important performance parameters of the two cogeneration systems and a boiler. For this purpose,

Table 2 Main performance data of combined cycle plant

		A to D	Max.	A + B	C	D
a) at plant site						
Q_{HO}	GWh	98.589	-	26.667	50.900	21.022
t	1000 h	6.20	-	1.00	3.00	2.20
$\dot{Q}_{HO}$	MW	15.90	33.33	26.67	16.97	9.56
T_a	°C	2.84	-15	-5	3	12
T_f	°C	91	120	104	90	75
T_r	°C	54	70	59	53	46
ε	-	9.15	7.0	8.0	9.2	11.0
P	MW	301.74	304.76	303.33	301.85	300.87
ΔP	MW	1.738	4.762	3.33	1.845	0.87
ΔQ_F	GWh	19.955	-	6.172	10.244	3.539
$\Delta Q_F/Q_{HO}$	-	0.202	0.265	0.231	0.201	0.168
b) after subtracting 10 % transmission losses						
Q_H	GWh	88.730	-	24.000	45.810	18.920
$\Delta Q_F/Q_H$	-	0.225	0.294	0.257	0.224	0.187

Table 3 Performance comparison of boiler, block heating station and back-pressure part of combined cycle plant

		Boiler	BHSt.	Comb. C. Backpr. P.
E	GWh	-	50.447	111.800
Q_H	GWh	88.730	88.730	88.730
ϵ	-	-	-	7.00
ν	-	0.90	0.86	0.87
ϑ	-	-	0.57	1.26
η	-	-	0.32	0.48

the combined cycle plant is thought of as having been split into two units. The first and larger one operates in condensing mode and produces electricity at the maximum possible thermal efficiency of 54 percent at generator terminals. It does not participate in the production of heating energy. The second unit, and in this case much smaller one, operates in back-pressure mode and supplies the required heating energy. Both units together produce 300 MW at generator terminals. The small combined heat and power production part can at any time be adjusted in an optimal manner to the heating demand.

This view of plant performance explains that for the same heating duty the combined cycle cogeneration plant produces more than twice as much electricity compared to the block heating station with gas engines.

Figure 5 depicts the fuel energies required by the various systems for delivering 100 percent heating energy. For the combined cycle plant, the corresponding values are also presented for the elements A to D and the peak demand.

It is noticed that the combined cycle plant needs nearly two thirds less fuel compared to the block heating station for producing the same amount of district heat, provided that the cogenerated electricity is evaluated corresponding to the state of technology.

6 Flexibility of the Combined Cycle Plant

Figure 6 displays the energy balances of a combined cycle plant without and with heat extraction up to back-pressure operation.

It is seen how the fictitious splitting-off of a combined heat and power plant with pure back-pressure operation functions. It can be done continuously depending on the heating energy demand.

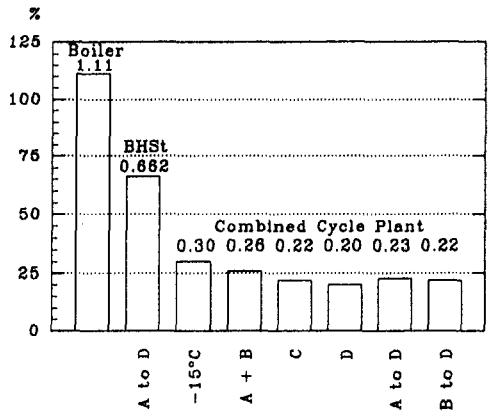

Fig. 5 Fuel energy input in percent of heating energy

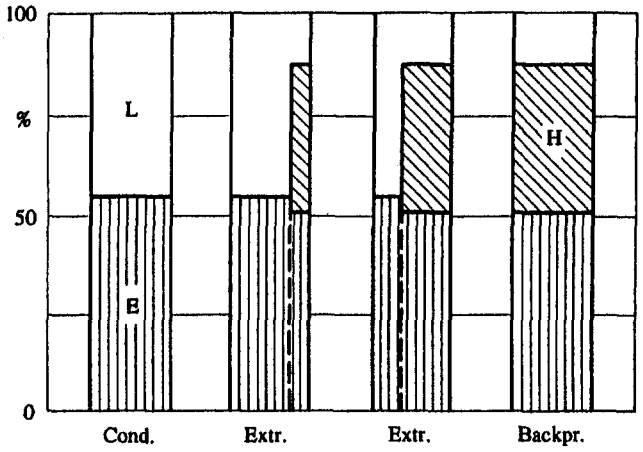

Fig. 6 Electricity and heat production by steam extraction in the combined cycle plant

Figure 7, finally, shows how the reduction of the electric output due to steam extraction is balanced due to the strong dependence of the electric output potential on ambient temperature. This characteristic is a consequence of the increase in compressor mass flow as the ambient temperature drops. It is a feature of the gas turbine that strongly affects the combined cycle plant. It is observed that heat extraction of 30 MW, as assumed in this paper, requires that the output of the cycle be raised by only a few megawatts.

The great power reserve of the plant, e.g., of 38 MW at an ambient temperature of −15°C, permits the additional production of very valuable "winter" electric energy at high thermal efficiencies.

7 Conclusions

The extraction of district heat from a modern combined cycle plan at constant electricity production and thermal efficiency consumes two to three times less fuel than a block heating station with gas engines.

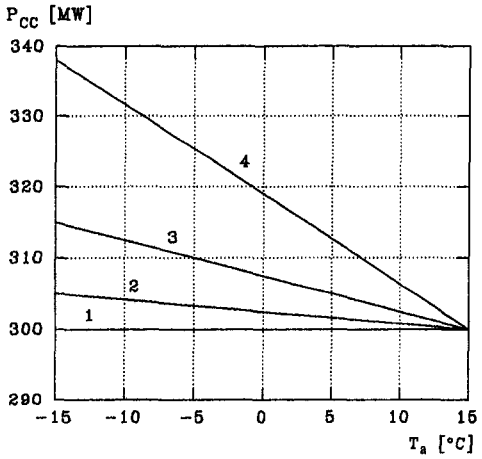

1 Nominal electric power of the combined cycle plant (ISO)

2 Cycle power output at 30 MW heat extraction and 300 MW at generator terminals

3 Cycle power output at 100 MW heat extraction and 300 MW at generator terminals

4 Maximum electric power of the combined cycle plant

Fig. 7 Electric energy generation potential of the combined cycle plant

Referred to the same fuel utilization factor and the same amount of heat energy, a modern combined cycle plant produces about twice as much electricity at the high thermal efficiency of cogeneration as gas engines.

When operating in extraction mode, the fictitiously split-off back-pressure combined heat and power plant benefits from a number of advantages of the large combined cycle plant. Two very important ones are that it profits from the high efficiency of the large power plant and that its heat output can be adjusted continuously to the demand.

Before deciding to build a block heating system, possibilities of heat extraction from an existing thermal power plant should be considered.

An economic comparison supplementing the technical data presented here has in the meantime been published in a separate paper (Rohrer, 1996).

References

Frutschi, H. U., 1995, "Gas Turbines With Sequential Combustion for Cogeneration of Heat and Power," *ABB Review,* No. 3, Baden, Switzerland, pp. 4–9.

Gas Turbine World, 1993, "The 1993–1994 Handbook," Vol. 15, Fairfield.

Piller, W., 1988, "Wärmeversorgung aus der Kraft-Wärme-Kopplung Leiningerwerk Block 5 der Isar-Amperwerke AG," *Fernwärme International—FWI,* No. 3, Frankfurt/Main, FRG, pp. 154–158.

Rohrer, A., 1996, "Comparison of Combined Heat and Power Generation," *ABB Review,* No. 3, Baden, Switzerland, pp. 24–32.

Stachel, K., Frutschi, H. U., and Haselbacher, H., 1995, "Thermodynamic Heating With Various Types of Cogeneration Plants and Heat Pumps," ASME JOURNAL OF ENGINEERING FOR GAS TURBINES AND POWER, Vol. 117, pp. 251–258.

K. Ito
Professor.
Mem. ASME

R. Yokoyama
Associate Professor.
Mem. ASME

Department of Energy Systems Engineering,
Osaka Prefecture University,
1-1, Gakuen-cho, Sakai, Osaka, 593 Japan

M. Shimoda
Senior Researcher,
Hitachi Research Laboratory,
Hitachi, Ltd.,
832-2, Horiguchi,
Hitachinaka, Ibaraki, 312 Japan

Optimal Planning of a Super Waste Incineration Cogeneration Plant

This paper is concerned with the evaluation of economic and energy-saving characteristics of a super waste incineration cogeneration plant, which is equipped with gas turbines as topping cycle to overcome the drawback of low power generating efficiency of conventional waste incineration cogeneration plants only with steam turbines. Economic and energy-saving characteristics are evaluated using an optimal planning method, which determines capacities and operational strategies of constituent equipment from their many alternatives so as to minimize the annual total cost. Through a case study, advantages of a super waste incineration cogeneration plant are shown in comparison with a conventional one. A parametric study is also carried out with respect to the amounts of waste collected and energy distributed.

Introduction

Concerned with global energy and environmental problems, waste management is nowadays one of the important issues to be grappled with. Waste incineration has been used as one of the main ways to manage waste in Japan. With an increase in the amount of waste generated from cities, waste incineration plants have been installed increasingly by local governments. Furthermore, some of the waste incineration plants have been equipped with steam turbine generators to utilize exhaust heat generated from waste incinerators and to generate electricity. However, these waste incineration power generation plants have a great drawback of a low power-generating efficiency of 10 to 15 percent or 20 percent at most. This value is due to relatively low temperature and steam pressure limited to prevent high-temperature corrosion caused by hydrogen chloride in combustion gas generated by burning waste.

To overcome this drawback of the conventional waste incineration power generation plants, a repowering plant has been proposed (Terasawa and Ogura, 1993). Equipped with gas turbines as topping cycle, this plant will utilize exhaust heat from gas turbines to superheat the steam generated by waste incinerators and to supply it to steam turbines. This will increase the power-generating efficiency and power output of steam turbine generators. This novel plant is called "super waste incineration power generation plant," and several plants are now under construction in Japan.

In addition to improvement of power-generating efficiency and augmentation of power output by repowering, cascaded utilization of exhaust heat after use by steam turbines is important from the viewpoint of energy efficient utilization. However, only a part of steam after use by steam turbines is utilized for thermal energy supply in most of the waste incineration power generation plants installed currently. In planning a new waste incineration plant, we should also conceive positive utilization of exhaust heat and extend a super waste incineration power generation plant into a cogeneration facility. Therefore, it is an important issue to evaluate the feasibility of a super waste incineration cogeneration plant from the viewpoints of economic and energy saving characteristics.

Contributed by the International Gas Turbine Institute and presented at the 41st International Gas Turbine and Aeroengine Congress and Exhibition, Birmingham, United Kingdom, June 10–13, 1996. Manuscript received at ASME Headquarters February 1996. Paper No. 96-GT-384. Associate Technical Editor: J. N. Shinn.

The objective of this paper is to evaluate economic and energy-saving characteristics of a super waste incineration cogeneration plant in comparison with those of a conventional one. An optimal planning method will be used to determine capacities and operational strategies of constituent equipment from their many alternatives and to evaluate the characteristics given above. A fundamental numerical study will be carried out by fixing the amounts of waste collected and energy distributed to investigate differences between the two plants in detail. A parametric study will also be carried out with respect to the amounts of waste collected and energy distributed to investigate how they affect the above characteristics.

Mathematical Model of Waste Incineration Cogeneration Plant

Waste Collection. We adopt a simplified model to estimate the amount of waste collected and incinerated. It is assumed that waste is collected from a circular area with a center at which a waste incineration cogeneration plant is located and with a radius of r_w. It is also assumed that the amount of waste generated is distributed uniformly within the area and remains constant throughout a year, and the amount of waste generated per day and per square meters is designated by R_w. It is further assumed that the amount of waste collected and incinerated per day is equal to that generated per day. On these assumptions, the daily total amount of waste generated, collected, and incinerated R_{day} is calculated by $R_{\text{day}} = \pi r_w^2 R_w$. If we add the assumption that waste is incinerated uniformly throughout each day of the year, the hourly amount of waste incinerated R is calculated by $R = R_{\text{day}}/24$.

Energy Distribution. A simplified model similar to that for waste collection is used to estimate the amounts of electrical and thermal energy distributed. It is assumed that a waste incineration cogeneration plant supplies electricity and cold/hot water to a circular area with a center at which the plant is located and with a radius of r_e. It is also assumed that electricity and cold/hot water demands are distributed uniformly within the area, and the amounts of electricity and cold/hot water demands per hour and per district are designated by E_e, Q_e^c, and Q_e^h, respectively. On these assumptions, the hourly total amounts of electricity and cold/hot water demands, E_d, Q_d^c, and Q_d^h, are calculated by $E_d = \pi r_e^2 D_e E_e$, $Q_d^c = \pi r_e^2 D_e Q_e^c$, and $Q_d^h = \pi r_e^2 D_e Q_e^h$, respectively, where D_e is the number of districts per

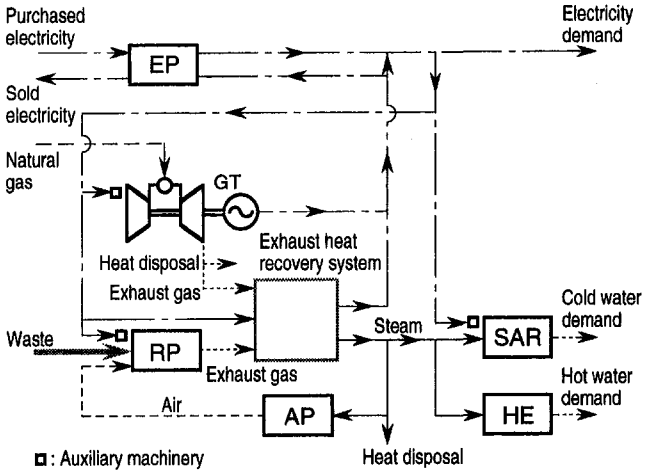

Fig. 1 Overall configuration of waste incineration cogeneration plant

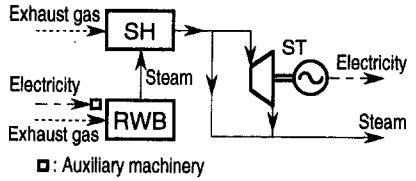

(a) Super waste incineration cogeneration plant (plant A)

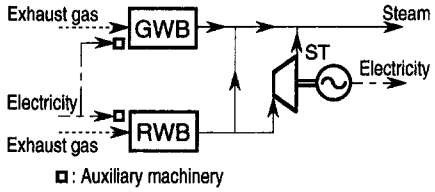

(b) Conventional waste incineration cogeneration plant (plant B)

Fig. 2 Configuration of exhaust heat recovery system

square meters. Note that energy demands change with season and time.

Waste Incineration Cogeneration Plant. To investigate the effects of waste incineration cogeneration and repowering, we treat the following three waste incineration plants:

Plant A: super waste incineration cogeneration plant,
Plant B: conventional waste incineration cogeneration plant combined with a gas turbine cogeneration plant, and
Plant C: conventional waste incineration plant without cogeneration plus a gas turbine cogeneration plant.

Figure 1 shows a schematic diagram for an overall configuration common to plants A and B. Figures 2(a, b) show schematic diagrams for configurations of exhaust heat recovery systems used in plants A and B, respectively, and they indicate differences between the two plants.

In plant A, waste is burned in waste incinerators (RP), and exhaust heat generated is recovered by waste heat recovery boilers (RWB) to generate low-temperature steam. On the other hand, gas turbine generators (GT) are operated using natural gas to generate electricity and exhaust heat, which is used by superheaters (SH) to superheat the low-temperature steam. Superheated steam is used to drive steam turbine generators (ST) with high-power generating efficiency. Low-pressure steam, after it is used by steam turbines, is used to supply thermal

Nomenclature

C = annual cost, yen/y
$C(\ )$ = capital cost of equipment as function of its capacity, yen
C_{car} = transportation fee per meter, yen/m
C_{pipe} = capital cost of piping per meter and per megawatt, yen/(m·MW)
D_e = number of districts per square meters, districts/m^2
D_w = number of collecting cars required per square meters, units/m^2
E = electric power, MWh/h
E_d, Q_d^c, Q_d^h = hourly demands of electricity and cold/hot water, MWh/h
E_e, Q_e^c, Q_e^h = hourly demands of electricity and cold/hot water per district, MWh/(h·district)
F = flow rate of natural gas, m^3/h
i = interest rate
L_{car} = transportation distance per day, m/d
L_{road} = length of road per square meters, m/m^2
N = number of equipment installed
P = annual primary energy consumption, MWh/y
p = coefficient to convert energy flow rate to primary energy consumption, MW/MW, MW/(m^3/h)
R = hourly amount of waste incinerated, t/h
R_{car} = capacity of collecting car, t/unit
R_{day} = daily amount of waste generated, collected, and incinerated, t/d
R_w = daily amount of waste generated per square meters, t/(d·m^2)
r_e = radius of circular area for energy distribution, m
r_w = radius of circular area for waste collection, m
s = ratio of salvage value to capital cost of equipment or piping
V = capital recovery factor of equipment or piping
γ = capacity parameter, MW
κ = life of equipment or piping, y
φ = rate of energy charge, yen/MWh, yen/m^3
Ψ = rate of customer charge, yen/month
ψ = rate of demand charge, yen/(MW·month), yen/(m^3/h·month)
$\overline{(\ )}$ = contract demand, MW, m^3/h

Subscripts

b = purchasing
C = cold water
d = demand
dmnd = demand charge
E = electricity
engy = energy charge
equip = equipment
G = natural gas
H = hot water
ppng = piping
s = selling
total = total cost
trans = transportation

Equipment symbols (subscripts)

AP = preheater
EP = equipment for receiving electricity
GT = gas turbine generator
GWB, RWB = waste heat recovery boiler
HE = heat exchanger
RP = waste incinerator
SAR = steam absorption refrigerator
SH = superheater
ST = steam turbine generator

energy for district heating and cooling. Heat exchangers (HE) and steam absorption refrigerators (SAR) are installed to supply hot and cold water, respectively. Low-pressure steam is also used by preheaters (AP) to preheat air supplied to waste incinerators. Electricity generated by operating both gas and steam turbine generators is distributed to districts and is used to drive auxiliary machinery in the plant. A shortage of electricity is supplemented through the equipment for receiving electricity (EP) from an outside electric power company. A surplus of electricity can be fed back to the company.

In plant B, conventional waste heat recovery boilers (GWB) are installed to recover exhaust heat from gas turbines, in place of superheaters. Steam generated from waste heat recovery boilers for waste incinerators is fed to steam turbines. On the other hand, steam generated from waste heat recovery boilers for gas turbines is used for district heating and cooling.

In plant C, a waste incineration plant equipped with incinerators without steam turbines, and a gas turbine cogeneration plant, are installed independently to burn waste and to supply energy to districts, respectively.

To model these three plants mathematically, we consider performance characteristics of each piece of constituent equipment as well as energy balance and supply–demand relationships as basic equations. As for the former, we formulate piecewise linear relationships between flow rates of input and output energy for each piece of equipment, using binary and continuous variables expressing on/off status of operation and energy flow rates, respectively. Here, we regard performance characteristic parameters for each piece of equipment as nonlinear functions of its capacity. As for the latter, we formulate linear relationships among energy flow rates for each kind of energy, using continuous variables expressing the flow rates (Yokoyama et al., 1995).

Evaluation of Economic and Energy-Saving Characteristics

To evaluate the feasibility of the super waste incineration cogeneration plant from the economic and energy-saving viewpoints, we define two evaluation criteria, i.e., annual total cost and annual primary energy consumption.

On the basis of the annualized costs method, the annual total cost C_{total} is basically evaluated as the sum of the following five items:

(a) capital cost of constituent equipment C_{equip},
(b) demand charge for utilities C_{dmnd},
(c) energy charge for utilities C_{engy},
(d) transportation cost for waste collection C_{trans}, and
(e) capital cost of piping for energy distribution C_{ppng}.

For the super waste incineration cogeneration plant, item (a) is evaluated as follows:

$$\left.\begin{aligned} C_{\text{equip}} &= \{V_{\text{equip}}(1 - s_{\text{equip}}) + is_{\text{equip}}\}\{N_{\text{RP}}C_{\text{RP}}(\gamma_{\text{RP}}) \\ &\quad + N_{\text{RWB}}C_{\text{RWB}}(\gamma_{\text{RWB}}) + N_{\text{GT}}C_{\text{GT}}(\gamma_{\text{GT}}) \\ &\quad + N_{\text{SH}}C_{\text{SH}}(\gamma_{\text{SH}}) + N_{\text{ST}}C_{\text{ST}}(\gamma_{\text{ST}}) \\ &\quad + N_{\text{AP}}C_{\text{AP}}(\gamma_{\text{AP}}) + N_{\text{SAR}}C_{\text{SAR}}(\gamma_{\text{SAR}}) \\ &\quad + N_{\text{HE}}C_{\text{HE}}(\gamma_{\text{HE}}) + C_{\text{EP}}(\gamma_{\text{EP}})\} \\ V_{\text{equip}} &= i(1 + i)^{\kappa_{\text{equip}}}/\{(1 + i)^{\kappa_{\text{equip}}} - 1\} \end{aligned}\right\} \quad (1)$$

where N, C, and γ are, respectively, the number, capital cost, and capacity parameter of each kind of equipment installed, V_{equip}, s_{equip}, and κ_{equip} are, respectively, the capital recovery factor, ratio of salvage value to capital cost, and life of equipment, and i is the interest rate.

Using the contract demands of purchased electricity and natural gas, $\bar{E}_b$ and $\bar{F}_b$, item (b) is evaluated as follows:

$$C_{\text{dmnd}} = \sum_{month} (\psi_{Eb}\bar{E}_b + \Psi_{Gb} + \psi_{Gb}\bar{F}_b) \quad (2)$$

where Ψ_{Gb} is the monthly rate for customer charge of natural gas, and ψ_{Eb} and ψ_{Gb} are the monthly rates for demand charge of electricity and natural gas, respectively. The summation in Eq. (2) means the annual sum of monthly values.

Item (c) is evaluated as the sum of hourly values of energy charge as follows:

$$C_{\text{engy}} = \sum_{\text{hour}} (\varphi_{Eb}E_b - \varphi_{Es}E_s - \varphi_{Ed}E_d + \varphi_{Gb}F_b - \varphi_{Cd}Q_d^c - \varphi_{Hd}Q_d^h) \quad (3)$$

where φ_{Eb}, φ_{Es}, φ_{Ed}, φ_{Gb}, φ_{Cd}, and φ_{Hd} are the hourly rates for energy charge of electricity purchased, electricity sold, electricity distributed, natural gas purchased, cold water distributed, and hot water distributed, respectively, and E_b, E_s, E_d, F_b, Q_d^c, and Q_d^h are their flow rates, respectively. The summation in Eq. (3) means the annual sum of hourly values.

A simplified model is used to evaluate item (d) as follows:

$$\left.\begin{aligned} C_{\text{trans}} &= 365C_{\text{car}}L_{\text{car}} \\ L_{\text{car}} &= \int_0^{r_w} 2\pi r 2r D_w dr + \int_0^{r_w} 2\pi r L_{\text{road}} dr \\ &= \frac{4}{3}\pi r_w^3 D_w + \pi r_w^2 L_{\text{road}} \\ D_w &= R_w/R_{\text{car}} \end{aligned}\right\} \quad (4)$$

where C_{car} is the transportation fee per meter, L_{car} is the total transportation distance per day, L_{road} is the total length of road per square meters used to collect waste, R_{car} is the capacity of a collecting car, and D_w is the number of collecting cars required per square meters.

A simplified model is also used to evaluate item (e). Assuming that diameters of piping are proportional to the square roots of the annual maxima of heat flow rates of cold and hot water, and that the price of piping is proportional to the length and the square of diameter, item (e) is evaluated as follows:

$$\left.\begin{aligned} C_{\text{ppng}} &= \{V_{\text{ppng}}(1 - s_{\text{ppng}}) + is_{\text{ppng}}\}C_{\text{pipe}} \\ &\quad \times \int_0^{r_e} 2\pi r\{\max_{\text{hour}} Q_e^c + \max_{\text{hour}} Q_e^h\}D_e r dr \\ &= \{V_{\text{ppng}}(1 - s_{\text{ppng}}) + is_{\text{ppng}}\}C_{\text{pipe}} \\ &\quad \times \frac{2}{3}\pi r_e^3 D_e\{\max_{\text{hour}} Q_e^c + \max_{\text{hour}} Q_e^h\} \\ V_{\text{ppng}} &= i(1 + i)^{\kappa_{\text{ppng}}}/\{(1 + i)^{\kappa_{\text{ppng}}} - 1\} \end{aligned}\right\} \quad (5)$$

where C_{pipe}, V_{ppng}, s_{ppng}, and κ_{ppng} are, respectively, the price per meter and per megawatt, capital recovery factor, ratio of salvage value to capital cost, and life of piping. The maximum operator in Eq. (5) means the annual maximum of hourly values.

The annual primary energy consumption P is evaluated as follows:

$$P = \sum_{\text{hour}} (p_{Eb}E_b - p_{Es}E_s + p_{Gb}F_b) \quad (6)$$

where p_{Eb}, p_{Es}, and p_{Gb} are respectively the coefficients used to convert the amounts of electricity purchased, electricity sold, and natural gas purchased to their primary energy consumptions.

Optimal Planning Method

To evaluate the annual total cost and its items as well as the annual primary energy consumption, we use an optimal planning method. The basic idea of the optimal planning method

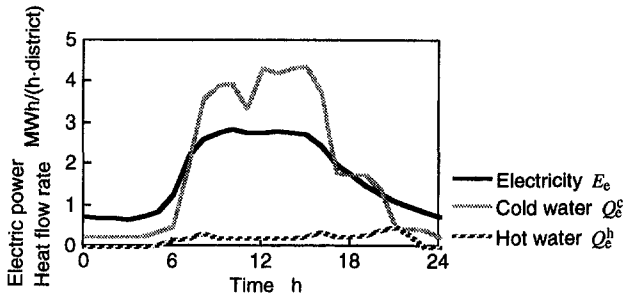

Fig. 3 Daily patterns of energy demands (August)

used here is based on that for simple cycle gas turbine cogeneration plants (Yokoyama et al., 1995). Only an outline of the method is described here.

We fix the amounts of waste collected and energy distributed as preconditions in advance of optimization calculation. Therefore, by optimization calculation, we determine equipment capacities and utility contract demands so as to optimize an objective function, in consideration of equipment operational strategies corresponding to seasonal and hourly variations of energy demands. The annual total cost is adopted here as the objective function to be minimized. We may exclude items (d) and (e) from the objective function, because they can be evaluated in advance from the amounts of waste collected and energy distributed. Performance characteristics of equipment as well as energy balance and supply–demand relationships are considered as constraints to be satisfied. Operational strategies to be determined include binary and continuous variables, which express on/off status of operation and energy flow rates, respectively.

To consider the operational strategies corresponding to seasonal and hourly variations of energy demands, the annual operational hours in a year are discretized by setting several representative days and by dividing each day into several sampling time intervals. Energy demands are estimated for each sampling time interval on each representative day, and the operational strategy is assessed correspondingly.

In order to solve this problem efficiently, a hierarchical optimization method is employed here: equipment capacities and utility contract demands are determined in the unit sizing problem at the upper level; the operational strategy is assessed in the operational planning problem at the lower level; both levels are interconnected with each other by a penalty method.

At the upper level, the optimal unit sizing problem is formulated as a nonlinear programming one, in which optimal values of equipment capacities and utility contract demands are searched so as to minimize the annual total cost. The sequential linear programming method is adopted as a solution method of this nonlinear programming problem (Cheney and Goldstein, 1959).

At the lower level, for a plant with the equipment capacities and utility contract demands given at each searching step, the operational strategy is assessed using an optimal operational planning method (Ito et al., 1990), and the annual energy charge is evaluated. This optimal operational planning problem is formulated as a mixed-integer linear programming problem, and it is solved by the branch and bound method (Garfinkel and Nemhauser, 1972). The specific algorithm adopted here is based on the Land–Doig (1960) method.

Numerical Study

Input Data. To estimate seasonal and hourly variations of energy demands, a year is divided into 12 representative days, each of which corresponds to each month, and further each representative day is divided into 24 sampling time intervals. For example, Fig. 3 shows the daily patterns of energy demands estimated per district on the representative day in August.

Table 1 Miscellaneous input data

Category	Symbol	Value	
Waste collection	R_w	1.27×10^{-3}	kg/m^2
Energy distribution	D_e	15.6×10^{-6}	districts/m^2
Equipment	κ_{equip}	15	y
	s_{equip}	0.0	
Transportation	C_{car}	1.0	yen/m
	R_{car}	1.0×10^{3}	kg/unit
	L_{road}	18.0×10^{-3}	m/m^2
Piping	C_{pipe}	0.30×10^{6}	yen/(MWh/h)/m
	κ_{ppng}	20	y
	s_{ppng}	0.0	
Others	i	0.10	
	p_{Eb}	2.58	MWh/h
	p_{Es}	2.58	MWh/h
	p_{Gb}	11.6×10^{-3}	MWh/m^3

Performance characteristics and capital costs of equipment are given as functions of their capacities. Linear functions are used here to express performance characteristics and capital costs in terms of capacities for all kinds of equipment. Representative performance characteristic values and capital unit costs are omitted here. It is assumed that one unit is installed for each kind of equipment in plants A–C.

Rates of utilities adopted here are standard ones used in Japan, and they are omitted here. Other miscellaneous input data are summarized in Table 1.

Results and Discussion

Fundamental Study. First, a fundamental case study is carried out by fixing the amounts of waste collected and energy distributed. The amount of waste collected per day is set at R_{day} = 400 t/d, which means that the radius of circular area from which waste is collected is set at r_w = 10 km. On the other hand, the radius of circular area to which energy is distributed is set at r_e = 350 m.

Table 2 shows the optimal values of equipment capacities and utility contract demands for plants A–C. The capacity of gas turbine generator for plant C is large enough to supply cold and hot water only by utilizing exhaust heat from the gas turbine. On the other hand, the capacity of gas turbine generator for plant A or B becomes much smaller. This is because exhaust heat from the waste incinerator can be utilized to generate electricity and steam. Comparing plants A and B, the capacity of steam turbine generator for plant A is larger by 33.8 percent than that for plant B. This is because the power-generating efficiency of steam turbine generator is increased by repowering.

Figure 4 compares plants A–C in terms of annual cost. Note that we exclude not only transportation cost for waste collection and capital cost of piping for energy distribution, but also capital cost of waste incinerator and energy charges of electricity and cold/hot water distributed from the annual total cost, because they remain constant for plants A–C with the values of r_w and r_e fixed. According to Fig. 4, the installation of the steam turbine generator in the waste incineration plant reduces the annual cost

Table 2 Optimal values of equipment capacities and utility contract demands (R_{day} = 400 t/d, r_e = 350 m)

Plant			A	B	C
Gas turbine generator	γ_{GT}	MW	6.5	3.7	13.5
Waste heat recovery boiler	γ_{GWB}	MW	—	6.5	24.3
Superheater	γ_{SH}	MW	14.8	—	—
Steam turbine generator	γ_{ST}	MW	12.6	9.4	—
Electricity	$\bar{E}_b$	MW	3.4	10.8	7.7
Natural gas	$\bar{F}_b$	$\times10^3$ m^3/h	2.1	1.2	4.3

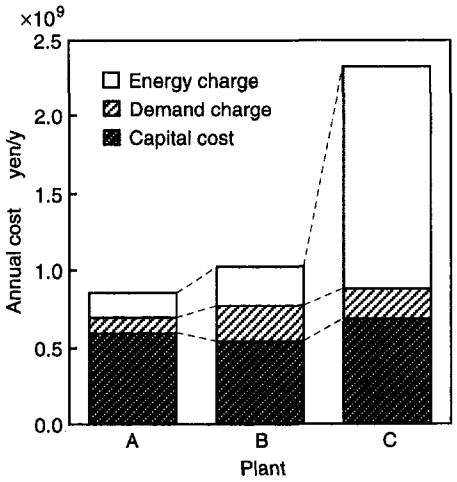

Fig. 4 Annual cost and its items (without items common to plants A to C, R_{day} = 400 t/d, r_e = 350 m)

by more than 50 percent. This is mainly due to a large reduction in energy charge obtained by utilizing exhaust heat generated from the waste incinerator. Plant A has an increase in capital cost in comparison with plant B due to larger capacities of both gas and steam turbine generators, but plant A has a possibility of reducing demand charge as well as energy charge. In this study, the annual cost for plant A is reduced by 16.4 percent in comparison with that for plant B. The results for annual primary energy consumption are similar to those for annual energy charge in Fig. 4. Plant B has a decrease of 90.2 percent in annual primary energy consumption as compared with plant C, while plant A has a decrease of 17.8 percent as compared with plant B.

Figures 5(a–c), respectively, show the optimal operational strategies for electricity supply for plants A–C on the representative day in August. Since the capacity of gas turbine generator is large for plant C, it is operated following electricity demand throughout the day. For plant B, the steam turbine generator is operated at base load. The gas turbine generator is operated only during the daytime from 8:00 to 20:00 with high electricity demand, and the electric output of steam turbine generator decreases during the time. This is because a large amount of cold water is demanded for space cooling during the daytime, and part of the steam generated by the waste incinerator must be distributed directly. During the nighttime, the electricity generated by the steam turbine generator is fed back to the electric power company. For plant A, the operation of the steam turbine generator during the nighttime is basically the same as that for plant B. However, the electric output of steam turbine generator during the daytime is augmented by repowering. Consequently, the electric power purchased for plant A becomes much lower than that for plant B.

Parametric Study. Second, a parametric study is carried out with respect to the amount of waste collected per day R_{day} and the radius of circular area to which energy is distributed r_e. The value of R_{day} ranges from 100 to 600 t/d (the value of r_w from 5 to 12.3 km), and the value of r_e from 100 to 600 m.

Figures 6(a, b) show the optimal capacity of gas turbine generator as a function of R_{day} and r_e for plants A and B, respectively, while Figs. 7(a, b) show the optimal capacity of steam turbine generator. The capacity of steam turbine generator for plant B remains constant against a change in r_e. This is because the capacity of the steam turbine generator basically depends only on the hourly maximum amount of waste incinerated or R_{day}. On the other hand, the capacity of gas turbine generator for plant B increases with the amount of energy distributed or r_e. The change in the capacity of gas turbine generator for plant A is similar to that for plant B. Because of repowering, this leads to an increase in the capacity of steam turbine generator with r_e.

Figure 8 compares plants A and B in terms of annual total cost as a function of R_{day} and r_e. Note that the annual total cost shown here includes all the items. For each amount of waste, there exists an optimal value of r_e that minimizes the annual total cost. This means the following: If we set the value of r_e at a smaller value, we cannot utilize exhaust heat generated from the waste incinerator, and the revenue obtained from energy distribution decreases; on the other hand, for a larger value of r_e the capital cost of piping significantly affects the annual total cost. The difference in annual total cost between plants A and B increases with an increase in r_e and with a decrease in R_{day}. This tendency is mainly due to the difference in capacity of steam turbine generator caused by repowering, as shown in Fig. 7.

Figure 9 compares plants A and B in terms of annual primary energy consumption as a function of R_{day} and r_e. The difference in annual primary energy consumption between plants A and B has a tendency similar to that in annual total cost.

Conclusions

The economic and energy saving characteristics of a super waste incineration cogeneration plant have been evaluated in

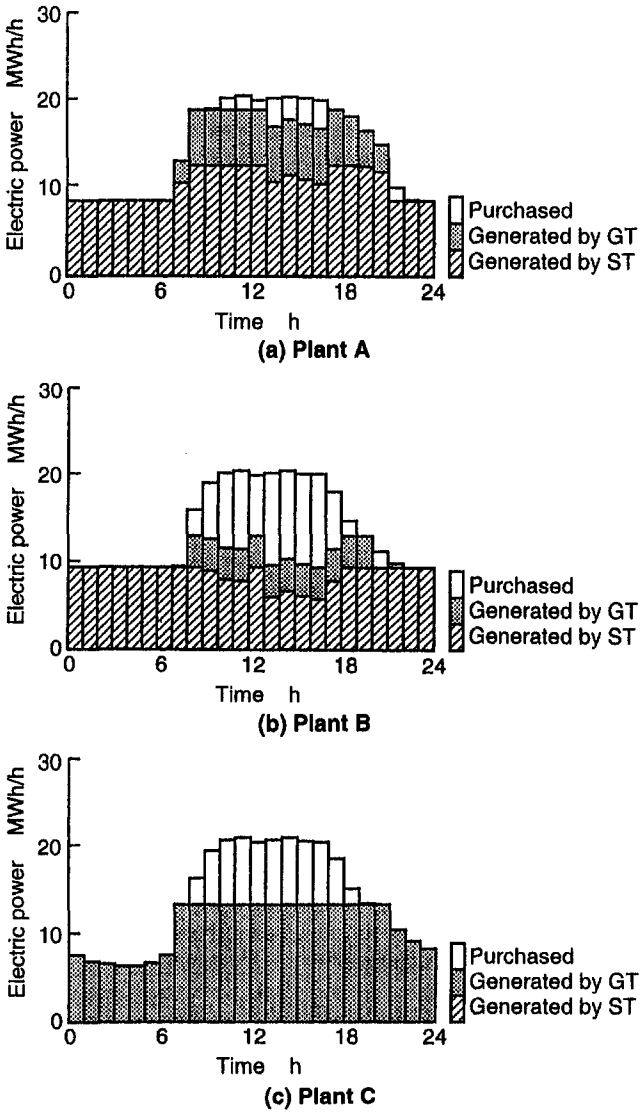

Fig. 5 Optimal operational strategies for electricity supply (R_{day} = 400 t/d, r_e = 350 m, August)

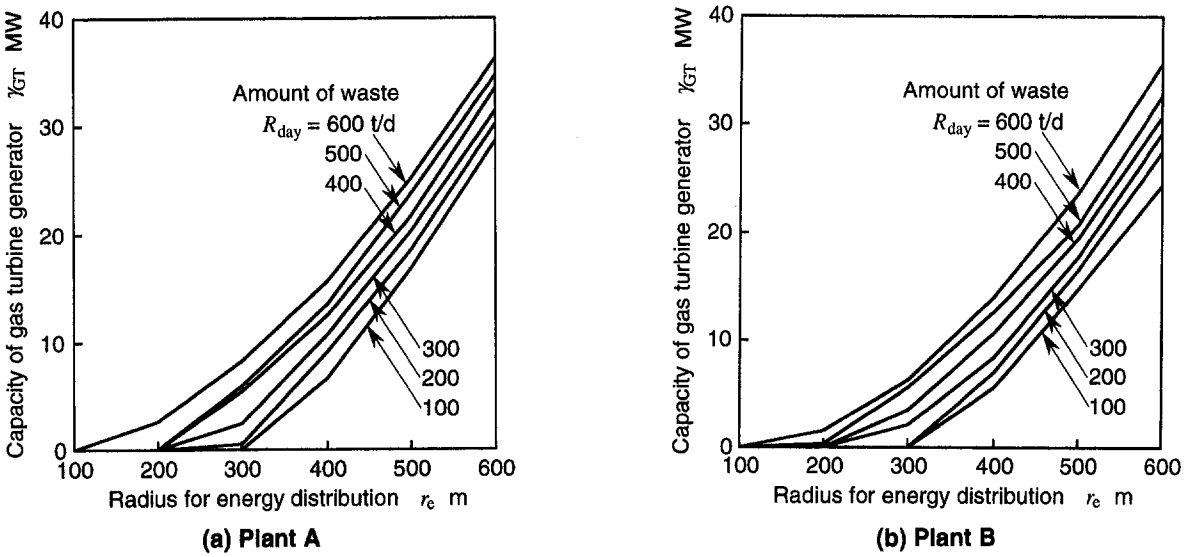

Fig. 6 Optimal capacities of gas turbine generator

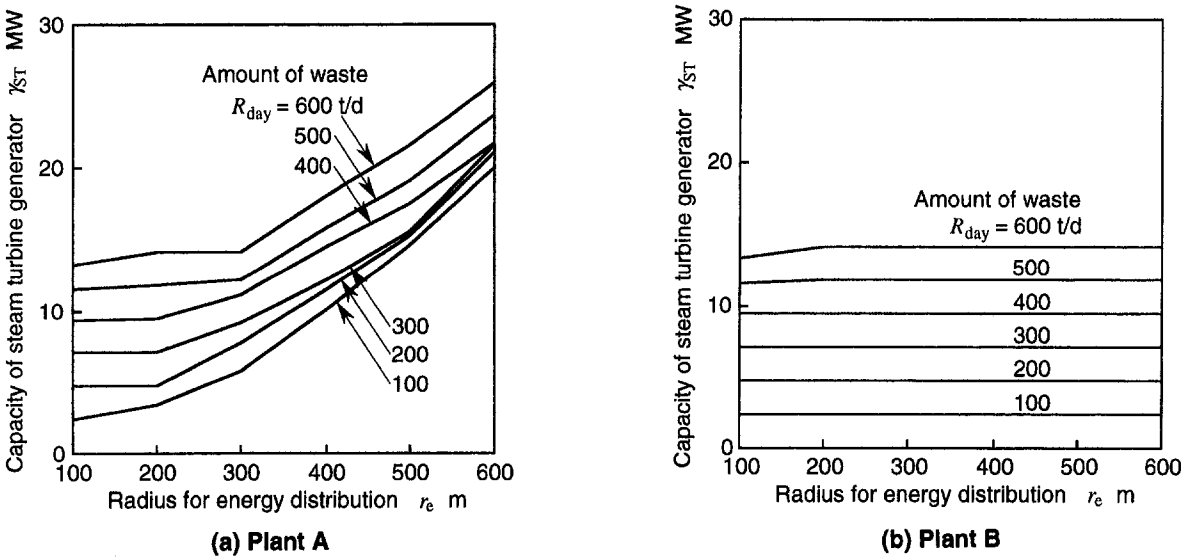

Fig. 7 Optimal capacities of steam turbine generator

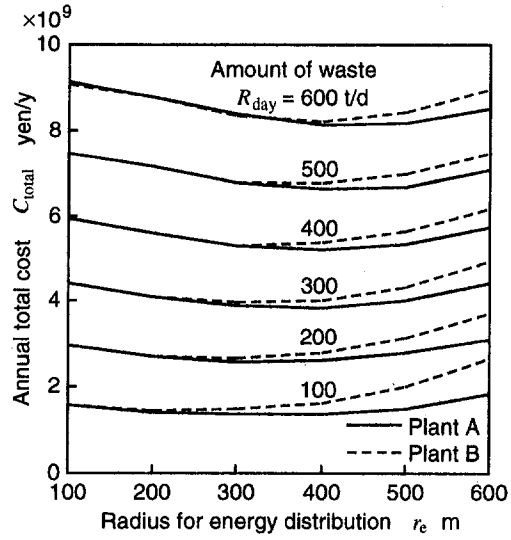

Fig. 8 Comparison of plants A and B in terms of annual total cost

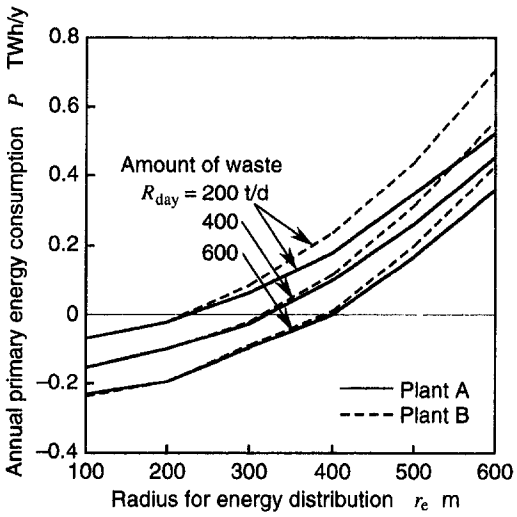

Fig. 9 Comparison of plants A and B in terms of annual primary energy consumption

comparison with those of a conventional one. An optimal planning method has been used to determine capacities and operational strategies of constituent equipment from their many alternatives and to evaluate the above characteristics. A numerical study has been carried out by changing the amounts of waste collected and energy distributed to investigate how they affect these characteristics. The following are main results obtained:

1 A super waste incineration cogeneration plant has a possibility of reducing annual total cost, by covering an increase in capital cost through decreases in both demand and energy charges.

2 As a result of repowering, the optimal capacity of steam turbine generator increases with the amounts of waste incinerated and energy distributed. Its increasing rate is high for a small amount of waste incinerated and a large amount of energy distributed.

3 Due to the difference in the increasing rate of capacity of steam turbine generator, the differences between super and conventional waste incineration cogeneration plants in both annual total cost and annual primary energy consumption increase, with a decrease in the amount of waste incinerated and with an increase in the amount of energy distributed.

Acknowledgments

The authors would like to thank Mr. Shuji Nishikawa, a graduate student of Osaka Prefecture University previously and an engineer of Osaka Gas Co., Ltd., currently, for his contribution to this research.

References

Cheney, E. W., and Goldstein, A. A., 1959, "Newton's Method for Convex Programming on Tchebycheff Approximation," *Numerische Mathematik,* Vol. 1, pp. 253–268.

Garfinkel, R. S., and Nemhauser, G. L., 1972, *Integer Programming,* Wiley, New York.

Ito, K., Yokoyama, R., Akagi, S., and Matsumoto, Y., 1990, "Influence of Fuel Cost on the Operation of a Gas Turbine-Waste Heat Boiler Cogeneration Plant," ASME JOURNAL OF ENGINEERING FOR GAS TURBINES AND POWER, Vol. 112, pp. 122–128.

Land, A. H., and Doig, A. G., 1960, "An Automatic Method of Solving Discrete Programming Problems," *Econometrica,* Vol. 28, pp. 497–520.

Terasawa, H., and Ogura, M., 1993, "System to Rationalize Energy Utilization at Waste Incineration Plants," *Proc. JSME–ASME International Conference on Power Engineering—93,* Vol. 2, pp. 591–594.

Yokoyama, R., Ito, K., and Matsumoto, Y., 1995, "Optimal Sizing of a Gas Turbine Cogeneration Plant in Consideration of Its Operational Strategy," ASME JOURNAL OF ENGINEERING FOR GAS TURBINES AND POWER, Vol. 116, pp. 32–38.

Sensitivity Analysis on Brayton Cycle Gas Turbine Performance

G. Negri di Montenegro

A. Peretto

DIEM—University of Bologna, Bologna, Italy

This paper evaluates the performance of a Brayton cycle gas turbine, in terms of power output and conversion efficiency. Sensitivity of this performance to the realistic value of each input variable considered is analyzed. Sensitivity is evaluated by introducing a parameter, defined as the ratio between the logarithmic differential of the power output or efficiency functions and the logarithmic differential of each variable considered. These analytical functions and their derivatives correspond to a gas turbine model developed by the authors. The above-mentioned sensitivity parameter can be also evaluated by means of a numerical procedure utilizing a common gas turbine power plant computational model. The values calculated with the two procedures turn out to be substantially the same. Finally, the present analysis permits the determination of the weight of the input variable and of its value on the obtainable numerical performance. Such weights are found to be less important for some variables, while they are of marked significance for others, thus indicating those input parameters requiring a very precise verification of their numerical values.

Introduction

The behavior of gas turbine power plants, like that of every energy system, is usually described by suitable models that, depending on their precision and complexity, reproduce working conditions more or less accurately.

These models are often employed to determine or verify the performance of an energy system, using numerical values of different input variables, which affect calculation results to a varying extent, according to their chosen value (El Masri, 1986; El Hadik, 1990). Such values may be estimated in the case of determination and deduced in that of verification.

If, as seems evident, each input variable has a different weight on the numerical results, the establishment of a sensitivity parameter defining this weight can be of considerable interest.

In addition, this parameter permits one to compare the relative incidence of each of the above-mentioned input variables and, therefore, to establish which of them require a more precise choice of the value to be attributed.

Sensitivity Parameter

The performance of any energy system can be represented by means of analytical expressions such as:

$$F = F(x_1, x_2, \ldots, x_n) \tag{1}$$

where $x_1, x_2, \ldots, x_n$, are the physical variables that define the behavior of the system. Each of these variables weighs on the F values to a greater or lesser extent, according to its assumed value and its functional link to the F function. This link depends on the analytical-computational model adopted to represent the system working conditions. To evaluate the influence of one variable alone, x_i, the f function can be introduced:

$$f(x_i) = F(x_{10}, x_{20}, \ldots, x_i, \ldots, x_{n0}) \tag{2}$$

where the subscripts 0 refer to the assumed value for each variable different from x_i.

The logarithmic differential of Eq. (2) is:

$$d[\ln (f(x_i))] = \frac{d[f(x_i)]}{f(x_i)}$$

and, indicating with a_i the derivative of $f(x_i)$ with respect to x_i, that is:

$$a_i(x_i) = \frac{d[f(x_i)]}{dx_i}$$

and with Φ_{fi}:

$$\phi_{fi} = \frac{\dfrac{d[f(x_i)]}{f(x_i)}}{\dfrac{dx_i}{x_i}}$$

we obtain:

$$\phi_{fi} = \frac{a_i(x_i)}{f(x_i)} x_i \tag{3}$$

The ϕ_{fi} parameter defined by Eq. (3) expresses the sensitivity of the f function to the x_i variable and is therefore called the sensitivity parameter. This dimensionless parameter seems more appropriate to express sensitivity than the derivative of the f function with respect to x_i, which is a dimensional quantity, less suitable for a comparative analysis among different physical quantities. Apart from the quantity x_i considered, Φ_{fi} values also depend on the assumed x_i value, as clearly represented in Eq. (3).

It can be observed that the derivation of $f(x_i)$ with respect to x_i, $a_i(x_i)$, may be particularly difficult. That occurs when the adopted model describing the performance is sophisticated and accurate. In this case it can be convenient to calculate this sensitivity parameter with a numerical procedure. With this procedure the sensitivity parameter is expressed by:

$$\phi_{fi} = \frac{\dfrac{\Delta f}{f(x_i)}}{\dfrac{\Delta x_i}{x_i}} \tag{4}$$

where $\Delta f = f(x_{i1}) - f(x_i)$, and $\Delta x_i = x_{i1} - x_i$. Obviously the Φ_{fi} evaluation with Eq. (4) must be performed with x_{i1} very close to x_i.

Sensitivity Parameter on Brayton Cycle Gas Turbine

In gas turbine plants, sensitivity analyses are carried out by considering the variables describing the system, whose perfor-

Contributed by the International Gas Turbine Institute and presented at Turbo Asia '96, Jakarta, Indonesia, November 5–7, 1996. Manuscript received at ASME Headquarters July 1996. Associate Technical Editor: J. W. Shinn. Paper No. 96-TA-37.

mance is expressed in terms of power output and conversion efficiency. For each of the variables the corresponding sensitivity parameter has been calculated, with both analytical and numerical procedures.

Analytical Procedure. For Φ_{fi} evaluation with an analytical procedure, the relationship between the performance and the above-mentioned variables must be expressed. The analytical model adopted to determine the relationships is represented by the following equations:

$$W = (W_t - W_c)\eta_m \tag{5}$$

where W_t is

$$W_t = (m_1 + m_f)[c_{p13s}(T_{3s} - T_1) - c_{p14}(T_4 - T_1)] \tag{6}$$

and W_c is

$$W_c = m_1 c_{p12}(T_2 - T_1) \tag{7}$$

with

$$\beta_e = (1 - \Delta P_{in})(1 - \Delta P_{cc})(1 - \Delta P_{st})\beta_c \tag{8}$$

$$T_2 = T_1\beta_c\left(\frac{k_{12} - 1}{k_{12}\eta_{pc}}\right) \tag{9}$$

$$T_4 = T_{3s}\beta_e - \left(\frac{k_{3s4} - 1}{k_{3s4}}\eta_{pe}\right) \tag{10}$$

$$m_f = \frac{(m_1 - m_c)[c_{p13}(T_3 - T_1) - c_{p12}(T_2 - T_1)]}{\eta_{cc}\mathrm{LHV} - c_{p13}(T_3 - T_1)} \tag{11}$$

$$T_{3s} = T_1 + \frac{m_c c_{p12}(T_2 - T_1) + m_3 c_{p13}(T_3 - T_1)}{(m_1 + m_f)c_{p13s}} \tag{12}$$

$$\eta = \frac{W}{m_f \mathrm{LHV}} \tag{13}$$

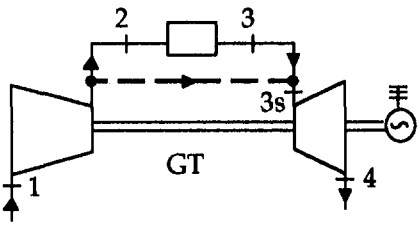

Fig. 1 Schematic layout of the gas turbine

The subscripts in the variables from Eqs. (6)–(12) refer to the gas turbine schematic layout represented in Fig. 1.

Temperature T_{3s}, as Eq. (12) shows, corresponds to the assumption that all the cooling mass flow rate mixes at the turbine inlet. This cooling mass flow rate has been calculated with a methodology presented by Benvenuti et al. (1993).

The specific heat at constant pressure, cp_{ij}, and specific heat ratio, k_{ij}, of the working gas mixtures are the average specific heat and the ratio of average specific heat between the physical state i and j.

To evaluate the sensitivity parameter referring to the power output, expressed by:

$$\phi_{Wi} = \frac{x_i}{W}\frac{dW}{dx_i}$$

it is necessary to determine the derivatives of the functions, expressed by Eq. (5) to (12), with respect to each x_i variable taken independently. The independent variables considered here are: β_c, η_{pc}, η_{pe}, T_1, T_3, m_1, m_c, LHV, η_{cc}, η_m, Δp_{in}, Δp_{cc}, and Δp_{st}. The analytical procedure applied to each independent variable is presented in the appendix, which refers only to variable T_3. It should be noted that in the derivative expressions, the derivatives of both cp_{ij} and k_{ij} are taken into account with respect to each variable.

The sensitivity parameter referred to the conversion efficiency, η, is expressed by:

$$\phi_{\eta i} = \frac{x_i}{\eta}\frac{d\eta}{dx_i}$$

Nomenclature

$a_i(x_i)$ = derivative expression of $f(x_i)$ function with respect to the variable x_i
c_{pi} = constant pressure specific heat in the physical state i
c_{pij} = average constant pressure specific heat between physical states i and j
$f(x_i)$ = F function in which all variables, except for x_i, are constant and set to the values in Table 1
F = function expressing performance of the system
k = specific heat ratio
k_{ij} = average specific heat ratio between physical states i and j
LHV = fuel lower heating value
m = mass flow rate
m_c = gas turbine cooling mass flow rate
m_f = fuel mass flow rate
T = temperature
W = gas turbine shaft power
W_t = expander power output
W_c = compressor power
X = x_i percentage variation referring to its value in Table 1
x_i = generic variable in the F function
β_c = compressor pressure ratio
β_e = gas turbine expansion pressure ratio
Δp_{cc} = gas turbine combustor relative pressure losses
Δp_{in} = gas turbine inlet relative pressure losses
Δp_{st} = gas turbine outlet relative pressure losses
Φ_{fi} = sensitivity parameter, relative to x_i variable, for f function
Φ_{Wi} = sensitivity parameter, relative to x_i variable, for function expressing gas turbine power output
$\Phi_{\eta i}$ = sensitivity parameter, relative to x_i variable, for function expressing gas turbine efficiency
η = gas turbine conversion efficiency
η_{cc} = gas turbine combustor efficiency
η_m = gas turbine mechanical efficiency
η_{pc} = polytropic compression efficiency
η_{pe} = polytropic expansion efficiency

Subscripts

1 = compressor inlet
2 = compressor outlet
3 = gas turbine combustor exit
3s = gas turbine expansion starting point (after mixing cooling mass flow rate with turbine inlet gas mass flow rate)
4 = gas turbine outlet

Acronyms

AD = aeroderivative gas turbine typology
GT = gas turbine
HD = heavy-duty gas turbine typology
SS = small-size gas turbine typology

Table 1 Gas turbine assigned variable values and performance

	HD	SS	AD
β_c	14	9	30
η_{pc}	0.910	0.895	0.905
η_{pe}	0.89	0.875	0.88
T_1 [K]	288	288	288
T_3 [K]	1523	1373	1553
m_1 [kg/s]	370	16	120
m_c [kg/s]	37.80	1.07	18.42
LHV [kJ/kg]	50000	50000	50000
η_{cc}	0.99	0.98	0.99
η_m	0.980	0.970	0.975
Δp_{in} [%]	1.8	2.5	2.0
Δp_{cc} [%]	2.2	3.0	2.5
Δp_{st} [%]	0.9	1.3	1.0
W [MW]	141.7	4.6	41.3
η	0.38	0.31	0.42

Taking Eq. (13) into account, this parameter may be written:

$$\phi_{\eta i} = \phi_{Wi} - \frac{x_i}{m_f}\frac{dm_f}{dx_i} - \frac{x_i}{\mathrm{LHV}}\frac{d\mathrm{LHV}}{dx_i} \qquad (14)$$

The second term in Eq. (14) contains the terms previously determined for the calculation of the sensitivity parameter for power.

Numerical Procedure. With this procedure the evaluation of Φ_{Wi} and $\Phi_{\eta i}$ was performed utilizing a common gas turbine power plant computational model that differs from the model employed for the analytical procedure. In fact, it considers the variation of k along compression and expansion, the cooling mass flow rate injected into each stage and bled at an appropriate compressor pressure, and the effective gas mixture composition in the different expansion stages.

Gas Turbine Power Plants

To determine Φ_{Wi} and $\Phi_{\eta i}$ values, it is necessary to define a gas turbine power plant and the variables describing its working conditions. This study deals with three gas turbine power plants representing the most commonly encountered typologies. They are: heavy-duty (HD), small-size (SS), and aeroderivative (AD) gas turbines.

Table 1 lists the assigned variable values that define the gas turbine plants, together with power output and efficiency.

The cooling mass flow rates reported in Table 1 were calculated adopting a computational procedure developed by Benvenuti et al. (1993).

Results

The evaluation of the sensitivity parameter for each of these variables was initially carried out assuming for each of them the value reported in Table 1.

Subsequently, the sensitivity parameter for each variable was calculated for different values from that reported in Table 1, within the range −6 percent to +6 percent. Obviously, at the same time, the remaining variables maintained the values reported in Table 1.

The wide range chosen seems to be realistic for this kind of analysis, as it refers to well-defined gas turbine typologies.

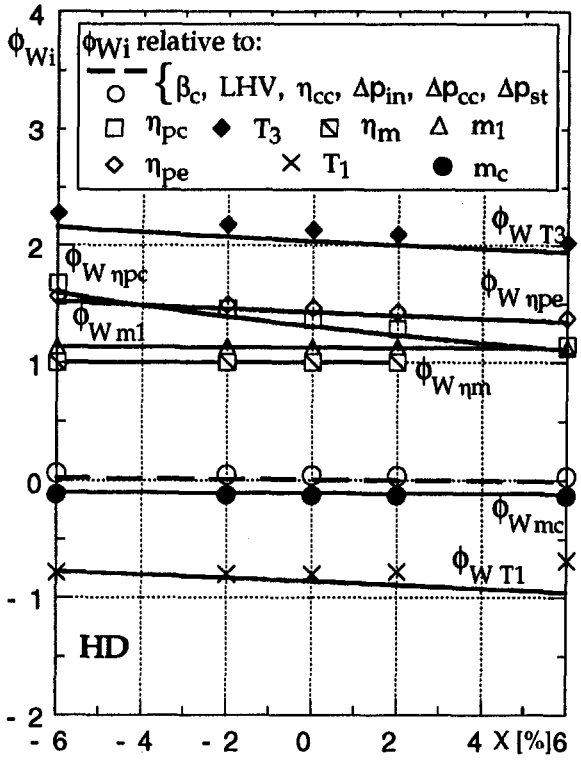

Fig. 2 Φ_{Wi} for the variables considered (HD case)

In Figs. 2–7 the results of the calculation of Φ_{Wi} and $\Phi_{\eta i}$, for both the analytical and numerical procedure, are represented versus X, that is the percentage variation of each variable, with reference to its value reported in Table 1.

Figures 2, 3, and 4 give the values of Φ_{Wi} versus X, for HD, SS, AD, respectively.

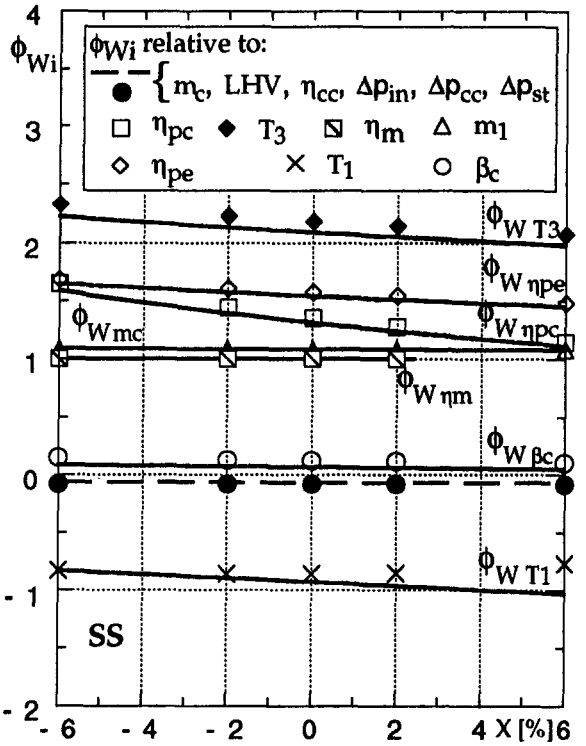

Fig. 3 Φ_{Wi} for the variables considered (SS case)

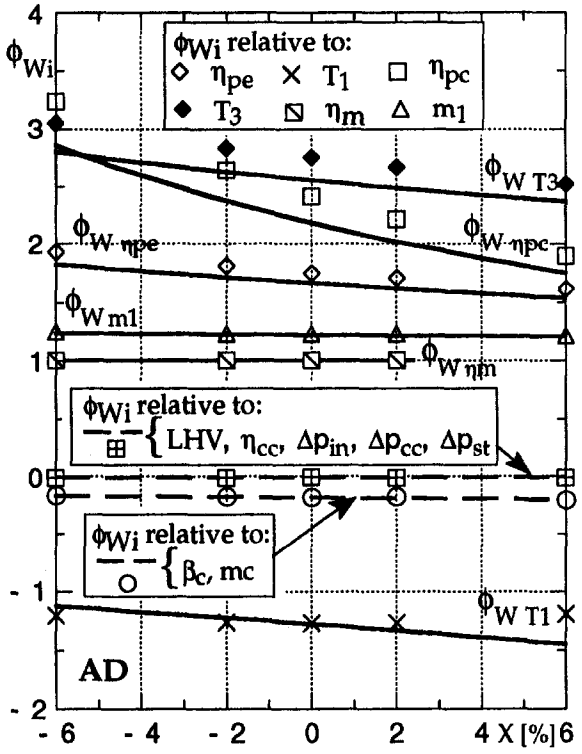

Fig. 4 Φ_{Wi} for the variables considered (AD case)

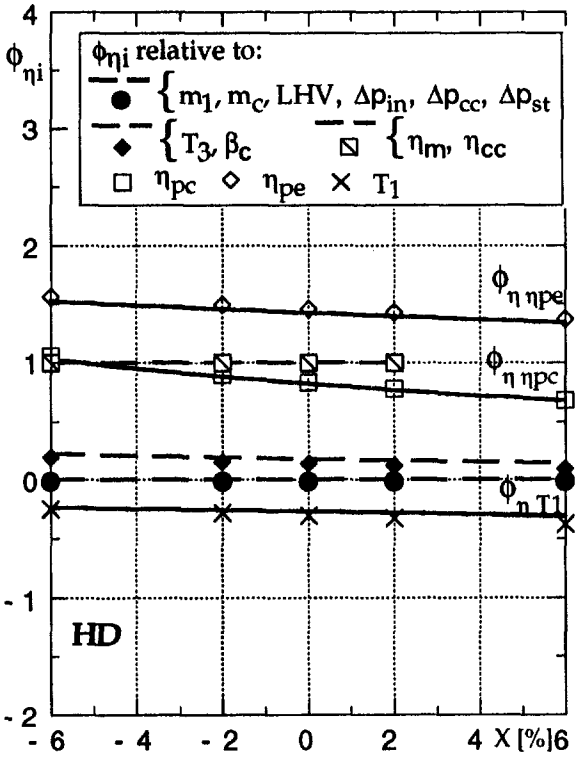

Fig. 5 $\Phi_{\eta i}$ for the variables considered (HD case)

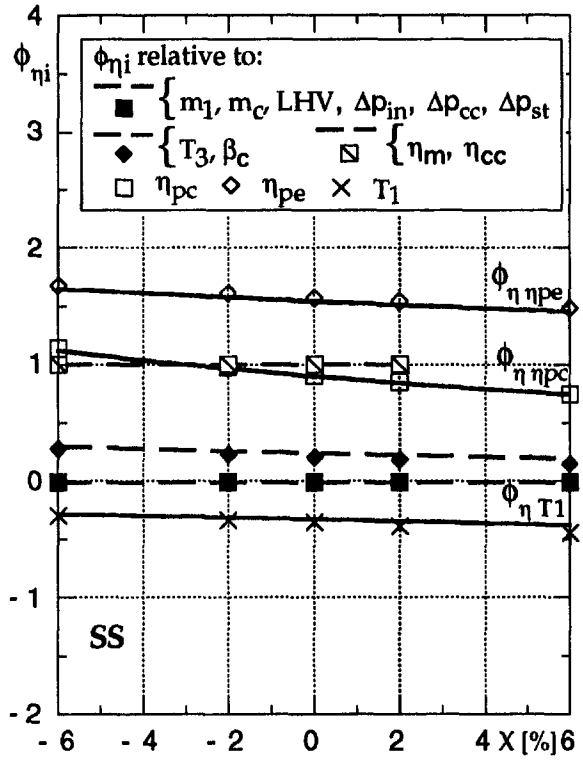

Fig. 6 $\Phi_{\eta i}$ for the variables considered (SS case)

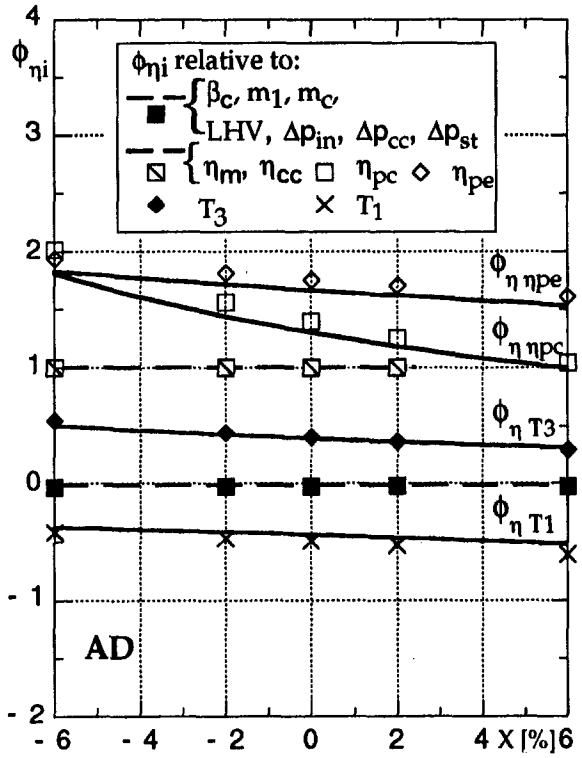

Fig. 7 $\Phi_{\eta i}$ for the variables considered (AD case)

Similarly, Figs. 5, 6, and 7 give the values of $\Phi_{\eta i}$ versus X for HD, SS, AD, respectively.

In all figures, the lines represent the results of the analytical procedure, while the markers correspond to the calculations performed using the numerical procedure. It should be pointed out that, for some of the variables considered, the sensitivity parameter values are, for a given X value, substantially the same, so that the curves would not be distinguishable. In such cases, the figures show a single dashed line or a single marker, for the analytical and numerical procedure, respectively.

The analysis of the figures shows that sensitivity parameter values, obtained with analytical and numerical procedures, are

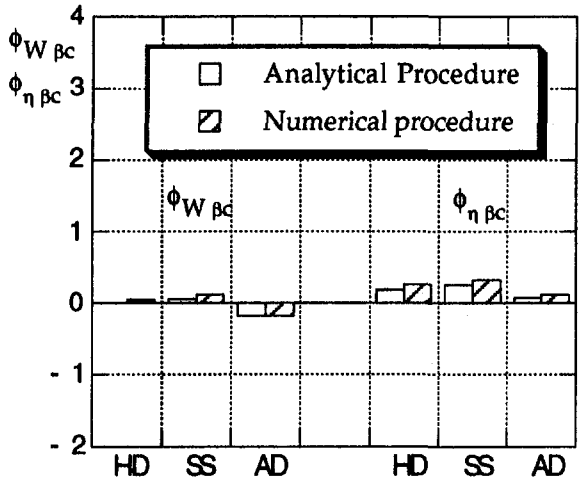

Fig. 8 $\Phi_{W\beta c}$ and $\Phi_{\eta\beta c}$ for HD, SS, AD

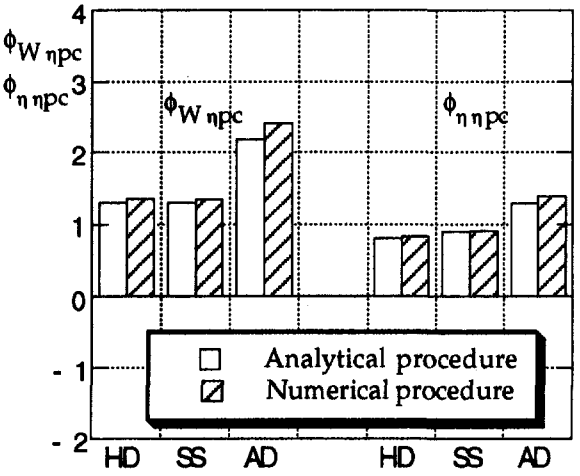

Fig. 9 $\Phi_{W\eta pc}$ and $\Phi_{\eta\eta pc}$ for HD, SS, AD

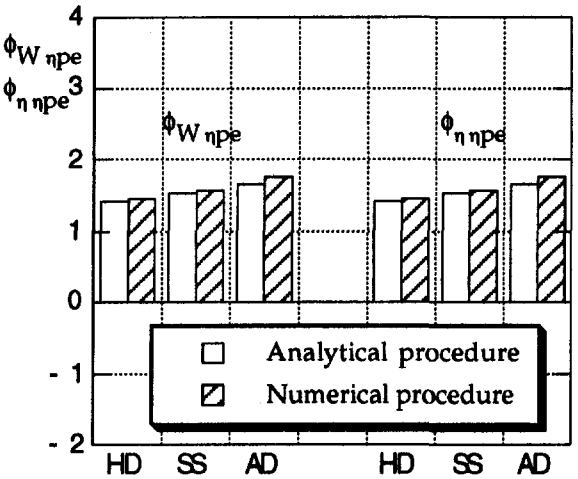

Fig. 10 $\Phi_{W\eta pe}$ and $\Phi_{\eta\eta pe}$ for HD, SS, AD

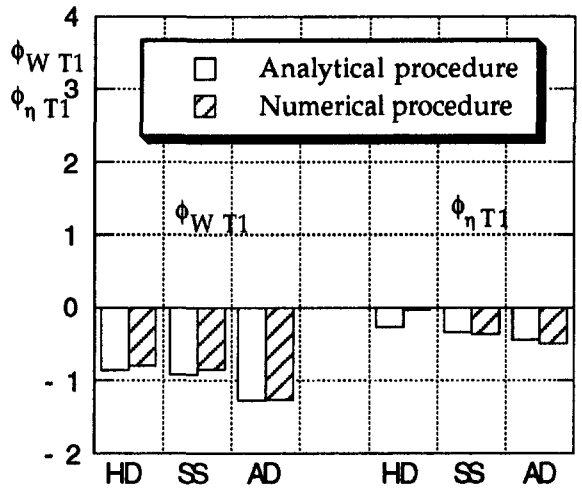

Fig. 11 Φ_{WT1} and $\Phi_{\eta T1}$ for HD, SS, AD

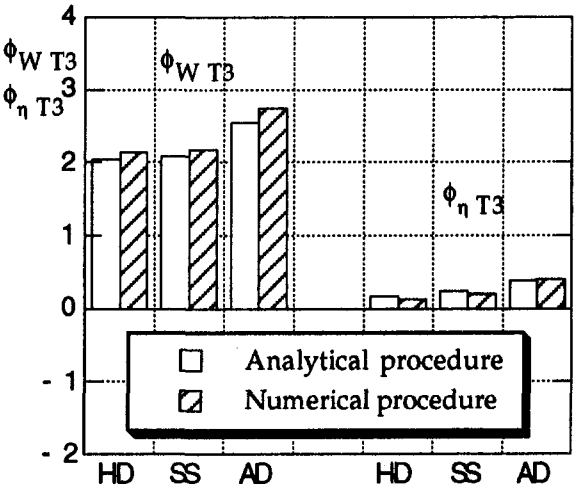

Fig. 12 Φ_{WT3} and $\Phi_{\eta T3}$ for HD, SS, AD

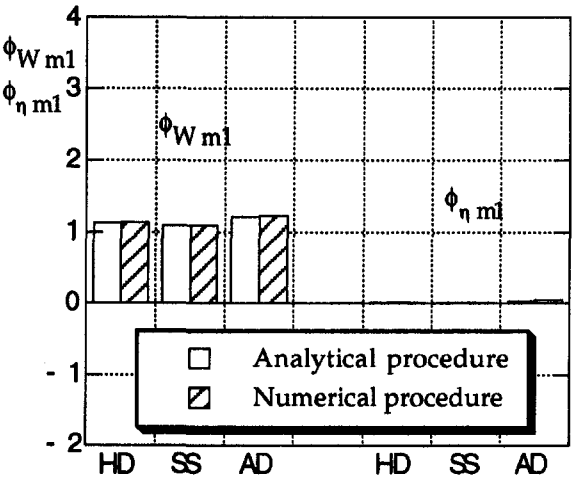

Fig. 13 Φ_{Wm1} and $\Phi_{\eta m1}$ for HD, SS, AD

substantially the same for most of the variables considered. In fact, appreciable differences are noted for the variables η_{pc} and T_3, only in the case of Fig. 4, relating to the sensitivity parameter for power in the aeroderivative gas turbine.

It should be pointed out that $\Phi_{\eta i}$ assumes significantly different values, according to the variable considered. The same occurs for Φ_{Wi} but with greater relevance.

It must be noted that in the HD and SS gas turbines, sensitivity parameters are, for a given variable, mainly independent of

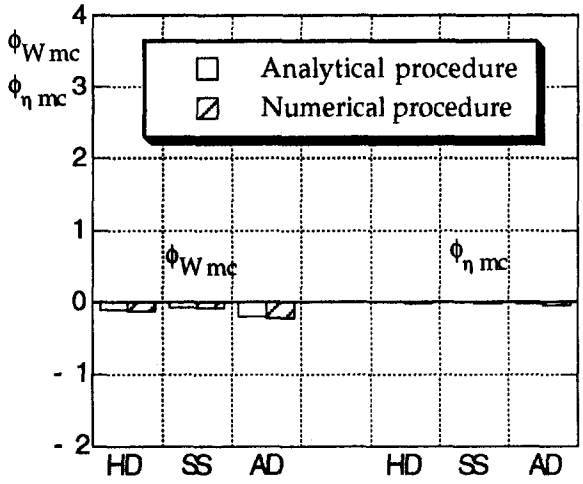

Fig. 14 Φ_{Wmc} and $\Phi_{\eta mc}$ for HD, SS, AD

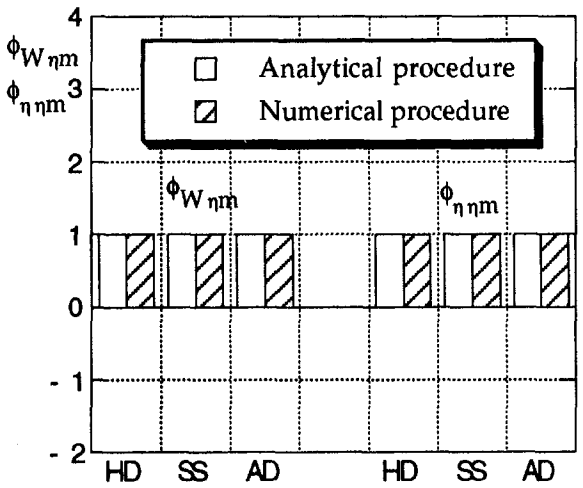

Fig. 15 $\Phi_{W\eta m}$ and $\Phi_{\eta\eta m}$ for HD, SS, AD

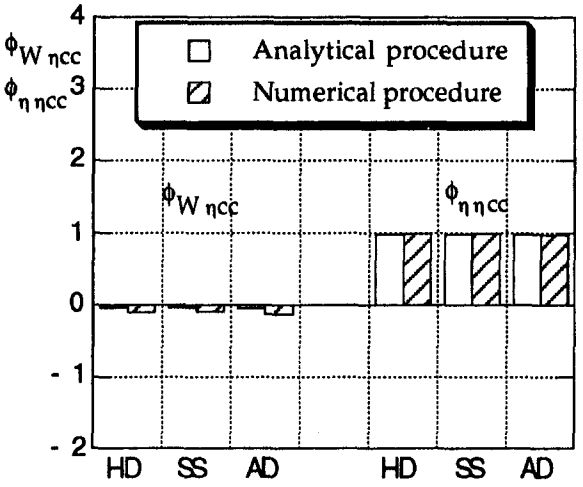

Fig. 16 $\Phi_{W\eta cc}$ and $\Phi_{\eta\eta cc}$ for HD, SS, AD

the value assigned to the variable. However, for the AD gas turbine, the sensitivity parameter values referring to power and conversion efficiency strongly depend on the assumed value in the case where the variable is η_{pc}. For example, $\Phi_{W_{\eta pc}}$, calculated using the analytical procedure is about 2.2 for η_{pc} equal to 0.905 (see Table 1), about 2.9 for η_{pc} equal to 0.851 (−6 percent), and about 1.8 for η_{pc} equal to 0.959 (+6 percent).

To compare the sensitivity parameter values calculated with the two procedures for the three gas turbine typologies, in Figs. 8–16 the relative histograms are reported, only for sensitivity parameters that turned out to be appreciably different from zero. The Φ_{Wi} and $\Phi_{\eta i}$ in these figures are the ones calculated by assigning the values reported in Table 1 to the variables. It should be noted that sensitivity parameters for HD and SS gas turbines are substantially the same, when referring to the same variable.

Analyzing Figs. 8–16 we also find that, for the variables T_3, T_1, η_{cc}, the corresponding sensitivity parameters for power and conversion efficiency have significantly different values.

Conclusions

The sensitivity parameter introduced in this paper assumes values that are substantially the same if evaluated with numerical or analytical procedures. It should be noted that the model adopted for the analytical procedure is less sophisticated than that employed in the numerical one.

This sensitivity parameter permits one to distinguish among the different variables those that weight more significantly on Brayton cycle gas turbine performance.

By way of example, the sensitivity parameters for power are about 2.1, 1.4, and −0.9 with reference to the variables T_3, η_{pe}, and T_1, respectively, in the case of a heavy-duty gas turbine for the variable values assigned in Table 1.

Conversely, for the same gas turbine and variable values, the sensitivity parameters for the efficiency are about 0.2, 1.4, and −0.2 with reference to the variables T_3, η_{pe}, and T_1, respectively. This example shows that the sensitivity parameter values can be very different when calculated for power and efficiency.

For this kind of gas turbine the assigned variable value does not substantially modify the value of the relative sensitivity parameter.

It should be noted that the sensitivity parameter value relative to each variable considered remains substantially unvaried, on passing from the small-size to heavy-duty gas turbine. Instead, in the case of the aeroderivative gas turbine, the sensitivity parameter values relative to some variables turn out to be very different. For example, with regard to the η_{pc} variable, the relative sensitivity parameter for power is about 1.4 for heavy-duty and small-size gas turbines and about 2.3 for the aeroderivative type.

It can therefore be affirmed that the parameter introduced is useful for identifying those variables that weight most heavily on performance, whose value must be carefully and precisely attributed.

Finally, it is observed that the adopted procedures for evaluating the Brayton cycle gas turbine sensitivity may be applied, for the same purpose, in any type of energy system.

References

Benvenuti, E., Bettocchi, R., Cantore, G., Negri di Montenegro, G., and Spina, P. R., 1993, "Gas Turbine Cycle Modeling Oriented to Component Performance Evaluation From Limited Design or Test Data," *Proc. VII ASME COGENTURBO,* Bournemouth, U.K., Sept. 21–23, pp. 327–337.

El Hadik, A. A., 1990, "The Impact of Atmospheric Conditions on Gas Turbine Performance," ASME JOURNAL OF ENGINEERING FOR GAS TURBINES AND POWER, Vol. 112, pp. 590–596.

El Masri, M., A., 1986, "On Thermodynamics of Gas-Turbine Cycles: Part 2—A Model for Expansion in Cooled Turbines," ASME JOURNAL OF ENGINEERING FOR GAS TURBINES AND POWER, Vol. 108, pp. 151–159.

Erbes, M. R., Gay, R. R., and Cohn, A., 1989, "GATE: A Simulation Code for Analysis of Gas-Turbine Power Plants," ASME Paper No. 89-GT-39.

Palmer, C., and Erbes, M. R., 1984, "Simulation Methods Used to Analyze the Performance of the GE PG6541B Gas Turbine Utilizing Low Heating Value Fuels," *Proc. ASME Cogen Turbo Power,* ASME IGTI-Vol. 9.

APPENDIX

The derivative of the gas turbine power output function with respect to temperature T_3 may be written:

$$\frac{dW}{dT_3} = \frac{\partial W}{\partial T_{3s}}\left(\frac{dT_{3s}}{dT_3} + \frac{\partial T_{3s}}{\partial m_f}\frac{dm_f}{dT_3}\right) + \frac{\partial W}{\partial m_f}\frac{dm_f}{dT_3} + \frac{\partial W}{\partial T_3}$$

where:

$$\frac{\partial W}{\partial T_{3s}} = -\eta_m(m_1 + m_f)\left(c_{p14}\beta_e^{-(((k_{34}-1)/k_{34})\eta_{pe})} + (T_4 - T_1)\frac{dc_{p14}}{dT_{3s}} - c_{p14}T_4\frac{\ln(\beta_e^{\eta_{pe}})}{k_{3s4}^2}\frac{dk_{3s4}}{dT_{3s}}\right)$$

$$\frac{dT_{3s}}{dT_3} = \frac{m_3\left(\frac{dc_{p13}}{dT_3}(T_3 - T_1) + c_{p13}\right) - (m_1 + m_f)(T_{3s} - T_1)\frac{dc_{p13s}}{dT_3}}{c_{p13s}(m_1 + m_f)}$$

$$\frac{\partial T_{3s}}{\partial m_f} = \frac{T_3 - T_{3s}}{m_1 + m_f}$$

$$\frac{dm_f}{dT_3} = \frac{\eta_m m_3}{\eta_{cc}\mathrm{LHV} - c_{p13}(T_3 - T_1)}\left(\frac{dc_{p13}}{dT_3}(T_3 - T_1) + c_{p13}\right)$$

$$\frac{\partial W}{\partial m_f} = \eta_m[c_{p13}(T_3 - T_1) - c_{p14}(T_4 - T_1)]$$

$$\frac{\partial W}{\partial T_3} = \eta_m m_3\left(\frac{dc_{p13}}{dT_3}(T_3 - T_1) + c_{p13}\right)$$

The derivative of average specific heat and specific heat ratio functions with respect to temperature T_{3s} may be written:

$$\frac{dc_{p14}}{dT_{3s}} = \frac{d}{dT_{3s}}\left(\frac{h_4 - h_1}{T_4 - T_1}\right) = \frac{\frac{dh_4}{dT_{3s}}(T_4 - T_1) - \frac{dT_4}{dT_{3s}}(h_4 - h_1)}{(T_4 - T_1)^2}$$

$$= \frac{c_{p4} - c_{p14}}{T_4 - T_1}\frac{dT_4}{dT_{3s}} \approx \frac{c_{p4} - c_{p14}}{(T_4 - T_1)}\beta_e^{-(((k_{34}-1)/k_{34})\eta_{pe})}$$

$$\frac{dc_{p3s4}}{dT_{3s}} = \frac{d}{dT_{3s}}\left(\frac{h_{3s} - h_4}{T_{3s} - T_4}\right)$$

$$= \frac{c_{p3s} - \frac{dh_4}{dT_4}\frac{dT_4}{dT_{3s}} - c_{p3s4}\left(1 - \frac{dT_4}{dT_{3s}}\right)}{(T_{3s} - T_4)}$$

$$\approx \frac{c_{p3s} - c_{p3s4} + (c_{p3s4} - c_{p4})\beta_e^{-(((k_{34}-1)/k_{34})\eta_{pe})}}{T_{3s} - T_4}$$

$$\frac{dk_{3s4}}{dT_{3s}} = \frac{d}{dT_{3s}}\left(\frac{c_{p3s4}}{c_{p3s4} - R_{3s4}}\right)$$

$$= \frac{(c_{p3s4} - R_{3s4})\frac{dc_{p3s4}}{dT_{3s}} - c_{p3s4}\frac{dc_{p3s4}}{dT_{3s}}}{(c_{p3s4} - R_{3s4})^2}$$

$$\approx \frac{-R_{3s4}}{(c_{p3s4} - R_{3s4})^2}\frac{dc_{p3s4}}{dT_{3s}}$$

Thermocyclic Behavior of Variously Stabilized EB-PVD Thermal Barrier Coatings

U. Schulz

K. Fritscher

M. Peters

DLR,
German Aerospace
Research Establishment,
Institute of Materials Research,
D-51170 Cologne,
Federal Republic of Germany

The demand for increasing gas inlet temperatures in modern gas turbines up to 1500°C and above is the main reason for the need for more reliable thermal barrier coatings. New ceramics should provide higher phase stability and better resistance against chemical attack by pollutants in the combustion gas. Electron-beam physical vapor deposition (EB-PVD) processed, ZrO_2-based TBCs were generated on bond-coated superalloy directionally solidified (DS) samples. Common yttria-stabilized zirconias of two different compositions, as well as novel stabilizers like CeO_2 and La_2O_3, were investigated. A columnar structure was established during high-rate deposition in all cases. Diameter, degree of ordering of the columns, and phase composition depended on stabilizer oxide and content. The role of differences of vapor pressures is addressed with regard to chemical homogeneity of the coatings. The performance of the TBCs having various stabilizers was investigated in a cyclic oxidation furnace test and in a burner rig at Mach 0.3. The results were correlated to the type and content of stabilizer with special emphasis on phase analyses. Evaporation of new ceramic compositions necessitates special precautions because the vapor pressures of the components may differ too much. A new dual-source evaporation coater allows the production of these innovative TBCs with close control of chemistry. The potential of the equipment will be discussed.

1 Introduction

Thermal barrier coatings (TBCs) on components in the high-pressure turbine allow an essential increase in gas inlet temperature. They are an integrated part of the design of blades and vanes in the new generation of high-bypass aero engines as well as in the latest generation of gas turbines for power generation. A further increase of gas inlet temperature is intended for future developments to increase the engine efficiency. Higher gas temperatures will cause higher thermal load on the components, mainly of those in the combustion chamber and in the high-pressure turbine. This necessitates materials that are capable of operation at temperatures much higher than currently acceptable.

There are two preferential methods to apply TBC systems on airfoils: Plasma Spraying (PS) and Electron-Beam Physical Vapor Deposition (EB-PVD). It is well known that the EB-PVD processed TBCs offer significantly extended lifetimes, smooth aerodynamically attractive surfaces, and only minor cooling hole closure. PS coatings, on the other hand, offer economic advantages and provide slightly better thermal isolation [1].

The superiority of EB-PVD TBCs is related to their columnar microstructure [2, 3]. They consist of densely packed 2 to 25 μm diameter columnar crystals. This specialty gives EB-PVD TBCs outstanding resistance against thermal shocks and strains.

Partially yttria-stabilized zirconia (PYSZ) is the current state-of-the-art material for thermal barrier coatings. Unfortunately, the material shows insufficient phase stability and accelerated sintering at temperatures above 1200°C. Therefore, the increase of gas inlet temperature up to 1500°C and above is the main reason for the search for alternative stabilizers, which should provide improved phase stability. Another argument for new stabilizers in zirconia or for completely new ceramics is the insufficient resistance of current thermal barrier coatings against chemical attack by pollutants in the combustion gas. Hot corrosive decay of TBCs by Na_2SO_4 and vanadates is reported, which involves leaching out of stabilizers from parent zirconia. The degradation occurs by transformation of high-temperature phases to monoclinic on cooling. This failure mode may be found mainly in heavy-duty engines and off-shore service, as referenced elsewhere [4].

An alternative composition for TBCs is ZrO_2-25 wt% CeO_2–2.5% Y_2O_3 (CeSZ). The benefits of Ce-stabilized TBCs are good corrosion resistance [5–7] and an excellent phase stability at high temperature [8, 9]. The mechanisms of vanadium attack on zirconia are not fully understood. Therefore the discussion in the literature is controversial [10, 11]. The thermal conductivity is found to be extremely low and some benefits for lifetime and thermocyclic resistance are reported too. This or similar Ce-containing compositions, however, were investigated only as plasma-sprayed TBCs. Two short contributions on EB-PVD TBCs are excepted: one that mentions the provision of ZrO_2–45wt.% CeO_2 [7] TBCs, the other presents preliminary random burner rig test results and phase analyses (100 percent tetragonal) of ZrO_2–23 wt% CeO_2 [12].

A different possibility to meet the above-mentioned requirements of phase stability at higher temperatures is to stabilize the cubic equilibrium phase in the ZrO_2–Y_2O_3 system. In this case, the content of yttria must be increased to near 20wt%. Several alternative stabilizers have been investigated, namely candidates from rare earth oxides like scandia [13], ytterbia [14], or india [15].

In this study, four EB-PVD processed ZrO_2-based TBC systems on IN100 substrates covered with a NiCoCrAlY bondcoat were examined. Samples were thermocycled in a furnace and in a high-velocity burner rig. Common yttria-stabilized zirconias of two different compositions as well as zirconias with novel stabilizers like CeO_2 and La_2O_3 were investigated. This work was intended to study the feasibility of novel TBC compositions by EB-PVD and to trace the potential of these coatings for future applications in turbines.

Contributed by the International Gas Turbine Institute and presented at the 41st International Gas Turbine and Aeroengine Congress and Exhibition, Birmingham, United Kingdom, June 10–13, 1996. Manuscript received at ASME Headquarters February 1996. Paper No. 96-GT-488. Associate Technical Editor: J. N. Shinn.

2 Experimental Procedure

Directionally solidified IN 100 pin samples of 6 mm diameter and 100 mm length were coated with a 75 to 90 μm thick NiCoCrAlY bond coat by EB-PVD. Table 1 gives the compositions of substrate and bond coat.

Samples were EB-PVD coated with variously stabilized TBCs after peening at an Almen intensity of 12 N to 14 N and a vacuum heat treatment at 1080°C for 4 h.

The coating equipment used in this study for both metallic and ceramic deposition was a 60 kW EB-PVD single-source coater with preheating chamber, facilities for rotating and moving the specimens on a 27 deg tilted axis, and an automated control system for power, electron beam movement, and gas flow (for detailed description see [16]).

The compositions of the 50 mm diameter ceramic ingot sources for evaporation and the respective designations of the TBCs are listed below:

PYSZ 6.5 wt% Y_2O_3
FYSZ 20 wt% Y_2O_3
CeSZ 25 wt% CeO_2–2.5 wt% Y_2O_3
LaSZ 8 wt% La_2O_3

The substrates were rotated on a planetary drive to achieve a uniform thickness distribution around the circumference of the pins. The temperature of the substrate pins was adjusted between 1000°C and 1050°C during thermal barrier coating deposition. Condensation rate was between 5 and 7 μm/min. The total pressure in the coating chamber was adjusted to 0.2 Pa by permanent oxygen bleed in during TBC deposition. For more details see [17].

Two alternative cyclic tests were used to quantify the lifetime of the coating systems: a burner rig and a furnace test. Cyclic burner rig tests were carried out on samples that are mounted on a rotating carousel (1000 min^{-1}) under high-velocity clean fuel gases of Mach 0.3–0.4. One cycle consisted of 57 min heating at 1150°C metal temperature and 3 min quench to RT in a Mach 0.1 air stream. Optical inspection and weighing of the samples were done every 11 hours. A local spallation of ceramic coating greater than 3 mm length in one direction was considered as failure. The furnace tests consisted of 9.3 min heating at 1100°C (temperature was reached within 90 s) and 6 min cooling in forced air down to 130°C. After each collective of 25 cycles, stereomicroscopic inspection was undertaken [18]. The number of samples of each type was three for each test.

Specimens were investigated before and after testing by scanning electron microscopy (SEM) with energy dispersive X-ray spectroscopy (EDS) and optical microscopy. Chemical contents were measured by XRF. Oxides were calculated from measured values of elements assuming normal stoichiometry. Phases were determined from XRD measurements using copper radiation.

3 Results

The surface image of the four TBCs in the as coated condition is shown in Fig. 1. A columnar structure is apparent in all cases with some noticeable differences between the various ceramics. FYSZ and CeSZ possess a larger column diameter and a higher degree of ordering as well. LaSZ, on the other hand, has the most nonuniform shape of the terminal section of columns, which can be seen in Fig. 1(*d*). Here many small protrusions on top of larger crystals can be found. The standard material PYSZ lies between these two extremes with more irregularities than CeSZ and FYSZ but not as many as with LaSZ. Some differences in the symmetry of the terminal faces must be considered. Because of the 27 deg tilted rotational axis all columns were also not perpendicular to the surface.

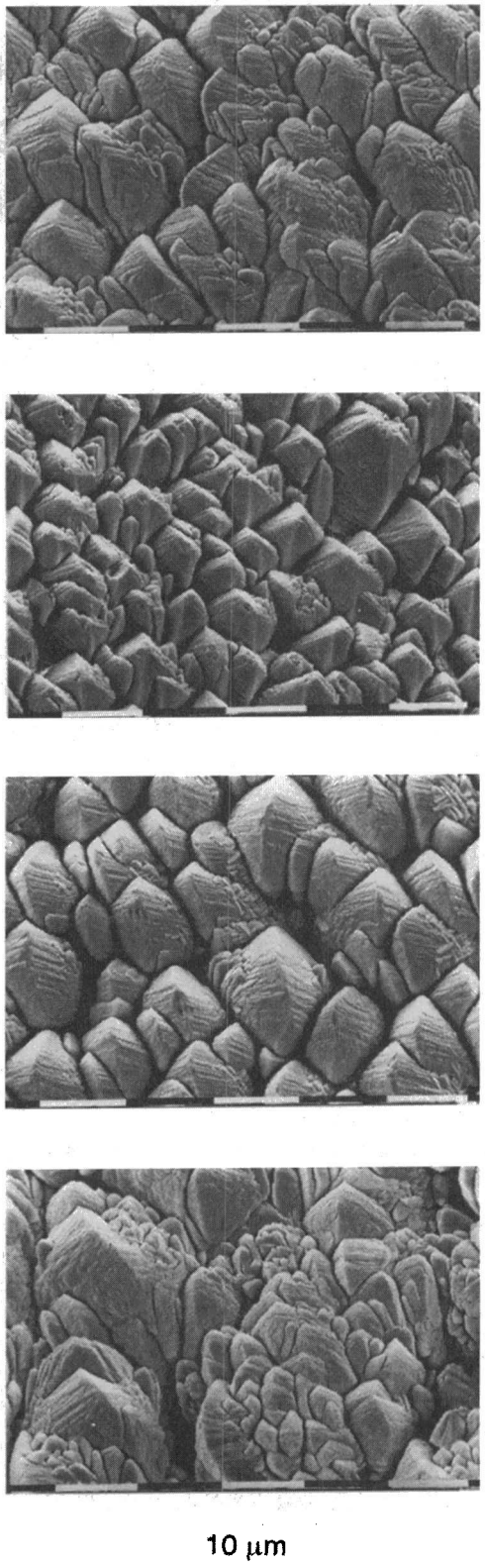

Fig. 1 Morphology of EB-PVD processed thermal barrier coatings: PYSZ, FYSZ, CeSZ, LaSZ (from top to bottom)

Table 1 Average composition of substrate and bond coat (wt%)

	Ni	Co	Cr	Al	Others
IN 100	64.1	14.1	8.6	5.1	5 Ti–2.3 Mo–0.8 V
NiCoCrAlY	46	22	20	12	0.1 . . . 0.15 Y

The results of phase analyses can be summarized as follows:

PYSZ fully metastable tetragonal t' phase
FYSZ fully equilibrium cubic phase
CeSZ mixture of cubic, tetragonal, and occasional monoclinic phases
LaSZ mixture of mainly tetragonal, minor cubic, and substantial amounts of monoclinic phases.

Phase analysis is described in more detail in [17]. The compositions of the three binary TBCs PYSZ, FYSZ, and LaSZ were close to the ingot compositions. In the case of the ternary composition ZrO_2–CeO_2–Y_2O_3, however, analyses show no constant but fluctuating compositions on traversing the cross section of the TBCs. Due to these variations, the surface content of ceria varied among test pieces of different deposition runs between 13 and 38 wt%.

Results of burner rig testing are summarized in Fig. 2. Rapid spallation of FYSZ and LaSZ TBCs was observed as characterized by high weight losses after short testing times. PYSZ proved as most stable coating over long times, followed by sudden spallation of TBC. CeSZ exhibits a different behavior. Here a quasi-continuous weight loss was observed after each inspection cycle. The different failure mode of CeSZ in comparison to "standard" failure by spallation of PYSZ is shown in Fig. 3.

A stepwise degradation in layers is established for the CeSZ TBCs instead of spallation of the whole TBC in one single event as shown in all other cases. A thin layer of ceramic was still present on top of the bond coat after the tests.

Figure 4 summarizes the results of cyclic furnace testing. Here a distinction is made between the time to first cracking as visible in stereomicroscope and the time to spallation. CeSZ was not examined in the furnace test because of the uncertainty of the composition (see above). The lifetime of PYSZ was much higher than that of FYSZ and LaSZ. Both these two thermal barrier coatings showed spallation after the first 25 cycles. Testing of PYSZ that still adhered to the bondcoat has to be stopped after 500 cycles. Termination was due to total consumption of IN 100 substrate material in the uncoated root area that is needed for fastening. EDS analyses give evidence that the main failure location was between thermally grown oxide (TGO) and bond coat, with some areas of failure between TGO and TBC in all three cases.

4 Discussion

The use of different source compositions like PYSZ, FYSZ, CeSZ, and LaSZ for the deposition of EB-PVD thermal barrier coatings bring about severe variations of the columnar structure (Fig. 1). A possible explanation for this observation is the following. Variations can be assumed to be mainly caused by differences of the respective homologous temperatures $T_{deposition}/T_{melting}$, which have a strong relation to diverse microstructural zones within common structural zone diagrams [19, 20]. Although the deposition temperature was nearly the same for all four versions of TBCs, their melting points differ widely. Thus, the "actual point" in these structure models for PVD processes will change, and consequently the structure will vary. CeSZ with a comparably lower melting point, for instance, comes closer to zone 3 according to its homologous temperature value of 0.47, compared to PYSZ, which is centrally located in zone 2 with reference to its homologous temperature value of 0.43. This shift in the structural diagrams results in a larger column diameter and in a more regular structure for CeSZ than for

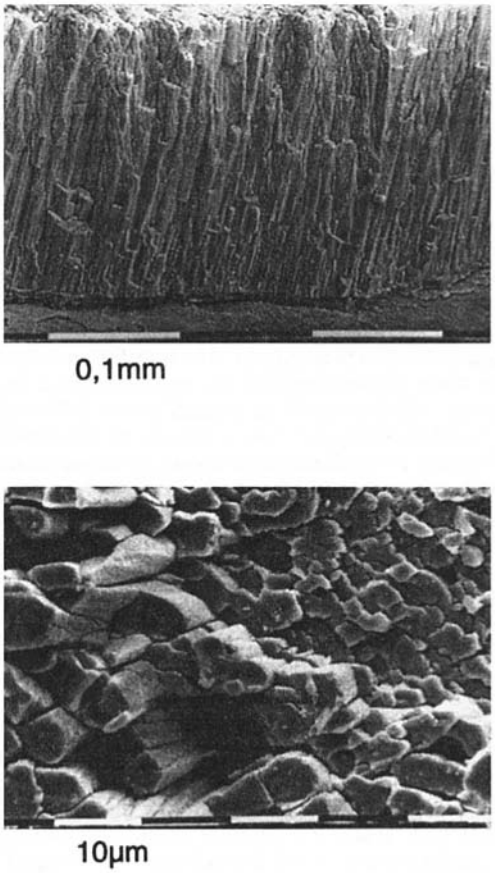

Fig. 3 SEM pictures of burner rig tested TBCs after 65 h at 1150°C: PYSZ (cross section, top); CeSZ (surface image, bottom)

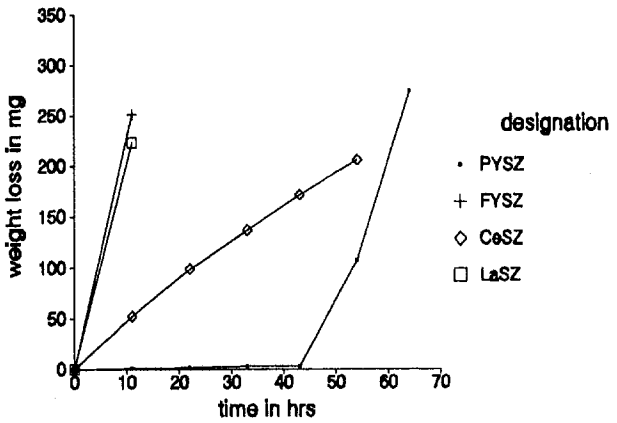

Fig. 2 Weight loss of cyclically burner rig tested samples versus time

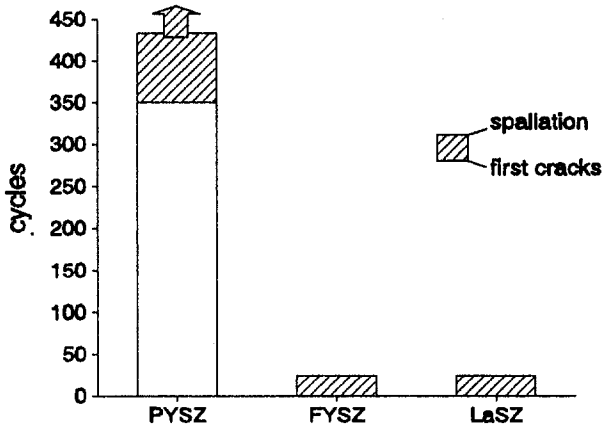

Fig. 4 Cyclic lifetime in furnace test between 1100°C and 130°C

PYSZ. Some other effects that may also affect the microstructure arise from variations in phase composition, ion radii, and surface energy aspects during condensation [17].

Analyses of composition and phase structure of the variously stabilized zirconias provide some help for understanding of the respective cyclic lifetimes. The only phase in 6.5 wt% Y_2O_3 stabilized zirconia EB-PVD TBCs is metastable nontransformable t'. This observation agrees with findings in the literature [21, 22] and with our previous investigations [18, 23]. The lack of high-temperature phase stability of PYSZ is supported by annealing experiments. Whereas EB-PVD TBCs are stable at temperatures up to 1150°C, they transfer after 100 h annealing at 1400°C to a mixture of 48% tetragonal + 48% cubic + 4% monoclinic (Mol%) phases [24]. The transformation processes to these three phases suggests the operation of a sequential mechanism, which consists of yttrium cation diffusion out of t' and destabilization of t' into c and t with subsequent phase transformation $t \rightarrow m$ during cool down. At temperatures below the stability point t' is still the most effective phase for durability in thermal barrier coatings, as can be seen in Fig. 2 and 4, respectively. Outstanding bending strength, high crack propagation energy, high fracture toughness values, and highly tolerant thermoshock behavior represent the microstructure of t'. Lattice distortion due to tetragonality, a domain structure, and the well-described tweed microstructure inside the t' grains [21] are supposed to be responsible for this excellent performance of PYSZ.

Formation of single cubic phase for FYSZ TBCs is in accordance with all findings on TBCs of EB-PVD and also PS origin. {112} pole figure measurements confirmed the absence of any t' phases. FYSZ suffers from low thermal shock resistance and poor fracture properties of the equilibrium cubic phase. Earlier reports on PS thermal barrier coatings [25, 26] have shown that FYSZ possesses poor thermocyclic behavior. Some inconsistency in the literature on EB-PVD TBCs of this composition must be recognized. The present study supports findings in [12] that the columnar structure is not able to overcome the intrinsic problems of FYSZ. The result is poor integrity of these coatings in both cyclic tests (Figs. 2 and 4). It must be pointed out that there is still a potential to improve the adherence of FYSZ EB-PVD thermal barrier coatings on top of latest generation bond coats. This potential may lead to a substantial increase in lifetime.

Monoclinic phases that undergo phase transformation during temperature variation will cause rapid spallation of EB-PVD TBCs. The volume change that is connected to the phase transformation $m \leftrightarrow t$ creates high stresses. Even strain-tolerant structures like columnar EB-PVD ones are not able to accommodate these stresses on transformation. Early spallation of LaSZ gives clear evidence of this mechanism. It must be noticed that phase composition depends strongly on the respective technique of manufacture. Above 7.5 wt% La_2O_3 in ZrO_2, exclusive cubic phase was reported for bulk materials [27]. In this study, however, mixtures of mainly tetragonal, minor cubic, and substantial amounts of monoclinic phases were identified for EB-PVD thermal barrier coatings of similar composition. It has to be taken into account that high rate condensation from a vapor phase is not necessarily a process that stabilizes equilibrium phases. Therefore, phase diagrams do not allow a safe prediction of phase structure of real coatings.

The most interesting behavior in the present study was exhibited by CeSZ. It was found that constant composition of this quality can not be obtained by single-source evaporation. The reason for that is the preferential evaporation of high vapor pressure components and an enrichment of low vapor pressure compounds in the pool. Unfortunately, it is not possible to solve the problem of too low evaporation escape of the low vapor pressure components by overrepresenting them in the liquid pool. The provision of a "starter" composition that balances the vapor pressure differences proved infeasible because of small thickness of melt due to high melting point and low thermal conductivity of the ceramic, although the pool depth is larger in case of CeSZ compared to PYSZ.

In order to understand the problem of composition control, the respective vapor pressures at 2500 K were compared: 5×10^{-2} Pa for ZrO_2, 10^{+3} Pa for CeO_2 [28]. They differ by a factor of 20,000 and probably even more at evaporation temperature, which indeed is too much for viable single-source EB-PVD processing.

Burner rig results of CeSZ, however, were promising (Fig. 2). Quasi-continuous weight loss and a degradation of the CeSZ TBCs in thin layers were found but no spallation. One reason for a stepwise loss is, of course, the fluctuation of composition across the thickness of the TBC. This may cause alternating layers of "weak" phases including monoclinic and "strong" phases like t'. Apparently, the coating will break first in weaker regions. Lattice misfits between the various layers may further contribute to less adhesion between the layers. Higher erosion rates of CeSZ that were found for PS TBCs [5, 9] may also account for this failure mode. The partial loss of this TBC may act as a strain/stress relief mechanism that allows the remainder part of the coating, which is thinner due to partial spallation, to adhere longer.

CeSZ apparently offers some potential in thermal barrier coatings, especially if a columnar microstructure can be utilized. Single-source EB-PVD has proved unsuccessful so far. Two-source evaporation, however, may bring about reproducible CeSZ TBCs of stable composition. First tests of dual source evaporation of ceramics, powered by one 150 kW gun using a "jumping beam technology," are promising. By adjusting dwell time and power distribution of the electron beam over each pool independently, the intended mixing of components in the vaporized state can be established.

Conclusions

Common yttria-stabilized zirconias of two different compositions as well as two innovative coating compositions with CeO_2 and La_2O_3 as stabilizers were produced by reactive high-rate EB-PVD. The results allow the following conclusions.

1 The lifetime of thermal barrier coating systems in a cyclic burner rig and in a cyclic furnace test can be correlated with phase content. PYSZ TBCs exhibit the longest lifetime; LaSZ and FYSZ are characterized by early spallation. CeSZ shows a failure mode consisting of continuous weight loss on stepwise degradation in thin layers. Thus no total spallation occurred.

2 Crystal habit and phase content strongly depend on chemistry. The phases formed on EB-PVD do not necessarily conform to equilibrium diagrams.

3 For CeSZ TBCs, remarkable compositional fluctuations across coating thickness were found. They are due to overcritical differences in the vapor pressures of the components, which become apparent during single-source EB-PVD processing. TBCs composed of components of widely differing vapor pressures require a dual source evaporation process.

References

1 Rhys-Jones, T. N., and Toriz, F. C., "Thermal Barrier Coatings for Turbine Applications in Aero Engines," *High Temp. Technol.*, Vol. 7, No. 2, 1989, pp. 73–81.

2 Demaray, R. E., Fairbanks, J. W., and Boone, D. H., "Physical Vapor Deposition of Ceramic Coatings for Gas Turbine Engine Components," ASME Paper No. 82-GT-264, 1982.

3 Meier, S. M., and Gupta, D. K., "The Evolution of Thermal Barrier Coatings in Gas Turbine Engine Applications," ASME JOURNAL OF ENGINEERING FOR GAS TURBINES AND POWER, Vol. 116, 1994, pp. 250–257.

4 Fritscher, K., Peters, M., Rätzer-Scheibe, H.-J., and Schulz, U., "Superalloys and Coatings," in: *Advanced Aerospace Materials*, H. Buhl, ed., Springer-Verlag Berlin–Heidelberg, 1992, pp. 84–107.

5 Toriz, F. C., Thakker, A. B., and Gupta, S. K., "Thermal Barrier Coatings for Jet Engines," ASME Paper No. 88-GT-279.

6 Nagaraj, B. A., and Wortmann, D. J., "Burner Rig Evaluation of Ceramic Coatings With Vanadium-Contaminated Fuels," ASME JOURNAL OF ENGINEERING FOR GAS TURBINES AND POWER, Vol. 112, 1990, pp. 536–542.

7 Nagaraj, B. A., Maricocchi, A. F., Wortmann, D. J., Patton, J. S., and Clarke, R. L., "Hot Corrosion Resistance of Thermal Barrier Coatings," ASME Paper No. 92-GT-44, 1992.

8 Vincenzini, P., Appiano, G., Brossa, F., and Meriani, S., "Stability of Thermal Barrier Coatings," *Proc. 3th Int. Symp. Ceramic Materials and Components for Engines,* Tennery, V. J., ed., 1989, pp. 201–210.

9 Taylor, R., Brandon, J. R., and Morrell, P., "Microstructure, Composition and Property Relationships of Plasma-Sprayed Thermal Barrier Coatings," *Surface and Coatings Technology,* Vol. 50, 1992, pp. 141–149.

10 Jones, R. L., and Williams, C. E., "Hot Corrosion Studies of Zirconia Ceramics," *Surface and Coatings Technology,* Vol. 32, 1987, pp. 349–358.

11 Siemers, P. A., and McKee, D. W., US Patent No. 4328 285, Apr. 5, 1982.

12 Anderson, N. P., and Sheffler, K. D., "Development of Strain Tolerant Thermal Barrier Coating Systems," NASA Contract NAS3-22548, report No. NASA-CR-168251, 1983.

13 Stecura, S., "New ZrO_2–Yb_2O_3 Plasma-Sprayed Coatings for Thermal Barrier Applications," *Thin Solid Films,* Vol. 150, 1987, pp. 15–40.

14 Jones, R. L., and Reidy, R. F., "Development of Hot Corrosion Resistant Scandia-Stabilized Zirconia Thermal Barrier Coatings," *Proc. ASM/TMS Materials Week,* 1994.

15 Jones, R. L., "The Development of Hot-Corrosion-Resistant Zirconia Thermal Barrier Coatings," *Materials at High Temperature,* Vol. 9, No. 4, 1991, pp. 228–236.

16 Fritscher, K., and Bunk, W., "Density-Graded TBC's Processed by EB-PVD," *1st International Symposium on Functionally Gradient Material. Proc.,* Yamanouchi, M., et al., eds., Society of Non-Traditional Technology, 1990, Tokyo, Japan, pp. 91–96.

17 Schulz, U., Fritscher, K., and Peters, M., "EB-PVD Y_2O_3 and CeO_2/Y_2O_3 Stabilized Zirconia Thermal Barrier Coatings—Crystal Habit and Phase Compositions," *Surface and Coatings Technology,* Vol. 82, 1996, pp. 259–269.

18 Schulz, U., and Fritscher, K., "Behavior of Subsurface-Modified EB-PVD Processed Thermal Barrier Coatings on Cyclic Tests," in: *Ceramic Coatings,* K. Kokini, ed., ASME MD-Vol. 44, 1993, pp. 163–172.

19 Thornton, J. A., "Influence of Substrate Temperature and Deposition Rate on Structure of Thick Sputtered Cu Coatings," *J. Vac. Sci. Technol.,* Vol. 12, No. 4, 1975, pp. 830–835.

20 Movchan, B. A., and Demchishin, A. V., *Fiz. Met. Metalloved.,* Vol. 28, 1969, pp. 83–90.

21 Lelait, L., Alperine, S., and Diot, C., "Microstructural Investigation of EBPVD Thermal Barrier Coatings," *Journal de Physique IV,* Colloque C9, Vol. 3, 1993, pp. 645–654.

22 Sohn, Y. H., Cho, K., Lee, E. Y., Biederman, R. R., and Sisson, R. D., Jr., "Phase Analysis of Physical Vapor Deposited ZrO_2–8wt% Y_2O_3 Thermal Barrier Coatings," in: *Materials for Advanced Power Engineering—Part II,* D. Coutsouradis et al., eds., Kluwer Academic Publishers, 1994, pp. 1345–1356.

23 Schulz, U., "Wachstum, Mikrostruktur und Lebensdauer von elektronenstrahlaufgedampften Wärmedämmschicht-Systemen für Turbinenschaufeln," *Shaker Verlag Aachen,* 1995, ISBN 3-8265-0754.

24 Fritscher, K., "Über das EB PVD-Verfahren erzeugte, mehrfach gradierte Wärmedämmschichten," *Workshop Gradientenwerkstoffe 1993,* W. A. Kaysser et al., eds., DLR Köln, 1993, pp. 6/1–4.

25 Stecura, S., "Effects of Compositional Changes on the Performance of a Thermal Barrier Coating System," NASA Technical Memorandum 78976, 1979.

26 Miller, R. A., and Berndt, C. C., "Performance of Thermal Barrier Coatings in High Heat Flux Environments," *Thin Solid Films,* Vol. 119, 1984, pp. 195–202.

27 Singh, P., Sainkar, S. R., Kuber, M. V., Gunjikar, V. G., Shinde, R. F., and Date, S. K., "La-Stabilized Zirconia: Synthesis and Characterization," *Materials Letters,* Vol. 9, No. 2/3, 1990, pp. 65–70.

28 Jacobson, N. S., "Thermodynamic Properties of Some Metal Oxide-Zirconia Systems," NASA TM 102351, 1989, pp. 1–63.

Temperature Estimation and Life Prediction of Turbine Blades Using Post-Service Oxidation Measurements

V. P. Swaminathan
Southwest Research Institute,
6220 Culebra,
San Antonio, TX 78228

J. M. Allen
Consulting Engineer,
Cupertino, CA 95014

G. L. Touchton
Electric Power Research Institute,
Palo Alto, CA 94304

The depth of internal oxidation and nitridation from the surface of the 16 cooling holes in a first-stage turbine blade was measured by optical microscopy after 32,000 hours of service. Maximum depth of penetration was 15.5 mils (0.4 mm) at the trailing edge hole. An effort was made to predict hole surface metal temperatures based on these measurements using the Arrhenius relationship between time and temperature with depth of oxidation assumed to be parabolic with time. Reasonable correlations were obtained between finite element analysis results and temperature estimates based on the oxidation measurements. In the thickest part of the airfoil, where metal temperature is minimum, intergranular cracks up to 12.6 mils (0.32 mm) in depth were found at the surface of the cooling holes. Measurable oxidation attack was only one to two mils (0.025–0.050 mm). Based on an approximate elastic-relaxation-local inelastic stress analysis, it was calculated that inelastic local strains of over one percent occur at the points of cracking. No cracking was observed in the more heavily oxidized, lower stressed, hotter holes. However, cracking occurred in a trailing edge tip cooling hole when weld repair of the tip squealer was attempted, due to embrittlement and grain boundary oxidation from service exposure. Temperature estimates suitable for life assessment purposes using oxidation measurements appears to be a possible technique that should be further developed and validated.

Introduction

Cooled gas turbine blade life is primarily limited by thermal-mechanical fatigue (TMF) or by surface degradation due to oxidation and corrosion. In peak load applications involving frequent startups and shutdowns, TMF will likely be the limiting mode of failure, while in combined cycle or cogeneration base loaded plants, oxidation and corrosion will govern life. In natural gas fired units, oxidation is the dominant mode of environmental attack.

Cooled blade airfoils are generally coated with a diffusion aluminide coating or a MCrAlY overlay coating. MCrAlY coatings consist of a NiCoCrAlY composition in varying amounts plus, in some cases, small additions of Hf, Si, Ta, or Re. Duplex coatings are also used where a diffused aluminude is applied over a MCrAlY coating, or vice versa. Without suitable coatings, satisfactory life cannot be achieved at the surface temperatures at which these blades operate.

Experience has shown that cooling passages near the surface also oxidize significantly during service. To address this problem, internal aluminization processes have been developed. Cooling hole passage oxidation is not so severe as on external surfaces because of the lower temperatures involved, but significant surface layer and grain boundary damage could be caused by internal oxidation and nitridation. Moreover, the highest tensile stresses occur on the colder surfaces on the inside of the blade.

Internal oxidation and nitridation reduce mechanical properties and increase risk of failure. It is therefore important to understand what impact such damage has on structural integrity and the rate at which it occurs. In this paper, cooling hole oxidation from a blade examined after 32,000 hours service is characterized and the feasibility of using oxidation measurements to estimate thermal history is explored. The surface cracking noted on certain cooling holes is also analyzed using an elastic stress calculation and Neuber's rule to estimate local inelastic strain around the holes.

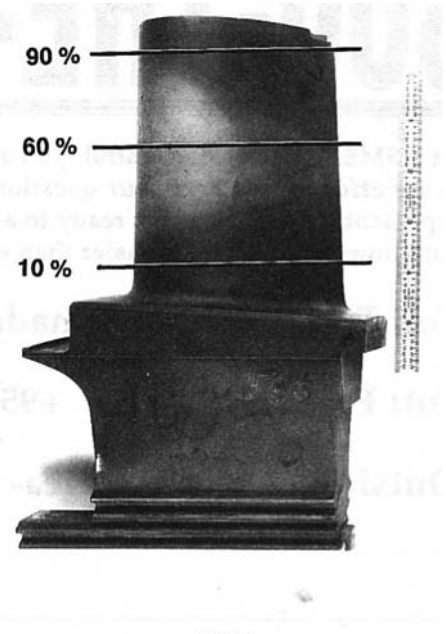

Fig. 1 First-stage blade and sectioning planes shown at three locations of the blade airfoil

[1] Trademark of Special Metals Corporation.

Contributed by the International Gas Turbine Institute and presented at the 41st International Gas Turbine and Aeroengine Congress and Exhibition, Birmingham, United Kingdom, June 10–13, 1996. Manuscript received at ASME Headquarters February 1996. Paper No. 96-GT-528. Associate Technical Editor: J. N. Shinn.

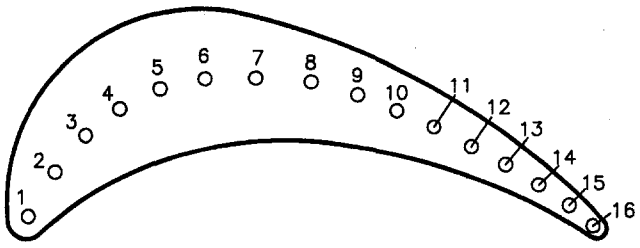

Fig. 2 Cross-sectional diagram of the blade airfoil showing the cooling hole numbering sequence

Material and Measurement Procedure

A first-stage turbine blade was metallurgically examined after 32,000 hours of base-loaded service in a W501D5 model gas turbine. The blades operated at a firing temperature of 2020°F (1104°C) for the first 16,000 hours, at which time they were recoated and reheat treated, and at 2065°F (1129°C) firing temperature for the second 16,000 hours. The blade material was UDIMET 520 (U-520)[1] with nominal composition of 57Ni19Cr12Co6Mo1W2Al3Ti.05C.005B. Standard heat treatment is 2025 F/4h/AC + 1550 F/24h/AC + 1400 F/16h/AC.

In addition to evaluations of external coating and general condition of the blade, the 16 cooling passages were examined by sectioning the blade at distances of 10, 60, and 90 percent of airfoil height (above the platform); see Fig. 1. The 60 percent height section, cooling hole pattern, and numbering convention are shown in Fig. 2. Hole No. 1 is at the leading edge and No. 16 at the trailing edge. The 16 cooling holes vary in diameter and are located along the camber line of the airfoil (line along the midthickness of the airfoil). The holes are electrochemically milled (ECM'd) from the airfoil tip to the base of the airfoil at one diameter and intersect larger diameter holes ECM'd from the root end of the blade.

Metallurgical mounts were prepared and examined under an optical microscope. Hole diameters were measured at the three airfoil heights. Since the hole shapes were not exactly round, maximum and minimum diameters were recorded. Each hole was examined, and the maximum depth of oxidation measured at the three radial locations. The maximum depth of intergranular oxidation (IGO) was also measured and recorded. In addition, the holes were examined for cracking, and crack depths and locations recorded where cracking was observed.

Results

Hole Diameter Measurements. The results from the hole diameter measurements are summarized in Table 1.

Table 1 lists the minimum and maximum diameter measurements for each hole at the 10, 60, and 90 percent height sections. The average diameter listed in column 5 in the table is the average of all six measurements for each hole, except for holes 5, 10, and 11, where diameter measurements could not be made at 90 percent height because sections had been locally cut out for other evaluations.

It can be seen from columns 2–4 in Table 1 that the cooling holes were generally round within +0.001/−0.001 in. The only exceptions were holes 13, 14, and 16 at the 10 percent height section. At this location, these holes were out-of-round by +0.0035/−0.0035 in., +0.005/−0.005 in. and +0.0035/−0.0035 in., respectively. At the 60 and 90 percent height locations, these holes were also round to within +0.001/−0.001 inches.

The holes were somewhat tapered. The average diameter at the 90 percent height section was 0.0015 to 0.0055 in. smaller than at the 10 percent section. Relative to the average diameters given in column 5 of Table 1, the 90 percent height diameters differed by +0.0003/−0.003 in. The average difference in tip to average hole diameter was only −0.0013 in.

It is significant to note that the diameters were largest in the lowest temperature section (10 percent section) where oxidation was much less than in the other two sections. Since the cooling holes were drilled to constant nominal diameters, it would therefore appear that the oxidation observed was primarily internal and that very little metal loss occurred. Original hole diameters were not available.

Oxidation Measurements. Figure 3 illustrates the typical oxidation at a cooling hole. Uniformly scattered dark oxide particles (aluminum oxide) and preferential grain boundary oxidation were present. Needle-shaped light grey particles are titanium nitride. The maximum depth of oxidation/nitridation (d) was measured in each hole at the three sections. The maximum depth of intergranular oxidation (IGO) was also measured. The results are shown in Table 2 and Fig. 4.

It can be seen from Table 2 and Fig. 4 that the depth of oxidation/nitridation and IGO is insignificant at the 10 percent height location, where metal temperatures are substantially lower than in the upper half of the blade. At the 60 and 90 percent height sections, depth of attack is significant in the holes

Table 1 Hole diameter measurements

Hole	Dia. at 10%	Dia. at 60%	Dia. at 90%	Avg. Dia.	Variation
1	.107x.107	.103x.103	.102x.103	.1042 in.	+.0028/-.002 in.
2	.100x.102	.101x.097	.095x.096	.0985	+.0035/-.0025
3	.103x.104	.101x.102	.103x.103	.1027	+.0013/-.0017
4	.106x.107	.103x.105	.103x.103	.1045	+.0025/-.0015
5	.101x.103	.102x.103	not meas.	.1023	+.0007/-.0013
6	.105x.105	.102x.101	.103x.103	.1032	+.0018/-.0022
7	.104x.106	.104x.105	.104x.103	.1043	+.0017/-.0013
8	.097x.098	.095x.093	.094x.094	.0952	+.0028/-.0022
9	.091x.089	.087x.087	.086x.086	.0877	+.0033/-.0017
10	.089x.090	.087x.088	not meas.	.0885	+.0015/-.0015
11	.079x.081	.078x.078	not meas.	.0790	+.0020/-.0010
12	.077x.079	.079x.078	.077x.076	.0777	+.0013/-.0017
13	.077x.081	.077x.078	.075x.077	.0775	+.0036/-.0025
14	.078x.088	.076x.077	.078x.078	.0792	+.0088/-.0032
15	.064x.063	.060x.059	.061x.060	.0612	+.0028/-.0022
16	.056x.063	.058x.058	.056x.054	.0575	+.0055/-.0035

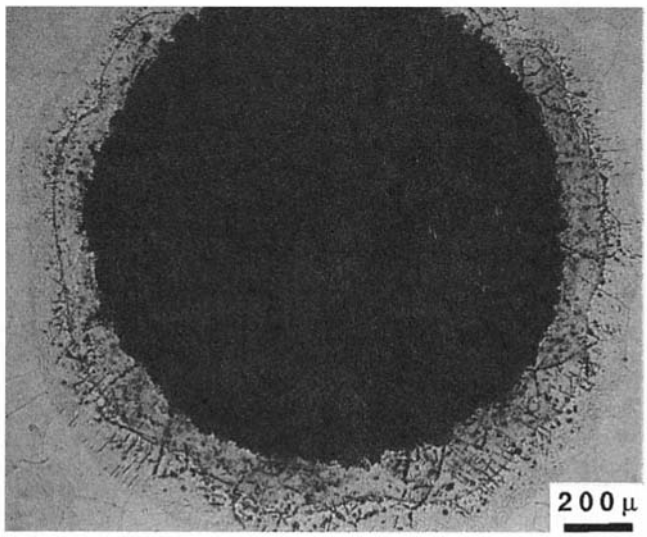

Fig. 3 Optical photos of oxidation of cooling hole number 16 (trailing edge hole) showing oxide particles (dark) and nitride phase (light grey)

closest to the blade surface, i.e., hole 1 at the leading edge of the airfoil and holes 12–16 in the trailing edge of the airfoil. The extent of the leading edge hole oxidation at 60 percent height is shown in Fig. 5.

It appears that there was no significant metal loss from oxidation because hole diameters in the most oxidized sections (60 and 90 percent sections) were slightly smaller than in the colder section (10 percent section) where virtually no internal oxidation was observed.

Cooling Hole Cracking. At the 60 percent height section, cracking was observed in holes 3–7. Typical cracking is shown in Fig. 6. The depths and locations are shown in Table 3 and Fig. 7 for each affected hole.

Analysis of Oxidation Measurements

It is known that internal oxidation and nitridation can cause embrittlement of superalloys [1], but it is not known to what extent blade life is actually reduced from the type of attack observed in these blades. Mechanical properties from similarly oxidized material under simulated turbine operating conditions are needed to answer this question. An important first step in this regard is to be able to relate oxidation measurements to the thermal history of the part. To explore the feasibility of doing this, the oxidation measurements made in this study were used to predict surface metal temperature of the cooling holes and the results evaluated in light of what is known about actual temperatures.

Metal Temperature Predictions. To predict metal temperature based on measurements, oxidation depth was assumed to be parabolic with time, based on the work by Chang [1], and to conform to the Arrhenius relationship between time and temperature, i.e.,

$$[\log C - \log (d^2/t)][T + 460] = Q/R \qquad (1)$$

where:

$\log C$ = const
d = depth of oxidation front, in.
t = time, hours
T = temperature, °F
Q = activation energy, ft-lb/lb
R = gas constant, ft/R

For blade alloy Rene 80, Chang [1] measured the constants C and Q/R in static furnace tests. The resulting relationship was

$$[4.300 - \log (d^2/t)][T + 460] = 25{,}700. \qquad (2)$$

Equation (2) was used to predict hole surface temperatures of the blade. Since the turbine operated at different firing temperatures and hence different metal temperatures for the two 16,000 hour periods, an equivalent operating time referenced to the higher firing temperature, 2065°F (1129°C), was computed using Eq. (2) and used in the analysis of the data. The equivalent time was computed to be 26,400 hours. The temperature estimates for the 60 and 90 percent height sections are shown in Figs. 8 and 9.

The results in Figs. 8 and 9 are plotted against hole camber line distance from the leading edge hole. Polynomial regression fits of the data are also shown in Figs. 8 and 9. The regression fits were made on the premise that actual hole temperatures in the blade vary smoothly along this line and hence deviations from the regression curves should provide reasonable estimates of measurement standard deviation. The standard deviations obtained were 31.7°F (17.6°C) for the 60 percent height section and 10.7°F (5.9°C) for the 90 percent height section. It can be seen from Fig. 8 that the relatively large standard deviation for the 60 percent height data is due to the large scatter in the oxidation measurements in the lowest temperature holes where oxidation is less than two mils and measurement accuracy is low.

Analysis of Hole Cracking

To evaluate the hole cracking that was observed, an approximate elastic stress analysis was performed to determine nominal elastic stress distribution through the thickness of the airfoil, and local strain at the edge of the holes was estimated using Nueber's Rule and stress-strain-creep properties of the material.

Elastic Stress Analysis. The hole cracking observed in holes 3–7, see Table 3 and Fig. 7, occurred in the thickest portion of the airfoil where temperature differences through the thickness are greatest. Figure 10 shows the estimated surface to cooling hole temperature difference distribution based on the temperature contours published in [2] for this blade. It can be seen that the maximum thru-the-thickness difference occurs in holes 3–7, where the cracking was observed. The estimated temperature distribution, also based on the contours in [2],

Table 2 Depth (d) of oxidation measurements at the three airfoil sections

Hole	d at 10%	d at 60%	d at 90%	IGO at 10%	IGO at 60%	IGO at 90%
1	.0007 in.	.0103 in.	.0066 in.	.0024 in.	.0090 in.	.0053 in.
2	.0002	.002	.0033	.0018	.0043	.0031
3	.0000	.0018	.0015	.0017	.0023	.0009
4	.0002	.0009	.0010	.0017	.0021	.0007
5	.0002	.0018	not meas.	.0013	.0016	not meas.
6	.0002	.0009	.0009	.0017	.0034	.0012
7	.0002	.0008	.0008	.0013	.0035	.0014
8	.0003	.0021	.0016	.0015	.0041	.0020
9	.0002	.002	.0018	.0012	.0050	.0012
10	.0002	.002	not meas.	.0008	.0030	not meas.
11	.0002	.0035	not meas.	.0013	.0040	not meas.
12	.0003	.0055	.0058	.0002	.0055	.0045
13	.0003	.0095	.008	.0004	.0065	.0068
14	.0005	.008	.0103	.0000	.0055	.0085
15	.0005	.0115	.0153	.0008	.0090	.0130
16	.0012	.0155	.0150	.0000	.0125	.0133

along a line perpendicular to the camber line and passing through hole number 5 is plotted in Fig. 11.

In this region of the airfoil, high steady-state elastic stresses occur in directions perpendicular to the cross section and in-the-plane perpendicular to the direction of cracking that was observed. A good estimate of this stress can be obtained by using the equation for thermal stress in a flat plate [3] as demonstrated in [4]. The nominal elastic stress distribution through the thickness was computed using the flat plate equation and temperature dependent coefficient of expansion and Young's modulus from [5] for similar alloy wrought U-500. The resulting stress distribution is also shown in Fig. 11.

At the surface of the holes, high local stresses and strains occur due to stress concentration from the holes. The peak value of stress occurs at the location of cracking and is a function of hole spacing to diameter ratio and the in-plane components of nominal stress perpendicular and parallel to the cracks. The stress concentration factor for the holes in question was estimated to be 2.5 based on stress concentration factors given in [6, 7] for a row of holes under biaxial loading conditions. This resulted in a peak elastic stress of 174 ksi (1199 MPa).

Inelastic Strain Analysis. Nominal stress, S versus time at the edge of the holes was estimated by using the equation for stress relaxation [8] and assuming power law creep. Creep properties were estimated based on a Monkman–Grant-type relationship between creep rate and time to rupture (creep rate $\times$ time to rupture = 0.02) and stress rupture data from [9] at a temperature of 1300°F (704°C).

Local strain was estimated using Neuber's rule [10], which states that

$$\sigma\epsilon = SeK_t^2 \tag{3}$$

where:

σ = local stress
ϵ = local strain
S = nominal stress
e = nominal strain = constant
K_t = elastic stress concentration factor

Assuming a power law relation between stress and strain,

$$e = kS^n \tag{4}$$

and

$$\epsilon = k\sigma^n \tag{5}$$

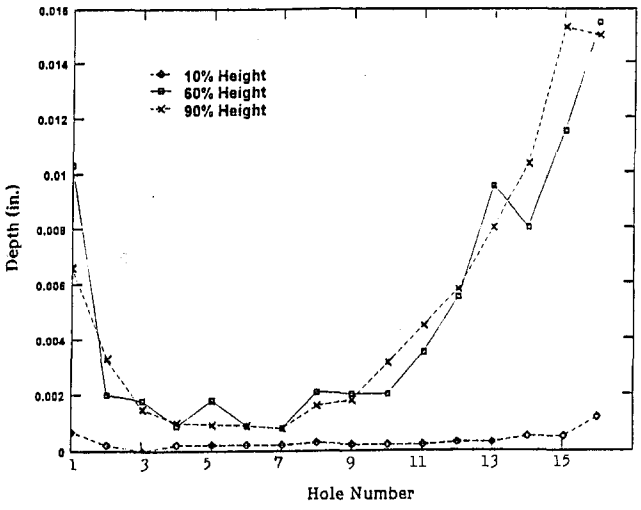

Fig. 4 Plot of depths of oxidation at 10, 60, and 90 percent heights for the 16 cooling holes

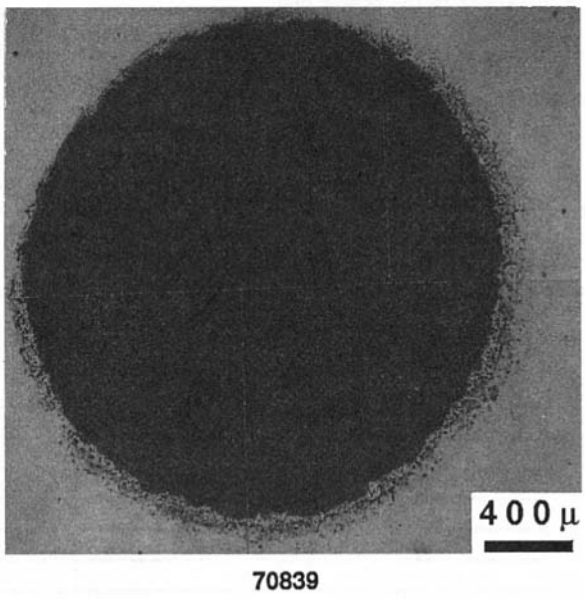

Fig. 5 Optical photomicrograph of leading edge hole (hole No. 1) oxidation at 60 percent height

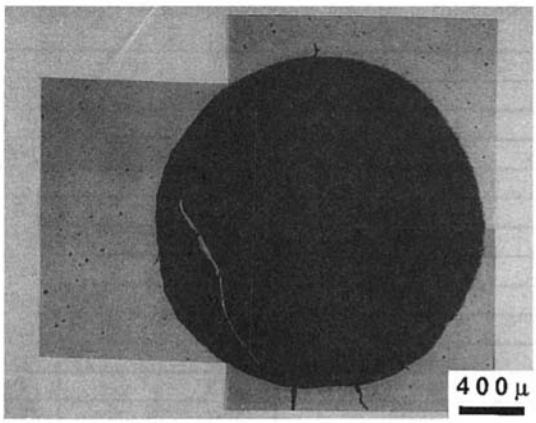

70115

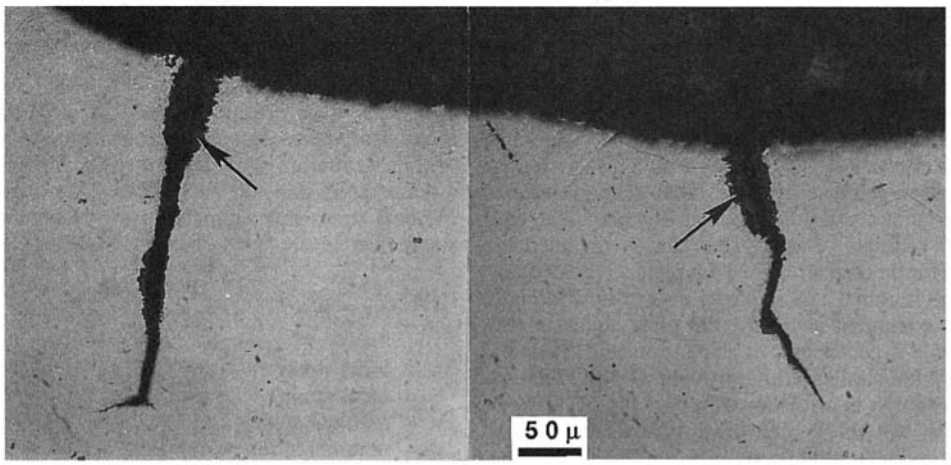

54776-77

Fig. 6 Intergranular cracking at cooling hole number 5 at 60 percent height. Maximum crack depth is about 0.009 in. (0.23 mm). Oxide can be seen on the crack surface (arrows).

where:

k = constant
n = exponent in the power law

Solving Eq. (4) for S and Eq. (5) for σ, and substituting the results into Eq. (3), yields the following equation between nominal and local strain:

$$\epsilon = eK_t^{2n/(n+1)} \tag{6}$$

Equations (6) and (3) were used to estimate local strain and then stress versus time at the edge of the hole with $n = 4.2$ when local stress is equal to the yield stress (107 ksi) and increasing to 6.3 as inelastic strain approaches total strain. The results are shown in Fig. 12. It can be seen that a total strain of about 1.3 percent results of which 1.2 percent is inelastic. Of the inelastic component, 0.7 percent is plastic strain and 0.5 percent is attributable to creep relaxation. Since the state of local deformation at the holes approaches that of plane strain, fracture strain would be expected to be low. While actual data are not available, it is not unreasonable to expect that it could be as low as 1.2 percent for nickel base superalloys under the conditions involved. In addition, although the temperature is relatively low (about 1300°F) in this location, the possibility of environmental effect cannot be ruled out in view of the very high tensile strains that are present and the observed oxidation of the cracks.

As has been noted, these cracks run longitudinally along the hole (radial direction of the blade) and probably arrest as they

Table 3 Cooling hole cracking at the 60 percent height section

Hole No.	Crack Depth	Location*	Crack Depth	Location*
3	.0045 inches	6:00 o'clock		
4	.0099	6:00 o'clock	.0086 inches	12:00 o'clock
5	.0088	6:00 o'clock	.0058	12:00 o'clock
6	.0126	6:00 o'clock	.0072	12:00 o'clock
7	.0078	7:00 o'clock	.0089	12:00 o'clock

* Positions 6:00 o'clock and 12:00 o'clock are perpendicular to the camber line of the airfoil with 12:00 o'clock toward the suction (convex) side and 6:00 o'clock toward the pressure (concave) side of the airfoil.

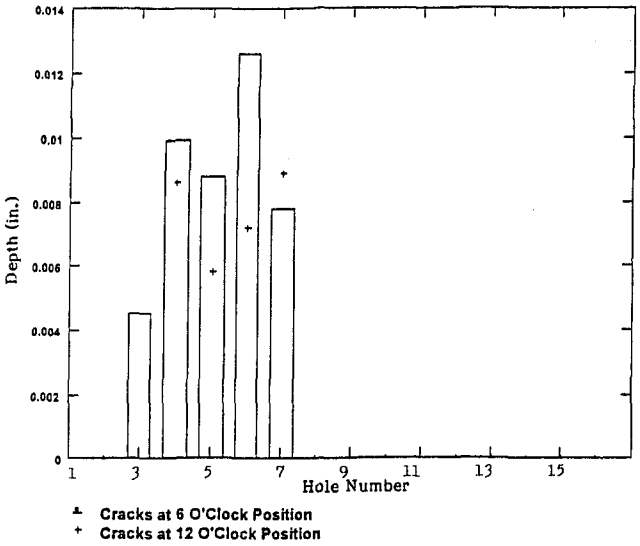

Fig. 7 Histogram of depth of intergranular cracks at 60 percent span

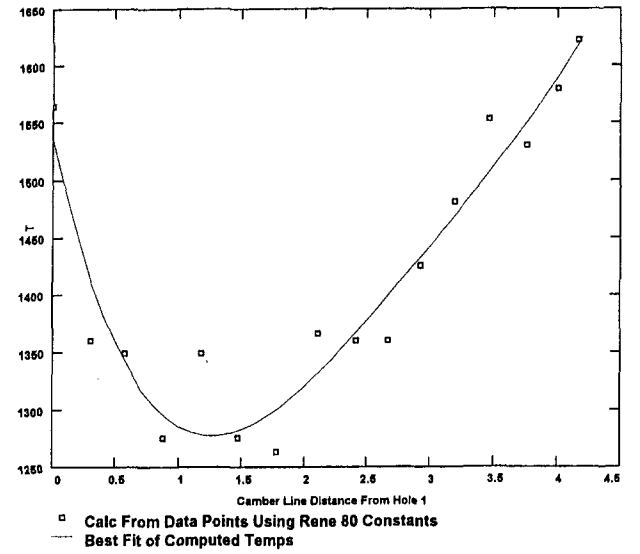

Fig. 8 Best fit of computed temperatures and calculated values at 60 percent span using oxidation depth and Rene 80 constants

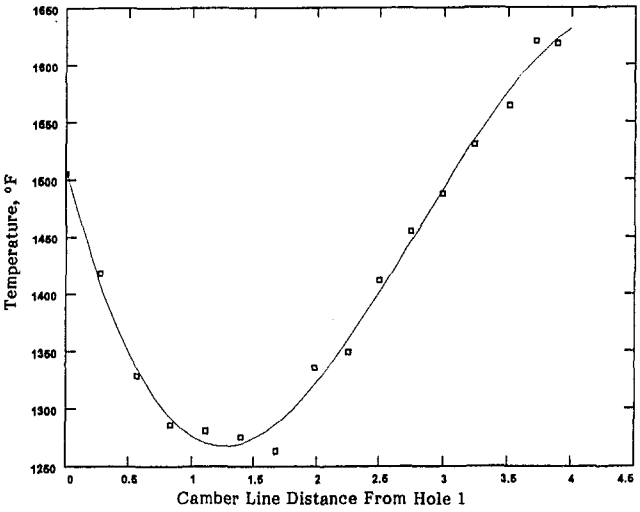

Fig. 9 Predicted temperatures at 90 percent span

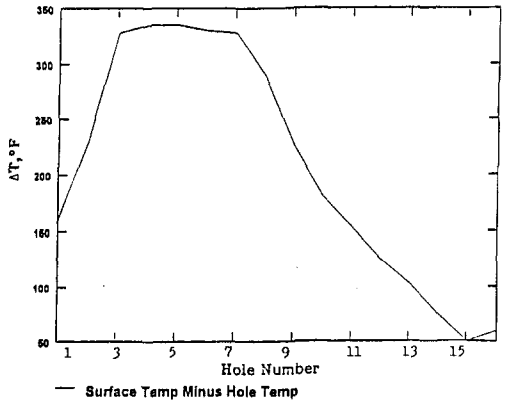

Fig. 10 Estimated through thickness temperature difference (ΔT) from outside surface to cooling hole

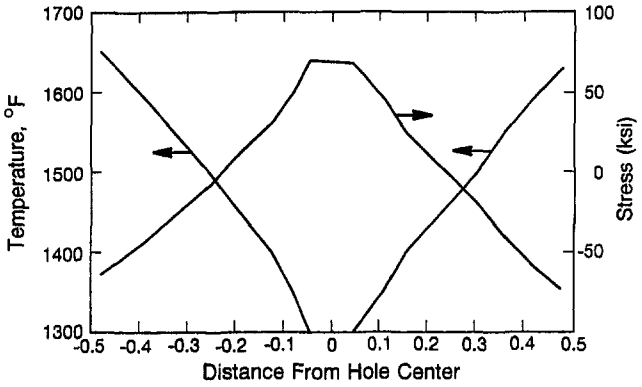

Fig. 11 Temperature and elastic stress distribution along line through hole number 5

propagate into lower stress regions and as the thermal stresses relax from creep. Since they are not normal to the direction of centrifugal stress, the risk of blade failure from these cracks would seem to be low.

Low Cycle Fatigue Analysis. Since the local strains are large, the possibility of LCF cracking was also considered. LCF data for U-520 material could not be found in the literature, but data for continuous cycling, as well as with one hour hold times, on sister alloy U-720 have been reported at 1350°F (732°C) [11], which is in the right temperature range for holes 3–7. As noted earlier, these blades had been cycled less than 50 times

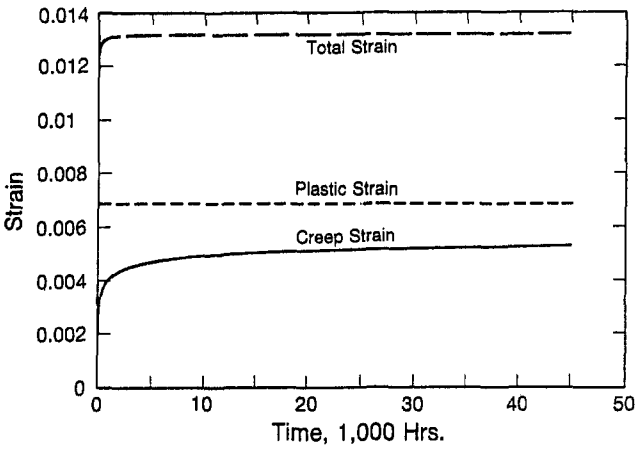

Fig. 12 Local strain at the edge of hole number 5

Table 4 Expected resistance of U-520 versus Rene 80 from metal loss measurements of other alloys and comparison of Al and Cr contents [12]

Alloy	% Aluminum	% Chromium	Relative Performance
IN713C	5.9	12.0	1.0 (Best)
U500	3.0	18.0	0.6
IN738	3.4	16.0	0.5
Rene 80	3.0	14.0	0.5 Expected
U520	2.0	19.0	<0.5 Expected

in service. The strain range required to cause LCF cracking of U-720 in 50 cycles is 3.6 percent. The actual cyclic strain assuming completely elastic behavior during cycling is estimated to be about 0.77 percent (0.67 percent tensile for startup to full load and perhaps −0.10 percent during shutdown).

The cyclic life for a strain range of 0.77 percent for U-720 is 3300 cycles. Because the cyclic strain is greater than the yield strain, it is probable that some cyclic plasticity and creep will occur after sufficient stress relaxation has occurred, which could perhaps increase the cyclic strain range to around 1 percent. In these circumstances, the estimated cycles to cracking is 1000 cycles. In view of these estimates, it does not appear that LCF is a primary cause of the cracking that was observed.

Discussion

Assessment of Temperature Predictions. While the predictions of temperature from this exercise appear to be reasonable, directly measured temperatures were not available for comparison. It is expected that they might possibly be somewhat too high in view of the following considerations:

First, because no data on U-520 or other nickel base blade alloys, except for alloy Rene 80, could be found on internal oxidation, the Rene 80 data were used for purposes of this study. This was considered to be reasonable in light of some metal loss data obtained in a three atmosphere combustor rig on pin samples of three other alloys (IN-713C, IN-738, and U-500) of varying aluminum and chromium compositions [12]. The relative performance of the three alloys and their aluminum and chromium contents are listed in Table 4. The aluminum and chromium contents of U-520 and Rene 80 are also shown for comparison purposes.

It can be seen that IN-713C performed significantly better than IN-738 and U-500 in these tests. That is undoubtedly because IN-713C has an aluminum content (5.9 percent) that is nearly twice as high as that for IN-738 (3.4 percent) and U-500 (3.0 percent). The Rene 80 aluminum content is 3.0 percent, while the U520 content is 2 percent. Based on this information, it is anticipated that Rene 80 would probably behave similarly to IN-738 and U-500 and that U-520 behavior would be somewhat worse. Thus, temperature predictions for U-520 using Rene 80 constants would be expected to be on the high side.

Another possible reason for the over prediction of temperature is that oxidation may occur more rapidly under turbine operating conditions than in a static furnace environment. In service, the hole surfaces are exposed to high velocity air and order of magnitude higher pressures than are samples exposed in an atmospheric furnace.

As far as actual temperatures of the subject blade are concerned, isotherms for the midheight section and some optical pyrometer traces are reported in [2], but without labels. Efforts were made to calibrate these isotherms by independent calculation using the EPRI computer program BLADE-CT [13]. While accurate blade geometry measurements were available for modeling of the blade, heat transfer boundary conditions had to be calculated based on imprecise information. Thus the accuracy of the calibrating calculations is also open to question. The results obtained were generally close to the predictions with maximum difference being 50–75°F (28–42°C) lower at the trailing edge holes, as shown in Fig. 13.

All things considered, the results suggest that prediction of temperature and temperature distributions from oxidation measurements is feasible and a practical, low-cost approach. It is evident, however, that data from samples exposed to properly simulated turbine environments must be used to obtain acceptable results. A properly simulated test environment is one that produces oxidation patterns like those seen in service and that has been further validated by comparisons of predicted temperatures with temperatures established by calculation and direct engine measurements.

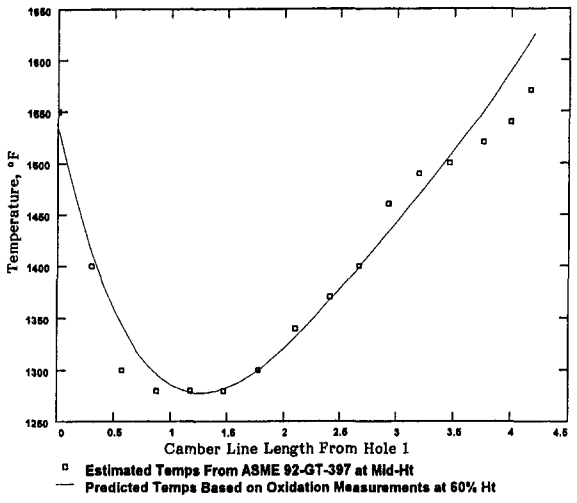

Fig. 13 Comparison of calculated temperatures and those estimated using data from [2]

Effect of Oxidation on Blade Integrity. The concern about the type of environmental attack seen in this investigation is the effect it has on mechanical properties. The environment is known to be embrittling [1, 14, 15], but whether sufficiently so to cause problems depends on the degree of embrittlement and the details of the loadings involved. The fact that no cracking was seen in the most severely oxidized holes in the blade examined in this study while cracks were seen in the least oxidized holes illustrates the point. It should also be noted that there was indirect evidence of embrittlement in the tip area of the blade because attempts to weld repair the squealer tip were unsuccessful due to cracking attributed to environmental embrittlement during service.

The ultimate goal of measuring internal oxidation of cooling passages is to be able to relate this information to remaining life or continued serviceability of the blade. However, this cannot be done on a simplistic basis if optimum use of the parts is to be realized. Mechanical properties of material that has been similarly exposed and detailed knowledge of the loadings on the blade in the affected areas are required for this purpose.

Summary and Conclusions

An exploratory study was made to predict the cooling hole surface temperature from oxidation measurements from the 16 cooling holes in a cooled first-stage turbine blade. The Arrhenius relationship between time and temperature was used with depth of oxidation assumed to be parabolic with time. Based on the results from this exercise, it appears that this is a feasible and practical approach. Correlations suitable for life assessment purposes must be established using data generated on samples exposed to test conditions that simulate the turbine operating environment and that have been validated by calculations and engine measurements.

The ultimate value of measuring internal oxidation of cooling passages is to be able to relate this information to the remaining useful life of the blade. This requires generation of mechanical properties from material that has been similarly exposed and a detailed knowledge of the loadings on the blade.

The hole cracking occurred in the lowest temperature holes in the thickest part of the airfoil where oxidation is minimum. In this region, through-the-thickness temperature difference is maximum and so is thermal stress. The local strain at the point of cracking was estimated using a nominal elastic and stress relaxation calculation and a local strain analysis using Neuber's rule. An inelastic strain of about 1.2 percent was estimated, which is believed to be sufficient to cause cracking for the type of geometry and the temperature (about 1300°F) (704°C) involved. Also, the presence of oxide scale and the intergranular morphology of cracks indicate that environment may play a role in the formation of these cracks. These cracks run longitudinally along the hole (parallel to the centrifugal stress direction) and probably do not threaten blade integrity.

Acknowledgments

The authors gratefully acknowledge the financial support of the Electric Power Research Institute (EPRI) for this study and publication thereof, and of ENRON Power Corp. for the metallurgical evaluation.

References

1 Chang, W. H., "Tensile Embrittlement of Turbine Blade Alloys After High-Temperature Exposure," *Superalloys,* 1972, pp. V-1 to V-41.

2 Whidden, G. L., and North, W. E., "Evolution of Spanwise-Hole Blade Cooling in Industrial Combustion Turbines," ASME Paper No. 92-GT-397, 1992.

3 Timoshenko, S., and Goodier, J. N., *Theory of Elasticity,* McGraw-Hill, New York, 1951, pp. 399–403.

4 Allen, J. M., "Effect of Temperature Dependent Mechanical Properties on Thermal Stress in a Cooled Gas Turbine Blade," ASME JOURNAL OF ENGINEERING FOR POWER, Vol. 104, 1982, pp. 349–353.

5 "Nickel Base Alloys," distributed by the Nickel Development Institute, courtesy of Inco Limited, 1987 printing.

6 Peterson, R. E., *Stress Concentration Design Factors,* Wiley, New York, 1953, p. 94.

7 Griffe, W., "Stress Concentration Factors for Plates With Holes," *Product Engineering,* Nov. 11, 1963, p. 112.

8 Timoshenko, S., "Strength of Materials, Part II," D. Van Nostrand Company, Inc., 3rd ed., Mar. 1956, pp. 530–533.

9 "Udimet 520 Alloy Performance Data," Special Metals Corp., New Hartford, NY, 1999.

10 Neuber, H., "Theory of Stress Concentration for Shear-Strained Prismatical Bodies With Arbitrary Stress-Strain Law," ASME *Journal of Applied Mechanics,* Vol. 28, 1961, pp. 544–550.

11 Whitlow, G. A., Johnson, R. L., Pridemore, W. H., and Allen, J. M., "Intermediate Temperature, Low Cycle Fatigue Behavior of Coated and Uncoated Nickel Base Superalloys in Air and Corrosive Sulfate Environments," ASME *Journal of Engineering Materials and Technology,* Vol. 106, 1984, pp. 43–49.

12 Lee, S. Y., Young, W. E., and Hussey, C. E., "Environmental Effects on the High-Temperature Corrosion of Superalloys in Present and Future Gas Turbines," ASME JOURNAL OF ENGINEERING FOR POWER, Vol. 94, 1972, pp. 149–153.

13 Wan, S. M., Lam, T. C. T., Allen, J. M., and McCloskey, T. H., "A Gas Turbine Blade Thermal/Structural Program With Linked Flow-Solid Modeling Capability," ASME Paper No. 94-GT-270, 1994.

14 Woodford, D. A., "Gas Phase Embrittlement of Superalloys—Implications for Life Assessment," *Proc. EPRI-ASM Life Assessment and Repair of Combustion Turbine Hot Section Components Conference,* Phoenix, Apr. 17–19, 1990, EPRI Report GS-7031, pp. 97–102.

15 Fox, H. M., "Gas Turbine Refurbishment Technology, A Perspective," *Proc. EPRI-ASM Life Assessment and Repair of Combustion Turbine Hot Section Components Conference,* Phoenix, Apr. 17–19, 1990, EPRI Report GS-7031, pp. 344–345.

Structural Integrity of a Gas Turbine Combustion System Subjected to Increased Dynamic Pressure

J. E. Barnes
Gas Turbine Engineering,
GE Company,
Schenectady, NY 12345

The effect of combustion dynamic pressure oscillations on the structural integrity of the MS 7001F dry low NO_x2 (DLN 2) combustion system has been evaluated using ANSYS [1] finite element analyses and high cycle fatigue material data. Analytical results were validated with laboratory measurements on the combustion system subjected to combustion dynamic pressure at actual gas turbine temperature and pressure operating conditions. The combustion liner, transition piece, impingement sleeve, and supports were proven to have excellent durability when subjected to dynamic loads. No risk of structural failure exists at anticipated dynamic pressures using assumptions shown to be conservative.

Introduction

The DLN 2 combustion system includes the liner and transition piece assemblies, which contain and direct the high-temperature combustion gases. These components are restrained at minimal locations and with adequate flexibility to allow for thermal expansion. The combustion process, especially premixed burning for low emissions, can have pressure oscillations at discrete frequencies due to flame stability. This stimulus combined with flexible attachments can result in considerable mechanical vibration. This vibration can cause fatigue cracking, which could lead to catastrophic failure.

Mechanical development of new combustion components and systems must trade off adequate flexibility to minimize thermal stress with sufficient stiffness to avoid vibration problems. Thermal stresses are routinely calculated for component design. However, vibratory stresses have not previously been adequately quantified. Structural dynamic analyses had not been utilized due to the complexity of the geometry, loading, and contact behavior. Measurements of strain were also of limited usefulness because critical locations are unknown and often inaccessible, and also owing to the high metal temperatures. Previous structural dynamic analysis of a simplified combustion model with components represented by rigid linkages and corresponding laboratory testing demonstrated that the system actively responds to the dynamic pressure [2]. However, no information regarding component vibratory stresses could be obtained from such analyses.

Historically, allowable limits on combustion dynamic pressure for structural integrity were based on field experience gained from years of operation. Direct application of field experience from different combustion systems to new designs was questionable. Analytical prediction of component life and development of a design methodology that considers dynamic pressure loading was therefore undertaken to assure the integrity of mechanical designs.

Nonlinear transient dynamic finite element analyses were necessary to predict the combustion system dynamic behavior that accurately compared with measured strains and accelerations. Component stiffnesses and masses as well as distributed pressure loading could then be accurately modeled. Contact behavior including the sliding friction at supports and seals was essential to computing the response. These numerous sliding interfaces add considerable damping to the system. Nonlinear gap conditions capable of maintaining or breaking physical contact according to relative displacements between components were also necessary. Attempts to utilize viscous damping and no-gap conditions to eliminate nonlinearities did not yield accurate results.

Modal analyses were used to compute natural frequencies and mode shapes. These results compared well with laboratory modal testing and were used to determine the proximity to resonance conditions.

Finite Element Model

The finite element model in Fig. 1 was constructed with particularly accurate representations in the areas of highest structural concern. These areas focus on the supports and regions of past structural problems. Accurate representation means geometry matches manufacturing drawings, fillets are included, and element size, shape, and aspect ratios are very good. This level of detail captures stress concentrations with the forced response analyses but would not be required for the modal analyses. Mesh density was initially based on past work with some refinement added as analyses were preformed. Nearly all eight noded brick elements were used to minimize the number of elements for what was expected to be a large model and a computationally intensive solution. Geometric symmetry was not exploited because future work may investigate effects of nonsymmetric loading and constraints. All results presented here are symmetric with respect to an axial–radial plane.

The transition piece assembly has accurate representations of the aft mount, body, and forward sleeve assembly. The aft frame has accurate stiffness and mass but the rib fillets are not included because these are near the neutral axis of the frame and therefore have low stress. The frame also lacks cooling holes. The impingement sleeve is accurate except for the lack of cooling holes. Stress concentration factors can be applied if large vibratory stresses occur near these holes.

The liner has accurate representations of the support stops, stiffening ribs, and cooling ring details except for the cooling holes. Again stress concentration factors can be applied if large vibratory stresses occur near the holes. Nodes around the liner

Contributed by the International Gas Turbine Institute and presented at the 41st International Gas Turbine and Aeroengine Congress and Exhibition, Birmingham, United Kingdom, June 10–13, 1996. Manuscript received at ASME Headquarters February 1996. Paper No. 96-GT-473. Associate Technical Editor: J. N. Shinn.

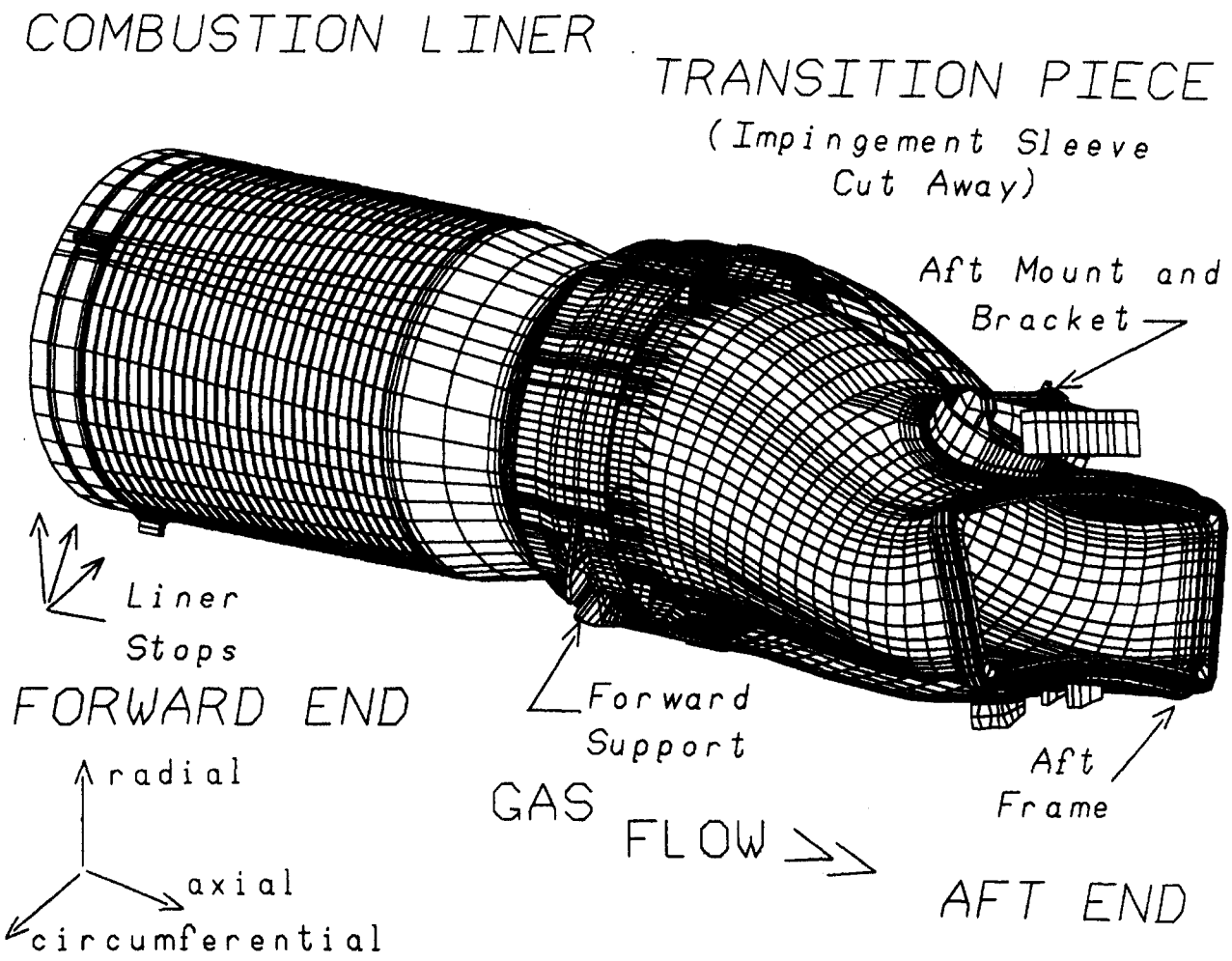

Fig. 1 Combustion system finite element model

align with the forward sleeve for point-to-point attachment of the hula seal.

The hula seals on the forward and aft ends of the liner are modeled as a combination of a normal spring and a tangential friction element. The hula seal has a stiffness computed with a small finite element model and a friction coefficient as measured in hula seal fretting tests.

Several notable details of the combustion system have not been included in the model. Seals at the aft end of the transition piece to the turbine section and adjacent transition pieces have not been modeled. Uncertainty exists regarding the contact force of these seals with the transition piece due to relative thermal expansion of the components. Due to the relatively small mass and stiffness of these seals, the only anticipated effect on the dynamic response is a reduction in damping. Therefore, this assumption is conservative. Crossfire tubes that connect adjacent combustion liners were not included. The connection of these relatively small tubes to the liner is very flexible so that minimal influence on the system behavior is expected. Also, because the crossfire tubes contact two different liners responding to dynamic pressure with some unknown phase difference, inclusion in this one-combustion-chamber model would be difficult.

The components modeled are considered to be far more flexible than the supporting structure, which is considered ground in this model.

Nonlinear Transient Dynamic Analyses

The transient dynamic finite element analysis determines the dynamic response of a structure to time dependent loads. The basic equation of motion is solved using finite element representations for the stiffness, mass, and damping of the structure. The direct integration method is used to solve for the unknown displacements at discrete time points. Numerous solutions are obtained at successive time points to represent the pressure oscillations.

The nonlinearities modeled are gap conditions and Coulomb friction. The hula seals at the liner forward end and between the liner and transition piece are prestressed, can maintain or break physical contact depending on relative displacements, and stick or slide tangentially with Coulomb friction. Gap conditions and Coulomb friction are also modeled on the liner stops and forward supports and on the aft mount to bracket, which also includes preload due to the bolt torque.

The pressure loading represents measurements from the laboratory while simulating actual machine conditions. Peak-to-peak pressure of 21 kPa at 160 Hz defines the combustion dynamics. Pressure measurements were made at several locations in the combustion system. The distribution of pressure was then predicted based on the theoretical shape of the dynamic combustion pressure wave.

System damping was specified using Rayleigh mass and stiffness damping constants. Ratios of actual to critical damping were measured for each individual component. Mass and stiffness constants were then calculated. The sensitivity of the response to the damping constants was tested, and very small effect was shown.

Superelements were utilized to reduce computer run times. This technique was well suited to this problem because linear

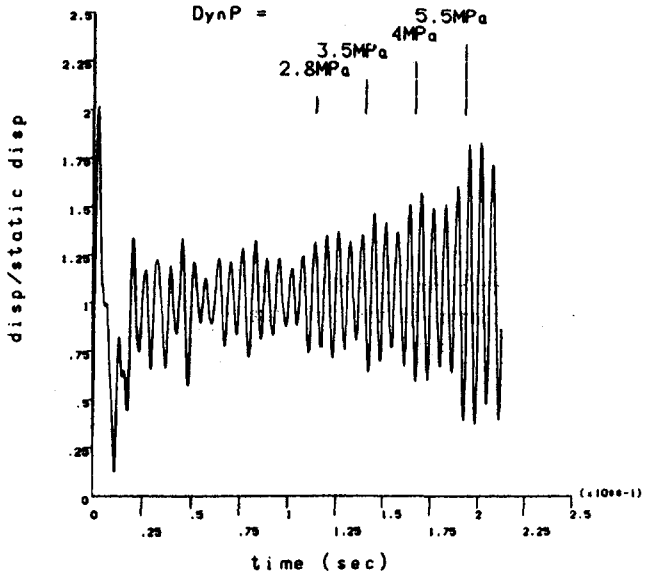

Fig. 2 Computed transition piece axial displacement versus time at forward end

portions of the model (superelements) are interconnected at relatively few points by the nonlinear contact elements.

Laboratory Validation

Strains and accelerations were measured in the laboratory at numerous locations. Figure 2 plots the computed oscillating axial displacement at an accelerometer location on the transition piece forward end. The ratio of dynamic displacement to the static displacement at 21 kPa dynamic pressure is 0.14. Integrating the measured acceleration at this location assuming a sinusoidal response yields a ratio of 0.16. The analysis has underpredicted displacement at this location by 12 percent. The location with the poorest correlation, radial motion at the aft end inner panel of the transition piece, had computed displacements five times greater than measured. In this case, the analysis predicted vibration of the inner panel of the transition piece. One possible explanation for this overprediction is that this vibration is actually damped by the seals, which are not included in the model. Subsequent wear and differences in component alignment during manufacturing could change this damping, so the assumption of no damping is conservative.

Circumferential vibratory strain divided by allowable strain between the aft mount and aft frame is plotted for several elements in Fig. 3. The time range in this plot is for two cycles and the dynamic pressure is 21 kPa. These elements cover an axial length of approximately 10 mm. A strain gage approximately centered in this region measured a ratio of 0.0038. Similarly good correlation exists at all gages with the exception of the gages associated with the inner panel vibration discussed above. Also, because the strain gages were positioned prior to completion of the analyses, half of the gages measured extremely low strain levels, as predicted by the analysis. In future testing, much better gage locations can be chosen based on the analytical results.

High Cycle Fatigue Life Prediction

High cycle fatigue is a function of vibratory stress, mean stress, metal temperature, and material type. Material testing was initiated before the vibratory stresses were computed but the mean stress and metal temperatures were known. Therefore, testing was limited to maximum mean stresses and metal temperature for each material over a range of vibratory stresses. Although the critical location may be at a lower mean stress

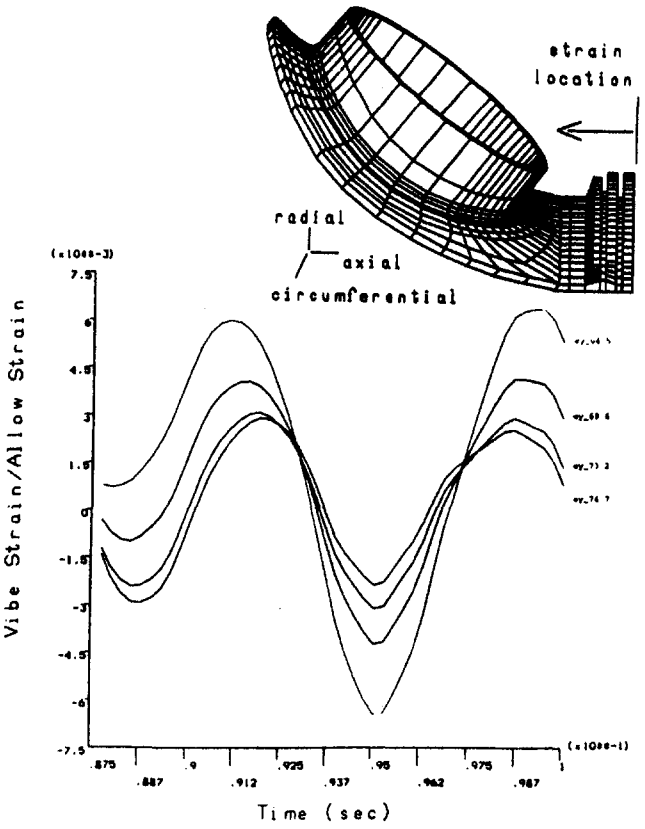

Fig. 3 Computed circumferential strain versus time for several elements located between the aft mount and aft frame on the centerline of the transition piece

and metal temperature, this material testing program determines a conservative limit for vibratory stress. Allowable dynamic strain was then established.

Critical locations were determined by computing dynamic strain range, the metal temperature, and mean stress at each element. Figure 4 is a plot of equivalent vibratory strain divided by allowable strain at one critical location. The strain is far

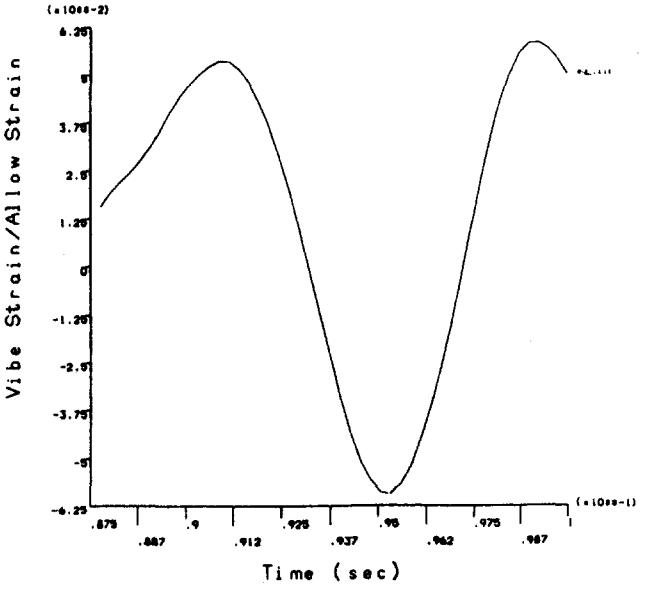

Fig. 4 Computed equivalent strain versus time at critical transition piece location

below the allowable level. Note that measuring strain at this location would not be feasible demonstrating the necessity for relying on analytical methods.

Impact Loading

The nonlinear transient dynamic analysis also predicted the response to the initial impact of the dynamic pressure. The pressure was conservatively assumed to begin oscillating at the full amplitude rather than ramping up as is probably more realistic. The highest dynamic amplification in the system occurs at the transition piece forward support (Fig. 5). The gap condition at this support is alternating between contacting and being free, resulting in nearly a factor of 12 increase over the static reaction at impact. Fortunately, the support areas are designed for higher impact load based on historical design practices.

Modal Analyses

In addition to predicting structural dynamic response for the particular frequency of interest, a wider frequency range was investigated to assure that slight variation in stimulus frequency would not be significant. Modal analyses were more expeditious than the nonlinear transient dynamic for evaluating frequency effects.

Experimental measurement of natural frequencies was performed to validate the finite element analyses. The testing was limited to individual components in a free support condition at room temperature.

The analytical prediction of natural frequencies agrees very well with the measurements, as do the mode shapes, which were compared by viewing animated displays. The variation of ± 7 percent is partly due to differences in mass and stiffness from manufacturing tolerances as well as measurement inaccuracies. The conclusion from this validation is that finite element analyses can be used with confidence to predict natural frequencies for actual support conditions and metal temperatures.

Modal analyses results for the combustion system with actual support conditions at operating metal temperature are given in Fig. 6. The combustion system consists of the liner and transition piece assemblies with radial spring elements for the hula seals. The hula seals are preloaded to represent the assembly interference and thermal expansion but do not develop force

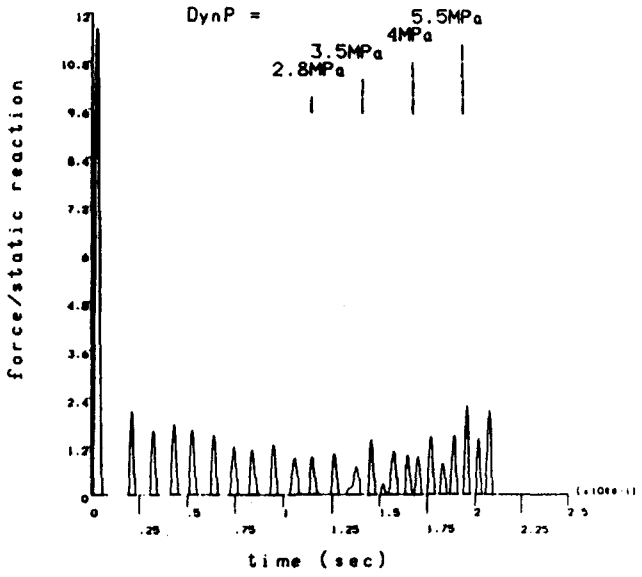

Fig. 5 Radial reaction versus time at transition piece forward support

	Fixed Brkt	Free Brkt	No Seal Prestress
Mode	Freq (hz)	Freq (hz)	Freq (hz)
1	90	90	90
2	108	106	106
3	159	117	154
4	169	169	156
5	203	203	190
6	212	211	197

Fig. 6 Computed natural frequencies of combustion system

due to axial sliding friction. Results without hula seal prestress are also given. The liner stops are restrained in the axial and circumferential directions relative to the axis of liner. The transition piece forward supports are restrained in the circumferential direction relative to the axis of liner. The aft bracket is fixed at the connection to the first-stage nozzle outer support ring. The bolted connection between the aft mount boss and aft bracket, which can actually slide after overcoming static friction, is modeled as both fixed and pinned, i.e., free to rotate, to test sensitivity since the actual condition cannot be represented.

The conclusion from these analyses is that several natural frequencies are very close to the combustion dynamic pressure, i.e., the third and fourth modes. The response to mode three was captured with the nonlinear transient dynamic analyses and did not cause structural concerns. Mode four is a liner natural frequency, which was analyzed separately and found to be of no consequence. The response is not extremely sensitive to the aft bracket rotation condition except for mode 3. Most importantly, no additional modes correspond to the combustion stimulus frequency due to variation in this boundary condition. The hula seal prestress also has minimal effect, especially in the frequency range of interest.

Conclusions

The analyses predict a large margin of safety against loss of structural integrity at possible dynamic pressure levels. Higher dynamic pressure than expected has also been analyzed to estimate the operational pressure limit with still no integrity concern. Modal analyses were also performed to be aware of nearby resonances.

The successful demonstration of this capability provides a powerful tool for gas turbine combustion development. Areas where the first signs of fatigue would most likely occur have been identified. Future strain measurements can be made at better locations as indicated by the analyses. Reactions including initial impact exerted on supporting components were determined, and are being used to design these components. Relative motions at interfaces were also computed and can be used to understand wear at these locations.

The analysis has several conservative assumptions, which caused overprediction of some measured accelerations and strains. Future work will include more interface components and the resulting friction, verification of the dynamic pressure distribution, and additional measurements of the component behavior.

References

1 ANSYS User's Manuals for Revision 5.0 Vols. I through IV, Swanson Analysis Systems, Inc., Houston, PA, 1992.

2 Bagepalli, B., Barnes, J., Dinc, S., Imam, I., and Slocum, G., 1992, "A System Dynamics Approach to Modeling Gas Turbine Combustor Wear," ASME Paper No. 92-GT-47.

Experience in Full-Load Testing of Natural Gas Centrifugal Compressors for Rotordynamics Improvements

A. Gelin

J.-M. Pugnet

D. Bolusset

Research and Development Department.

P. Friez

Compressor Department.

FRAMATOME Division THERMODYN, Le Creusot, France

During full-load shop tests under natural gas, two multistage centrifugal compressors exhibited subsynchronous vibrations. Both of them are low-flow, high-pressure, high rotational speed compressors, and are fitted with tilting pad bearings and dry gas seals. A rotating stall problem was first eliminated by a modification of the diffuser geometry. Then, aerodynamic excitations caused the rotors to operate at their stability limit, and high vibration levels were observed at the first natural frequency. A complete rotordynamics analysis was performed in order to model precisely all the fluid–structure interactions. Modifications of the rotor designs were implemented, consisting in optimizing conveniently the bearing pads, replacing the toothed labyrinth seals of the balance pistons by damping honeycomb seals, fitting them with improved shunt hole systems. In addition, the dry gas seals were found to have been damaged, due to thermal effects, and further modifications were implemented to eliminate this problem. Final full load tests demonstrated a satisfactory behavior of both centrifugal compressors.

Introduction

In 1993, two centrifugal compressors were ordered by two oil firms for enhanced oil recovery. The first one was dedicated to a reinjection process in Asia, and the other one to a gas lift process in Africa, but both of them were for offshore applications, and full-load, full-pressure tests with natural gas were specified (Fig. 1). Both of them are also low flow coefficient and rather high-pressure compressors, and fitted with dry gas seals.

Although both centrifugal compressors complied rigorously with the rotordynamics requirements of API 617, vibration problems occurred during the shop tests. These requirements mainly deal with synchronous unbalanced response of the rotor, and are not related to the problems encountered during the tests, which concerned subsynchronous vibrations induced by gas flows, that is to say the stability.

When the gas crosses through the compressor channel, many distortions occur in the velocity distributions all along the impellers, the diffusers, the channel returns, the inlet guide vanes, and the volutes. This induces unstationary forces in particular on the rotor, the prediction of which is of a very high complexity.

The aerodynamic forces on the rotor may be classified into two different categories. Both types were particularly active in the case of the centrifugal compressors involved in this paper.

The first type of aerodynamic force is generated directly by the flow itself and is considered as a forced excitation, such as, for instance, the rotating stall phenomenon, which is an unstability of the flow at low flow rates. The rotating stall was found on both compressors, due to the low flow coefficients of these machines. Prediction criteria of this phenomenon exist, but they are not accurate enough in the case of low flow coefficient, high-pressure centrifugal compressors, which remain a difficult application field.

The second type of aerodynamic forces regarding rotordynamics are applied in regions where the handled fluid is confined; a rotor displacement induces local disturbances in pressure and velocity, the resultant of which can be considered as a special gas bearing reaction. This will be called later self-induced aerodynamic excitation, or fluid–structure interaction. These fluid–structure interactions took a major importance, because the compressors were equipped with a high number of impellers and therefore a high number of labyrinths where the gas is confined. Fluid–structure interactions are found in the interstage and piston labyrinths, for which modeling exists (Childs, 1993). They are also developed around the impellers, for which empiric formulae are available (Wachel and Von Nimitz, 1981).

There is no doubt that, in a near future, new suitable models, issued probably from unsteady three-dimensional calculations using Euler (Fatsis et al., 1995), or Navier–Stokes solvers (Dawes, 1994), will be efficiently established. But these problems are not readily solved, and a lot of research is still needed.

The tendency to increase the application range of centrifugal compressors to high pressures, low flow rates, high rotational speeds, high pressure ratio (impeller number) makes such methods necessary. Some guidelines are commonly used (Fulton, 1984), but the deeper present knowledge of compressor manufacturers is also widely based upon experience, which appears in excellent papers (Zeidan et al., 1993; Kuzdzal et al., 1994), for some of the most recent ones.

On the other hand, the dry gas seal use is more and more popular in centrifugal compressors. This leads to longer bearing spans and heavier shaft ends than in the case of oil film ring equipped compressors. The natural frequencies are lower, and the absence of stiffness and damping effect makes rotordynamics different.

Description of Equipment

The main characteristics of the two natural gas centrifugal compressor trains are given in Table 1. The first one is a re-injection compressor, driven by a variable-speed electric motor through a gear. The second one is dedicated to a gas lift application, and is driven by a fixed speed electric motor through a gear. The rotor of the second compressor can be seen in Fig. 2.

Contributed by the International Gas Turbine Institute and presented at the 41st International Gas Turbine and Aeroengine Congress and Exhibition, Birmingham, United Kingdom, June 10–13, 1996. Manuscript received at ASME Headquarters February 1996. Paper No. 96-GT-378. Associate Technical Editor: J. N. Shinn.

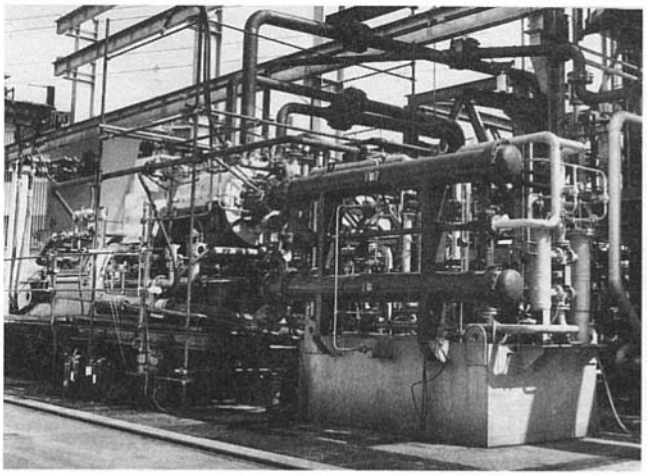

Fig. 1 Full-load test of centrifugal compressor

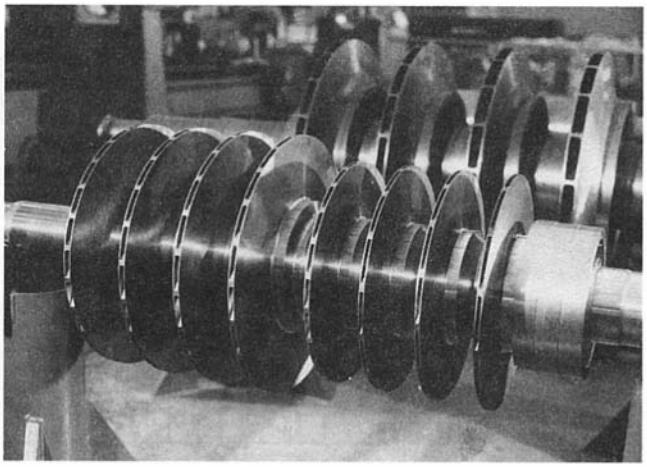

Fig. 2 Compressor rotor

Table 1 Main compressor characteristics

Compressor application	reinjection	gas lift
Impeller number	3 + 4	4 + 4
Suction pressure (bar a)	70	18
Suction temp. (°C)	50	35
Discharge pres. (bar a)	205	141
Discharge temp. (°C)	107	118
Molecular weight	21.9	23.4
Gas power (kW)	5670	5270
Nominal speed (RPM)	12258	13802
Bearing span (m)	1.426	1.379

Both compressors are fitted with tilting pad bearings from Glacier, with a length-diameter ratio of 0.4, and with dry gas seals in a tandem arrangement of the 28AT type from John Crane. Each of them is split into two sections for intermediate cooling of the gas. Cross sections of these compressors can be seen in Figs. 3 and 4.

Due to the high gas pressure level, the re-injection compressor had a high stiffness rotor, with a part of the gas path machined in the shaft at the impeller eye locations. The gas lift compressor had conventional impellers and sleeves.

Though the applications need very low flow coefficient impellers, the diffusers were initially of the vaneless type.

Low-Pressure Performance Tests

Both compressors were initially tested at low pressure, under inert gas condition, according to ASME PTC 10 Class III.

During these performance tests, the gas lift compressor exhibited high vibration levels at very low frequency. The subsynchronous peak appeared at about 7 percent rotational speed, which is characteristic of rotating stall excitation. The diffuser widths of the four impellers of the second compression section were progressively reduced, and vaned diffusers were implemented, which eliminated the rotating stall problem.

The reinjection compressor had good vibratory behavior during these low-pressure performance tests.

Full-Load Tests

Both compressor trains being dedicated to offshore applications had to be submitted to full-load, full-pressure tests under natural gas according to ASME PTC 10 Class I. Each of them had a behavior different from that during the low-pressure tests.

Reinjection Compressor. During the first full-load test, subsynchronous vibrations at 7 percent rotational speed appeared. In addition, an unacceptable vibration amplitude was found at the first natural lateral frequency of the rotor (Fig. 5).

At first, the rotating stall problem, which did not appear at low pressure, was investigated by decreasing the widths of the last diffuser of each section, and then by using vaned diffusers in the second section and for the last impeller of the first section. An extra modification was performed, regarding the last diffuser length. The rotating stall problem was easily eliminated, with these conventional means, and the influence of these modifications on the aerodynamic performance map was acceptable for the service of the compressor.

But the first natural frequency peak was always present in the vibration spectrum (Fig. 6), and the unstationary excitations by the rotating stall were no longer involved to explain a possible response of the lateral modes of the rotor. Several investiga-

Nomenclature

$[C]$ = damping matrix
$[C_b]$ = bearing damping matrix
$[C_f]$ = fluid–structure damping matrix
$[C_g]$ = gyroscopic antisymmetric matrix
C = direct damping
c = cross-coupled damping
$F(t)$ = forced excitation vector
$[K]$ = stiffness matrix
$[K_b]$ = bearing stiffness matrix
$[K_f]$ = fluid–structure stiffness matrix
$[K_s]$ = shaft symmetrical matrix
K = direct stiffness
k = cross-coupled stiffness
$[M]$ = symmetric mass matrix
WFR = whirl frequency ratio
x = nodal displacement vector
x' = nodal velocity vector
x'' = nodal acceleration vector
Ω = rotational speed
ω = pulsation

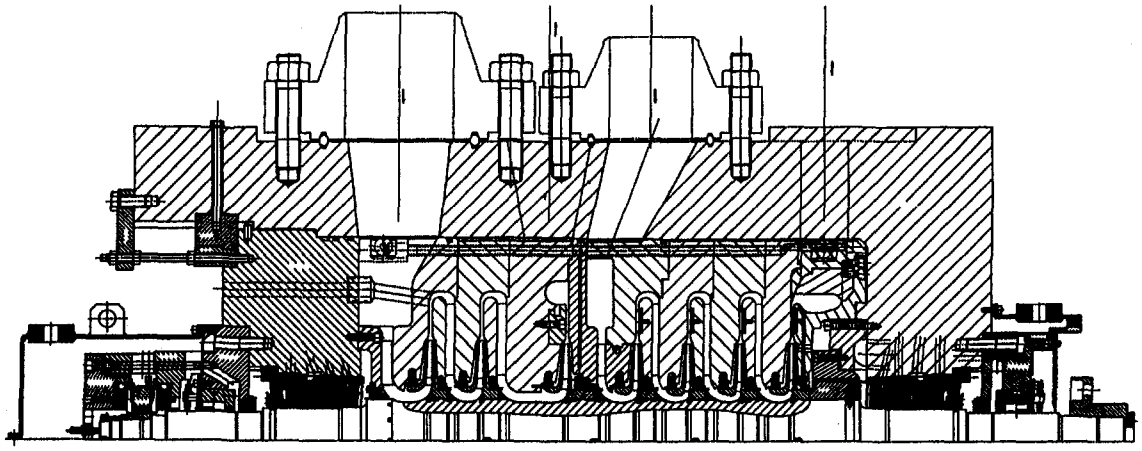

Fig. 3 Re-injection compressor cross section

tions were carried out in order to solve this instability problem, the final solution of which consisted in, by decreasing order of efficiency:

- installing a honeycomb damping seal instead of the initial toothed labyrinth on the balance piston,
- optimizing the tilting pad bearings with an higher stiffness in order to decrease the influence of the aerodynamic forced excitations, and to increase the first natural frequency,
- designing a new shunt hole system on the balance piston, in order to feed the piston seal with gas directly from the last impeller outlet (and not from the discharge volute) and to assure a gas preswirl as low as possible at the inlet of the piston seal.

Thus, the subsynchronous vibrations were eliminated, and the vibratory behavior of the compressor was very safe.

Gas Lift Compressor. During the first full-pressure tests, the gas lift compressor exhibited a high vibration level at the natural frequency of the first bending mode of the rotor, when the compressor was working at high flow rate. An important incident occurred very rapidly under the following conditions:

- rotational speed 13,800 rpm,
- suction pressure 17 bar,
- discharge pressure 125 bar,
- inlet flow about 100 percent on each section.

When dismantling the machine, the tilting pads of the outside thrust-bearing, the thrust collar, and the dry gas seal of the nondrive end were found to have been destroyed. Important traces of contact were visible on the impeller shroud, and the drive end dry gas seal was damaged. But the radial bearings and the internal labyrinths were intact. So, it was very strange that a radial vibration instability should lead to a major incident in the axial direction without notable radial damages.

Of course, the rotordynamics analysis had to be re-examined. But it was also necessary to widen the investigation field to the aerodynamic excitations assessment by a three-dimensional flow analysis using a Navier–Stokes method, and to the aerodynamic and thermal behavior of the dry gas seals.

Finally, it was determined that two different phenomena happened together, but without evident correlation: a vibration instability of the first bending mode, under particular operating conditions, and a thermal problem with the dry gas seals. The final modifications of the compressor allowed a satisfactory operation under full-load and full-pressure tests, and consisted of, by decreasing order of efficiency:

- a rotor with a reinforced stiffness shaft, according to the same technique as the reinjection compressor,
- a damping honeycomb seal on the balance piston,
- a new shunt hole system on this damping seal,
- a new adjustment of the tilting pads of the radial bearings,
- a new design of the inlet and discharge volutes of the second section.

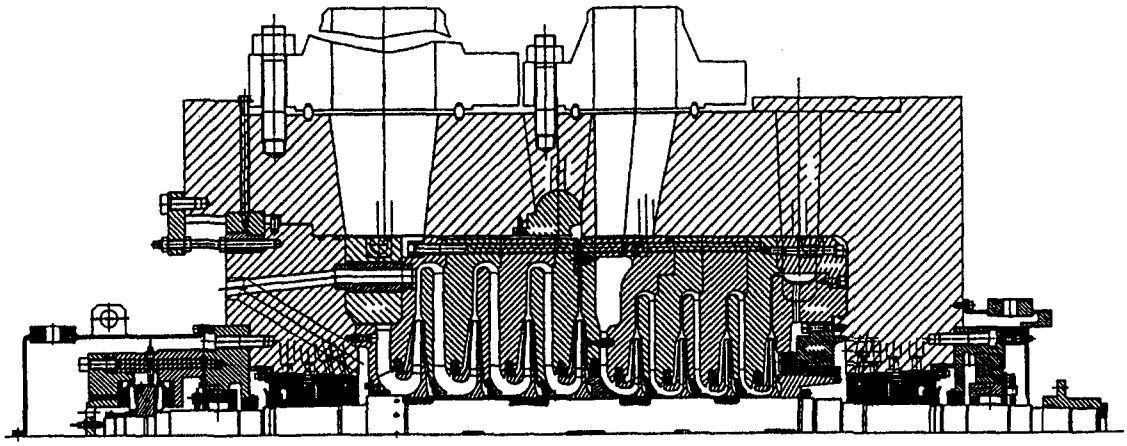

Fig. 4 Gas lift compressor cross section

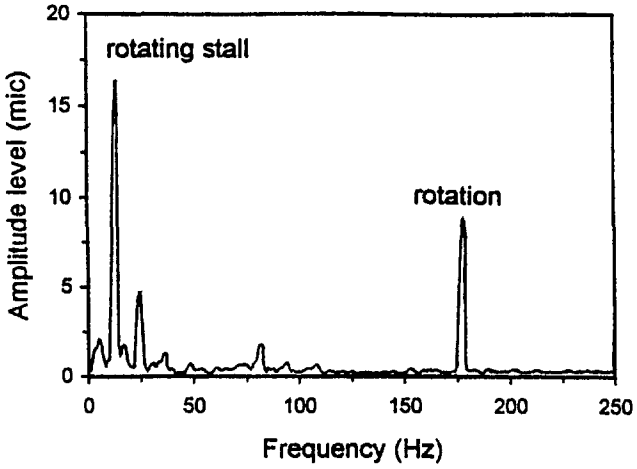

Fig. 5 Typical rotating stall spectrum

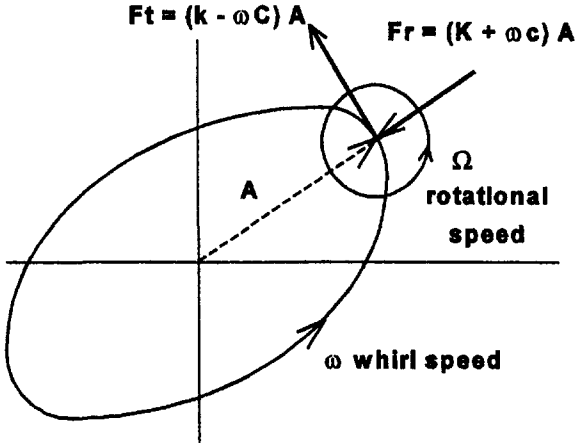

Fig. 7 Forces acting on a whirling and rotating element

The full-load test campaigns were carried out initially with the driver, the gear, the skid, and the lube oil system of the contract, then with the equipment of the test facility, in order to allow the erection of the skid in the module of the offshore platform, and the piping installation.

Subsynchronous Vibration Diagnostic and Rotordynamic Analysis

Rotordynamics. The shaft of the rotor is modeled with beam finite elements, each node having four degrees of freedom (two radial displacements, and two slopes). All the rotating components, such as the coupling, the impellers, the balance piston, the dry gas seals . . . , are modeled as pure masses and inertias without stiffness term.

The radial tilting pad bearings are modeled by complete stiffness $[K_b]$ and damping $[C_b]$ matrices, including cross-coupling terms due to the pad inertia. The dry gas seals are considered only as pure masses and inertias, without any stiffness or damping properties.

Fluid structure interactions due to impellers and internal seals are modeled, like the radial bearings, by stiffness $[K_f]$ and $[C_f]$ matrices, which have the following form:

$$[K_f] = \begin{bmatrix} K & k \\ -k & K \end{bmatrix} \quad \text{and} \quad [C_f] = \begin{bmatrix} C & c \\ -c & C \end{bmatrix}$$

In order to characterize the influence of the fluid–structure interactions on the rotor stability, the difference $k - C\omega$ is calculated, because it represents the destabilizing cross coupled force intensity. On Fig. 7, the represented resultant $k - C\omega$ is in the same direction as the whirl velocity, and is therefore destabilizing.

The general rotordynamics equation can be written as follows:

$$[M]x'' + ([C_g] + [C_b] + [C_f])x' + ([K_s] + [K_b] + [K_f])x = F(t) \quad (1)$$

The eigenvalues of the finite element equation (1) (Lalanne and Ferraris, 1990) contain the natural frequency (imaginary part), and the associated damping (real part), which are among the most important parameters to be analyzed.

Bearing Modeling and Optimization. The finite element models of the compressor rotors are composed of about 100 nodes (400 degrees of freedom).

The stiffness and damping matrices of the radial bearings come from the resolution of the Reynolds equation with a perturbation introduction (Frene et al., 1990). The thermal equilibrium on each pad is verified to estimate the actual oil viscosity and the bearing geometry (clearance and preload). The pad inertias are taken into account for the determination of the cross-coupling terms. The numerical resolution method uses an iterative procedure based on a finite difference scheme.

The bearing optimization uses the rotor modeling and is performed by a parametric analysis. The natural frequencies and their associate damping (logarithmic decrement) are computed at nominal speed versus tilting pad geometry (couples of radial clearance and preload) from Eq. (1) without the right-hand-side term.

The corresponding chart for the first lateral mode in the forward direction for the reinjection compressor is given in Fig. 8, where the diametral clearances are related to the bearing diameter (per thousand), and the preload expressed as usual. This diagram allows to choose the optimum geometry, leading to a natural frequency high enough, and with a good damping. It is important to note that small pad geometry variations lead to high rotordynamics changes, and a special attention is to be paid in the clearance and preload definition.

Table 2 indicates the original set of values, calculated for both rotors without taking into account any fluid–structure interaction. The Campbell diagram of the re-injection compressor is shown in Fig. 9.

Dry Gas Seal Influence. As mentioned above, the dry gas seals are more and more often used for sealing the compressor shaft ends, instead of oil film ring seals. Due to their operation

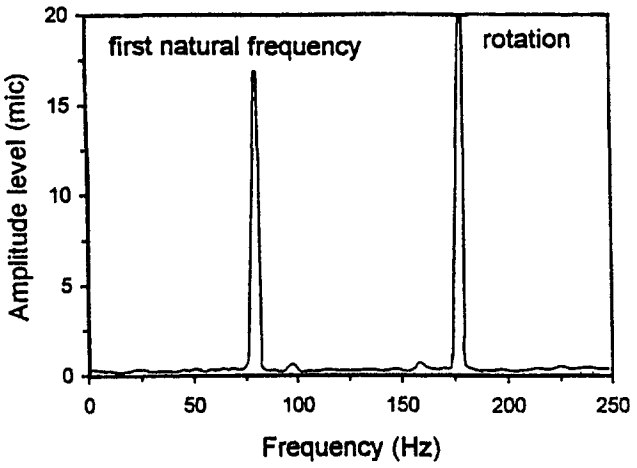

Fig. 6 Typical first mode instability spectrum

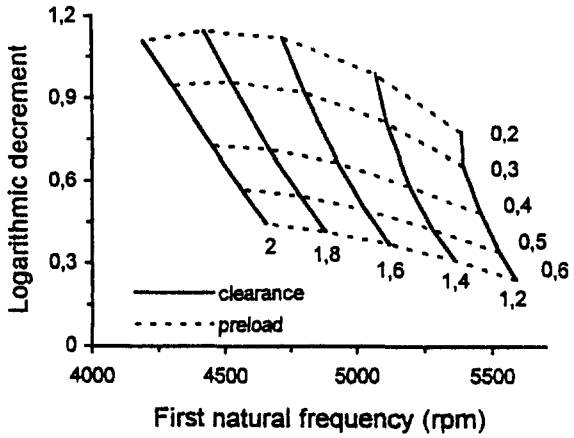

Fig. 8 Bearing optimization chart (re-injection compressor)

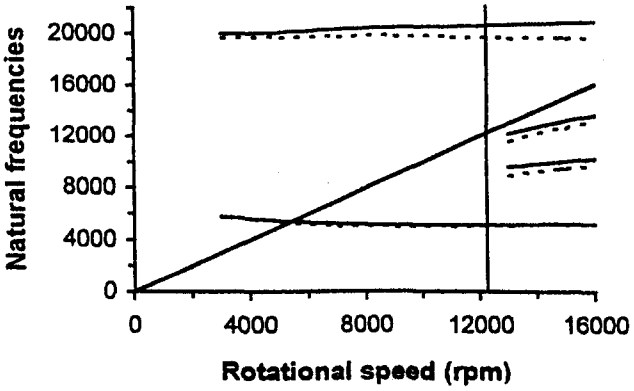

Fig. 9 Campbell diagram

principle, the dry gas seals do not develop any reaction directly affecting the rotor stability.

From a rotordynamics point of view, the rotating part of the dry gas seals are modeled as pure mass and inertia. So the dry gas seals tend to decrease the first natural frequency, and thus, increase the rotor sensitivity to fluid–structure interactions, as opposed to the oil film ring seals, which develop stiffness and damping terms.

Sensitivity to Fluid–Structure Interactions. In order to verify that the rotor-bearing system was able to withstand the destabilizing effects of the impellers, a sensitivity analysis was carried out. These fluid–structure interactions were modeled only by a purely destabilizing cross-coupled stiffness concentrated at midspan of the rotor, in a pessimistic way.

Table 2 Original first natural frequency without internal seal influence

Compressor application	reinjection	gas lift
Relative clearance (‰)	1.75	1.95
Geometric preload	0.26	0.35
Nominal speed (rpm)	12258	13802
1st natural frequency (rpm)	4511	4139
1st natural frequency (%)	37	30
Logarithmic decrement	1.1	0.56

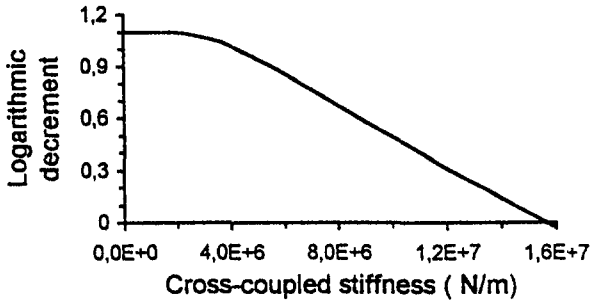

Fig. 10 Cross coupled stiffness rotor sensitivity diagram (without internal seal influence)

The evolution of the logarithmic decrement of the natural frequency is plotted versus the cross-coupled stiffness (Fig. 10). The k value for a logarithmic decrement equal to zero gives the stability threshold. This value is compared to the empirical cross-coupled stiffness estimated by the works of the Southwest Research Institute (Wachel and Von Nimitz, 1981) for the different impellers. The ratio between these two values gives the stability margin.

Table 3 indicates these stability margins, calculated without taking into account any internal seal influence.

It appeared that the initial stability margin of the gas-lift compressor was not high enough and a new rotor fitted with a reinforced stiffness shaft has been designed. Only the aerodynamic part of the rotor has been modified (the shaft diameter was increased from 127 mm to 146 mm for the first section, and to 140 mm for second one). The shaft end dry gas seals, the bearings, the thrust bearing, and the coupling were not changed.

A new tilting pad optimization of the radial bearing has been performed, as shown in Table 4. It can be noted that this arrangement leads to a better damping improvement rather than a frequency increase.

Internal Seal Influence. In spite of the bearing geometric optimizations, both compressors still exhibited subsynchronous vibration at the first natural frequency during full-load tests.

So, it was suspected that the main origin of the destabilizing cross-coupled forces came from internal seals where the com-

Table 3 Stability margin without internal seal influence

Compressor	reinjection	gas lift
k (10^6N/m)	15.8	6.8
stability margin	3.4	1.3

Table 4 Gas lift compressor rotor arrangements (without internal seal influence)

Compressor rotor	initial	reinforced
Relative clearance (‰)	1.95	1.7
Geometric preload	0.36	0.3
1st natural frequency (rpm)	4139	4485
1st natural frequency (%)	30	33
Logarithmic decrement	0.56	0.74
Stability margin	1.3	2.1

Table 5 Complete rotordynamics comparison taking all the effects into account

Compressor application		Reinjection				Gas lift			
Arrangement		initial		final		initial		final	
Bearings	Radial clearance (‰)	1.75		1.43		1.95		1.7	
	Geometric preload	0.26		0.39		0.35		0.30	
Balance piston seal	Type	toothed labyrinth		honeycomb		toothed labyrinth		honeycomb	
	Inlet gas preswirl ratio (%)	0	50	0	50	0	50	0	50
Rotordynamics results	First natural frequency (rpm)	4487	4432	6956	6875	4096	4022	5564	5375
	Logarithmic decrement	1.13	1.18	1.63	1.16	0.61	0.47	1.80	1.08
	Stability margin	3.9	2.9	9.2	6.6	1.8	0.8	6.5	4.1

pressed gas is confined. Initially, all the internal seals (impeller eyes and balance piston) were of the toothed labyrinth type (teeth-on-stator), with only a shunt hole system on the balance piston of the gas lift compressor, and a separation wall between the last impeller and the balance piston in the reinjection compressor.

Very extensive investigations were performed to predict with enough accuracy fluid–structure interactions due to these internal seals.

The toothed labyrinth seal behavior was computed by using the Childs modeling (1993), and the main following results have been observed:

- The influence of all the impeller eyes is negligible, compared to the influence of the balance piston labyrinth seal.
- The cross-coupled stiffness increases with the cavity number, and is mainly related to the inlet preswirl (tangential velocity).
- For more than four or five cavities, the direct stiffness is negative, and becomes more and more negative when the cavity number increases. During the full-load tests of both compressors, no decrease in the first natural frequency value, due to a negative direct stiffness on the rotor, has been observed, as predicted by computational results, so this particular term was no longer taken into account in the rotordynamics calculation.

The main results are given in Table 5 for two different assumptions of the inlet gas preswirl ratio: 0 and 50 percent rotational speed.

It can be noted that the gas lift compressor is on its stability limit when the preswirl ratio is about 40 percent rotational speed. We note that the solution of the initial rotating stall problem consisted in implementing width reduced vaned diffusers, which develop overly high losses at high flow rates. In the case of high flow rates, the shunt hole system was no longer effective, because the pressure in the discharge volute was lower than the pressure at the last impeller outlet, and the gas inlet into the toothed labyrinth came directly from this impeller outlet, with a high preswirl. Thus, the instability observed on this gas lift compressor was fully explained. In order to eliminate these undesirable conditions, the following modifications were implemented:

- implementation of the reinforced rotor with the new radial bearing adjustment,
- installation of a damping honeycomb seal to improve the global damping capacity,
- improvement of the shunt hole system feeding,
- installation of a separation wall between the last impeller and the balance piston to reduce the inlet preswirl if the shunt hole system is not yet efficient enough.

A damping honeycomb seal on the balance piston was also designed and implemented on the reinjection compressor, and though this problem was less critical for this compressor, the gas feeding of the shunt hole system was also improved. The technology of both compressors became quite similar.

The design of the honeycomb seal was performed using the recent software developed by Scharrer and Pelletti (1995). The main results are summarized in Table 5 with the two different preswirl ratios of 0 and 50 percent.

The use of honeycomb seals on the balance piston instead of the initial toothed labyrinth seals confers two very interesting characteristics to both compressors, from a rotordynamics point of view (see Fig. 11):

- a first natural frequency increase, this one becoming less sensitive to fluid–structure interactions. This increase is mainly due to the direct stiffness of the honeycomb seals, the high-pressure gas being very well confined in the honeycomb cavities, compared to those of the tooth labyrinth seal.
- an important damping increase (logarithmic decrement) of the first natural frequency, due to the high damping capacity of honeycomb seals, and which is accompanied with a high stability margin.

The corresponding mode shapes of the first natural frequency of the reinjection compressor are shown in Fig. 12 (Fig. 12.1 with the toothed labyrinth arrangement, and Fig. 12.2 for the honeycomb one). The difference in shape is related to the direct high stiffness of the honeycomb seal.

Final Full-Load Test Results. After implementing these modifications, both compressors were again full-load tested, and demonstrated their good vibratory behavior.

The subsynchronous vibration of the reinjection compressor completely disappeared from the vibration spectrum (Fig. 13), on the whole operating range.

The gas lift compressor, which was the most sensitive one, taking into account its relatively low first natural frequency, exhibited a subsynchronous vibration level quite in accordance with the limit of API 617 standard at high flow rate. At nominal flow, the subsynchronous peak completely disappeared (Fig. 14).

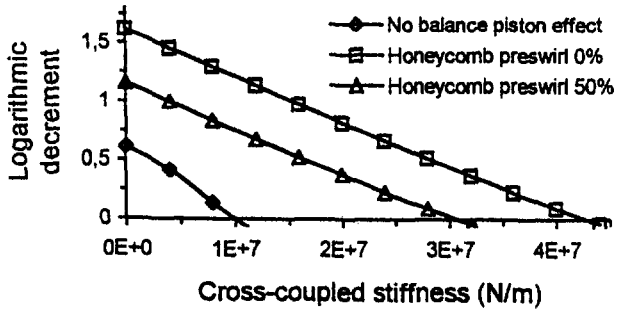

Fig. 11 Cross-coupled stiffness sensitivity diagram of the rotor fitted with damping honeycomb seal

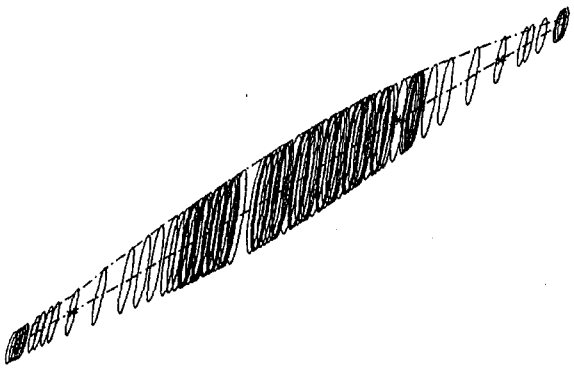

Fig. 12-1 With toothed labyrinth

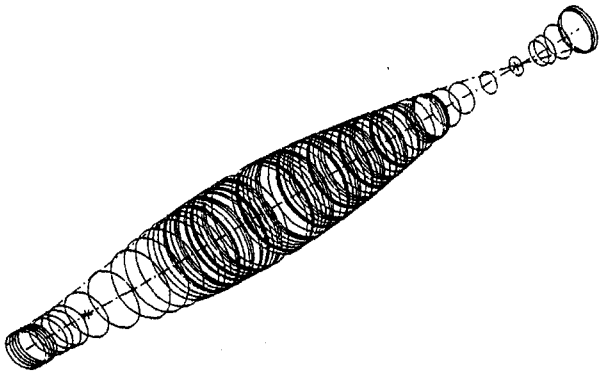

Fig. 12-2 With honeycomb seal

Fig. 12 First mode shape

Dry Gas Seal Behavior

The dry gas seal arrangement is a tandem seal with an intermediate labyrinth for both compressors. An equilibrium connection was installed in order to have exactly the same pressure to be sealed at each shaft end. This is particularly interesting in the case of the reinjection compressor to obtain a better thrust definition, but both shaft ends become hot.

In order to minimize the rotor length, for rotordynamics reasons, taking into account the high impeller numbers, the dry gas seal configuration shown in Fig. 15 was chosen. The labyrinth that separates the buffer gas from the process gas was directly installed around the rotating seat shroud.

During the shop tests of the compressors, some slight, but abnormal marks were detected, mainly on the primary seals: their rotating seats exhibited "island shape" traces between each groove at their inner diameter, and their mating rings some traces more or less all around the circumference.

Microscopic electron beam examinations of the damaged parts detected antimonia particles inside the rotating rings, and tungsten inside the mating faces, which demonstrated that contacts occurred during operation.

A more detailed analysis of the dry seal running conditions showed that the temperature gradients in the seals are greater than those obtained when the separation labyrinth is directly assembled on the compressor shaft.

Computer simulations, which take into account the actual boundary conditions in the compressors, and a long duration test at the test rig of the dry gas seal supplier, showed a seat deflection in a "wave shape," which may induce such slight local contacts.

These contacts generate heat. This reinforces the influence of the phenomenon, and explains the destruction of the dry gas seal of the gas lift compressor during one of the first full-load tests, as previously mentioned. Thus, both problems of rotordynamics stability and of seal thermics were coexisting on this compressor, but without relation between each other.

Two main improvements have been implemented:

- the number of grooves has been increased in order to minimize the wave deformation phenomenon in operation,

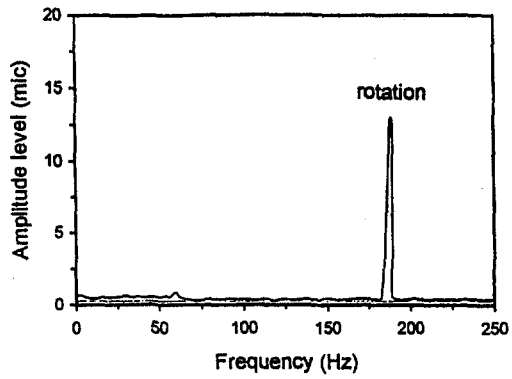

Fig. 13 Final vibration spectrum: re-injection compressor

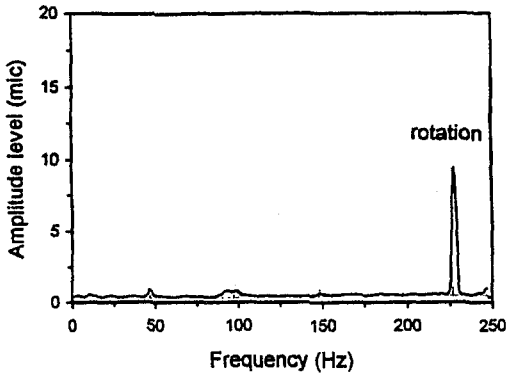

Fig. 14 Final vibration spectrum: gas lift compressor

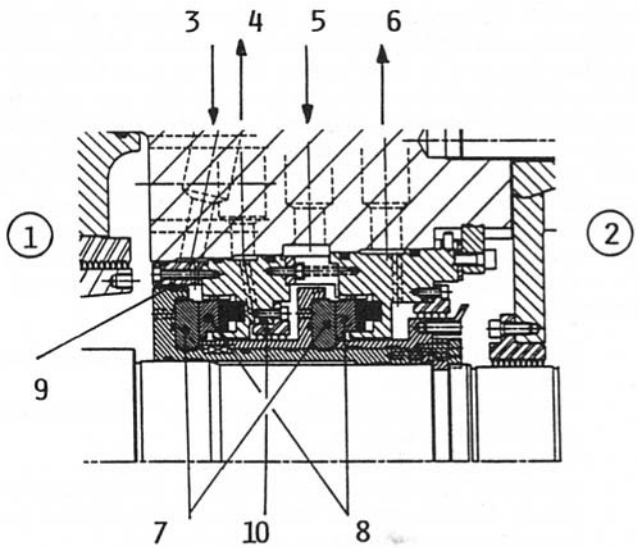

Fig. 15 Initial dry gas seal arrangement: (1) compressor side; (2) bearing side; (3) internal buffer gas inlet; (4) to flare; (5) external buffer gas; (6) vent; (7) grooved rotating rings; (8) stationary mating rings; (9) internal labyrinth; (10) intermediate labyrinth

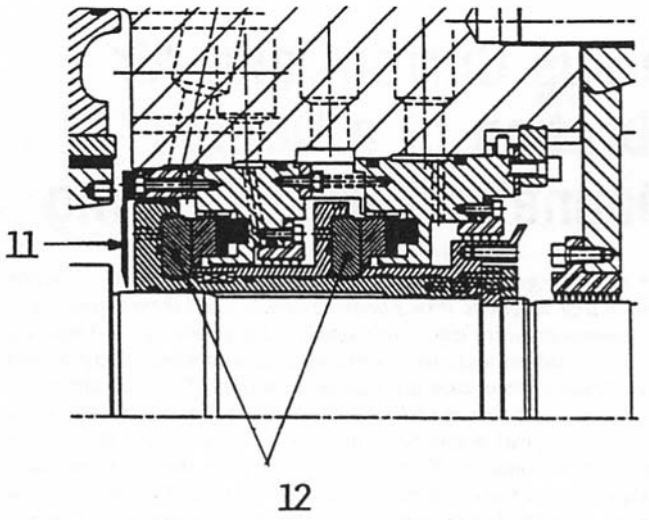

Fig. 16 Final dry gas seal arrangement: (11) added deflector; (12) changed number of grooves

- a deflector has been installed between the buffer gas and the process gas so that the dry gas seals remain as cool as possible, thus limiting temperature gradients in the dry gas seals (see Fig. 16).

The modified dry gas seals were retested under severe conditions and for a long duration, and no anomaly was detected after inspection.

Conclusion

Rotordynamics analysis of high-pressure, high-speed multistage centrifugal compressors should consider all the fluid–structure interactions that influence the rotor stability. The use of dry gas seals with long shafts makes the rotor more sensitive to aerodynamic excitations, and it is possible that the damping capacity of tilting pad bearings becomes insufficient to allow safe vibratory behavior of such rotors.

Subsynchronous vibrations appeared on two centrifugal compressors during full-load tests under natural gas.

A rotating stall phenomenon on both compressors was first eliminated by a modification of the diffuser geometry.

The understanding and solution of the problem of high subsynchronous vibrations at the first natural frequency requires one to model all the fluid–structure interactions all along the rotor, and not only in the bearings (and the lubricated seals, if any). The most recent theories have to be used to characterize the aerodynamic behavior of toothed labyrinths, honeycomb seals, and impellers.

It appeared that the most destabilizing effect of internal seals was located on the balance piston. The initial toothed labyrinths were replaced by honeycomb seals, in order to increase the seal damping and stiffness. Thus, the first natural frequency increases and its damping is improved, and the compressor stability margin versus aerodynamic excitations is considerably reinforced.

From a rotordynamics point of view, it should be noted that the design of such compressors requires appropriate, sophisticated, and up-to-date modeling of the flow-induced forces, the evolution of these methods being in accordance with the application domain of centrifugal compressors.

In addition dry gas seals troubles occurred during the full-load tests, one of them being very severe. It was previously assumed that this was connected to the vibration problem; it appears that these troubles were due to thermal environment problems, which were solved separately.

After relevant modifications, both compressors again showed satisfactory vibratory behavior during the last full-load tests with natural gas, and were delivered to be installed in off-shore platforms for enhanced oil production.

At this time (end of 1995), the re-injection compressor has been commissioned on site, and its behavior confirms the efficiency of the implemented modifications.

Acknowledgments

The authors would like to thank the oil companies for their kind authorization to publish this paper, and to present the main characteristics of the two centrifugal compressors involved.

References

American Petroleum Institute, 1995, "Centrifugal Compressors for Petroleum, Chemical and Gas Service Industries," API Standard 617, 6th ed., Feb.

American Society of Mechanical Engineers, 1974, "Compressors and Exhausters," Power test code 10, (1965 reaffirmed 1979), ANSI PTC 10 (1974).

Childs, D. W., 1993, *Turbomachinery Rotordynamics,* Wiley, New York.

Dawes, W. N., 1995, "A Simulation of the Unsteady Interaction of a Centrifugal Impeller With Its Vaned Diffuser: Flow Analysis," ASME *Journal of Turbomachinery,* Vol. 117, pp. 213–222.

Fatsis, A., Pierret, S., and Van den Braembussche, R. A., 1997, "3D Unsteady Flow and Forces in Centrifugal Impellers With Circumferential Distortion of the Outlet Static Pressure," ASME *Journal of Turbomachinery,* Vol. 119, pp. 94–102.

Frene, J., Nicolas, D., Degueurce, B., Berthe, D., and Gaudet, M., 1990, *Lubrification Hydrodynamique,* Eyrolles Editions.

Fulton, J. W., 1984, "The Decision to Full Load Test a High Pressure Centrifugal Compressor in Its Module Prior to Tow-Out," presented at the IMechE Second European Congress on Fluid Machinery for Oil, Petrochemical, and Related Industries, The Hague (Netherlands), Mar.

Kuzdzal, M. J., Hustak, J. F., and Sorokes, J. M., 1994, "Identification and Resolution of Aerodynamically Induced Subsynchronous Vibration During Hydrocarbon Testing of a 34,000 HP Centrifugal Compressor," presented at the IFToMM, Fourth International Conference on Rotordynamics, Chicago (Illinois), Sep. 7–9.

Lalanne, M., and Ferraris, G., 1990, *Rotordynamics Prediction in Engineering,* Wiley, New York.

Scharrer, J. K., and Pelletti, J. M., 1995, "Gasseal™ Software Operating Manual," Rotordynamics-Seal Research, North Islands, CA.

Wachel, J. C., and Von Nimitz, W. W., 1981, "Ensuring the Reliability of Offshore Gas Compression Systems," presented at the European Offshore Petroleum Conference and Exhibition, EUR 205.

Zeidan, F. Y., Perez, R. X., and Stephenson, E. S., 1993, "The Use of Honeycomb Seals in Stabilizing Two Centrifugal Compressors," *Proc. 22nd Turbomachinery Symposium,* Dallas, TX, pp. 3–15.

Force Versus Current and Air Gap Calibration of a Double Acting Magnetic Thrust Bearing

D. O. Baun

R. L. Fittro

E. H. Maslen

Mechanical, Aerospace, and Nuclear Engineering Department, University of Virginia, Charlottesville, VA 22903

Force versus current and air gap measurements were obtained for the actuator component of a double acting magnetic thrust bearing constructed from a powdered metal. Static force measurements were made for various air gap settings and bearing current combinations. The resulting data were reduced and an optimized expression representing the force versus current and air gap relationship of the actuator was found. In addition, a theoretical force model was developed using simple magnetic circuit theory and constant material magnetic properties. The theoretical model predicted force magnitudes approximately 20 percent greater than the experimentally measured values. Hysteresis tests were conducted with the thrust disk in the centered position for various current perturbation amplitudes about the design bias current. Hysteresis effects were shown to cause a difference between the measured force as the current was increasing as compared to when the current was decreasing. This difference varied from 10 to 7 percent of the peak force from each respective hysteresis loop. A second-order polynomial expression was developed to express the coercive force as a function of the perturbation current amplitude. The bearing frequency response was examined by injecting sinusoidal currents of varying frequencies into the bearing. An actuator bandwidth of at least 700 Hz was determined. Above 700 Hz the bearing frequency response could not be distinguished from the test fixture frequency response.

Introduction

Magnetic bearings provide a strong diagnostic capability, which has been widely discussed in the literature (Humphris, 1992; Imlach et al., 1991; Ulbrich, 1988, Wagner et al., 1988). This capability stems, fundamentally, from the fact that the magnetic actuator component produces a force acting on the shaft, which depends primarily on clearances within the actuator and its electromagnet coil currents. These quantities are all readily measured while the bearing is in operation, thereby providing direct access to the forces applied by the bearing.

Such direct measurability of the bearing applied force enables two general classes of application not possible with conventional bearings: (*i*) As a diagnostic tool for rotating machinery—a knowledge of the forces at the bearings can be a significant indication of both the rotor dynamic condition and the operating point of the machine. (*ii*) As a measurement tool for turbomachines—an accurate knowledge of the loads at the bearings can be used to evaluate hydrodynamic or aerodynamic forces acting on the rotor.

In understanding this use of the bearing as a measurement device, it is important to distinguish the components of the bearing. A magnetic bearing is a feedback based device (Allaire et al., 1994a) which employs three distinct components: a position sensor to detect the position of the supported shaft, a magnetic actuator that applies the bearing force to the shaft, and a feedback controller that determines what force to apply based on the shaft position measurement. The static and dynamic properties of the bearing are thus a composite of the properties of each of these three components.

When the bearing is to be treated as a diagnostic or measurement device, attention is focused solely on the properties of the actuator itself. In this case, the forces generated by the actuator are related to the actuator air gaps and coil currents by a static calibration relationship, $F_b = f(i, g)$. The performance of the bearing as a force measurement or diagnostic tool is determined primarily by the accuracy to which this actuator calibration relationship can be determined. In addition, the nonlinear effects due to material hysteresis, eddy currents, leakage, and fringing need to be understood and quantified in order to assess their effect on measurement uncertainty. In this paper, the calibration function and the nonlinearities for a double acting magnetic thrust bearing actuator are investigated.

For the design of magnetic bearing actuators the force versus current and air gap relationship must be known not only in crude form but in detail. Typically, a model using linear magnetic circuit theory is used for preliminary design, and a finite element analysis may be conducted for a more detailed design (Allaire et al., 1994a). However, not much work has been done to compare these relationships to the actual performance of the bearings. Ulbrich (1988) and Hawkins et al. (1991) used magnetic bearings as a force input device for system excitation and the evaluation of system dynamics. Imlach et al. (1991) examined the application of magnetic bearings to measure force, stiffness, and damping in a centrifugal pump. Wagner and Pietruska (1988) constructed a magnetic bearing for measuring hydrodynamic forces in a turbocompressor. Humphris (1992) discussed magnetic bearings as a diagnostic tool for rotating machinery. Guinzburg and Buse (1994) measured the static radial and axial reaction forces on a single stage end suction pump rotor through calibrated magnetic bearings. The bearings were calibrated by applying known loads on the suspended shaft. The calibration was reported to be independent of load frequency. In addition, hysteresis was deemed insignificant. Pottie et al. (1994) used active magnetic bearings for the support and excitation of a boiler feed pump rotor. Bearing reaction force measurements were used to determine on-line frequency response functions from which dynamic fluid/rotor interaction forces were evaluated. A static calibration of the bearings was conducted by measuring bearing-generated forces acting on the shaft via

Contributed by the International Gas Turbine Institute and presented at the 41st International Gas Turbine and Aeroengine Congress and Exhibition, Birmingham, United Kingdom, June 10–13, 1996. Manuscript received at ASME Headquarters February 1996. Paper No. 96-GT-121. Associate Technical Editor: J. N. Shinn.

a stiff linkage and load cell assembly. The calibration was found to be a function of shaft position about the bearing center. In addition, hysteresis effects were found to cause significant variation in the measured forces. Frequency effects were not reported. Allaire et al. (1995) examined the force versus current characteristic for a single-sided magnetic thrust actuator machined from solid iron. They demonstrated that the nonlinear effects of hysteresis and eddy currents can cause significant deviation of the actuator performance as compared to a force model based on linear theory.

The magnetic thrust bearing actuator discussed in this paper is intended for use as a load cell to measure axial forces acting on a single stage end suction centrifugal pump rotor.

Test Apparatus

The double acting thrust actuator was tested using the apparatus shown in Fig. 1. The upper and lower air gaps were controlled by adjusting the relative position of the thrust disk between the two actuator halves and were measured with machinist's thickness gages at four equally spaced locations around the disk circumference. Axial alignment and perpendicularity between the thrust disk and the actuator halves were maintained by the linear bearing and the guide block located on the top and bottom of the apparatus assembly, respectively. The net magnetic force acting on the thrust disk was transmitted to a 200 lbf (890 N) load cell.

The magnetic thrust actuator discussed in this document is shown in Fig. 2. Design details of this actuator are identical to those described by Allaire et al. (1995), with the exception that the actuator components (both stators and the thrust disk) were constructed from a powdered metal, Anchor Steel TC-80 (Oliver et al., 1995) chosen for its low core loss properties at high frequencies. The actuator has an inner diameter, $D_1 = 1.75$ in (44.4 mm), coil inner diameter, $D_2 = 2.4$ in (60.9 mm), coil outer diameter, $D_3 = 3.09$ in (78.5 mm), actuator outer diameter, $D_4 = 3.5$ in (88.9 mm), back iron length, $L_b = 0.28$ in (7.1 mm), stator length, $L_t = 0.76$ in (19.3 mm) and thrust collar length, $L_r = 0.56$ in (14.2 mm). These actuator dimensions give a mean magnetic path length in the iron, $L_i = 2L_t + L_b + L_r/2 + (D_4 + D_3)/2 - (D_2 + D_1)/2 = 3.301$ in (83.9 mm). It was designed for a maximum thrust load of 42 lbf (185 N). The coil windings, N, consist of 300 turns of #22 wire. The design bias current, i_b, was 1.75 A, with operating range between 0.95 A and 2.55 A. The nominal air gap of the actuator, g_0, is 0.030 in (0.76 mm).

Based on an independent magnetic material property test conducted to ASTM standard A773-91, an initial relative permeability and a coercive force, $\mu_r = 139$ and $H_c = 4.94$ Oe, respectively were found for Anchor Steel TC-80. A graphic summary of the test results are shown on the B-H curve in Fig. 3. In addition the core loss was measured to be 10.6 W/kg at 60 Hz and a peak induction of 10,000 Gauss.

Static Force/Current Testing

Theoretical force relationships for magnetic thrust actuators using linear magnetic circuit theory have been well documented by Allaire et al. (1994a). The theoretical force in a single sided thrust actuator is given by

$$F_{th} = \epsilon \frac{\mu_o N^2 i_1^2 A_g}{(2g_1 + b_{th})^2} \tag{1}$$

The net force in a double acting magnetic thrust actuator can be expressed as the difference between the magnetic forces developed in each side of the actuator:

$$F_{th} = F_1 - F_2 \tag{2}$$

For the thrust actuator discussed in this paper, the expression for the theoretical net force is given by

$$F_{th} = \epsilon k_{th}\left[\frac{i_1^2}{(2g_1 + b_{th})^2} - \frac{i_2^2}{(2g_2 + b_{th})^2}\right] \tag{3}$$

where $k_{th} = \mu_0 A_g N^2 = (0.05383$ lbf in.^{2}/A^2 (154.475 N mm^2/A^2) and $b_{th} = L_t/\mu_r = 0.02375$ in (0.603 mm), where the initial permeability, $\mu_r = 139$, was used.

A systematic testing procedure was established where air gaps, $g_2 = g_0 - \Delta g$, and, $g_1 = g_0 + \Delta g$, were varied from 0.015 in to 0.045 in. (0.381 mm to 1.143 mm) in increments of 0.005 in (0.127 mm) for a total of seven discrete position settings. Simultaneously, the nominal currents, i_2 and i_1, were varied in the range of 0 and 3.5 A depending on the nominal air gap setting such that the maximum net force was less than approximately 70 lb (310 N). A total of 5400 discrete data points were obtained for the static calibration. Before the start of each new current trajectory, both sides of the actuator were degaussed to remove any residual magnetism from the magnet iron, thereby reducing hysteresis effects. For the static tests the eddy current effects were minimized by slowly incrementing the actuator currents in discrete positive steps. The effective current time rate of change for the static tests varied between 0.07 and 0.1 A/s.

The static calibration data was evaluated with an optimization routine, based on Powell's method (Press et al., 1986), that solved for values of k_{exp} and b_{exp} to be used in a force calibration equation of the same form as Eq. (3). Optimal values of k_{exp} and b_{exp} were those that minimized the root-mean-square error between the experimental actuator force, as measured by the load cell, and the force as calculated by the force calibration equation. The rms error was minimized to 0.52 lbf (2.31 N)

Nomenclature

A_g = actuator pole face area
B = magnetic flux density
b_{exp} = equivalent iron length (experimental)
b_{th} = equivalent iron length (theoretical)
D_1 = actuator inner diameter
D_2 = coil inner diameter
D_3 = coil outer diameter
D_4 = actuator outer diameter
F_b = actuator force (calibration equation)
F_c = coercive force
F_m = actuator force (measured)
F_{th} = actuator force (theoretical)
g_0 = nominal air gap
Δg = change in air gap (positive up)
g_1 = lower air gap = $g_0 + \Delta g$
g_2 = upper air gap = $g_0 - \Delta g$
H = magnetic field intensity
i_1 = lower coil current
i_2 = upper coil current
i_c = effective coercive current
i_b = bias current
i_p = perturbation current
$j = \sqrt{-1}$
k_{exp} = proportionality constant (experimental)
k_{th} = proportionality constant (theoretical)
K = combined actuator/apparatus DC gain
L_i = magnetic path in iron
L_r = thrust collar length
N = number of coil turns
$R = \omega/\omega_n$
μ_o = permeability of free space
μ_r = relative permeability
μ_{rexp} = relative permeability (experimental)
ϵ = derating factor
ξ = damping factor
ω = frequency, rad/s
ω_n = natural frequency, rad/s

TEST APPARATUS

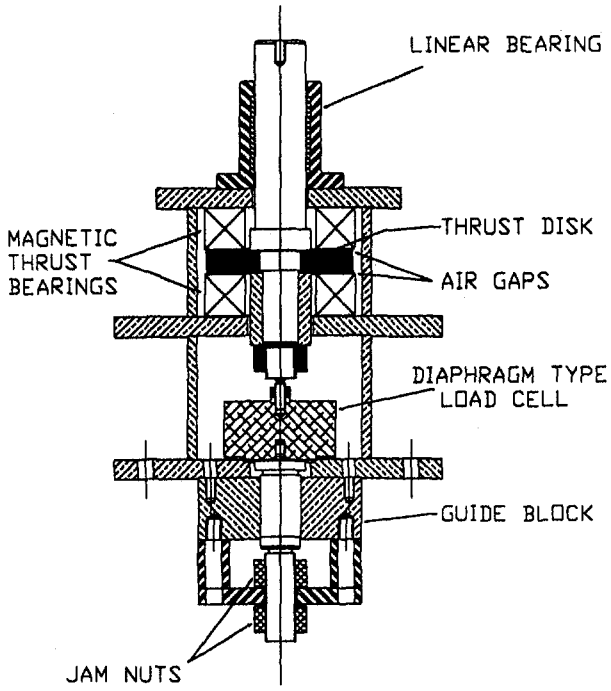

Fig. 1 Thrust actuator test apparatus

with corresponding optimal values of k_{exp} and b_{exp} found to be 0.05076 lbf in.^{2}/A^2 (145.68 N mm^2/A^2) and 0.03499 in. (0.889 mm), respectively. The optimized calibration function is given by

$$F_b = 0.05076\left[\frac{i_1^2}{(2g_1 + 0.03499)^2} - \frac{i_2^2}{(2g_2 + 0.03499)^2}\right] \quad (4)$$

where 0.05076 is compared to ϵk_{th} in Eq. (3).

Figure 4 shows a plot of the experimentally measured force versus calculated force, where Eq. (4) was used to evaluate the calculated force based on the measured coil currents and air gaps from the static calibration data.

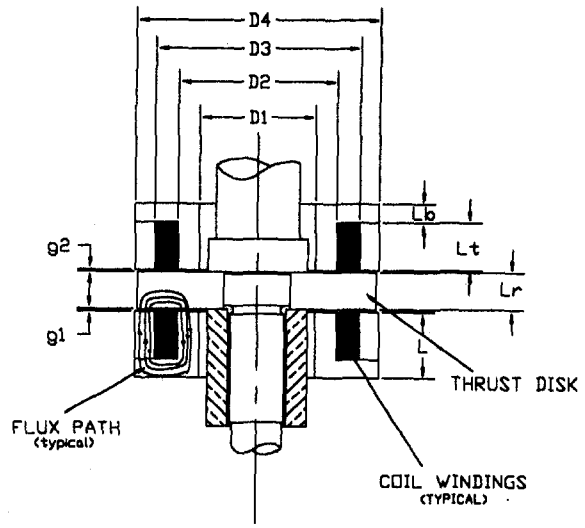

Fig. 2 Double-acting thrust actuator

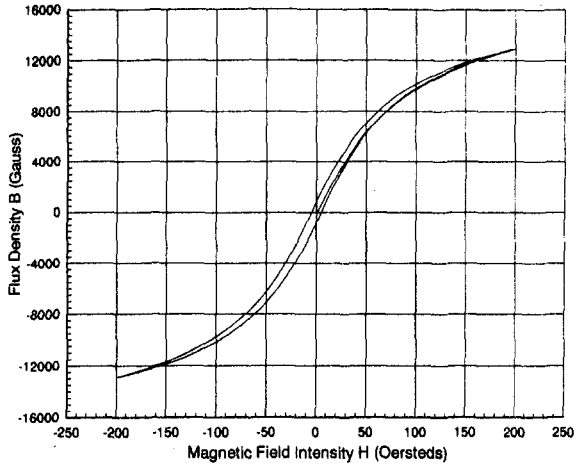

Fig. 3 TC-80 B-H curve

A test was conducted to determine the saturation force level of the actuator. The results of this test are shown in Fig. 5. Above force levels of about 50 lbf (222.5 N), the measured actuator force begins to drop below the force as calculated from Eq. (4). This is likely due to a decrease in the bearing materials relative permeability at higher induction levels. Figure 3 shows that the relative permeability (slope of the B-H curve) of Anchor Steel TC-80 is a function of field intensity H, $\mu = \mu(H)$, and as such the relative permeability will vary with field intensity or coil current in the case of the thrust actuator.

Some comparisons between k_{th} and k_{exp} can be made. It is common practice when using the theoretical bearing force equations to include a derating factor, ϵ, to account for magnetic leakage and fringing effects. A value of $\epsilon = 0.9$ is commonly used with thrust bearings (Allaire et al., 1994a). For this particular bearing, a derating factor, ϵ, can be explicitly calculated from the ratio

$$\epsilon = \frac{k_{exp}}{k_{th}} = 0.943 \quad (5)$$

This value of, ϵ, is of the same magnitude as those cited in references.

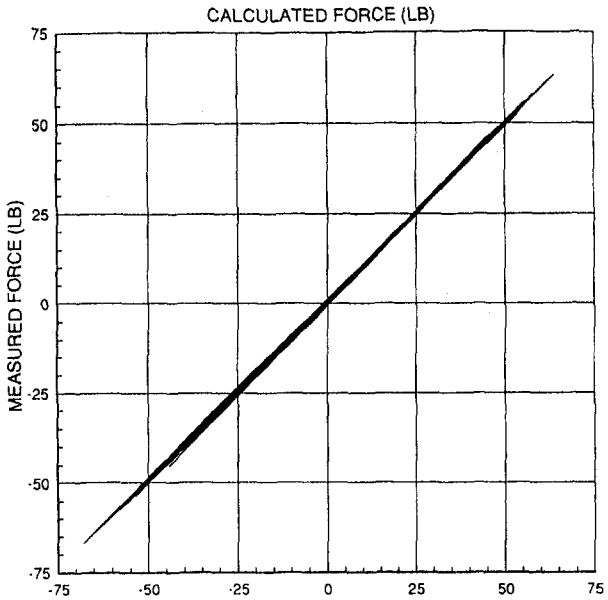

Fig. 4 Calculated force versus measured force

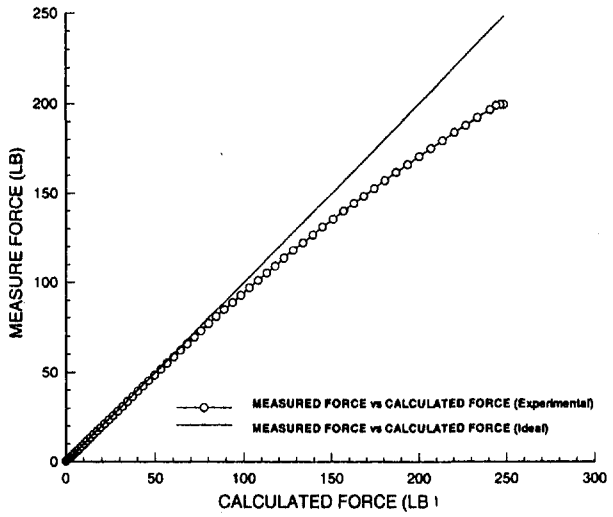

Fig. 5 Actuator saturation

Some comparisons between b_{th} and $b_{\exp}$ can also be made. There is a significant difference between the theoretically calculated equivalent iron length, b_{th}, and the experimentally determined equivalent iron length, $b_{\exp}$. The theoretical equivalent iron length, $b_{th} = 0.02375$ in. (0.603 mm), was calculated using the initial permeability, $\mu_r = 139$ (a constant), and is about 32 percent lower than the experimentally determined value, $b_{\exp} = 0.03499$ in (0.889 mm). An explanation for this difference may be attributed to: (*i*) dependence of the material's relative permeability on the magnetic field intensity (Fig. 3); (*ii*) variability of the magnetic material's relative permeability due to the manufacturing process of a powdered metal part (Oliver et al., 1995). An estimation of the effective material relative permeability applicable over the magnetic field intensity range of the tests can be made using $b_{\exp}$, $\mu_{r\exp} = L_i/b_{\exp} = 94$.

The scattering in the calibration data is apparent from the varying thickness of the calibration curve shown in Fig. 4. A scatter plot of the calibration data in the range of ±20 lbf (89 N), Fig. 6, shows that the calibration data is tightly banded, with most of the scatter skewed toward the lower side of the band. This could suggest: (*i*) Error was incurred whereby the calculated force from Eq. (4) was consistently lower than the measured force; (*ii*) the force model, Eq. (4), does not fully account for all the physical phenomena related to the magnetic flux in the bearing. The first hypothesis likely applies due to minor compliance in the test apparatus combined with a drift in the zero of the strain gauge amplifier. However, an estimate of the combined effect of these two factors showed them to be insignificant compared to the scatter observed in Fig. 6. Thus, the scatter is likely due to limitations of the linearized force model Eq. (4) to model all magnetic phenomena occurring in the bearing. This conclusion is all the more plausible given the variation of the bearing material's permeability with magnetic field intensity. In addition, extreme air gaps (very small or very large) may cause a nonlinear variation in the leakage and/or fringing. Extending the force model to account for material property, fringing, and leakage nonlinearities is beyond the scope of the present study, but would be a logical extension.

Figure 7 shows the distribution of the deviation between the measured force data and the calculated force predicted by Eq. (4). The percent error is normally distributed with a mean of −0.226 percent and a standard deviation of 7.8 percent. This relatively high standard deviation is due to: (*i*) data points with very small magnitudes of measured force and the definition of percent error as given by %error = $(F_m - F_b)/F_m$ (% error is normalized with respect to the measured force); (*ii*) limitations of the linearized force model. The slight concentration of error occurrences at +1.5 percent is likely the result of the one-sided bias of the data as discussed previously.

An uncertainty analysis was performed to determine the uncertainty of the force predicted from the calibration equation due to the uncertainties in $k_{\exp}$ and $b_{\exp}$. A Monte Carlo type perturbation analysis (based on the uncertainty of the measured calibration variables) was performed on the calibration data to obtain a large sample of values for $k_{\exp}$ and $b_{\exp}$ from which a statistical analysis was conducted to find the uncertainty in these parameters. Using a 95 percent confidence interval, the uncertainties in $k_{\exp}$ and $b_{\exp}$ were found to be ±0.000048 lbf in^2/A^2 (±0.1377 N mm^2/A^2), and ±0.000052 in (±0.00132 mm), respectively. From this result, uncertainty in the *in situ* actuator force (as given by (4)), due to the combined uncertainty of the calibration and the *in situ* measured actuator variables, can be calculated.

An estimate of the *in situ* actuator force uncertainty can be made by making a representative calculation. At an operating force of 30 lbf (133.5 N), air gap uncertainty of approximately ±0.00025 in. (±0.0064 mm), current uncertainty of ±0.005 A, $k_{\exp}$ and $b_{\exp}$ uncertainties given above, the total force uncertainty

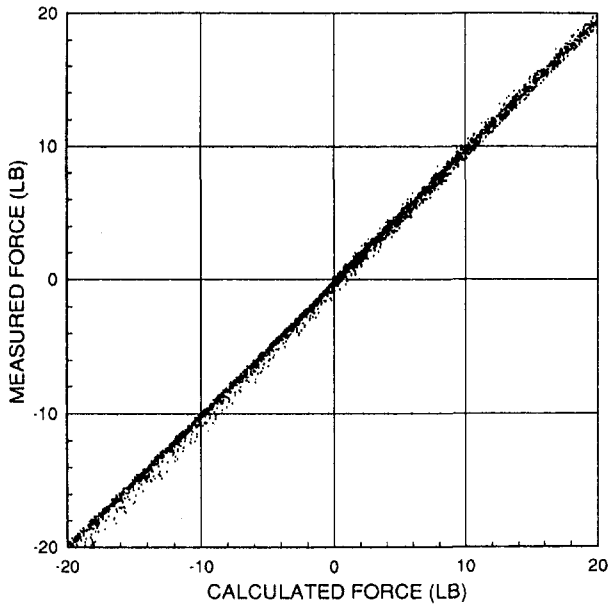

Fig. 6 Scatter in calibration data

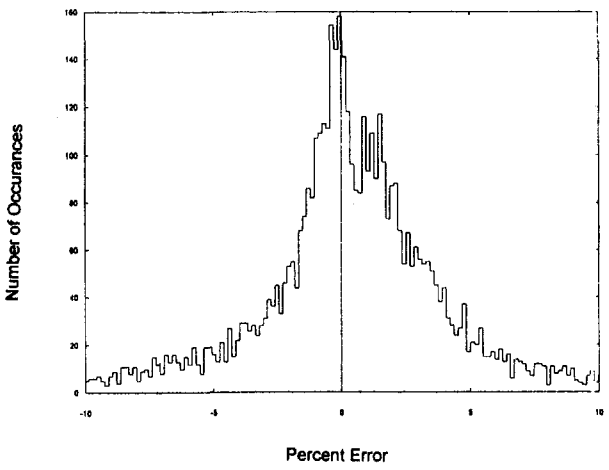

Fig. 7 Distribution of percent error

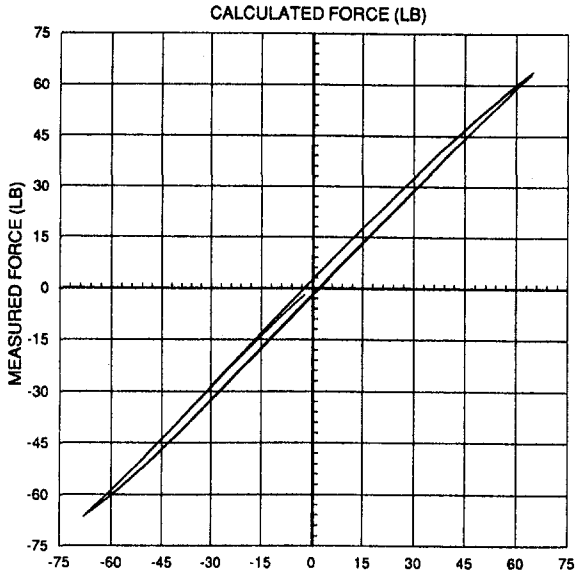

Fig. 8 Hysteresis loop test (i_p = 1.75 A)

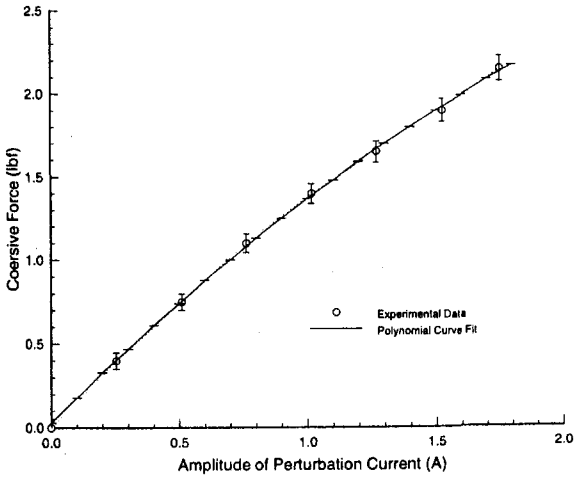

Fig. 10 Coercive force versus perturbation current amplitude

will be ±0.58 lbf (±2.58 N). Thus the calculated *in situ* actuator force uncertainty is approximately the same as the rms error in the actuator static calibration. It is of interest to note that the uncertainty in the air gaps contributes most of this total force uncertainty.

Hysteresis Testing

Hysteresis effects of a magnetic material typically produce a variation in the flux density between an increasing and decreasing magnetizing field. Thus in a dynamic environment uncertainty is introduced in any calculated bearing force based on a linear single valued force versus current model.

All hysteresis testing was conducted about the operating bias current of 1.75 A with the thrust disk in the centered position. A cyclical triangular perturbation current, i_p, of varying amplitude was then superimposed onto the bias current in each bearing. The current cycle rate was held constant at approximately 0.1 A/s. Seven tests were conducted with the amplitude of the perturbation current varying from 1.75 A to 0.25 A corresponding to minimum and maximum bearing currents of 0.0 to 3.5 A and 1.5 to 2.0 A, respectively.

Figures 8 and 9 show plots of the actuator hysteresis for a 1.75 A and a 0.25 A amplitude current loop. From Fig. 8, the maximum variation of calculated force between one side of this loop (force increasing) and the other side of the loop (force decreasing) occurs at the origin and is about 4.3 lbf (19.14 N). Figure 9 represents force variations that more closely resemble actual bearing operation. For this case, the largest force variation between one side of the hysteresis loop and the other is about 0.8 lbf (3.56 N), or expressed as a coercive force, F_c = 0.4 lbf (1.78 N).

The results from all seven hysteresis tests were combined to obtain a relationship between perturbation current, i_p, and measured coercive force, F_c. A second-order polynomial relating the amplitude of the perturbation current, i_p, and the coercive force, F_c, was found and is given by,

$$F_c = 0.0293 + 1.521 i_p - 0.1832 i_p^2. \quad (6)$$

Figure 10 shows a plot of the coercive force, F_c, versus perturbation current amplitude, i_p. Also included on this figure is a plot of Eq. (6) (solid line). From this figure, or by using Eq. (6) it will be possible to estimate the uncertainty in the *in*

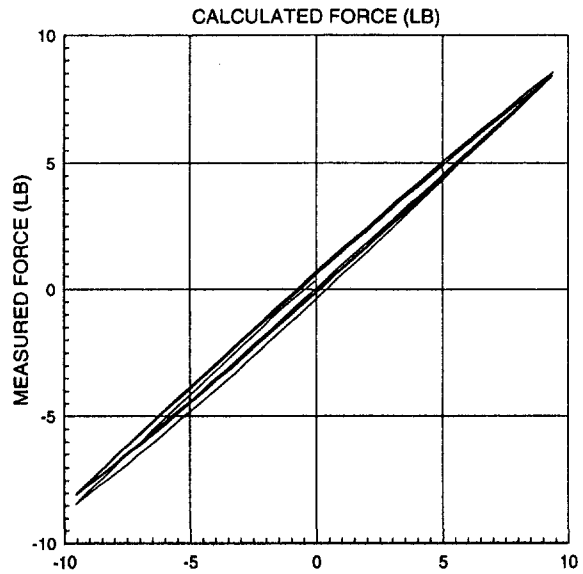

Fig. 9 Hysteresis loop test (i_p = 0.25 A)

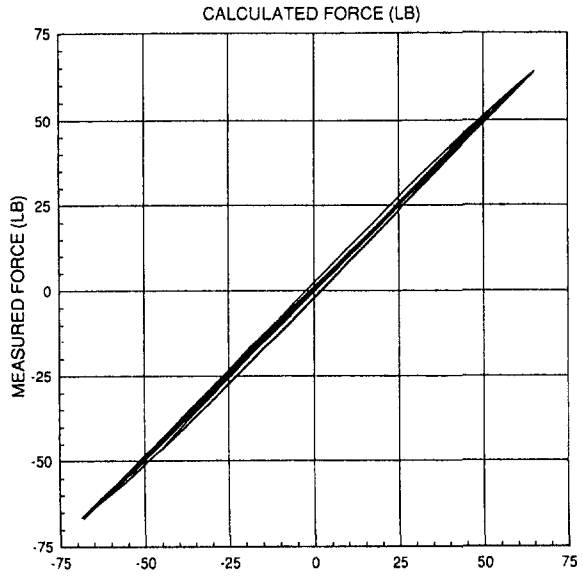

Fig. 11 Static calibration data with hysteresis test (i_p = 1.75 A)

situ actuator force, as given by Eq. (4) due to material hysteresis, if the *in situ* actuator perturbation current, i_p, is known.

Figure 11 superimposes Figs. 4 and 8 to show that the combined effects of all systematic errors in the calibration plus limitations of the linear force model result in calculated static actuator forces that lie within the bounds of force variation as dictated by the magnetic material's major hysteresis loop. When employed in a dynamic environment, the minimum uncertainty in the *in situ* actuator force is at least as large as the actuator hysteresis loop that corresponds to the amplitude of the largest actuator perturbation current encountered during the bearing operation.

Frequency Testing

The force versus current characteristic of a magnetic bearing actuator is frequency dependent due to eddy current effects. The net actuator force for a quickly varying magnetic field intensity (large i_p frequency) is less than it would be if a static field of the same instantaneous intensity (constant i_p) were applied to the actuator. In addition, the resultant actuator force develops a time delay (phase lag) with respect to the current that produced it. This type of behavior could be detrimental to, or at least limit the usefulness of, a magnetic bearing actuator as a measurement tool in a dynamic environment such as the support of a turbomachine rotor.

Frequency testing of the actuator was conducted in order to determine its bandwidth. All frequency testing was conducted about the design bias current, i_b = 1.75 A, with the thrust disk in the centered position. A sinusoidal perturbation current with a controlled cycle frequency between 1 Hz and 1 kHz and a frequency dependent amplitude was superimposed on the bias current. The actuator gain versus frequency characteristic was determined by establishing a reference at 1 Hz of the resultant actuator force versus the actual actuator current. Actuator gain at all other test frequencies was then normalized with respect to this reference.

The results of the frequency testing are shown in Fig. 12: The magnitude of the normalized actuator force (circles) and the phase of the actuator force (squares) versus frequency are plotted together with the test apparatus structural dynamic response. Figure 13 is a block diagram representation of the frequency testing model, where,

$G_b(j\omega)$ = actuator transfer function
$G_{app}(j\omega)$ = test apparatus transfer function
$G_{lc}(j\omega)$ = load cell *c/w* load cell amplifier transfer function
K = load cell static sensitivity
$i_p(j\omega)$ = actuator current
$F_b(j\omega)$ = actuator force

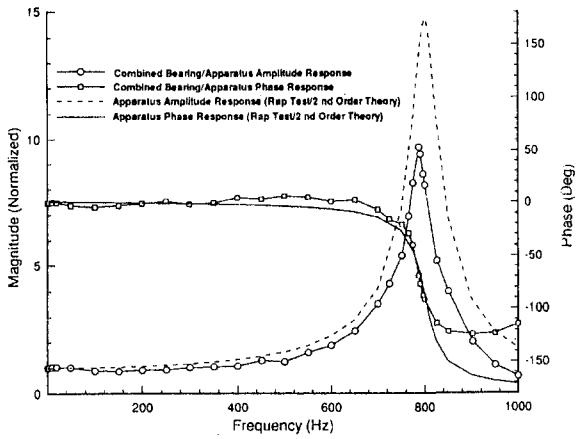

Fig. 12 Actuator frequency response

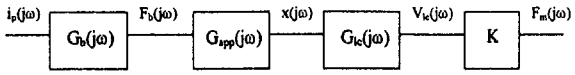

Fig. 13 Frequency testing block diagram

$x(j\omega)$ = test apparatus deflection strain
$V_{lc}(j\omega)$ = load cell amplifier output voltage
$F_b(j\omega)$ = measured force.

The apparatus structural dynamic characteristic, $F_m(j\omega)/F_b(j\omega) = KG_{app}(j\omega)G_{lc}(j\omega)$, was determined by applying a mechanical impulse to the system and measuring the transient response. The dynamic characteristic of the apparatus corresponded to a lightly damped second-order system. The natural frequency, ω_n, was estimated as 4085 (±60) rad/s (800 Hz) with a damping factor, ζ, of 0.037 (±0.0015) Using these values of ω_n and ζ, the normalized amplitude and phase versus frequency response of the apparatus assembly was modeled as

$$\frac{F_m(j\omega)}{F_b(j\omega)} = \frac{\hat{K}}{\sqrt{[1 - (R)^2]^2 + 4\zeta^2 R^2}} \tag{7}$$

and

$$\phi = \tan^{-1}\frac{2\zeta R}{R^2 - 1} \tag{8}$$

respectively. Equations (7) and (8) are plotted in Fig. 12 as a baseline to which the combined actuator/apparatus, $F_m(j\omega)/i_p(j\omega) = KG_b(j\omega)G_{app}(j\omega)G_{lc}(j\omega)$, frequency response can be compared.

As can be seen from Fig. 12, the combined actuator/apparatus frequency response, $F_m(j\omega)/i_p(j\omega)$, follows the apparatus frequency response, $F_m(j\omega)/F_b(j\omega)$. The combined actuator/apparatus phase response remains at about zero degrees up to a frequency of about 700 Hz, where it decreases due to the influence of the apparatus structural natural frequency. At frequencies above 800 Hz, the combined phase response begins to recover as compared with the theoretically predicted phase response of the apparatus alone, which asymptotically approaches −180 deg. This phase recovery may be the effect of higher apparatus modes. The normalized amplitude response of the combined bearing/apparatus, $F_m(j\omega)/i_p(j\omega)$, matches that of the structure quite well except for a slightly lower resonance peak. This is likely due to limitations of the model Eqs. (7) and (8) in completely describing the dynamics of the apparatus. The lower resonance peak may also indicate the presence of some additional damping when the bearing is operating. The only definite conclusion that can be drawn from these measurements is that, below 700 Hz, the actuator exhibits no significant eddy current effects. Above 700 Hz, the actuator frequency response was masked by structural effects. This actuator bandwidth is a significant improvement over the case of the solid iron actuator (Allaire et al., 1995), which had a reported bandwidth of approximately 2 Hz.

Summary

A double-acting magnetic thrust actuator constructed from a powdered metal was calibrated to characterize the actuator force as a function of coil currents and air gaps. The nonlinear effects of hysteresis, eddy currents, leakage, and fringing were also quantified. All actuator testing was done with the actuator operating in a differential configuration.

A static calibration test was conducted to determine a linearized functional relationship between the actuator force and the coil currents and air gaps. The functional relationship found was suitable for actuator air gap variations of ±0.015 in (±0.38 mm) about the nominal, and up to actuator force levels of 50 lbf (222.5 N). The calibration relationship was also compared

to a theoretical force relationship, based on linear magnetic theory and constant material magnetic properties. Discrepancies between the experimental and theoretical relationships were attributed to a variable relative permeability and also to possible nonlinear variations of leakage and fringing at extreme air gaps. The root-mean-square error between the experimental relationship and the measured actuator force from the static calibration test was minimized to 0.52 lbf (2.31 N). The error was normally distributed with a mean of −0.23 percent and standard deviation of 7.8 percent. In addition, a detailed error analysis procedure was developed for predicting the uncertainty of the *in situ* actuator force. The estimated *in situ* actuator force uncertainty was estimated to be of the same order of magnitude as the rms uncertainty in the static calibration.

Hysteresis testing was conducted to quantify the magnitude of actuator force variation due to material hysteresis. The coercive force was shown to depend on the specific current trajectory and the amplitude of bearing perturbation currents. A quadratic relationship was found to relate bearing coercive force to perturbation current amplitude. This relationship can be used to predict variations in actuator force due to material hysteresis if the maximum amplitude of the actuator perturbation current is known. The variation in actuator force due to hysteresis represents the minimum achievable uncertainty of the *in situ* actuator force measurement for current perturbation frequencies below the cut-off frequency.

The actuator frequency response was tested up to 1000 Hz. Due to the dynamic interference of the testing apparatus, it was only possible to verify that the bandwidth of the actuator is at least 700 Hz.

References

Allaire, P., Imlach, J., McDonald, J., Humphris, R., Lewis, D., Blair, B., Claydon, J., and Flack R., 1989, "Design, Construction, and Test of a Magnetic Bearing in an Industrial Canned Motor Pump," *Proc. Texas A&M Pump Symposium,* Houston, TX, May.

Allaire, P. E., Maslen, E. H., Humphris, R. R., Knospe, C. R., and Lewis, D. W., 1994a, "Magnetic Bearings," *Handbook of Lubrication and Tribology,* Vol. III, CRC Press, pp. 577–600.

Allaire, P. E., Maslen, E. H., Lewis, D., and Flack, R., 1994b, "Magnetic Thrust Bearing Operation and Industrial Pump Application," ASME Paper No. 94-*GT*-???.

Allaire, P. E., Fittro, R. L., Maslen, E. H., and Wakefield, W. C., 1995, "Eddy Currents, Magnetic Flux and Force in Relations in Solid Magnetic Thrust Bearings," *Proc. Fourth International Symposium on Magnetic Bearings,* Zurich, Aug.

Flack, R. D., and Allaire, P. E., 1984, "Lateral Forces on Pump Impellers: A Literature Review," *Shock and Vibration Digest,* Vol. 16, No. 1, January, pp. 5–14.

Guinzburg, A., and Buse, F. W., 1994, "Axial and Radial Forces on a Pump Impeller Obtained With a Magnetic-Bearing Force Measurement Rig," *Proc. Fourth International Symposium on Magnetic Bearings,* Hochschulverlag AG, Zurich, Switzerland, Aug. 23–26, pp. 537–542.

Hawkins, L. A., Murphy, B. T., and Lang, K. W., 1991, "The Rocketdyne Multifunction Tester: Operation of a Radial Magnetic Bearing as an Excitation Source," *Proc. ROMAG '91, Magnetic Bearings and Dry Gas Seals International Conference,* University of Virginia, Mar. 13–15, pp. 1–13.

Humphris, R. R., 1992, "A Device for Generating Diagnostic Information for Rotating Machinery," *Proc. MAG '92, Magnetic Bearings, Magnetic Drives, and Dry Gas Seals Conference & Exhibition,* July, Technomics Publication Co., pp. 123–135.

Imlach, J., Blair, B. J., and Allaire, P. E., 1991, "Measured and Predicted Force and Stiffness Characteristics of Industrial Magnetic Bearings," ASME *Journal of Tribology,* Vol. 113, pp. 784–788.

Oliver, C. G., and Rutz, H. G., 1995, "Powder Metallurgy in Electro Magnetic Applications," *Proc. Conference & Exposition on Powder Metallurgy & Particulate Materials,* Seattle, WA.

Pottie, K., Wallays, G., Verhoeven, J., Sperry, R., Gielen, L., De Vis, D., Neumer, T., Matros, M., and Jayawant, R., 1994, "Active Magnetic Bearings Used in BW/IP Centrifugal Pump," *Proc. Fourth International Symposium on Magnetic Bearings,* Hochschulverlag AG, Zurich, Switzerland, Aug. 23–26, pp. 463–477.

Press, W. H., Flannery, B. P., Teukololsky, S. A., and Vettlerling, W. T., 1986, *Numerical Recipes in Fortran, The Art of Scientific Computing,* 2nd ed., Cambridge University Press.

Ulbrich, H, 1988, "New Test Techniques Using Magnetic Bearings," *Proc. First International Conference on Magnetic Bearings,* June, Springer-Verlag, pp. 281–289.

Wagner, N. G., and Pietruszka, W. D., 1988, "Identification of Rotor Dynamic Parameters on a Test Stand With Active Magnetic Bearings," *Proc. First International Conference on Magnetic Bearings,* June, Springer-Verlag. pp. 289–302.

Wakefield, W. C., 1994, "Magnetic Bearings/Load Cells for a Centrifugal Pump: Design Construction and Testing," M.S. Thesis, University of Virginia.

The Acoustic Influence of Cell Depth on the Rotordynamic Characteristics of Smooth-Rotor/Honeycomb-Stator Annular Gas Seals

G. F. Kleynhans
Graduate Research Assistant.

D. W. Childs
Jordan Professor of Mechanical Engineering.

Turbomachinery Laboratory,
Texas A&M University,
College Station, TX 77843-3257

A two-control-volume model is employed for honeycomb-stator/smooth-rotor seals, with a conventional control-volume used for the throughflow and a "capacitance-accumulator" model for the honeycomb cells. The control volume for the honeycomb cells is shown to cause a dramatic reduction in the effective acoustic velocity of the main flow, dropping the lowest acoustic frequency into the frequency range of interest for rotordynamics. In these circumstances, the impedance functions for the seals cannot be modeled with conventional (frequency-independent) stiffness, damping, and mass coefficients. More general transform functions are required to account for the reaction forces, and the transfer functions calculated here are a lead-lag term for the direct force function and a lag term for the cross-coupled function. Experimental measurements verify the magnitude and phase trends of the proposed transfer functions. These first-order functions are simple, compared to transfer functions for magnetic bearings or foundations. For synchronous response due to imbalance, they can be approximated by running-speed-dependent stiffness and damping coefficients in conventional rotordynamics codes. Correct predictions for stability and transient response will require more general algorithms, presumably using a state-space format.

Introduction

The use of honeycomb annular seals in gas compressors and turbines is an attractive retrofit or design implementation due to their favorable static and dynamic characteristics. Honeycomb seals are most often employed in the following two distinct ways: (*a*) A honeycomb-stator/smooth-rotor configuration for enhancing rotor stability, (*b*) an abradable honeycomb-stator with a labyrinth-rotor for superior leakage control. The latter configuration is typical for aircraft gas turbines, while the former is used frequently in high-pressure centrifugal compressors in the petrochemical industry and is the configuration of interest here. In the balance of this paper, "honeycomb seals" will refer to this configuration.

Honeycomb seals were initially used to eliminate a stability problem with the High-Pressure Oxygen Turbopump (HPOTP) of the Space Shuttle Main Engine (SSME) (Scharrer, 1989). Recently, these seals have been used to eliminate rotordynamic instability problems with high-pressure compressors (Zeidan et al., 1993; Sorokes et al., 1994). The authors are aware of several other compressors plus at least one steam turbine that have been "cured" of rotordynamic instability problems via retrofits of honeycomb seals.

For small motion about a centered position, the conventional force/motion model used for annular seals is

$$-\begin{Bmatrix} F_x \\ F_y \end{Bmatrix} = \begin{bmatrix} K & k \\ -k & K \end{bmatrix} \begin{Bmatrix} x \\ y \end{Bmatrix} + \begin{bmatrix} C & c \\ -c & C \end{bmatrix} \begin{Bmatrix} \dot{x} \\ \dot{y} \end{Bmatrix} + M \begin{Bmatrix} \ddot{x} \\ \ddot{y} \end{Bmatrix} \quad (1)$$

For annular gas seals, c and M have typically been assumed to be negligible. Nelson (1984, 1985) developed the initial analysis for rotordynamic coefficients of annular seals. Nelson developed a bulk-flow model comprised of: (*a*) a compressible-flow continuity equation, (*b*) an axial-momentum equation, (*c*) a circumferential-momentum equation, (*d*) an energy equation, and (*e*) a perfect-gas equation of state. The honeycomb surface was treated as a solid wall. The only influence of the honeycomb surface was an increased friction factor in the momentum equations. This model did a notably poor job in predicting measured rotordynamic coefficients. Various improvements were attempted, starting with Elrod et al. (1989, 1990) who developed an improved model for the inlet loss. Ha and Childs (1994) implemented friction-factor data from flat-plate measurements to improve the friction-factor model for honeycomb surfaces. In a response to a discussion of their paper, Ha and Childs expanded the model to allow radial transient flow into the honeycomb surface. Their analysis uses a two-control-volume model.

An implicit requirement in all of the analyses leading to the model of Eq. (1) is that the acoustic frequencies of the gas within an annular seal be substantially above the rotordynamic frequencies of interest. This paper will use the two-control-volume model of Ha and Childs (1994) to demonstrate that this requirement is generally not met, and consequently, honeycomb seals cannot be modeled adequately with frequency-independent stiffness, damping, and mass coefficients.

Two-Control-Volume Model. The prior governing equations for plain and honeycomb gas seals (Nelson, 1985; Ha and Childs, 1994) employ a single control volume. However, the honeycomb seal geometry can clearly allow flow to enter and exit the honeycomb cells radially. In essence, the honeycomb seal land acts as a porous surface. Hence, as indicated in the authors' response of Ha and Childs (1994), the use of an additional control volume (adjacent to the main flow control volume), which allows flow to enter and exit only in the radial direction, can better describe the physical nature of the flow.

Contributed by the International Gas Turbine Institute and presented at the 41st International Gas Turbine and Aeroengine Congress and Exhibition, Birmingham, United Kingdom, June 10–13, 1996. Manuscript received at ASME Headquarters February 1996. Paper No. 96-GT-122. Associate Technical Editor: J. N. Shinn.

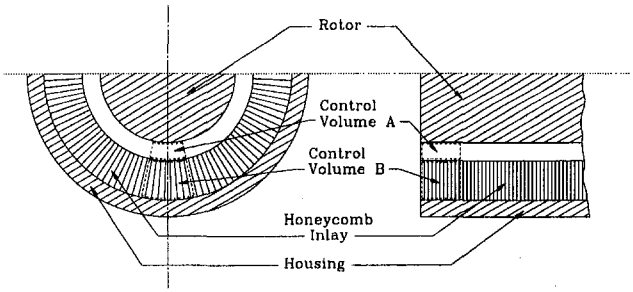

Fig. 1 Control volume locations within seal

Figure 1 shows the locations of the two control volumes in a honeycomb seal with the clearance exaggerated for clarity. The nature of flow between the control volumes is shown in Fig. 2. Note that the cell depth H_d can be more than ten times the clearance, H. For control volume A in Fig. 2, the continuity equation is

$$\frac{\partial}{\partial t}(\rho H) + \frac{1}{R}\frac{\partial}{\partial \Theta}(\rho U H) + \frac{\partial}{\partial Z}(\rho W H) + \rho V = 0, \quad (2)$$

and for control volume B,

$$\rho V = H_d \frac{\partial \rho}{\partial t} \quad (3)$$

Note that for a centered seal without a clearance perturbation, $V = 0$. A clearance perturbation is required to generate flow between volumes A and B.

A summation of the forces in the Z and Θ directions yields the following momentum equations:

Axial Momentum Equation

$$-H\frac{\partial P}{\partial Z} = \tau_{sz} + \tau_{rz} + \rho W V + \frac{\partial}{\partial t}(\rho W H) + \frac{1}{R}\frac{\partial}{\partial \Theta}(\rho U W H) + \frac{\partial}{\partial Z}(\rho W^2 H) \quad (4)$$

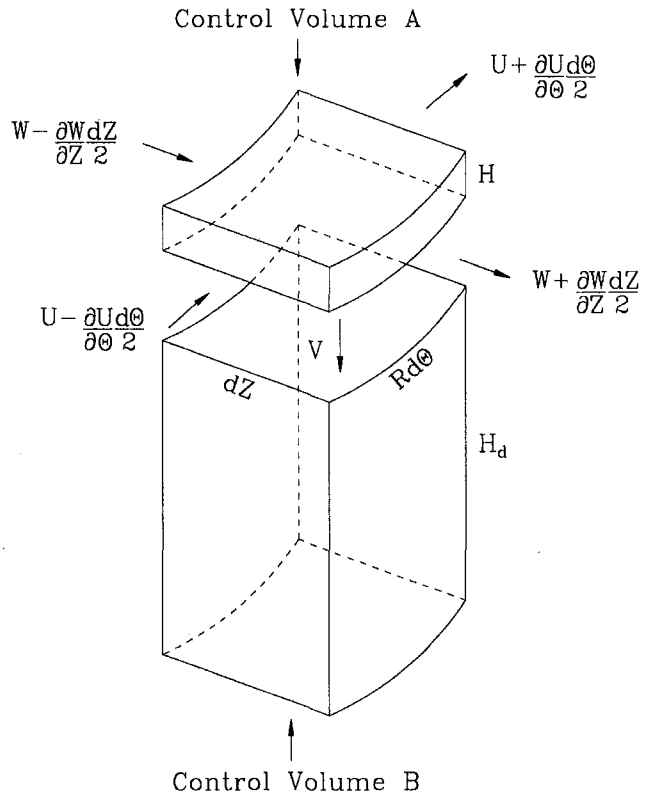

Fig. 2 Flow in and out of control volumes

Circumferential Momentum Equation

$$-\frac{H}{R}\frac{\partial P}{\partial \Theta} = \tau_{s\Theta} + \tau_{r\Theta} + \rho U V + \frac{\partial}{\partial t}(\rho U H) + \frac{1}{R}\frac{\partial}{\partial \Theta}(\rho U^2 H) + \frac{\partial}{\partial Z}(\rho U W H) \quad (5)$$

Nomenclature

c_0 = effective sonic speed, L/t
c_r = rotor damping, Ft/L
C, c = direct and cross-coupled damping, Ft/L
C_r = seal inlet clearance, L
$\mathbf{D}$ = direct impedance, F/L
e = Precession amplitude, L
$\mathbf{E}$ = Cross-coupled impedance, F/L
f = Ω/ω-nondimensional excitation frequency
f_{res} = resonant frequency, l/t
F_X, F_X = seal reaction forces, F
H = seal clearance, L
H_d = honeycomb cell depth, L
h_d = H_d/H-nondimensional honeycomb cell depth
I_r, I_Θ = Radial and tangential impedances, F/L
$j = \sqrt{-1}$
K, k = direct and cross-coupled stiffness, F/L
K_D = direct transfer function constant, F/L
K_E = cross-coupled transfer-function constant, FT/L
k_r = rotor stiffness, F/L
L = seal length, L
M = direct added mass, M
m_r = rotor mass, M
p_e = P_S/P_R = ratio of absolute sump to reservoir pressures
P = pressure, F/L^2
P_R = reservoir (upstream, inlet) pressure, F/L^2
P_S = sump (downstream, back) pressure, F/L^2
r_0 = excitation amplitude, L
R = seal radius, L
R_g = gas constant, FL/MT
s = complex variable for Laplace transforms, $1/t$
t = time, t
T = fluid bulk temperature, T
U = circumferential bulk fluid velocity, L/t
V = radial bulk fluid velocity, L/t
W = axial bulk fluid velocity, L/t
x, y = seal/rotor relative displacement, L
$\dot{x}, \dot{y}$ = seal/rotor relative velocities, L/t
$\ddot{x}, \ddot{y}$ = seal/rotor relative accelerations, L/t^2
x, y = frequency domain seal/rotor relative displacement, L/t
Z = axial coordinate, L
Z_c = gas compressibility factor
α, β, γ = transfer function frequencies, $1/t$
ϵ = perturbation in eccentricity ratio
Θ = circumferential coordinate
ρ = fluid density, M/L^3
τ = shear stress, F/L^2
ξ, ξ_e = entrance loss and exit recovery factors
ω = rotor rotational frequency, $1/t$
Ω = rotor precession frequency, $1/t$

Subscripts

0, 1 = zeroth and first order
r, Θ = radial and circumferential
$rz, r\Theta$ = rotor axial and circumferential
$sz, s\Theta$ = stator axial and circumferential

The variable V is eliminated by substituting the continuity equation for Control Volume B into the continuity equation of Control Volume A and the momentum equations. The shear-stress terms are modeled via the bulk-flow theory of Hirs (1973). The relationship between pressure P and density ρ is modeled by the equation of state for an ideal gas,

$$\rho = \frac{P}{Z_c R_g T} \tag{6}$$

For this analysis an isothermal flow is assumed; hence, the energy equation is not required. The bases for assuming isothermal flow are the following: (a) experimental measurements for honeycomb seals tested at the Turbomachinery Laboratory of Texas A&M University have shown less than 5 percent temperature change through the seal, and (b) dynamic pressure measurements inside the honeycomb cells by Ha et al. (1992) indicated that the fundamental frequencies are above audible range (0 to 18 kHz); according to Potter and Foss (1982) flow with that high a frequency content is best approximated as being isothermal.

The solution of these equations follows the procedure outlined by Childs (1993) and employs a perturbation of the variables P, H, W, and U in the following manner:

$$\begin{aligned} P &= P_0 + \epsilon P_1 \\ H &= H_0 + \epsilon H_1 \\ W &= W_0 + \epsilon W_1 \\ U &= U_0 + \epsilon U_1 \end{aligned} \tag{7}$$

The small parameter ϵ is the perturbed eccentricity ratio about a centered position. For solution, the parameters are nondimensionalized via

$$p = \frac{P}{P_r} \quad h = \frac{H}{C_r} \quad w = \frac{W}{\sqrt{Z_c R_g T}} \quad u = \frac{U}{\sqrt{Z_c R_g T}}$$

$$z = \frac{Z}{L} \quad h_d = \frac{H_d}{C_r} \quad \tau = t\omega \tag{8}$$

The clearance function is

$$h = h_0 - x(t)\cos\Theta - y(t)\sin\Theta \tag{9}$$

Thus, from Eqs. (7) and (8)

$$\epsilon h_1 = -x\cos\Theta - y\sin\Theta \tag{10}$$

Given this relation for h_1, the following separation-of-variable solution is assumed for the dependent perturbation variables:

$$\begin{aligned} w_1(z, \tau, \Theta) &= w_{1c}(z, \tau)\cos\Theta + w_{1s}(z, \tau)\sin\Theta \\ u_1(z, \tau, \Theta) &= u_{1c}(z, \tau)\cos\Theta + u_{1s}(z, \tau)\sin\Theta \\ p_1(z, \tau, \Theta) &= p_{1c}(z, \tau)\cos\Theta + p_{1s}(z, \tau)\sin\Theta \end{aligned} \tag{11}$$

This assumed solution established a sinusoidal response of the perturbed variables in the $R\Theta$ direction. The Θ dependency is eliminated by substituting the relations of Eqs. (10) and (11) into the first order equations. Equating coefficients of $\sin\Theta$ and $\cos\Theta$ terms yields six real equations. Introducing the following complex variables:

$$\begin{aligned} \bar{\mathbf{w}}_1 &= w_{1c} + jw_{1s} \quad \bar{\mathbf{u}}_1 = u_{1c} + ju_{1s} \\ \bar{\mathbf{p}}_1 &= p_{1c} + jp_{1s} \quad \epsilon\mathbf{h}_1 = -(x + jy), \end{aligned} \tag{12}$$

reduces the problem to three complex equations in t and z. The time dependency is eliminated by assuming a precessional seal motion of the form,

$$\epsilon\mathbf{h}_1 = -\left(\frac{R_0}{C_r}\right)e^{j\Omega t} = -r_0 e^{jft}, \tag{13}$$

where Ω is the precessional frequency for the rotor, and

$$f = \frac{\Omega}{\omega}. \tag{14}$$

Corresponding separation-of-variables solutions for the perturbed dependent variables are:

$$\bar{\mathbf{w}}_1 = \mathbf{w}_1 e^{jft} \quad \bar{\mathbf{u}}_1 = \mathbf{u}_1 e^{jft} \quad \bar{\mathbf{p}}_1 = \mathbf{p}_1 e^{jft} \tag{15}$$

Finally, after substituting these variables and simplifying, the governing equations are

$$[A(z)]\frac{d}{dz}\begin{Bmatrix}\mathbf{w}_1\\ \mathbf{p}_1\\ \mathbf{u}_1\end{Bmatrix} + [B(z,f)]\begin{Bmatrix}\mathbf{w}_1\\ \mathbf{p}_1\\ \mathbf{u}_1\end{Bmatrix} = \left(\frac{r_0}{\epsilon}\right)\{C(z,f)\} \tag{16}$$

The boundary conditions required to solve Eq. (16) can be obtained by applying the perturbations of Eq. (7) to the entrance-loss equation,

$$1 - p(0, \Theta, t) = \frac{(1+\xi)}{2}p(0, \Theta, t)w^2(0, \Theta, t), \tag{17}$$

and exit-recovery equation,

$$p(1, \Theta, t) - p_e = -\frac{(1-\xi_e)}{2}p(1, \Theta, t)w^2(1, \Theta, t) \tag{18}$$

The resultant perturbed expressions are

$$\mathbf{p}_1(0) = -\frac{(1+\xi)}{2} \times [\mathbf{p}_1(0)w_0^2(0) + 2p_0(0)w_0(0)\mathbf{w}_1(0)], \tag{19}$$

and,

$$\mathbf{p}_1(1) = -\frac{(1-\xi_e)}{2} \times [\mathbf{p}_1(1)w_0^2(1) + 2p_0(1)w_0(1)\mathbf{w}_1(1)] \tag{20}$$

For choked flow, Eq. (20) is replaced with the requirement that the exit isothermal Mach number be constant, which yields the alternative perturbed boundary condition $w_1(1) = 0$. Note, choked flow implies that the coefficient of the dp_0/dz term is zero and thus, the pressure gradient becomes infinite. The third boundary condition is $\mathbf{u}_1(0) = 0$. Using a transition-matrix approach, the missing boundary conditions at the entrance ($\mathbf{p}_1(0)$ and $\mathbf{w}_1(0)$) are found that satisfy Eqs. (19) and (20).

Integration of the perturbed pressure for discrete frequencies gives the following perturbation impedances:

$$\begin{aligned} I_r(f) &= -\pi\int_0^1 \mathrm{Re}[\mathbf{p}_1(f)]dz \\ I_\Theta(f) &= -\pi\int_0^1 \mathrm{Im}[\mathbf{p}_1(f)]dz \end{aligned} \tag{21}$$

If the force/motion relationship conforms to the model in Eq. (1), least-square curvefits of impedance versus frequency provide:

Table 1 Input data from test measurement

Absolute Inlet Pressure	18.3 bar
Absolute Back Pressure	4.4 bar
Inlet Temperature	302 K
Rotational Speed	15960 rpm
Seal Length	0.101 m
Seal Diameter	0.101 m
Seal Clearance	0.2 mm
Honeycomb Cell Width	1.59 mm
Honeycomb Cell Depth	2.29 mm
Inlet Preswirl Ratio	0.0
Entrance Loss Factor	0.5

$$I_r(f) = (K - Mf^2) + cf$$
$$I_\Theta(f) = k - Cf \qquad (22)$$

With the force coefficients found, the analysis is complete. The example provided in the following section will demonstrate the inadequacy of Eq. (1) in matching calculated impedances due to an acoustic phenomenon.

Solution Example for a Long (L/D = 1) Honeycomb Seal

Test conditions of a honeycomb seal that was tested at the Turbomachinery Laboratory of Texas A&M University are used in this study to define an example calculation. A description of the test facility is provided by Childs et al. (1985) and Pelletti and Childs (1991). The appropriate input data are shown in Table 1. The required gas properties conform to dry air at these pressures and temperature.

Figures 3 and 4 show the calculated impedances in the radial and circumferential directions, respectively, with honeycomb cell depth as a parameter. Note that varying h_d will vary the shear stresses; however, here the shear stresses are held constant and h_d is allowed to vary to examine its effect on the impedances. For h_d = 0, the models of Eq. (22) are adequate for precessional frequencies that range out to four or five times running speed. For deeper cell depths, the model of Eq. (22) and by inference Eq. (1) cannot describe the force/motion relationship at higher frequencies. More importantly, when the cell depth increases, Fig. 4 shows resonances, i.e., local minima or maxima, at frequencies (f_{res}) that are less than running speed. Clearly, the form of Eq. (1) cannot accommodate these resonances; specifically, $I_r(f)$ can not be modeled by a quadratic function, and $I_\theta(f)$ cannot be modeled by a straight line over the frequency range of interest. The resonances appear because the enclosed cell depth yields a reduction of the effective sonic speed caused by the increased effective volume. An explanation of the phenomenon is provided below.

Acoustic Model. To perform an acoustic study, the perturbed governing equations of flow are reduced in a manner described by Thompson (1988). The reduction of the general perturbation equations to an undamped wave equation entails eliminating the convection terms in the perturbed variables and the shear stress terms. For simplicity, excitation terms due to perturbations in the clearance function are also neglected. After these simplifications, and using dimensional variables for clarity, the following equations result:

Continuity

$$\frac{\partial}{\partial t}[\rho_1(H_0 + H_d)] + \rho_0 H_0\left(\frac{1}{R}\frac{\partial U_1}{\partial \Theta} + \frac{\partial W_1}{\partial Z}\right) = 0 \qquad (23)$$

Axial Momentum

$$-H_0\frac{\partial P_1}{\partial Z} = \rho_0 H_0\frac{\partial W_1}{\partial t} \qquad (24)$$

Circumferential Momentum

$$-\frac{H_0}{R}\frac{\partial P_1}{\partial \Theta} = \rho_0 H_0\frac{\partial U_1}{\partial t} \qquad (25)$$

Taking the divergence of the combination of Eqs. (24) and

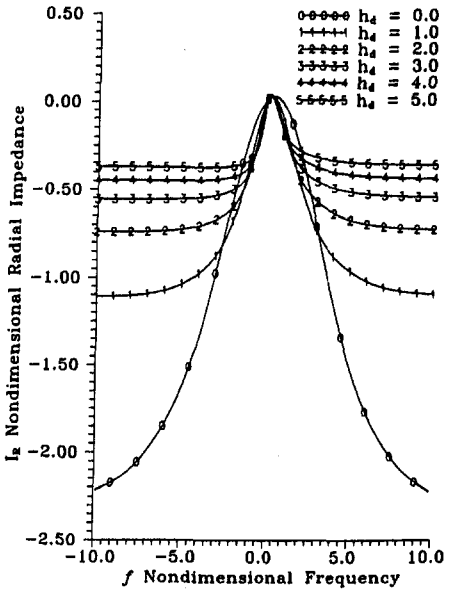

Fig. 3 Radial impedance versus frequency

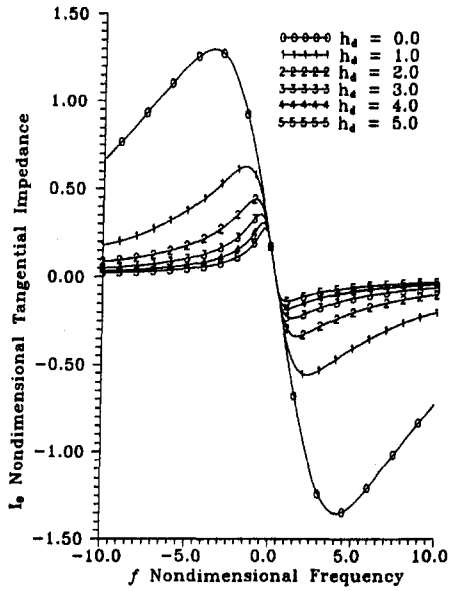

Fig. 4 Tangential impedance versus frequency

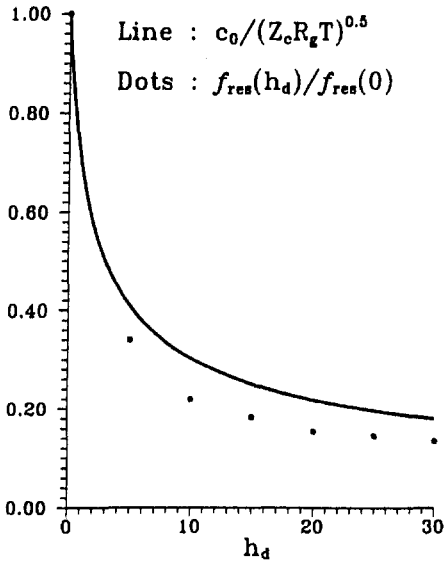

Fig. 5 Effective sonic speed versus honeycomb cell depth

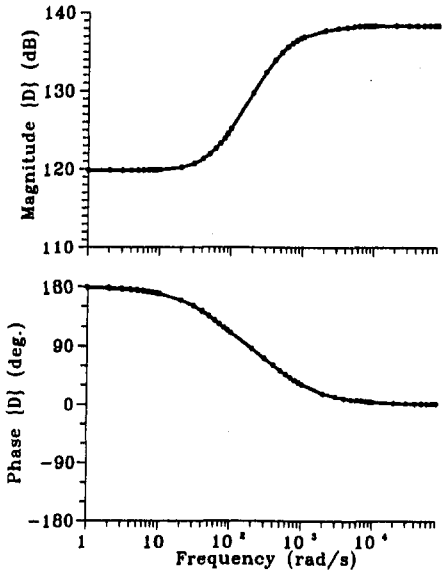

Fig. 6 Magnitude and phase of calculated direct impedance versus frequency

(25) and subtracting the result from the partial derivative of Eq. (23) with respect to time yields

$$(H_0 + H_d)\frac{\partial^2 \rho_1}{\partial t^2} - H_0 \nabla^2 P_1 = 0 \tag{26}$$

Simplifying Eq. (26) with the equation of state, Eq. (6), and rearranging provides,

$$\frac{\partial^2 P_1}{\partial t^2} = \frac{Z_c R_g T}{\left(1 + \dfrac{H_d}{H_0}\right)} \nabla^2 P_1 = c_0^2 \nabla^2 P_1, \tag{27}$$

which is the wave equation in terms of perturbed pressure where c_0 is the effective acoustic velocity. Note that setting $H_d = 0$ yields $c_0 = \sqrt{Z_c R_g T}$ the isothermal sonic speed (Potter and Foss, 1982).

A comparison of the reduction of c_0 and the resonant frequencies (f_{res}) of Fig. 4 versus h_d is shown in Fig. 5. The effective sonic speed is nondimensionalized by the isothermal sonic speed, the resonant frequencies are nondimensionalized by the resonant frequency for $h_d = 0$, and the honeycomb cell depth is nondimensionalized by the operating clearance.

In performing the acoustic analysis, the velocity disturbances, ($\mathbf{w}_1$ and $\mathbf{u}_1$), are assumed to be small in comparison to the sonic speed, i.e., (Mach number)$^2 \ll 1$. However, the flow within a seal can approach the choked condition, Mach number = 1 at seal exit. Hence, applying the acoustic analysis may be questionable for some conditions. Nevertheless, the acoustic model explains the reduction of the resonant frequencies shown in Fig. 4. In Fig. 5, the rate of decrease of the resonant frequencies with increased cell depth is consistent with the rate of decrease of the effective sonic speed from the acoustic solution. This parallel validates the acoustic-model explanation of cell-depth influence on the effective sonic speed and, consequently, on the resonances shown in Fig. 4.

General-Transfer-Function Model

Because the acoustic resonant frequencies in a honeycomb seal can be less than the operating speed, causing the force/motion model in Eq. (1) to be inadequate, a new model is required for the reaction force components and the following Laplace transform model is proposed:

$$-\begin{Bmatrix} \mathbf{F}_x(s) \\ \mathbf{F}_y(s) \end{Bmatrix} = \begin{bmatrix} \mathbf{D} & \mathbf{E} \\ -\mathbf{E} & \mathbf{D} \end{bmatrix} \begin{Bmatrix} \mathbf{x}(s) \\ \mathbf{y}(s) \end{Bmatrix} \tag{28}$$

where the form of $\mathbf{D}$ and $\mathbf{E}$ is to be determined based on the solution of Eq. (16) and the boundary conditions of Eqs. (19) and (20). Following Bolleter et al. (1989), for circular precession the impedances of Eq. (21) in terms of $\mathbf{D}$ and $\mathbf{E}$ are,

$$\begin{aligned} I_r^+ &= -\mathrm{Re}[\mathbf{D}] - \mathrm{Im}[\mathbf{E}] \\ I_r^- &= -\mathrm{Re}[\mathbf{D}] + \mathrm{Im}[\mathbf{E}] \\ I_\Theta^+ &= \mathrm{Re}[\mathbf{E}] - \mathrm{Im}[\mathbf{D}] \\ I_\Theta^- &= \mathrm{Re}[\mathbf{E}] + \mathrm{Im}[\mathbf{D}], \end{aligned} \tag{29}$$

where the "+" power indicates positive excitation frequencies and the "−" power indicates negative excitation frequencies. By adding and subtracting terms in Eq. (29), $\mathbf{D}$ and $\mathbf{E}$ can be found from the solutions shown in Figs. 4 and 5.

To obtain analytical expressions for the transfer functions, magnitude and phase plots for $\mathbf{D}$ and $\mathbf{E}$ are required. Figures 6 and 7 show the magnitude and phase for $\mathbf{D}$ and $\mathbf{E}$, respectively.

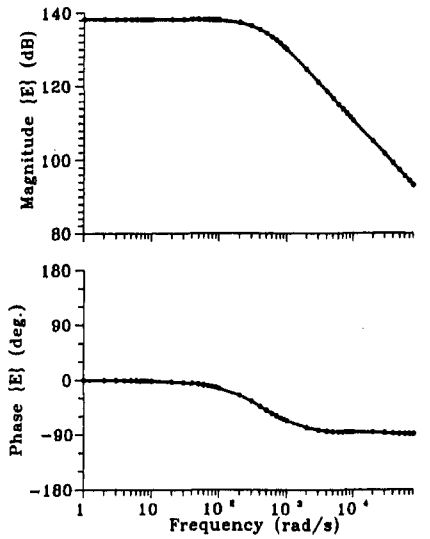

Fig. 7 Magnitude and phase of calculated cross-coupled impedance versus frequency

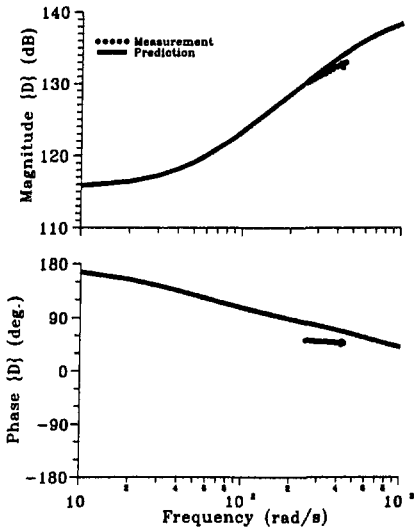

Fig. 8 A comparison of measured (dots) and predicted (thin line) magnitude and phase for direct impedance *D*

The approximate transfer functions resulting from the solutions are:

$$\mathbf{D}(s) = \frac{K_D(s + \alpha)}{(s + \beta)}, \tag{30}$$

and,

$$\mathbf{E}(s) = \frac{K_E}{(s + \gamma)} \tag{31}$$

For the plots depicted in Figs. 6 and 7, the terms in these expressions are approximately; $K_D = 10.75$ MN/m, $K_E = 2108$ MNs/m, $\alpha = -84$ rad/s, $\beta = 600$ rad/s, and $\gamma = 470$ rad/s. Note that α, β, and γ are less than running speed ($\sim$1670 rad/s). The model format for **D** and **E** shown in Eqs. (30) and (31) has been found to be appropriate for a wide range of honeycomb seal configurations over a wide range of operating conditions. However, alternative formats may yet be required for some cases; e.g., second-degree denominator polynomials might result from calculated seal impedances.

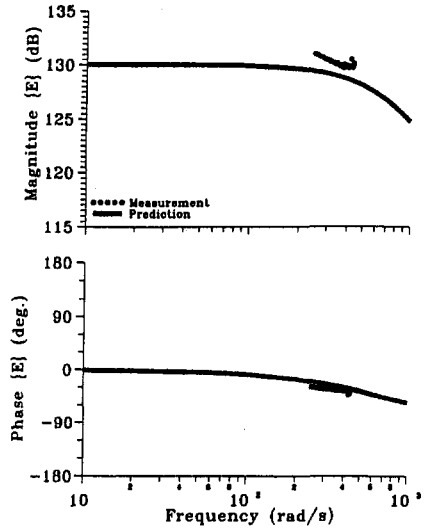

Fig. 9 A comparison of measured (dots) and predicted (thin line) magnitude and phase for cross-coupled impedance *E*

Figures 8 and 9 show comparisons of measured and predicted magnitude and phase of **D** and **E**, respectively, for the example case of Table 1. The predicted trends of magnitude and phase for both **D** and **E** are verified by the measurements. A large message provided by Figs. 8 and 9 is that data are required over a much larger frequency range to verify the predicted model format of Eqs. (30) and (31) more adequately. Unfortunately, the frequency range of the investigators test rig cannot be extended.

Having arrived at valid transfer functions for honeycomb seals, the next question is: How can these models be integrated into rotordynamic analyses?

General Transfer Function Models and Rotordynamic Analyses

Rotordynamic analyses generally involve solution for synchronous response due to imbalance, stability analyses, and nonlinear transient simulations. For synchronous response, the transfer functions of Eqs. (30) and (31) can be converted into running-speed-dependent stiffness and damping coefficients in the same way that people have traditionally modeled foundations, gas bearings, flexibly-supported tilting-pad bearings, etc. The effective (running-speed-dependent) stiffness and damping are found by returning to Eq. (28). The bottom (y-direction) term is multiplied by **j** and added to the top term, yielding the complex expression,

$$-[\mathbf{F}_x(s) + j\mathbf{F}_y(s)] = [\mathbf{D}(s) - j\mathbf{E}(s)][x(s) + jy(s)] \tag{32}$$

Next, Eqs. (30) and (31) are substituted for $\mathbf{D}(s)$ and $\mathbf{E}(s)$ and s is replaced by $\mathbf{j}\Omega$. Dividing the force (left-hand-side) by the motion (extreme right-hand-side) provides the following complex expression:

$$-\frac{[\mathbf{F}_x(\Omega) + j\mathbf{F}_y(\Omega)]}{[\mathbf{X}(\Omega) + j\mathbf{Y}(\Omega)]} = \frac{K_D[\Omega^2 + \alpha\beta]}{\Omega^2 + \beta^2} - \frac{K_E\Omega}{\Omega^2 + \gamma^2} + j\left[\frac{K_D\Omega(\beta - \alpha)}{\Omega^2 + \beta^2} - \frac{K_E\gamma}{\Omega^2 + \gamma^2}\right] \tag{33}$$

From this relation, the real part of the right-hand-side provides the effective stiffness and the imaginary part of the right-hand-side, divided by Ω, provides the effective damping, i.e.,

$$K_{\text{eff}} = \frac{K_D[\Omega^2 + \alpha\beta]}{\Omega^2 + \beta^2} - \frac{K_E\Omega}{\Omega^2 + \gamma^2}$$

$$C_{\text{eff}} = \frac{K_D[\beta - \alpha]}{\Omega^2 + \beta^2} - \frac{K_E\gamma}{\Omega(\Omega^2 + \gamma^2)} \tag{34}$$

Figures 10 and 11 show the predicted effective stiffness and damping, in dimensional units, for the impedances shown in Figs. 3 and 4, respectively. Note that increased cell depth decreases the effective damping. At low frequencies ($f < 0.15$) the effective damping is negative because of a relatively large cross-coupled stiffness ($K_E\gamma$) term.

An approximate and iterative stability analysis can be performed by selecting a frequency, e.g., running speed, calculating equivalent stiffness and damping coefficients for this speed from Eq. (34), and then calculating damped eigenvalues. The natural frequency of the mode that is of concern with respect to stability can then be used to recalculate equivalent stiffness and damping coefficients, and the cycle is repeated until convergence is achieved between the assumed frequency and the imaginary part of the damped eigenvalue of interest. Aside from the iterative nature of this approach, an additional drawback is that the results obtained for damped eigenvalues at other than the converged natural frequency are not correct.

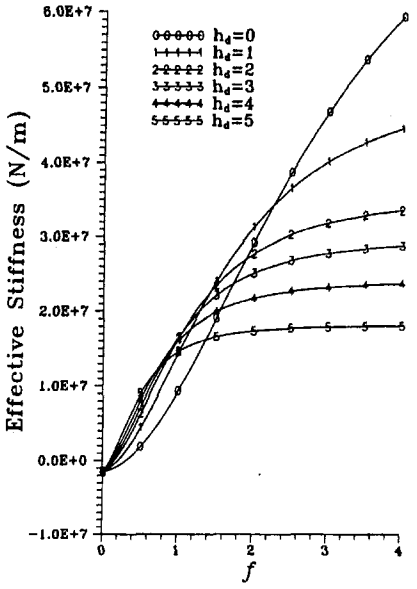

Fig. 10 Effective stiffness versus frequency

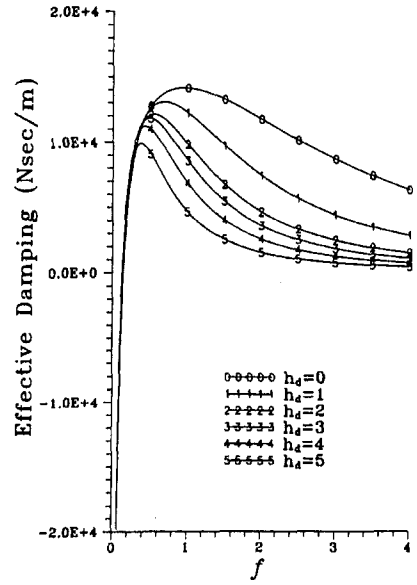

Fig. 11 Effective damping versus frequency

Beyond the weight of past practice, there is no compelling reason to continue forcing models to conform to a stiffness, damping, and inertia format. Conventional linear systems analysis (e.g., Melsa and Shultz, 1969) provides a quite adequate foundation for handling the type of reaction-force transfer function models provided by Eqs. (30) and (31). The approach can be demonstrated by a Jeffcott model formulation. Applying the reaction-force model of Eqs. (28), (30), and (31) to the mass of a Jeffcott model would yield

$$(m_r s^2 + c_r s + k_r)x(s) + \frac{K_D(s+\alpha)x(s)}{(s+\beta)} + \frac{K_E y(s)}{(s+\gamma)} = F_x(s)$$

$$(m_r s^2 + c_r s + k_r)y(s) - \frac{K_E x(s)}{(s+\gamma)} + \frac{K_D(s+\alpha)y(s)}{(s+\beta)} = F_y(s) \quad (35)$$

in the Laplace domain. By defining the new variables

$$x_1(s) = \frac{K_D(s+\alpha)x(s)}{(s+\beta)}, \quad y_2(s) = \frac{K_E y(s)}{(s+\gamma)}$$

$$x_2(s) = \frac{K_E x(s)}{(s+\gamma)}, \quad y_1(s) = \frac{K_D(s+\alpha)y(s)}{(s+\beta)}, \quad (36)$$

The following more useful Laplace-domain model is obtained

$$(m_r s^2 + c_r s + k_r)x(s) + x_1(s) + y_2(s) = F_x(s)$$
$$(s+\beta)x_1(s) - K_D(s+\alpha)x(s) = 0$$
$$(s+\gamma)y_2(s) - K_E y(s) = 0$$
$$(m_r s^2 + c_r s + k_r)y(s) - x_2(s) + y_1(s) = F_y(s)$$
$$(s+\gamma)x_2(s) - K_E x(s) = 0$$
$$(s+\beta)y_1(s) - K_D(s+\alpha)y(s) = 0 \quad (37)$$

Note that while the original Jeffcott model has a fourth-order characteristic equation in s, Eq. (37) yields an eight-order polynomial. Modeling the seal forces with frequency-dependent stiffness, damping, and inertia terms hides the degrees of freedom which are contained in the transfer-function denominators of **D** and **E**.

A time-domain, state-variable format for the model of Eq. (37) is

$$\dot{x} - v_x = 0$$
$$m_r \dot{v}_x + c_r v_x + k_r x + x_1 + y_2 = F_x(t)$$
$$\dot{x}_1 + \beta x_1 - K_D v_x - \alpha K_D x = 0$$
$$\dot{y}_2 + \gamma y_2 - K_E y = 0$$
$$\dot{y} - v_y = 0$$
$$m_r \dot{v}_y + c_r v_y + k_r y - x_2 + y_1 = F_y(t)$$
$$\dot{x}_2 + \gamma x_2 - K_E x = 0$$
$$\dot{y}_1 + \beta y_1 - K_D v_y - \alpha K_D y = 0 \quad (38)$$

Again, this is an eight-order system versus the fourth-order system of the original Jeffcott model. Equation (38) can be stated in matrix form as

$$[G_1](\dot{z}) + [G_2](z) = (f)$$

or

$$(\dot{z}) + [G](z) = [A]^{-1}(f), \quad [G] = [G_1]^{-1}[G_2]$$

The eigenvalues for $[G]$ can be calculated directly (versus iteratively), e.g., using the QR algorithm.

Due to space limitations, the following simplified eigenvalue analysis is provided as insight for the application of a transfer-function honeycomb seal force/motion model to the Jeffcott rotor. For this analysis, the Jeffcott rotor is assigned: (a) a mass of 100 kg, (b) a natural frequency of 0.75ω, (c) viscous damping corresponding to 2 percent of critical damping, (d) the calculated values of K_D, K_E, α, β, and γ for the input of Table 1 over a range of h_d from 0 to 5. Eigenvalue solutions indicate that the overall system critical damping, for forward precession, decreases from 10.4 percent, at $h_d = 0$, to 5.1 percent, at $h_d = 5$.

The Jeffcott model used in this demonstration is obviously simpler than a general rotordynamics model involving stiffness, damping, and inertia matrices. However, the state-variable formulation demonstrated above can be readily extended to general rotor models, and has previously been employed for rotors on magnetic bearings (Palazzolo et al., 1993).

Discussion and Conclusions

The analysis presented demonstrates that the cells of honeycomb act to reduce the effective acoustic velocity of flow through the seal, which can drop seal acoustic natural frequencies into the frequency range of interest for rotordynamics. In these circumstances, the conventional (frequency-independent) rotordynamic-coefficient model is invalid, and a more general transfer-function model is required. The transfer functions calculated here are a lead-lag function for the direct term and a simple lag function for the cross-coupled term.

Given that the lowest axial acoustic mode natural frequency is approximately $\pi c_0/L$ and the lowest circumferential mode frequency is approximately c_0/R where c_0 is the effective acoustic velocity, conventional (frequency-independent) models may work for short seals with small diameters and (comparatively) low speeds. For all other cases, general transfer functions should be employed. General transfer-function models for honeycomb seals require nonconventional rotordynamics tools for stability and/or transient analysis. For synchronous response due to imbalance, running-speed-dependent stiffness and damping coefficients can be used with conventional analyses.

A reasonable question to consider at this point is: Does the new model fit test data better than the old model? Unfortunately, the answer is inconclusive with respect to the authors' test data, because our feasible frequency range of excitation (40 to 70 Hz) is too restricted. Test data are needed from low frequencies out to frequencies in excess of running speed to verify the predictions of the present analysis. The test apparatus described by Childs and Hale (1994) for testing hydrostatic bearings has the required frequency range and has been modified to test liquid annular seals (Lindsey and Childs, 1995). The test rig is currently being considered for future air-seal testing.

References

Bolleter, U., Leibundgut, E., Stürchler, R., and McCloskey, T., 1989, "Hydraulic Interaction and Excitation Forces of High Head Pump Impellers," in: *Pumping Machinery—1989,* Proceedings of the Third Joint ASCE/ASME Mechanics Conference, La Jolla, CA, pp. 187–194.

Childs, D., Nelson, C., Nicks, C., Scharrer, J., Elrod, D., and Hale, K., 1986, "Theory Versus Experiment for the Rotordynamic Coefficients of Annular Gas Seals: Part I—Test Facility and Apparatus," ASME *Journal of Tribology,* Vol. 108, pp. 426–432.

Childs, D., 1993, *Turbomachinery Rotordynamics: Phenomena, Modeling, and Analysis,* Wiley, New York, NY, pp. 243–248.

Childs, D., and Hale, K., 1994, "A Test Apparatus and Facility to Identify the Rotordynamic Coefficients of High-Speed Hydrostatic Bearings," ASME *Journal of Tribology,* Vol. 116, pp. 337–344.

Elrod, D., Nelson, C., and Childs, D., 1989, "An Entrance Region Friction Factor Model Applied to Annular Seals Analysis: Theory vs. Experiment for Smooth and Honeycomb Seals," ASME *Journal of Tribology,* Vol. 111, pp. 337–343.

Elrod, D., Childs, D., and Nelson, C., 1990, "An Annular Gas Seal Analysis Using Empirical Entrance and Exit Region Friction Factors," ASME *Journal of Tribology,* Vol. 112, pp. 254–258.

Ha, T. W., Morrison, G. L., and Childs, D., 1992, "Friction-Factor Characteristics for Narrow-Channels With Honeycomb Surfaces," ASME *Journal of Tribology,* Vol. 114, pp. 714–721.

Ha, T., and Childs, D., 1994, "Annular Honeycomb-Stator Turbulent Gas Seal Analysis Using New Friction-Factor Model Based on Flat Plate Tests," ASME *Journal of Tribology,* Vol. 116, pp. 352–360.

Hirs, G., 1973, "A Bulk-Flow Theory for Turbulence in Lubricating Films," ASME *Journal of Lubrication Technology,* Vol. 95, pp. 137–146.

Lindsey, W. T., and Childs, D. W., 1995, "The Effects of Converging and Diverging Axial Taper on the Rotordynamic Coefficients of Liquid Annular Pressure Seals: Theory Versus Experiment," presented at the 1995 ASME Vibration Conference, Boston, MA, Sept.

Melsa, J., and Shultz, D., 1969, *Linear Control Systems,* McGraw-Hill, New York.

Nelson, C., 1984, "Analysis for Leakage and Rotordynamic Coefficients of Surface-Roughened Tapered Annular Gas Seals," ASME JOURNAL OF ENGINEERING FOR GAS TURBINES AND POWER, Vol. 106, pp. 927–934.

Nelson, C., 1985, "Rotordynamic Coefficients for Compressible Flow in Tapered Annular Seals," ASME *Journal of Tribology,* Vol. 107, pp. 318–325.

Palazzolo, A. B., Tang, P., Brown, G., DiRusso, E., and Kascak, A., 1993, "An Electromechanical Simulation Method for Active Vibration Control of a Magnetic Bearing Supported Rotor," ASME Paper No. 93-GT-382.

Pelletti, J., and Childs, D., 1991, "A Comparison of Experimental Results and Theoretical Predictions for the Rotordynamic Coefficients of Short (L/D = 1/6) Labyrinth Seals," *Proc. 1991 ASME Design Technical Conference,* ASME DE-Vol-35, pp. 69–76.

Potter, M., and Foss, J., 1982, *Fluid Mechanics,* Great Lakes Press, Inc., Okemos, MI, pp. 477–481.

Scharrer, J., 1989, discussion of the paper, "Annular Honeycomb Seals: Test Results for Leakage and Rotordynamic Coefficients; Comparisons to Labyrinth and Smooth Configurations," by Childs et al., ASME *Journal of Tribology,* Vol. 111, pp. 293–301.

Sorokes, J., Kuzdzal, M., Sandberg, M., and Colby, G., 1994, "Recent Experiences in Full Load Full Pressure Shop Testing of a High Pressure Gas Injection Centrifugal Compressor," *Proc. Twenty-Third Turbomachinery Symposium,* The Turbomachinery Laboratory, Texas A&M University, College Station, TX, pp. 3–17.

Thompson, P., 1988, *Compressible-Fluid Dynamics,* pp. 155–234.

Zeidan, F., Perez, R., and Stephenson, E., 1993, "The Use of Honeycomb Seals in Stabilizing Two Centrifugal Compressors," *Proc. Twenty-Second Turbomachinery Symposium,* The Turbomachinery Laboratory, Texas A&M University System, College Station, TX, pp. 3–15.

DISCUSSION

D. A. Elrod[1]

The authors are commended for this insightful contribution in the area of honeycomb seal rotordynamic analysis. The authors provide calculated impedances for a laboratory seal and a brief description of a Jeffcott rotor application. Can the authors discuss the importance of using the present two-control-volume model in the analysis of a seal in an industrial application?

Authors' Closure

Dr. Elrod's comments are appreciated. In response to his inquiry on the application of the predictions of the present model to a "real" seal, operating and geometric data for the balance-piston seal of a typical natural-gas compressor are provided below. Figures D.1 and D.2 illustrate calculated values for K_{eff} and C_{eff} for this seal configuration. In these figures, the running-speed predictions correspond to a nondimensional frequency of one. At $f = 1$, the calculated value for C_{eff} is about thirty times greater than corresponding calculated values for a tooth-on-stator (TOS) labyrinth. Calculated K_{eff} values for a TOS seal are negative and comparatively small, while the calculated K_{eff} values for the honeycomb seal are positive and large enough to

[1] University of Alabama in Huntsville.

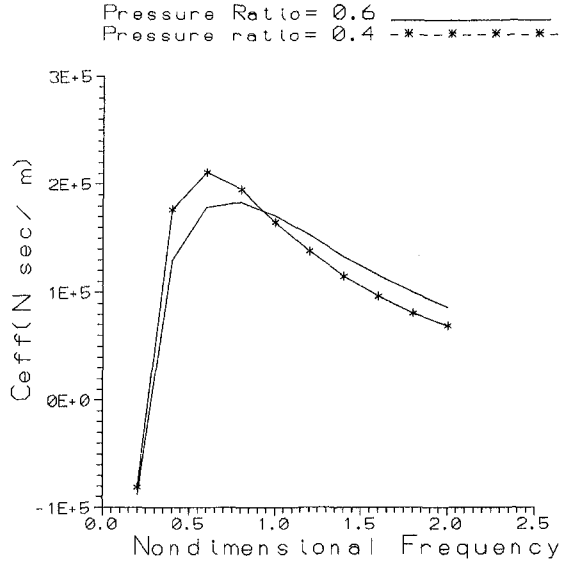

Fig. D.1 C_{eff} versus nondimensional precession frequency $f = \Omega/\omega$ for a typical balance piston seal of natural-gas compressor using back-to-back (pressure ratio = 0.6) or flow-through (pressure ratio = 0.4) designs

Discussion and Conclusions

The analysis presented demonstrates that the cells of honeycomb act to reduce the effective acoustic velocity of flow through the seal, which can drop seal acoustic natural frequencies into the frequency range of interest for rotordynamics. In these circumstances, the conventional (frequency-independent) rotordynamic-coefficient model is invalid, and a more general transfer-function model is required. The transfer functions calculated here are a lead-lag function for the direct term and a simple lag function for the cross-coupled term.

Given that the lowest axial acoustic mode natural frequency is approximately $\pi c_0/L$ and the lowest circumferential mode frequency is approximately c_0/R where c_0 is the effective acoustic velocity, conventional (frequency-independent) models may work for short seals with small diameters and (comparatively) low speeds. For all other cases, general transfer functions should be employed. General transfer-function models for honeycomb seals require nonconventional rotordynamics tools for stability and/or transient analysis. For synchronous response due to imbalance, running-speed-dependent stiffness and damping coefficients can be used with conventional analyses.

A reasonable question to consider at this point is: Does the new model fit test data better than the old model? Unfortunately, the answer is inconclusive with respect to the authors' test data, because our feasible frequency range of excitation (40 to 70 Hz) is too restricted. Test data are needed from low frequencies out to frequencies in excess of running speed to verify the predictions of the present analysis. The test apparatus described by Childs and Hale (1994) for testing hydrostatic bearings has the required frequency range and has been modified to test liquid annular seals (Lindsey and Childs, 1995). The test rig is currently being considered for future air-seal testing.

References

Bolleter, U., Leibundgut, E., Stürchler, R., and McCloskey, T., 1989, "Hydraulic Interaction and Excitation Forces of High Head Pump Impellers," in: *Pumping Machinery—1989,* Proceedings of the Third Joint ASCE/ASME Mechanics Conference, La Jolla, CA, pp. 187–194.

Childs, D., Nelson, C., Nicks, C., Scharrer, J., Elrod, D., and Hale, K., 1986, "Theory Versus Experiment for the Rotordynamic Coefficients of Annular Gas Seals: Part I—Test Facility and Apparatus," ASME *Journal of Tribology,* Vol. 108, pp. 426–432.

Childs, D., 1993, *Turbomachinery Rotordynamics: Phenomena, Modeling, and Analysis,* Wiley, New York, NY, pp. 243–248.

Childs, D., and Hale, K., 1994, "A Test Apparatus and Facility to Identify the Rotordynamic Coefficients of High-Speed Hydrostatic Bearings," ASME *Journal of Tribology,* Vol. 116, pp. 337–344.

Elrod, D., Nelson, C., and Childs, D., 1989, "An Entrance Region Friction Factor Model Applied to Annular Seals Analysis: Theory vs. Experiment for Smooth and Honeycomb Seals," ASME *Journal of Tribology,* Vol. 111, pp. 337–343.

Elrod, D., Childs, D., and Nelson, C., 1990, "An Annular Gas Seal Analysis Using Empirical Entrance and Exit Region Friction Factors," ASME *Journal of Tribology,* Vol. 112, pp. 254–258.

Ha, T. W., Morrison, G. L., and Childs, D., 1992, "Friction-Factor Characteristics for Narrow-Channels With Honeycomb Surfaces," ASME *Journal of Tribology,* Vol. 114, pp. 714–721.

Ha, T., and Childs, D., 1994, "Annular Honeycomb-Stator Turbulent Gas Seal Analysis Using New Friction-Factor Model Based on Flat Plate Tests," ASME *Journal of Tribology,* Vol. 116, pp. 352–360.

Hirs, G., 1973, "A Bulk-Flow Theory for Turbulence in Lubricating Films," ASME *Journal of Lubrication Technology,* Vol. 95, pp. 137–146.

Lindsey, W. T., and Childs, D. W., 1995, "The Effects of Converging and Diverging Axial Taper on the Rotordynamic Coefficients of Liquid Annular Pressure Seals: Theory Versus Experiment," presented at the 1995 ASME Vibration Conference, Boston, MA, Sept.

Melsa, J., and Shultz, D., 1969, *Linear Control Systems,* McGraw-Hill, New York.

Nelson, C., 1984, "Analysis for Leakage and Rotordynamic Coefficients of Surface-Roughened Tapered Annular Gas Seals," ASME JOURNAL OF ENGINEERING FOR GAS TURBINES AND POWER, Vol. 106, pp. 927–934.

Nelson, C., 1985, "Rotordynamic Coefficients for Compressible Flow in Tapered Annular Seals," ASME *Journal of Tribology,* Vol. 107, pp. 318–325.

Palazzolo, A. B., Tang, P., Brown, G., DiRusso, E., and Kascak, A., 1993, "An Electromechanical Simulation Method for Active Vibration Control of a Magnetic Bearing Supported Rotor," ASME Paper No. 93-GT-382.

Pelletti, J., and Childs, D., 1991, "A Comparison of Experimental Results and Theoretical Predictions for the Rotordynamic Coefficients of Short (L/D = 1/6) Labyrinth Seals," *Proc. 1991 ASME Design Technical Conference,* ASME DE-Vol-35, pp. 69–76.

Potter, M., and Foss, J., 1982, *Fluid Mechanics,* Great Lakes Press, Inc., Okemos, MI, pp. 477–481.

Scharrer, J., 1989, discussion of the paper, "Annular Honeycomb Seals: Test Results for Leakage and Rotordynamic Coefficients; Comparisons to Labyrinth and Smooth Configurations," by Childs et al., ASME *Journal of Tribology,* Vol. 111, pp. 293–301.

Sorokes, J., Kuzdzal, M., Sandberg, M., and Colby, G., 1994, "Recent Experiences in Full Load Full Pressure Shop Testing of a High Pressure Gas Injection Centrifugal Compressor," *Proc. Twenty-Third Turbomachinery Symposium,* The Turbomachinery Laboratory, Texas A&M University, College Station, TX, pp. 3–17.

Thompson, P., 1988, *Compressible-Fluid Dynamics,* pp. 155–234.

Zeidan, F., Perez, R., and Stephenson, E., 1993, "The Use of Honeycomb Seals in Stabilizing Two Centrifugal Compressors," *Proc. Twenty-Second Turbomachinery Symposium,* The Turbomachinery Laboratory, Texas A&M University System, College Station, TX, pp. 3–15.

DISCUSSION

D. A. Elrod[1]

The authors are commended for this insightful contribution in the area of honeycomb seal rotordynamic analysis. The authors provide calculated impedances for a laboratory seal and a brief description of a Jeffcott rotor application. Can the authors discuss the importance of using the present two-control-volume model in the analysis of a seal in an industrial application?

Authors' Closure

Dr. Elrod's comments are appreciated. In response to his inquiry on the application of the predictions of the present model to a "real" seal, operating and geometric data for the balance-piston seal of a typical natural-gas compressor are provided below. Figures D.1 and D.2 illustrate calculated values for K_{eff} and C_{eff} for this seal configuration. In these figures, the running-speed predictions correspond to a nondimensional frequency of one. At $f = 1$, the calculated value for C_{eff} is about thirty times greater than corresponding calculated values for a tooth-on-stator (TOS) labyrinth. Calculated K_{eff} values for a TOS seal are negative and comparatively small, while the calculated K_{eff} values for the honeycomb seal are positive and large enough to

[1] University of Alabama in Huntsville.

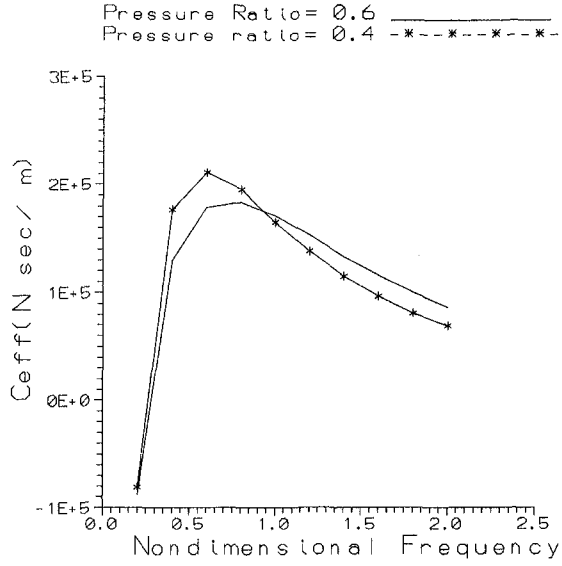

Fig. D.1 C_{eff} versus nondimensional precession frequency $f = \Omega/\omega$ for a typical balance piston seal of natural-gas compressor using back-to-back (pressure ratio = 0.6) or flow-through (pressure ratio = 0.4) designs

Modeling of Friction Contact and Its Application to the Design of Shroud Contact

B.-D. Yang

C.-H. Menq

Department of Mechanical Engineering,
The Ohio State University,
Columbus, OH 43210

Designers of aircraft engines frequently employ shrouds in turbine design. In this paper, a variable normal load friction force model is proposed to investigate the influence of shroudlike contact kinematics on the forced response of frictionally constrained turbine blades. Analytical criteria are formulated to predict the transitions between stick, slip, and separation of the interface so as to assess the induced friction forces. When considering cyclic loading, the induced friction forces are combined with the variable normal load so as to determine the effective stiffness and damping of the friction joint over a cycle of motion. The harmonic balance method is then used to impose the effective stiffness and damping of the friction joint on the linear structure. The solution procedure for the nonlinear response of a two-degree-of-freedom oscillator is demonstrated. As an application, this procedure is used to study the coupling effect of two constrained forces, friction force and variable normal load, on the optimization of the shroud contact design.

Introduction

Designers of aircraft engines frequently employ platform dampers and shrouds in turbine design to attenuate the resonant vibration of blades and at the same time to increase their aeroelastic stability. During the engine operation, the platform dampers constrain the blade motions along the contact plane. The contact normal force determined by the damper mass and engine rpm is nearly constant. Therefore, their effect on the dynamic response of blades was usually investigated by using a simple friction contact model assuming constant normal load [1–8]. On the other hand, the protruding shrouds constrain the blade motions not only along the contact plane but also along the normal direction of the plane, resulting in complex contact kinematics, in which the relative motion has a slip motion on the contact planes and an additional component normal to the plane. While the slip motion induces friction to dissipate energy, the component normal to the plane causes normal load variation and possible separation of the contact surfaces producing lift-off, an effect that cannot be adequately modeled by a simple friction contact model having constant normal load.

The influence of variable normal load on the vibration of frictionally constrained blades was first studied by Menq et al. [9, 10]. In their studies, the component of the relative motion causing normal load variation was assumed to be in phase with the relative slip motion on the contact surface. However, in real shrouded blade systems, due to the existence of the interblade phase angle and/or possible multiple mode vibration, the in-phase assumption is often not possible. Therefore, it is essential to be able to include the phase angle between the normal component of the relative motion and the slip motion in the proposed variable normal load friction force model if the model is to be applied to real shrouded blade systems.

The paper presents a generalized variable normal load friction force model and discusses its application to the prediction of the forced response of a frictionally constrained structure. In the generalized model, the friction force is related to two independent variables: linear slip motion and normal load variation. This leads to a more complex stick-slip condition and the determination of the transitions between various states, including stick, slip, and separation, is not as obvious as that in the case of constant normal load and of in-phase variable normal load. For example, when assuming constant normal load or in-phase variable normal load, the interface that slips becomes struck when the vibration motion reaches an extreme; on the other hand, this is often not the case in the generalized problem since the independent variable normal load may decrease to keep the interface remaining slipping when the motion reverses. Hence, it is critically important to develop analytical criteria that can be used to determine the transitions between various states of the interface when experiencing variable normal load. These criteria can be used to produce hysteresis loops of the friction interface when subjected to cyclic loading. These hysteresis loops can then be incorporated with the harmonic balance method to solve the forced responses of shrouded blade systems.

Contact Kinematics

When a part-span shroud is brought into contact with its neighboring shroud by the centrifugal force during the engine rotation, the relative motion of the two contact surfaces, depending on the shroud geometry and the vibratory motions of the two neighboring blades, is often not parallel to the contact plane and results in an additional component normal to the contact plane that causes variation of the contact normal load. This complex contact kinematics can be illustrated in Fig. 1, where two neighboring blades of a shrouded blade system are shown in their top-view perspective. A "substructure" can be used to represent the friction interface that consists of a contact plane and small portions of the two neighboring shrouds. Compared to the otherwise massive structure, the substructure can be modeled as two massless elastic elements that are held together by a preload n_0. The points A and B are the outermost points of these two elastic elements; the difference of their respective motions can describe the relative motion of the two neighboring shrouds. It is apparent that this relative motion may contain two components: one tangential to the contact plane (slip motion), the other normal to the plane (normal motion). The slip motion accounts for the occurrence of friction slip, but the normal component can cause the normal load to vary during a cycle of motion. Since the elastic elements are assumed to be massless, the variation of the normal load is proportional to the normal motion. This implies that the phase difference between

Contributed by the International Gas Turbine Institute and presented at the 41st International Gas Turbine and Aeroengine Congress and Exhibition, Birmingham, United Kingdom, June 10–13, 1996. Manuscript received at ASME Headquarters February 1996. Paper No. 96-GT-472. Associate Technical Editor: J. N. Shinn.

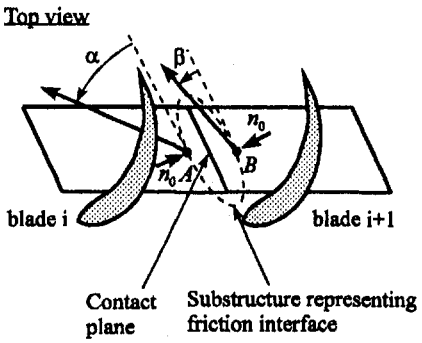

Fig. 1 The contact interface of two neighboring shrouds

the variable normal load and the slip motion is equivalent to that between the normal motion and the slip motion. If the vibrations of the two blades are dominated by a single mode, the motions of the point A and B can be assumed to be linear motions. Moreover, if the effect of the interblade phase angle of the two neighboring blades is negligible, these two linear motions can be assumed to be in phase with each other and therefore result in a linear relative motion. Thus, one can conclude that the normal motion causing normal load variation is in phase with the slip motion. This is the case that has been thoroughly investigated by Menq et al. [10]. However, when considering the existence of the interblade phase angle and/or multiple mode vibration of the two blades, it can be shown that the relative motion may not have a linear trajectory and thus the normal motion may not be in phase with the slip motion [11].

Friction Interface Model

Since the friction force in the proposed model is completely characterized by the relative motion, it will not lose generality to assume one of the two contact surfaces is a fixed ground. In addition, in the proposed model, the friction element is assumed to obey the Coulomb friction law. While the Coulomb friction law has many limitations [12–14], it has been shown to be useful in various applications where the prediction of the forced response of frictionally constrained structures is desired [2, 5, 9, 10]. With these assumptions, a friction interface model is proposed and its schematic is depicted in Fig. 2. In this model, u and v are the input slip motion and normal motion of the substructure, respectively; w describes the slip motion of the contact plane. The stiffness of the substructure is characterized by two massless springs, k_u and k_v, which account for the shear and normal stiffnesses, respectively, μ is the friction coefficient, and n_0 is the preload. This model allows a negative preload to represent the situation when the interface has an initial gap; and the equivalent preload across the interface with a gap e is calculated as $-k_v e$. The variable normal load n and the induced friction force f, acting on the ground, can be expressed as follows:

$$n = \begin{cases} n_0 + k_v v & \text{when} \quad v \geq -n_0/k_v \\ 0 & \text{when} \quad v < -n_0/k_v \end{cases} \tag{1}$$

$$f = k_u(u - w) \tag{2}$$

Stick, Slip, and Separation. When the vibratory motion is small, the contact surface sticks and the friction force is proportional to the slip motion u. Its magnitude is always limited by the slip load $\pm\mu n$. During the course of vibration, the interface may reach a point where the friction force tends to exceed the positive slip load μn and the contact surface starts to slip toward the positive u direction. Subsequently, the friction force remains equal to the varying slip load until the contact surface sticks again. Here, it should be pointed out that the location where the interface changes back to the stick state does not correspond to an extreme of the slip motion u. The reason is that the transition from slip to stick depends on the slip motion u as well as the variable normal load; and in the process the normal load may decrease to reduce the slip load so that the occurrence of the transition can be postponed to some point after the extreme of the slip motion u. When the interface moves toward the negative u direction, the interface repeats the process in the opposite direction. During the cycle of motion, the applied normal load may vanish and cause the interface to separate; consequently, the friction force is not present.

The stick-slip phenomenon becomes complicated due to the variation of the contact normal load and the possible separation of the interface. Therefore, the transitions between various states cannot be determined by a simple "rule of thumb," e.g., the slip-to-stick transition occurs when the slip motion reverses its direction. Instead, for the proposed model, analytical criteria are developed to predict the transitions so as to establish accurately the relationship between the relative motion and its induced friction force. The formulations of these criteria are documented in [12].

Hysteresis Loop. When considering a cyclic relative motion, $u = a \sin \theta$ and $v = b \sin (\theta + \phi)$, the induced periodic friction force can be segmented into a sequence of stick, slip, and separation regions, and it can be broken into three cases:

(a) No-slip case: When the input relative motion is small, the interface sticks all the time and it cannot contribute any damping to the system. Therefore, the relative motion and the induced friction force do not form a hysteresis loop.

(b) Slip-but-no-separation case: When the amplitude of the relative motion increases to some extent causing the interface to slip but still remain contact, the interface undergoes an alternating stick-slip motion. Similar to the cases of the constant and in-phase normal load, the resulting hysteresis loop consists of four alternating stick and slip regions. Figure 3 shows four typical examples, in which $k_u = k_v = 1$, $\mu = 0.4$, $n_0 = 1.2$, $a = b = 1$, and the phase angles (ϕ) between u and v for each example have distinct values and they are shown in the figure. It can be seen that the shapes of these hysteresis loops are complicated, except for the in-phase case ($\phi = 0$ deg), which consists of four straight lines.

(c) Separation case: When the relative motion becomes larger and larger, the interface will separate for a while during a cycle of motion. The occurrence of the separation complicates the stick-slip friction phenomenon and thus the resulting hysteresis loop becomes complex. Figure 4 shows four typical hysteresis loops for the separation case. In these examples, the interface parameters and the relative motion are the same as those in the slip-but-no-separation case, except $n_0 = 0.8$. As can be seen, the shapes of the hysteresis loops have significant variations due to the phase angles.

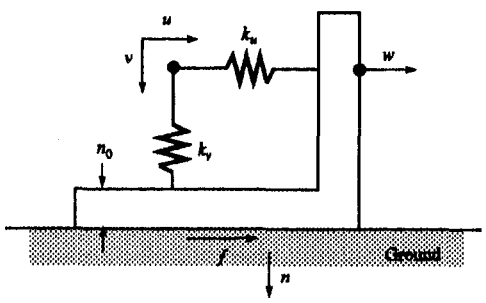

Fig. 2 Friction interface model having linear slip motion and variable normal load

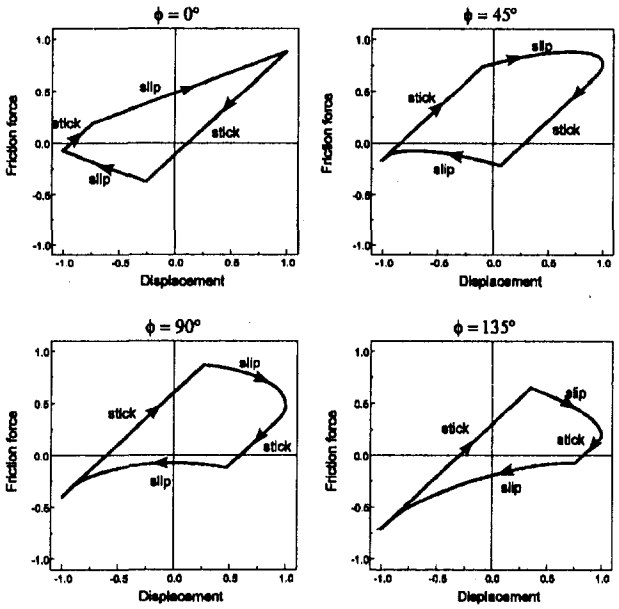

Fig. 3 Typical hysteresis loops for the slip-but-no-separation case

Nonlinear Friction Force. The dynamic analysis of a frictionally constrained structure is a nonlinear problem due to the presence of the nonlinear friction force. In this study, we intend to solve this nonlinear problem by the approximate method using harmonic balance technique. Therefore, the induced periodic friction force due to the harmonic (say sinusoidal) relative motion needs to be further approximated by its equivalent damping and effective stiffness. This can be done using Fourier series expansion once the hysteresis loop is established.

Considering the time-invariant term and the first harmonic terms of the Fourier series, the nonlinear friction force can be approximated as:

$$f(\theta) \approx f_b + f_s \sin\theta + f_c \cos\theta \tag{3}$$

where f_b, f_s, and f_c are defined in the usual way:

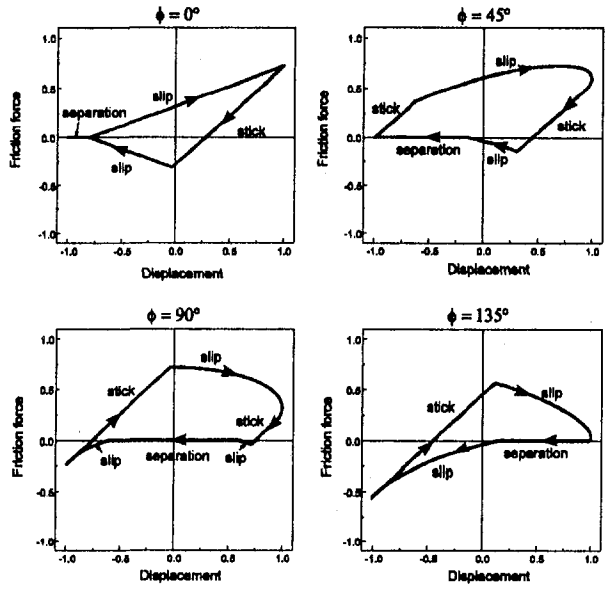

Fig. 4 Typical hysteresis loops for the separation case

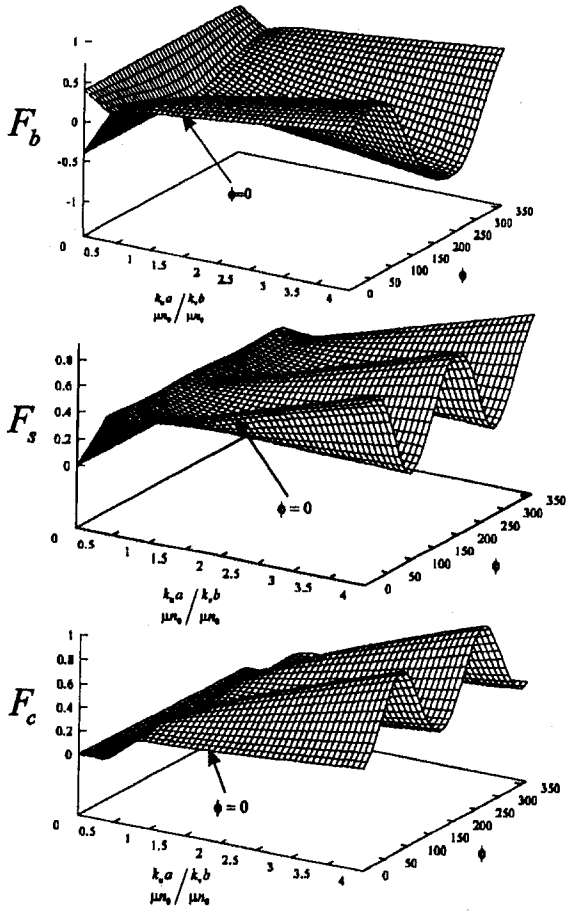

Fig. 5 Dimensionless Fourier coefficients (with a preload)

$$f_b(a, b, \phi, n_0; \mu, k_u, k_v) = \frac{1}{2\pi}\int_0^{2\pi} f(\theta)d\theta \tag{4}$$

$$f_s(a, b, \phi, n_0; \mu, k_u, k_v) = \frac{1}{\pi}\int_0^{2\pi} f(\theta)\sin\theta d\theta \tag{5}$$

$$f_c(a, b, \phi, n_0; \mu, k_u, k_v) = \frac{1}{\pi}\int_0^{2\pi} f(\theta)\cos\theta d\theta \tag{6}$$

The inclusion of the time-invariant term f_b in the dynamic analysis is important. The reason is that it may cause a static component of the variable normal load, which may alter the resulting friction damping.

The Fourier coefficients expressed above can be nondimensionalized with respect to the slip load μn_0:

$$F_b(k_u a/\mu n_0, k_v b/\mu n_0, \phi) = f_b/\mu n_0 \tag{7}$$

$$F_s(k_u a/\mu n_0, k_v b/\mu n_0, \phi) = f_s/\mu n_0 \tag{8}$$

$$F_c(k_u a/\mu n_0, k_v b/\mu n_0, \phi) = f_c/\mu n_0 \tag{9}$$

By assigning $k_u a/\mu n_0$ to be proportional to $k_v b/\mu n_0$, these functions can be visualized as three-dimensional surfaces. Typical results depicting these dimensionless functions are shown in Figs. 5 and 6. The dimensionless Fourier coefficients for the interface with a preload are shown in Fig. 5, and those for the interface with an initial gap are shown in Fig. 6. It is noticed that the time-invariant term F_b is not unique but within two bounds for the no-slip case, in which the interface sticks for the whole cycle of motion. This can be seen in Fig. 5, which shows this uncertainty by its upper and lower bound for small slip motion. This uncertainty of F_b cannot affect the dynamic response of the structure because the interface does not dissipate

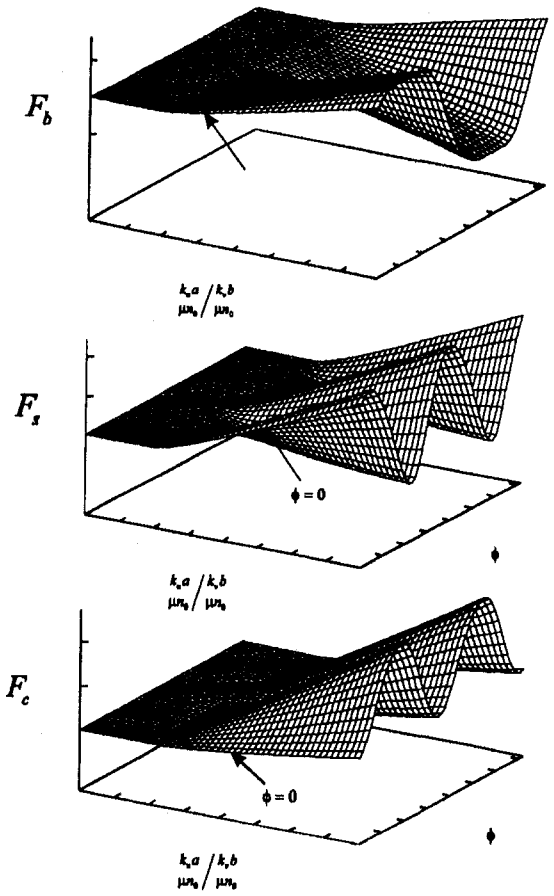

Fig. 6 Dimensionless Fourier coefficients (with an initial gap)

any vibratory energy and its friction damping is always zero. It should also be noticed that those curves for $\phi = 0$ are those for the in-phase case that was thoroughly studied by Menq et al. [10].

Nonlinear Normal Load. Similar to the friction force, the variable normal load must also be expressed as a harmonic function. Since it cannot contribute to damping and therefore must be in phase with the response, it may be approximated as:

$$n(\theta) \approx n_0[N_b(k_v b/n_0) + N_s(k_v b/n_0) \sin(\theta + \phi)] \quad (10)$$

where N_b and N_s are the dimensionless Fourier coefficients, and their analytical forms can be found in [10].

Prediction of Forced Response

Since the normal load variation is induced by the normal motion, the existence of a static component of this motion, say v_d, can cause the static component of the variable normal load to change from the preload n_0 to $n_0 + k_v v_d$; thus the resulting friction damping and effective stiffness may change accordingly. To consider this effect, one can assume the response in the following form:

$$u = a \sin \theta \quad (11)$$

$$v = v_d + b \sin(\theta + \phi) \quad (12)$$

where $\theta = \omega t + \psi$. It can be seen that there are five unknowns, a, b, v_d, ϕ, and ψ, that need be solved. Applying the approximate procedure using the harmonic balance method as presented in [9], one can obtain five nonlinear, algebraic equations with these five unknowns. Due to the presence of the normal load variation, there may exist multiple solutions to these nonlinear equations. Thus, in this study, a combined scheme of the continuation method [15] and the Newton–Raphson method is used to find the possible multiple solutions. This combined scheme takes the advantage of the continuation method to find the multiple solutions with less accuracy; then these solutions can provide good initial guess for the Newton–Raphson method to improve the accuracy of the solutions further.

Forced Response of a Two-Degree-of-Freedom Oscillator

When constrained by a friction interface experiencing variable normal load, a system is subjected to two constrained forces: friction force and variable normal load. Since these two constrained forces have a coupled effect on the response of the constrained system and their individual influences are different, it is important to examine their individual influences and coupled effect. A two-degree-of-freedom oscillator is used for this purpose. For a specific vibration mode of the oscillator, the modal displacement can have two components, ϕ_u and ϕ_v, which correspond to the u and v directions, respectively. Depending on the parametric values of the oscillator, the ratio between ϕ_u and ϕ_v can be different. It is evident that when ϕ_u is large, slip motion dominates and so does friction force. However, when ϕ_v is large, normal motion dominates and the effect of variable normal load becomes significant. In this paper, an "influence ratio" γ is defined as follows:

$$\gamma = \frac{k_u|\phi_u|}{k_v|\phi_v|} \quad (13)$$

According to the defined influence ratio, three different cases are studied.

(a) $\gamma = \infty$: This case can be regarded as the situation in which the normal load is constant. Figure 7 shows typical responses of this case. The results show that the resonant responses are bounded within two linear cases: fully slip case and fully stuck case. The first case occurs when the normal load is not present and therefore neither is the friction force. As the normal load increases to a certain large value ($n_0 > 90$ in this case), the friction interface is fully stuck. In this case, the friction interface does not dissipate energy at all; however, it provides additional stiffness to the system to cause a higher resonant frequency. In between, the resonant responses of the system are damped; and the resonant frequency increases as the

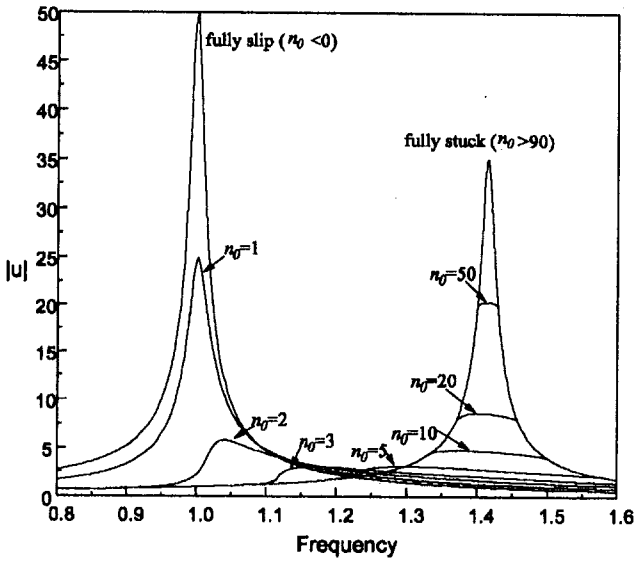

Fig. 7 Forced responses of the oscillator ($\gamma = \infty$)

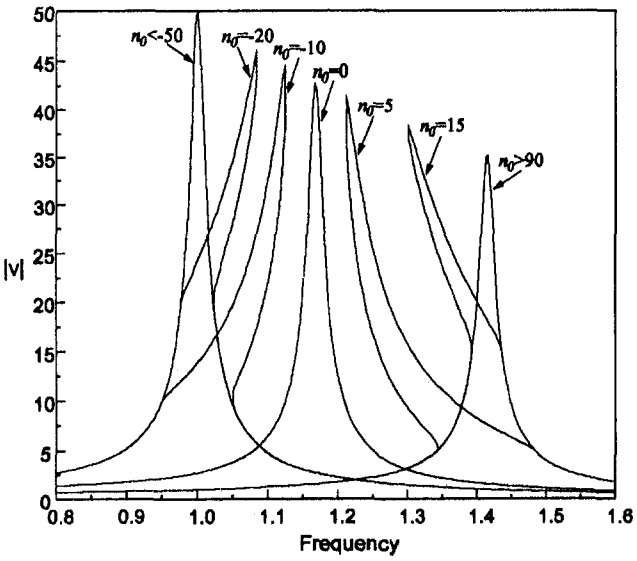

Fig. 8 Forced responses of the oscillator ($\gamma = 0$)

normal load increases. The damping effect is contributed by the slip motion occurring in the friction interface.

(b) $\gamma = 0$: This case can occur when the modal displacement is normal to the friction interface; as a result, no slip motion is induced to develop any friction and only the nonlinearity of the variable normal load will affect the response of the system. The typical responses due to this nonlinearity are shown in Fig. 8. It can be seen that these responses are also bounded by two linear responses, which correspond to the situation of a large initial gap ($n_0 < -50$ in this case) and of a large preload ($n_0 > 90$ in this case). When the interface has a large initial gap, the response of the system is not large enough to cause any contact in the interface; and, thus, the system responds without any constraint of the interface. On the contrary, when the preload exceeds some value, the interface remains in contact during the cycle of motion and the interface provides a linear spring force to stiffen the system to a higher resonant frequency. Between these two linear responses, two different kinds of nonlinear response are observed. One is the nonlinear response that occurs when the interface has a moderate initial gap; as the amplitude of the vibratory motion increases, the interface will stay in contact for some period to impose a "harden spring" effect on the response, causing the resonant peak to bend toward higher frequencies. The other nonlinear response, however, takes place as a moderate preload is applied to the interface. The increase in the amplitude of the motion causes the preloaded interface to separate and, as a result, the interface cannot provide stiffness to the system temporarily. The overall effect of the temporary separation is similar to the effect of a softened spring that gives rise to the nonlinear response with a resonant peak bending toward lower frequencies.

(c) $\gamma = 1$: Figure 9 shows the typical responses for a small influence ratio. As expected, the friction damping effect and the jump phenomenon due to the variable normal load are observed in these responses as a result of the coupled effect of the two constrained forces. It can be seen that the jump phenomenon dominates the responses in the situations when the interface has initial gaps or small preload, and on the other hand, the friction damping effect dominates the responses in the situations when the preload is large.

Design of Shroud Contact

As indicated in the previous discussions, the normal load variation induced by the normal component of the relative motion may cause the harmonic response of the structure to have a jump phenomenon and thus often impose a detrimental effect on structural dynamics. On the other hand, the slip motion can provide the damping to attenuate the resonance and the effectiveness increases as the magnitude of the slip motion increases. Therefore, maximizing the influence ratio of the contact interface can be considered as an important guideline for designing an effective shroud contact.

Depending on the shroud angle, the influence ratio of the shroud interface varies. Therefore, maximization of the influence ratio can be obtained by designing a proper shroud angle. Since a shroud contact often experiences an elliptical relative motion due to the effect of the interblade phase angle or multimode excitation, the shroud angle can be designed according to the principal axes of the ellipse. This effective shroud contact can better use the relative motion to induce the friction slip and at the same time suppress the normal load variation as much as possible.

Conclusions

Motivated by the application of shroud contact to the control of blade vibration, a friction force model has been developed to investigate the influence of a friction interface experiencing variable normal load on resonant vibration of frictionally constrained structures. When compared with the constant normal load and in-phase variable normal load, the variable normal load can lead the interface to a more complex friction phenomenon, in which the determination of the transition between stick, slip, and separation of the interface is not straightforward.

When constrained by a friction interface experiencing variable normal load, a system is subjected to two constrained forces: friction force and variable normal load. The former often results in damped resonant responses while the latter often imposes a detrimental effect on the responses, which may exhibit a so-called "jump phenomenon." In the design of shroud contact, the detrimental effect of the variable normal load can be minimized by designing a proper shroud angle. Moreover, since the nonlinear response due to these two constrained forces can be accurately predicted over a wide range of preload, the optimal preload of the interface can be obtained to maximize the performance of the shroud contact.

This proposed friction model has been integrated into a computer code BDAMPER, which was developed to predict the forced response of frictionally constrained turbine blades. The application of BDAMPER to the dynamic analysis and design of shroud contact has been reported by Griffin and Labelle [16].

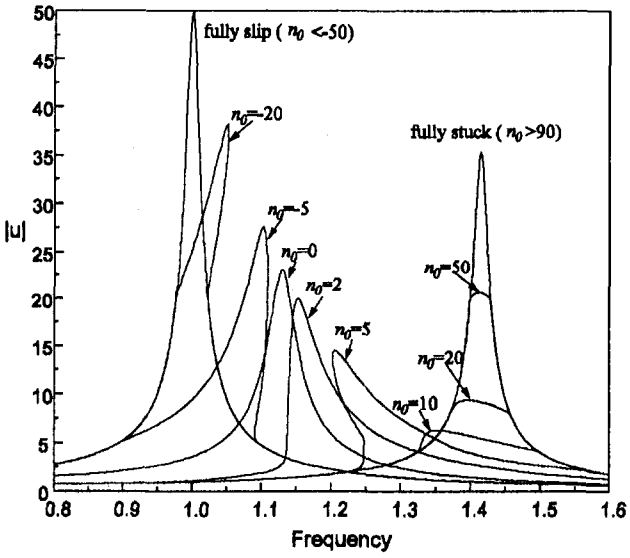

Fig. 9 Forced responses of the oscillator ($\gamma = 1$)

Acknowledgments

This material is based on the work supported by the GUIde Consortium under contract No. P.O. H210353. Any opinions, findings, and conclusions or recommendations expressed in this material are those of the authors and do not necessarily reflect the views of the GUIde Consortium.

References

1 Earles, S. W. E., and Williams, E. J., 1972, "A Linearized Analysis for Frictionally Damped Systems," *Journal of Sound and Vibration,* Vol. 24, No. 4, pp. 445–458.

2 Griffin, J. H., 1980, "Friction Damping of Resonant Stresses in Gas Turbine Engine Airfoils," ASME JOURNAL OF ENGINEERING FOR POWER, Vol. 102, pp. 329–333.

3 Plunkett, R., 1980, "Friction Damping," in: *Damping Applications for Vibration Control,* ASME AMD-Vol. 8, by P. J. Torvik, ed.

4 Dowell, E. H., and Schwartz, H. B., 1983, "Forced Response of a Cantilever Beam With a Dry Friction Damper Attached, Part I: Theory," *Journal of Sound and Vibration,* Vol. 91, No. 2, pp. 255–267.

5 Menq, C. H., and Griffin J. H., 1983, "A Comparison of Transient and Steady State Finite Element Analyses of the Forced Response of a Frictionally Damped Beam," ASME *Journal of Vibration, Acoustics, Stress, and Reliability in Design,* Vol. 107, pp. 19–25.

6 Muszynska, A., and Jones, D. I. G., 1983, "A Parametric Study of Dynamic Response of a Discrete Model of Turbomachinery Bladed Disk," ASME *Journal of Vibration, Acoustics, Stress, and Reliability in Design,* Vol. 105, pp. 434–443.

7 Srinivasan, A. V., and Cutts, D. G., 1983, "Dry Friction Damping Mechanisms in Engine Blades," ASME JOURNAL OF ENGINEERING FOR POWER, Vol. 105, pp. 332–341.

8 Griffin, J. H., and Sinha, A., 1985, "The Interaction Between Mistuning and Friction in the Forced Response of Bladed Disk Assemblies," ASME JOURNAL OF ENGINEERING FOR GAS TURBINES AND POWER, Vol. 107, Jan., pp. 205–211.

9 Menq, C. H., Griffin, J. H., and Bielak, J., 1986a, "The Forced Response of Shrouded Fan Stages," ASME *Journal of Vibration, Acoustics, Stress, and Reliability in Design,* Vol. 108, pp. 50–55.

10 Menq, C. H., Griffin, J. H., and Bielak, J., 1986b, "The Influence of a Variable Normal Load on the Forced Vibration of a Frictionally Damped Structure," ASME *Journal of Engineering for Gas Turbines and Power,* Vol. 108, pp. 300–305.

11 Yang, B. D., 1996, "The Resonant Response of Frictionally Constrained Turbine Blades," Ph.D. Dissertation, The Ohio State University.

12 Oden, J. T., and Pires, E. B., 1983, "Nonlocal and Nonlinear Friction Laws and Variational Principles for Contact Problems in Elasticity," ASME *Journal of Applied Mechanics,* Vol. 50, pp. 67–76.

13 Menq, C. H., Griffin, J. H., and Bielak, J., 1986, "The Influence of Microslip on Vibratory Response; Part 1: A New Microslip Model," *Journal of Sound and Vibration,* Vol. 107, pp. 279–293.

14 Menq, C. H., Bielak, J., and Griffin, J. H., 1986, "The Influence of Microslip on Vibratory Response; Part 2: A Comparison With Experimental Results," *Journal of Sound and Vibration,* Vol. 107, pp. 295–307.

15 Allgower, E. L., and Georg, K., 1990, *Introduction to Numerical Continuation Methods,* Springer-Verlag, Berlin–Heidelberg–New York.

16 Griffin, J. H., and Labelle, R. F., 1996, "A Rational Method for Optimizing Shroud Damping," ASME Paper No. 96-GT-402.

Nonplanar Crack Growth Using the Surface Integral Method

S. C. Forth

W. D. Keat

Department of Mechanical and Aeronautical Engineering, Clarkson University, Potsdam, NY 13699

A surface integral formulation, based on representing a crack as a distribution of force dipoles, has been developed for modeling the propagation of a three-dimensional nonplanar fracture. The minimum strain energy density and maximum circumferential stress theories were used to determine the direction of crack growth. The extension of the fracture surface was based on the Paris law for fatigue. Remeshing of the fracture during growth was accomplished by adding a ring of elements to the existing mesh at the conclusion of each increment of crack growth. This promoted the efficiency of the algorithm by eliminating the need to recalculate the entire coefficient matrix. Use of the surface integral method, coupled with growth criteria, has yielded an accurate model for three-dimensional nonplanar crack growth under mixed mode loading conditions. The study of several penny-shaped precracks under mixed-mode loading conditions produced the expected growth trajectory, and compared favorably to existing two-dimensional, three-dimensional, and experimental results found in the literature.

Introduction

Explicit modeling of three-dimensional crack growth poses a significant numerical challenge because of the computational intensity of the problem as well as logistical complexities associated with having to remesh a three-dimensional crack front. Much of the recent work in this area has been accomplished using the direct boundary element method [1], the dual boundary element method [2], and the finite element method [3].

In contrast to the methods just cited, the three-dimensional surface integral method is an indirect boundary element method that models the fracture as a distribution of force multipoles. It has been applied to model mode 1 crack growth in an infinite region [4], and extended to finite bodies by coupling it with a finite element method [5]. The three-dimensional formulation was recently generalized to stationary nonplanar fractures in an infinite region by Forth and Keat [6].

In this paper, the surface integral method for three-dimensional nonplanar fracture analysis is further developed in order to investigate out-of-plane crack growth as well as to evaluate the suitability of the method for this application. Discussion of the computational capability begins with a review of the surface integral formulation and then proceeds to detail the fracture criterion and the remeshing strategy. Growth results are presented for a penny-shaped crack initially inclined at various angles with respect to a far field tensile stress. The results generated compared favorably with published two-dimensional [7], three-dimensional [2], and experimental [8] results.

Surface Integral Method

The surface integral method models a fracture by means of multipole or dislocation superposition. The concept of force dipoles is based on the idea that a nucleus of strain can be represented by a pair of equal but opposing concentrated forces separated by an infinitesimal distance (see, e.g., Love [9]). Systems of force dipoles, known as multipoles, can be used to model a mixed-mode fracture event. Assuming linear elasticity, one can superimpose the effects of the multipoles to determine accurately the stresses and displacements induced by a fracture of known opening and slip.

The tractions induced by a fracture can thus be represented by the integral equation

$$t_k = \iint_A \Gamma_{km} n_m \delta_n \, dA \tag{1}$$

where t_k is the traction vector, A is the surface area of the nonplanar fracture, Γ_{kmn} is the stress influence function, n_m is the normal to the fracture surface, and δ_n represents variations of crack displacement where δ_1 is crack opening, and δ_2, δ_3 are orthogonal components of crack shear.

Traction boundary conditions are enforced at collocation points located at the element centroids. In the vicinity of a collocation point, the traction integral becomes singular due to the presence of terms in the form of $1/R^3$, x^2/R^5, etc. in the fundamental solution, where R is the distance between the field point and source point. By subtracting off the integral equivalent of a rigid body displacement, one can modify the singular integrand so that it can be evaluated in the Cauchy principal-value sense [5].

The traction equation then becomes

$$t_k = \iint_{A_{NS}} \Gamma_{kmn} n_m h_n \hat{\delta}_n \, dA + \oint_{A_S} N_k \cdot \nabla \phi_{kn} \hat{\delta}_n \, dS + \iint_{A_S} \Gamma_{kmn} n_m (h_n - I_n) \hat{\delta}_n \, dA \tag{2}$$

where A_S identifies the singular crack element containing the collocation point, A_{NS} is the surface area of the fracture minus A_S, $\hat{\delta}_n$ is the crack opening at the collocation point, h_n is the interpolation function for crack opening, I_n is the identity matrix, N_k is the outward unit normal to the contour enclosing A_S, and

$$\Gamma_{kmn} = \nabla_m \cdot \nabla \phi_{kn} \tag{3}$$

where "$\cdot$" implies a dot product, and Γ_{kmn} and ϕ_{kn} are continuously differentiable along the closed contour and functions of two in-plane spatial variables x and y. Note that the line integral was introduced to avoid having to discretize beyond the fracture perimeter.

Each element on the fracture has associated with it a unique set of local coordinates (see Fig. 1). The origin of each local coordinate system is located at the third node of the element as defined by the element connectivities.

The introduction of these local coordinate systems involved the use of rotation matrices to represent the transformations

Contributed by the International Gas Turbine Institute and presented at the 41st International Gas Turbine and Aeroengine Congress and Exhibition, Birmingham, United Kingdom, June 10–13, 1996. Manuscript received at ASME Headquarters February 1996. Paper No. 96-GT-539. Associate Technical Editor: J. N. Shinn.

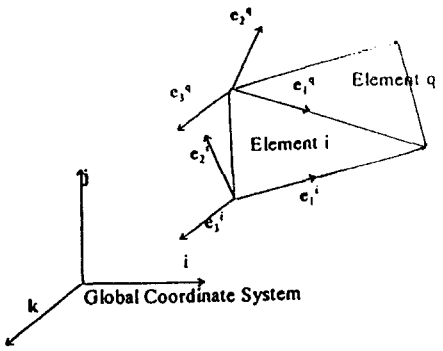

Fig. 1 Local coordinate systems of fracture elements

between the local and global coordinate systems. For example, $Q_{kl}^{(i,q)}$ represents the rotation matrix from element i to q.

A specialized element interpolation function was derived to accommodate the rapidly changing displacements near the crack front. Type A and B tip elements were formulated since the crack front may correspond either to a triangle edge or node, respectively, as shown in Fig. 2.

The general form of the interpolation function for crack opening displacements is taken from the well-known elasticity solution for a plane strain fracture, according to which near-tip displacements vary as the square root of the perpendicular distance from the crack front. In addition, the interpolation function is required to equal one at the element centroid. The general form of the interpolation function is given by

$$h = \sqrt{\frac{2\rho}{\rho_{\max}}} \tag{4}$$

where ρ is the perpendicular distance from the crack front, $\rho_{\max}$ is the perpendicular distance to the back edge of the tip element under inspection.

The interior elements are assumed to have constant crack opening displacements such that $h = 1$. Equation (2) then becomes

$$t_k^{(q)} = \sum_{\substack{i=1 \\ i \neq q}}^{Nele} \iint_{A_{NS}} Q_{kl}^{(i,q)} \Gamma_{lmn}^{(i)} Q_{mp}^{(q,i)} n_p^{q(q)} h_n^{(i)} \hat{\delta}_n^{(q)} dA + \oint_{A_S} N_k^{(q)} \cdot \nabla \phi_{kn}^{(q)} \hat{\delta}_n^{(q)} dS + \iint_{A_S} \Gamma_{knm}^{(q)} n_m^{q(q)} (h_n^{(q)} - I_n) \hat{\delta}_n^{(q)} dA \tag{5}$$

where *Nele* is the number of elements representing the fracture surface. Using shorthand notation, Eq. (5) can be rewritten as

$$t_k^{(q)} = C_{kn}^{(i,q)} \hat{\delta}_n^{(i)} \tag{6}$$

where C_{kn} represents the coefficient matrix. The system of equations defining the surface integral method are generated by writing Eq. (6) at each of the collocation points that have been located at the element centroids.

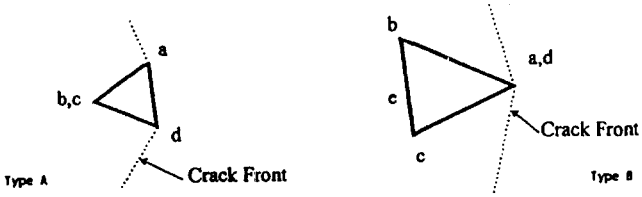

Fig. 2 Definition of tip elements

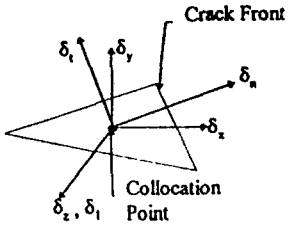

Fig. 3 Local normal-tangential, and Cartesian coordinate systems of a tip element

Stress Intensity Factors

The stress intensity factors (SIF) were calculated by substituting tip element displacements into the plane strain definitions of the stress intensity factors given below:

$$K_I = \frac{G}{(1-\nu)} \frac{\delta_1}{2\sqrt{2\rho/\pi}}$$

$$K_{II} = \frac{G}{(1-\nu)} \frac{\delta_n}{2\sqrt{2\rho/\pi}}$$

$$K_{III} = \frac{G\delta_t}{2\sqrt{2\rho/\pi}} \tag{7}$$

where K_I, K_{II}, and K_{III} are the stress intensity factors corresponding to the three fundamental modes, G is the shear modulus, ν is Poisson's ratio, r is the perpendicular distance from the crack front to the collocation point of the element under inspection, and δ_i is the crack opening displacement vector resolved in the local normal, tangential, and opening directions of the tip element under consideration.

The normal-tangential directions associated with the tip elements are defined with respect to the crack front. These directions were defined when the interpolation function for crack opening was derived for the tip elements. The displacements are calculated in the local Cartesian coordinate system for each tip element, then transformed to the normal-tangential directions for calculating the stress intensity factors, where δ_l, δ_n, δ_t correspond to modes I, II, and III, respectively (see Fig. 3).

Crack Propagation Models

Three criteria were considered for locally predicting the direction of crack growth along the crack front [10]: maximum circumferential stress (MCS) [11], minimum strain energy density (SED) [12], and three-dimensional maximum circumferential stress (3DMCS). In all cases, the Paris law was used to determine the magnitude of crack extension.

Minimum Strain Energy Density. The SED method was selected due to the ease with which it could be integrated into the existing fracture calculations. The direction of crack propagation was determined using the minimum strain energy density function defined by Sih [2] as

$$S = a_{11}K_I^2 + 2a_{12}K_IK_{II} + a_{22}K_{II}^2 + a_{33}K_{III}^2 \tag{8}$$

where

$$a_{11} = \frac{1}{16G}(3 - 4\nu - \cos\theta)(1 + \cos\theta)$$

$$a_{12} = \frac{1}{8G}\sin\theta\,(\cos\theta - 1 + 2\nu)$$

$$a_{22} = \frac{1}{16G}[4(1-\nu)(1-\cos\theta) + (3\cos\theta - 1)(1 + \cos\theta)]$$

$$a_{33} = \frac{1}{4G} \tag{9}$$

where S is the strain energy density factor, and θ is the angle relating the normal to the growth direction in the local normal-tangential coordinate system of the tip element, as shown in Fig. 4.

SED theory assumes that the crack will propagate in the direction that minimizes the strain energy density function. At a given point on the crack front, this direction corresponds to the value of θ that satisfies the following conditions:

$$\frac{dS(\theta)}{d\theta} = 0 \quad \text{and} \quad \frac{d^2S(\theta)}{d\theta^2} > 0 \quad i = 1, N \tag{10}$$

Since the values of the stress intensity factors vary along the crack front, this minimization must be repeated for each of the tip elements. Note from Eqs. (8) and (9) that the contribution of K_{III} to strain energy density does not vary with the angle θ. As a result, K_{III} does not influence the direction of crack growth.

Maximum Circumferential Stress. The MCS method was also chosen for ease of implementation and because it is a widely used in two-dimensional applications. The direction of crack propagation was determined by maximizing the circumferential stress (σ_{qq}):

$$\sigma_{\theta\theta} = \sigma_{11} \sin^2 \theta - 2\sigma_{12} \cos \theta \sin \theta + \sigma_{22} \cos^2 \theta \tag{11}$$

where σ_{ij} is the plane strain asymptotic stress solution and θ is the angle relating the normal to the growth direction in the local normal-tangential coordinate system of the tip element, as shown in Fig. 4.

MCS theory predicts that the fracture will propagate in a path perpendicular to the maximum circumferential stress. The angle θ can then be found from iterating (a closed-form solution is available [14], and is being implemented) the following equation:

$$K_I \sin \theta + K_{II}(3 \cos \theta - 1) = 0 \tag{12}$$

Note once again that the resulting direction is independent of K_{III}.

Three-Dimensional Maximum Circumferential Stress. The three-dimensional maximum circumferential stress criteria was developed to incorporate the effects of K_{III}. Like the previous two theories, it is applied locally at points along the crack front. This theory is an expansion of the maximum circumferential stress theory in that the angle θ is maximized independently, then the angle ϕ, as defined in Fig. 4, is calculated. Equations (12) and (13) are solved in sequence to define the direction of crack growth.

$$0 = K_I\left(\nu - 1 - \sin\frac{\theta}{2}\sin\frac{3\theta}{2}\right) - K_{II}\left(\nu \tan\frac{\theta}{2} + \sin\frac{\theta}{2}\cos\frac{3\theta}{2}\right) + K_{III}(\tan \phi - \cot \phi) \tag{13}$$

Note the presence of K_{III} in Eq. (13).

Paris Law for Fatigue. The Paris law is implemented using the following equation defining the rate of crack growth:

$$\frac{da}{dN} = C\Delta K_I^m \tag{14}$$

where da is the crack extension, dN is the number of cycles, C and m are material constants, and ΔK_I is defined as

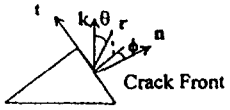

Fig. 4 Definition of local coordinate systems at the crack tip

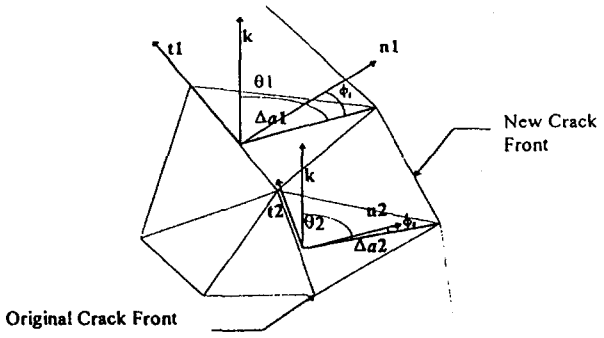

Fig. 5 Construction of new tip elements

$$\Delta K_I = K_{I_{\max}} - K_{I_{\min}} \tag{15}$$

All the tip elements are searched for the element with the largest ΔK_I. The largest allowable crack front increment is defined as $\Delta a_{\max}$ and occurs at the element associated with $\Delta K_{I_{\max}}$. The number of cycles linked with $\Delta a_{\max}$ can be determined by

$$\Delta N = \frac{\Delta a_{\max}}{C\Delta K_{I_{\max}}^m} \tag{16}$$

Assume that ΔN is the number of cycles corresponding to all points along the crack front. The crack extension at each tip element is then

$$\Delta a_i = C\Delta K_{I_i}^m \Delta N \tag{17}$$

where i corresponds to the ith tip element. However, if $K_{I_i} \leq K_{I_{TH}}$, where $K_{I_{Th}}$ is the threshold stress intensity (a material property), then the point will not advance. The total number of cycles is then additive for each additional time step.

Fracture Remeshing and Stepping Strategy. Only type A tip elements were used in determining the magnitude and path of crack extension. This decreased the calculation time by eliminating the need to evaluate the type B elements for growth criteria and proved to be accurate in predicting the mesh growth.

The stepping of the fracture was accomplished by adding a ring of elements to the initial mesh. A new type B tip element was generated by using the midpoint of the type A tip element lying on the previous crack front as an origin, and defining a new crack front node by the point, (Δa_i, θ, ϕ). This procedure is carried out in the local normal-tangential coordinate system defined by the type A tip element using one of the three growth criteria previously described. These coordinates, when transformed to the global coordinate system, define the node of a type B element lying on the new crack front as shown in Fig. 5. A type A tip element is created by connecting the adjacent crack front nodes of the new type B tip elements.

The procedure employed for time stepping the fracture was:

(*i*) Use an automatic mesh generator initially to model the fracture surface using triangular elements.
(*ii*) Local Cartesian (and normal-tangential for tip elements) coordinate systems are set up for the entire mesh.
(*iii*) The stress intensity factors are computed using the surface integral method.
(*iv*) The stress intensity factors are used to determine the angle θ, and ϕ from Eqs. (8), (12), and/or (13) for each type A tip element.
(*v*) The magnitude of crack extension is then determined using the Paris law, Eqs. (16) and (17).
(*vi*) Construction of the new type B tip elements from the existing type A tip elements is done in the local nor-

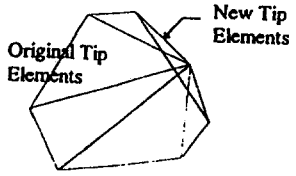

Fig. 6 Overlapping tip elements

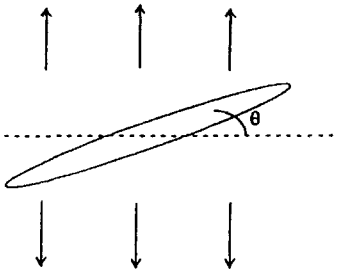

Fig. 7 Crack orientation

mal-tangential coordinate system. The new type A tip elements are constructed by connecting the outer vertices of the new type B tip elements.

(*vii*) The nodal coordinates defining the new mesh are transformed to the global coordinate system.

(*viii*) The flags for the old tip elements are changed to interior elements, and the new tip elements are flagged as type A and B tip elements, respectively.

(*ix*) Repeat the process, from step (*ii*) on, for a predefined number of time steps.

The use of triangular elements along the crack front results in topological peaks that must be controlled through prudent selection of step size in order to avoid overlapping of elements (see Fig. 6). Topological peaks exist when the crack front nodal point corresponding to a type B tip element exists at a larger radial distance from the center of the fracture, after crack advance, than the face of the adjacent type A element. A trial and error approach found that the minimum value for Δa was $0.07r$, where r is the current crack radius, to eliminate the possibility of overlapping.

Results. The growth of a nonplanar fracture under mixed-mode loading conditions was modeled by placing an elliptical precrack under a uniform tensile loading at various angles, as illustrated in Fig. 7. The precrack was modeled by 110 triangular elements, which yielded accurate stress intensity factors (less than 2 percent error) consistently for nonplanar geometries [6].

A comparison of minimum strain energy density theory, maximum circumferential stress theory, and three-dimensional maximum circumferential stress theory was conducted using the case of a penny-shaped precrack inclined at 45 deg. The Paris law was used to determine the amount of crack extension. The resulting growth trajectories of points lying on the plane of symmetry of the fracture are shown in Fig. 8. As indicated by the figure, all three theories yielded very similar predictions.

Initial growth studies used Sih's minimum strain energy density theory both to determine the direction of crack growth as

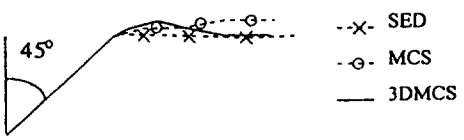

Fig. 8 Comparison of growth theories

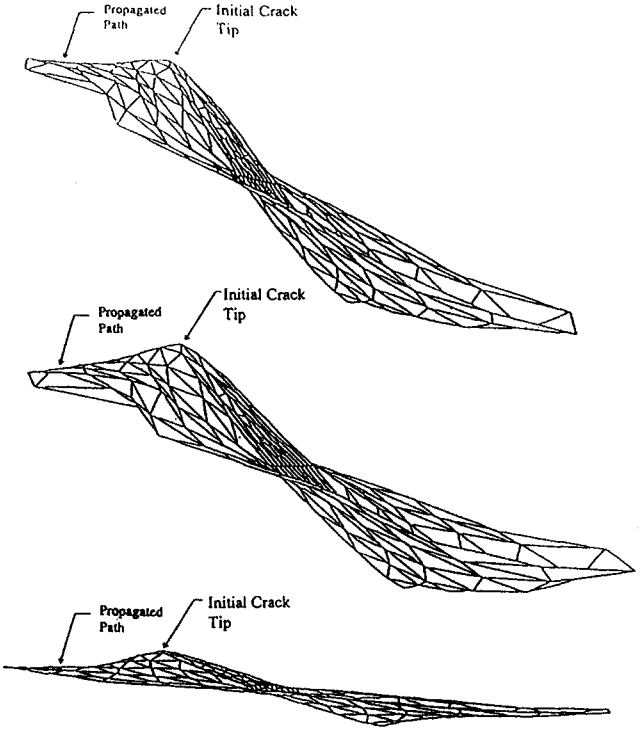

Fig. 9 Growth of a three-dimensional penny-shaped crack under a uniform tensile loading at 30, 45, and 60 deg

well as the amount of crack extension. Results are presented in Figure 9 for penny-shaped cracks oriented at three different angles with respect to the tensile field. In each case the growth trajectory was smooth and tended to align itself perpendicular to the direction of the far-field stress. Also, good correlation was obtained with results reported in the literature for a crack inclined at 45 deg. As shown in Fig. 10, Annigeri's [7] two-dimensional surface integral model for a through crack, Pustejovsky's [8] experimental results for a through crack growing in fatigue, and a fully three-dimensional dual boundary element model of the growing penny-shaped crack by Mi and Aliabadi [2] all tracked along paths closely approximated by the three-dimensional surface integral result.

The computer time required to evaluate a static fracture of 5 rings and 10 sectors (110 elements) using the surface integral method was roughly 15 minutes on a 60 MHz Pentium PC, with 16MB of RAM, under OS/2 3.0. The growth of the fracture initially took approximately 45 minutes for five time steps. The computer algorithm was then made more efficient by eliminating the need to recalculate the coefficient matrix by simply adding rows and columns to the existing matrix for each time

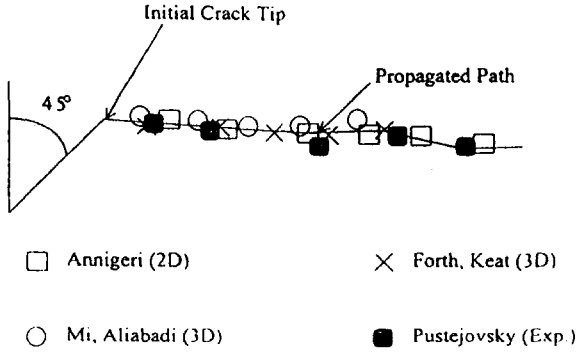

Fig. 10 Comparison with published results

step. This reduced the run time to only 30 minutes for five time steps. This is highly efficient considering the computer code is being run on a PC. The accuracy of the algorithm was not compromised in this efficiency study.

Conclusions

It has been demonstrated that an indirect boundary element formulation, based on superposition of force multipoles, can effectively model the growth of three-dimensional fractures under mixed-mode loading conditions. Since only the surface of the fracture needs to be discretized, numerical efficiency and remeshing simplicity are gained by adopting the strategy of adding rings of crack elements to model the evolving fracture. Fracture criteria for plane strain, when applied pointwise along the three-dimensional crack front, led to growth trajectories that correlated well with two-dimensional and three-dimensional published results.

The question as to which fracture criterion is best to use remains unresolved at this time. Candidate criteria must be evaluated both in terms of numerical considerations, e.g., ease of implementation and efficiency, as well as degree of correlation with physical experiments. Both MCS and SED have the appeal of being very easy to implement. MCS may have the advantage in numerical efficiency with Eq. (12) having a closed-form solution, but this edge is ever so slight. MCS also has the advantage over SED of conforming more closely with physical intuition. For example, Ingraffia [14] has noted exceptions that are in disagreement with the assumptions of SED theory.

However, both MCS and SED share the same weakness in that they are essentially two-dimensional theories, i.e., they ignore the near-tip stress fields induced by mode 3 behavior. The implications of this assumption may be observed in the results of Mi and Aliabadi [2] who conducted numerical experiments with SED, very similar to those presented here, for a penny-shaped crack inclined at 45 deg with respect to a tensile field. While the values of K_I along the crack front tended to become more uniform and the values of K_{II} died out, the magnitudes of K_{III} were virtually unaffected. This seems inconsistent with energy approaches that take into account all three modes, e.g., in the definition of energy release rate. Experimental results [15] have confirmed the tendency for a crack to grow out of plane under mixed mode I/III conditions.

The 3DMCS theory was introduced, not to settle the issue, but rather was intended to bring attention to the fact that the two-dimensional criteria have some deficiencies. The computational capability described in this paper should prove useful as a test bed for evaluating this and other growth criteria that may be proposed in the future.

References

1 Blandford, G. E., Ingraffia, A. R., and Liggett, J. A., "Two Dimensional Stress Intensity Factor Computations Using the Boundary Element Method," *International Journal of Numerical Engineering,* Vol. 17, 1981, pp. 387–404.

2 Mi, Y., and Aliabadi, M. H., "Dual Boundary Element Method for Three-Dimensional Crack Growth Analysis," *Boundary Element,* Vol. XV(2), 1993, pp. 249–260.

3 Sham, T. L., "A Unified Finite Element Method for Determining Weight Functions in Two and Three Dimensions," Department of Mechanical Engineering, Aeronautical Engineering and Mechanics, Rensselear Polytechnic Institute, 1985.

4 Narendran, V. M., and Cleary, M. P., "Elastic Interaction of Multiple Arbitrary Shaped Cracks in Plane Inhomogeneous Regions," *Engineering Fracture Mechanics,* Vol. 19, No. 3, 1984, pp. 481–506.

5 Keat, W. D., "Surface Integral and Finite Element Hybrid Method for the Analysis of Three Dimensional Fractures." PhD Thesis, Department of Mechanical Engineering, Massachusetts Institute of Technology, 1989.

6 Forth, S. C., and Keat, W. D., "Three Dimensional Nonplanar Fracture Model using the Surface Integral Method," *Int. J. of Fracture,* in press.

7 Annigeri, B. S., "Surface Integral Finite Element Hybrid Method for Localized Problems in Continuum Mechanics," Sc.D. Thesis. Department of Mechanical Engineering, M.I.T., 1984.

8 Pustejovsky, M. A., "Fatigue Crack Propagation in Titanium Under General In-Plane Loading—I: Experiments; II: Analysis," *Engrg. Fract. Mech.,* Vol. 11, 1979, pp. 9–15, 17–31.

9 Love, A. E. H., *A Treatise on the Mathematical Theory of Elasticity,* Dover Publications, New York, 1944.

10 Selcuk, S., Hurd, D. S., Crouch, S. L., and Gerberich, W. W., "Prediction of Interfacial Crack Path: A Direct Boundary Integral Approach and Experimental Study," *Int. J. of Fracture,* Vol. 67, 1994, pp. 1–20.

11 Erdogan, F., and Sih, G. H., ASME *Journal of Basic Engineering,* Vol. 89, 1963, pp. 159–525.

12 Sih, G. C., *Mechanics of Fracture Initiation and Propagation,* Kluwer Academic Publishers, 1991.

13 Palaniswamy, K., and Knauss, W. G., "On the Problem of Crack Extension in Brittle Solids Under General Loading," Report SM-74-8, Graduate Aeronautical Laboratory, California Institute of Technology, 1972.

14 Ingraffia, A. R., "Discrete Fracture Propagation in Rock: Laboratory Tests and Finite Element Analysis," PhD Thesis. University of Colorado, Boulder, 1977.

15 Hull, D., "The Effect of Mixed Mode I/III on Crack Evolution in Brittle Solids," *Int. J. of Fracture,* Vol. 70, 1995, pp. 59–79.

A New Experimental Method to Study Combined Fatigue of Actual Turbine Disk Mortise Teeth at Elevated Temperatures

Rongqiao Wang

Jingxu Nie

Jet Propulsion Department,
Beijing University of Aeronautics
and Astronautics,
Beijing, People's Republic of China

This paper presents a new experimental system to study the L-HCCF of an actual turbine disk mortise teeth at elevated temperature, using an actual disk as experimental component. This system ingeniously achieves combined loading (simulating low cycle radial centrifugal force and high cycle crosswise vibration of blade), high-frequency induction local heating (550°C constant temperature), control of high cycle vibrating frequency and amplitude, and crack real-time detection. The experimental result is identical with the practical flight failure. This method can be easily popularized to study the L-HCCF of many components.

Introduction

Along with the working conditions of a turbine blade, the mortise teeth of an aeroengine turbine disk are affected by the Low-High Cycle Combined Fatigue (L-HCCF). The low cycle load stems from the centrifugal force of the blade and the heating stress, and the high cycle vibration is from gas force and system vibration. Because of the interaction of the low and high cycle loadings, the fatigue damage of a component is largely increased. The result is crack growth and failure, which can seriously endanger the aircraft. Therefore, it is becoming extremely urgent to study L-HCCF.

Usually, the standard L-HCCF testing machine is used to study the characteristics of material, and is suitable for a standard specimen only, not for a large-scale component. However, the actual crack growth and fracture failure of the mortise teeth are not only determined by the characteristics of the material, but are also affected by the structure, dimension, and the teeth space of the mortise. Therefore, we require a special experimental method, using the actual disk to find the practical L-HCCF rule of the mortise teeth. For this reason, we developed a new experimental system using a Ferris Wheel (a low cycle fatigue tester) to simulate the L-HCCF of the actual mortise teeth with low cycle radial pulse loading overlapping the high cycle winding loading at elevated temperature. This ingeniously achieved combined loading in a simple mechanical way, high-frequency induction local heating (550°C constant temperature), control of high cycle vibration frequency and amplitude, and crack real-time detection. The experimental loading spectrum and temperature field are coincident with the reality, and the experimental result is identical with practical flight failure. This method can be easily popularized to study L-HCCF in many components.

New Experimental Loading Method

The loading method is the key technique of this experiment to achieve failure rendition. The diagrammatic sketch of the actual loading is shown in Fig. 1. P is the low cycle loading simulating the centrifugal force of the blade, and M is simulating the vibration bending moment.

The most important problem we encounter is the rational and noninterfering treatment of the low- and high-cycle loading (P and M). We have tried two methods. The first, that is, the conventional method (Fig. 2), has its serious disadvantage: First, when the low cycle large loading directly exerts on the bearing ear (see (5) in Fig. 2) of the blade, the high cycle loading cannot transmit to the mortise tooth because it is offset by the large friction between the ear and the drawplate (see (1) in Fig. 2). That means we cannot achieve the interaction of low and high cycle loading; second, the stress distribution on the mortise teeth cannot be identical with the actual stress.

The above options is proven by the stress measurement using the dynamic strain gage; when the low cycle loading is larger than 40 kN, the stress on the mortise teeth has no changes even though the high cycle vibration loading is acting. The stress on the first teeth is smaller than that on the fifth; however, the crack appears in the first tooth first, that means the actual stress on the first teeth is the biggest.

To achieve the successful transmission of the high cycle vibration and the rational stress distribution, the best way is to cause the low cycle load to push on the blade root from the back of the blade. Meanwhile, we move the vibrating center point to the back of the mortise and place a bearing on this point to reduce the friction of vibrating transmission; however, the actuating cylinder of the Ferris Wheel cannot directly complete this action because only tension force can be exerted on the component. Therefore, we ingeniously present the second loading method. The sketch is shown in Fig. 3.

The new loading method moving the low cycle load exerting point to the back of the mortise through the load-bearing bar (see (10) in Fig. 3), then transmiting the loading using a pair of load-transmiting plates (see (5) in Fig. 3) to the bearing ear (see (8) in Fig. 3). Thus, the high cycle vibrating center point moves backward and lengthens the arm of the high cycle vibration; meanwhile, when the blade vibrates around the center point, the vibrating force reachs the mortise teeth first, then the low cycle load exerting point. Therefore, the vibrating force can transmit to the mortise teeth without any loss. This is proven by the stress measurement: When the vibrating force is constant, the vibrating stress on the mortise teeth keeps approximately constant as the low cycle loading changes from 40 kN to 70 kN; meanwhile, the vibrating stress on the teeth is well distributed.

Experimental Load Spectrum

Based on the actual service load spectrum of the mortise teeth on a certain aeroengine second-stage turbine disk, we have

Contributed by the International Gas Turbine Institute and presented at Turbo Asia '96, Jakarta, Indonesia, November 5–7, 1996. Manuscript received at ASME Headquarters July 1996. Associate Technical Editor: J. W. Shinn. Paper No. 96-TA-20.

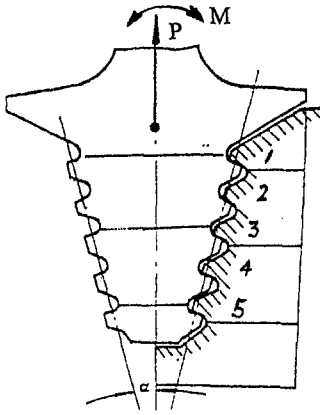

Fig. 1 Sketch of loading

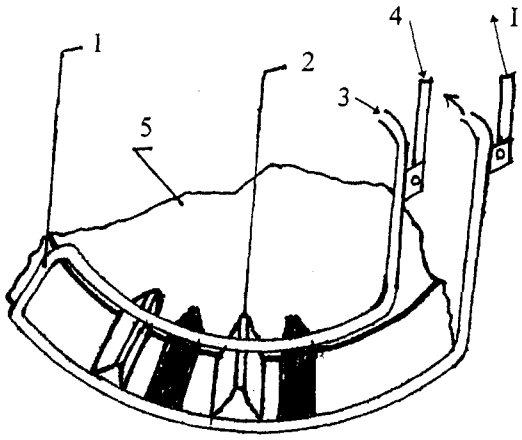

1 Heating ring 2 Experimental mortise 3 Cooling water
4 Connecting high-frequency induction heater 5 Actual disk

Fig. 5 Sketch of local heating

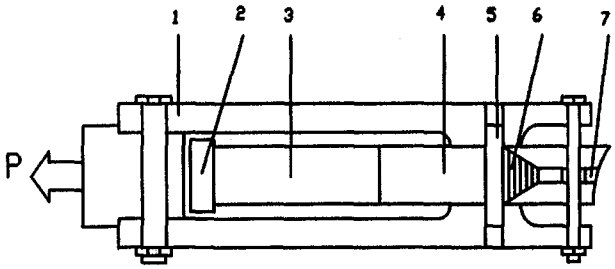

1 Drawplate 2 Vibrating point 3 Extending plate
4 Simulating blade 5 Bearing ear 6 Mortise 7 Actual turbine disk

Fig. 2 Sketch of conventional loading method

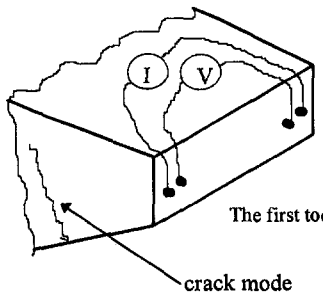

Fig. 6 Lead wire of crack detection system

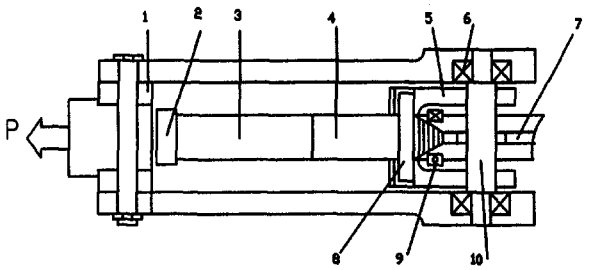

1 Drawplate 2 Vibrating point 3 Extending plate 4 Simulating blade
5 Load-transmissing plate 6 Bearing 7 Actual turbine disk
8 Bearing ear 9 Heating ring 10 Load-bearing bar

Fig. 3 Sketch of new loading method

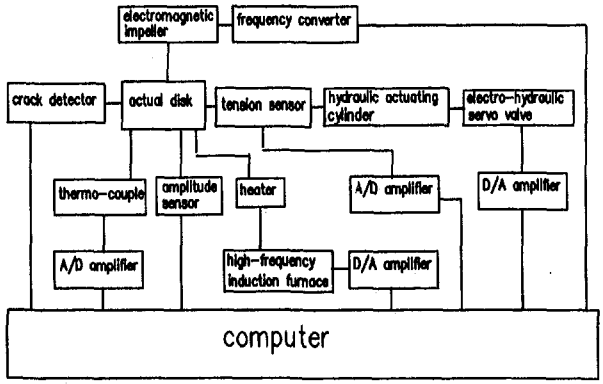

Fig. 7 Block diagram of the experimental system

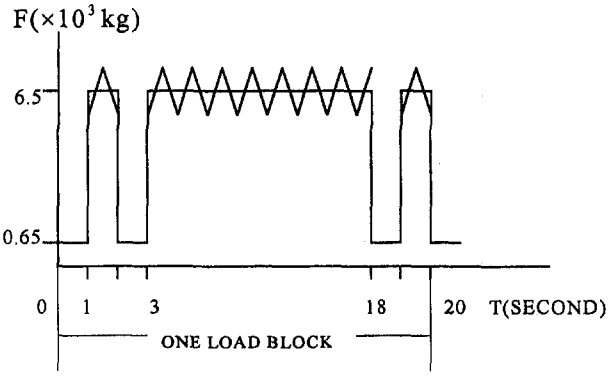

Fig. 4 Sketch of experimental load spectrum (one load block)

designed an experimental loading spectrum, as shown in Fig. 4.

The low cycle loading exerted by the actuating cylinder and controlled by the computer simulates the centrifugal force of the blade (about 65 kN). The period of each loading block is about 20 seconds. The two short blocks simulate the climbing and landing, and the big loading block is simulating the cruising of the aircraft. On the big loading block, overlapping is the high cycle vibration, which simulates the resonance vibration of the blade during aircraft operation. Using an electromagnetic impeller as the vibration source, the vibrating frequency can be changed from 0 to 650 Hz, and the vibrating force acts on the extending part of the simulating blade. Its amplitude can be adjusted according to the service loads. By measuring the vibration amplitude on the vibrating point (see (2) in Fig. 3) using

Table 1 Constituents of GH36

Mn	Si	Cr	Ni	Ti	V	Mo	Nb	C	S	P	Fe	
8.02	0.43	12.75	8.3	0.02	1.40	1.34	0.32	0.35	0.07	0.019	the	rest

Table 2 Properties of GH36 (550°C)

Young's Modulus (E), GPa	0.2% Yield Strength ($\sigma_{0.2}$), MPa	Tensile Strength (σ_S), MPa	Reduction in Area %	Elongation %
136	522	661	45.6	16.1

Table 3 Maximum principal stress of each tooth (mPa)

No. of teeth	1	2	3	4	5
σ_H	81.5	79.6	78.3	75.4	77.4
σ_L	408.5	400.2	402.3	396.9	410.3

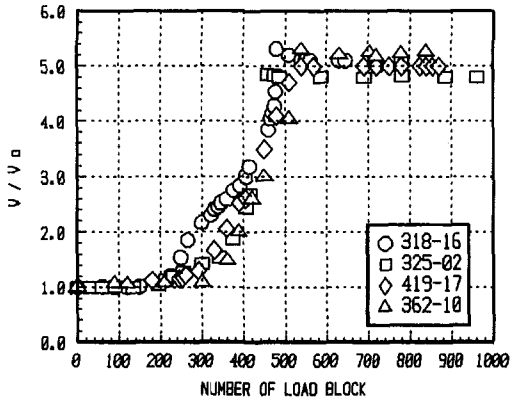

Fig. 8 L-HCCF result

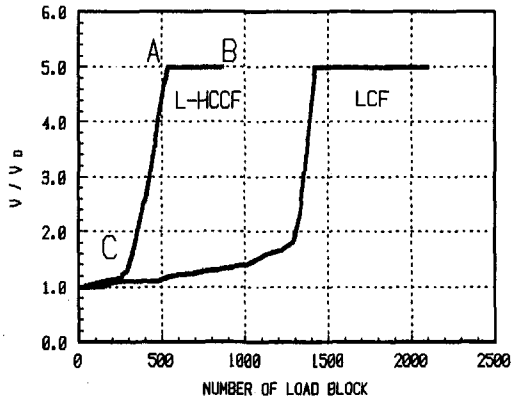

Fig. 9 Comparison of L-HCCF and LCF

a ZZF6-1 eddy current vibrating amplitude measuring apparatus, the dynamic stress on the mortise teeth can be well controlled. That means the low- and high-cycle stress ratio on the mortise teeth can be varied to suit the different experimental needs. Of course, the relationship between the dynamic stress on the first teeth and the vibrating amplitude on the vibrating point must be calibrated beforehand.

High-Frequency Induction Heating and Crack Real-Time Detection

Using a high-frequency induction heater, local heating of the experimental mortise is achieved. The diagrammatic sketch of heating is shown in Fig. 5. Measured by an electric thermocouple and controlled by computer, the temperature around the experimental mortise can be changed from 0°C to 1000°C, and the measuring deviation is within ±3°C. No obvious temperature gradient exists along the depth of the mortise.

Owing to the elevated temperature and the confined monitoring space of mortise teeth, the common method of crack propagation detection is difficult to use. Therefore, we adopt the direct-current electrical potential technique, using the recently developed MDF-1 D-C measurement system. Real-time monitoring of the crack propagation of the first teeth is thus achieved, combining with the micrometer to monitor the radial displacement of the simulating blade, determining the failure of the second teeth. The lead wire for crack measurement is shown in Fig. 6. Thus, the whole process of crack initiation, growth, and fracture can be well monitored.

Experimental System of Combined Fatigue at Elevated Temperature

Combining these techniques, we established an experimental system of combined fatigue at elevated temperature. This system mainly consists of the Ferris Wheel system, the low cycle hydraulic system, the high cycle vibration system, the high-frequency induction heating system, the real-time crack detection system, computer control system, etc. The block diagram of the system is illustrated in Fig. 7.

Experimental Results and Discussion

The purpose of this experiment is: (1) studying the crack propagation life of the first mortise teeth for a turbine disk; (2) determining the residual life of the other four teeth after the first teeth become inoperative.

The material of the actual disk is a superalloy GH36; its constituents are shown in Table 1, and the properties at 550°C in Table 2.

For comparison, the Low-High Cycle Combined Fatigue (L-HCCF) and the Low Cycle Fatigue (LCF) tests of the mortise with the same low cycle loading have been performed. Keeping temperature constant at 550°C, the low-cycle loading of the

experiment has been given in section 3, and the impeller frequency acting on the blade is 50 Hz. The maximum principal stress of each tooth, σ_H due to the high- and σ_L due to the low-cycle loads, is illustrated in Table 3. It is obvious that the low- and high-cycle stress ratio of each tooth is about 1:0.2.

Eight mortises in four actual disk, two in each disk (one for L-HCCF) and another for LCF), have been tested in this experiment. The results are illustrated in Figs. 8 and 9, in which *V/Vo* is the relative potential corresponding to the crack size, *Vo* is the potential of the initial state without any crack, and *N* is the number of the low cycle block. In Fig. 9, point A states the invalidity of the first tooth, and point B relates to the invalidity of the second tooth, which is also the complete failure of the mortise.

The first tooth's fractograph of experimental L-HCCF, which is different from the LCF's, is identical with the actual's. That shows the failure of the actual mortise teeth is due to the L-HCCF, not LCF. From Figs. 8 and 9, we can see that:

1 The whole L-HCCF life of the mortise is less than half of the LCF life. So the conventional failure criterion of the disk based on the LCF is too optimistic, and in fact, causes a lot of accidents. The failure criterion can be amended based on L-HCCF experiment.

2 Even though the first tooth reaches complete failure (point A), the remaining four teeth have about 40 percent residual life (from A to B).

That also proves the new L-HCCF experimental method is simple, rational, and feasible, and can be used as a criterion for lifing many components.

References

Hudak, and Bucci, 1981, *Fatigue Crack Growth Measurement and Data Analysis,* ASTM STP 738, PP103-119.

Powell, B. E., et al., 1982, "The Influence of Minor Cycles on Low Cycle Fatigue Crack Propagation," *Int. J. Fatigue,* Vol. 4, No. 1.

Improved Turbine Cylinder Bolting System

M. C. Gosling
Manager, Total Quality and Manufacturing Technology, Westinghouse Canada Inc., P.G.M.D. (Hamilton) P.G.B.U., Hamilton, Ontario, Canada

This paper describes the design and development of a new cylinder bolting system to replace the main joint hardware for both combustion (and steam) turbine applications. The new bolts are designed to be hydraulically tensioned to the specified preload and utilize ultrasonic verification of elongation. The new bolting system uses a reduced number of components in each assembly and the individual components themselves are of a simplified design. The new hardware can be applied to new equipment without modification and retrofitted to customer-owned equipment as a direct replacement for existing joint hardware. The prototype, production, and field testing of this hardware, the installation tooling; and ultrasonic elongation measuring equipment are described. This testing has shown significant savings in assembly and disassembly cycle times even after prolonged exposure to turbine operating temperatures in a corrosive environment. The new design of bolting is now standard equipment for the CW251B11/B12 combustion turbine manufactured by Westinghouse P.G.B.U.

Introduction

Industry standard turbine cylinder bolting design has remained essentially unchanged for many years. This paper describes a simplified bolting system designed to take advantage of modern methods of manufacture, preloading, and elongation measurement.

The new bolting system incorporates:

- Rolled parallel male threads
- Hydraulic tensioning
- Load distributing nut design
- Ultrasonic elongation verification

The new bolting hardware is configured such that it is a direct replacement for existing reverse taper studs (and bolts) fitted with extension nuts, nitrided washers, and closing screws.

This paper describes the analysis, rig testing, and field testing that were carried out to support this design change.

Background

On review of the published work relating to high-temperature, high-preload bolting, the work of Goodier (1939) and Stoeckly and Macke (1951) stand out. Both of these lines of analysis and testing looked at the stress distribution in different styles of thread on the one hand and the effect of thread taper on the other.

Working on from the above published work, it was decided to investigate the stress (strain) distribution in threaded assemblies that comprised parallel threaded studs fitted with flexible insert nuts to redistribute stress along the length of the engaged thread. The intention was to establish that an acceptable stress level could be achieved at the first engaged thread without recourse to tapering either the male and/or the female thread. This would make thread rolling of the male thread practical for production and allow for simplified nut manufacture as well.

In all cases initially back-to-back testing was carried out with standard nuts for reference purposes so that the new test data could be correlated with published data. This approach made it possible to complete this program quickly and cost effectively.

Contributed by the International Gas Turbine Institute and presented at the 41st International Gas Turbine and Aeroengine Congress and Exhibition, Birmingham, United Kingdom, June 10–13, 1996. Manuscript received at ASME Headquarters February 1996. Paper No. 96-GT-524. Associate Technical Editor: J. N. Shinn.

Testing in Detail

Test Series 1. Table 1 describes the overall test program. ∅ 1.5 in. 8 T.P.I. (38.1 mm dia. × 3.175 mm pitch) parallel thread test samples were manufactured from specified materials and assembled as shown in Fig. 1.

A test nut and standard nut were preloaded against a tubular spacer. Prior to preloading, the test elements were strain gaged as shown. Each nut was instrumented with miniature gages oriented to measure hoop strain in several axial positions. The spacer was also instrumented with miniature strain gages positioned such that the local compressive strain adjacent to nut interface could be measured. As can be seen, the test nut containing the flexible insert had an aspect ratio of 1.5:1.0, whereas the standard nut used had an aspect ratio of 1.0:1.0.

In all cases the miniature strain gages were used and connected to a standard calibrated strain gage read-out unit. The assembly was preloaded in a tensile testing machine and strain gage readings were taken each time. The micro strain readings were analyzed and plotted against percent axial position along the length of each nut.

Figure 2 shows a typical plot of hoop strain against axial position for a test nut (flexible insert) and a standard nut. It should be noted that:

- For the test nut the hoop strain falls to zero at the interface with the flange (at the first engaged thread).
- For the standard nut the hoop strain trends toward a maximum value at the flange interface (this is consistent with published data).
- The test nut (fitted with the flexible insert) demonstrates zero hoop strain (stress) over the first 30 percent of its axial length and therefore could be shortened from an aspect ratio of 1.5:1.0 to 1.0:1.0 with no detrimental effect.

The results from the strain gages attached to the spacer measuring compressive strain were inconclusive, so it was decided to investigate this area in more detail in the second series of tests.

Test Series 2. For this series of tests, only the tubular spacer between the test nut and the standard nut was strain gaged as shown in Fig. 3. Eight miniature strain gages were arranged equispaced at each end as close to the nut interfaces as practical and aligned to measure compressive strain. In addition, four strain gages were arranged, equispaced, at the center plane of

Table 1

TEST PROGRAM	
Series	Description
1	Hoop strain distribution in the body of the test nut and standard nut.
2	Interface compressive strain (stress) distribution for both the test nut and a standard nut.
3	Hydraulic tooling load to nut load transfer performance and preload loss measurement.
4	Prototype engine hardware performance measurement. Installation tooling testing and ultrasonic elongation equipment testing.
5	High temperature load rig testing.
6	Corrosive environment load rig testing.
7	Prototype engine hardware field testing.

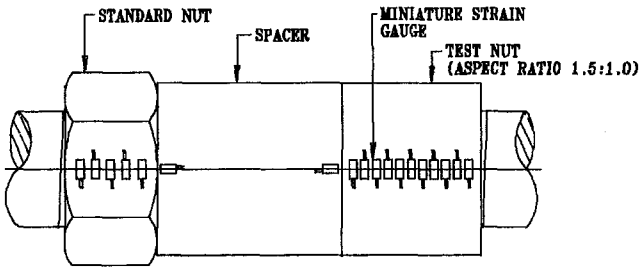

Fig. 1 Strain gage array for test series 1 hoop strain axial distribution

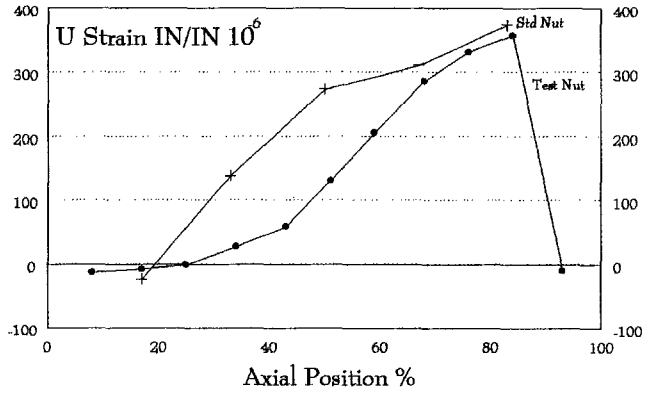

Fig. 2 Strain versus axial position test series 1

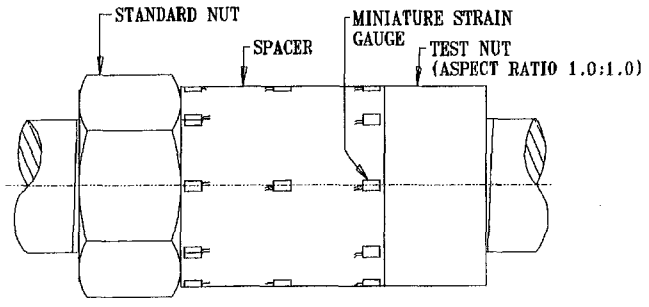

Fig. 3 Strain gage array for test series 2 compressive strain in spacer

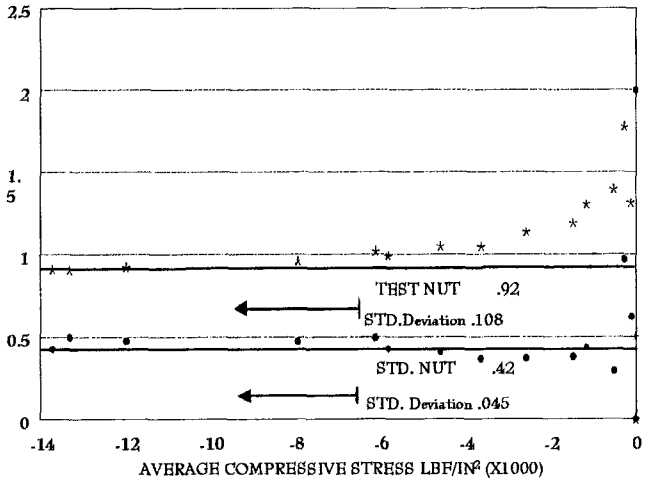

Fig. 4 Strain ratio (local/average) in spacer versus compressive stress test series 2

the spacer oriented to measure compressive strain (average value for the system).

For this series of tests and for all subsequent tests the aspect ratio of the test nut (fitted with the flexible insert) was reduced from 1.5:1.0 to 1.0 to 1.0 as suggested by Series 1 test results.

Again the miniature strain gages were connected to a standard calibrated readout unit and system preloading was provided by a calibrated tensile testing machine. The spacer strain ratio (local to average) at each interface was plotted against average compressive stress (calculated from mid plane strain readings in the spacer). As can be seen from Fig. 4 the strain ratio is greater than unity at lower levels of compressive spacer stress for both the test and standard nut but in both cases becomes asymptotic to a horizontal line as stress levels are increased. In the case of the test nut the value of the asymptote is 0.92 and for the standard nut it is 0.42. In an ideal situation the asymptote would have a value of 1.0, showing that the compressive stress is constant over the full contact area.

We make the following assumptions:

- The stress gradient is linear over the relatively small radial contact distance.
- The nut and the spacer are in continuous contact over the full radial distance.

Based on these reasonable assumptions, Table 2 was constructed. This shows that the standard nut data compares well (within 0.5 percent) with comparable available published data (Stoeckly and Macke, 1951), which validates the new data presented here. In addition this table shows that the flexible insert nut is superior to thread tapering in its ability to unload the first engaged thread and produce a flat compressive contact stress profile at the nut/flange interface.

Table 2

Comparison of Results. Peak to average stress ratio (at nut inner diameter close to first engaged thread) equal preload			
Hamilton Data		Stoeckly & Macke Data	
Standard Nut	2.38	2.37	Parallel Thread
Test Nut	1.09	----	----------
----------	-----	1.50	.003 in/in tapered
----------	-----	.83	.006 in/in tapered

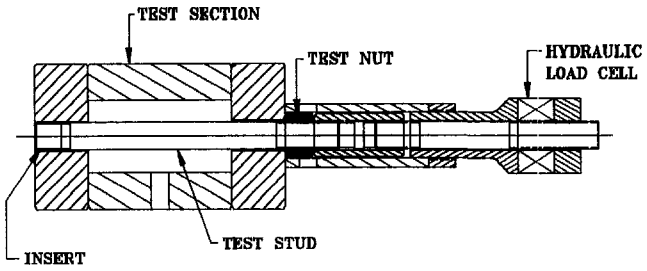

Fig. 5 Test rig series 3 tests

Test Series 3. Again the test samples were ∅ 1.5 in. 8 T.P.I. (38.1 mm dia × 3.175 mm pitch) parallel thread manufactured from specified materials.

The test stud was strain gaged with two miniature gages, positioned diametrically opposite at midspan, arranged to compensate for any bending that might be present.

The instrumented test stud was assembled into the test section of the rig shown in Fig. 5. The test section simulated a thick engine cylinder flange. Special tensioning tooling was designed to bear down on the flange around the test nut while the extended thread on the end of the stud was tensioned. This tooling provided access for taking up the axial slack at the nut through a port.

The necessary axial load was generated by a standard hydraulic load cell. Hydraulic pressure was supplied by a standard hand pump through a flexible hose. The stud strain gages were connected to a standard calibrated read-out unit.

By loading the stud in stages and taking up the axial slack at the nut it was possible to:

- Compare strain gage readings against hydraulic load
- Measure preload in the test stud with the hydraulic pressure reduced to zero.

Figure 6 shows a typical plot for this series of tests. Hydraulic pressure is plotted against bolt stress (calculated from measured strain readings). The effect of load transfer from tooling to upper nut can be clearly seen.

Figure 7 plots the same typical data but as overstress ratio (calculated from the stud strain gage readings with and without the hydraulic pressure applied at each test point) against residual bolts stress (or prestress). As can be seen the test nut (fitted with the flexible insert) has an overstress asymptote of 1.45 at 40,000 LBF/In^2 (5.8 Pascals)[1] stud stress and the standard nut

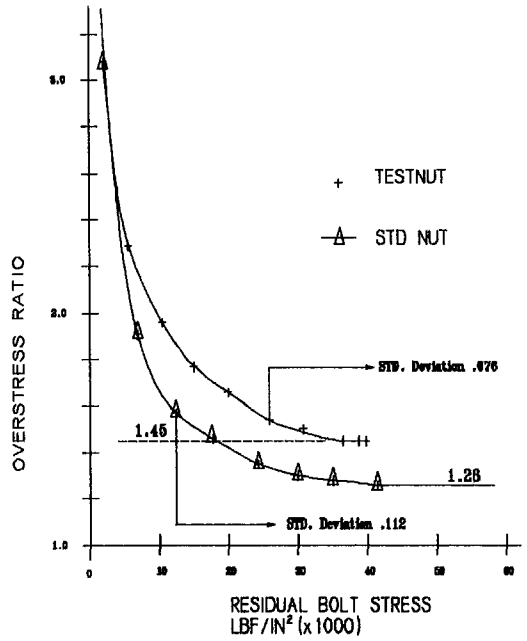

Fig. 7 Overstress ratio versus residual bolt stress series 3 tests

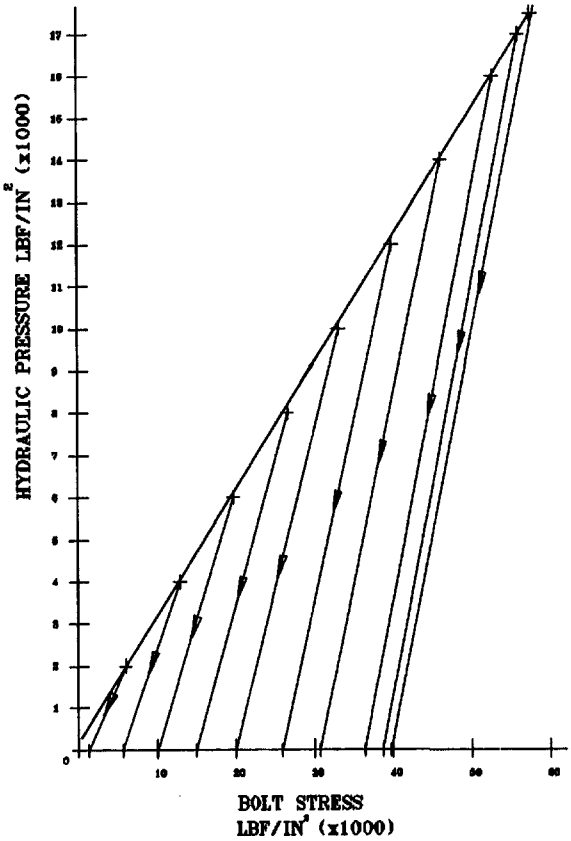

Fig. 6 Hydraulic pressure-bolt stress series 3 tests

[1] Conversion factor: 1 Pascal = 1.450 × 10^{-4} LBF/in.^{2}.

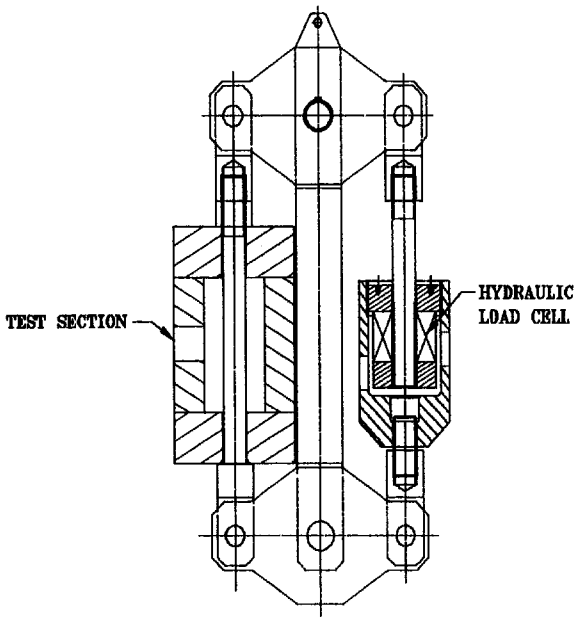

Fig. 8 Parallel action bolt tensioner

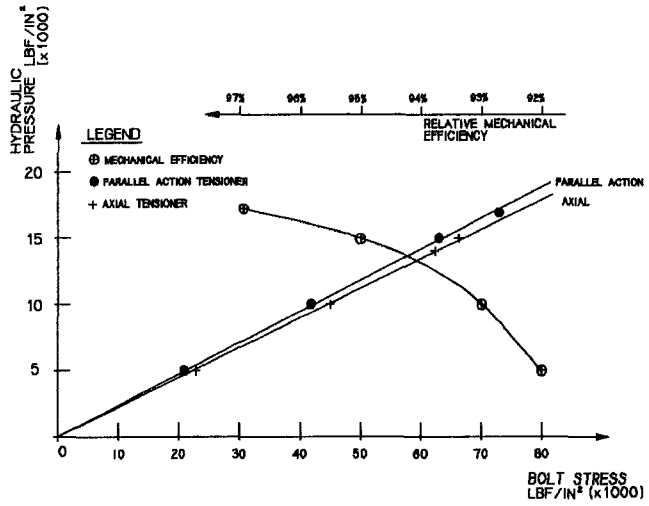

Fig. 9 Parallel action bolt tensioner hydraulic pressure versus bolt stress and relative mechanical efficiency

has an overstress asymptote of 1.26 at the same level of stress. It should be noted that the test sample stud had cut and not rolled threads, had the stud had rolled parallel threads lower values would be demonstrated. These values will also change with changing stud active length and aspect ratio.

This testing was carried out with axial or in-line tooling, a parallel action tensioning tool was also designed and manufactured to explore the practicality of working around the flange rather than through the flange to tension the stud (or bolt). Figure 8 shows this prototype parallel action tooling, which used the same hydraulic load cell as the axial tensioner. The parallel action tensioner, although somewhat cumbersome to cope with the high bending loads generated, worked well at commendable levels of mechanical efficiency (95–97 percent at normal levels of bolt stress) as shown by Fig. 9.

For most applications the use of the in-line (or axial) tensioning tooling is recommended due to its simpler configuration and lower cost, as shown in Figs. 5 and in 10.

Test Series 4. This series of tests was completed using prototype engine hardware of each size, length/diameter with rolled parallel threads. A special spacer rig was made to take

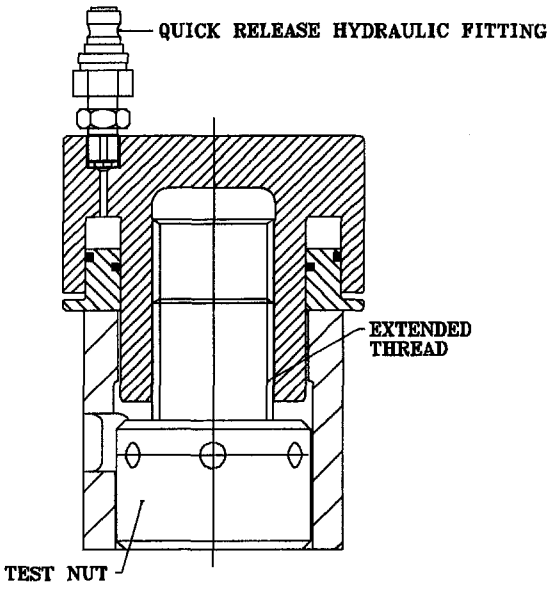

Fig. 10 Typical custom-designed factory tooling

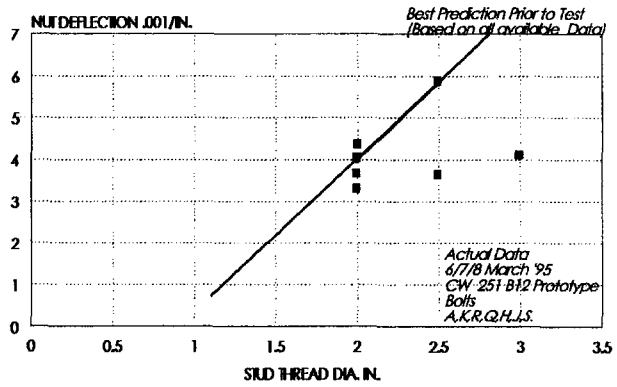

Fig. 11 Prototype engine hardware test results series 4 tests

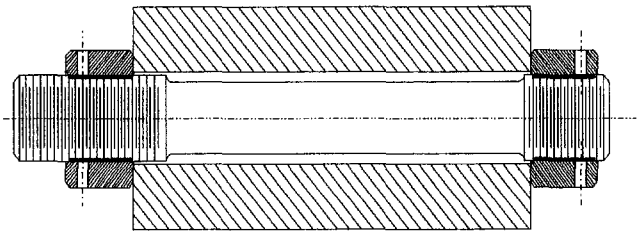

Fig. 12 Thermal cycle rig for series 5 tests

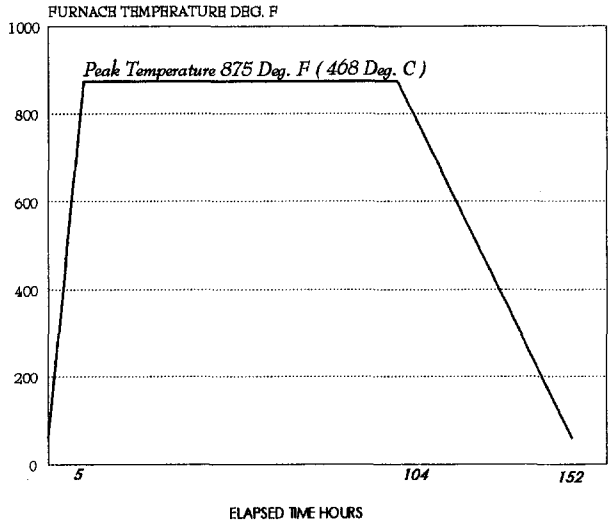

Fig. 13 Typical bolt test furnace heat cycle

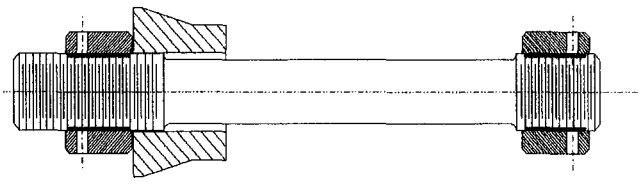

Fig. 14 Prototype engine field test hardware for test series 7

the seven different size combinations of stud and utilized the custom designed factory installation hydraulic tensioning tooling.

Figure 10 shows a typical shop hydraulic tensioning tool (which was similar in operation to that used in the test rig shown in Fig. 5 for series 3 tests) and Fig. 11 shows typical test data from this series of tests.

In this case the data were reduced to nut deflection against thread size so that these results could be compared with available published (and nonpublished data) from all sources. The assumption was that all of the loss of preload during load transfer was due to nut deflection.

As can be seen, the prototype engine hardware performed equal to, or better than, all other test data. The hydraulic tooling worked well and well within its maximum rating. It was possible to establish hydraulic pressures for preloading each stud (length and diameter) to design values during this series of tests. Furthermore, the ultrasonic elongation measuring system was checked out during these tests and accurately calibrated for each stud size. Calibration was verified by direct micrometer measurement.

Test Series 5. This series of tests was carried out to investigate the performance of the new style hardware during and after being subjected to repeated thermal cycles equivalent to engine operating cycles.

Figure 12 shows the test sample configuration. The test stud was preloaded to its design value and the assembly was loaded into an electric stress relieving furnace. Figure 13 shows a typical thermal cycle; this cycle was repeated many times and the hardware was disassembled and reassembled after each cycle. No galling or seizing was experienced on any components or at any time during this series of tests.

Test Series 6. The same test setup was used as for test series 5 (refer to Fig. 12). The exposed thread was sprayed with a saturated salt water solution several times a day and the assembly was left exposed to the outside atmosphere. The test assembly was subjected to this hostile environment for many days, after which it was disassembled without difficulty, was still serviceable, could be reassembled and preloaded as before.

Test Series 7. Figure 14 shows the prototype hardware that was designed as a direct replacement for existing engine bolting components. This prototype engine hardware was fitted to two customer-owned and operated engines at different locations with the intention of field testing and evaluation. Many thousands of hours of operation, followed by successful disassembly and reassembly, have been completed with no problems being experienced.

Conclusion

As a result of this successful program, the new hardware is now fitted as standard equipment, where appropriate, to the CW251B11/B12 Industrial Combustion Turbine manufactured by Westinghouse PGBU at the Hamilton Facility.

All aspects of the new bolting system's performance equal or exceed those for conventional reverse taper thread studs fitted with extension nuts, nitrided washers and closing screws.

In practice the major benefits from making this change are a significant reduction in assembly and disassembly times and a greater control of stud preloading.

References

Goodier, J. N., 1939, "The Distribution of Loads on the Threads of Screws," presented at the ASME Annual Meeting, Philadelphia, PA, Dec. 8.

Stoeckly, E. E., and Macke, H. J., 1951, "Effect of Taper on Screw Thread Load Distribution," contributed by the Power and Fuels Divisions and presented at the ASME Spring Meeting, Atlanta, GA, Apr. 2–5.

Two-Dimensional Computational Model for Wave Rotor Flow Dynamics

G. E. Welch
U.S. Army Research Laboratory,
Vehicle Technology Center,
NASA Lewis Research Center,
Cleveland, Ohio 44135

A two-dimensional (θ, z) Navier–Stokes solver for multiport wave rotor flow simulation is described. The finite-volume forms of the unsteady thin-layer Navier–Stokes equations are integrated in time on multiblock grids that represent the stationary inlet and outlet ports and the moving rotor passages of the wave rotor. Computed results are compared with three-port wave rotor experimental data. The model is applied to predict the performance of a planned four-port wave rotor experiment. Two-dimensional flow features that reduce machine performance and influence rotor blade and duct wall thermal loads are identified.

Introduction

The wave rotor is a machine designed to transfer energy efficiently between gas streams of differing energy density. The energy exchange is accomplished within shrouded rotor passages (see Fig. 1) by axially propagating shock and expansion waves. The waves are initiated as the ends of the wave rotor passages open and close to the relatively steady flows in stationary inlet and outlet ports in a timed sequence set by the rotor speed and the tangential positions of the port walls. Various wave rotor cycles can be achieved by varying the sequence of passage charging and discharging events dictated by the wave timing. These include three-port divider cycles (Kentfield, 1969; Wilson and Fronek, 1993) and four-port cycles (e.g., Mathur, 1985; Moritz, 1985; Zauner et al., 1993), which promise attractive specific fuel consumption and specific power improvements in gas turbine engines (e.g., see Taussig, 1984, and Welch et al., 1997). The interesting history of the wave rotor and its applications has been documented elsewhere (see, for example, Azoury, 1965–66, Rose, 1979, Taussig and Hertzberg, 1984, and Shreeve and Mathur, 1985).

Wave rotor performance depends in part on proper wave timing. The asymmetric opening and closing of the rotor passages to the port flows reduce effective one-dimensional wave speeds (e.g., see Paxson, 1993) and significantly influence the shape and subsequent distortion of contact discontinuities within the rotor (cf. Eidelman, 1985). Machine performance is degraded by viscous, heat transfer, and shock losses within the rotor passages, leakage to and from the rotor passages and ports, and mixing of nonuniform port flow fields and at gas/gas interfaces. Arguably, the gas dynamic wave timing can be modeled either analytically or by the method-of-characteristics (e.g., see Burri, 1958); however, the inherent multidimensionality and nonlinearity of many of the wave rotor loss mechanisms provide impetus for applying computational fluid dynamics (CFD) methods to simulate the wave rotor flow dynamics.

One-dimensional, single rotor passage, CFD models (e.g., see Zehnder, 1971, Thayer et al., 1980, Wen and Mingzheng, 1982, Taussig, 1984, and Paxson, 1995) that use time-varying boundary conditions to represent the inlet and outlet port conditions accurately predict the gas dynamics within straight rotor passages having aspect (length-to-width) ratios typical of pressure-exchangers (i.e., ≥ 10). Given properly calibrated loss models, the one-dimensional solvers can also accurately simulate machine performance. Multidimensional CFD models have to date assumed inviscid flow. These include single passage, two-dimensional solvers for (r, z) coordinates (Hong-De, 1983; Zhang and So, 1990) and (θ, z) coordinates (Eidelman, 1985) and a single passage, three-dimensional (r, θ, z) solver (Larosiliere, 1995). Lear and Candler (1993) proposed a two-dimensional Euler solver that assumes one-dimensional flow in infinite aspect ratio rotor passages and two-dimensional (θ, z) steady-state flow in multiple ports. It is the understanding of the author that a two-dimensional (θ, z) code for unsteady, inviscid flow in multiple passages and ports has been developed by A. L. Ni of the Moscow Academy of Science (private communication, A. Pfeffer and R. Althaus, Asea-Brown-Boveri, 1994).

The CFD model described in this work addresses a need to simulate inherently two-dimensional flow features routinely encountered in the stator/rotor/stator configuration of multiport wave rotors. These include viscous phenomena such as flow separation (e.g., off the stator end-wall during rotor passage opening and closing, off the trailing edge of rotor blades, and in shock/boundary layer interactions) and inviscid phenomena such as Rayleigh–Taylor flows (including shock/contact and fan/contact interactions), gas dynamic waves emitted from the rotor passages into the ports, and passage-to-passage flow recirculation via the inlet and outlet ports. An overview of the computational model is first provided. Computed results are then compared with three-port experimental data. Finally, the model is applied to a planned four-port wave rotor experiment both to predict machine performance and to identify flow features that influence machine design and performance.

Computational Model

The multiregion geometry and important fluid dynamic features of the wave rotor may be appreciated by considering the passage charging problem shown in Fig. 2. In this view (looking radially inward), the wave rotor passages are unwrapped from the periphery of the rotor. The rotor passages gradually open (and close) to the inlet port as dictated by the rotor speed and the passage width. As the low-pressure fluid in a rotor passage is first exposed to the high total pressure inlet port flow, compression waves move into the rotor passage, compress and set into motion the on-board "driven fluid," and thus allow the inlet port "driver" fluid to enter the rotor passage. Simultaneously, an expansion wave moves into the inlet port region and reduces the total pressure and total temperature of the entering driver fluid. In general, temperature and density are discontinuous at the distorted interface of the driver and driven gases. The right moving compression wave steepens into a shock wave, which then reflects off the right-hand wall. The reflected

Contributed by the International Gas Turbine Institute and presented at the 41st International Gas Turbine and Aeroengine Congress and Exhibition, Birmingham, United Kingdom, June 10–13, 1996. Manuscript received at ASME Headquarters February 1996. Paper No. 96-GT-550. Associate Technical Editor: J. N. Shinn.

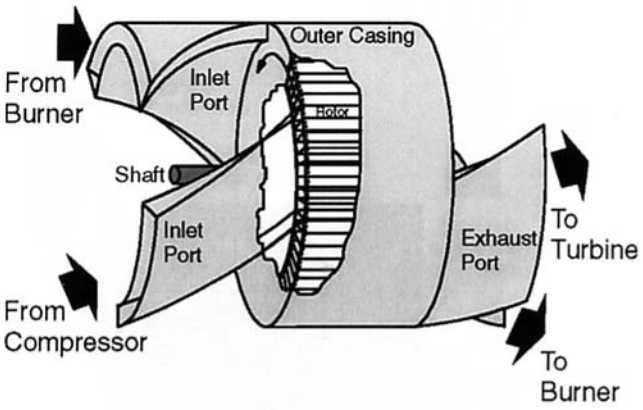

Fig. 1 Four-port wave rotor schematic diagram

(lambda) shock moves leftward, interacts with the established boundary layer, and compresses the driven and driver gases. The contact is significantly distorted by vorticity deposited along the contact by the reflected shock. Richtmeyer–Meshkov (or shock-excited Rayleigh–Taylor) instability theory suggests that the contact distortion scales with the density difference and the strength of the shock (e.g., see Sturtevant, 1987). The inlet port is designed so that the rotating passages close just as the reflected shock reaches the rotor/port interface. The reflected shock wave is emitted into the inlet port. The gradual closing of the passage generates a pair of counterrotating vortices.

Model Restrictions. Centripetal forces establish a tangential baroclinic torque along contact discontinuities (interfaces) between gases of differing density: this can cause significant interface skewing (cf. Keller, 1984). The distortion is expected to scale with the square of rotor Mach number and the rotor hub-to-tip ratio (cf. Larosiliere, 1995). Optimum rotor Mach numbers based on peak cycle temperature are low (≤ 0.3) and optimum hub-to-tip ratios are likely at or above $\frac{2}{3}$ (cf. Welch, 1997); centripetal and Coriolis forces are neglected in this work and the rotor passages and inlet ports are solved at passage midspan, in $z-\theta$ (or $x-y$) coordinates. Leakage flows, both from the rotor passages to the space between the rotor and the outer casing and from passage to passage, are neglected in this work. In practice leakage is mitigated by minimizing rotor/end-wall clearance and/or by using seals; however, it is noted that leakage substantially reduces the performance (e.g., see Wilson and Fronek, 1993), and can impact the radial and tangential port flow profiles, of some machines. Fluid-to-wall heat transfer is another potentially significant loss mechanism neglected in the present work in which the passage walls are adiabatic.

The inlet port flow fields in many applications are likely turbulent. The character (laminar, transitional, or turbulent) of the boundary layer flow within the rotor passages is not known, but will certainly be influenced by the turbulence intensity of the incoming driver flow. The viscous flow of this work is modeled using laminar transport properties, under the thin-layer approximation (cf. Baldwin and Lomax, 1978). Turbulence-enhanced mixing (e.g., at gas/gas interfaces and in nonuniform outflow port flow fields) and turbulence-enhanced diffusion (e.g., of vorticity and heat) are neglected. Assessing the impact of neglecting the streamwise diffusion terms by the thin-layer approximation remains for future work.

Solution Method. The wave rotor flow field is modeled by the two-dimensional, unsteady, compressible, thin-layer Navier–Stokes equations with laminar viscosity. The gas is assumed calorically and thermally perfect. The finite-volume form of the governing equations are integrated in time using a second-order accurate explicit four-stage Runge–Kutta scheme (Jameson et al., 1981). The time step is dictated by the grid resolution and the CFL number, nominally set at 1.5. In the cell-centered finite-volume formulation used, the inviscid and viscous flux vectors are calculated at the cell interfaces defined by lines connecting the grid points. The inviscid flux vectors are computed using a multidimensional, boundary-fitted (ξ, η) coordinates formulation (Grossman and Walters, 1989; Walters and Thomas, 1989) of Roe's (1981) approximate Riemann solution scheme with the entropy condition fix of Harten and Hyman (1983). The "left" and "right" states of the Riemann problem are set by MUSCL interpolation (van Leer, 1979) with Mulder limiting (cf. Anderson et al., 1986). In general, four grid-aligned cells are involved in the interpolation for each cell face value, so that an inviscid spatial flux derivative involves a five-cell stencil and is at least second-order accurate. The shear stress and heat flux components of the viscous flux vector are central-differenced at the cell interfaces using the primitive variables of the adjacent cells and transport properties evaluated at the arithmetic mean of the static temperatures in the adjacent cells. The overall method is second-order accurate in space and time.

Port/Rotor Interfaces. The multiple rotor passages are solved on identical grid blocks. At the beginning of each time step, the rotor grids are advanced according to the current time step and the rotor linear speed. A schematic diagram of the interface at the left end of the rotor at some arbitrary time is provided in Fig. 3. The interface is represented by a zone in which zero volume cells are artificially created by the overlapping of constant-η grid lines from the left and right grid blocks. This definition ensures that each interior cell communicates with an integer number of artificial interface cells. The left and the right face of each interface cell are set by the MUSCL interpolation, where now the four point stencil involves both the left and right grid blocks. For example, the interpolation for the primitive variables at the left face of an interface cell involves two interior cells of the left grid block and one interior cell of the right block. Likewise, the interpolation for the primitive variables at the right face of the grid block involves two points in the right grid block and one in the left. In the case where one or more of the interface cell faces is a wall (e.g., a stator surface or a rotor blade), the wall boundary conditions described in the following section are imposed. If both interface cell faces are walls, interpolation is not required; i.e., that interface cell does not affect any interior cell. After the left and right faces of the artificial interface cells are set, an approximate Riemann solution provides the primitive variables and fluxes at

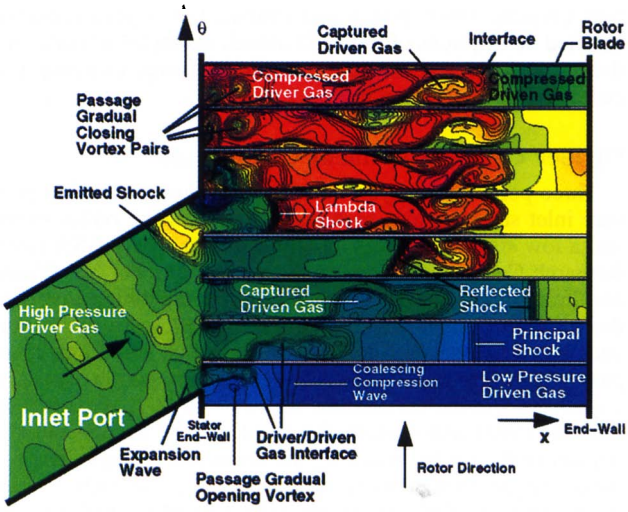

Fig. 2 Prototypical inlet port/passage charging process showing computed density contours (nondimensional values: dark blue = 0.6 and magenta = 4.6)

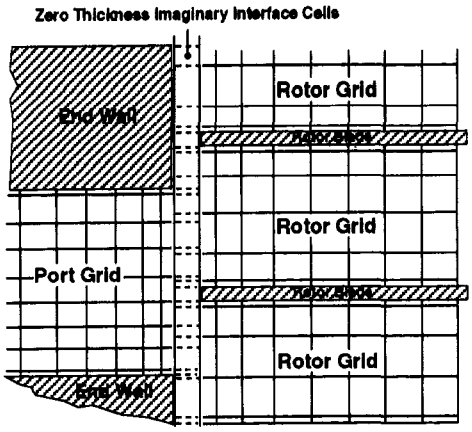

Fig. 3 Schematic diagram of instantaneous port/passage imaginary interface cell construction

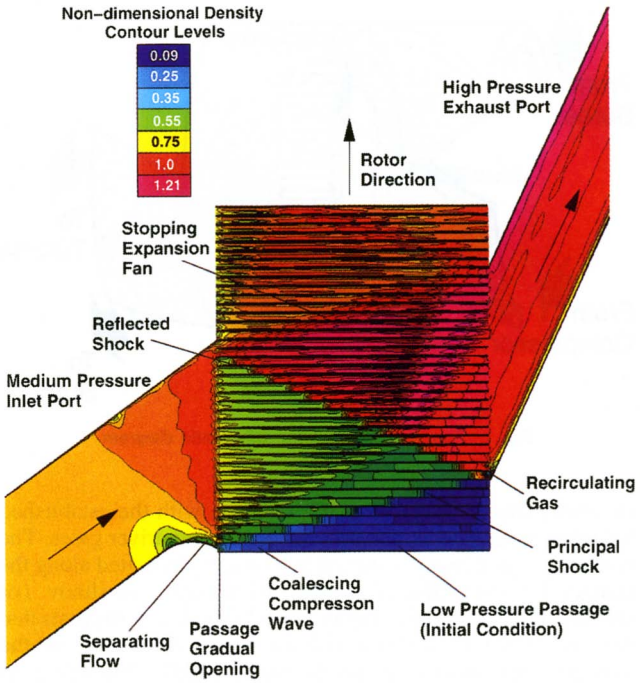

Fig. 4 Computed instantaneous density contours in medium pressure inlet port and high pressure outlet port portion of NASA LeRC three-port divider cycle experiment

the interface. For a given interior cell, the product of the inviscid flux times cell area is obtained by summing the flux/area products of the integer number of interface cells that correspond to that interior cell. For example, if the interior cell in the right grid block is spanned by three interface cells, the flux/area product values for the three interface cells are summed and the total flux/area product is applied at the left face of the interior cell. In this way overall flux conservation is imposed by the interface routine at the beginning of each time step.

Port Boundary Conditions. Phantom cells are used to impose subsonic boundary conditions at the inlet port inflow boundary and at the exhaust port outflow boundary. Standard one-dimensional nonreflecting boundary conditions are used in which the Riemann variables are based on the streamwise covariant velocity component. The normal derivative of pressure and the normal velocity component are required to be zero at walls. In inviscid computations, the streamwise covariant velocity component is allowed to slip at the wall. In viscous computations, phantom cells internal to walls are used to ensure that the streamwise covariant velocity component and the normal derivative of temperature are zero at the wall. The local wall temperature itself is therefore very nearly the fluid temperature in the adjacent cell, and can be inferred at any time.

Chima's (1987) single-block quasi-three-dimensional rotor viscous code (RVCQ3D) provided a skeletal structure for the multi-block (WROTOR2D) solver described above. Earlier papers (Welch, 1993; Welch and Chima, 1993) have presented detailed descriptions of the CFD model, examples of code validation, and applications to wave rotor passage charging processes (e.g., that shown in Fig. 2).

Divider Cycle Experiment Comparison

Three-port divider cycles divide a medium stagnation pressure inlet stream into a high stagnation pressure outlet stream and a low stagnation pressure outlet stream. The NASA Lewis Research Center three-port wave rotor experiment (cf. Wilson and Fronek, 1993) was simulated by a computation involving the medium pressure inlet port, the high-pressure outlet port, and 39 rotor passages (see Fig. 4). The initial conditions in the passage about to open to the medium pressure port are set using a one-dimensional calculation courtesy of D. E. Paxson (see Paxson, 1993) and contain the "history" of the unsimulated portion of the cycle, including the impact of leakage. The two ports can be characterized by the ratio of the high-pressure discharge mass flow rate to the inlet port mass flow rate and the ratio of average total pressures in these ports. Given the inlet port stagnation conditions and outlet port static conditions from the experiment, the code predicted mass flow rate fraction and pressure ratio of 0.434 and 1.222, respectively, while the experimental data showed a 0.371 mass flow rate fraction and 1.195 pressure ratio. The discrepancies between the computed and experimental results are arguably attributable to the impact of the leakage flows in the experiment, which are not accounted for in the simulated portion of the wave rotor (Fig. 4). Computed and measured total velocity tangential distributions in the inlet port region of the experiment are compared in Fig. 5. The measurements were taken approximately 1 in. (2.5 cm) upstream of the rotor blades. The comparison shows excellent agreement between the experimental and computed velocities, including the inflection caused in part by the rounding of the leading port wall, near the rotor/port interface. The inlet port rounding effects a flow area increase, which decelerates the flow just upstream of the rotor as indicated by the increase in the density contour levels (see Fig. 4). Also evident in Fig. 4 is that the density of the fluid entering the rotor decreases

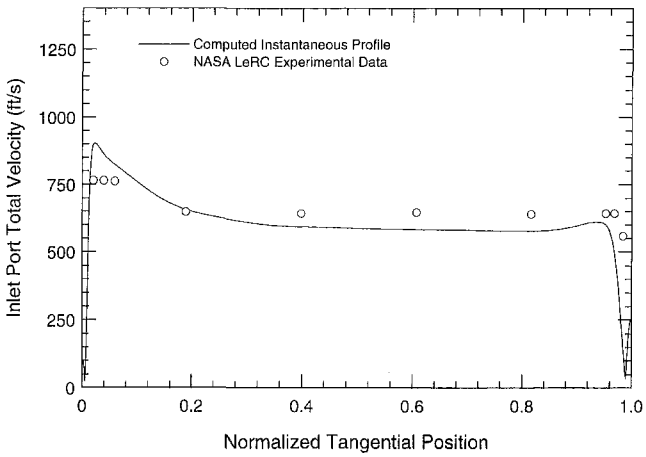

Fig. 5 Comparison of computed and measured (Wilson and Fronek, 1993) NASA LeRC three-port divider cycle experiment medium pressure inlet port total velocity as a function of normalized tangential position

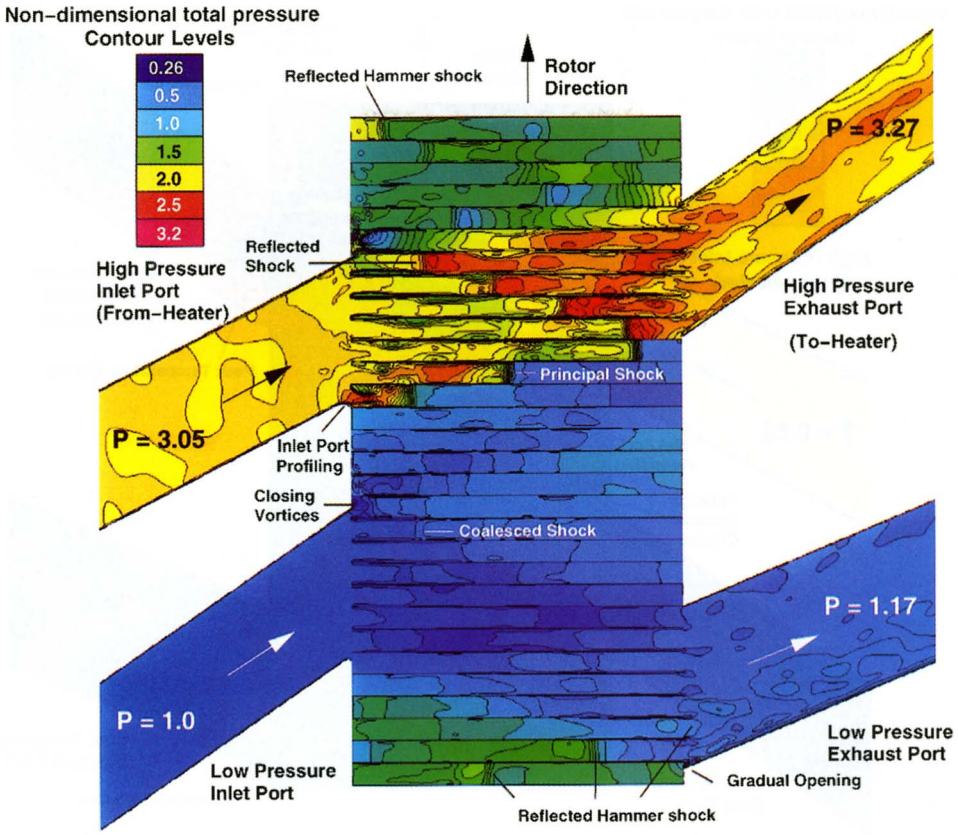

Fig. 6 Computed instantaneous total pressure contours and normalized mixed-out port pressures of planned four-port wave rotor experiment

abruptly at the rotor interface as a result of the sudden decrease in flow area caused by the 7.4 percent blade blockage.

Four-Port Wave Rotor Application

A simulation of the design-point operation of a planned four-port wave rotor experiment is discussed in this section. The four-port experiment calls for an external heater to add the energy that, in practice, is added in the burner of a gas turbine engine. The heater and four-port wave rotor combine to effect a Brayton cycle in which the rotor provides pressure gain (i.e., the exhaust port total pressure is higher than the inlet port total pressure) while producing zero net work by design. Only the wave rotor is modeled in the present work. The heat addition and heater pressure drop are implicit in the specified boundary conditions. Cycle timing and rotor dimensions were set by Paxson's (1995) one-dimensional code and the rotor optimization scheme described by Wilson and Paxson (1996). The wave rotor has one wave cycle per rotor and 30 passages per cycle. The rotor length is 10.5 in. (26.7 cm), the hub-to-tip ratio is 0.675, and the passage aspect (rotor length to blade-to-blade distance) ratio at the tip is 13.5. The rotor blade thickness is 8 percent of the blade-to-blade distance at midspan. The rotor tip speed is 367 ft/s (112 m/s) at 10,500 rpm. The design mass flow rate is 1.45 lb_m/s (0.658 kg/s) at an exhaust port total temperature to inlet port total temperature ratio of 2.0, with inlet port conditions of 400 R (222 K) and 1 atm (0.101 MPa).

Calculation. Each rotor passage is discretized by a 115 × 41 H-grid with spacing adjacent to the blades of 3.5×10^{-3} in. (8.9×10^{-3} cm). The grid is stretched in the tangential-direction to provide gradual transition to 2.5×10^{-2} in. (6.4×10^{-2} cm) cell spacing near the passage centerline. The inlet and outlet port flow fields are each solved on 85 × 151 sheared H-grids, except for the low-pressure exhaust port, which is solved on a 85 × 165 grid. The same 3.5×10^{-3} in. (8.9×10^{-3} cm) near-wall grid spacing is used. The port and rotor grids are also stretched in the axial direction to provide gradual transition between the 2.5×10^{-2} in. (6.4×10^{-2} cm) spacing at the port/rotor interfaces and the 0.1 in. (0.25 cm) spacing of the interior cells. The inlet port leading wall is rounded at the port/rotor interface. The high-pressure port has a rounding radius of 0.33 in. (0.84 cm) and the low-pressure inlet port has a rounding of 0.2 in. (0.51 cm). The inlet and outlet port angles are set using the mean axial velocities from the one-dimensional design code and the specified rotor speed. A Reynolds number of 0.8295×10^6/in. (0.3266×10^6/cm) is prescribed for the low-pressure inlet port reference conditions of 400 R (222 K) and 1 atm (0.101 MPa). The boundary conditions are also obtained from a one-dimensional design-point calculation, although in the course of the simulation the high-pressure (to-heater) exhaust port back pressure is adjusted to enforce equal mass flow rates in the low pressure ports. The two-dimensional calculation requires approximately a cpu-month on the Cray-YMP.

Flow Mechanics. An "unwrapped" view of the wave rotor solution is provided in Figs. 6 and 7, which show instantaneous total pressure and total temperature contours for the time-periodic (converged) solution. Time-averaged mixed-out port total properties are also noted. At the instant in time shown, the lowest passage is beginning to open to the low-pressure exhaust port where, in this discussion, "low-pressure" refers to the bottom two ports and "high-pressure" refers to the top two ports.

Low-Pressure Ports. The low-pressure port region serves to draw unheated, relatively cold air on-board the rotor from the inlet port and to expand and discharge high-pressure, high-temperature passage fluid to the exhaust port. As a passage gradually opens to the low-pressure exhaust port, an expansion

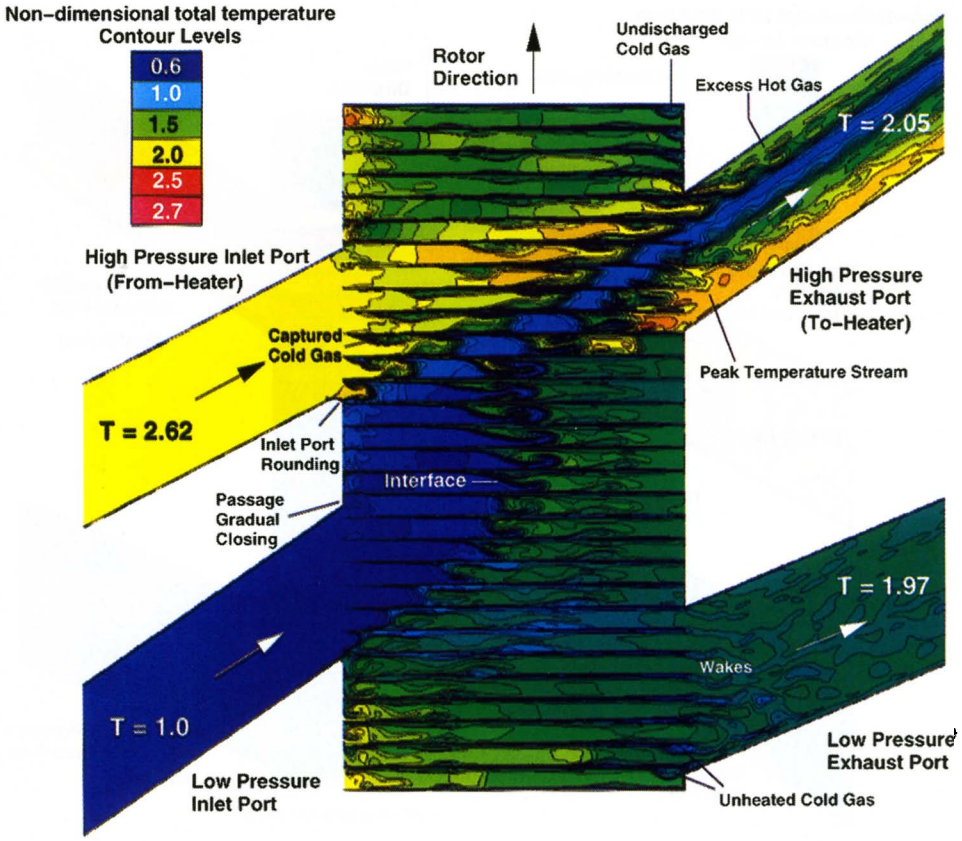

Fig. 7 Computed instantaneous total temperature contours and normalized mixed-out port temperatures of planned four-port wave rotor experiment

fan moves into the passage and reduces the on-board pressure as the passage content is discharged to the exhaust port. The principal fan traverses the passage, reflects off the inlet port side of the rotor, and returns to the exhaust port. This is evident in the low pressure of the preceding passages. The passages are timed to open to the inlet port flow just as the static pressure in the rotor passage at the rotor/passage interface equals the inlet port relative total pressure. The inlet port flow is drawn onto the rotor as the fan establishes a negative (axial and tangential) pressure gradient at the rotor/inlet port interface. Figure 7 shows that the interface between the cold inlet port flow and the hot exhaust port flow is skewed: The principal expansion wave/interface interaction is a Rayleigh–Taylor flow. A radial baroclinic torque is established (i.e., radial vorticity is deposited) along the interface, which is unstable to the acceleration established by the fan. The interface skews partly because of this baroclinic torque. The interface skewing is also likely affected by the velocity field induced by the vortices created as each passage gradually closes off to the high-pressure inlet port (see discussion below). As the right running once-reflected fan reaches the rotor/exhaust port interface, it reflects as left running compression waves off the (relatively uniform static pressure surface at the) rotor/exhaust port interface. As the fan reflects, the axial velocity at the rotor/exhaust port interface is reduced inversely with time (or tangential position), ideally to zero as the exhaust port ends. Nonuniformities caused by the fan, the rotor wakes, and the gradual opening of passages to the exhaust port lead to the (instantaneous) axial velocity profile shown in Fig. 8. The nonuniform velocity (or total pressure) profile effectively leads to mixing losses in the port. The compression waves generated by the twice-reflected expansion wave coalesce as they traverse the rotor back to the inlet port. Significant skewing of the cold/hot air interface occurs as the shock formed by the coalesced waves interacts with the interface. This Richtmeyer–Meshkov interaction results in vorticity deposition at the already distorted interface evidenced by the subsequent evolution of the interface. The inlet port ends (is "closed") as the coalesced shock in each passage reaches the rotor/inlet port interface. A pair of fairly strong counterrotating vortices is created as each passage gradually closes off from this port.

High-Pressure Ports. The high-pressure port region provides the main compression of the unheated air that enters the rotor in the low pressure inlet port. This gas, already slightly compressed by the coalesced shock wave of the low-pressure port region, is compressed another three to four times in the high-pressure port region. As a passage gradually opens to the

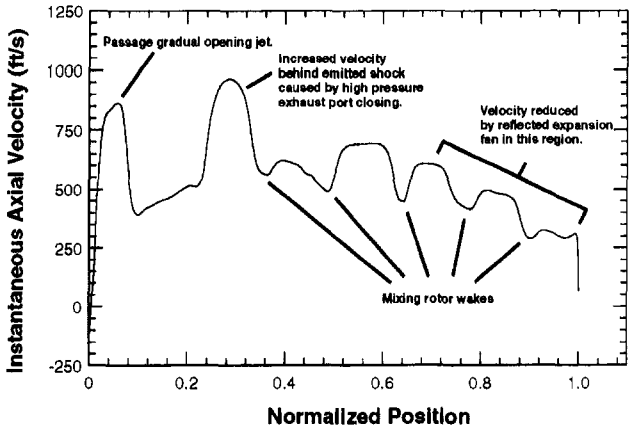

Fig. 8 Computed instantaneous axial velocity as a function of position in low-pressure exhaust port, one passage width from rotor face, showing features contributing to exhaust port nonuniformity

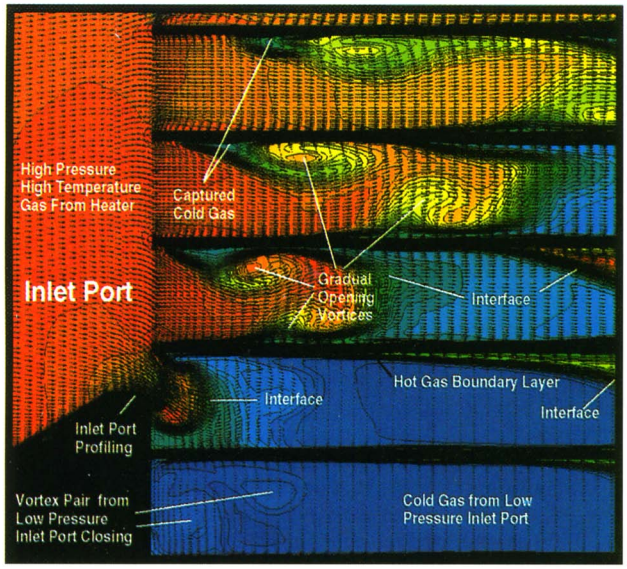

Fig. 9 Computed instantaneous static temperature contours and velocity vectors showing close-up view of passage gradual opening process and two-dimensional flow features contributing to redistribution of hot and cold gases

high-pressure inlet (from heater) port, compression waves—eventually steepening into a shock wave—move on-board, and compress and set into motion the on-board "driven" gas. This allows the incoming "driver" gas to enter the rotor passage. Simultaneously, an expansion wave moves into the port and reduces the total pressure and temperature of the incoming driver gas. Figure 9 shows a close-up view of instantaneous static temperature contours and velocity vectors during the passage charging process. The evolution of the hot driver gas/cold driven gas interface is influenced by the local relative velocity, which is effected by the inlet port rounding and blade profiling (after Keller, 1984, and see Welch, 1993). Note that a pocket of driven gas is captured by the driver gas due to incidence at the passage leading edge during opening. The principal shock traverses the rotor passage and reflects off the end-wall just as the high-pressure exhaust (to heater) port begins. The left-running reflected (lambda) shock interacts strongly with the boundary layer established by the principal shock. The principal shock interacts with the cold-gas/hot-gas interface established earlier as the cold gas entered the low-pressure inlet port. The reflected shock interacts with both this interface and the interface between the high-pressure driver gas and cold driven gas. These Richtmeyer–Meshkov interactions impact the vorticity along the interfaces. The cold driven gas and the hot gas that was not discharged during the low-pressure exhaust process, now compressed by both the principal and reflected shock waves, are discharged to the stratified exhaust port. The high-pressure inlet port ends as the reflected shock arrives back at the inlet port/rotor interface. As a passage gradually closes off from the inlet port, a pair of strong counterrotating vortices is created, and an expansion fan is initiated that eventually brings the passage flow to rest relative to the rotor. The fan traverses the passage and brings the axial velocity at the rotor/exhaust port interface to zero, and is reflected in a manner similar to the fan in the low pressure exhaust port. In the presented simulation, the axial velocity in fact does not quite reach zero; a weak hammer shock merges with the coalescing wave produced as the fan reflects off the exhaust port. This wave can be barely discerned in Fig. 6 as it traverses, and is emitted from, the rotor during the low-pressure exhaust port discharge process (as noted in Fig. 8).

Impact of Two-Dimensional Effects. The flow discharged to the heater is highly stratified (see Fig. 7), composed of both the cold air originally from the low-pressure inlet port and the hot air not discharged in the low-pressure exhaust process. In a gas turbine engine application, the hot air (exhaust gas recirculation) is previously burned. This hot gas is twice-compressed and is the hottest fluid in machine. Its entropy is that of the burner exhaust gas, plus that produced in the low-pressure port region, plus that produced during recompression by the principal and reflected shocks back up to the peak cycle (to-heater) pressure. The two-dimensional total temperature contours of Fig. 7 illustrate that the particular (throughflow) four-port cycle simulated here creates high wall temperatures in the high-pressure exhaust port.

Figure 7 shows that hot driver gas coats the trailing end of the high pressure exhaust port: More hot gas is discharged to the heater than anticipated by the one-dimensional design analysis. At the same time, the captured cold (driven) air, which by design was to be exhausted to the heater, remains on board the rotor and is discharged instead to the low-pressure exhaust port. Exhaust port temperature nonuniformity is thus increased and less fresh air is discharged to the heater (burner) than intended. This redistribution (capturing) of cold and hot air is caused by the asymmetric gradual opening of passages to the high-pressure inlet port and the subsequent evolution of the interface between the hot driver (from heater) gas and cold driven gas. The redistribution accounts for a discrepancy between the actual 1.97 temperature ratio effected by the specified boundary conditions and the 2.0 temperature ratio effected by the same boundary conditions in the one-dimensional design code. Figures 6 and 7 show that the low-pressure exhaust port is nonuniform in both total temperature and total pressure, in part due to this redistribution. Further, the trailing wall of the high-pressure exhaust port is washed by hot fluid rather than cold, leading to higher duct wall thermal loads than projected by the initial one-dimensional design.

In addition to redistribution caused by the passage gradual opening process, redistribution of cold and hot gas occurs by interface skewing (discussed earlier) and by boundary layer dynamics; the latter leads to an inversion in the expected rotor blade (adiabatic) temperature profile. Figure 10 shows that the time-averaged free-stream (passage centerline) gas temperature is lower on the inlet end of the wave rotor than on the outlet end. This is expected because cold flow enters, and spends the greatest fraction of the cycle time, on the inlet end of the rotor. Strictly one-dimensional analysis will suggest that the wall temperature distribution qualitatively follows the mean free-stream

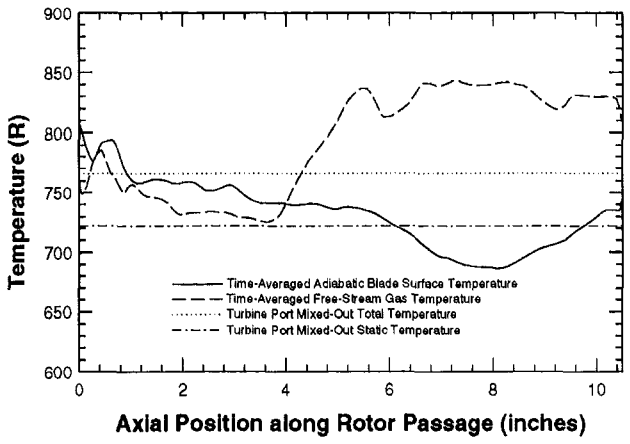

Fig. 10 Comparison of computed axial distributions of time-averaged passage free-stream temperature and rotor blade surface temperature for planned NASA Lewis Research Center four-port wave rotor experiment at design point

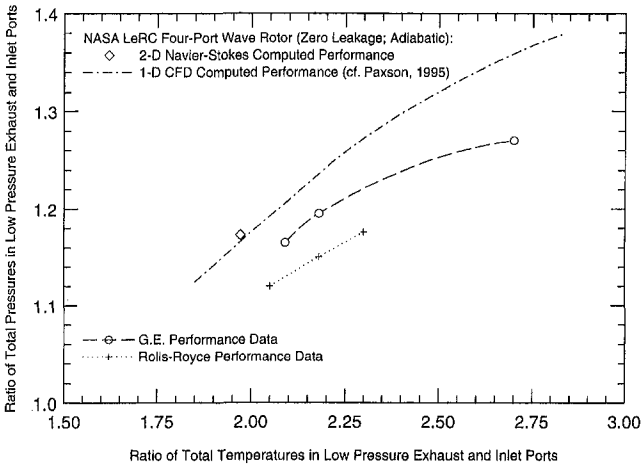

Fig. 11 Comparison of computed performance of planned NASA Lewis Research Center four-port wave rotor with G. E. experimental data (reported by Mathur, 1985) and Rolls-Royce experimental data (reported by Moritz, 1985)

temperature; however, the predicted mean adiabatic wall temperature distribution of this work suggests that the wall temperature is higher on the inlet end of the rotor than the outlet end, and that the wall temperature gradient is reduced in magnitude from that of the free stream. The time-averaged adiabatic wall temperature—i.e., the time-averaged temperature of the boundary layer fluid adjacent to the wall—reflects the time-dependent boundary layer temperature distribution rather than the free-stream temperature distribution. Indeed, the entering cold flow moves over the hot boundary layer fluid attached to the rotor rather than displacing it as assumed in one-dimensional analysis. Similarly, at the discharge end of the rotor, some of the cold fluid remains in the boundary layers rather than being discharged to the high-pressure exhaust port (heater). As a result, the mean rotor adiabatic wall temperature is lower than the mean free-stream temperature: The mean time-averaged free-stream temperature is near the averaged low-pressure exhaust port total temperature whereas the mean time-averaged wall temperature is more like the colder exhaust port mixed-out static temperature. There is a hot spot at the inlet end of the rotor. The rotor wall temperature distribution will in general affect rotor design through thermal growth, stress, and (in some applications) rotor cooling considerations.

Machine Performance Levels. Wave rotor performance levels are compared in Fig. 11 in terms of the ratio of the low-pressure exhaust and inlet port mixed-out total pressures versus the ratio of total temperatures in the same ports as predicted by the present work and by the one-dimensional design/analysis code (Paxson, 1995). The one and two-dimensional model results agree surprisingly well at the design-point operating condition considered in this work. The two-dimensional simulation accounts for entropy production in shock/boundary-layer interactions and rotor wakes, which is not accounted for in the one-dimensional simulation; on the other hand, by using a suitable hydraulic diameter, the one-dimensional simulation accounts for entropy production in the rotor hub and tip-shroud boundary layers (i.e., rotor end-wall flows), which is not accounted for in the two-dimensional calculation carried out at midspan. Evidently these modeling differences very nearly offset one another. Performance data from the General Electric (cf. Mathur, 1985) and Rolls-Royce (cf. Moritz, 1985) pressure-exchanger experiments are also provided in Fig. 11 to provide a context in which to assess the predicted adiabatic zero-leakage performance of the planned four-port experiment.

Summary

A two-dimensional (θ, z), thin-layer Navier–Stokes solver developed to simulate unsteady, two-dimensional flow in the stator/rotor/stator geometry of multiport wave rotors was described. Good agreement between computed results and three-port wave rotor experimental measurements was shown. The model was used to predict the design-point performance level of a planned four-port wave rotor experiment. The predicted performance agrees well with that predicted by the one-dimensional code used to design the experiment. Important two-dimensional flow features were identified: skewing of the interface between hot and cold gases is caused by unstable Rayleigh–Taylor flows established by shock/contact (Richtmeyer–Meshkov) and expansion fan/contact interactions; vortices are created during passage gradual opening and closing processes and can influence the evolution of the cold gas/hot gas interfaces; separating flows due to rotor wakes and (lambda) shock/boundary layer interactions contribute to entropy production (i.e., loss). Interface skewing, boundary layer flow dynamics, and passage gradual opening lead to the redistribution of hot and cold gas within the wave rotor passages in ways not accounted for by one-dimensional codes. The two-dimensional redistribution of hot and cold gas in the rotor impacts rotor blade and duct wall thermal loads. The impact of redistribution of hot and cold gas can be reduced by minimizing the relative amount of cold driven gas "captured" behind the hot driver gas during passage charging process in the high-pressure port; this suggests increasing the rotor passage aspect ratio beyond the optimum determined by one-dimensional design analysis.

Acknowledgments

Parts of this work were done while the author held a National Research Council-NASA LeRC Research Associateship. The author is grateful for the generous encouragement and technical support offered during the course of this work by NASA LeRC Turbomachinery Technology branch members Dr. Lawrence J. Bober, Dr. Rodrick V. Chima, and Dr. Jack Wilson (NYMA, Inc.) and System Dynamics branch member Dr. Daniel E. Paxson.

References

Anderson, W. K., Thomas, J. L., and van Leer, B., 1986, "Comparison of Finite Volume Flux Vector Splittings for the Euler Equations," *AIAA J.*, Vol. 24, No. 9, Sept., pp. 1453–1460.

Azoury, P. H., 1965–66, "An Introduction to the Dynamic Pressure Exchanger," *Proc. Inst. Mech. Eng.*, Vol. 180, Part 1, pp. 451–480.

Baldwin, B. S., and Lomax, H., 1978, "Thin-Layer Approximation and Algebraic Model for Separated Turbulent Flows," Paper No. AIAA-78-257.

Burri, H. U., 1958, "Non-steady Aerodynamics for the Comprex Supercharger," ASME Paper No. 58-GTP-15.

Chima, R. V., 1987, "Explicit Multigrid Algorithm for Quasi-Three-Dimensional Viscous Flows in Turbomachinery," *J. of Propulsion and Power*, Vol. 3, No. 5, Sept.–Oct., pp. 397–405.

Eidelman, S., 1985, "The Problem of Gradual Opening in Wave Rotor Passages," *J. Propulsion and Power*, Vol. 1, No. 1, Jan.–Feb., pp. 22–28.

Grossman, B., and Walters, R. W., 1989, "Flux-Split Algorithms for the Multidimensional Euler Equations With Real Gases," *Computers and Fluids*, Vol. 17, No. 1, pp. 99–112.

Harten, A., and Hyman, J. M., 1983, "Self Adjusting Grid Methods for One-Dimensional Hyperbolic Conservation Laws," *J. Comp. Phys.*, Vol. 50, pp. 235–269.

Hong-De, J., 1983, "Two-Dimensional Unsteady Flow in Comprex Rotor," *Proc. 1983 Tokyo International Gas Turbine Congress*, Oct., pp. 463–470.

Jameson, A., Schmidt, W., and Turkel, E., 1981, "Numerical Solutions of the Euler Equations by Finite Volume Methods Using Runge-Kutta Time-Stepping," Paper No. AIAA-81-1259.

Keller, J. J., 1984, "Some Fundamentals of the Supercharger Comprex," in: Sladky, 1984, pp. 47–54.

Kentfield, J. A. C., 1969, "The Performance of Pressure-Exchanger Dividers and Equalizers," ASME *J. Basic Engineering*, Sept., pp. 361–370.

Larosiliere, L. M., 1995, "Wave Rotor Charging Process: Effects of Gradual Opening and Rotation," *J. Propulsion and Power*, Vol. 11, No. 1, Jan.–Feb., pp. 178–184.

Lear, W. E., Jr., and Candler, G., 1993, "Analysis of the Accuracy of Wave Rotor Boundary Conditions Using a Novel Computational Method," Paper No. AIAA-93-2524.

Mathur, A., 1985, "A Brief Review of G.E. Wave Engine Program (1958–1963)," in: Shreeve and Mathur, 1985, pp. 171–193.

Moritz, R., 1985, "Rolls-Royce Study of Wave Rotors 1965–1970," in: Shreeve and Mathur, 1985, pp. 116–124.

Paxson, D. E., 1993, "An Improved Numerical Model for Wave Rotor Design and Analysis," AIAA-93-0482; also NASA TM-105915.

Paxson, D. E., 1995, "Comparison Between Numerically Modeled and Experimentally Measured Wave-Rotor Loss Mechanisms," *J. Propulsion and Power,* Vol. 11, No. 5, Sept.–Oct., pp. 908–914; also NASA TM-106279.

Roe, P. L., 1981, "Approximate Riemann Solvers, Parameter Vectors, and Difference Schemes," *J. Comp. Phys.,* Vol. 43, pp. 357–372.

Rose, P. H., 1979, "Potential Applications of Wave Machinery to Energy and Chemical Processes," Lifshitz, A., and Rom, J., eds., *Shock Tubes and Wave, Proc. 12th Int. Symposium on Shock Tubes and Waves,* The Magnes Press, Jerusalem, Israel, July, pp. 3–30.

Shreeve, R. P., and Mathur, A., eds., 1985, *Proc. 1985 ONR/NAVAIR Wave Rotor Research and Technology Workshop,* Report NPS-67-85-008, Naval Postgraduate School, Monterey, CA, May.

Sladky, J. F., Jr., ed., 1984, *Machinery for Direct Fluid-Fluid Energy Exchange,* AD-07, Winter Annual Meeting of The ASME, New Orleans, LA, Dec. 9–14.

Sturtevant, B., 1987, "Rayleigh–Taylor Instability in Compressible Fluids," Gronig, H., ed., *Shock Tubes and Waves, Proc. of the Sixteenth Int. Symp. on Shock Tubes and Waves,* Achen, West Germany, July, VCH, Federal Republic of Germany, pp. 89–100.

Taussig, R. T., 1984, "Wave Rotor Turbofan Engines for Aircraft," in: Sladky, 1984, pp. 9–45; also see *Mech. Engineering,* Nov., 1984, pp. 60–66.

Taussig, R. T., and Hertzberg, A., 1984, "Wave Rotors for Turbomachinery," in: Sladky, 1984, pp. 1–7.

Thayer, W. J., III, Vaidyanathan, T. S., and Zumdieck, J. F., 1980, "Measurements and Modeling of Energy Exchanger Flow," *Proc. Intersociety Energy Conversion Engineering Conference,* Vol. 3, Aug., pp. 2368–2379.

van Leer, B., 1979, "Towards the Ultimate Conservative Difference Scheme. V. A Second-Order Sequel to Godunov's Method," *J. Comp. Phys.,* Vol. 32, pp. 101–136.

Walters, R. W., and Thomas, J. L., 1989, "Advances in Upwind Relaxation Methods," Noor, A. K. and Oden, J. T., eds., *State-of-the-Art Surveys on Computational Mechanics,* The American Society of Mechanical Engineers, New York, U.S.A., pp. 145–183.

Welch, G. E., 1993, "Two-Dimensional Numerical Study of Wave Rotor Flow Dynamics," Paper No. AIAA-93-2525.

Welch, G. E., and Chima, R. V., 1993, "Two-Dimensional CFD Modeling of Wave Rotor Flow Dynamics," *Proc. 11th Computational Fluid Dynamics Conference,* Part 1, AIAA-93-3318-CP, July, pp. 234–247; also NASA TM-106261.

Welch, G. E., 1997, "Macroscopic Balance Model for Wave Rotors," *J. Propulsion and Power,* Vol. 13, No. 4, July–Aug., pp. 508–516.

Welch, G. E., Jones, S. M., and Paxson, D. E., 1997, "Wave-Rotor-Enhanced Gas Turbine Engine," ASME JOURNAL OF ENGINEERING FOR GAS TURBINES AND POWER, Vol. 119, pp. 469–477.

Wen, W., and Mingzheng, C., 1982, "Some Result [sic] of Theoretical Analysis, Calculation and Experimental Research of Pressure Wave Supercharger," *J. Engineering Thermophysics,* Vol. 3, No. 1, Feb., pp. 33–38.

Wilson, J., and Fronek, D., 1993, "Initial Results from the NASA Lewis Wave Rotor Experiment," Paper No. AIAA-93-2521; also NASA TM-106148.

Wilson, J., and Paxson, D. E., 1996, "Optimization of Wave Rotors for Use as Gas Turbine Engine Topping Cycles," *J. Propulsion and Power,* Vol. 12, No. 4, July–Aug., pp. 778–785.

Zauner, E., Chyou, Y.-P., Walraven, F., and Althaus, R., 1993, "Gas Turbine Topping Stage Based on Energy Exchangers: Process and Performance," ASME Paper No. 93-GT-58.

Zehnder, G., 1971, "Calculating Gas Flow in Pressure-Wave Machines," *Brown-Broveri Review,* Rev. 4/5, pp. 172–176.

Zhang, H. S., and So. R. M. C., 1990, "Calculation of the Material Interface in a Pressure-Wave Supercharger," *Proc. Inst. Mech. Eng., Part A: J. of Power and Energy,* Vol. 204, No. A1, pp. 151–161.